University of Colorado, Boulder
CU Scholar

Aerospace Engineering Sciences Graduate Theses & Dissertations

Aerospace Engineering Sciences

Spring 1-1-2019

Level-Set-XFEM-Density Topology Optimization of Active Structures: Methods and Applications

Markus Josef Geiss
University of Colorado at Boulder, Markus.Geiss@Colorado.edu

Follow this and additional works at: https://scholar.colorado.edu/asen_gradetds

Part of the Aerospace Engineering Commons, Applied Mechanics Commons, and the Computer Sciences Commons

Level-Set-XFEM-Density Topology Optimization of Active Structures: Methods and Applications

by

Markus Josef Geiss

M.Sc. Aerospace Engineering, University of Colorado Boulder, 2016

B.Eng. Mechatronics Engineering, University of Applied Sciences Munich,

Germany, 2014

A thesis submitted to the

Faculty of the Graduate School of the

University of Colorado in partial fulfillment

of the requirements for the degree of

Doctor of Philosophy

Ann and H.J. Smead Department of Aerospace Engineering Sciences

2019

This thesis entitled:
Level-Set-XFEM-Density Topology Optimization of Active Structures: Methods and Applications
written by Markus Josef Geiss
has been approved for the Ann and H.J. Smead Department of Aerospace Engineering Sciences

_____

Prof. Kurt Maute

_____

Prof. Carlos Felippa

Date _____

The final copy of this thesis has been examined by the signatories, and we find that both the content and the form meet acceptable presentation standards of scholarly work in the above mentioned discipline.

Geiss, Markus Josef (Ph.D., Aerospace Engineering)

Level-Set-XFEM-Density Topology Optimization of Active Structures: Methods and Applications

Thesis directed by Prof. Kurt Maute

Abstract

To unlock the potential of advanced manufacturing technologies like additive manufacturing, an inherent need for sophisticated design tools exists. In this thesis, a systematic approach for designing printed active structures using a combined level-set (LS) extended finite element (XFEM) density topology optimization (TO) scheme is developed. This combined scheme alleviates the downsides of both LS and density based TO approaches while building upon the advantages of either method. Thus, a superior design optimization approach is created, which, when coupled with the XFEM, yields a highly accurate physical modeling method. The unique capabilities of this combined approach include hole nucleation and minimum feature size control while retaining a crisp and unambiguous definition of the material interface. Different stabilization and regularization schemes are developed to maximize the robustness of the proposed method. Ensuring sufficient numerical stability during the TO process is especially critical when using large deformation nonlinear elasticity models. Without sufficient stabilization, divergence in the analysis or optimization process is frequently encountered. Therefore, a novel explicit LS regularization scheme, based on the construction of a signed distance field (SDF) for every design iteration, is developed in this thesis. It is also demonstrated that the obtained SDF can be used for minimum feature size control and control of the mean curvature during a TO process. Numerical design examples in 2D and 3D are presented to demonstrate the applicability of the proposed combined TO method. Physical specimens of 4D printed samples are used to validate the accuracy of the predicted structural performance by the developed thermomechanical large-strain XFEM model. Finally, conclusions and recommendations for future work are presented and the original contributions made in this thesis are summarized.

Kurzfassung

Von Natur aus existiert ein Bedürfnis nach fortgeschrittenen Konstruktionsverfahren, um das volle Potential von zukunftsweisenden Fertigungstechnologien zu erschließen. Nicht nur deshalb wird in dieser Dissertation eine systematische Herangehensweise zur Auslegung von aktiven Strukturen anhand einer kombinierten Level-Set (LS) Extended Finite Element (XFEM) Dichte Topologieoptimierungs (TO) Methode präsentiert. Diese kombinierte Methode reduziert die Nachteile der jeweilig einzelnen TO Verfahren und verbindet gleichzeitig die Vorteile von LS und Dichte Methoden. Dadurch entsteht ein übergeordnetes TO Verfahren, welches in Kombination mit der XFEM ein hochgenaues physikalisches Modellierungsverfahren liefert. Die Alleinstellungsmerkmale dieses Designoptimierungsverfahrens beinhalten die Entstehung von Leerstellen, ein Kontrollmechanismus über kleinstmögliche Kenngrößen, und eine klare und eindeutige Definition der Materialgrenzflächen. Dabei werden verschiedene Stabilisierungs- und Regularisierungsmaßnahmen diskutiert, um die Robustheit der neu entwickelten TO Methode zu maximieren. Hierbei muss vor allem ausreichend numerische Stabilität gegeben sein, wenn große Verschiebungen und nichtlineare Phänomene während eines TO Vorgangs in Betracht gezogen werden. Ohne eine ausreichende Stabilisierung tritt häufig Divergenz während der Analyse oder des Optimierungsprozesses auf. Deshalb wird in dieser Arbeit ein neuartiges Regularisierungsverfahren für explizite LS TO, basierend auf der Konstruktion einer Signierten Distanz Funktion (SDF), entwickelt und getestet. Außerdem kann die SDF zur Kontrolle der kleinstmöglichen Kenngröße und der mittleren Krümmung der Materialgrenzfläche während eines TO Prozesses eingesetzt werden. Numerische Designbeispiele in 2D und 3D werden präsentiert, um die Anwendbarkeit der vorgeschlagenen kombinierten TO Methode zu demonstrieren. Die Gültigkeit und Genauigkeit des entwickelten thermomechanischen Modells unter großen Verschiebungen werden anhand von 4D gedruckten Teststrukturen validiert. Zum Abschluss der Arbeit werden ein Fazit gezogen und Empfehlungen für zukünftige Studien angeführt. Schlussendlich wird eine Zusammenfassung der ursprünglichen Beiträge dieser Dissertation präsentiert.

Dedication

To Marion,

Christine and Josef

Acknowledgements

First and foremost I would like to thank my thesis advisor Prof. Kurt Maute for his endless patience, support and ideas that lead to this dissertation over the past four-and-a-half years. Moreover, I would like to thank my committee members Prof. Carlos Felippa, Prof. Alireza Doostan, Prof. John Evans, and Prof. Richard Reguerio for their time and valuable feedback on my work. Furthermore, I want to acknowledge Prof. Martin Dunn, Prof. Oliver Weeger, and Dr. Narasimha Boddeti for their guidance and expertise during my time at the Singapore University of Technology and Design (SUTD) in 2017. I would also like to thank the German Academic Scholarship Foundation (Studienstiftung des deutschen Volkes) and the German Federal Ministry for Economic Affairs and Energy (Bundesministerium für Wirtschaft und Energie) for partial support of this work.

For their help and advice in support of my research, I would like to thank my fellow graduate students. In particular, I would like to thank my former office mate Jorge Luis Barrera Cruz for many fruitful discussions and his constructive feedback on my research. In addition, I would like to thank my friends and family for their motivation and patience throughout the course of my graduate studies. Finally, I express my deepest gratitude to my wife Marion and our son Maximilian without whom I could not have completed this work.

Contents

Figures

Chapter 1

Introduction

With the advent of novel manufacturing technologies like additive manufacturing (AM), unprecedented design freedom is unlocked across various fields of engineering. Through the use of multi-material 3D printing, active structural components can be manufactured with increased accuracy. This is achieved by placing materials with different thermal, mechanical and "active" properties on a build-tray with an accuracy in the order of tens of microns. The shape-changing property of the structure is inherently built-in through the AM process and can be triggered by an external stimulus like light, mechanical load, thermal load or a change in radiation conditions. The concept of a 3D printed structure undergoing a subsequent shape change was introduced by [184] and named "4D printing", where time is seen as the fourth dimension. To date, this concept has been used for designing shape-changing shape memory polymer (SMP) structures [65] and active origami structures [64]. Building upon the shape-memory effect of 3D printed polymers, [125] proposed a design methodology for SMPs using topology optimization (TO) combined with a small strain linear elastic SMP model. More recently, [45] developed a direct 4D printing approach where a built-in "printing" strain is responsible for the shape change, alleviating the need for a complex training and activation cycle as required by classical SMPs. In essence, direct 4D printing hinges on the fact that multiple materials with a tunable inelastic printing strain can be combined through multi-material 3D printing, yielding an active structure upon activation. Direct 4D printing was used by [199] and [44] for designing shape-changing 1D rod structures where the initial design

layout, yielding a desired target shape, could be determined by intuition.

Exploring more complex designs, density-based TO with a small strain linear elastic mechanical model has been applied by [61] for designing shape-changing liquid crystal elastomer structures. To determine optimal folding lines of technical origami, a commonly used approach is the ground structure approach as studied by [31], [59], [58] and [62]. While it reduces the number of design variables and thus simplifies the design problem, only a subset of all possible designs is explored. Similarly, [105] used a simplified TO approach for the determination of optimal crease patterns of self-folding origami and kirigami structures. Just recently, [205] used the concept of moving morphable components (MMC) to optimize cut patterns of post-buckled 3D kirigami structures.

Especially in the field of aerospace engineering, the advantages provided by 3D and 4D printing are just starting to be exploited. Traditionally, deployable structures have been actuated mechanically or electrically; however, the use of active structures or structural components to replace classical hinges is promising. This is especially true for remote applications like space telescopes or satellites, where high reliability of the deployment mechanism is required to guarantee mission success. Moreover, active structures can be used in applications where a small volume is desired during transportation (e.g., launch) but a large surface area is required in the deployed state (e.g., space antennas, drag sails).

The goal of this thesis is to combine state of the art simulation and optimization techniques for developing a systematic design and analysis framework for active structures. This is achieved through a hybrid formulation between density-based and level-set (LS)- based TO approaches in combination with the extended finite element (XFEM) method. More details on the goals of this thesis and the approaches taken to achieve them are provided in the following section.

1.1 Goals and Approach

While 3D printing and, more recently, 4D printing are becoming established fabrication technologies, systematic design approaches utilizing the vast design freedom are widely missing. To address this issue, various simulation schemes have been proposed in literature. One commonality to all those simulation approaches is the fact that they only focus on a subset of all feasible designs due to the simplifications made either in the analysis method or the optimization scheme used. The overarching goal of this thesis is therefore:

The Development of a systematic Design Approach for Active Structures
using combined LS-XFEM-Density Topology Optimization.

To achieve this, various aspects of computational modeling and design optimization are expanded in terms of accuracy, robustness and applicability. In addition, a large deformation XFEM simulation framework is developed for nonlinear thermoelastic structures. This is a key aspect for simulating shape-changing structures which undergo large deformations and rotations. Using the XFEM versus classical FEM provides advantages in terms of design freedom and modeling accuracy during TO. The geometry description of the XFEM is naturally suited for 3D printing without the need for post-processing. In order to accurately capture the physical response of active structures which are oftentimes slender in shape, a higher-order XFEM scheme is used. To take advantage of the benefits of both density-based and LS-based TO approaches, various combined TO schemes are developed and applied in this thesis. Classically, both methods have been used by their respective research communities where the drawbacks as well as the benefits of either method have been studied extensively. Comprehensive reviews of both density-based and LS-based TO approaches are provided in [188, 168, 43]. However, the combination of them has been largely unexplored to date. In this thesis, complementary features of density-based and LS-based TO approaches are identified and a superior TO approach building on the strengths of either method, while eliminating their respective weaknesses, is developed. Moreover, to improve the stability of LS-based TO, an explicit LS regularization scheme based on a signed distance function (SDF) is developed and applied to

various optimization problems in 2D and 3D. This approach is further extended to minimum feature size control via the skeleton method [78] and a scheme to control the mean curvature of optimized structures using LS-XFEM TO is derived. Finally, a combined LS-XFEM-density approach is used for solving multi-material TO problems to design active structures undergoing small and large deformation. The obtained designs are 4D printed and activated to demonstrate the applicability of the developed design approach for solving real-world design optimization problems in a structured and systematic manner.

1.2   Thesis Organization

The remainder of this thesis is structured as follows: The physics models relevant for this thesis are introduced in Chapter 2. Chapter 3 discusses relevant computational approaches, namely the XFEM, higher-order XFEM and the enhanced assumed strain (EAS) method. The aim of Chapter 4 is to discuss design optimization, with a special focus on TO. After a review of density-based and LS-based TO approaches, different combined LS-density TO schemes are proposed. In addition, stability considerations are discussed and an explicit LS regularization scheme is introduced. After that, a discussion on minimum feature size control as well as mean curvature control follows. A brief introduction to design sensitivity analysis and to the formulation of an end-stiffness constraint relevant for 4D printed active structures is given. The aim of Chapter 5 is to demonstrate the applicability of the developed optimization methods for solving TO problems. This is achieved through numerical studies and examples in 2D and 3D. First, the developed large strain thermoelastic XFEM model is validated before a combined LS-density approach is used for TO of active structures. Different features of the proposed combined LS-density approach are studied to demonstrate the superiority of the novel TO scheme. Finally, the explicit LS regularization scheme, minimum feature size control and the mean curvature control are applied to numerical examples. Conclusions and future work are presented in Chapter 6. The original contributions made in this thesis are summarized in Chapter 7 and publications leading up to this thesis are included in Appendices B - D for completeness.

Chapter 2

Physics Models

The physics models relevant for this thesis are summarized in this chapter. These include transient heat conduction, (static) linear elasticity and (static) nonlinear hyperelasticity in a total Lagrangian setting.

All problems considered in this section are boundary value problems (BVP) defined over a volumetric and boundary domain, Ω_0 and Γ_0, respectively. The domain boundary is further divided into a Dirichlet (essential) boundary Γ_D and a Neumann (natural) boundary Γ_N such that $\Gamma_D \cup \Gamma_N = \Gamma_0 = \partial \Omega_0$.

Graphically, this is illustrated in Figure 2.1. Prescribed Dirichlet and Neumann boundary conditions for a general (scalar- or vector-valued) state variable φ are denoted with $\bar{\varphi}_D$ and $\bar{\vartheta}_N$, respectively. The unit normal on the Neumann boundary is denoted with $\mathbf{N}$, and $\mathbf{B}$ is a generic volumetric load. Following the notation of [86], quantities in the undeformed (reference) configuration are denoted by a capital letter (e.g., $\mathbf{N}$) or a subscript 0 (e.g., Ω_0). Consequently, quantities in the deformed (current) configuration are denoted by lower case letters (e.g., $\mathbf{n}$) or have no subscript (e.g., Ω). More details regarding different configurations are discussed in Section 2.3 and illustrated in Figure 2.2.
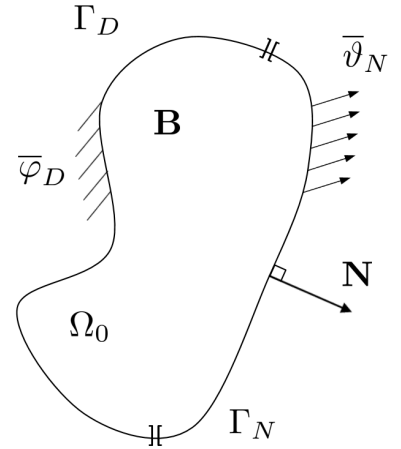
Figure 2.1: General BVP domain decomposition.

2.1   Transient Heat Conduction

To model the diffusive process of a temperature field in space and time, the transient linear parabolic heat partial differential equation (PDE) is solved. Referring back to the general description of a BVP introduced in Figure 2.1, the temperature state variables are denoted by $\varphi = \theta$. In Cartesian coordinates, the strong form of the problem is:

Find $\theta(\mathbf{X}) : \bar{\Omega} \to \mathbb{R}$, such that

$$\rho c_p \dot{\theta} + \nabla \cdot (-\kappa \nabla \theta) = 0 \qquad \text{in} \quad \Omega_0$$
$$\theta = \bar{\theta}_D \quad \text{on} \quad \Gamma_D \tag{2.1.1}$$
$$(-\kappa \nabla \theta)\mathbf{N} = \bar{q}_N \quad \text{on} \quad \Gamma_N$$

where ρ is the physical density, c_p is the specific heat capacity and κ is the thermal conductivity. The prescribed Dirichlet and Neumann boundary conditions are denoted by $\bar{\theta}_D$ and $\bar{q}_N = \bar{\vartheta}_N$, respectively. The time derivative of the temperature state variable is denoted by $\dot{\theta} = \partial\theta/\partial t$. In this thesis, a semi-discrete formulation (i.e., first discretization in space to then solve in time) is used. The time derivative at the current time step $q + 1$ is obtained using an implicit Euler backward scheme as:

$$\dot{\theta}^{q+1} = \frac{\theta^{q+1} - \theta^q}{\Delta t} \tag{2.1.2}$$

where θ^q is the temperature at the previous time step q and Δt is the time step size.

Multiplying the strong form of the governing equation stated in Eqn.(2.1.1) with an arbitrary test (weighting) function $\delta\theta$, performing integration by parts and applying the divergence theorem yields the weak form of the governing equation. It is stated as:

Find $\theta(\mathbf{X}) \in \mathcal{S}$, such that

$$\int_{\Omega_0} \rho \, c_p \, \delta\theta \, \dot{\theta} \, dV + \int_{\Omega_0} \delta\nabla\theta(\kappa \, \nabla\theta) \, dV = \int_{\Gamma_N} \delta\theta(k \, \nabla\theta) \, \mathbf{N} \, dA \quad \forall \quad \delta\theta \in \mathcal{V} \tag{2.1.3}$$

where $\mathcal{S}$ denotes the scalar-valued trail solution space defined as $\mathcal{S} = \{\theta(\mathbf{X}) : \bar{\Omega} \to \mathbb{R}; \ \theta = \theta_D \text{ on } \Gamma_D\}$. The scalar-valued weighting function space is defined as $\mathcal{V} = \{\delta\theta(\mathbf{X}) : \bar{\Omega} \to \mathbb{R}; \ \delta\theta = 0 \text{ on } \Gamma_D\}$.

This classical weak form is augmented by additional terms to enable weak enforcement of Dirichlet boundary conditions using Nitsche's method [136]. A more detailed discussion of weak enforcement of boundary conditions is presented in Section 3.1.2, along with the spatial discretization used in this work.

2.2 Small Strain Elasticity

Cauchy's first equation of motion is the governing equation for linear elasticity [86]. Assuming accelerations to be zero, Cauchy's equation of equilibrium for elastostatics is:

$$\nabla \cdot \boldsymbol{\sigma} + \mathbf{B} = \mathbf{0} \tag{2.2.1}$$

where $\boldsymbol{\sigma}$ is the Cauchy stress tensor and $\mathbf{B}$ is a body force vector. It should be noted that in linear elastic small strain theory, no distinction is made between reference (Ω_0) and current configuration (Ω) as deformations and rotations are assumed to be infinitesimal (i.e., $\Omega_0 \equiv \Omega$). Therefore, the choice of stress measure is arbitrary. Most commonly, the Cauchy stress tensor, also called true stress tensor, is used. This stress tensor is symmetric (i.e., $\boldsymbol{\sigma} = \boldsymbol{\sigma}^T$) in the absence of body moments, satisfying the conservation of angular momentum in a solid [23]. The strong form of the linear elastic BVP for the vector valued state variables (i.e., displacements) $\varphi = \mathbf{u}$ can be formulated as:

Find $\mathbf{u}(\mathbf{X}) : \bar{\Omega} \to \mathbb{R}^d$, such that

$$
\begin{aligned}
\nabla \cdot \boldsymbol{\sigma} + \mathbf{B} &= \mathbf{0} && \text{in} \quad \Omega_0 \\
\mathbf{u} &= \bar{\mathbf{u}}_D && \text{on} \quad \Gamma_D \\
\boldsymbol{\sigma}\mathbf{N} &= \bar{\mathbf{T}} && \text{on} \quad \Gamma_N
\end{aligned}
\tag{2.2.2}
$$

where the prescribed traction is $\bar{\mathbf{T}} = \bar{\vartheta}_N$ for consistency with Figure 2.1. The Helmholtz free energy function $\Psi(\boldsymbol{\epsilon}_M)$ for linear elastic materials is defined as [23]:

$$\Psi(\boldsymbol{\epsilon}_M) = \frac{1}{2}\boldsymbol{\epsilon}_M \ \boldsymbol{D} \ \boldsymbol{\epsilon}_M \tag{2.2.3}$$

where $\boldsymbol{D}$ denotes the fourth-order material tensor. When considering small strain thermoelasticity, the mechanical small strain tensor $\boldsymbol{\epsilon}_M$ is defined as:

$$\boldsymbol{\epsilon}_M = \boldsymbol{\epsilon} - \boldsymbol{\epsilon}_\theta \tag{2.2.4}$$

as a function of the infinitesimal strain tensor $\boldsymbol{\epsilon} = 1/2(\nabla \mathbf{u}^T + \nabla \mathbf{u})$ and the thermal strain tensor $\boldsymbol{\epsilon}_\theta$. It should be noted, that the thermal strain is also referred to as inelastic eigenstrain in this thesis. The thermal strain tensor is defined as:

$$\boldsymbol{\epsilon}_\theta = \alpha(\theta - \theta_0)\mathbf{I} \tag{2.2.5}$$

where α is the linear isotropic coefficient of thermal expansion (CTE), θ_0 is a reference temperature, and the second-order identity tensor is denoted by $\mathbf{I}$. The fourth-order material tensor for isotropic, linear elastic homogeneous materials is defined in terms of the Lamé constants λ_L and μ_L as:

$$\boldsymbol{D} = D_{ijkl} = \lambda_L \delta_{ij}\delta_{kl} + \mu_L(\delta_{ik}\delta_{jl} + \delta_{il}\delta_{jk}) \tag{2.2.6}$$

where δ_{ij} is the Kronecker delta (i.e., the equivalent of $\mathbf{I}$ in index notation). The Lamé constants can be expressed as a function of the Young's modulus E and the Poisson's ratio ν as:

$$\lambda_L = \frac{\nu E}{(1+\nu)(1-2\nu)}, \qquad \mu_L = \frac{E}{2(1+\nu)} \tag{2.2.7}$$

Using Eqn.(2.2.6) and Eqn.(2.2.7), the Helmholtz free energy function for linear elastic isotropic compressible solids (Eqn.(2.2.3)) can be re-written as:

$$\Psi(\boldsymbol{\epsilon}_M) = \mu_L \operatorname{tr}((\boldsymbol{\epsilon}_M)^2) + \frac{\lambda_L}{2} \left(\operatorname{tr}(\boldsymbol{\epsilon}_M)\right)^2 \tag{2.2.8}$$

Finally, the Cauchy stress is obtained by differentiation of the free energy function with respect to the mechanical strain tensor as:

$$\boldsymbol{\sigma}(\boldsymbol{\epsilon}_M) = \frac{\partial \Psi(\boldsymbol{\epsilon}_M)}{\partial \boldsymbol{\epsilon}_M} = 2\mu_L \boldsymbol{\epsilon}_M + \lambda_L \operatorname{tr}(\boldsymbol{\epsilon}_M)\boldsymbol{I} \tag{2.2.9}$$

Alternatively, the small strain constitutive relationship (Eqn. (2.2.9)) can be stated using the fourth-order material tensor $\boldsymbol{D}$. This yields the well-known linear elastic stress-strain relationship

in 3D for small strains:

$$\boldsymbol{\sigma} = \boldsymbol{D}\boldsymbol{\epsilon}_M \tag{2.2.10}$$

It should be noted that the thermal strain tensor $\boldsymbol{\epsilon}_\theta$ does not contribute to any mechanical stress in the solid; therefore, the Cauchy stress is solely a function of mechanical strain tensor $\boldsymbol{\epsilon}_M$.

Applying the vector-valued test functions $\delta\mathbf{u}$ to the strong form of the linear elastic governing equation (Eqn.(2.2.2)), performing integration by parts and applying the divergence theorem yields the variational form of the linear elastic static problem. This can be stated as:

Find $\mathbf{u}(\mathbf{X}) \in \boldsymbol{\mathcal{S}}$, such that

$$\int_{\Omega_0} \delta\boldsymbol{\epsilon} : \boldsymbol{\sigma} \; dV = \int_{\Omega_0} \delta\mathbf{u} \; \boldsymbol{B} \; dV + \int_{\Gamma_N} \delta\mathbf{u} \; \bar{\mathbf{T}} \; dA \quad \forall \quad \delta\mathbf{u} \in \boldsymbol{\mathcal{V}} \tag{2.2.11}$$

where $\boldsymbol{\mathcal{S}}$ denotes the vector-valued trail solution space defined as $\boldsymbol{\mathcal{S}} = \{\mathbf{u}(\mathbf{X}) : \bar{\Omega} \rightarrow \mathbb{R}; \; \mathbf{u} = \mathbf{u}_D \text{ on } \Gamma_D\}$. The vector-valued weighting function space is defined as $\boldsymbol{\mathcal{V}} = \{\delta\mathbf{u}(\mathbf{X}) : \bar{\Omega} \rightarrow \mathbb{R}; \; \delta\mathbf{u} = 0 \text{ on } \Gamma_D\}$.

2.3   Finite Strain Hyperelasticity

Before formulating the strong and the weak form of the hyperelastic governing equations, finite strain kinematics, different stress measures, and three hyperelastic constitutive models are discussed.

2.3.1   Finite Strain Thermomechanical Kinematics

The nonlinear kinematic relationship between displacements and strains at large deformations is discussed first. When considering elasticity at finite strains, it is crucial to (at least) distinguish between quantities in the reference (undeformed) configuration Ω_0 and in the current (deformed) configuration Ω. In case of finite strain thermoelasticity an additional, intermediate, non-physical configuration $\tilde{\Omega}$ exists. See Figure 2.2 for a schematic illustration. The deformation of a point between undeformed ($\mathbf{X}$) and deformed configuration ($\mathbf{x}$) is characterized by the deformation gradient tensor $\mathbf{F}$, defined as:

$$\mathbf{F} = \frac{\partial \mathbf{x}}{\partial \mathbf{X}} \tag{2.3.1}$$
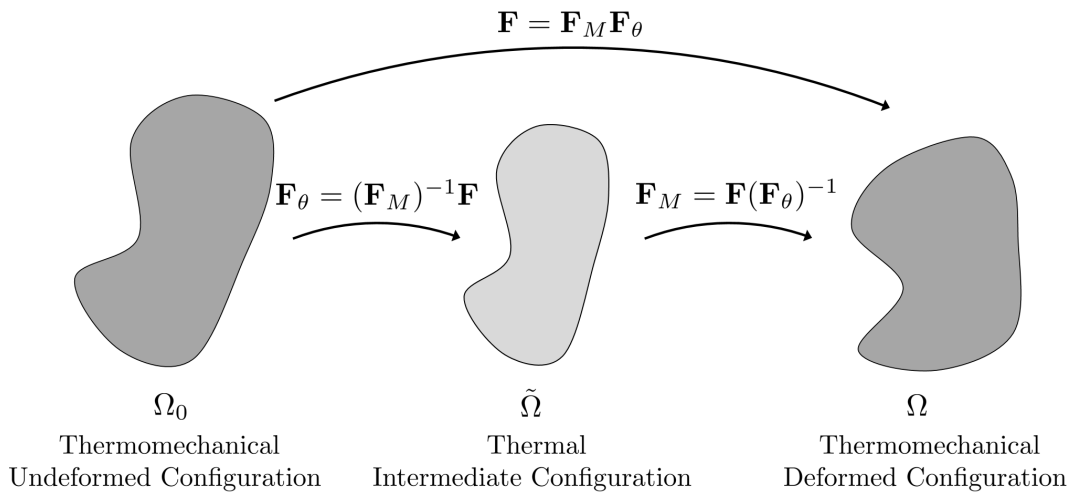
Figure 2.2: Multiplicative decomposition of the total deformation gradient $\mathbf{F}$ into mechanical deformation gradient $\mathbf{F}_M$ and thermal deformation gradient $\mathbf{F}_\theta$.

Note that in general $\mathbf{F}$ is not symmetric. The relationship between current coordinates ($\mathbf{x}$) and reference coordinates ($\mathbf{X}$) is given by $\mathbf{x} = \mathbf{u} + \mathbf{X}$. This leads to the definition of the deformation gradient tensor in terms of the displacement gradient tensor $\mathbf{H} = \partial \mathbf{u}/\partial \mathbf{X}$ as:

$$\mathbf{F} = \mathbf{H} + \mathbf{I} \tag{2.3.2}$$

In a total Lagrangian setting, the governing equations are evaluated in the undeformed configuration, whereas other quantities like certain stress measures might be defined in the deformed configuration, or even in the intermediate configuration. Considering the case of thermoelasticity, the total deformation gradient $\mathbf{F}$ can be multiplicatively decomposed into a mechanical deformation gradient $\mathbf{F}_M$ and a thermal deformation gradient $\mathbf{F}_\theta$ as:

$$\mathbf{F} = \mathbf{F}_M \mathbf{F}_\theta \tag{2.3.3}$$

It should be noted that for the case of isotropic thermal swelling where $\mathbf{F}_\theta$ only contains normal (diagonal) components, the decomposition order of the deformation is arbitrary. In that case Eqn.(2.3.3) is equivalent to $\mathbf{F} = \mathbf{F}_\theta \mathbf{F}_M$. By definition, the thermal deformation leads to a stress-free state and only the mechanical deformation leads to a mechanical stress in the body.

The thermal deformation for isotropic materials is described by [192, 86]:

$$\mathbf{F}_\theta = \vartheta(\theta)\mathbf{I} \tag{2.3.4}$$

where $\vartheta(\theta)$ is the thermal stretch ratio in an arbitrary direction. Using an exponential thermal expansion model, the thermal stretch ratio is defined as:

$$\vartheta(\theta) = e^{\int_{\theta_0}^{\theta} \alpha(\theta)dT} \tag{2.3.5}$$

where in general, the CTE $\alpha(\theta)$ is a function of temperature. For materials with a constant CTE, the thermal deformation gradient is determined as:

$$\mathbf{F}_T = e^{\alpha(\theta - \theta_0)}\mathbf{I} \tag{2.3.6}$$
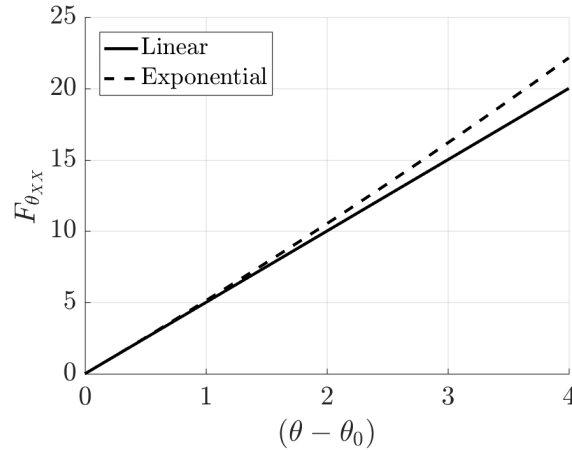
Figure 2.3: Thermal deformation gradient component $F_{\theta_{XX}}$ over temperature difference, for $\alpha = 0.05$.

Alternatively, a linear thermal expansion model, similar to the small strain equivalent of Eqn.(2.2.5) can be considered. In this case, the thermal deformation gradient is computed as:

$$\mathbf{F}_\theta = (1 + \alpha(\theta - \theta_0))\mathbf{I} \tag{2.3.7}$$

A comparison of the exponential and the linear thermal expansion model, Eqn.(2.3.6) and Eqn.(2.3.7), respectively, is shown in Figure 2.3. The $F_{\theta_{XX}}$ component of each model is shown over temperature difference for a constant CTE of $\alpha = 0.05$.

Good agreement between the two models can be seen, especially if the temperature difference is small. As the temperature difference increases, deviations between the linear and the exponential temperature model are seen, as expected. Given that generally a maximum temperature difference of 1 is considered in this thesis, combined with a CTE of, for example 0.05, the choice of thermal expansion model is insignificant.

Using solely the mechanical deformation gradient obtained from Eqn.(2.3.3) as $\mathbf{F}_M = \mathbf{F}(\mathbf{F}_\theta)^{-1}$, the (symmetric) right Cauchy-Green deformation tensor is obtained as:

$$\mathbf{C}_M = (\mathbf{F}_M)^T \mathbf{F}_M \tag{2.3.8}$$

Using that, the (symmetric) Green-Lagrange strain tensor is defined as:

$$\mathbf{E}_M = \frac{1}{2}(\mathbf{C}_M - \mathbf{I}) \tag{2.3.9}$$

which is the finite strain equivalent to the infinitesimal strain tensor introduced in Eqn.(2.2.4).

2.3.2 Stress Tensors

Various stress measures are associated with large strain kinematics. For completeness, they are discussed in the following section. The Cauchy stress tensor, introduced in Eqn.(2.2.1), is a symmetric stress tensor which is defined fully in the current (deformed) configuration. It physically represents the force (in the deformed configuration) per unit area in the deformed configuration. It is derived from Cauchy's stress theorem as [86]:

$$\mathbf{t} = \boldsymbol{\sigma}_M \mathbf{n} \tag{2.3.10}$$

where $\mathbf{t}$ is the traction vector and $\mathbf{n}$ is the outward surface normal vector, both in the deformed configuration.

Using the Piola transformation, the Cauchy stress can be transformed to the first Piola-Kirchhoff stress tensor $\mathbf{P}_M$ as:

$$\mathbf{P}_M = J_M \boldsymbol{\sigma}_M (\mathbf{F}_M)^{-T} \tag{2.3.11}$$

where J_M is the determinant of the mechanical deformation gradient $J_M = \det(\mathbf{F}_M)$, indicating the volume ratio between an undeformed and a deformed body. The first Piola-Kirchhoff stress tensor, also referred to as nominal stress tensor, represents the force (in the current, deformed configuration) per unit area of the mechanically undeformed solid (in the intermediate configuration). Due to this duality, it has no real physical significance attributed to it. It should be noted that the first Piola-Kirchhoff stress tensor is in general not symmetric (i.e., $\mathbf{P}_M(\mathbf{F}_M)^T = \mathbf{F}_M(\mathbf{P}_M)^T$ [86]).

The second Piola-Kirchhoff stress tensor $\mathbf{S}$ is introduced here as a third stress tensor, which is fully defined in the mechanically undeformed (thermomechanical intermediate) configuration. It is related to the first Piola-Kirchhoff stress tensor by:

$$\mathbf{P}_M = \mathbf{F}_M \mathbf{S}_M \tag{2.3.12}$$

Combining Eqn.(2.3.12) and Eqn.(2.3.11) leads to the relationship between the second Piola-Kirchhoff stress and the Cauchy stress tensor as:

$$\sigma_M = (J_M)^{-1} \mathbf{F}_M \mathbf{S}_M (\mathbf{F}_M^T) \tag{2.3.13}$$

It should be noted that $\mathbf{S}_M$ is a symmetric stress tensor representing a force (in the mechanically undeformed configuration) per unit area of the mechanically undeformed configuration.

2.3.2.1   Remarks on Notation

In general, the convention of [86] and [186] for the definition of the stress components of the Cauchy stress is followed in this thesis. The Cauchy stress (in index notation) is defined as $(\sigma_{ij})_M$ where the first index i corresponds to the component of the traction vector $\mathbf{t}$ (force) and the second index j corresponds to the unit normal $\mathbf{n}$ characterizing the plane $\mathbf{t}$ is acting on. Therefore, Cauchy's formula is defined as presented in Eqn.(2.3.10). This is different from other authors, like [23] or [15], who define the Cauchy stress tensor as the transpose of what is presented here. In general, this does not affect the Cauchy stress tensor and the second Piola-Kirchhoff stress tensor in particular, since both of them are symmetric. The first Piola-Kirchhoff stress tensor is not symmetric, which leads to the fact that special care needs to be taken when referring to the notation of different authors.

2.3.2.2   Stress mapping into Thermomechanical Undeformed Configuration

Due to the existence of three configurations in the context of large strain thermomechanics (see Figure 2.2), mechanical stresses are only defined with respect to the intermediate configuration ($\tilde{\Omega}$) or the deformed configuration (Ω). The Piola transformation (Eqn.(2.3.11)) is used for mapping back the second Piola-Kirchhoff stress from the thermomechanical intermediate configuration ($\tilde{\Omega}$) to the true undeformed configuration (Ω_0) as:

$$\mathbf{S} = (\mathbf{F}_\theta)^{-1} \mathbf{S}_M (\mathbf{F}_\theta)^{-T} J_\theta \tag{2.3.14}$$

where J_θ is the Jacobian of the thermal deformation gradient $J_\theta = \det(\mathbf{F}_\theta)$. It should also be noted that from a global perspective, the mechanical second Piola-Kirchhoff stress $\mathbf{S}_M$ is defined with respect to the intermediate configuration. Only after the Piola transformation (Eqn.(2.3.14)) is the second Piola-Kirchhoff stress defined in the true or global reference configuration. The first Piola-Kirchhoff (nominal) stress in the undeformed configuration is computed similar to Eqn.(2.3.12) as:

$$\mathbf{P} = \mathbf{FS} \tag{2.3.15}$$

where $\mathbf{F}$ is the total deformation gradient defined in Eqn.(2.3.3).

2.3.3 Hyperelastic Constitutive Relations for Compressible Isotropic Solids

In general, a Helmholtz free energy function Ψ defined per unit volume exists for a hyperelastic material [86]. Three hyperelastic constitutive relations are considered in this thesis, which in parts are a second source of nonlinearity besides the nonlinear kinematics discussed in Section 2.3.1. As the thermal deformation does not lead to stresses in the solid (for unconstrained isotropic thermal expansion), only mechanical deformations are considered in the following.

2.3.3.1 Saint Venant-Kirchhoff Constitutive Model

The Saint Venant-Kirchhoff constitutive model is a simple extension of the linear elastic material model (Eqn.(2.2.10)) to large strains. The Helmholtz free energy function in the undeformed configuration Ω_0 of the hyperelastic Saint Venant-Kirchhoff model is defined as [86]:

$$\Psi(\mathbf{E}_M) = \mu_L \ \mathrm{tr}((\mathbf{E}_M)^2) + \frac{\lambda_L}{2} \ \mathrm{tr}(\mathbf{E}_M)^2 \tag{2.3.16}$$

where μ_L and λ_L are the Lamé parameters defined in Eqn.(2.2.7) and $\mathbf{E}_M$ is the Green-Lagrange strain tensor (Eqn.(2.3.9)). Using the fourth-order material tensor $\boldsymbol{D}$ (Eqn.(2.2.6)), the Helmholtz free energy function for the Saint Venant-Kirchhoff material model can alternatively be written as:

$$\Psi(\mathbf{E}_M) = \frac{1}{2}\mathbf{E}_M \ \boldsymbol{D} \ \mathbf{E}_M \tag{2.3.17}$$

A similarity between Eqn.(2.3.17) and Eqn.(2.2.3) can be seen where the only difference lies in the strain measures used. In the small strain case, the small strain tensor ϵ_M is used, which is based on linearized displacement gradients. Large strains and rotation cannot be captured with this infinitesimal strain measure. Therefore, the Green-Lagrange strain tensor $\mathbf{E}_M$ is used in the large strain extension of the model which more accurately captures large strains and large rotations. Using Eqn.(2.3.16) or Eqn.(2.3.17), the second Piola-Kirchhoff stress tensor is obtained as:

$$\mathbf{S}_M(\mathbf{E}_M) = \frac{\partial \Psi(\mathbf{E}_M)}{\partial \mathbf{E}_M} = \boldsymbol{D} : \mathbf{E}_M = 2\mu_L \mathbf{E}_M + \lambda_L \, \text{tr}(\mathbf{E}_M)\mathbf{I} \tag{2.3.18}$$

Alternatively, Eqn.(2.3.18) can be written in terms of the right Cauchy-Green deformation tensor as:

$$\mathbf{S}_M(\mathbf{C}_M) = \mu_L(\mathbf{C}_M - \mathbf{I}) + \frac{\lambda_L}{2} \, \text{tr}(\mathbf{C}_M - 3)\mathbf{I} \tag{2.3.19}$$

Compressibility is assumed in the hyperelastic constitutive models treated in this thesis, which means the material is not necessarily volume preserving during large deformations. Considering the fact that the Saint Venant-Kirchhoff material is an extension of the linear elastic constitutive model to large strains, it can only be applied in special cases, namely when small strains but large rotations or displacements are present in a modeling situation.

2.3.3.2   Neo-Hookean Constitutive Model for isotropic compressible Solids

The Neo-Hookean material model is the simplest form of a hyperelastic material model considering both geometric and material nonlinearities. The strain energy density function for it is defined as [15]:

$$\Psi(\mathbf{C}_M) = \frac{\lambda_L}{2} \left(\ln(J_M)\right)^2 - \mu_L \, \ln(J_M) + \frac{\mu_L}{2} \left(\, \text{tr}(\mathbf{C}_M) - 3\right) \tag{2.3.20}$$

where, again, the Lamé parameters (Eqn.(2.2.7)) are used. From Eqn.(2.3.20) the second Piola-Kirchhoff stress is obtained as:

$$\mathbf{S}_M(\mathbf{C}_M) = \frac{\partial \Psi(\mathbf{C}_M)}{\partial \mathbf{C}_M} = \left(\lambda_L \, \ln(J_M) - \mu_L\right)(\mathbf{C}_M)^{-1} + \mu_L \mathbf{I} \tag{2.3.21}$$

The Cauchy stress follows from Eqn.(2.3.21) by a push-forward operation to the current configuration as:

$$\boldsymbol{\sigma}(\mathbf{b}_M) = \frac{1}{J_M}\mathbf{F}_M\mathbf{S}_M(\mathbf{C}_M)\mathbf{F}_M^T = \frac{1}{J_M}\left[(\lambda_L \ln(J_M) - \mu_L)\mathbf{I} + \mu_L\mathbf{b}_M\right] \tag{2.3.22}$$

where $\mathbf{b}_M$ is the mechanical left Cauchy-Green deformation tensor $\mathbf{b}_M = \mathbf{F}_M\mathbf{F}_M^T$. Again, this constitutive model implies compressibility and is therefore not fully volume-preserving.

2.3.3.3   Alternative Formulation of Neo-Hookean Constitutive Model

An alternative formulation of the Neo-Hookean material model, found in [180], is introduced next:

$$\Psi(\mathbf{C}_M) = \frac{\lambda_L + \frac{2}{3}\mu_L}{2}\left(J_M - 1\right)^2 + \frac{\mu_L}{2}\left(\operatorname{tr}(\mathbf{C}_M)(J_M)^{-\frac{2}{3}} - 3\right) \tag{2.3.23}$$

where $\lambda_L + \frac{2}{3}\mu_L = K$ can also be represented as the bulk modulus K to yield a more compact form. In some literature, the term $\operatorname{tr}(\mathbf{C}_M)(J_M)^{-\frac{2}{3}} = \bar{I}_1$ is represented as the first modified invariant $\bar{I}_1$ of the right Cauchy-Green deformation tensor. As before, the Lamé parameters defined in Eqn.(2.2.7) are used. Using the modified version of the first invariant of the right Cauchy-Green deformation tensor, Eqn.(2.3.23) can be re-stated in more compact form as:

$$\Psi(\mathbf{C}_M) = \frac{K}{2}\left(J_M - 1\right)^2 + \frac{\mu_L}{2}\left(\bar{I}_1 - 3\right) \tag{2.3.24}$$

From Eqn.(2.3.23) the second Piola-Kirchhoff stress is obtained as:

$$\mathbf{S}_M(\mathbf{C}_M) = \mu_L(J_M)^{-\frac{2}{3}}\mathbf{I} + \left(-\frac{\mu_L}{3}\operatorname{tr}(\mathbf{C}_M)(J_M)^{-\frac{2}{3}} + K((J_M)^2 - J_M)\right)(\mathbf{C}_M)^{-1} \tag{2.3.25}$$

2.3.3.4   Comparison of Constitutive Models

A comparison of the four constitutive models discussed previously (i.e., linear elasticity, Saint Venant-Kirchhoff, Neo-Hookean, alternative Neo-Hookean) is presented next. For that, a simplified 1D problem with a prescribed axial displacement gradient is simulated and the obtained first Piola-Kirchhoff stress component P_{XX} is plotted over the first component of the displacement gradient (H_{XX}) in Figure 2.4.
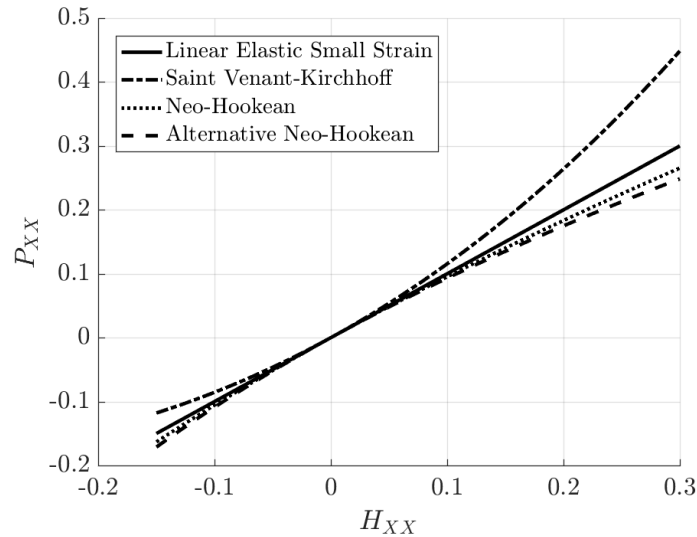
Figure 2.4: Comparison of uniaxial stress obtained by a linear elastic, Saint Venant-Kirchhoff, and two different Neo-Hookean constitutive models for a uniaxial displacement gradient.

It can be seen that the stresses obtained from all four constitutive models agree quite well for small deformations (i.e., $-0.01 \leq H_{XX} \leq 0.01$), both in tension and in compression. A significantly different behavior is, however, observed for larger deformations. It is especially noticeable that the Saint Venant-Kirchhoff material over-predicts the stress across the entire range compared to both Neo-Hookean models and even the linear elastic material law. In addition, it is interesting to observe a significant difference between the linear elastic small strain and the large strain material model (Saint Venant-Kirchhoff) introduced solely by nonlinear kinematics.

It is also apparent from Eqn.(2.3.21) and Eqn.(2.3.25) that, as a compressible deformation of -100% is approached, both Neo-Hookean materials approach a stress singularity (i.e., as $J_M \rightarrow 0$) while the two other material models (i.e., linear elastic and Saint Venant-Kirchhoff) can capture compression beyond that. However, a compressive deformation of 100% is physically meaningless, as it means the body of interest has been compressed to zero volume in the deformed configuration.

2.3.4   Strong Form and Weak Form of the Finite Strain BVP

The strong form of the finite strain hyperelastic BVP for the vector valued state variables (displacements) $\varphi = \mathbf{u}$ can be formulated as:

Find $\mathbf{u}(\mathbf{X}) : \bar{\Omega} \to \mathbb{R}^d$, such that

$$\nabla \cdot \boldsymbol{P} + \mathbf{B} = \mathbf{0} \quad \text{in} \quad \Omega_0$$
$$\mathbf{u} = \bar{\mathbf{u}}_D \quad \text{on} \quad \Gamma_D \tag{2.3.26}$$
$$\boldsymbol{P}\,\mathbf{N} = \bar{\mathbf{T}} \quad \text{on} \quad \Gamma_N$$

where similar to the linear elastic case, the prescribed traction is $\bar{\mathbf{T}} = \bar{\vartheta}_N$ for consistency with Figure 2.1. As before, applying the vector-valued test functions $\delta\mathbf{u}$ on the strong form of Eqn.(2.3.26), performing integration by parts and applying the divergence theorem yields the variational form of the finite strain hyperelastic problem. This can be stated as:

Find $\mathbf{u}(\mathbf{X}) \in \boldsymbol{\mathcal{S}}$, such that

$$\int_{\Omega_0} \delta\boldsymbol{F} : \boldsymbol{P}\; dV = \int_{\Omega_0} \delta\mathbf{u}\,\boldsymbol{B}\; dV + \int_{\Gamma_N} \delta\mathbf{u}\,\bar{\mathbf{T}}\; dA \quad \forall \quad \delta\mathbf{u} \in \boldsymbol{\mathcal{V}} \tag{2.3.27}$$

where the same vector-valued trail solution space and weighting function space as in Eqn.(2.2.11) are used.

Chapter 3

Computational Approaches

Computational approaches relevant to this thesis are discussed in this chapter. These include the XFEM, for both first-order and higher-order spatial discretization and the Enhanced Assumed Strain (EAS) method to avoid shear locking of slender structures.

3.1   The Extended Finite Element Method

The XFEM, an immersed boundary method, was originally proposed by [13] for applications in crack modeling. Since then, the XFEM, or sometimes also called the CutFEM [26], has been widely used in fracture mechanics, material modeling and design optimization [14, 188]. It enables modeling of intra-element discontinuities on a non-conforming background mesh by enriching the standard FE shape functions with additional shape functions [54]. A high geometric resolution is enabled by this approach, on rather coarse background meshes. Multiple levels of enrichment are required to avoid spurious coupling or load transfer between disconnected material sub-domains [121, 185]. Enforcement of boundary and interface conditions is achieved by, for example, the Lagrange multiplier method [70] or via Nitsche's method [12, 29].

3.1.1   Heaviside-Enriched XFEM

A generalized Heaviside enrichment strategy [82, 183] is employed in this thesis, where the degrees of freedom within each unique subphase are approximated using standard FE shape functions. This approach is ideally suited for modeling of strong discontinuities due to the discontinuous nature

of the Heaviside step function. Using this approach, the state variable vector $\hat{\mathbf{u}}_i(\mathbf{X})$ at node i of a two material problem (phase I, phase II) is approximated as:

$$\hat{\mathbf{u}}_i(\mathbf{X}) = \sum_{l=1}^{L} \left(H(-\phi(\mathbf{X})) \sum_{k=1}^{N_N^e} N_k(\mathbf{X})\delta_{lq}^k \mathbf{u}_{il}^{k,I} + H(\phi(\mathbf{X})) \sum_{k=1}^{N_N^e} N_k(\mathbf{X})\delta_{lq}^k \mathbf{u}_{il}^{k,II} \right) \tag{3.1.1}$$

where H is the Heaviside function as a function of the LS value $\phi(\mathbf{X})$ defined as:

$$H(\phi) = \begin{cases} 1, & \forall \ \phi(\mathbf{X}) > 0 \\ 0, & \forall \ \phi(\mathbf{X}) < 0 \end{cases} \tag{3.1.2}$$

The maximum number of enrichment levels is denoted by L, $N_k(\mathbf{X})$ is the elemental shape function and δ_{lq}^k is the Kronecker delta which selects the active enrichment level q for node k. δ_{lq}^k ensures that displacements at node k are only interpolated by a single set of degrees of freedom (DOFs) defined at node position $\mathbf{X}$ such that the partition of unity principle is satisfied [109]. The number of nodes per element is denoted by N_N^e. For more details about the generalized Heaviside enrichment strategy employed in this work, the interested reader is referred to [121], [183], and [185]. It should be noted that the XFEM framework employed in this thesis uses bi-linear or tri-linear LS interpolation in 2D and 3D, respectively. This means, from a geometrical point of view, every edge of a background element can only be intersected at most once. More details about this simplification in combination with higher-order spatial XFEM discretization are discussed in Section 3.2.

3.1.2 Weak Enforcement of Interface and Boundary Conditions

To achieve continuity of the solution field and the tractions across a discontinuous material interface $\Gamma_0^{I,II}$, Nitsche's method [136] is used in this work. To that extent, the governing equation (Eqn.(2.1.3), Eqn.(2.2.11) or Eqn.(2.3.27)) is augmented by an additional contribution. For the large strain hyperelastic case (Eqn.(2.3.27)), the additional (unsymmetrical) interface Nitsche residual contribution in vector form is:

$$\mathbf{R}_{IF} = -\int_{\Gamma_0^{I,II}} [\![\delta\mathbf{u}]\!]\{\mathbf{P}(\mathbf{u})\}\mathbf{N}dA + \int_{\Gamma_0^{I,II}} \{\mathbf{P}(\delta\mathbf{u})\}\mathbf{N}[\![\mathbf{u}]\!]dA + \gamma_N \int_{\Gamma_0^{I,II}} [\![\delta\mathbf{u}]\!][\![\mathbf{u}]\!]dA \tag{3.1.3}$$

where the jump operator $[\![\bullet]\!]$ is defined as:

$$[\![\mathbf{u}]\!] = \mathbf{u}^I - \mathbf{u}^{II} \,, \qquad [\![\delta\mathbf{u}]\!] = \delta\mathbf{u}^I - \delta\mathbf{u}^{II} \tag{3.1.4}$$

and the state variables in phase I and phase II are denoted by $\mathbf{u}^I$ and $\mathbf{u}^{II}$, respectively. The weighted sum of the stresses is denoted by $\{\bullet\}$, such that:

$$\{\mathbf{P}(\mathbf{u})\} = w^I\mathbf{P}(\mathbf{u}^I) + w^{II}\mathbf{P}(\mathbf{u}^{II}) \tag{3.1.5}$$

Following the work of [91], the interface parameter γ_N is obtained from:

$$\gamma_N = 2c_N \frac{\mathrm{meas}(\Gamma_0^{I,II})}{\mathrm{meas}(\Omega_0^I)/E^I + \mathrm{meas}(\Omega_0^{II})/E^{II}} \tag{3.1.6}$$

where c_N is a user-defined penalty parameter and E^I and E^{II} denote the Young's modulus of the material in phase I and phase II, respectively. It should be noted that even though a higher penalty parameter increases the enforcement of Eqn.(3.1.3), it may also lead to ill-conditioning of the linear system [162]. The Lebesgue measure is denoted by $\mathrm{meas}(\bullet)$ corresponding to a line length or surface area in 2D and a surface area or a volume measure in 3D. Similar to Eqn.(3.1.6), the weights of Eqn.(3.1.5) are obtained as:

$$w^m = \frac{\mathrm{meas}(\Omega_0^m)/E^m}{\mathrm{meas}(\Omega_0^I)/E^I + \mathrm{meas}(\Omega_0^{II})/E^{II}} \tag{3.1.7}$$

where the superscript m denotes either material phase, i.e., $m = [I, II]$. The first term of Eqn.(3.1.3) corresponds to the consistency term, the second one is the adjoint consistency and the final term is a penalty on the jump in state variables.

A consistent tangent stiffness matrix is required for an iterative nonlinear solver and for computations of shape sensitivities using the adjoint method (see Section 4.6.1). The derivative of the Nitsche residual (Eqn.(3.1.4)) with respect to the discretized state variables $\hat{\mathbf{u}}$, i.e., Jacobian matrix, is computed as:

$$\begin{aligned}
\frac{\partial R_{IF}}{\partial \hat{\mathbf{u}}} = &- \int_{\Gamma_0^{I,II}} [\![\delta\mathbf{u}]\!] \left\{\frac{\partial\mathbf{P}(\mathbf{u})}{\partial\hat{\mathbf{u}}}\right\} \mathbf{N} dA \\
&+ \int_{\Gamma_0^{I,II}} \left(\left\{\frac{\partial\mathbf{P}(\delta\mathbf{u})}{\partial\hat{\mathbf{u}}}\right\} [\![\delta\mathbf{u}]\!] + \{\mathbf{P}(\delta\mathbf{u})\} \frac{\partial[\![\delta\mathbf{u}]\!]}{\partial\hat{\mathbf{u}}}\right) dA \\
&+ \gamma_N \int_{\Gamma_0^{I,II}} [\![\delta\mathbf{u}]\!] \frac{\partial[\![\mathbf{u}]\!]}{\partial\hat{\mathbf{u}}} dA
\end{aligned} \tag{3.1.8}$$

It should be pointed out that the evaluation of Eqn.(3.1.8) requires the second derivative of the stress tensor with respect to the state variables in order to compute $\frac{\partial \mathbf{P}(\delta \mathbf{u})}{\partial \hat{\mathbf{u}}}$. For small strain kinematics, this term vanishes, but for large strain kinematics (see Section 2.3.1) this involves computation of a fifth-order tensor which is non-trivial and can be computationally costly.

A simplified version of Eqn.(3.1.3) is used for application of Dirichlet boundary conditions weakly. This is achieved by neglecting the second material phase and applying the jump operator (Eqn.(3.1.4)) with respect to a prescribed Dirichlet boundary condition value.

Weak enforcement of Neumann boundary conditions is achieved by evaluation of the boundary term in Eqn.(2.3.27) as:

$$\mathbf{R}_T = \int_{\Gamma_N} \delta \mathbf{u} \bar{\mathbf{T}} dA \tag{3.1.9}$$

Alternatively, XFEM interface conditions can be enforced using a stabilized Lagrange multiplier method [28]. This requires a local solve on an elemental level and therefore increases the computational cost of the XFEM approach. In this thesis, Nitsche's method is used exclusively to apply XFEM interface conditions and weak boundary conditions.

3.1.2.1   1D Bar Example

To illustrate the basic concept of Heaviside-enriched XFEM, a simple bar example in 1D is presented in Appendix A. Nitsche's method is used to enforce the XFEM interface condition and the influence of the interface location on the different residual components is analyzed.

3.1.3   Face Oriented Ghost Stabilization

To prevent the occurrence of an ill-conditioned system, face-oriented ghost stabilization, as introduced by [30], is used in the vicinity of the XFEM interface. Ill-conditioning arises when the XFEM interface $\Gamma_0^{I,II}$ moves too close to a FE node, which leads to a vanishing zone of influence of certain DOFs as well as significant jumps in the solution gradients. Face-oriented ghost stabilization cures this, independent of the intersection configuration. In a general sense, all spatial gradients

up to the degree to which these are captured by the spatial interpolation of the underlying finite element, need to be stabilized. This is formulated as [157]:

$$\mathbf{R}_G = \sum_{F \in F_{cut}} \sum_{p=1}^{k} \int_F \gamma_G h^{2(p-1)+1} [\![D^p(\delta\mathbf{u})]\!] [\![D^p(\mathbf{u})]\!] dA \qquad (3.1.10)$$

where h is the element edge length, k is the highest polynomial order and, $D^p(\bullet)$ denotes the normal derivative of order p on the face between two adjacent elements Ω_{e_1} and Ω_{e_2}. The ghost penalization parameter is denoted by γ_G and $F_{cut} = F_{cut}^I \cup F_{cut}^{II}$ contains all element faces in the immediate vicinity of the interface for which at least one of the two adjacent elements is intersected [190]. The selection of the faces on which ghost penalization is applied is schematically illustrated in Figure 3.1.
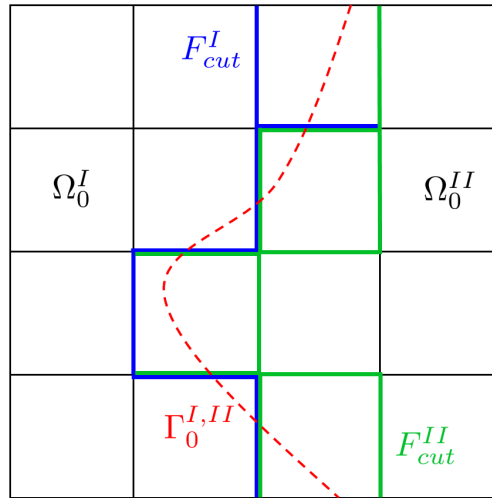
Figure 3.1: Domain decomposition for ghost stabilization applied to a material-material XFEM problem.

3.2   Higher-Order XFEM

Combining the XFEM with higher-order spatial interpolation is an attractive means to overcome limitations of linear element basis functions. These include, but are not limited to, element locking, inability to compute higher-order spatial gradients, and the need for high levels of mesh refinement to accurately capture physical phenomena. Additionally, a more accurate capturing of (potentially curved) interfaces is enabled by higher-order XFEM [34, 47]. This has extensively been studied in the context of fracture mechanics [181, 106, 172] and fluid-structure interaction [126]. Higher-order XFEM for modeling and optimizing slender structures where shear locking occurs in linear elements has been applied by [68, 69]. In the work considered in this thesis, linear interpolation of the LS field defining the XFEM interface $\Gamma_0^{I,II}$ is assumed. This is true regardless of the interpolation order of the background element. Therefore, only straight interfaces which intersect a background element edge at most once are considered.

3.2.1   Different Higher-Order Ghost Penalization Formulations

Based on Eqn.(3.1.10), different ghost penalization formulations are derived. Representative for higher-order ghost penalization, first and second-order ghost penalization expressions are discussed in the context of this thesis. As before, large strain kinematics (see Section 2.3) and the associated stress and strain measures are used for this purpose.

3.2.1.1   Displacement Gradient based Formulation

Using the displacement gradient based ghost formulation as originally proposed by [30], the residual equation penalizing jumps in first and second-order spatial displacement gradients is stated as:

$$
\begin{aligned}
R_G =& h\gamma_G E \sum_{F \in F_{cut}} \int_F [\![\delta\nabla\mathbf{uN}]\!][\![\nabla\mathbf{uN}]\!]\ dA \\
&+ h^3\gamma_G E \sum_{F \in F_{cut}} \int_F [\![\delta\nabla(\nabla\mathbf{uN})]\!][\![\nabla(\nabla\mathbf{uN})]\!]\ dA
\end{aligned}
\tag{3.2.1}
$$

where the normal derivative $D(\bullet)$ is explicitly written as the spatial gradient of a quantity dotted with the normal vector. Scaling of Eqn.(3.2.1) with (in structural problems) the elastic modulus E is performed in order to achieve consistent units of the residual equation. This is the simplest formulation of ghost penalization; however it is only valid if the material within one phase is homogeneous and not spatially varying.

3.2.1.2   Stress-based Formulation

The displacement gradient based ghost stabilization (Eqn.(3.2.1)) directly penalizes jumps in displacement gradients, which need to vanish between elements of the same phase. When using a spatially varying material within one phase, jumps in displacement gradients exist by construction. In order to not falsely penalize jumps caused by varying material properties, but only by numerical artifacts of the XFEM discretization, a stress-based ghost penalization is proposed. This, most general form of ghost penalization is formulated as:

$$
\begin{aligned}
R_G = & \frac{h}{\tilde{E}} \gamma_G \sum_{F \in F_{cut}} \int_F [\![\mathbf{P}(\delta\mathbf{u})\mathbf{N}]\!][\![\mathbf{P}(\mathbf{u})\mathbf{N}]\!] \ dA \\
& + \frac{h^3}{\tilde{E}} \gamma_G \sum_{F \in F_{cut}} \int_F [\![\nabla\mathbf{P}(\delta\mathbf{u})\mathbf{N}]\!][\![\nabla\mathbf{P}(\delta\mathbf{u})\mathbf{N}]\!] \ dA
\end{aligned}
\tag{3.2.2}
$$

where $\tilde{E}$ is a scaling parameter computed as the geometric mean of the Young's moduli of the two adjacent elements within one material phase (see Figure 3.1). Using Eqn.(3.2.2), no jumps caused by varying material properties are taken into account as the scaling of the ghost residual contribution is performed element-wise constant. This most general formulation has the drawback of requiring the computation of a seventh-order tensor for linearization of the variation of the gradient of the stress $\partial(\nabla\mathbf{P}(\delta\mathbf{u}))/\partial\hat{\mathbf{u}}$. This significantly increases computational complexity and, therefore, the stress-based ghost stabilization formulation is less suitable for practical means.

3.2.1.3   Virtual Work based Formulation

A hybrid formulation based on the principle of virtual work is adopted to combine the benefits of the two previous stabilization formulations. The ghost stabilization contribution in residual form

is:

$$R_G = h\gamma_G \sum_{F \in F_{cut}} \int_F [\![\delta\nabla\mathbf{uN}]\!][\![\mathbf{P(u)N}]\!] \, dA$$
$$+ h^3\gamma_G \sum_{F \in F_{cut}} \int_F [\![\delta\nabla(\nabla\mathbf{uN})]\!][\![\nabla\mathbf{P}(\delta\mathbf{u})\mathbf{N}]\!] \, dA \tag{3.2.3}$$

This formulation is an extension of Eqn.(3.2.1) suitable for varying material parameters within a phase. However it should be noted, that subphase constant material properties (within an element) are assumed in any further treatment of Eqn.(3.2.3) in order to simplify the dependencies arising from the spatial gradient of the stress tensor. If material properties would be spatially varying within one element (i.e., below subphase resolution), derivatives of the stress tensor with respect to the material parameters (E, α) arise when computing $\nabla\mathbf{P(u)}$ and its derivative with respect to the state variables $\mathbf{u}$. This is of special importance when performing combined LS-Density TO, as discussed in Section 4.1.3. It is also worth noting that both the displacement gradient based formulation (Eqn.(3.2.1)) and the stress-based formulation (Eqn(3.2.2)) are guaranteed to be strictly positive due to their formulation based on an L^2 norm of the respective quantity. This is an important property for ghost stabilization in order to act as a penalty on the jump terms. The virtual work based formulation, as it is a hybrid formulation, does not necessarily exhibit this property and, therefore, needs to be used with care. As its contributions can also become negative, it can potentially be exploited by the solver to increase the ghost penalization jumps in order to cancel out some other, equal but opposite residual contribution while reducing the overall residual.

3.2.1.4 Shape Function Derivatives

To compute higher-order ghost stabilization terms, higher-order spatial derivatives of discretized quantities are needed (see Eqn.(3.1.10)). Using the chain rule, derivatives of shape functions with respect to natural coordinates and derivatives of natural coordinates with respect to physical coordinates need to be computed. The (first-order) relationship between natural and physical

coordinates for a 3D hexahedral element is defined by the geometric Jacobian $\mathbf{J}$ as [52]:

$$\mathbf{J} = \begin{bmatrix} \dfrac{\partial X_1}{\partial \xi} & \dfrac{\partial X_2}{\partial \xi} & \dfrac{\partial X_3}{\partial \xi} \\[2ex] \dfrac{\partial X_1}{\partial \eta} & \dfrac{\partial X_2}{\partial \eta} & \dfrac{\partial X_3}{\partial \eta} \\[2ex] \dfrac{\partial X_1}{\partial \zeta} & \dfrac{\partial X_2}{\partial \zeta} & \dfrac{\partial X_3}{\partial \zeta} \end{bmatrix} \tag{3.2.4}$$

where ξ, η, ζ are the natural coordinates in X_1, X_2, and X_3 direction, respectively. Consequently, the first-order derivatives of shape functions with respect to physical coordinates are obtained from:

$$\begin{bmatrix} \dfrac{\partial N_i}{\partial X_1} \\[2ex] \dfrac{\partial N_i}{\partial X_2} \\[2ex] \dfrac{\partial N_i}{\partial X_3} \end{bmatrix} = \mathbf{J}^{-1} \begin{bmatrix} \dfrac{\partial N_i}{\partial \xi} \\[2ex] \dfrac{\partial N_i}{\partial \eta} \\[2ex] \dfrac{\partial N_i}{\partial \zeta} \end{bmatrix} \tag{3.2.5}$$

where the derivatives of shape functions with respect to natural coordinates are omitted here for brevity.

A similar concept is applied to obtain second-order spatial derivatives of shape functions with respect to physical coordinates. Following the work of [193], a second-order geometric Jacobian matrix $\bar{\mathbf{J}}$ is defined as:

$$\bar{\mathbf{J}} = \begin{bmatrix} \left(\dfrac{\partial X_1}{\partial \xi}\right)^2 & \left(\dfrac{\partial X_2}{\partial \xi}\right)^2 & \left(\dfrac{\partial X_3}{\partial \xi}\right)^2 & 2\dfrac{\partial X_1}{\partial \xi}\dfrac{\partial X_2}{\partial \xi} & 2\dfrac{\partial X_1}{\partial \xi}\dfrac{\partial X_3}{\partial \xi} & 2\dfrac{\partial X_2}{\partial \xi}\dfrac{\partial X_3}{\partial \xi} \\[2ex] \left(\dfrac{\partial X_1}{\partial \eta}\right)^2 & \left(\dfrac{\partial X_2}{\partial \eta}\right)^2 & \left(\dfrac{\partial X_3}{\partial \eta}\right)^2 & 2\dfrac{\partial X_1}{\partial \eta}\dfrac{\partial X_2}{\partial \eta} & 2\dfrac{\partial X_1}{\partial \eta}\dfrac{\partial X_3}{\partial \eta} & 2\dfrac{\partial X_2}{\partial \eta}\dfrac{\partial X_3}{\partial \eta} \\[2ex] \left(\dfrac{\partial X_1}{\partial \zeta}\right)^2 & \left(\dfrac{\partial X_2}{\partial \zeta}\right)^2 & \left(\dfrac{\partial X_3}{\partial \zeta}\right)^2 & 2\dfrac{\partial X_1}{\partial \zeta}\dfrac{\partial X_2}{\partial \zeta} & 2\dfrac{\partial X_1}{\partial \zeta}\dfrac{\partial X_3}{\partial \zeta} & 2\dfrac{\partial X_2}{\partial \zeta}\dfrac{\partial X_3}{\partial \zeta} \\[2ex] \dfrac{\partial X_1}{\partial \xi}\dfrac{\partial X_1}{\partial \eta} & \dfrac{\partial X_2}{\partial \xi}\dfrac{\partial X_2}{\partial \eta} & \dfrac{\partial X_3}{\partial \xi}\dfrac{\partial X_3}{\partial \eta} & \dfrac{\partial X_1}{\partial \xi}\dfrac{\partial X_2}{\partial \eta}+\dfrac{\partial X_2}{\partial \xi}\dfrac{\partial X_1}{\partial \eta} & \dfrac{\partial X_1}{\partial \xi}\dfrac{\partial X_3}{\partial \eta}+\dfrac{\partial X_3}{\partial \xi}\dfrac{\partial X_1}{\partial \eta} & \dfrac{\partial X_2}{\partial \xi}\dfrac{\partial X_3}{\partial \eta}+\dfrac{\partial X_3}{\partial \xi}\dfrac{\partial X_2}{\partial \eta} \\[2ex] \dfrac{\partial X_1}{\partial \xi}\dfrac{\partial X_1}{\partial \zeta} & \dfrac{\partial X_2}{\partial \xi}\dfrac{\partial X_2}{\partial \zeta} & \dfrac{\partial X_3}{\partial \xi}\dfrac{\partial X_3}{\partial \zeta} & \dfrac{\partial X_1}{\partial \xi}\dfrac{\partial X_2}{\partial \zeta}+\dfrac{\partial X_2}{\partial \xi}\dfrac{\partial X_1}{\partial \zeta} & \dfrac{\partial X_1}{\partial \xi}\dfrac{\partial X_3}{\partial \zeta}+\dfrac{\partial X_3}{\partial \xi}\dfrac{\partial X_1}{\partial \zeta} & \dfrac{\partial X_2}{\partial \xi}\dfrac{\partial X_3}{\partial \zeta}+\dfrac{\partial X_3}{\partial \xi}\dfrac{\partial X_2}{\partial \zeta} \\[2ex] \dfrac{\partial X_1}{\partial \eta}\dfrac{\partial X_1}{\partial \zeta} & \dfrac{\partial X_2}{\partial \eta}\dfrac{\partial X_2}{\partial \zeta} & \dfrac{\partial X_3}{\partial \eta}\dfrac{\partial X_3}{\partial \zeta} & \dfrac{\partial X_1}{\partial \eta}\dfrac{\partial X_2}{\partial \zeta}+\dfrac{\partial X_2}{\partial \eta}\dfrac{\partial X_1}{\partial \zeta} & \dfrac{\partial X_1}{\partial \eta}\dfrac{\partial X_3}{\partial \zeta}+\dfrac{\partial X_3}{\partial \eta}\dfrac{\partial X_1}{\partial \zeta} & \dfrac{\partial X_2}{\partial \eta}\dfrac{\partial X_3}{\partial \zeta}+\dfrac{\partial X_3}{\partial \eta}\dfrac{\partial X_2}{\partial \zeta} \end{bmatrix} \tag{3.2.6}$$

With that, the second-order derivatives of shape functions with respect to physical coordinates are

obtained by solving the following linear system:

$$
\begin{bmatrix}
\dfrac{\partial^2 N_i}{\partial X_1 \partial X_1} \\[2ex]
\dfrac{\partial^2 N_i}{\partial X_2 \partial X_2} \\[2ex]
\dfrac{\partial^2 N_i}{\partial X_3 \partial X_3} \\[2ex]
\dfrac{\partial^2 N_i}{\partial X_1 \partial X_2} \\[2ex]
\dfrac{\partial^2 N_i}{\partial X_1 \partial X_3} \\[2ex]
\dfrac{\partial^2 N_i}{\partial X_2 \partial X_3}
\end{bmatrix}
= \bar{\mathbf{J}}^{-1}
\left[
\begin{pmatrix}
\dfrac{\partial^2 N_i}{\partial \xi \partial \xi} \\[2ex]
\dfrac{\partial^2 N_i}{\partial \eta \partial \eta} \\[2ex]
\dfrac{\partial^2 N_i}{\partial \zeta \partial \zeta} \\[2ex]
\dfrac{\partial^2 N_i}{\partial \xi \partial \eta} \\[2ex]
\dfrac{\partial^2 N_i}{\partial \xi \partial \zeta} \\[2ex]
\dfrac{\partial^2 N_i}{\partial \eta \partial \zeta}
\end{pmatrix}
-
\begin{pmatrix}
\dfrac{\partial^2 X_1}{\partial \xi \partial \xi} & \dfrac{\partial^2 X_2}{\partial \xi \partial \xi} & \dfrac{\partial^2 X_3}{\partial \xi \partial \xi} \\[2ex]
\dfrac{\partial^2 X_1}{\partial \eta \partial \eta} & \dfrac{\partial^2 X_2}{\partial \eta \partial \eta} & \dfrac{\partial^2 X_3}{\partial \eta \partial \eta} \\[2ex]
\dfrac{\partial^2 X_1}{\partial \zeta \partial \zeta} & \dfrac{\partial^2 X_2}{\partial \zeta \partial \zeta} & \dfrac{\partial^2 X_3}{\partial \zeta \partial \zeta} \\[2ex]
\dfrac{\partial^2 X_1}{\partial \xi \partial \eta} & \dfrac{\partial^2 X_2}{\partial \xi \partial \eta} & \dfrac{\partial^2 X_3}{\partial \xi \partial \eta} \\[2ex]
\dfrac{\partial^2 X_1}{\partial \xi \partial \zeta} & \dfrac{\partial^2 X_2}{\partial \xi \partial \zeta} & \dfrac{\partial^2 X_3}{\partial \xi \partial \zeta} \\[2ex]
\dfrac{\partial^2 X_1}{\partial \eta \partial \zeta} & \dfrac{\partial^2 X_2}{\partial \eta \partial \zeta} & \dfrac{\partial^2 X_3}{\partial \eta \partial \zeta}
\end{pmatrix}
\cdot
\begin{pmatrix}
\dfrac{\partial N_i}{\partial X_1} \\[2ex]
\dfrac{\partial N_i}{\partial X_2} \\[2ex]
\dfrac{\partial N_i}{\partial X_3}
\end{pmatrix}
\right]
\tag{3.2.7}
$$

This approach is used in this thesis to compute the second-order shape function derivatives of Lagrange and Serendipity elements in 2D and 3D (i.e., 4 node quadrilateral, 8 node quadrilateral, 8 node hexahedral, and 20 node hexahedral elements).

3.2.2   Mesh Refinement Studies

To verify the performance of higher-order XFEM, mesh refinement studies are conducted. First, the effectiveness of face-oriented ghost stabilization introduced in Section 3.2.1 is demonstrated and ghost stabilized XFEM results are compared against analytical solutions. Then an h-refinement study is performed to investigate the convergence rates of first- and second-order XFEM simulations.

3.2.2.1   Verification of Higher-Order Ghost Stabilization

To verify the higher-order ghost stabilization introduced in Section 3.2.1 against analytical solutions, a spherical inclusion of radius $a = 0.5$ embedded in an infinitely large host matrix is used. The problem setup, with dimensions, is shown in Figure 3.2 (a). The L^2 error norm of the solution field and the H^1 error semi-norm of the solution field gradient are computed in the entire domain.
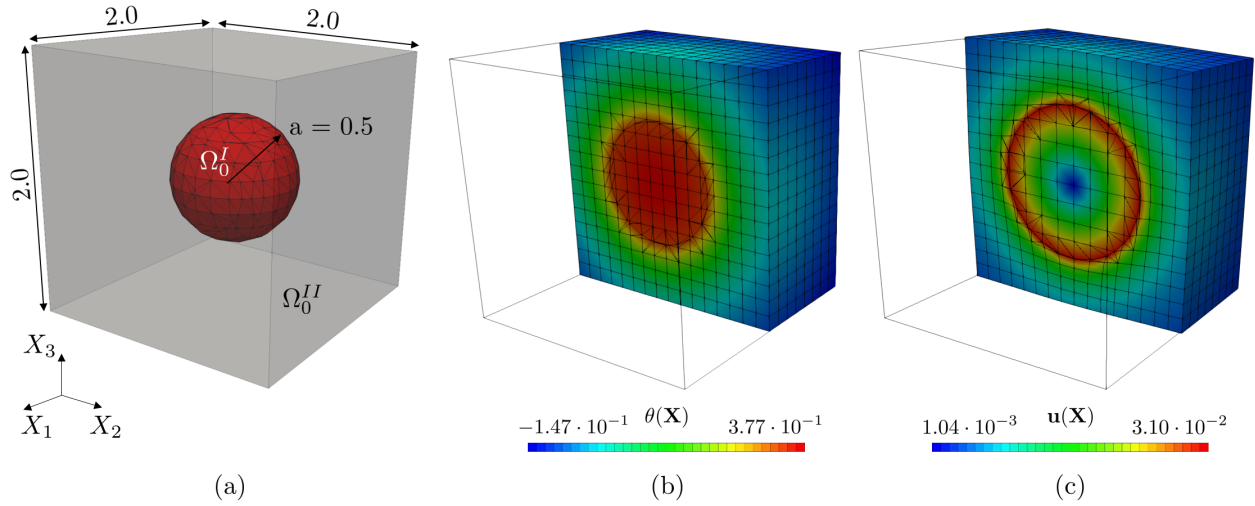
Figure 3.2: Spherical inclusion problem in cubical host matrix. (a) Problem setup, (b) linear diffusion solution (cut-away view), and (c) warped mechanical solution (cut-away view).

Those (absolute) error norms are defined as:

$$\text{Absolute } L^2 \text{ Error Norm } = \sqrt[2]{\int_{\Omega_0} (\mathbf{u} - \bar{\mathbf{u}})^2 dV} \tag{3.2.8}$$

and

$$\text{Absolute } H^1 \text{ Error Semi-Norm } = \sqrt[2]{\int_{\Omega_0} (\nabla\mathbf{u} - \nabla\bar{\mathbf{u}})^2 dV} \tag{3.2.9}$$

where $\bar{\mathbf{u}}$ and $\nabla\bar{\mathbf{u}}$ are the prescribed analytical solution and the prescribed solution gradient, respectively. To demonstrate robustness of the face-oriented ghost stabilization, randomly perturbed center locations of the spherical inclusion are used during the subsequent mesh refinement studies. This shows the effectiveness of the stabilization in the presence of critical intersection configurations.

For both the linear heat conduction problem and the mechanical problems considered in this study, analytical reference solutions defined on an infinitely large host domain are used. To draw correct comparisons between analytical solutions and XFEM solutions, "infinity" boundary conditions need to be applied in the numerical model. This is achieved by prescribing the analytical solution as a Dirichlet boundary condition weakly along all six phases of the cubical simulation domain of size $2.0 \times 2.0 \times 2.0$. For all subsequent studies discussed in the following, a ghost penalty parameter of $\gamma_G = 0.001$ is used.

Heat Conduction

For the heat conduction problem, the host matrix is a finite domain (phase II) with a conductivity of $\kappa = 0.125$ and no volumetric heat flux (i.e., $Q = 0.0$). The inclusion is modeled by a spherical domain (phase I) which has a conductivity of $\kappa = 1.0$ and a volumetric heat flux of $Q = 1.0$. Within the XFEM framework, interface conditions and boundary conditions are applied weakly using Nitsche's method (see Section 3.1.2). An analytical solution is developed for a linear heat conduction problem of a heated spherical inclusion in an infinite host domain.

In Cartesian coordinates, the strong form of the 1D heat conduction equation with constant generation is:

$$\frac{d^2\theta}{dX^2} + \frac{Q}{\kappa} = 0 \tag{3.2.10}$$

with the solution $\theta(X) = -\frac{QX^2}{2\kappa} + AX + B$. The integration constants are denoted by A and B which depend on the boundary and interface conditions. In spherical coordinates, Eqn.(3.2.10) becomes:

$$\frac{d}{dR}\left(\frac{d\theta}{dR}\right) + R^2\frac{Q}{\kappa} = 0 \tag{3.2.11}$$

The general solution of Eqn.(3.2.11) is $\theta(R) = -\frac{QR^2}{6\kappa} + \frac{A}{R} + B$ and the integration constants are determined by the following boundary conditions:

- Prescribed temperature at the origin: $\theta(R)|_{R=0} = 0.375$

- Zero temperature gradient at the origin: $\left.\frac{d\theta(R)}{dR}\right|_{R=0} = 0.0$

- Temperature continuity at the material interface: $\left.\theta^I(R)\right|_{R=a} = \left.\theta^{II}(R)\right|_{R=a}$

- Temperature gradient continuity at the material interface: $\left.\frac{d\theta^I(R)}{dR}\right|_{R=a} = \left.\frac{d\theta^{II}(R)}{dR}\right|_{R=a}$

Using the coordinate transformation between Cartesian and spherical coordinates, the analytical temperature in phase I in spherical coordinates is:

$$\theta^I(R) = -\frac{R^2}{6} + \frac{3}{8} \tag{3.2.12}$$

In phase II, the host matrix, it is:

$$\theta^{II}(R) = \frac{1}{3R} - \frac{1}{3} \tag{3.2.13}$$

where the radius is computed as $R(X_1, X_2, X_3) = \sqrt{(X_1 - X_{1_c})^2 + (X_2 - X_{2_c})^2 + (X_3 - X_{3_c})^2}$. The randomly perturbed center coordinates of the spherical inclusion are denoted by X_{1_c}, X_{2_c} and X_{3_c}, respectively. Similarly, the analytical temperature gradient in phase I is obtained as:

$$\frac{d\theta^I(R)}{d\mathbf{X}} = \frac{d\theta^I(R)}{dR} \frac{dR}{d\mathbf{X}} \tag{3.2.14}$$

where $\frac{d\theta^I(R)}{dR} = -\frac{R}{3}$ and $\frac{dR}{d\mathbf{X}} = \frac{\mathbf{X} - \mathbf{X}_c}{R}$. The analytical temperature gradient in phase II is obtained by:

$$\frac{d\theta^{II}(R)}{d\mathbf{X}} = \frac{d\theta^{II}(R)}{dR} \frac{dR}{d\mathbf{X}} \tag{3.2.15}$$

with $\frac{d\theta^{II}(R)}{dR} = -\frac{1}{3R^2}$.

Using the heat conduction problem setup and the analytical solution developed above as a reference, a mesh refinement study is conducted. The goal of the study is to understand the influence of the higher-order ghost stabilization on the temperature solution, its spatial gradient, and the condition number of the linear system as linear and quadratic XFEM meshes are refined. Element edge lengths of $h = [0.5, 0.25, 0.125, 0.0625]$ are used.

As can be seen from Figure 3.3 (a) and (b), second-order ghost stabilization has no significant effect on the convergence behavior of the L^2 norm and the H^1 semi-norm of the temperature field, respectively. Also, comparing the convergence behavior of quadratic versus linear XFEM elements shows only marginal differences. This is not expected and will be investigated in more detail in Section 3.2.2.2. However, a significant effect of higher-order ghost stabilization on the condition number is seen (see Figure 3.3 (c)). An increased condition number is expected when using higher-order (e.g., HEX20) elements, due to the increased number of DOFs per element. This drawback is almost entirely compensated through the use of second-order ghost stabilization, as can be seen from Figure 3.3 (c), where reasonable condition numbers are achieved through face-oriented ghost stabilization.
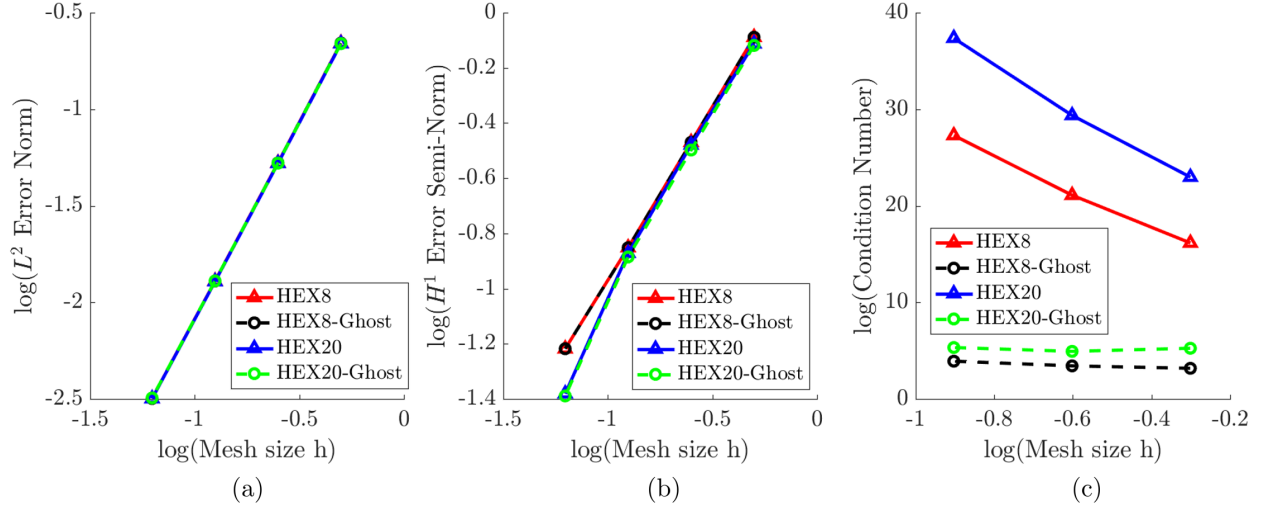
Figure 3.3: Mesh refinement results for the heat conduction problem. (a) L^2 error norm, (b) H^1 error semi-norm, and (c) condition number with and without ghost stabilization.

Linear Elasticity

A similar approach as for the heat conduction problem is followed to study the effect of higher-order ghost penalization for linear elastic problems. For that, both the inclusion material and the host matrix have an elastic modulus of $E = 10.0$ and a Poisson's ratio of $\nu = 0.3$. The inclusion material has a CTE of $\alpha^I = 0.1$, while the host matrix has no eigenstrain (i.e., $\alpha^{II} = 0.0$). Interface and boundary conditions are weakly enforced via Nitsche's method.

An analytical solution for stress and strain fields of a spherical inclusion embedded in an infinite linear elastic isotropic solid was first derived by [194]. This approach is the basis for the derivation of a linear elastic reference solution, which is summarized (in index notation) in the following. A constant eigenstrain is assumed in phase I, defined as:

$$\bar{\epsilon}_{ij}^I = \alpha^I \delta_{ij} \tag{3.2.16}$$

The uniform strain field within the spherical inclusion is obtained from the Eshelby tensor S_{ijkl}^* as:

$$\epsilon_{ij}^I = S_{ijkl}^* \bar{\epsilon}_{kl}^I \tag{3.2.17}$$

where the (constant) fourth-order Eshelby tensor for a spherical inclusion is computed as:

$$S^*_{ijkl} = \frac{5\nu - 1}{15(1 - \nu)}\delta_{ij}\delta_{kl} + \frac{4 - 5\nu}{15(1 - \nu)}(\delta_{ik}\delta_{jl} + \delta_{il}\delta_{jk}) \tag{3.2.18}$$

The analytical reference displacement within the spherical inclusion (i.e., Ω_0^I) is then obtained by integration of the strain field (assuming zero displacement at the origin):

$$u_i^I(\mathbf{X}) = \epsilon_{ij}^I X_j \tag{3.2.19}$$

The spatial derivative of the displacement field is equal to the strain field:

$$\frac{\partial u_i^I}{\partial X_j} = \epsilon_{ij}^I \tag{3.2.20}$$

Following the work of [133], an analytical solution for stress and strain fields outside the spherical inclusion, in the infinite host matrix, can also be obtained. From that, the analytical displacement field is obtained using Papkovich-Neuber potentials [149, 135]. A transformation stress $\bar{\sigma}_{ij}^I$ is computed using the isotropic eigenstrain $\bar{\epsilon}_{ij}^I$ as [23]:

$$\bar{\sigma}_{ij}^I = \frac{E}{1 + \nu}\left(\bar{\epsilon}_{ij}^I + \frac{\nu}{1 - 2\nu}\bar{\epsilon}_{kk}^I\delta_{ij}\right) \tag{3.2.21}$$

The resulting Papkovich-Neuber potentials $(\Psi_{PN})_i$ and ϕ_{PN} are computed as:

$$(\Psi_{PN})_i = \frac{a^3\bar{\sigma}_{ij}X_j}{3R^3} \quad \text{and} \quad \phi_{PN} = \frac{a^3\bar{\sigma}_{ij}}{15R^3}\left((5R^2 - a^2)\delta_{ij} + 3a^2\frac{X_iX_j}{R^2}\right) \tag{3.2.22}$$

where the distance from the origin is denoted by $R = \sqrt{X_kX_k}$ and $a = 0.5$ is the inclusion radius. The displacement field outside the spherical inclusion is then obtained using:

$$u_i^{II}(\mathbf{X}) = \frac{2(1 + \nu)}{E}\left((\Psi_{PN})_i + \frac{1}{4(1 - \nu)\frac{\partial}{\partial X_i}(\phi_{PN} - (\Psi_{PN})_kX_k)}\right) \tag{3.2.23}$$

Combining Eqn.(3.2.22) and Eqn.(3.2.23) finally yields the displacement field outside the spherical inclusion (i.e., Ω_0^{II}) as:

$$u_i^{II}(\mathbf{X}) = \frac{(1 + \nu)a^3}{2(1 - \nu)E}\left(\frac{2\bar{\sigma}_{ik}X_k + \bar{\sigma}_{kk}X_i}{15R^5}(3a^2 - 5R^2) + \frac{\bar{\sigma}_{jk}X_iX_jX_k}{R^7}(R^2 - a^2) + \frac{4(1 - \nu)\bar{\sigma}_{ik}X_k}{3R^3}\right)$$

$$\tag{3.2.24}$$
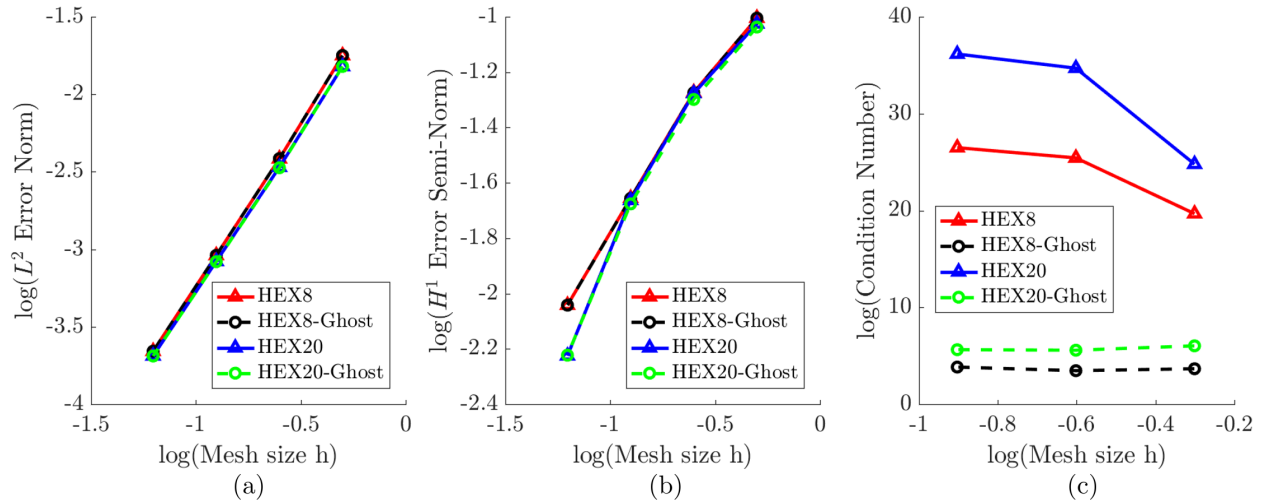
Figure 3.4: Mesh refinement results for the linear elastic problem. (a) L^2 error norm, (b) H^1 error semi-norm, and (c) condition number with and without ghost stabilization.

The spatial derivative of Eqn.(3.2.24), $\partial u_i^{II}/\partial X_j$, is obtained using symbolic differentiation and omitted here for brevity.

Similar to the heat conduction case, a mesh refinement study is conducted and compared against the analytical solution developed above. The same mesh sizes as in the heat conduction case are used. The results of the mesh refinement study for the linear elastic spherical inclusion with eigenstrain embedded in an infinite host matrix are shown in Figure 3.4. In order to simulate an infinite host domain, the analytical reference solution (Eqn.(3.2.24)) is applied to the six faces of the domain boundary of the XFEM mesh as a weak Dirichlet boundary condition. Similar to Figure 3.3, very little influence of higher-order ghost stabilization is seen on the convergence behavior of the L^2 norm and H^1 semi-norm. See Figure 3.4 (a) and (b), respectively. Since a much higher convergence rate is expected when using quadratic elements, further analyses are performed in Section 3.2.2.2 to understand the observed behavior. With respect to the condition number, a large improvement is observed when using higher-order ghost stabilization in combination with quadratic XFEM elements (see Figure 3.4 (c)).

Nonlinear Hyperelasticity

To understand the impact of higher-order ghost stabilization on nonlinear hyperelasticity considering large deformation, a similar mesh-refinement study is repeated. Due to the lack of an analytical solution for a nonlinear hyperelastic case, the previously developed linear elastic reference solution is used. In order for this to be valid, the isotropic eigenstrain in the spherical inclusion is reduced to $\alpha = 0.01$. The results of this mesh refinement study are presented in Figure 3.5. Mesh sizes of $h = [0.5, 0.25, 0.125]$ are used.

As in the previous studies, only marginal effects of higher-order ghost stabilization are observed with respect to the convergence behavior of L^2 norm and H^1 semi-norm. The fact that no increased convergence rates are obtained for higher-order XFEM with h-refinement has previously been reported by [172, 130] for cases when an element is sub-divided only using straight faces. See Figure 3.5 (a) and (b), respectively. A drastic reduction in condition number is, however, seen for both linear and quadratic elements when face-oriented ghost penalization is applied. This is especially critical for nonlinear analyses as a well-conditioned matrix is crucial to facilitate convergence of an iterative nonlinear solver (e.g., Newton-Raphson).
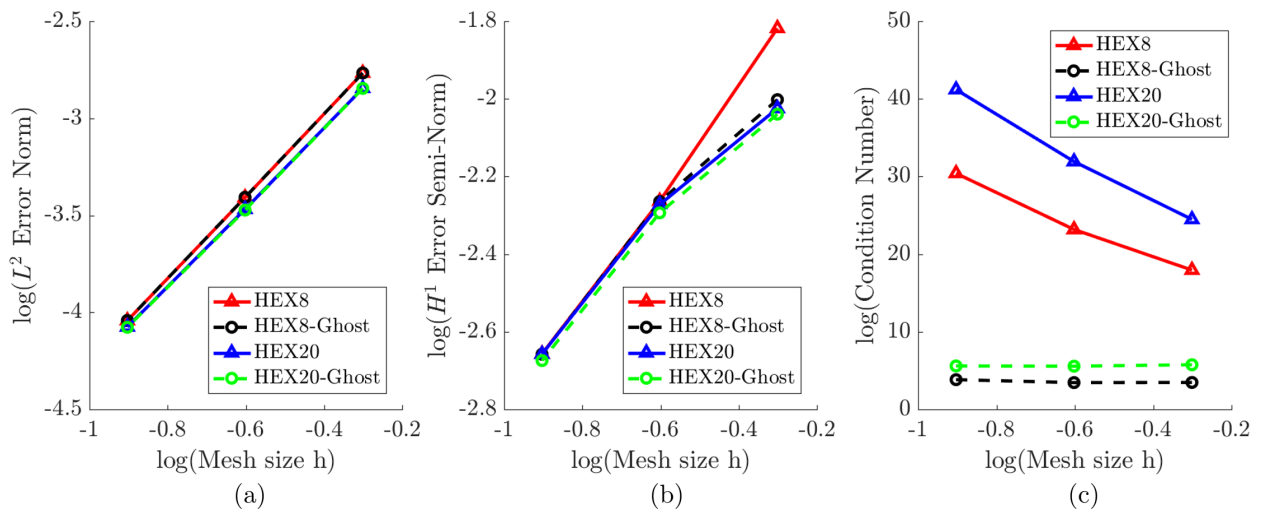
Figure 3.5: Mesh refinement results for the nonlinear hyperelastic problem. (a) L^2 error norm, (b) H^1 error semi-norm, and (c) condition number with and without ghost stabilization.

3.2.2.2   Mesh Refinement Studies using Higher-Order XFEM

The convergence behavior of higher-order XFEM elements with mesh refinement is studied in this section. To achieve that, a pseudo-1D linear elastic bar problem is studied with a quadratic, space dependent body force $b = 2.0(X_1)^2$ applied. The 1D bar governing equation is stated as:

$$\frac{EA}{L}\frac{d^2u}{dX_1^2} + b = 0 \tag{3.2.25}$$

with homogenous Dirichlet boundary conditions applied at $X_1 = 0.0$. The Young's modulus used is $E = 10.0$, the Poisson's ratio is $\nu = 0.0$ (to have no 3D effects), and the cross-sectional area is $A = 0.25$. A unit-length is assumed for the bar (i.e., $L = 1.0$). The analytical displacement solution of this second-order differential equation is given by a fourth-order polynomial as:

$$u(X_1) = \frac{b}{12EA}\left(4L^3X_1 - (X_1)^4\right) \tag{3.2.26}$$

From Eqn.(3.2.26) the analytical 1D displacement gradient is a third-order polynomial given as:

$$\frac{du(X_1)}{dX_1} = \frac{b}{3EA}\left(L^3 - (X_1)^3\right) \tag{3.2.27}$$

Using Eqn.(3.2.26) and Eqn.(3.2.27) as a reference solution, L^2 error norms and H^1 error semi-norms are computed in the following sections for different interface geometries. In order for the previously developed 1D reference solution to be valid, the same material properties are used in Ω_0^I and Ω_0^{II} and only the interface geometry in between them is varied.

Planar Interface Geometries

First, a set of simple (planar) interface geometries are considered for a mesh refinement study as shown in Figure 3.6. Planar intersections in the X_1, X_2, and X_3 plane are studied as shown in Figure 3.6 (a), (b), and (c), respectively. Moreover, an inclined plane as depicted in Figure 3.6 (d) is studied. Mesh sizes of $h = [0.5, 0.25, 0.125, 0.0625, 0.03125]$ are used. The convergence rates of the L^2 error norm and H^1 error semi-norm with mesh refinement are shown in Figure 3.7. It can clearly be seen that regardless of the intersection configuration, the expected convergence rates of
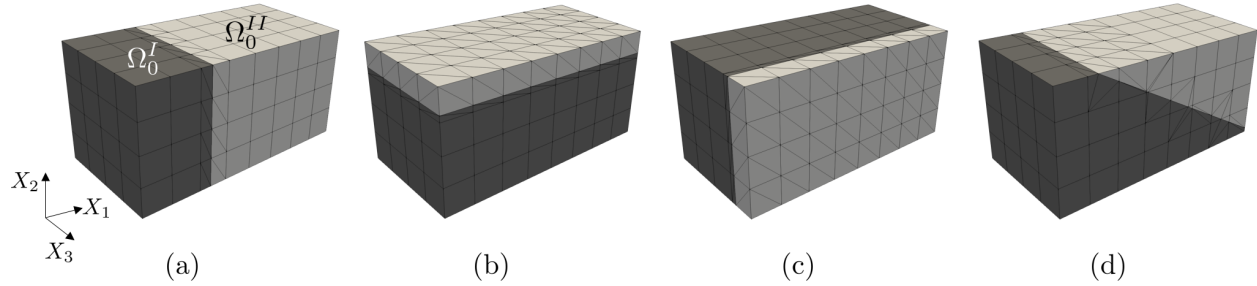
Figure 3.6: Simple planar interface geometries for the pseudo 1D bar problem. (a) Plane in X_1 direction, (b) plane in X_2 direction, and (c) plane in X_3 direction, (d) inclined plane in $X_1 - X_2$ direction.

about 2.0 and 3.0 are obtained in the L^2 error norms for linear and quadratic elements, respectively. Similarly, the expected convergence rates of about 1.0 and 2.0 are achieved in the H^1 semi-norms, again for linear and quadratic elements, respectively. This first study successfully demonstrates the expected convergence behavior of higher-order XFEM for a set of simple interface geometries.
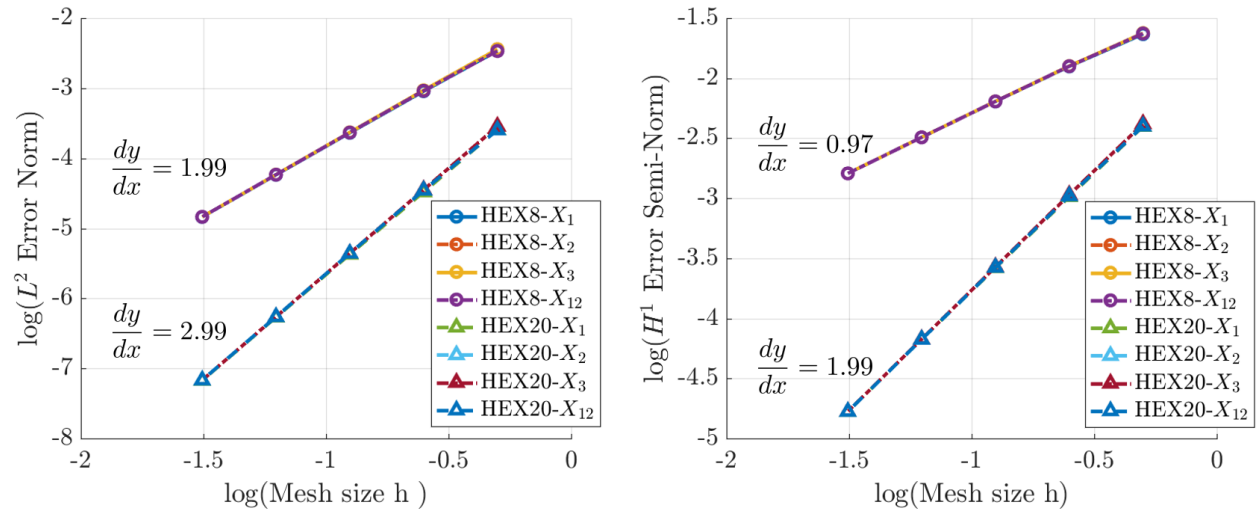
Figure 3.7: Mesh refinement results for different planar intersection configurations using a pseudo 1D bar problem. (a) L^2 error norm and (b) H^1 error semi-norm.

Spherical Interface Geometry

The same mesh refinement study is repeated for a spherical inclusion in the rectangular domain used before. The domain decomposition for mesh sizes of $h = [0.5, 0.25, 0.125, 0.0625]$ is shown in Figure 3.8. Using the coarsest mesh (Figure 3.8 (a)) as a starting point, two different refinement studies are performed. First, both the spatial discretization and the geometric representation of the immersed sphere are refined simultaneously (see Figure 3.8 (b)). This is done by default when using XFEM for geometric representation, as the accuracy at which an immersed geometry is discretized highly depends on the discretization of the background mesh. Secondly, only the spatial discretization of the XFEM is refined while the immersed sphere geometry is kept constant (see Figure 3.8 (c)). This is achieved by interpolating the nodal LS field, which defines the material interface $\Gamma_0^{I,II}$, from the coarsest mesh (Figure 3.8 (a)) to all finer meshes, without re-computing the nodal LS values using a new (finer) background mesh. The L^2 norm and H^1 semi-norm results of both refinement strategies are shown in Figure 3.9 for linear and quadratic elements.

It can be seen that for linear background elements regardless of the refinement approach, the
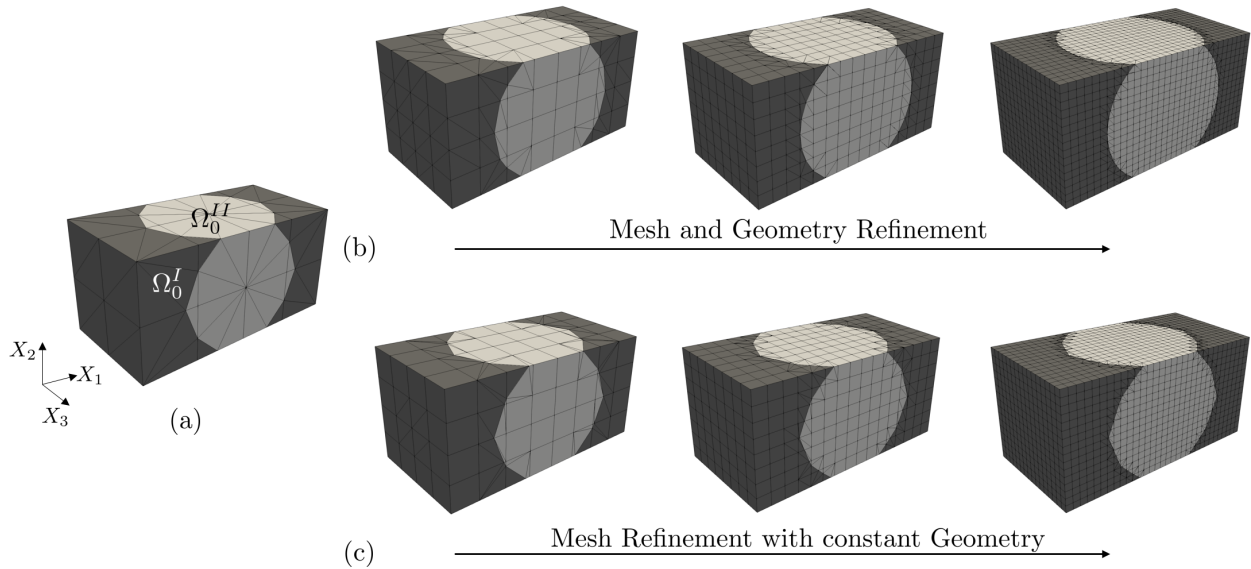
Figure 3.8: Pseudo 1D bar problem with a spherical inclusion. (a) Coarsest mesh as a starting point, (b) simultaneous mesh and geometry refinement, and (c) mesh refinement with constant geometry.
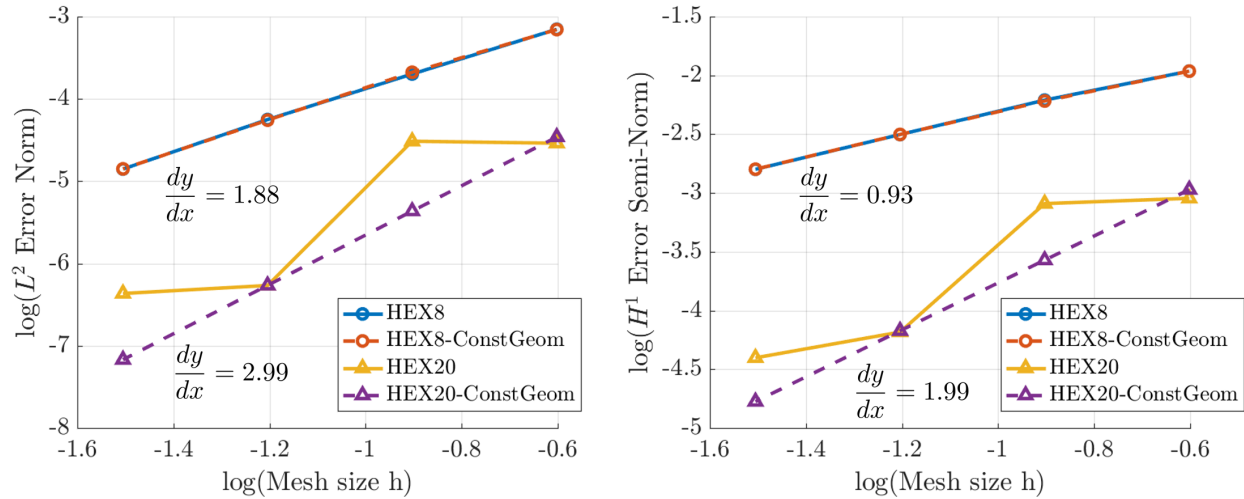
Figure 3.9: Mesh refinement results for the pseudo 1D bar problem with a spherical inclusion using different refinement approaches. (a) L^2 error norm and (b) H^1 error semi-norm.

expected convergence rates of about 2.0 and 1.0 are obtained in the L^2 norm and H^1 semi-norm, respectively. For quadratic elements, when the mesh and the geometry is refined simultaneously, degenerated convergence rates are obtained (see Figure 3.9 (a) and (b)). When the geometry is kept constant at the initial representation of the spherical inclusion stemming from the coarsest mesh, expected higher-order convergence rates are obtained for quadratic elements. This can be explained by the fact that the initial geometric representation has straight faces and only captures the spherical geometry roughly in form of a diamond. As this interface representation is constant throughout mesh-refinement, the interface geometry does not change and can be fully captured regardless of the mesh size of the background elements. In case of a changing interface geometry, linear/planar intersections insufficiently capture the geometry of the sphere and only converge to a truly spherical representation of the shape with mesh refinement. This means, depending on the level of refinement of the background mesh, a different representation of the spherical inclusion is captured. Therefore, a different XFEM problem is solved at every step of the refinement process and a comparison between the differently refined meshes is not meaningful. Higher-order convergence rates can, therefore, not be expected if both the spatial discretization and the geometric representation are refined at the same time. To mitigate this large dependency of the geometric representation on the background

discretization, curved interface capturing is required when using higher-order XFEM. The identified need for consistent geometric representation of an (in general curved) interface in order to obtain improved convergence rates with higher-order XFEM discretization is in agreement with findings reported by [113, 34]. The results of this study also explain why no higher-order convergence rates were obtained in Section 3.2.2.1 where simultaneous refinement of the background mesh and the spherical inclusion geometry was performed, despite the fact that quadratic XFEM elements were employed.

3.2.3   Higher-Order XFEM for Slender Structures

Besides increasing accuracy, higher-order spatial interpolation also mitigates numerical artifacts like shear locking when modeling slender structures [49, 87]. This is a well-known approach to circumvent the modeling deficiency of low-order finite elements. When using the XFEM for modeling slender structures, a similar effect is observed as shown in Figure 3.10. A bi-layer cantilevered beam of dimensions $80.0 \times 2.5 \times 1.0$ is modeled with linear and quadratic XFEM elements. The beam consists of two distinct material layers where the top layer (Ω_0^I) has a Young's modulus of $E = 0.6$, a Poisson's ratio of $\nu = 0.0$, and a uniaxial eigenstrain of 0.045 in X_1 direction. The bottom layer (Ω_0^{II}) has a Young's modulus of $E = 6.0$, a Poisson's ratio of $\nu = 0.0$ but no eigenstrain. Isotropic expansion of the top layer due to its eigenstrain causes downward curling of the beam. A strong influence of spatial discretization on the deformation of the beam is observed, especially when using linear hexahedral elements (see Figure 3.10 beams in red). Even for a highly refined mesh, the linear XFEM elements do not converge towards the analytical Timoshenko beam model prediction. However, using quadratic 20 node hexahedral Serendipity elements leads to a much faster convergence towards the analytical beam model prediction. Even for the coarsest mesh considered in this study, a much better prediction by the XFEM is obtained. To quantify the superiority of higher-order XFEM for modeling slender structures, a comparison of tip displacement L^2 error norms for both small strain and large strain kinematics models is shown in Table 3.1. It should be noted that each kinematics model is only compared against a consistent beam model based on
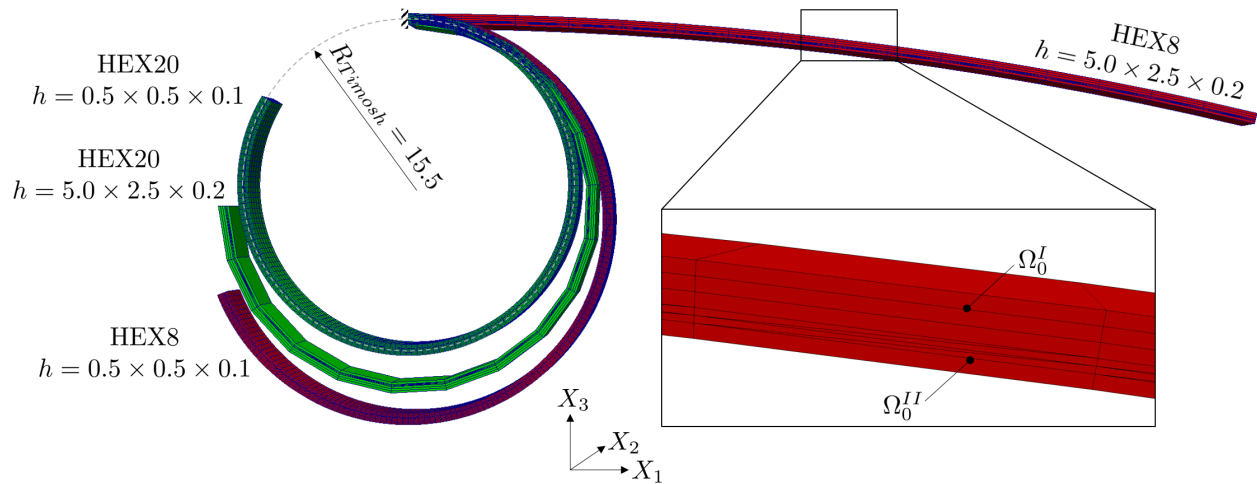
Figure 3.10: Deformation of a bi-layer cantilevered beam using linear and quadratic XFEM element of different mesh sizes.

the same kinematics, as a cross-comparison between small strain and finite strain results would be meaningless.

From Table 3.1 it can be seen that, irrespective of the kinematics model used, a significant underperformance of linear elements is observed due to shear locking. This numerical artifact is reduced with spatial mesh refinement, but never fully vanishes for HEX8 elements. When using quadratic elements, a good prediction of the tip displacement is obtained even with coarse XFEM meshes. Therefore, a strong need for higher-order XFEM is identified when modeling slender structures with solid brick elements in order to obtain realistic performance predictions.

Table 3.1: Comparison of the tip displacement L^2 norm against a 1D Timoshenko model using small deformation and large deformation kinematics.

	Small Deformation		Large Deformation	
Mesh Size	HEX8	HEX20	HEX8	HEX20
h = $5.0 \times 2.5 \times 0.2$	93.6 %	3.7 %	90.1 %	4.3 %
h = $0.5 \times 0.5 \times 0.1$	14.7 %	2.6 %	6.3 %	1.2 %

3.2.4 Local Interpolation Order Reduction

To address ill-conditioning of higher-order XFEM linear systems, local reduction of the spatial interpolation order can be used in addition to higher-order ghost stabilization. This approach initially applied to finite difference schemes [79, 179] was then adopted to XFEM problems for the wave equation by [173]. While only marginally sacrificing convergence rates, a drastic decrease in condition number was reported by [173] for 2D XFEM problems. In order to not have hanging nodes (i.e., nodes which are not shared by all of its neighboring elements) at the transition between, e.g., quadratic elements (p) and linear element ($p-1$), a weakly enforced interpolation constraint is proposed. This scheme allows for operating on a higher-order mesh (i.e., of order p) in the entire domain and only adds additional residual components to elements close to the interface such that their spatial interpolation order is reduced by one order (i.e., $p-1$). Using the weak form of the large strain hyperelastic problem (Eqn.(2.3.27)) as an example, this additional residual contribution is formulated as:

$$R_{Red} = \gamma_R \int_{\Omega_0} \boldsymbol{F}(\delta\tilde{\mathbf{u}}) : \boldsymbol{P}(\tilde{\mathbf{u}})dV \tag{3.2.28}$$

where γ_R is a reduction penalty parameter and the modified displacements $\tilde{\mathbf{u}}$ are obtained from:

$$\tilde{\mathbf{u}} = \left(\sum_{i=1}^{N_N^e} N_i^p - \sum_{i=1}^{N_N^e} N_i^{p-1} \right) \hat{\mathbf{u}}_i \tag{3.2.29}$$

where N_i^p is the vector of shape functions corresponding to the original interpolation order p and N_i^{p-1} is the vector of shape functions corresponding to the reduced interpolation order $p-1$. Similar to Eqn.(3.2.29), a constraint displacement gradient can be obtained, which is the basis for computing the constrained deformation gradient $\boldsymbol{F}(\delta\tilde{\mathbf{u}})$ and the constrained stress tensor $\boldsymbol{P}(\tilde{\mathbf{u}})$ used in Eqn.(3.2.28). It should be noted that while, an increase in stability is seen through this approach, numerical artifacts like shear locking are potentially still exhibited by the reduced-order elements in the vicinity of the interface.

3.3   Enhanced Assumed Strain Method

Before the EAS concept is introduced and applied to XFEM problems, a brief summary of locking phenomena in 3D solid finite elements is given. It should be noted that within the scope of this thesis, only 2D linear elastic problems are considered regarding the EAS method both for classical FEM and for XFEM.

3.3.1   Locking of 3D Solid Finite Elements

Locking is a phenomenon experienced in FE when a severe underestimation of displacements occurs due to overly stiff elements [53]. This is caused by the existence of parasitic strains and stresses caused by the inability of a FE to correctly capture certain deformation modes. Different types of locking exist:

- **Volumetric Locking**: Over-stiffening of a FE with respect to incompressibility of a material ($K \to \infty$, $\nu \to 0.5$). Where K is the bulk modulus and ν is the Poisson's ratio. One way to mitigate these effects is by applying the so-called Incompatible Modes approach by [201] or the EAS method. Alternatively, the F-bar method proposed by [42] can be employed to alleviate volumetric locking.

- **Shear Locking**: Inability of a FE to model pure bending without any shear since both deformations are directly coupled through the element formulation. This is mainly caused by high-aspect ratio elements. It can be cured by Selective Reduced Integration (SRI), the Assumed Natural Strain (ANS) method, the Discrete Strain Gap (DSG) method, the Incompatible Modes method, or the EAS method [98].

- **Trapezoidal Locking**: Occurs if curved structures are modeled using trapezoidal-shaped elements. The driving parameter for this phenomenon is the element aspect ratio and the curvature of the structure. It was first studied by [120, 19] and can be cured by the ANS method and the DSG method.

- **Membrane Locking**: Occurs if element faces of slender structures are warped (do not lay within a plane), when, for example, double-curved structures are modeled. However, implications for tri-linear elements are relatively small. More details regarding this phenomenon and measures to avoid it are found in [98, 99].

It should be noted that the last three locking types listed above are also categorized as geometric locking effects where element over-stiffening occurs due to the violation of certain kinematic constraints. More details regarding locking of 3D solid FEs and numerical approaches to mitigate them can be found in [10, 20].

3.3.2 Classical Enhanced Assumed Strain Method

As the EAS method is most relevant for the work presented in this thesis, a more detailed discussion follows. The EAS method was initially proposed by [171] for 2D linear elasticity and extended to nonlinear kinematics by [169]. The method was then applied to 3D problems by [170] and [9]. The EAS method is formulated based on the Fraeijs de Veubeke-Hu-Washizu (VHW) three-field variational principle. It defines enhanced strains as a field of internal variables which are discontinuous across element boundaries.

3.3.2.1 FE Formulation

The variational basis for the EAS method is the VHW formulation with independent variables $\mathbf{u}, \boldsymbol{\epsilon}, \boldsymbol{\sigma}$, stated as [10]:

$$U_{int}(\mathbf{u}, \boldsymbol{\epsilon}, \boldsymbol{\sigma}) = \int_{\Omega_0} \frac{1}{2}\boldsymbol{\epsilon} : \boldsymbol{D} : \boldsymbol{\epsilon} \, - \, \boldsymbol{\sigma} : \boldsymbol{\epsilon} \, + \, \boldsymbol{\sigma} : \boldsymbol{\epsilon}^u \, dV \tag{3.3.1}$$

where the internal energy is denoted by U_{int} and Dirichlet and Neumann boundary conditions are assumed to be homogeneous. The displacement-based strain is denoted by $\boldsymbol{\epsilon}^u$ and the remaining quantities follow the small strain notation introduced in Section 2.2. Total strain $\boldsymbol{\epsilon}$ is composed of the displacement-based strain $\boldsymbol{\epsilon}^u$ and an enhanced strain $\tilde{\boldsymbol{\epsilon}}$, such that:

$$\boldsymbol{\epsilon} = \boldsymbol{\epsilon}^u + \tilde{\boldsymbol{\epsilon}} \tag{3.3.2}$$

Using Eqn.(3.3.2), Eqn.(3.3.1) becomes:

$$U_{int}(\mathbf{u}, \boldsymbol{\epsilon}, \boldsymbol{\sigma}) = \int_{\Omega_0} \frac{1}{2}(\boldsymbol{\epsilon}^u + \tilde{\boldsymbol{\epsilon}}) : \boldsymbol{D} : (\boldsymbol{\epsilon}^u + \tilde{\boldsymbol{\epsilon}}) \ - \boldsymbol{\sigma} : \tilde{\boldsymbol{\epsilon}} \ dV \qquad (3.3.3)$$

Considering the stress orthogonality condition between the independent stress field $\boldsymbol{\sigma}$ and the enhanced strain $\tilde{\boldsymbol{\epsilon}}$:

$$\int_{\Omega_0} \boldsymbol{\sigma} : \tilde{\boldsymbol{\epsilon}} \ dV = 0 \qquad (3.3.4)$$

Eqn.(3.3.3) reduces to a two-field variational form as:

$$U_{int}(\mathbf{u}, \boldsymbol{\epsilon}) = \int_{\Omega_0} \frac{1}{2}(\boldsymbol{\epsilon}^u + \tilde{\boldsymbol{\epsilon}}) : \boldsymbol{D} : (\boldsymbol{\epsilon}^u + \tilde{\boldsymbol{\epsilon}}) \ dV \qquad (3.3.5)$$

where $\boldsymbol{\epsilon}^u = 1/2(\nabla \mathbf{u}^T + \nabla \mathbf{u})$. The enhanced strain is interpolated from nodal internal variables $\hat{\boldsymbol{\alpha}}$ as:

$$\tilde{\boldsymbol{\epsilon}} = \mathbf{M}\hat{\boldsymbol{\alpha}} \qquad (3.3.6)$$

where the interpolation matrix $\mathbf{M}$ is defined as:

$$\mathbf{M} = \frac{\det(\mathbf{J}_c)}{\det(\mathbf{J})}\mathbf{T}_c^{-T}\mathbf{M}_\xi \qquad (3.3.7)$$

where $\mathbf{J}$ is the element Jacobian matrix of the isoparametric map and a subscript c denotes quantities evaluated at the element centroid, i.e., $\xi = \eta = 0$. The properties of $\mathbf{M}$ are such that [182]:

$$\int_{\Omega_0^e} \mathbf{M} \ dV = 0 \qquad (3.3.8)$$

where Ω_0^e denotes the domain of element e. Eqn.(3.3.8) states that enhanced strain contributions $\tilde{\boldsymbol{\epsilon}}$ vanish over an element when the strain field can exactly be represented by the displacement-based strain $\boldsymbol{\epsilon}^u$. Moreover, the transformation matrix $\mathbf{T}_c$ is defined for the 2D case as:

$$\mathbf{T}_c = \begin{bmatrix} (J_{11})^2 & (J_{21})^2 & 2J_{11}J_{21} \\ (J_{12})^2 & (J_{22})^2 & 2J_{12}J_{22} \\ J_{11}J_{12} & J_{21}J_{22} & J_{11}J_{22} + J_{12}J_{21} \end{bmatrix}_{\xi=\eta=0} \qquad (3.3.9)$$

where J_{ij} corresponds to the respective entry of the elemental Jacobian matrix in 2D. The interpolation matrix $\mathbf{M}_\xi$ for a 4 parameter EAS formulation is:

$$\mathbf{M}_\xi = \begin{bmatrix} \xi & 0 & 0 & 0 \\ 0 & 0 & 0 & \eta \\ 0 & \xi & \eta & 0 \end{bmatrix} \tag{3.3.10}$$

It should be noted that the columns of $\mathbf{M}_\xi$ are linearly independent and therefore their order is arbitrary. Using the interpolation of the enhanced strains (Eqn.(3.3.6)) and the classical interpolation of nodal state variables $\hat{\mathbf{u}}$, the extended discretized elemental linear system becomes:

$$\begin{bmatrix} \mathbf{K}_{uu} & \mathbf{K}_{u\alpha} \\ \mathbf{K}_{u\alpha}^T & \mathbf{K}_{\alpha\alpha} \end{bmatrix} \begin{bmatrix} \hat{\mathbf{u}} \\ \hat{\boldsymbol{\alpha}} \end{bmatrix} = \begin{bmatrix} \mathbf{R} \\ \mathbf{0} \end{bmatrix} \tag{3.3.11}$$

where the sub-matrices for linear elasticity under small strains are defined as:

$$\mathbf{K}_{uu} = \int_{\Omega_0^e} \mathbf{B}^T \boldsymbol{D} \mathbf{B} \; dV \tag{3.3.12}$$

$$\mathbf{K}_{\alpha u} = \mathbf{K}_{u\alpha}^T = \int_{\Omega_0^e} \mathbf{B}^T \boldsymbol{D} \mathbf{M} \; dV \tag{3.3.13}$$

$$\mathbf{K}_{\alpha\alpha} = \int_{\Omega_0^e} \mathbf{M}^T \boldsymbol{D} \mathbf{M} \; dV \tag{3.3.14}$$

Due to the discontinuity of the internal variable field, static condensation can be used to eliminate the enhanced strain parameters $\hat{\boldsymbol{\alpha}}$ on an elemental level. This yields the elemental stiffness matrix $\mathbf{K}$ as:

$$\mathbf{K} = \mathbf{K}_{uu} - \mathbf{K}_{\alpha u}^T \mathbf{K}_{\alpha\alpha}^{-1} \mathbf{K}_{\alpha u} \tag{3.3.15}$$

Because of the elemental condensation of the enhanced strain internal variables, the EAS formulation can conveniently be included in any existing computational FEM framework.

3.3.3   Enhanced Assumed Strain Method for XFEM

To extend the EAS method to XFEM, where intra-element discontinuities are considered, the approach proposed by [46] for quadrilateral elements with discontinuous strain enhancement is followed. A general review of enhanced element formulations with discontinuities can be found in [92]. A generalized Heaviside enrichment strategy (see Section 3.1.1) is applied to both the state variables and the EAS internal variables. Extending the EAS interpolation condition (Eqn.(3.3.8)) to allow for intra-element discontinuities, a piecewise constant stress field is assumed in intersected elements, such that:

$$\int_{\Omega_0^{I^e}} \mathbf{M}\ dV = 0 \quad , \qquad \int_{\Omega_0^{II^e}} \mathbf{M}\ dV = 0 \tag{3.3.16}$$

where $\Omega_0^{I^e}$ and $\Omega_0^{II^e}$ denote the complementary sub-regions of an intersected element corresponding to phase I and phase II, respectively, such that $\Omega_0^e = \Omega_0^{I^e} \cup \Omega_0^{II^e}$. For a sub-element of phase $m = [I, II]$, the enhanced strain field is interpolated by a shifted interpolation matrix $\bar{\mathbf{M}}_\xi^m$. For a four-parameter EAS formulation, it is:

$$\bar{\mathbf{M}}_\xi^m = \begin{bmatrix} \xi - \bar{\xi}^m & 0 & 0 & 0 \\ 0 & 0 & 0 & \eta - \bar{\eta}^m \\ 0 & \xi - \bar{\xi}^m & \eta - \bar{\eta}^m & 0 \end{bmatrix} \tag{3.3.17}$$

where $\bar{\xi}^m$ and $\bar{\eta}^m$ denote the subphase centroid coordinates in the local coordinate system of the respective sub-domain. In vector notation these are obtained as:

$$\bar{\boldsymbol{\xi}}^m = \begin{bmatrix} \bar{\xi}^m \\ \bar{\eta}^m \end{bmatrix} = \frac{\int_{-1}^1 \boldsymbol{\xi}^m d\tilde{\boldsymbol{\xi}}^m}{\int_{-1}^1 d\tilde{\boldsymbol{\xi}}^m} \tag{3.3.18}$$

It should be noted that for unintersected elements, the standard interpolation matrix (Eqn.(3.3.10)) is recovered from Eqn.(3.3.17) as $\bar{\xi}^m = \bar{\eta}^m = 0$. In order to use the EAS method for XFEM, the classical interpolation matrix Eqn.(3.3.10) needs to be replaced by a shifted interpolation matrix per unique subphase (Eqn.(3.3.17)) for intersected elements. Furthermore, enrichments of EAS variables needs to be performed just like for the global state variables (see Section 3.1.1). The remainder of the formulation is identical to EAS for regular FEM as discussed in Section 3.3.2.1.

3.3.4   2D Beam Examples

To demonstrate the performance of the EAS method, the bending behavior of a set of slender cantilevered beam examples is studied in 2D. The beam problems are analyzed under a plane stress assumption using FEM and XFEM with linear and quadratic elements as well as linear elements with EAS. As shear locking phenomena are mitigated on finer meshes, mesh refinement studies are conducted to examine the improved convergence behavior of linear elements with EAS using coarse spatial discretizations.

3.3.4.1   Intersections Aligned with Background mesh

First, a clamped beam of size $10.0 \times 1.0 \times 1.0$ is considered, where a point load of $T_{X_2} = -1.0$ is applied at the free end in vertical direction. The beam has a Young's modulus of $E = 5000.0$ and Poisson's ratio of $\nu = 0.0$. The coarsest FE mesh and the coarsest XFEM mesh of the same problem is shown in the insert in Figure 3.11 (a) and (b), respectively. Figure 3.11 (a) also shows the tip displacement for different levels of mesh refinement and different elements. These include 4 node quadrilaterals (Q4), 4 node quadrilaterals with a 4 parameter EAS formulation (Q4-EAS), and 8
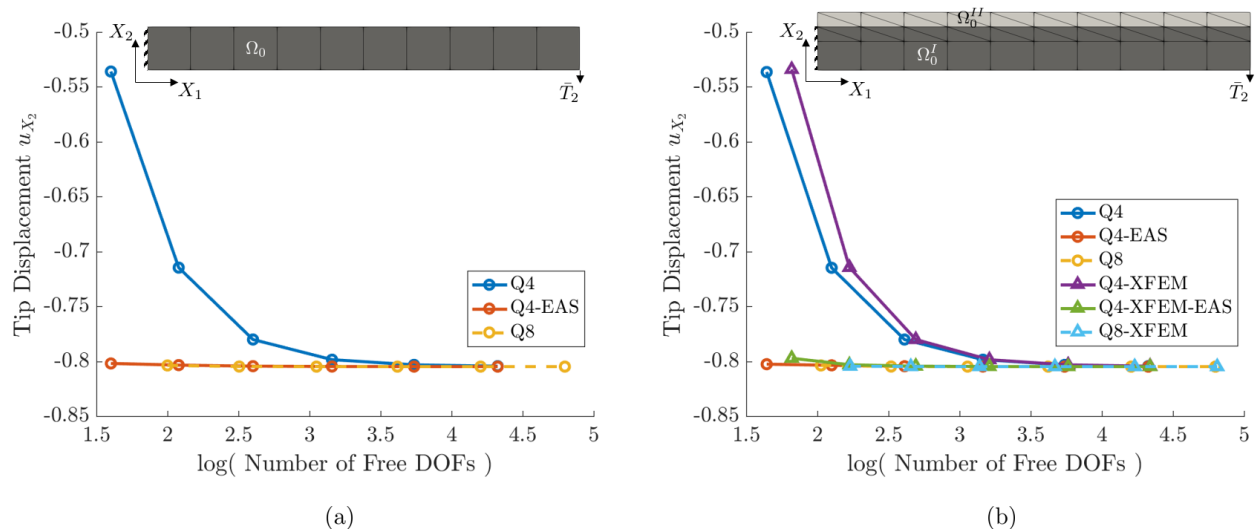
Figure 3.11: Tip displacement of a cantilevered beam over number of free DOFs for (a) FEM and (b) XFEM using different plane stress elements.

node quadrilaterals (Q8). In Figure 3.11 (b), these are complemented by their XFEM analogues. As expected, a significant underestimation of the tip displacement is seen by linear elements on coarse meshes, both using FEM (Q4) and XFEM (Q4-XFEM). Using higher-order spatial interpolation alleviates this issue. This is in agreement with findings presented in Section 3.2. However, this comes at the cost of a significant increase in number of DOFs. To avoid this, linear elements with EAS can be used, which show superior performance both for FEM (Q4-EAS) and XFEM (Q4-XFEM-EAS). From Figure 3.11 it can also be seen that all studied cases converge to the same tip displacement for very fine meshes, regardless of the interpolation order or geometry description (FEM or XFEM).

3.3.4.2   Arbitrary Intersections

Next, 2D beam examples resulting in more complex intersection configurations with respect to a regular background mesh are studied. First, a slender beam with comparable aspect ratio and loading as the one studied in Section 3.3.4.1 is addressed. It is, however, aligned diagonally with respect to the coordinate system, as shown in the insert in Figure 3.12 (a) for the coarsest XFEM mesh. The bottom left edges are clamped and a diagonal tip load is applied at the top right. From Figure 3.12 (a), it can be seen that Q4-EAS, Q8, and Q8-XFEM elements show good performance
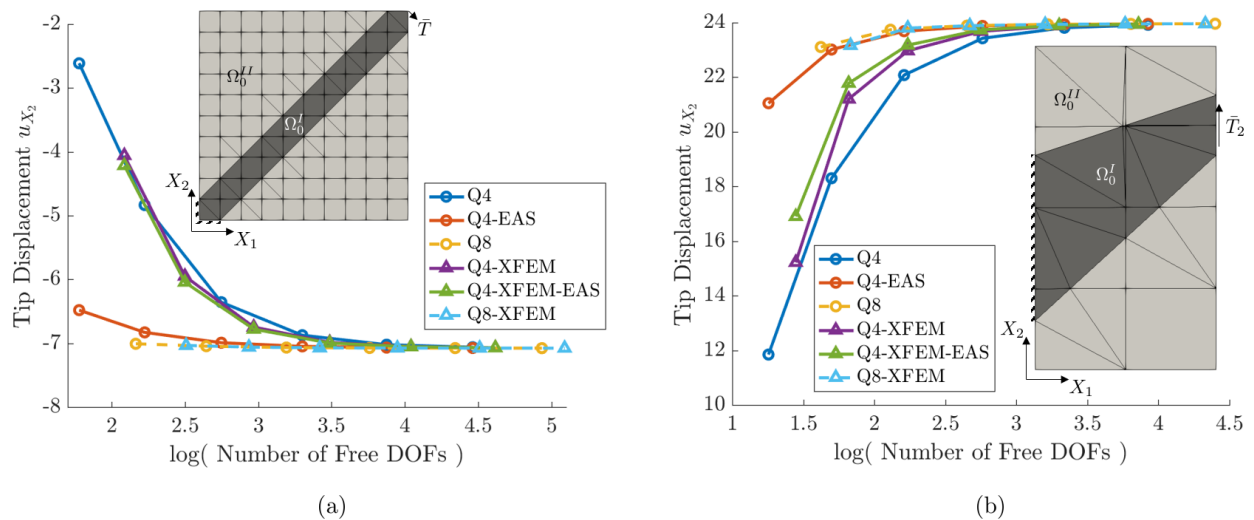
Figure 3.12: Tip displacement of cantilevered beam examples over number of free DOFs. (a) Diagonally aligned beam and (b) Cook's beam example using different FEM and XFEM elements.

for coarse meshes. In contrast, regular Q4 and Q4-XFEM elements show significant amounts of locking and therefore largely underestimate the tip displacement as expected for a coarse spatial discretization. Different than for the aligned beam presented in Section 3.3.4.1, the Q4-EAS-XFEM elements also show poor behavior for coarse meshes. Their bad performance is almost unaffected compared to regular Q4-XFEM elements.

Next, Cooks beam example [38], a classical benchmark problem for bending dominated problems is studied using FEM and XFEM. The coarsest XFEM mesh is shown in the insert in Figure 3.12 (b). A force of 1.0 is applied to the beam on the right edge in X_2 direction and a Young's modulus of $E = 1.0$ along with a Poisson's ratio of $\nu = 0.33$ is used. The problem dimensions are adopted from [32]. As in the previous example, superior convergence behavior is seen from Q4-EAS, Q8, and Q8-XFEM elements. The expected element shear locking and the resulting underestimated deformation of the linear Q4 and Q4-XFEM elements can also be seen. Again, the performance Q4-EAS-XFEM is unsatisfactory, as almost no improvement is observed compared to the same XFEM element without EAS.

Based on these results, it is assumed that the EAS XFEM formulation presented in Section 3.3.3 requires a close alignment of the XFEM interface $\Gamma_0^{I,II}$ with the background elements in order to perform well. This is, in general, not the case and further studies are required to sufficiently generalize the EAS concept for non-aligned XFEM intersections. One possibility is the introduction of a local coordinate rotation between the EAS frame (which is aligned with the interface) and the background element's frame of reference such that the non-alignment of the interface and the background mesh is accounted for. Another possibility is the formulation of the EAS contributions directly on the triangles in 2D or tetrahedrons in 3D which are used for volume integration of intersected XFEM elements. In this approach, a map between triangular/tetrahedral coordinates and DOFs and quadrilateral/hexahedron coordinates and DOFs of the background elements is required. More information regarding EAS for triangular elements is provided in [35]. The further examination and generalization of the EAS for XFEM should be addressed in future work.

3.4 Staggered Block Solution Approach

Block solvers are used to maximize efficiency of solving large multi-physics problems. Solving a one-way or two-way coupled system, for example by using a Block Gauss Seidel method, has multiple benefits. It is possible to make use of the symmetry of sub-matrices, as non-diagonal matrices are transformed to the Right-Hand-Side (RHS). Furthermore, the (potential) linearity of sub-systems can be taken advantage of, which enhances convergence. And lastly, the memory requirements are drastically reduced as sub-matrices are significantly smaller in size compared to the combined linear system [152]. In case of a two-way coupling between the sub-systems, the BGS method is applied in an iterative fashion. As only one-way coupled systems are considered in this thesis, it is the focus of the following discussion.

Suppose two linear fields, $\theta(\mathbf{X})$ and $\phi_{SD}(\mathbf{X})$ which are physically coupled in a one-way fashion. The combined linear system can be summarized as:

$$\begin{bmatrix} \mathbf{K}_{\theta\theta} & 0 \\ \mathbf{K}_{\phi_{SD}\theta} & \mathbf{K}_{\phi_{SD}\phi_{SD}} \end{bmatrix} \begin{bmatrix} \boldsymbol{\theta} \\ \boldsymbol{\phi}_{SD} \end{bmatrix} = \begin{bmatrix} \mathbf{R}_{\theta} \\ \mathbf{R}_{\phi_{SD}} \end{bmatrix} \tag{3.4.1}$$

The first linear system is solved in a classical sense for $\boldsymbol{\theta}$ as:

$$\mathbf{K}_{\theta\theta}\boldsymbol{\theta} = \mathbf{R}_{\theta} \tag{3.4.2}$$

where $\mathbf{K}_{\theta\theta}$ is the tangent stiffness matrix and $\mathbf{R}_{\theta}$ is the residual vector of θ. Next, the second linear sub-system is solved for $\boldsymbol{\phi}_{SD}$ as:

$$(\mathbf{K}_{\phi_{SD}\phi_{SD}})\boldsymbol{\phi}_{SD} = \mathbf{R}_{\phi_{SD}} - \mathbf{K}_{\phi_{SD}\theta}\boldsymbol{\theta} \tag{3.4.3}$$

where the coupling matrix $\mathbf{K}_{\phi_{SD}\theta}$ multiplied with the solution vector of the previous linear system ($\boldsymbol{\theta}$) is appended to the RHS. This block solution approach, which decomposes large linear systems into smaller sub-systems based on coupled physics, can be seen as a domain-decomposition method [152]. It is highly efficient when used with parallel linear solvers and therefore widely used in the work of this thesis.

Chapter 4

Design Optimization

Design optimization is highly relevant to various fields of engineering and science. Especially in aerospace engineering, increasing performance, reducing the number of parts, and the overall weight of a design is of special interest. The origins of design optimization are found in structural design optimization and can be traced back to the seminal work of Galileo and Hooke in continuum mechanics [51]. Initially, analytical design optimization approaches however were very limited due to the available, simplified physical models and analysis methods. This was drastically changed with the advent of the FEM and numerical analysis techniques [140, 141]. Ever since, design optimization has been applied to various fields of engineering, including but not limited to structural mechanics, fluid mechanics, and heat transfer [17, 43, 168].

In general, a design optimization problem seeks to find the geometry, size, and shape of a body and/or distribution of materials within that body such that an objective function is minimized/ maximized and a set of given constraints is satisfied [124]. The objective function is formulated to quantify the performance of the design and constraints are enforced to limit the design space in a certain manner. Both, objective and constraints are formulated in terms of design criteria, like strain energy, power dissipation, drag, manufacturability or cost of a part [191]. Based on their geometric design freedom, different types of design optimization are being distinguished. The simplest form is size optimization, where only a few, geometric design parameters (e.g., dimensions) exist. Shape optimization, allows for more design freedom where not only the size of geometric components but also their shape is subject to change. The most general form of design optimization is TO, which encompasses all
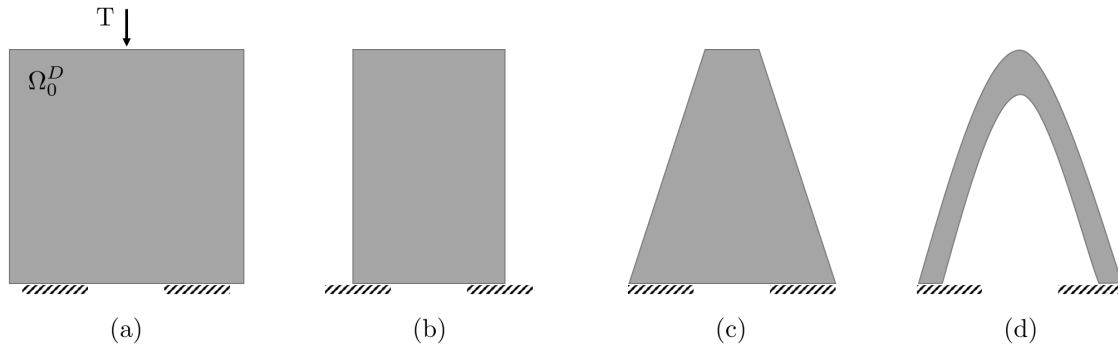
Figure 4.1: Illustration of different types of structural design changes for a structure in compression. (a) Initial design, (b) changes in size, (c) changes in shape, (d) changes in topology.

previously mentioned sub-sets of design optimization and in addition allows for topological changes during the optimization process. Compared to size and shape optimization, TO does not require a close to optimal initial design and is able to generate optimal designs where intuitive design approaches fail [17]. However, this enhanced flexibility comes at the cost of increased complexity in formulating and solving the design optimization problem [124]. A conceptual illustration of the three approaches of design optimization is shown in Figure 4.1 for a simple structural optimization problem in 2D. Figure 4.1 (a) shows the initial design which defines the design space Ω_0^D and Figure 4.1 (b) shows a size optimized design where the width of the structure was altered. An optimized shape of the same problem is shown in Figure 4.1 (c) while the design of Figure 4.1 (d) also underwent topological changes.

Mathematically, a design optimization problem is formulated as a minimization problem of some objective function z such that a set of N_g constraints g_j are satisfied. This is stated as:

$$
\begin{aligned}
\min_{\mathbf{s}} \quad & z(\mathbf{s}, \mathbf{u}(\mathbf{s})) \\
\text{s.t.} \quad & g_j(\mathbf{s}, \mathbf{u}(\mathbf{s})) \leq 0 \qquad j = 1 \dots N_g \\
& \mathbf{s} \in \Pi = \{\mathbb{R}^{N_s} | \mathbf{s}_L \leq \mathbf{s} \leq \mathbf{s}_U\} \\
& \mathbf{u}(\mathbf{s}) \in \mathbb{R}^{N_u}
\end{aligned}
\tag{4.0.1}
$$

where $\mathbf{s}$ is the vector of design variables of length N_s bounded by its lower bounds $\mathbf{s}_L$ and its upper bounds $\mathbf{s}_U$. The vector of state variables as a function of the design variables is denoted by $\mathbf{u}(\mathbf{s})$ and

the number of state variables is N_u. In general, equality constraints could be enforced explicitly in Eqn.(4.0.1) in addition to the inequality constraints g_j. In the scope of this thesis, when necessary to enforce an equality constraint, it is converted into a set of bounding inequality constraints which for all practical means is equivalent.

A nested analysis and design (NAND) approach [11] is used in this thesis where the state variables $\mathbf{u}$ are considered dependent variables of the design variables $\mathbf{s}$ satisfying the governing equations for every design. This allows for the flexibility to use a different solution algorithm for the "forward" analysis problem (see Chapter 2) and the optimization problem (Eqn.(4.0.1)).

To solve the parameter optimization problem at hand, different types of solution algorithms can be employed. These can be grouped in gradient-free and gradient-based optimization schemes. The advantage of gradient-free methods is their ease of use and the fact that they do not require a differentiable formulation of objective and constraints. For a large number of design variables (like it is the case in TO), the computational cost increases significantly when using gradient-free approaches [167]. In contrast, gradient-based solution approaches use design sensitivity information of objective and constraints with respect to the design variables for solving the optimization problem. This requires a consistent linearization of the optimization problem and the forward problem, however significantly increases convergence when compared to gradient-free methods [167]. For the work presented in this thesis, the gradient-based nonlinear programming scheme Globally Convergent Method of Moving Asymptotes (GCMMA) of [177, 178] is used without inner iterations. The design sensitivities are obtained by the adjoint method which is an efficient means to obtain design sensitivities for parameter optimization problems involving a large number of design variables. More details regarding design sensitivity analysis are discussed in Section 4.6.

4.1   Topology Optimization

TO, the design optimization approach allowing for the most design freedom, is a particular class of mathematical optimization problems which uses the solution of a set of PDEs in order to quantify the performance of the system to be optimized [124]. Referring back to the conceptual example shown in Figure 4.1, this could mean to find the optimal geometry within the design space Ω_0^D which minimizes the strain energy of the structure under a certain traction load T while subject to a volume constraint on the structural domain. The origins of TO are found in the work by [128] on minimizing the mass of quasi-continuous truss structures. This was later expanded by [85] and [153] for solving similar truss structure optimization problems. Comprehensive reviews of recent developments in TO are found in [17, 168, 43, 51, 188].

4.1.1   Density-based Topology Optimization

Using the concept of material homogenization, density-based TO has become one of the most popular forms of TO, ever since it was introduced by [18]. In this approach, a nodal or elemental design variable field, most commonly called fictitious densities $0 \leq s^\rho(\mathbf{X}) \leq 1$, is introduced for interpolation of the physical material properties. This continuous interpolation of material properties relaxes the original integer optimization problem which seeks to find the optimum design composed of either material A ($s^\rho(\mathbf{X}) = 0$) or material B ($s^\rho(\mathbf{X}) = 1$) and makes it possible to use a nonlinear programming algorithm to determine its solution. To penalize intermediate material associated with intermediate fictitious densities ($0 < s^\rho(\mathbf{X}) < 1$), different penalization schemes have been introduced [17].

4.1.1.1   Solid Isotropic Material with Penalization

The most common one is called Solid Isotropic Material with Penalization (SIMP) [16, 211, 129] which uses a nonlinear power-law to define the relationship between the design variables and the

physical material properties. For a two material problem, the SIMP material interpolation is:

$$p(s_i^\rho) = p^A + (p^B - p^A)(s_i^\rho)^{\beta_S} \tag{4.1.1}$$

where p denotes a generic material property with the properties corresponding to material A and material B being denoted by p^A and p^B, respectively. The nodal fictitious density design variables are denoted by s_i^ρ, and β_S is the so-called SIMP exponent. The penalization effect is not enforced by the power-law (Eqn.(4.1.1)) itself, but only in combination with the appropriate definition of a competing objective and constraint [124]. For example, for a compliance minimization problem, a constraint on the allowable mass of the structure needs to be enforced to achieve the desired penalization effect of intermediate material densities. This is usually achieved by using a linear interpolation for the physical density of either material (i.e., $\beta_S = 1.0$) and a nonlinear interpolation for the stiffness of the material (i.e., $\beta_S = 3.0$). Using $\beta_S = 3.0$ for nonlinear material interpolation has also been shown to lead to desirable density gradients in linear elasticity [8].

4.1.1.2 Rational Approximation of Material Properties

To alleviate convergence issues of the SIMP approach due to zero gradients for $s^\rho(\mathbf{X}) = 0$, the Rational Approximation of Material Properties (RAMP) approach was introduced by [175, 174]. For a two material problem the RAMP interpolation is stated as:

$$p(s_i^\rho) = p^A + \frac{s_i^\rho}{1 + q_R(1 - s_i^\rho)}(p^B - p^A) \tag{4.1.2}$$

where the nonlinearity of the interpolation is determined by q_R. For $q_R = 0$ a linear interpolation is achieved. As pointed out by [17], the RAMP interpolation is more physical than the SIMP interpolation for a two material problem with respect to the Hashin-Shtrikman bounds [84].

4.1.1.3 Filtering and Projection

To increase numerical stability and to enhance convergence of the optimization problem, filtering of nodal (or elemental) design variables was introduced. Filtering for examples mitigates

checker-boarding and widens the area of influence of each design variable. The simplest filter, a linear averaging filter of design variables within a certain filter radius [24, 22], is mathematically formulated as:

$$\tilde{\rho}_i = \frac{\sum_{j=1}^{N_n} w_{ij} s_j^{\rho}}{\sum_{j=1}^{N_n} w_{ij}} \ , \qquad w_{ij} = \max(0, r_f - |\mathbf{X}_i - \mathbf{X}_j|) \qquad (4.1.3)$$

where N_n is the number of FE nodes within the filter radius, r_f, and $|\mathbf{X}_i - \mathbf{X}_j|$ is the Euclidean distance between node i and j. Index i denotes the current node for which the filtered fictitious density value $\tilde{\rho}_i$ is computed and index j denotes each node within the filter radius contributing to $\tilde{\rho}_i$. Alternatively, a similar filtering effect can be achieved using a Helmholtz-type PDE filter as proposed by [111, 94]. Besides introducing smoothing into the field of (filtered) design variables, numerical artifacts like checker boarding encountered in density-based TO with low-order elements can be alleviated using a filter on the design variables [151]. Moreover, when using a constant filter radius, mesh-independent designs are obtained.

To counteract the blurriness in the physical material properties introduced through linear filtering, projection schemes are most commonly applied [165, 204]. Using a smoothed Heaviside approximation for thresholding, [74] proposed the following projection scheme:

$$\hat{\rho}_i = 1 - e^{-\gamma_P \tilde{\rho}_i} + \tilde{\rho}_i e^{-\gamma_P} \qquad (4.1.4)$$

where γ_P is the projection sharpness parameter. Allowing also for a variable projection threshold, a smoothed Heaviside projection scheme proposed by [112] can be used instead:

$$\hat{\rho}_i = \frac{\tanh(\gamma_P(\tilde{\rho}_i - \eta_P)) + \tanh(\gamma_P \ \eta_P)}{\tanh(\gamma_P(1 - \eta_P)) + \tanh(\gamma_P \ \eta_P)} \qquad (4.1.5)$$

where η_P is the projection threshold parameter. An advantage of filtering the density design variables in combination with the appropriate projection scheme is minimum feature size control. This is enforced due to the definition of Eqn.(4.1.3) and an appropriate projection scheme, along with the material interpolation law which desires fictitious densities of either 0 or 1. It should however be noted that when using the projection scheme of Eqn.(4.1.5) with intermediate projection threshold values (i.e., $\eta_P \neq 0$ or $\eta_P \neq 1$) it does not allow for proper feature size control. To avoid additional

nonlinearities in the optimization problem, a continuation approach is most commonly used to gradually enforce the projection sharpness after a converged design is obtained [151].

In case linear filtering and projection of the design variables are used, the projected fictitious density values $\hat{\rho}_i$ are used for nonlinear material interpolation instead of the density design variables s_i^ρ directly. See Eqn.(4.1.1) and Eqn.(4.1.2), respectively.

4.1.1.4   Discussion

In summary, certain advantages of density-based TO can be identified. First of all, its ease of implementation and use within a FE framework lead to its great popularity especially in commercially available TO codes [51]. Moreover, it is relatively simple to control the minimum obtained feature size through appropriate filtering and projection. Another great advantage of density-based TO methods is the fact that the optimization process is usually started from a homogeneous, initial design variable field (e.g., $s^\rho(\mathbf{X}) = 0.5$ in the entire design domain Ω_0^D). This leads to the fact that no dependency of the final, optimized design is created on the initial design, as no initial seeding of the design space with distinct material phases is required.

A disadvantage of density-based TO can be the fact that an appropriate formulation of the optimization problem is needed to achieve the required penalization effect. While this might not be an issue for compliance minimization problems in structural mechanics, the formulation of other (mostly purely geometrical) optimization problems might not be straightforward. The major drawback of the density method is most certainly the blurry definition of the interface due to a finite (i.e., at least the width of an element) transition zone between two material phases. This is a limitation inherently built into the method which can only be mitigated but never fully removed by for example local mesh refinement of the background mesh. The jagged boundaries due to the density-based mapping of material properties on a fixed background mesh introduce inaccuracies when modeling the physical response [161]. Modeling of interface phenomena like fluid-structure interaction or contact is therefore hardly possible [124]. Due to the inexact definition of the material interface, additional post-processing is required when extracting the optimized design

geometry for manufacturing [68]. This does not only mean additional steps need to be performed but interpretation of the optimized design in a post-processing step leads to deviations from the determined optimum due to the manual extraction of the design geometry.

4.1.2   Level-Set-based Topology Optimization

Addressing some of the disadvantages of density-based TO, level-set (LS) TO is the second most popular TO approach. Initially, the level set method (LSM) was introduced by [145] for modeling moving boundaries. Since then, it has been widely used in image processing [144], computer graphics, computational geometry and computational physics [71, 143]. Due to the ability to implicitly describe a geometric boundary using a higher-order level-set function (LSF), the LSM is naturally suited for describing topological changes in TO. The LSM was first applied to TO by [81, 159, 41] and has gained great popularity since then. It is especially popular because of the crisp and unambiguous definition of the material interface [168, 188]. A conceptual illustration of a LSF $\phi(\mathbf{X})$, the corresponding material sub-domains Ω_0^I, Ω_0^{II}, and the material interface $\Gamma_0^{I,II}$ in-between is shown in Figure 4.2 (a) and (b), respectively. Moreover, Figure 4.2 shows how topological changes are described using the higher-order implicit LSF. In a two-material TO context, the domain decomposition is defined as:

$$\phi(\mathbf{X}) < 0, \forall\ \mathbf{X} \in \Omega_0^I$$
$$\phi(\mathbf{X}) > 0, \forall\ \mathbf{X} \in \Omega_0^{II} \tag{4.1.6}$$
$$\phi(\mathbf{X}) = 0, \forall\ \mathbf{X} \in \Gamma_0^{I,II}$$

where the entire design domain Ω_0^D is comprised of $\Omega_0^D = \Omega_0^I \cup \Omega_0^{II}$ and the interface between them is obtained by $\Gamma_0^{I,II} = \partial\Omega_0^I \cap \partial\Omega_0^{II}$[163]. The external boundaries of either material domain is denoted by $\partial\Omega_0^I$ and $\partial\Omega_0^{II}$, respectively.

Following [188], two categories of LSMs can be defined, namely implicit and explicit LSMs which are distinguished based on the update procedure and the interpretation of the design variables. In implicit LSM, the solution of a Hamilton-Jacobi (HJ) PDE is used to update the material
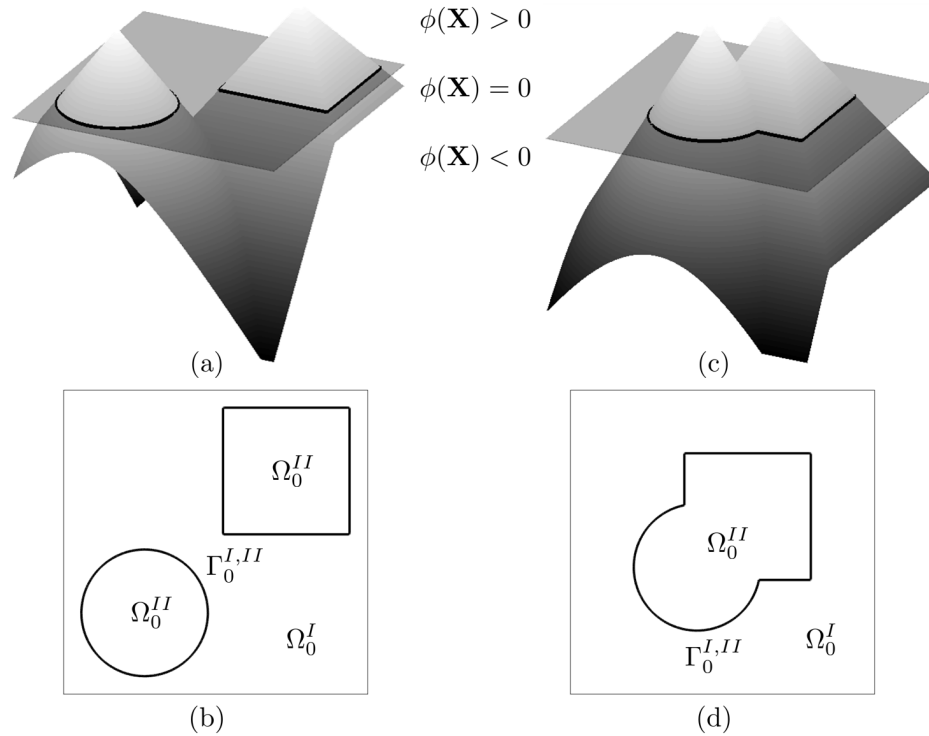
Figure 4.2: Higher-order LSF and corresponding zero iso-contour generated using LS primitives. (a) LSF of two distinct geometric primitives, (b) zero iso-contour of the LSF of (a), (c) LSF of two merged primitives, (d) corresponding iso-contour to the LSF of (c).

interface at every design step, using design velocities as design variables [5, 146]. While a PDE solution-based evolution of the LSF has advantages with respect to the evolution of the interface, stabilization techniques are required to limit the spatial gradient of the LSF [158]. If the HJ equation is solved using an explicit time integration scheme, the design step size is limited by the Courant-Friedrichs-Lewy (CFL) condition, which inherently limits the evolutionary speed of the design problem [67]. Further examples of applications of implicit LSMs for TO are found in [196, 200].

In contrast, explicit LSMs use a parametrized LSF and nodal LS values as design variables, which are updated using mathematical programming techniques [137, 103, 189, 119]. Even though no underlying PDE needs to be solved, and therefore no limitation on the design step size is given, a strong need for regularization exists. Further details regarding explicit LS regularization are found in [67] and are discussed in more depth in Section 4.3.

As identified by [189] and [101], design optimization using LS-based TO exhibits a large dependency on the initial design. To mitigate this influence, a large number of initial holes is used most commonly to initiate the TO process [125, 89, 78]. Alternatively, topological derivatives [7] or an additional reaction term with the HJ equation [25] can be used to nucleate new holes during the optimization process. For more details regarding implicit LSMs, the reader is referred to [63, 188].

4.1.2.1 Nodal LS Design Variables

As the work in this thesis exclusively uses the explicit, or parametric LSM, it is discussed in more detail hereinafter. A nodally discretized LSF $\phi_i(\mathbf{X})$ is used to distinguish between different material phases, according to Eqn.(4.1.6). Similar to Eqn.(4.1.3) a linear filter is used to define an explicit relationship between the design variables $\mathbf{s}^\phi$ and the LSF:

$$\phi_i = \frac{\sum_{j=1}^{N_n} w_{ij} s_j^\phi}{\sum_{j=1}^{N_n} w_{ij}} \, , \qquad w_{ij} = \max(0, r_f - |\mathbf{X}_i - \mathbf{X}_j|) \tag{4.1.7}$$

Just as in density-based TO, linear filtering of the design variables enhances convergence due to widening the zone of influence of every design variable [188] and introduces smoothing and stability during the optimization process [102]. However, no feature size control is achieved by Eqn.(4.1.7) in LS-based TO. More details on how to enforce minimum feature size control in LS-based TO are presented in Section 4.4.

4.1.2.2 Geometric Primitives as Design Variables

Instead of using design velocities or nodal LS values as design variables, definition of geometric primitives or MMCs as a function of a reduced set of parameters has been introduced recently. The material layout is then defined by a density map [138] or mapped by a LSF [77]. This allows for directly including minimum feature size control into the design optimization process [207] and drastically reduces the number of design variables. This typically regularizes the optimization problem. The LSF for a set of (spherical or cubical) primitives is defined as:

$$\phi(\mathbf{X}) = 1 - \min_i(\phi_{P_i}(\mathbf{X})) \tag{4.1.8}$$

where i denotes the index over all primitives N_P and the LSF of an individual primitive is denoted by $\phi_{P_i}(\mathbf{X})$. For spherical or cubical primitives the LSF is defined as:

$$\phi_{P_i}(\mathbf{X}) = \left(\left(\frac{X_1 - \tilde{X}_{1_i}}{r_{1i}} \right)^{n_i} + \left(\frac{X_2 - \tilde{X}_{2_i}}{r_{2_i}} \right)^{n_i} + \left(\frac{X_3 - \tilde{X}_{3_i}}{r_{3_i}} \right)^{n_i} \right)^{\frac{1}{n_i}} \tag{4.1.9}$$

where $\mathbf{r}_i$ is the radius of the i-th primitive, and $\tilde{\mathbf{X}}_i$ is the position of the center of the i-th primitive in X_1, X_2 and X_3 direction, respectively. The roundness parameter of a primitive is denoted by n_i. In case of primitives, the vector of design variables $\mathbf{s}^\phi$ contains explicit geometric properties like center coordinates of the primitives, their orientation or their radii. For the 2D example of $N_P = 2$ primitives shown in Figure 4.2 (a), $n_1 = 2.0$ to obtain a circular primitive and $n_2 = 100.0$ to yield a rectangular primitive. To obtain a differentiable definition of the LSF, the non-differentiable $\min(\bullet)$ (or $\max(\bullet)$) operator is oftentimes replaced by a Kreisselmeier-Steinhauser (KS) function defined as [100]:

$$\phi(\mathbf{X}) = 1 + \frac{1}{\beta_{KS}} \ln \left(\sum_{i=1}^{N_P} e^{\beta_{KS} \phi_{P_i}(\mathbf{X})} \right) \tag{4.1.10}$$

where the sharpness of the min/max approximation is determined by β_{KS}. More details and a general overview over recent developments using geometric primitives can be found in [161]. Numerical design optimization examples using LS primitives as design variables are presented in Section 5.2.

4.1.3 Combined Level-Set-XFEM-Density Approach

While comparisons of density-based and LS-based TO methods have presented by [189, 200, 88], a combination of LS-based and density-based approaches for TO has been largely unexplored to date. One work roughly related to this topic is by [93] where a classical SIMP approach is used for material interpolation while a LSM is employed to include void domains into the TO process. However, the shape and topology of the void domains described by LSFs is not subject to optimization. Similarly, in the work of [27] where non-design spaces described by CutFEM are embedded into the design space optimized by density-based TO. One key contributions of this thesis is therefore the development and testing of combined LS-density TO approaches where both, the LSF and the
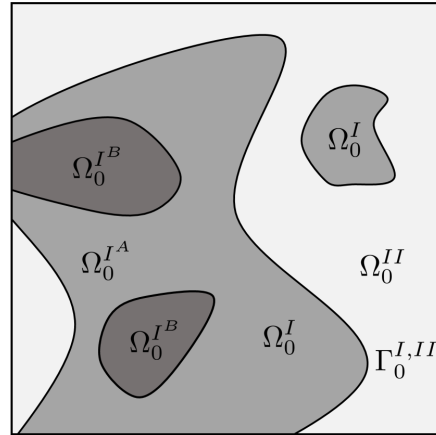
Figure 4.3: Multi-material design domain decomposition into phase I (Ω_0^I) and phase II (Ω_0^{II}) sub-domains along the interface ($\Gamma_0^{I,II}$) using LS-XFEM. Within the phase I domain, a further distinction is made between material A ($\Omega_0^{I^A}$) and material B ($\Omega_0^{I^B}$).

density field are being optimized simultaneously. An introduction and discussion of two different combination methods is presented hereinafter. The point of departure are two independent sets of design variables, denoted as $\mathbf{s}^\phi$ and $\mathbf{s}^\rho$. These are related to the LS approach and the density approach, respectively, and constitute the vector of design variables such that $\mathbf{s} = [\mathbf{s}^\phi, \mathbf{s}^\rho]$.

4.1.3.1   Uncoupled Level-Set and Density Fields

Assuming no relationship between the two sets of (independent) design variables, an uncoupled LS-density approach can for example be used for solving multi-material design optimization problems. Classically, multi-material TO using a pure density method has been demonstrated by [164] where multiple sets of density design variables are combined in an extended SIMP interpolation scheme to represent multiple material phases. Using a pure LS approach, color-LSs have been proposed by [196] for representation of multiple materials. In the color-LS approach n_m LSFs are needed in order to distinguish between 2^{n_m} number of different phases.

Here, an uncoupled LS-density approach is proposed where the benefits of both density methods and LSMs are exploited simultaneously. To this extent, a two-phase LSM and a two-material density interpolation are combined in an uncoupled manner to demonstrate the approach.

Without the loss of generality, this approach can be extended to incorporate both, multiple LSs and/or multiple density interpolation schemes. A conceptual multi-material domain decomposition using the combined LS-density approach discussed here is shown in Figure 4.3. A LSF (see Section 4.1.2) is used to distinguish between phase I (Ω_0^I) and phase II (Ω_0^{II}) along the interface $\Gamma_0^{I,II}$. In addition, a classical density interpolation scheme (see Section 4.1.1) is introduced to distinguish between material A ($\Omega_0^{I^A}$) and material B ($\Omega_0^{I^B}$) within phase I.

Directly inheriting the properties of either method, the combined approach does not only allow for an easy treatment of multi-material TO problems, but can efficiently be used to solve solid void two-material TO problems. This was demonstrated by [68, 69] and further examples are presented in Section 5.3. It should be noted that by introducing a material interpolation scheme within a LS-XFEM approach, special care needs to be taken due to the spatially varying material properties with a phase. This is a true deviation from classical LS-XFEM work where typically homogeneous material properties are assumed with a phase. In practice, special considerations need to be accounted for when using face-oriented ghost penalization in a combined LS-XFEM density approach. As discussed in Section 3.2.1, the classical displacement gradient-based ghost stabilization formulation is no longer valid and a, for example, virtual work-based formulation needs to be employed. Furthermore, when using a combined LS-density approach assuming subphase constant material properties greatly simplifies handling of material properties and their spatial variation on a discretized XFEM mesh. Therefore, this assumption is used for all numerical examples using a combined LS-density approach presented in Section 5.3.

4.1.3.2   Loosely-Coupled Level-Set and Density Fields

In contrast to the combined LS-density approach discussed in Section 4.1.3.1, a loosely-coupled relationship between the two independent design variable fields $\mathbf{s}^\phi$ and $\mathbf{s}^\rho$ is proposed next. Loose coupling between the two sets of design variables is achieved through the formulation of inequality constraints. The advantage of this combined TO approach is the fact that benefits exhibited by either method separately are combined in a sequential manner, in order to eliminate their mutual

drawbacks and thus create a superior TO approach. The combined scheme is capable of hole nucleation, minimum feature size control and LS regularization as design sensitivities exits in the entire design domain (properties of density methods) while yielding a crisp material interface (property of LS methods). For demonstration purposes, the approach is discussed in the following using a single material, solid-void example problem where a SIMP scheme is combined with explicit LS-XFEM TO for structural TO.

Coupling Penalty Formulations

To establish a hole nucleation capability for the LS field, a lower penalty coupling the filtered and projected nodal densities $\hat{\rho}$ with the nodal LS values ϕ is defined as:

$$p_L = \max((-\hat{\rho} + \hat{\rho}_{TL}), 0) \cdot \max((-\phi + \phi_{TL}), 0) \tag{4.1.11}$$

where $\hat{\rho}_{TL}$ is a lower density threshold and ϕ_{TL} is a lower LS threshold. The penalty landscape of the lower penalty function (Eqn.(4.1.11)) is depicted in Figure 4.4 (a) for $\hat{\rho}_{TL} = 0.1$ and $\phi_{TL} = 0.1$. As can be seen from Figure 4.4 (a), the lower penalty function p_L linearly penalizes any (negative) LS values below ϕ_{TL} when low density values below $\hat{\rho}_{TL}$ are present. In other words: in areas of low density (i.e., weak material), a positive LS value (i.e., void) needs to be present which leads in a TO process to the desired hole nucleation in areas of low density.

Similar to a penalty on the lower end of the density range, an upper penalty can be formulated as:

$$p_U = \max((\hat{\rho} - \hat{\rho}_{TU}), 0) \cdot \max((\phi - \phi_{TU}), 0) \tag{4.1.12}$$

where $\hat{\rho}_{TU}$ is an upper density threshold and ϕ_{TU} is an upper LS threshold. The corresponding penalty landscape for the upper penalty as a function of the filtered and projected density and the LS value is shown in Figure 4.4 (b). The upper penalty penalizes any (positive) LS value above ϕ_{TU} in areas of high density above $\hat{\rho}_{TU}$. From a TO perspective, this means that areas occupied by high density (i.e., strong) material, need to have a negative LS value (i.e., solid) which prevents the LSF from undercutting high-density areas in the design domain.
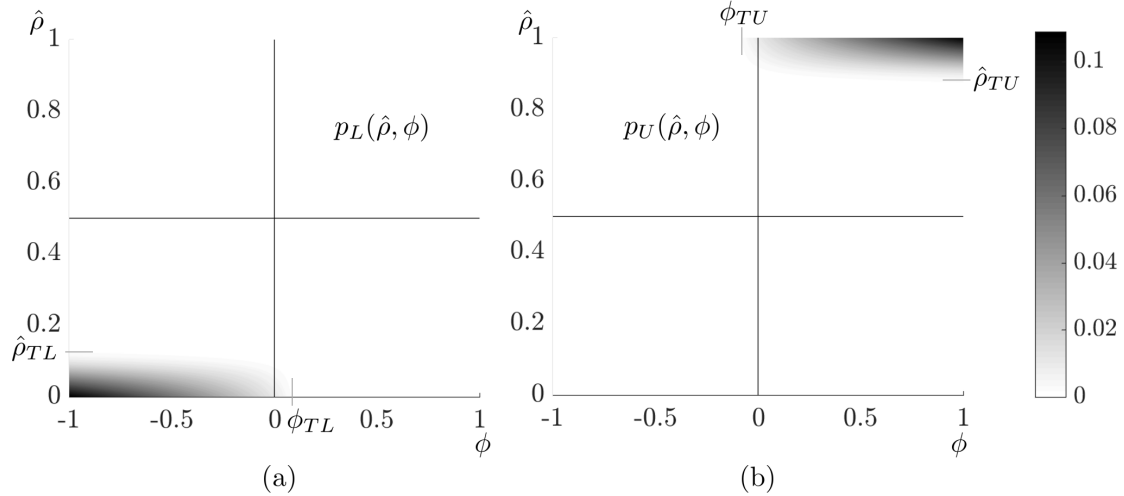
Figure 4.4: Penalization landscape for a loosely-coupled LS-density approach. (a) Lower penalty function, (b) upper penalty function.

It should be noted that both the lower penalty (Eqn.(4.1.11)) and the upper penalty (Eqn.(4.1.12)) exhibit a non-constant penalty front both with respect to $\hat{\rho}$ and with respect to ϕ. This can also be seen in Figure 4.4, where a smooth (rounded) transition from zero penalization to a maximum penalization in the respective corner of the penalization landscape is shown. This non-uniform penalty function with its maxima in the respective extrema (corners) of the penalization space is crucial, in order to provide non-zero design sensitivities which, in turn, lead to a hole nucleation (by the lower penalty) or prevent under-cutting (by the upper penalty).

Smooth Coupling Penalty Formulations

To obtain differentiable penalty formulations, the lower penalty (Eqn.(4.1.11)) and the upper penalty (Eqn.(4.1.12)) are approximated smoothly using a product of KS functions (see Eqn.(4.1.10)). In particular, the lower penalty is approximated smoothly as

$$\tilde{p}_L = m_L^1 \cdot m_L^2 \tag{4.1.13}$$

where

$$m_L^1 = \frac{1}{\beta_{KS}} \ln(e^{\beta_{KS}(-\hat{\rho}+\hat{\rho}_{TL})} + 1) \tag{4.1.14}$$

and

$$m_L^2 = \frac{1}{\beta_{KS}} \ln(e^{\beta_{KS}(-\phi+\phi_{TL})} + 1) \tag{4.1.15}$$

Similarly, the upper penalty is approximated smoothly as:

$$\tilde{p}_U = m_U^1 \cdot m_U^2 \tag{4.1.16}$$

where

$$m_U^1 = \frac{1}{\beta_{KS}} \ln(e^{\beta_{KS}(\hat{\rho}-\hat{\rho}_{TU})} + 1) \tag{4.1.17}$$

and

$$m_U^2 = \frac{1}{\beta_{KS}} \ln(e^{\beta_{KS}(\phi-\phi_{TU})} + 1) \tag{4.1.18}$$

It should be noted that for each of the smooth approximations of the max($\bullet$) operator presented above, the KS parameter is typically set to $\beta_{KS} = 75.0$.

Global Mass Measure considering Phase I and Phase II

The first approach explored is a combined LS-XFEM-density method where a mass constraint is globally enforced, i.e., in phase I and phase II of the LS-XFEM problem. Using this method, holes are initiated by virtue of the lower penalty of Eqn.(4.1.11) where in areas of low densities positive LS values are obtained. The upper penalty (Eqn.(4.1.12)) is not active as undercutting is globally prevented by the mass constraint on both, phase I and phase II. It is however observed, that intermediate density values are obtained in phase I elements close to the XFEM interface. Since all elements (in the solid and in the void) contribute to the total mass of the structure, intersected elements are only filled as much as needed with high density (i.e., material), in order to not place unnecessary mass into the void domain where no structural stiffness is gained. The optimizer rather sacrifices a small loss of stiffness from intermediate material near the structural boundary, than to unnecessarily contribute to the mass of the structure in phase II (void). This leads to the effect that some blurry (intermediate) material is obtained near the crisp LS-XFEM intersection in phase I.

Since both, phase I and phase II contribute to the total mass of the structure and therefore no undercutting of the LSF is possible, minimum feature size control from filtering of the density field is obtained. This enables feature size control of the LSF through filtering of the densities. Due to the global mass constraint, a rather strong coupling effect between densities and LS variables is seen and an independent evolution of one or the other is not possible. Numerical examples using a loosely coupled LS-density approach with a global mass constraint are presented in Section 5.4.3.

Influence of Density Projection

A strong influence of the density projection parameter γ_P (Eqn.(4.1.4) or Eqn.(4.1.5)) on the convergence of the combined LS-density approach has been observed. This is caused by the hole nucleation process which is drastically sped up when projection is used. With projection, small density values are projected to zero which means a positive LS field is obtained through the lower penalty of Eqn.(4.1.11). A density projection removes small oscillations in the density values and therefore yields a sharper and faster hole creation process. It should however be noted, that using high projection values (even through a continuation approach) drastically increases the nonlinearity of the design space and therefore inherently makes it harder for the optimization problem to be solved. Once a local minimum is identified, the projection scheme most likely will prevent the optimizer from leaving this locally optimal configuration. High projection values, by adding to the increased non-convexity of the problem, can also cause instabilities in the design optimization problem and in the worst case may prevent finding a solution at all.

The most practical strategy is therefore to only enable the LS-density penalty functions (i.e., start the hole nucleation process) after the density field has sufficiently converged, close to a 0-1 design. This can be achieved either with or without projection, only differing in the necessary number of optimization iterations to create an XFEM interface.
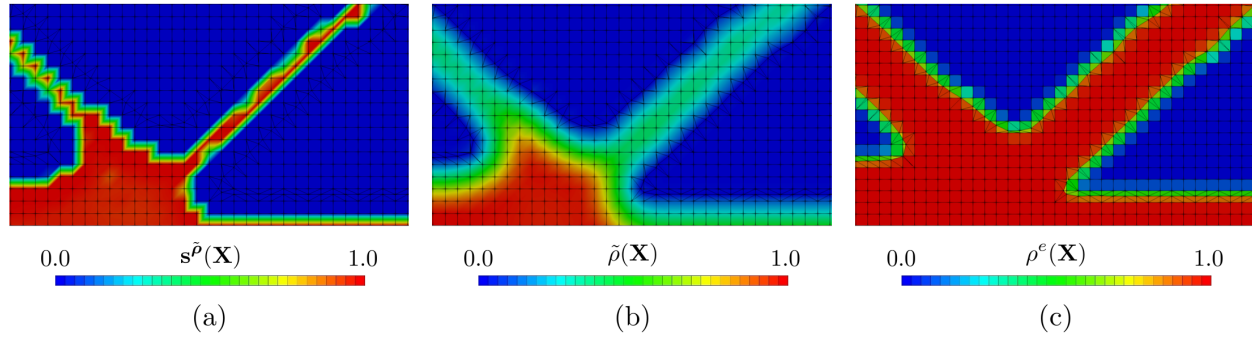
Figure 4.5: Different fields during a combined LS-XFEM density TO approach. (a) Nodal density design variables, (b) nodal filtered densities, and (c) subphase constant or elementally constant physical density.

Different Coupling Strategies

The choice of variables for coupling the density and the LSF through Eqn.(4.1.11) or Eqn.(4.1.12) is not unique. Either the raw design variable fields (i.e., $\mathbf{s}^{\phi}$ and $\mathbf{s}^{\rho}$) could be coupled or any choice of filtered or projected quantity derived from them. On the LS side, using filtered LS values (i.e., ϕ) is most advisable to operate on a smoothed field which is directly used for domain decomposition (see Eqn.(4.1.6)). With regards to the density values, it is most advantageous to use the nodally filtered and projected density field (i.e., $\hat{\rho}$) since smoothness and feature size control is gained through that. Compared to elemental density fields, a nodal density field greatly increases the design freedom through increased spatial resolution. This, in turn, improves the smoothness of the XFEM interface which closely traces the density design variable field. Especially, when the density boundary is not aligned with the background mesh, a jaggedly tracing XFEM boundary might be obtained when elementally constant densities are used for coupling the density field and the LS field.

In order to use a SIMP type approach for material interpolation, the following sequence is used to obtain elementally constant physical material properties from nodally defined density design variables:

(1) The optimizer operates on nodal density design variables $\mathbf{s}^{\rho}$.

(2) Filtered nodal density values $\tilde{\rho}$ are obtained.

(3) Projected nodal density variables $\hat{\rho}$ are calculated and used for coupling between the density and the LSF.

(4) SIMP interpolation is used to compute nodal physical material properties.

(5) Evaluation of elementally constant material properties for XFEM computation at element centroid (unintersected elements) or subphase centroid (intersected elements).

An example of three of the fields discussed above is shown in Figure 4.5. The (raw) nodal density design variable field $\mathbf{s}^\rho(\mathbf{X})$ is shown in Figure 4.5 (a), the filtered density field $\tilde{\rho}(\mathbf{X})$ is shown in Figure 4.5 (b) and Figure 4.5 (c) shows the elementally constant physical density field $\rho^e(\mathbf{X})$ after projection and interpolation using SIMP.

It should be pointed out that for intersected elements, as noted in Section 4.1.3.1, elementally constant material properties are used per unique subphase. This further increases the resolution of the material property field as intra-elementally changing but subphase constant material properties can be achieved in intersected elements.

Based on numerical experiments, it has been determined that during a combined LS-density optimization problem, the physics drives densities and the densities control the LSF (which follows closely). The reason for this one-way coupling is seen in the fact that the density field possesses global design sensitivities while the LS sensitivities are localized and only non-zero in the vicinity of the XFEM interface, once the hole-nucleation process has taken place. Initially, only design sensitivities with respect to the density design variables exist.

A complete hand-over from a pure density problem (which does not need holes to initiate the design, but produces intermediate density values and a jagged material interface at convergence) to a pure LS-XFEM problem (which needs initial holes but converges to a pure binary material problem with a crisply defined interface) can be performed in a continuation approach. After initial holes were seeded by the density field creating a locally positive LSF, all density design variables

within phase I can be fixed to 1, whereas all density design variables in phase II are set to 0. After that, the LSF is evolving independently from the underlying initial density field and homogeneous materials of pure solid ($\mathbf{s}^\rho = 1$) and pure void ($\mathbf{s}^\rho = 0$) are maintained in phase I and phase II, respectively. The independent evolution of the LSF then also allows for drastic changes in topology which were not possible by the density method, due to locking of the design into a local minimum. However, feature size control obtained through a continuously coupled LSF to the underlying density field is lost.

In summary, when a global mass measure considering both, the mass in phase I and in phase II is enforced, hole nucleation and minimum feature size control are achieved. Holes are nucleated through the lower penalty while preventing the LS field from undercutting the density field is achieved through the global mass measure.

Local Mass Measure only on Phase I

Instead of considering contributions from both phase I and phase II in the evaluation of the mass of a structure, it is physically more meaningful to only consider phase I (solid domain). Using this approach, a nice 0-1 design is obtained from the density field, while the LS-XFEM takes care of satisfying the mass constraint. The downside of this approach is that the density field (i.e., SIMP problem) only sees a mass constraint until void areas emerge using LS-XFEM. Since the mass constraint is not evaluated within those void areas, as much high density material as desired can be placed there since it does not contribute to the overall mass of the structure. Therefore, material in phase II does neither contribute to the mass nor to the stiffness of the overall design as this phase is excluded from the structural analysis (void phase). Without any further treatment, undercutting of the density field is not prevented and therefore feature size control of the LSF is lost as the interface can move (somewhat) independently from density field. The upper penalty (Eqn.(4.1.12)) enforces a coupling between the density and the LSF with respect to high density values and a negative LSF (solid). This mitigates undercutting and ties back the LSF to the density field as global mass

constraint did. Similar transition zones between purely solid and purely void elements are again seen in the vicinity of the XFEM interface.

Without the enforcement of the upper penalty, the local mass measure in phase I in combination with the lower penalty only yields the hole nucleation feature, as LS undercutting of the density field is not prevented.

Numerical examples in Section 5.4.1 are used to illustrate the combined LS-density approach with a mass constraint only enforced on phase I.

4.1.3.3   Other Level-Set and Density Field Coupling Approaches

In addition to the two combined LS-density approaches discussed above, a strongly coupled LS-density approach could be envisioned. The strong coupling stems from the fact that, for example, only a single field of design variables is used. If only a LSF is present, the material interpolation can be performed as a function of the LSF, or alternatively if only a density field is used the iso-contours of the density field could be used to define the material interface in a crisp manner. Using this strongly coupled approach, only partial benefits exhibited by either method are obtained and therefore this approach is not considered further in this thesis.

4.2   Stability Considerations

To achieve the required robustness of the XFEM analysis model for TO applications, different approaches and stability considerations are discussed. These include preconditioning, shifting of the XFEM interface and ghost stabilization. Ill-conditioning of the linear system occurs with Heaviside-enriched XFEM when the material interface gets too close to a FE node of the background mesh. During a TO process or any other XFEM simulation where the interface evolves, this situation is encountered frequently. As XFEM sub-domains reduce in area/volume, the area of influence of the associated DOFs vanishes which results in an increased condition number of the associated linear system. Ill-conditioning can harm or prevent convergence of the linear and nonlinear solve and overall affects the convergence of the optimization problem.

Using a geometric preconditioner, as proposed by [107] largely mitigates this issue. In this work, a preconditioning scheme is computed which balances the influence of all DOFs in the system based on their area of influence. If the area of influence of a certain DOF is too small, i.e., its contribution to the condition number of the system is too large, the respective DOF is eliminated. This only slightly affects the accuracy of the solution while drastically improving stability.

Instead of a preconditioner, face-oriented ghost penalization as proposed by [30] can be employed to achieve intersection-independent stabilization with XFEM. A discussion and an extension of ghost stabilization for linear and higher-order XFEM is presented in Section 3.1.3 and Section 3.2.1, respectively.

An alternative approach for stabilization of higher-order XFEM is local interpolation order reduction near intersected elements. It was first proposed by [173] and a brief discussion is presented in Section 3.2.4.

In addition to the stabilization approaches discussed, a Jacobi preconditioner on the nonlinear system, consistent LS shifting and selective structural springs are presented hereinafter to further improve the robustness of the LS-XFEM framework for TO. The nonlinear Jacobi preconditioner is discussed in the subsequent section.

4.2.1   Jacobi Preconditioner

To improve the condition number of a nonlinear system, a Jacobi preconditioning scheme is introduced. Following the work of [107], the original discretized FE problem $\mathbf{K} \cdot \mathbf{u} = \mathbf{R}$ is transformed and solved in a non-physical space. The consistent tangent stiffness matrix is $\mathbf{K}$, $\mathbf{u}$ is the solution vector containing all free DOFs and $\mathbf{R}$ is the global (free) residual vector including external forces. After a solution is obtained, scaling it back to physical space provides the correct solution of the initial, discretized problem. This is necessary for badly conditioned nonlinear systems which, if purely solved in the physical space, would lead to high solution inaccuracies and/or divergence of iterative nonlinear solvers. It should be noted that this purely algebraic preconditioner is commonly performed by linear solvers. The distinction here is that preconditioning is applied on the nonlinear system. This means the preconditioning matrix $\mathbf{T}_0$ is only computed once, using the first linearized system, and then used for all subsequent linearized systems within the same Newton-Raphson solve. The preconditioning matrix is obtained as:

$$\mathbf{T}_0 = \frac{1}{\sqrt{\text{diag}(|\mathbf{K}_0|)}} \mathbf{I} \tag{4.2.1}$$

such that $\mathbf{T}_0$ is a diagonal matrix $(\mathbf{T}_0 = (\mathbf{T}_0)^T)$ containing the inverse of the absolute of the square root of the diagonal entries of the initial stiffness matrix $\mathbf{K}_0$ as its entries. Taking the absolute is necessary in case instable systems with negative entries on the diagonal of the Jacobian matrix are considered. At this point in the algorithm, a check for strictly positive diagonal entries can be added to ensure a non-singular linear system.

With Eqn.(4.2.1), the transformed stiffness matrix and residual vector in non-physical (solution) space for any linearized system with a Newton-Raphson solve are obtained as:

$$\tilde{\mathbf{K}} = (\mathbf{T}_0)^T \mathbf{K} \mathbf{T}_0 \tag{4.2.2}$$

$$\tilde{\mathbf{R}} = (\mathbf{T}_0)^T \mathbf{R} \tag{4.2.3}$$

where $\tilde{\bullet}$ denotes quantities in the transformed, non-physical space.

Using the Jacobian and the residual vector transformed into non-physical space, the new linear

system to be solved is:

$$\tilde{\mathbf{K}} \cdot \tilde{\mathbf{u}} = \tilde{\mathbf{R}} \tag{4.2.4}$$

After a solve in non-physical space, all quantities are scaled back to physical space using:

$$\mathbf{K} = (\mathbf{T}_0)^{-T}\tilde{\mathbf{K}}(\mathbf{T}_0)^{-1} \tag{4.2.5}$$

$$\mathbf{R} = (\mathbf{T}_0)^{-T}\tilde{\mathbf{R}} \tag{4.2.6}$$

$$\mathbf{u} = \mathbf{T}_0\tilde{\mathbf{u}} \tag{4.2.7}$$

This approach can be used in combination with face-oriented ghost stabilization to enhance convergence of nonlinear systems during LS-XFEM TO.

4.2.2 Consistent Level-Set Shifting

As it was shown by [191], shifting of LS values is critical, in order to avoid intersections too close to FE nodes of the background mesh. The reason that XFEM intersections cannot coincide with or be close to a background node stems from the fact that the generalized Heaviside enrichment function (Eqn.(3.1.1)) is singular in this case. Traditionally, simple shifting of LS values below a certain critical LS threshold has been used. Since, in general, a unit gradient of the LSF is not guaranteed, shifting of the LS value itself might not necessarily lead to the desired shifting of the XFEM interface away from a FE node. If for instance, a very steep LSF is considered and a LS shift of $\delta\phi$ is performed, the shifted distance might be much less than the anticipated δX. In turn, for very flat LSFs, a shifting of $\delta\phi$ at a node might lead to a shift of the XFEM interface by much more than the intended δX, see Figure 4.6 (b). Therefore, a consistent LS shifting approach is developed hereinafter which is guaranteed to achieve the desired spatial shift through consistently shifting the LS value while taking the local LS gradient into account. It is assumed that the LSF which is used for XFEM decomposition is always interpolated linearly within a background FE, regardless of the interpolation order of the background mesh. This leads to the fact that every element edge can at most be intersected once by the XFEM. See Section 3.2 for more details.
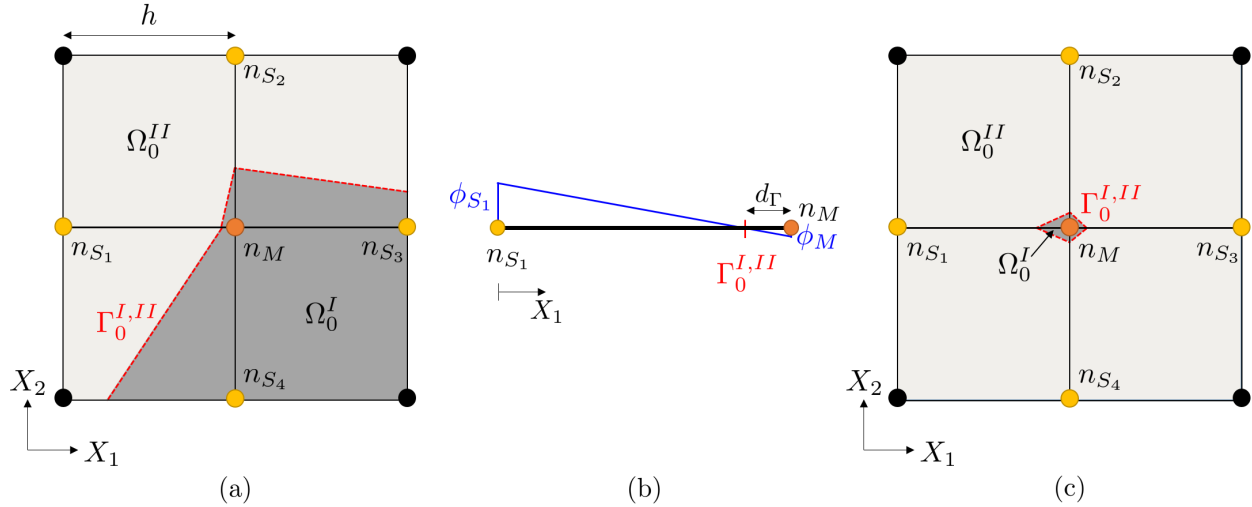
Figure 4.6: Critical intersection configurations with respect to the center (master) node n_M. (a) Violation of critical distance between master node n_M and slave node 1 n_{S_1}, (b), associated LS values of master node n_M and slave node 1 n_{S_1} leading to a critical intersection, and (c) violation of critical distance between master node n_M and all four connected slave nodes leading to an isolated inclusion.

For a consistent shifting scheme, only the LS values of element corner nodes need to be considered because LS values of element middle nodes (if any exist) are always dependent variables of the corresponding corner nodes. Within the scope of this thesis, middle node LS values are not considered for XFEM triangulation and enrichment, therefore shifting with respect to those nodes is not required.

The following LS shifting scheme is iterative in nature and repeated until no more shifts in LS values occur in the entire domain, meaning that all criteria (e.g., minimum distance away from a node) are satisfied.

4.2.2.1 Achievement of Critical Minimum Distance

The first characteristic of the consistent LS shifting scheme is the achievement of a critical minimum (spatial) distance of the intersection away from a FE node. Consider the case depicted in Figure 4.6 (a) where the XFEM interface violates the critical minimum distance with respect to the master node in the middle (n_M) on the edge n_{S_1}–n_M. Therefore, the LS value at the master node

needs to be adjusted accordingly, in order to sufficiently shift away the XFEM interface from the master node. The consistent LS shifting scheme therefore considers all (slave) nodes connected to the current master node connected via shared edges and obtains their LS values. In 2D up to 4 slave nodes are connected to a master node via the shared edges (see Figure 4.6 (a)) and in 3D up to 8 slave nodes are connected to a master node. To identify any edge on which the minimum critical distance is violated, the LS value of each slave node is compared with the LS value of the master node. If they are of the same sign, the edge is unintersected and therefore not treated further. If they are of opposite sign, an intersection is present and the distance d_Γ between the master node and the XFEM intersection is computed using the intercept theorem as:

$$d_\Gamma = \frac{|\phi_M|\,h}{|\phi_M| + |\phi_{S_i}|} \tag{4.2.8}$$

where ϕ_M is the LS value at the current master node, ϕ_{S_i} is the LS value at the current slave node, and h is the element edge length. If the obtained distance is below a minimum critical distance ϵ_d, such that $d_\Gamma < \epsilon_d$, the master LS value needs to be updated, in order for the minimum critical distance condition to be satisfied. The new LS value at the master node is computed as:

$$\tilde{\phi}_M = \text{sign}(\phi_M)\frac{|\phi_{S_i}|\,\epsilon_d}{h - \epsilon_d} \tag{4.2.9}$$

where $\tilde{\phi}_M$ is the shifted LS value at the master node. In practice, the critical minimum distance is defined as a function of the element edge length, e.g., $\epsilon_d = 1 \cdot 10^{-5}h$.

4.2.2.2 Elimination of Isolated Inclusions

A second critical scenario, which is not addressed by solely shifting of the master LS value, is if small isolated inclusions are encountered. This is conceptually shown in Figure 4.6 (c). Oftentimes, isolated material inclusions arise in the presence of very shallow LSFs. In order to detect and eliminate small isolated inclusions, a loop over all slave nodes connected to a master node is performed, and the distance between the master node and the XFEM interface is summed over, using Eqn. (4.2.8). In case an edge is not intersected, $d_\Gamma = h$ is added to the summation over all

edges. The sum over all edge distances i is determined as:

$$S_{d_\Gamma} = \sum_{i=1}^{n_S} d_{\Gamma_i} \qquad (4.2.10)$$

while the minimum required sum of distances is

$$S_{\epsilon_d} = \sum_{i=1}^{n_S} \epsilon_d \qquad (4.2.11)$$

where n_S is the number of slave nodes associated with the current master node. If the sum over all distances is less than the sum over all critical distances, i.e., $S_{d_\Gamma} < S_{\epsilon_d}$, the mean of all slave node LS values is used to update the master node LS value. Mathematically, this means:

$$\tilde{\phi}_M = \frac{\sum_{i=1}^{n_S} \phi_{S_i}}{n_S} \qquad (4.2.12)$$

Eqn.(4.2.12) therefore eliminates small isolated inclusions by replacing the master LS value (which is different in sign compared to all corresponding slave node LS values) with the mean of all slave node LS values.

4.2.2.3   Discussion

After applying both, the consistent LS shifting scheme (Section 4.2.2.1) and the isolated inclusions elimination scheme (Section 4.2.2.2), either critical situations shown in Figure 4.6 (a) and (c) would be resolved. However, it should be noted that any shifting scheme introduces (slight) non-differentiable design changes which are not seen by the optimization algorithm. Therefore it is crucial to use a small thresholding value ($\epsilon_d \ll 1.0$) which provides sufficient stability without impeding the optimization process. This is especially important with respect to design sensitivity analysis. It has been shown by [163], that globally finite differenced design sensitivities are meaningless as soon as LS shifting is evoked for a certain design variable. When using the adjoint method, consistent design sensitivities are obtained if LS shifting is accounted for properly. As mentioned before, consistent LS shifting and elimination of isolated domains is especially critical when no LS regularization is used (i.e., when no signed distance character of the design LSF can be guaranteed). More details regarding a SDF regularization are discussed in Section 4.3.

4.2.3 Selective Structural Springs

A special stability consideration in solid-void LS-XFEM TO is the stabilization of disconnected solid sub-domains (Ω_0^I) if the void domain (Ω_0^{II}) is excluded from the XFEM analysis. It is crucial to stabilize those unconstrained solid sub-domain embedded in the void to prevent rigid body motion (RBM) and ill-condition of the linear system. This can be achieved by globally applying a small stiffness contribution to the diagonal of the global stiffness matrix for every DOF. Physically, this represents attaching weak springs globally to every DOF in the entire domain. This has successfully been demonstrated by [189] for small strain linear elastic problems using linear brick elements. Alternatively, disconnected material sub-domains can be identified and a spring stiffness is only added to DOFs associated with isolated material domains. This is especially crucial for large deformation structural problems using higher-order XFEM elements, where globally applied weak springs heavily impede the deformation prediction using XFEM. Therefore, a selective springs approach initially proposed by [190, 191] for fluid problems is adopted in this thesis for large strain nonlinear structural problems.

To identify disconnected solid sub-domains in a solid-void LS-XFEM setting, an auxiliary indicator field $\tilde{\theta}(\mathbf{X})$ is used. The indicator field is modeled as a linear diffusion problem with bulk convection within the solid domain (Ω_0^I).
The weak form of the governing equation of the auxiliary indicator field in residual form is:

$$\mathbf{R}_{Aux} = \int_{\Omega_0^I} \delta \nabla \tilde{\theta} \ (\kappa \nabla \tilde{\theta}) + \delta \tilde{\theta} \ h_B (\tilde{\theta} - \tilde{\theta}_{ref}) dV \qquad (4.2.13)$$

where κ is the thermal conductivity, h_B is the bulk convection coefficient, and $\tilde{\theta}_{ref}$ is the reference indicator value. Typical numerical values for the conductivity and bulk convection are $\kappa = 30.0$ and $h_B = 0.01$, respectively. In order to identify mechanically disconnected solid sub-domains surrounded by void (see Figure 4.7 (a)), Dirichlet boundary conditions of $\bar{\tilde{\theta}} = 0.0$ on the auxiliary indicator field are applied everywhere where mechanical boundary conditions are applied to the structural problem (i.e., on Γ_D). Along with a reference indicator value of $\tilde{\theta}_{ref} = 1.0$, the solution of Eqn.(4.2.13) yields indicator values of close to zero in mechanically connected domains and indicator
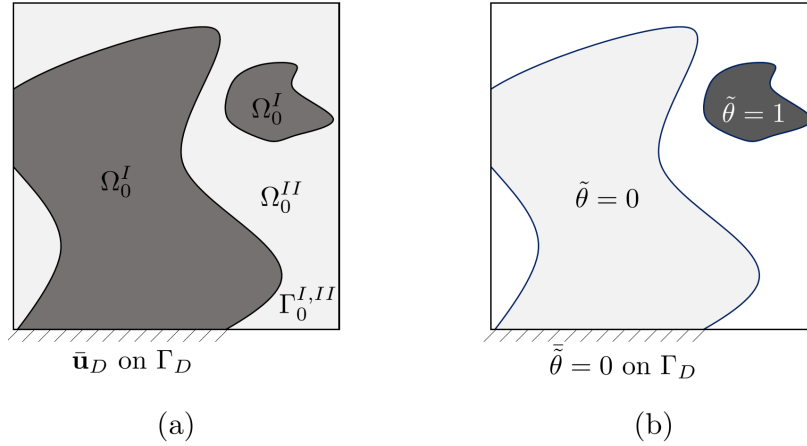
Figure 4.7: Domain decomposition using LS-XFEM for a solid-void problem. (a) Mechanical domain decomposition and boundary conditions, (b) auxiliary indicator field solution and boundary conditions.

values of close to one in isolated solid domains, see Figure 4.7 (b). It should be noted that by adding a bulk convection term to Eqn.(4.2.13), ill-conditioning of the auxiliary indicator problem in the presence of disconnected sub-domains is prevented.

To project the indicator values, to either exactly 0.0 or exactly 1.0, a smoothed Heaviside projection is used which is defined as:

$$\bar{\theta} = \frac{1}{2} + \frac{1}{2} \tanh(k_w(\tilde{\theta} - k_t \tilde{\theta}_{ref})) \tag{4.2.14}$$

where $\bar{\theta}$ is the projected indicator value, k_w is the projection sharpness parameter, and k_t is the projection threshold. Typically a projection sharpness of $k_w = 1000.0$ and a threshold of $k_t = 0.9$ are used. After the auxiliary indicator field solution has been projected, the residual of the nonlinear structural problem is augmented by the following selective spring stiffness term:

$$\mathbf{R}_{Spr} = \int_{\Omega_0^I} \mathbf{u} \, \mathbf{I} \, r_s \, E \, \bar{\theta} \, dV \tag{4.2.15}$$

where the relative spring stiffness ratio is r_s, and E is the Young's modulus of the solid material. Typically, relative spring stiffness ratios in the order of $r_s = 1.0 \cdot 10^{-10}$ or smaller are sufficient to stabilize the structural problem.

In this work, the auxiliary indicator field is solved separately and prior to the physical governing equations using a one-way coupled block solver (see Section 3.4). Design sensitivities of the selective structural springs are neglected as selectively enabled springs introduce a non-differentiability in the design process. As isolated material inclusions are typically eliminated by the optimizer within a few design iterations, constraining their deformation to stabilize the linear system has proven to not hinder a proper design evolution. Numerical studies indicated the validity of this approach. More details regarding structural selective springs are found in Appendix B and Appendix C.

4.3 Explicit Level-Set Regularization

A strong need for LS regularization has been identified for both, implicit and explicit LSMs. This is due to the fact that a locally too flat or too steep LSF negatively affects the stability and the rate of convergence of an optimization problem. In turn, having a uniform, uniquely defined LSF greatly improves those desired properties. To date, different regularization schemes have been proposed [188]. Perimeter regularization is used to achieved a well-posed optimization problem [80] and Tikhonov regularization is oftentimes employed to improve the smoothness of the LS gradient [147, 206]. Uniqueness of the LSF is however not guaranteed by these regularization techniques and a flat LSF may still be obtained. As identified by [188], a strong need for regularization schemes still exists. For the case of explicit LSMs, a signed-distance field regularization scheme is therefore developed and applied to multiple numerical design optimization examples in this thesis.

As a unit norm gradient of the LSF (i.e., $|\nabla\phi| = 1.0$) is desired in the vicinity of the material interface in LS-based TO, a SDF is commonly used for reinitialization, as it supports a unit norm gradient by construction. During the evolution of the design optimization process, the signed distance character typically vanishes [73] and therefore additional regularization terms need to be incorporated into the optimization problem formulation to retain a SDF characteristic of the LSF [36, 90, 114, 115, 176, 212, 213]. For implicit LSM, an auxiliary HJ equation is solved or fast marching methods [158] are used for periodic reinitialization of the LSF during an optimization. The intermittent reinitialization process however introduces discontinuities in the design optimization process as the zero LS iso-contour is slightly shifted [83, 143]. This, in turn, negatively affects the convergence of the optimization problem.

Alternatively, energy functionals have been proposed as penalty terms to the objective function to penalize the deviation of the LSF from a SDF [36, 55, 114, 197, 212]. While the gradient in the vicinity of the interface can somewhat be controlled via these energy functionals, gradient oscillations away from the interface are observed [115, 213]. Therefore, double-well potential functions were introduced [90, 115, 213] to not only enforce a unit norm gradient near the interface but also zero
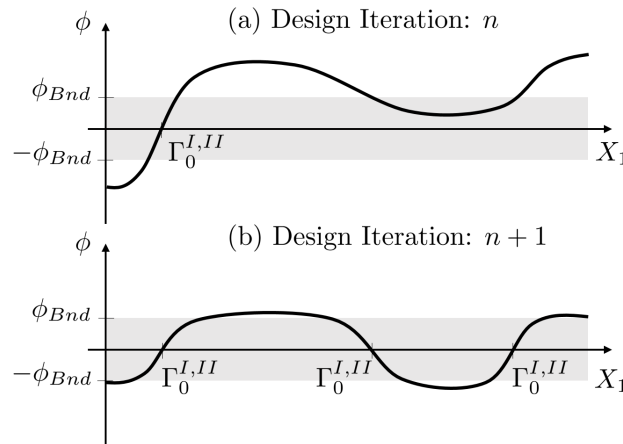
Figure 4.8: Drawback of local LS regularization, illustrated for two subsequent design iterations, (a) and (b).

gradient of the LSF away from the interface. As identified by [67], a limitation of these local regularization methods is the fact that they directly operate on the local LS value, or its gradient, and have no notion about the global distance to the actual material interface. This can lead to undesirable material inclusions away from the material interface, due to the inability of those local methods to distinguish between points of the same LS value but with a different distance to the interface. This limitation is conceptually illustrated in Figure 4.8 for two subsequent design iterations. Using a simple 1D example, a unit gradient is enforced at all points where the LS values are between some bounds $-\phi_{Bnd} \leq \phi \leq \phi_{Bnd}$ at design iteration n (see Figure 4.8 (a)). This however leads to new material intersections in the subsequent design iteration $n + 1$, regardless of their benefit for improving the design (see Figure 4.8 (b)). Due to the lack of local measures to distinguish between areas where $-\phi_{Bnd} \leq \phi \leq \phi_{Bnd}$ and an interface is present and areas where $-\phi_{Bnd} \leq \phi \leq \phi_{Bnd}$ without any interface, spurious material inclusions are frequently created. This is due to the enforcement of $|\nabla \phi| = 1.0$ anywhere where the LS value is between certain bounds $\pm \phi_{Bnd}$. Using energy functionals to achieve LS regularization as part of the objective is therefore very challenging and requires careful tuning for a specific problem.

Addressing the limitations of the regularization schemes discussed, an explicit LS regularization scheme which minimizes the difference between a globally defined target LSF and the design LSF

$\phi(\mathbf{X})$ is proposed. The target LSF is reconstructed at every design step using an extension of the Heat Method (HM) [39, 40] for a given interface, which is in turn defined by the design LSF. The target LSF is globally defined, unique, smooth, and treated as a prescribed field for a certain design iteration. The proposed penalty formulation is differentiable and therefore alleviates the need for discontinuous reinitialization during the design process.

4.3.1   The Heat Method

Classically, either fast marching approaches [158] or fast sweeping approaches [202] are used for SDF computation. To circumvent the implementation challenges associated with those classical approaches, and to alleviate the parallelization difficulties, the HM is used instead for SDF computation. To obtain the SDF, a transient heat conduction problem is solved first. The strong form of the governing equation is identical to the one discussed in Section 2.1 where all material parameters are taken as unity. Moreover, zero initial conditions are applied and a unit Dirichlet heat source is applied weakly at the XFEM interface, i.e., $\theta(\Gamma_0^{I,II}) = 1.0$.

The distance field $\phi_D(\mathbf{X})$ is then obtained as a solution of a Poisson's equation with the negative normalized temperature gradient as the volumetric heat source. The strong form of the governing equation of the distance field is:

$$\Delta\phi_D = \nabla \cdot \left(-\frac{\nabla\theta}{|\nabla\theta|} \right) \tag{4.3.1}$$

where the Laplacian is denoted by Δ and $\nabla\cdot$ is the divergence operator. The boundary conditions on the distance field are homogeneous Dirichlet at the XFEM interface, i.e., $\phi_D(\Gamma_0^{I,II}) = 0.0$. By enforcing this homogeneous boundary condition at the interface, it is guaranteed that the distance field $\phi_D(\mathbf{X})$ and the design LSF $\phi(\mathbf{X})$ are identical at the XFEM interface. This yields the desired property that no spatial fluctuations are introduced when reconstructing the (signed) distance field. Finally, the SDF $\phi_{SD}(\mathbf{X})$ is computed using the sign information of the design LSF $\phi(\mathbf{X})$, as:

$$\phi_{SD} = \text{sign}(\phi)\phi_D \tag{4.3.2}$$
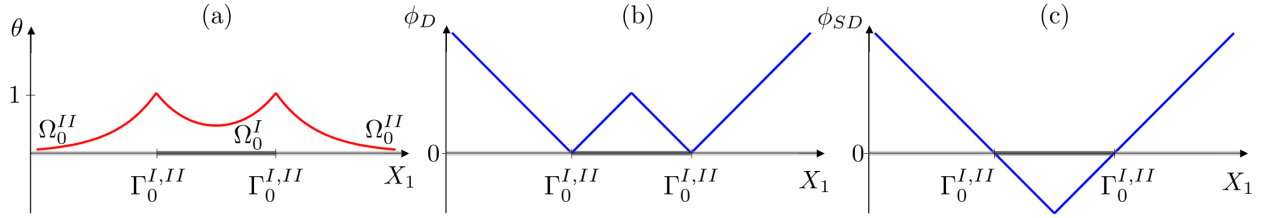
Figure 4.9: Computation of the SDF using the HM. (a) A heat conduction problem is solved with a heat source ($\theta = 1$) at the XFEM interface, (b) the distance field is obtained from normalized temperature gradient, and (c) the SDF is computed using sign information of each phase.

The three steps are conceptually shown in Figure 4.9 (a), (b), and (c) for a simple 1D problem with two interfaces. It is important to again point out the difference between design LSF $\phi(\mathbf{X})$ and the reconstructed SDF $\phi_{SD}(\mathbf{X})$. The design LSF is an explicit function of the design variables (see Eqn.(4.1.7)) and used for LS-XFEM domain decomposition, see Eqn.(4.1.6). The XFEM interface $\Gamma_0^{I,II}$ is then the starting point for the HM from which the SDF $\phi_{SD}(\mathbf{X})$ is obtained.

The weak form of the transient heat conduction problem follows Eqn.(2.1.3) where an explicit Euler backward scheme (Eqn. (2.1.2)) is used for time integration. To achieve maximum accuracy of the SDF, a time step size of $\Delta t = h^2$ is recommended by [40]. On the other hand, in order to increase the efficiency of the HM, solving the transient temperature problem for only a single time step is recommended. In order to obtain a meaningful SDF, the time step size needs to be sufficiently large to obtain a non-zero temperature gradient in the entire design domain. Solving the heat conduction problem for only a single (sufficiently large) time step significantly reduces the computational cost while only slightly impeding the accuracy of the SDF away from the interface.

Combining Eqn.(4.3.1) and Eqn.(4.3.2), the weak form of the governing equation for the SDF is:

$$\int_{\Omega_0^D} \delta \nabla \phi_{SD}(\nabla \phi_{SD} - \mathbf{G}) \, dV - \int_{\Gamma_0} \delta \phi_{SD}(\nabla \phi_{SD} \mathbf{N} - \mathbf{GN}) \, dA = 0 \qquad (4.3.3)$$

where $\delta \phi_{SD}$ is an admissible test function and the source term $\mathbf{G}$ is computed as:

$$\mathbf{G} = -\text{sign}(\phi) \left(\frac{\nabla \theta}{|\nabla \theta|} \right) \qquad (4.3.4)$$

Assuming that the projected SDF and the projected normalized temperature field are identical along external boundaries, the last term in Eqn.(4.3.3) vanishes. This corresponds to homogeneous Neumann boundary conditions on the SDF.

Both, the temperature field $\theta(\mathbf{X})$ and the SDF $\phi_{SD}(\mathbf{X})$ are discretized using the XFEM (see Section 3.1) and are evaluated over the entire design domain $\Omega_0^D = \Omega_0^I \cup \Omega_0^{II}$. Interface conditions and boundary conditions are applied weakly using Nitsche's method (see Section 3.1.2). In addition, face-oriented ghost stabilization (Section 3.1.3) is employed for both, the temperature field and the SDF.

4.3.2 Formulation of Regularization Penalty

To achieve continuous regularization of the design LSF, a penalty term is added to the objective function which minimizes the squared difference between the design LSF $\phi(\mathbf{X})$ and a target LSF $\tilde{\phi}(\mathbf{X})$ as well as the difference in spatial gradients. The regularization penalty term p_{Reg} is formulated as:

$$p_{Reg} = \frac{\int_{\Omega_0^D}(\phi - \tilde{\phi})^2 dV}{\int_{\Omega_0^D}(\phi_{Bnd})^2 dV} + \frac{\int_{\Omega_0^D}(|\nabla\phi - \nabla\tilde{\phi}|)^2 dV}{\int_{\Omega_0^D} dV} \tag{4.3.5}$$

where the target LSF $\tilde{\phi}(\mathbf{X})$ is obtained from the SDF. As the design LSF matches the target LSF, both terms of Eqn.(4.3.5) vanish. Also, the sensitivities of p_{Reg} vanish at convergence. Minimizing the difference in spatial gradients in addition to minimizing the difference in values between design LSF and target LSF improves the effectiveness of the penalty (Eqn.(4.3.5)) as it reduces spatial oscillations. Weighting both terms in Eqn.(4.3.5) equally yields a good balance between matching the target LSF and avoiding spatial oscillations. To remove length-scale dependence, both terms in Eqn.(4.3.5) are normalized.
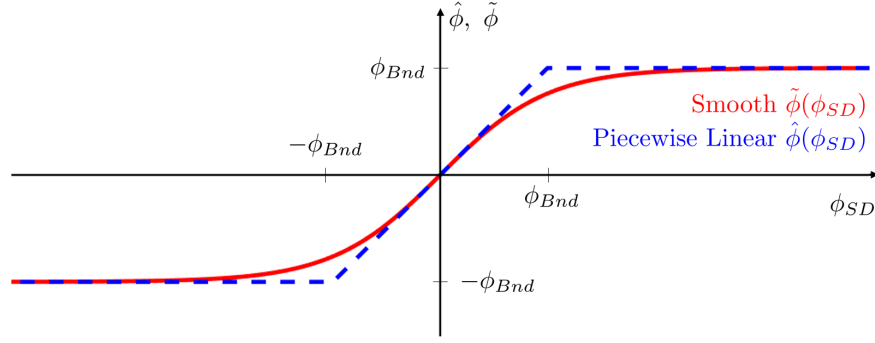
Figure 4.10: Construction of the target LSF, using either a piecewise linear or a smooth approximation.

To obtain a bounded design LSF away from the interface, the following piece-wise linear truncated LSF is proposed:

$$\hat{\phi}(\mathbf{X}) = \begin{cases} -\phi_{Bnd} & ,\forall \quad \phi_{SD}(\mathbf{X}) \leq -\phi_{Bnd} \\ \phi_{SD}(\mathbf{X}) & ,\forall \quad -\phi_{Bnd} < \phi_{SD}(\mathbf{X}) < \phi_{Bnd} \\ \phi_{Bnd} & ,\forall \quad \phi_{SD}(\mathbf{X}) \geq \phi_{Bnd} \end{cases} \quad (4.3.6)$$

Using Eqn.(4.3.6) the SDF is matched near the interface, whereas the lower bound $-\phi_{Bnd}$ is matched in Ω_0^I and the upper bound ϕ_{Bnd} is assumed in Ω_0^{II} (see Figure 4.10). To retain differentiability of the target LSF, a smooth target field is used to approximate Eqn.(4.3.6). Using a sigmoid function, the smooth target field $\tilde{\phi}(\mathbf{X})$ is formulated as:

$$\tilde{\phi}(\mathbf{X}) = \left(\frac{2}{1 + e^{\left(\frac{-2\phi_{SD}}{\phi_{Bnd}}\right)}} - 1 \right) \phi_{Bnd} \quad (4.3.7)$$

A comparison between the piece-wise linear target field (Eqn.(4.3.6)) and the smooth approximation (Eqn.(4.3.7)) is shown in Figure 4.10.

In order for the LS regularization term of Eqn.(4.3.5), not to dominate the overall objective and therefore the evolution of the XFEM interface, an appropriate weighting of the penalty contribution p_{Reg} is required. As shown in the work of [67], a penalty weight of $w \leq 0.1$ yields good results. However, implicit dependencies of the penalty term on the design variables through the SDF state variables might hinder an unaffected evolution of the interface. The target LSF and therefore the

reconstructed SDF should be treated as a prescribed target at every design iteration, and therefore only explicit dependencies of p_{Reg} on the design variables $\mathbf{s}^\phi$ are considered. Unlike in classical LS-XFEM TO, design sensitivities of p_{Reg} exist in the entire design domain. By neglecting implicit design sensitivity contributions of Eqn.(4.3.5), the computational cost of the sensitivity analysis is significantly reduced. More details about design sensitivity analysis are discussed in Section 4.6.

By treating the target LSF $\tilde{\phi}(\mathbf{X})$ as a prescribed field without any dependencies on the design variables, makes the regularization penalty Eqn.(4.3.5) behave as a "clean-up" procedure which follows the XFEM interface. It is important to note that the regularization mainly affects LS values away from interface and maintains a unit slope in the vicinity of the interface. Therefore, it does not influence the zero LS iso-contour which defines the material interface. As the target LSF is achieved, the penalty contribution and its sensitivities vanish. Therefore, instead of formulating the regularization term (Eqn.(4.3.5)) as a penalty, it could alternatively be used as a constraint, e.g., $p_{Reg} \leq \epsilon_p$ where $\epsilon_p \ll 1$.

Numerical examples in 2D and 3D for multiple physics using the explicit LS regularization approach are presented in Section 5.5. Additional features like the influence of the penalty weight, the number of time steps, and the influence of including implicit design sensitivities are studied. An additional discussion of the regularization approach can be found in Appendix D.

4.4 Feature Size Control

Controlling the size of minimum features within TO has been widely-discussed and is a long-standing issue in TO. It is not only critical to prevent small features from a numerical point of view in order to obtain sufficient stability, accuracy, and mesh-independence (e.g., robust design), but also from a manufacturing point of view it is highly desirable to control the size of features. While in density-based TO approaches feature size can be controlled by filtering and projection [76, 74, 75, 165, 166], much less work is found for feature size control in LS methods. In implicit LS-based TO, the SDF is obtained through re-initialization which, in turn, can be used for feature size control. This can either be achieved though identification of the skeleton of a structure [78, 203, 116] or by locating off-sets to the zero LS iso-contour [4, 127, 3, 198]. Alternatively, quadratic energy functionals can be formulated to achieve control of features [33, 118] which regularize the design problem. To obtain a well-posed optimization problem, control of features and regularization of the design is critical. To date, a strong need still exists for better control of minimum features [168], however keeping in mind that no feature size control method is (yet) perfect [4].

In this thesis, a novel approach to control minimum feature size in an explicit LS-XFEM TO process is developed and studied in 2D and 3D, as this has not yet been addressed in literature. Attempts to achieve minimum feature size control for explicit LS-XFEM TO were made by [191] and [37] where explicit geometric distance measures were used to control the size of minimum features. The proposed method utilizes the SDF obtained by the HM (see Section 4.3.1) to identify the shape skeleton on which the value of the SDF is probed, in order to enforce minimum feature size. The basic idea follows the work of [78] where it was applied to implicit LSMs for 2D structural problems. Extending the approach by [78] to an explicit LS-XFEM framework requires to overcome a set of challenges, including computation of higher-order derivatives, discontinuities introduced by the XFEM, and the calculation of a well-resolved skeleton for every design iteration. Moreover, in the work of [78], inconsistencies in the design sensitivities are present which might harm or even prevent the convergence of the optimization problem. In this thesis, a local, fully differentiable minimum
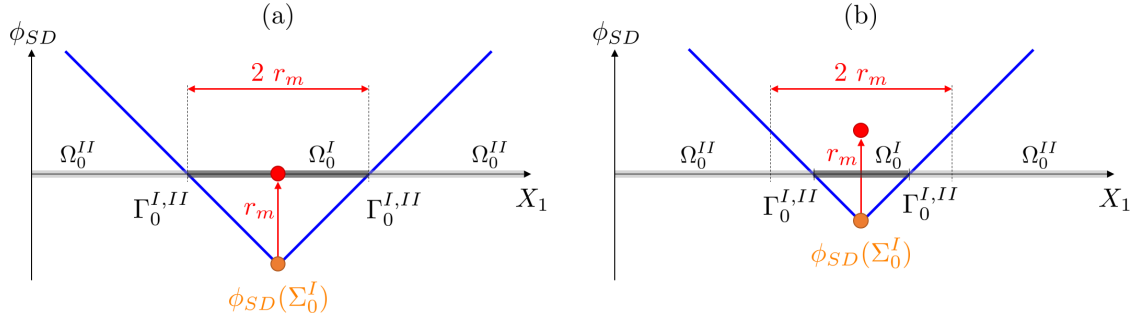
Figure 4.11: Illustration of minimum feature size measure where in (a) the feature size measure is met and in (b) the minimum feature size is violated.

feature size measure is therefore developed and applied to several numerical examples.

As demonstrated by [78], the minimum size of geometric features described by a LSM can be controlled by constraining the signed distance value at specific parts of the design domain. In particular, this set of points is called the medial surface [50], structural skeleton or the ridge of the SDF [4]. The set of all points belonging to the skeleton are denoted by Σ_0 and a mathematical definition of it is presented in Section 4.4.1. An explicit minimum feature size penalty within phase I (Ω_0^I) can therefore be formulated as:

$$p_{FS} = \int_{\Omega_0^I, \Sigma_0^I} \max((\phi_{SD} + r_m), 0) \, dV \qquad (4.4.1)$$

where r_m is the desired minimum feature size radius and the skeleton of phase I is denoted by Σ_0^I. The measure of Eqn.(4.4.1) is zero where ever the minimum feature size is met and non-zero where the minimum feature size is violated. At points where the minimum feature size is not met, the value of p_{FS} corresponds to the signed distance value at the skeleton shifted by the minimum feature size radius, i.e., $\phi_{SD}(\Sigma_0^I) + r_m$. Visually, this is depicted in Figure 4.11, where in Figure 4.11 (a) the minimum feature size is met and in Figure 4.11 (b) it is violated. In this 1D example, the skeleton of the SDF Σ_0^I only consists of a single point which is located at the minimum of ϕ_{SD}. It should be noted that even though the measure of Eqn.(4.4.1) is one single integral over the skeleton of phase I, it is an explicit feature size measure which is enforced locally, i.e., at every integration point at which the volume integral is evaluated. This is an important aspect as the minimum feature size

penalty of Eqn.(4.4.1) can for example be enforced by a single penalty contribution to the objective or by a single constraint.

As can be seen from the formulation of Eqn.(4.4.1), two issues arise. First, Eqn.(4.4.1) is non-differentiable due to the $\max(\bullet)$ operator and second, the identification of the skeleton of phase I Σ_0^I is crucial for this formulation. Suppose the skeleton is described by some field $\lambda(\mathbf{X})$ and points of interested at which Eqn.(4.4.1) should be evaluated are defined where $\lambda(\mathbf{X}) > \bar{\lambda}$ (a more detailed discussion of the skeleton is presented in Section 4.4.2 and 4.4.1). Then, a smooth and differentiable formulation of Eqn.(4.4.1) reads:

$$\tilde{p}_{FS} = \int_{\Omega_0^I} \frac{1}{\beta_{KS}} \ln(e^{\beta_{KS}(\phi_{SD}+r_m)} + 1) \left(\frac{1}{2} + \frac{1}{2}\tanh(\gamma_{SH}(\lambda - \bar{\lambda}))\right) \ dV \qquad (4.4.2)$$

where the $\max(\bullet)$ operator is approximated by a KS function (see Eqn.(4.1.10)). The condition $\lambda(\mathbf{X}) > \bar{\lambda}$ for identifying points on the skeleton is approximated by a smoothed Heaviside function which acts as a weight interpolating between zero and one. The projection sharpness for the KS function is denoted by β_{KS} and γ_{SH} denotes the weighting sharpness of the smoothed Heaviside function. For the work presented in this thesis, these values are set to $\beta_{KS} = 5.0$ and $\gamma_{SH} = 75.0$ which provides a sufficient approximation while maintaining differentiability and smoothness of the feature size measure. The formulation of Eqn.(4.4.2) as a penalty or as a constraint will be explored through numerical examples presented in Section 5.6.

4.4.1 Discussion on the Skeleton

The skeleton Σ_0 or ridge of a shape is the location of discontinuities in the SDF gradients [2, 96]. Alternatively, the skeleton of a shape is defined as a set of all points which have at least two closest points on the material interface $\Gamma_0^{I,II}$ [78]. Yet another, geometry-based, definition of the skeleton states: The skeleton is the location of centers of maximum circles (in 2D) or spheres (in 3D) contained in the shape, i.e., bounded by the zero LS iso-contour [4, 131]. Example skeletons for different shapes described by the zero LS iso-contour $\Gamma_0^{I,II}$ are shown in Figure 4.12.

By definition, a skeleton exists in both phase I and phase II. Since feature size control only within phase I is within the scope of this thesis, only the skeleton of phase I (Σ_0^I) is considered here.
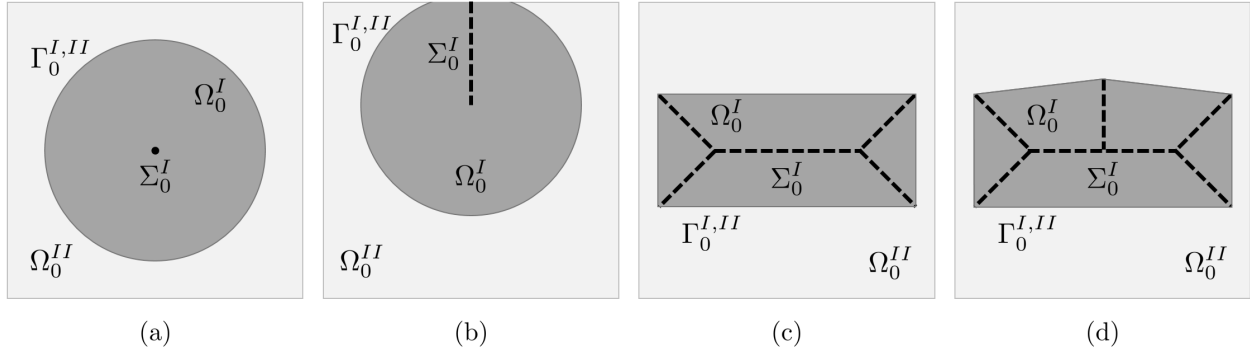
Figure 4.12: Examples of skeletons for different phase I domains embedded in phase II, where the external domain boundary is not described by the zero LS iso-contour.

Moreover, domain boundaries (e.g., the external boundaries of the boxes shown in Figure 4.12) are not described by the zero LS iso-contour and therefore not considered for the skeleton. This is apparent in Figure 4.12 (b) which has a drastically different skeleton than the very similar shape of Figure 4.12. The important difference between shapes of Figure 4.12 (a) and (b) is however that the zero LS iso-contour of Figure 4.12 (b) is open for which a vertical line is the skeleton. The skeleton of a closed circle (Figure 4.12 (a)) is in contrast just a single point. For phase boundaries comprised of straight edges (e.g., a rectangle), drastically different skeletons are obtained for slight boundary perturbations, see Figure 4.12 (c) and (d) [4].

4.4.2 Laplacian of the SDF

The identification of the skeleton of phase I Σ_0^I is crucial for the minimum feature size measure of Eqn.(4.4.1). Following the work of [50], the skeleton of a structure defined by a LSF can be obtained by non-zero values of the Laplacian of the corresponding SDF. Mathematically, these are the locations of discontinuities in the LS gradients which are defined by the Laplacian of the SDF in phase I as [78]:

$$\Sigma_0^I(\mathbf{X}) = \{\mathbf{X}|\ \phi(\mathbf{X}) < 0,\ |\Delta\phi_{SD}| > 0\} \tag{4.4.3}$$

To evaluate the Laplacian of the SDF, second-order spatial derivatives of the SDF need to be computed. In the work of [78], this is done using a finite difference approach proposed by [50] in

combination with a line sweep algorithm to compute the Laplacian and select all points which are part of the skeleton. While conceptually simple, this approach is limited to operate on regular (rectangular) background meshes and poses difficulties for parallelization. In addition, no explicit control of boundary conditions on the LSF or its first and second spatial derivative are possible. This limits the approach in selectively including domain boundaries in the feature size measure calculation.

To circumvent these limitations, operator splitting is used in this thesis to compute higher-order derivatives of the SDF on a linear background mesh using the HM (see Section 4.3.1). Additional scalar and vector fields are solved to compute the gradient of the SDF and the Laplacian, as well as the gradient of the temperature field used as a source in the HM. This allows for explicit control of each field as it is obtained as the solution of a Helmholtz-type PDE. Using a Helmholtz-type PDE for linear filtering has previously been applied to scalar design sensitivities by [110] and to scalar design variable fields by [111, 123]. Solving for each derivative as a separate scalar or vector field provides therefore additional smoothing and continuity across the XFEM interface which leads to increased stability when identifying Σ_0^I. For all fields based on a Helmholtz-type PDE, homogeneous Neumann boundary conditions are assumed, as suggested in [111].

However, when computing higher-order derivatives of the SDF which is obtained by the HM, boundary effects on the SDF are potentially amplified through spatial differentiation. To mitigate boundary effects on the SDF stemming from boundary conditions on the temperature field, it is suggested by [39] to use an average temperature field as the gradient source for the SDF (see Eqn.(4.3.4)). The two averaged temperature fields are obtained from homogeneous Dirichlet and homogeneous Neumann boundary conditions on the domain boundaries which yields the most accurate SDF. The source term used in Eqn.(4.3.4) is therefore computed as:

$$\theta = \frac{1}{2}(\theta^N + \theta^D) \tag{4.4.4}$$

where θ^N and θ^D denote the solution of a homogeneous Neumann and homogeneous Dirichlet temperature problem, respectively. While this adds the solution of an additional temperature field

to the problem, boundary effects on the SDF are significantly reduced through Eqn.(4.4.4).

Alternatively, immersion of the design domain as for example performed by [78] can be used. This approach is especially advantageous in combination with the HM, where boundary effects are largely caused when an XFEM interface intersects with the domain boundary. This is prevented by construction when using a fully immersed design domain. Due to the simplicity of this approach it is the preferred choice for all numerical examples presented in Section 5.6.

4.4.2.1 Normalized Temperature Gradient Field

To obtain a smooth source term (using the normalized temperature gradient) for computing the SDF using the HM (Eqn.(4.3.4)), a vector-valued field $\boldsymbol{\gamma}(\mathbf{X})$ is constructed. To mitigate boundary effects on the SDF, the spatial gradient of the average temperature field (Eqn.(4.4.4)) is used. The strong form of the Helmholtz-type governing equation is:

$$-r_H^2 \Delta \boldsymbol{\gamma} + \boldsymbol{\gamma} = \frac{\nabla \theta}{|\nabla \theta|} \tag{4.4.5}$$

where the Helmholtz filter radius is denoted by r_H and related to a physical smoothing radius r_s by [111]:

$$r_H = \frac{r_s}{2\sqrt{3}} \tag{4.4.6}$$

In the current thesis, the physical smoothing radius is set as a function of the mesh size h, e.g., $r_s = 1h$. Alternatively, a spatially varying smoothing radius can be employed, as discussed in Section 4.5.1.

After multiplying the strong form of the governing equation (Eqn.(4.4.5)) by admissible test functions $\delta\boldsymbol{\gamma}$, performing integration by parts and applying the divergence theorem, the weak form of the governing equation of the normalized temperature gradient field is obtained. It is stated as:

$$r_H^2 \int_{\Omega_0} \delta\nabla\boldsymbol{\gamma}\nabla\boldsymbol{\gamma} \, dV + \int_{\Omega_0} \delta\boldsymbol{\gamma}\left(\boldsymbol{\gamma} - \frac{\nabla\theta}{|\nabla\theta|}\right) dV = 0 \tag{4.4.7}$$

where homogeneous Neumann boundary conditions are assumed.

4.4.2.2   Signed Distance Normal Field

After the SDF is computed using the HM (Eqn.(4.3.3)), the normalized spatial gradient of $\phi_{SD}(\mathbf{X})$ is solved for using the vector-valued field $\boldsymbol{\eta}(\mathbf{X})$. The normalized spatial gradient of the SDF is also known as the LS normal [6] in LSM, i.e., $\boldsymbol{\eta} = \frac{\nabla \phi_{SD}}{|\nabla \phi_{SD}|}$. The strong form of governing equation for the LS normal field $\boldsymbol{\eta}(\mathbf{X})$ is:

$$-r_H^2 \Delta \boldsymbol{\eta} + \boldsymbol{\eta} = \frac{\nabla \phi_{SD}}{|\nabla \phi_{SD}|} \tag{4.4.8}$$

Applying the previously discussed steps leads to the weak form of the governing equation for the signed distance normal field as:

$$r_H^2 \int_{\Omega_0} \delta \nabla \boldsymbol{\eta} \nabla \boldsymbol{\eta} \; dV + \int_{\Omega_0} \delta \boldsymbol{\eta} \left(\boldsymbol{\eta} - \frac{\nabla \phi_{SD}}{|\nabla \phi_{SD}|} \right) dV = 0 \tag{4.4.9}$$

where the admissible test functions are denoted by $\delta \boldsymbol{\eta}$.

4.4.2.3   Signed Distance Laplacian Field

Finally, the Laplacian of the SDF $\lambda(\mathbf{X})$ is computed as the divergence of the LS normal field, i.e., $\lambda = \Delta \phi_{SD} = \nabla \cdot \boldsymbol{\eta}$. The scalar-valued governing equation in strong form for Helmholtz smoothing and L^2 projection of the Laplacian field is:

$$-r_H^2 \Delta \lambda + \lambda = \nabla \cdot \boldsymbol{\eta} \tag{4.4.10}$$

The weak form of Eqn.(4.4.10) is obtained as:

$$r_H^2 \int_{\Omega_0} \delta \nabla \lambda \nabla \lambda \; dV + \int_{\Omega_0} \delta \lambda \left(\lambda - \nabla \cdot \boldsymbol{\eta} \right) dV = 0 \tag{4.4.11}$$

where the admissible test functions are denoted by $\delta \lambda$.

4.4.2.4   Skeleton Fields - Summary

In summary, six scalar and vector fields are used to obtain a smooth and continuous Laplacian of the SDF within an XFEM framework, see Figure 4.13. Smoothing effects stem first of all from the

Figure 4.13: Computation of the SDF skeleton using 6 fields and the HM. (a) A homogeneous Neumann temperature field is combined with (b) a homogeneous Dirichlet temperature field to obtain (c) the normalized temperature gradient. From that, (d) the SDF is computed and subsequently (e) the LS normal field and (f) the LS Laplacian field are obtained.

XFEM discretization and the operator splitting to compute higher-order derivatives. In addition, employing Helmholtz smoothing on the projected quantities further introduces smoothing of sharp discontinuities in spatial derivatives. This leads to approximation of step functions as observed for the normalized temperature gradient field $\boldsymbol{\gamma}(\mathbf{X})$ (Figure 4.13 (c)) and the LS normal field $\boldsymbol{\eta}(\mathbf{X})$ (Figure 4.13(e)). Furthermore, the Laplacian field, which mathematically is described by a Dirac delta function, is smooth and finite in width in a discretized setting (see Figure 4.13(f)).

Mathematically, the linear system resulting from the 6 different fields and the coupling between them can be summarized as:

$$
\begin{bmatrix}
K_{\theta^N\theta^N} & & & & & \\
& K_{\theta^D\theta^D} & & & & \\
K_{\gamma\theta^N} & K_{\gamma\theta^D} & K_{\gamma\gamma} & & & \\
& & K_{\phi\gamma} & K_{\phi\phi} & & \\
& & & K_{\eta\phi} & K_{\eta\eta} & \\
& & & & K_{\lambda\eta} & K_{\lambda\lambda}
\end{bmatrix}
\begin{bmatrix}
\theta^N \\
\theta^D \\
\boldsymbol{\gamma} \\
\phi \\
\boldsymbol{\eta} \\
\lambda
\end{bmatrix}
=
\begin{bmatrix}
R_{\theta^N} \\
R_{\theta^D} \\
R_{\gamma} \\
R_{\phi} \\
R_{\eta} \\
R_{\lambda}
\end{bmatrix}
\tag{4.4.12}
$$

As most of those additional gradient fields have a similar structure, pre-factorization of the system matrices (e.g., in LU-decomposition) can be used to significantly offset the additional computational

cost. In addition, a block solver is used to take advantage of the linearity of each sub-system while considering the coupling terms between each system. More details regarding a staggered block solution approach are presented in Section 3.4.

4.4.3 Skeleton-based Feature Size Control

A clear identification and computation of a SDF skeleton without noise is a key characteristic for skeleton-based feature size control. Since this is the goal of this thesis, see Eqn.(4.4.2), additional numerical steps are required for this to be successful. Mathematically, any non-zero Laplacian in phase I uniquely defines the skeleton Σ_0^I, due to its Dirac delta character. In a discretized setting, this would however require an infinitely fine mesh to properly resolve the discontinuity in the SDF gradients and a perfectly smooth (non-oscillating) SDF as well as its higher-order derivatives. In practice, numerical discretization leads to smoothing and therefore blurs sharply defined derivative discontinuities, see Figure 4.13 (c) - (f). To obtain a sharply and unambiguously defined SDF Laplacian in a discretized setting, two different approaches are discussed in the following. First, a smooth Laplacian projection is considered and secondly a smooth Laplacian truncation strategy is discussed.

4.4.3.1 Smooth Laplacian Truncation

Smooth truncation of the Laplacian is proposed in this work to regularize the discretized Laplacian field. Alternatively, normalization of the Laplacian field by the global maximum/minimum was used by [78, 203, 116] to achieve similar numerical stability.

The truncated Laplacian values $\hat{\lambda}_T$ are therefore obtained as a function of λ as:

$$\hat{\lambda}_T(\lambda) = \max(\min(\lambda, \lambda_{Bnd}), -\lambda_{Bnd}) \tag{4.4.13}$$

where λ_{Bnd} denotes the bounding or truncation value of the Laplacian. Considering the fact that $\min(a, b) = -\max(-a, -b)$ and using a KS function to approximate the non-differentiable $\max(\bullet)$ operator, a smooth Laplacian truncation can be formulated as:
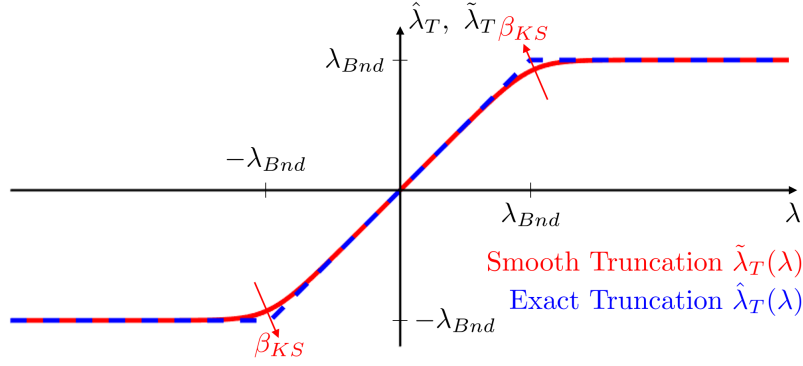
Figure 4.14: Truncation of the Laplacian field, either exact using min($\bullet$) max($\bullet$) operations or approximate using KS functions.

$$\tilde{\lambda}_T(\lambda) = \frac{1}{\beta_{KS}} \ln(e^{\beta_{KS} m_s} + e^{-\beta_{KS} \lambda_{Bnd}}) \,, \qquad m_s(\lambda) = \frac{-1}{\beta_{KS}} \ln(e^{-\beta_{KS} \lambda} + e^{-\beta_{KS} \lambda_{Bnd}}) \qquad (4.4.14)$$

A comparison of the exact truncation (Eqn.(4.4.13)) and the smooth approximation (Eqn.(4.4.14)) is shown in Figure 4.14. With an increasing KS parameter β_{KS} the approximation assumes the exact truncation constructed from min($\bullet$) max($\bullet$) operations, while removing the discontinuities at $\pm\lambda_{Bnd}$. Furthermore, Eqn.(4.4.14) maintains a unit gradient near the origin, which is a clear distinction from, for example, a tanh($\bullet$) sigmoid function. While the smooth truncation used for LS regularization (Eqn.(4.3.7)) does retain a unit gradient, its approximation sharpness cannot be adjusted. The smooth approximation presented in Eqn.(4.4.14) exhibits both of these features and is therefore superior.

4.4.3.2   Smooth Laplacian Projection

Instead of just truncating the Laplacian at certain bounds λ_{Bnd}, a projection approach can be used. This is a more intrusive way of introducing regularity into the Laplacian field using a piecewise constant function defined as:

$$\hat{\lambda}_P(\lambda) = \begin{cases} -1.0, & \forall \quad \lambda < -\lambda_P \\ 0.0, & \forall \quad -\lambda_P \le \lambda \le \lambda_P \\ 1.0, & \forall \quad \lambda > \lambda_P \end{cases} \qquad (4.4.15)$$
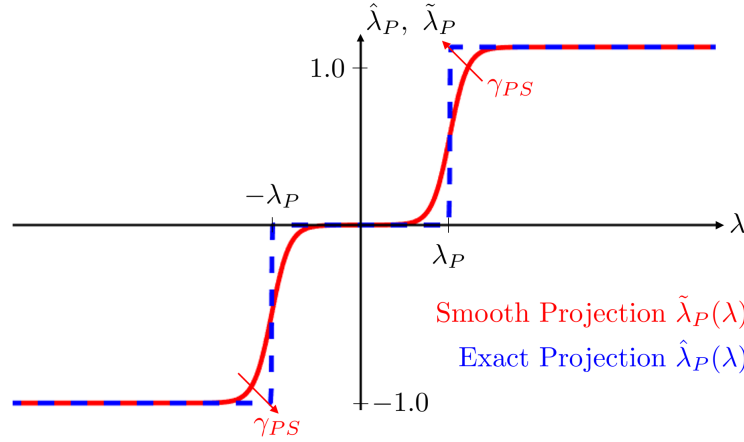
Figure 4.15: Projection of the Laplacian field, either exact using piecewise constant functions or approximate using smoothed Heaviside functions.

where λ_P is a Laplacian projection threshold parameter at which the distinction between projection to 0.0 and ± 1.0 is made. Schematically, this function is plotted in Figure 4.15. In order to obtain differentiability of this projection function, a product of smoothed Heaviside functions is used to approximate Eqn.(4.4.15). The smooth projection is computed as:

$$\tilde{\lambda}_P(\lambda) = \tanh(\gamma_{PS}\lambda)\left(\frac{1}{2} + \frac{1}{2}\tanh(\gamma_{PS}(|\lambda| - \lambda_P))\right) \tag{4.4.16}$$

where γ_{PS} is a projection sharpness parameter which determines how close the approximation of Eqn.(4.4.16) is to the exact projection of Eqn.(4.4.15). The first term in Eqn.(4.4.16) performs a signed normalization of the Laplacian and the second term either selects the signed normalized value or 0.0. An example of Eqn.(4.4.16) is compared in Figure 4.15 against the exact projection of Eqn.(4.4.15). It should however be noted that when using the smooth projection, the Laplacian field at the XFEM interface is projected to zero and therefore any mean curvature information is lost. A more detailed discussion of mean curvature is presented in Section 4.5.

4.4.3.3   General Discussion of the SDF Skeleton

In addition to smooth truncation of the Laplacian field, a Laplacian threshold $\bar{\lambda}$ is used in Eqn.(4.4.2) to identify Laplacian values which are part of the phase I skeleton Σ_0^I on which minimum

feature size is enforced. As pointed out by [78], a FEM discretized SDF necessarily yields a skeleton band with a finite width as opposed to an infinitely thin ridge. This leads to the fact that the minimum features are always greater than twice the minimum feature size radius, i.e., $x_{min} > 2r_m$ and therefore exact feature size can only be achieved on infinitely fine meshes. The lower the Laplacian threshold is set, the wider the skeleton band is and therefore the greater the practically obtained minimum feature size is. Due to the operator splitting and smoothing applied in this thesis for computing the SDF Laplacian (see Section 4.4.2.4), spreading of the skeleton cannot be avoided. From numerical studies presented in Section 5.6, it is apparent that the minimum achievable feature size r_{min} is:

$$r_{min} \geq r_m + 2h \tag{4.4.17}$$

where r_m is the minimum feature size radius specified in Eqn.(4.4.1) and h is the element edge width. The increase in feature size by $2h$ comes from the operator splitting required to compute higher-order spatial derivatives on a linear background mesh.

Despite the popularity of skeleton-based approaches for feature size control in both LS and density-based TO methods [208] certain limitations of this approach can be identified. As discussed above, smoothness and higher-order continuity of the SDF is required to construct a crisp and regular skeleton. To achieve that, operator splitting and Helmholtz smoothing are employed in this work. As pointed out by [40], boundary effects of the HM play a significant role on the SDF and its higher-order derivatives. These boundary effects can successfully be addressed by immersion of the design domain to avoid intersection of the domain boundary by the XFEM interface. Finally, as discussed by [4] small perturbations of the zero LS iso-contour, i.e., $\Gamma_0^{I,II}$ lead to non-differentiabilities in the SDF skeleton. This is conceptually illustrated in Figure 4.12. Comparing Figure 4.12 (a) and (b) and comparing Figure 4.12 (c) and (d) illustrates this issue. While the interface is only slightly changed, a drastically different skeleton is obtained. This might lead to oscillations in the design evolution, especially on very fine meshes.

4.5   Curvature Measure

To regularize the zero LS iso-contour during a LS-TO process, curvature measures are commonly used in implicit LSM [188]. Using the previously discussed computation of the SDF and its Laplacian, this concept is extended to explicit LS-XFEM TO in this thesis.

Mathematically, curvature quantifies the amount of change of a normal or tangent vector to a curve or surface, when traveling along that object. This means, a perfectly flat curve or surface have zero curvature, whereas at sharp changes (e.g., corners or kinks) the curvature is infinite. On the other hand, a perfect circle or sphere has constant curvature everywhere.

In the context of LSM, the mean curvature H_κ can directly be obtained from the SDF as [196, 195, 119, 6]:

$$H_\kappa = -\nabla \cdot \frac{\nabla \phi_{SD}}{|\nabla \phi_{SD}|} = -\nabla \cdot \frac{\boldsymbol{\eta}}{|\boldsymbol{\eta}|} = -\lambda \tag{4.5.1}$$

It should be noted that Eqn.(4.5.1) is only valid in 2D, whereas in 3D the mean curvature is defined as $H_\kappa = -2\lambda$. Following the work of [142, 191], a squared mean curvature penalty at the material interface can be formulated as:

$$p_\kappa = \frac{\int_{\Gamma_0^{I,II}} \lambda^2 \, dA}{\int_{\Gamma_0^{I,II}} dA} \tag{4.5.2}$$

which is an integrated squared mean curvature measure over the entire material interface. The mean curvature penalty p_κ is normalized by the perimeter of the interface to achieve length-scale independence. It is well-known that p_κ regularizes the XFEM interface/perimeter during design optimization [188], but so-far this concept has only been applied to implicit LSM using some form of HJ equation. Instead of minimizing the mean curvature squared in Eqn.(4.5.2), a regularized absolute of the (signed) mean curvature measure could alternatively be considered.

4.5.1   Spatially Varying Helmholtz Smoothing

As a curvature measure quantifies local spatial oscillations in the material interface, a large degree of smoothness in the Laplacian field is required. This guarantees that Eqn.(4.5.2) truly only

measures oscillations of the XFEM interface and does not pickup numerical noise from the XFEM discretization of the zero LS iso-contour. While continuity in the LS normal and LS Laplacian field across the XFEM interface are enforced using Nitsche's method (see Eqn.(3.1.3)), additional smoothing is desired to guarantee stability in the Laplacian field. This could simply be achieved by applying a larger Helmholtz smoothing radius to the LS normal field (Eqn.(4.4.9)) and the LS Laplacian field (Eqn.(4.4.11)). This global smoothing approach would however drastically decrease the sharpness at which the Laplacian is resolved for identification of the skeleton. To only apply an increased smoothing in the vicinity of the interface, the following spatially varying Helmholtz smoothing radius is defined:

$$\tilde{r}_s = \tilde{f} \ r_s(1 - (\tanh(\phi_{SD}))^2) + r_s \qquad (4.5.3)$$

which continuously increases the original smoothing radius r_s by a factor of $\tilde{f}$ at the interface as a function of the SDF $\phi_{SD}(\mathbf{X})$. Using a filter amplification factor of, for example $\tilde{f} = 1.5$ delivered a sufficient amount of smoothing at the XFEM interface, such that the mean curvature could be obtained well. While Eqn.(4.5.3) smoothly increases the Helmholtz smoothing radius to a maximum value at the interface, it should be noted that an additional (direct) dependency of the LS normal field $\boldsymbol{\eta}(\mathbf{X})$ (Eqn.(4.4.9)) and the LS Laplacian field $\lambda(\mathbf{X})$ (Eqn.(4.4.11)) on the SDF $\phi_{SD}(\mathbf{X})$ are introduced. These appear as off-diagonal entries in the elemental stiffness matrix and are not yet accounted for in Eqn.(4.4.12).

The previously developed mean curvature measure along with a spatially varying Helmholtz smoothing is demonstrated in Section 5.7 through a numerical example.

4.6   Design Sensitivity Analysis

In the context of gradient-based design optimization, the derivatives of objective and constraints with respect to the design variables need to be computed to update the design. This can either be done by global finite-differencing, the direct method, the adjoint method or automatic differentiation. Whereas global finite differencing is the most straight-forward approach to obtain design sensitivities, it is computationally very costly, especially when a large number of design variables are considered. As this is typically the case in TO, the design sensitivities of objective and constraints are most efficiently computed using the adjoint method. Computing design sensitivities using the adjoint method is therefore briefly discussed in the following for a static monolithic case and a transient staggered example.

4.6.1   Static Monolithic Adjoint Method

Following the work of [102, 101, 72, 68], the derivative of the objective z with respect to the vector of design variables $\mathbf{s}$ for a (quasi-) static case is:

$$\frac{dz}{d\mathbf{s}} = \frac{\partial z}{\partial \mathbf{s}} + \left(\frac{\partial z}{\partial \mathbf{u}}\right)^T \frac{d\mathbf{u}}{d\mathbf{s}} \tag{4.6.1}$$

where the first term represents explicit dependencies while the second term represents the implicit sensitivities. Considering the two sets of nodal design variables, $\mathbf{s}^\phi$ and $\mathbf{s}^{\tilde{\rho}}$, and the filtering and projection relationships defined in Section 4.1.1.3, the total derivative of Eqn.(4.6.1) can be further expanded into:

$$\frac{d\mathbf{u}}{d\mathbf{s}} = \begin{cases} \frac{\partial \mathbf{u}}{\partial \boldsymbol{\phi}} \frac{d\boldsymbol{\phi}}{d\mathbf{s}^\phi} \\ \\ \frac{\partial \mathbf{u}}{\partial \hat{\boldsymbol{\rho}}^e} \frac{\partial \hat{\boldsymbol{\rho}}^e}{\partial \bar{\boldsymbol{\rho}}^e} \frac{\partial \bar{\boldsymbol{\rho}}^e}{\partial \boldsymbol{\rho}^e} \frac{d\boldsymbol{\rho}^e}{d\mathbf{s}^\rho} \end{cases} \tag{4.6.2}$$

A fundamental assumption of the NAND approach used in this work for solving the optimization problem of Eqn.(4.0.1), is that a set of state variables $\mathbf{u}$ has been found which satisfy the governing equations. In other words, the total residual $\tilde{\mathbf{R}} = \sum_i^{N_R} \mathbf{R}_i = 0$ where $\mathbf{R}_i$ are the number of residuals N_R individual residual components. Under the assumption of $\tilde{\mathbf{R}} = \mathbf{0}$, the derivative $d\mathbf{u}/d\mathbf{s}$ can be

computed from:

$$\frac{d\tilde{\mathbf{R}}}{d\mathbf{s}} = \frac{\partial \tilde{\mathbf{R}}}{\partial \mathbf{s}} + \frac{\partial \tilde{\mathbf{R}}}{\partial \mathbf{u}}\frac{d\mathbf{u}}{d\mathbf{s}} = \mathbf{0} \tag{4.6.3}$$

Solving Eqn.(4.6.3) for $d\mathbf{u}/d\mathbf{s}$ and combining it with Eqn.(4.6.1) yields:

$$\frac{dz}{d\mathbf{s}} = \frac{\partial z}{\partial \mathbf{s}} - \left(\frac{\partial z}{\partial \mathbf{u}}\right)^T \left(\frac{\partial \tilde{\mathbf{R}}}{\partial \mathbf{u}}\right)^{-1} \frac{\partial \tilde{\mathbf{R}}}{\partial \mathbf{s}} \tag{4.6.4}$$

where the following adjoint problem can be identified:

$$\left(\frac{\partial \tilde{\mathbf{R}}}{\partial \mathbf{u}}\right)^T \boldsymbol{a} = \frac{\partial z}{\partial \mathbf{u}} \tag{4.6.5}$$

The adjoint solution is denoted by $\boldsymbol{a}$, which is used to finally compute the expression for the design sensitivities as:

$$\frac{dz}{d\mathbf{s}} = \frac{\partial z}{\partial \mathbf{s}} - \boldsymbol{a}^T \frac{\partial \tilde{\mathbf{R}}}{\partial \mathbf{s}} \tag{4.6.6}$$

It should be noted that in this thesis, the explicit contribution $\partial z/\partial \mathbf{s}$ and the post-multiplication term $\partial \tilde{\mathbf{R}}/\partial \mathbf{s}$ are obtained via finite differences on an elemental level. In a similar fashion as discussed above, the design sensitivities of the constraints with respect to the design variables can be obtained. For more details regarding the computation of design sensitivities with the XFEM, the interested reader is referred to [163].

4.6.2 Transient Staggered Adjoint Method

In case of a time dependency in the forward analysis, additional contributions need to be accounted for when computing design sensitivities via the adjoint method. This also applies in case a staggered block solution approach is employed in the forward analysis, as discussed in Section 3.4. The transient staggered solution approach is discussed in the following using the HM (Section 4.3.1) as one specific example. Furthermore, only the evaluation of the adjoint problem (Eqn.(4.6.5)) is discussed, as the remainder of the computation is assumed to be identical to the one presented in Section 4.6.1. The HM in its simplest form requires the solution of two fields. First, a (1) transient temperature field $\theta \mathbf{X}$ is solved and using its solution, a (2) (static) signed distance field $\phi_{SD}(\mathbf{X})$

is computed. This simple example is therefore sufficient to discuss the transient staggered adjoint analysis approach for two distinct fields which are one-way coupled. A more general treatment of transient (monolithic) adjoint analysis is discussed in [102, 72].

The coupled adjoint system for time step q is therefore summarized as:

$$\begin{bmatrix} \mathbf{K}_{\theta\theta}^q & 0 \\ \mathbf{K}_{\phi_{SD}\theta}^q & \mathbf{K}_{\phi_{SD}\phi_{SD}}^q \end{bmatrix}^T \begin{bmatrix} \boldsymbol{a}_\theta^q \\ \boldsymbol{a}_{\phi_{SD}}^q \end{bmatrix} = \begin{bmatrix} \frac{\partial z}{\partial \boldsymbol{\theta}^q} \\ \frac{\partial z}{\partial \boldsymbol{\phi_{SD}}^q} \end{bmatrix} \tag{4.6.7}$$

where the total adjoint solution vector $\boldsymbol{a}^q$ at time step q is comprised of $\boldsymbol{a}^q = [\boldsymbol{a}_\theta^q, \boldsymbol{a}_{\phi_{SD}}^q]$.

Following the same structure as in a monolithic transient analysis, the performed time steps of the forward analysis need to be evaluated backwards in the adjoint problem. A similar concept is applied to the block solves of the forward problem, which also need to be evaluated backwards in the sensitivity analysis. For a two system, two time step problem this yields for the first adjoint problem (time step 2, linear system 2 ($\phi_{SD}(\mathbf{X})$)):

$$\left(\mathbf{K}_{\phi_{SD}\phi_{SD}}^2\right)^T \boldsymbol{a}_{\phi_{SD}}^2 = \frac{\partial z}{\partial \phi_{SD}^2} \tag{4.6.8}$$

where $\mathbf{K}_{\phi_{SD}\phi_{SD}}^2$ is the stiffness matrix of the signed distance field at time step 2, ϕ_{SD}^2 is the solution of the signed distance state variables at time step 2 and $\boldsymbol{a}_{\phi_{SD}}^2$ is the signed distance adjoint solution at time step 2. Stepping back to linear system 1 ($\theta(\mathbf{X})$), still at the second time step, the next adjoint system to be solve is:

$$\left(\frac{\mathbf{C}_\theta^2}{\Delta t} + \mathbf{K}_{\theta\theta}^2\right)^T \boldsymbol{a}_\theta^2 = \frac{\partial z}{\partial \boldsymbol{\theta}^2} - \left(\mathbf{K}_{\phi_{SD}\theta}^2\right)^T \boldsymbol{a}_{\phi_{SD}}^2 \tag{4.6.9}$$

where $\mathbf{C}_\theta^2$ is the capacitance matrix at time step 2, Δt is the time step size, and $\mathbf{K}_{\theta\theta}^2$ is the tangent stiffness matrix of the temperature system at time step 2 and $\mathbf{K}_{\phi_{SD}\theta}^2$ is the coupling stiffness matrix between SDF DOFs and temperature DOFs. Similar to a forward block solve, the solution of the previous system $\boldsymbol{a}_{\phi_{SD}}^2$ multiplied with the coupling matrix is added to the system's RHS. With Eqn.(4.6.9) the backward loop over both linear systems at time step 2 is complete. Next, looping back in time, the adjoint solution of the SDF at time step 1 is solved for. It is computed as:

$$\left(\mathbf{K}_{\phi_{SD}\phi_{SD}}^1\right)^T \boldsymbol{a}_{\phi_{SD}}^1 = \frac{\partial z}{\partial \phi_{SD}^1} \tag{4.6.10}$$

Since the SDF is static, no contributions from the SDF adjoint vector of the previous time step $(\boldsymbol{a}^2_{\phi_{SD}})$ are added to Eqn.(4.6.10). The quantities are therefore equivalent to Eqn.(4.6.8) except they are evaluated at time step 1.

Finally, the adjoint solution of the temperature DOFs at time step 1 is computed. As the temperature system is transient, it contains contributions from the temperature adjoint solution vector of the previous time step $(\boldsymbol{a}^2_\theta)$ and from the SDF adjoint vector of the current time step $(\boldsymbol{a}^1_{\phi_{SD}})$ on the RHS. It is computed as:

$$\left(\frac{\mathbf{C}^1_\theta}{\Delta t} + \mathbf{K}^1_{\theta\theta}\right)^T \boldsymbol{a}^1_\theta = \frac{\partial z}{\partial \theta^1} - \left(\mathbf{K}^1_{\phi_{SD}\theta}\right)^T \boldsymbol{a}^1_{\phi_{SD}} - \left(-\frac{\mathbf{C}^1_\theta}{\Delta t}\right)^T \boldsymbol{a}^2_\theta \tag{4.6.11}$$

where as before, the same quantities as in Eqn.(4.6.9) are used on the left-hand side, but evaluated at time step 1. The last term on the RHS of Eqn.(4.6.11) is the coupling term from the previous time step.

To be consistent with the staggered block solve used for forward analyses, within every time step, a loop over all sub-systems is performed. Within one time step, coupling matrices and solutions of previous systems are appended to the RHS, while in-between different time steps only coupling information related to the transient part of system matrices is transferred to the previous time step. This transient staggered adjoint solution approach is used in this thesis when design sensitivities of the HM considering multiple time steps are computed.

4.7   End Stiffness Constraint

In the context of design optimization of active structure it is crucial to ensure the structural integrity of the final design. Applying a perturbation load opposite to the desired deformation and measuring the amount of deformation (e.g., in terms of change in strain energy) can be used to achieve that. The formulation of a follower Neumann BC defined in the deformed configuration and the formulation of an end-stiffness constraint are presented in this section.

4.7.1   Follower Pressure Load

A deformation dependent (i.e., follower) Neumann boundary condition is employed, which is formulated in the deformed configuration and mapped back to the undeformed configuration for integration purposes. Using Nanson's formula [86], the relationship between surface areas in the undeformed and deformed configuration is defined as:

$$da \; \mathbf{n} = J \; \mathbf{F}^{-T} dA \; \mathbf{N} \tag{4.7.1}$$

where da is an infinitesimal surface area in the deformed configuration, $\mathbf{n}$ is the surface normal corresponding to it, $J = \det(\mathbf{F})$ is the determinant of the deformation gradient $\mathbf{F}$, dA is an infinitesimal surface area in the undeformed configuration, and $\mathbf{N}$ is the surface normal corresponding to the surface area in the undeformed configuration.

The non-conservative follower pressure can be evaluated in the deformed or the undeformed configuration as follows:

$$\mathbf{R}_{\Gamma P} = -\int_{\Gamma_{\bar{T}}^0} \delta \mathbf{u} \; \mathbf{n} \; \bar{p} \; da = -\int_{\Gamma_{\bar{T}}^0} \delta \mathbf{u} \; (\mathbf{F})^{-T} \; \mathbf{N} \; J \; \bar{P} \; dA \tag{4.7.2}$$

where $\bar{p}$ is the surface pressure scalar in the deformed and $\bar{P}$ is the surface pressure scalar in the undeformed configuration. For simplicity it is assumed here that both $\bar{p}$ and $\bar{P}$ are not state dependent. As the work in this thesis is based on a total Lagrangian approach, integration of the governing equations is performed in the undeformed (reference) configuration. Therefore, the second expression of Eqn.(4.7.2) is used. Since however the mapping from the deformed (where the
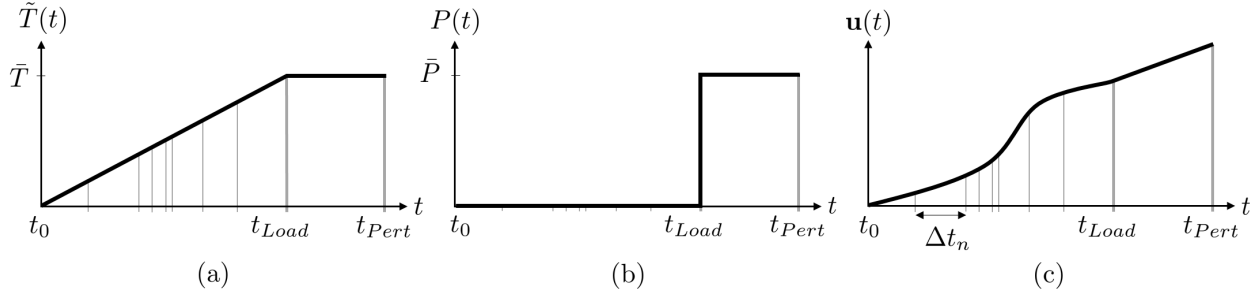
Figure 4.16: Evolution of (a) pseudo temperature load, (b) follower pressure, and (c) structural displacement response as a function of pseudo time.

follower pressure is applied) to the undeformed configuration (where the integration is performed) is depending on the states, a non-zero stiffness matrix contribution exists. It is computed as:

$$\frac{\partial \mathbf{R}_{\Gamma_P}}{\partial \mathbf{u}} = - \int_{\Gamma_{\tilde{T}}^0} \left(\frac{\partial \mathbf{F}^{-T}}{\partial \mathbf{u}} \ \det(\mathbf{F}) + \mathbf{F}^{-T} \frac{\partial \det(\mathbf{F})}{\partial \mathbf{u}} \right) \ \mathbf{N} \ \bar{P} \ dA \tag{4.7.3}$$

where the contributions defined previously are used.

4.7.2   Adaptive Load Stepping Approach

To efficiently predict the nonlinear deformation of slender structures undergoing large deformation, an adaptive load-stepping scheme is used for the XFEM analysis, as initially demonstrated in [68]. Schematically, the evolution of an external traction load $\tilde{T}(t)$, an applied follower load $P(t)$ and the corresponding displacement response $\mathbf{u}(t)$ as a function of pseudo time t is depicted in Figure 4.16. An adaptive pseudo time-stepping scheme is used such that the initially set pseudo time step size Δt_0 is reduced by a factor f_{TS} in case a Newton-Raphson solve does not converge to an equilibrium solution for a set maximum number of nonlinear iterations. The pseudo time step size of the current pseudo time step q is therefore computed as:

$$\Delta t^{q+1} = f_{TS} \Delta t^q \tag{4.7.4}$$

where Δt^m is the pseudo time step size of the previous pseudo time step q. A pseudo time step reduction factor of $f_{TS} = 0.25$ is a good balance between stability and numerical efficiency. An adaptive time step reduction is, for example, encountered when domains of intermediate (weak)

material dominate the structural response during a combined LS-XFEM-density TO process. In such an event, the pseudo time step is adaptively reduced until a specified number of (converged) nonlinear solutions are obtained at the reduced pseudo time step. After that, the original time step size is gradually restored. The total number of pseudo time steps is adjusted accordingly to reach the final loading time t_{Load}. The external traction load $\tilde{T}(t)$ is increased linearly between t_0 and t_{Load} to achieve a maximum value $\bar{T}$ while the follower surface pressure load $P(t)$ is zero during this time. Conceptually, this is shown in Figure 4.16 (a) and (b), respectively. Between t_{Load} and t_{Pert} the external pseudo temperature load is kept constant at $\bar{\theta}$ while a constant non-zero follower perturbation load $\bar{P}$ is applied. The magnitude of the non-zero follower perturbation load is chosen sufficiently small, in order to achieve fast convergence of the nonlinear solver, ideally in a single iteration. This is valid for enforcing an end-stiffness constraint measuring the change in total strain energy-based on a linear concept. Numerical design optimization examples exhibiting this adaptive load stepping approach are presented in Section 5.3.2.

4.7.3   Formulation of End Stiffness Constraint

To control the stiffness of self-deforming structures in the activated state, an end-stiffness constraint is enforced. Following the work initially proposed by [95], it is formulated as:

$$g_e = \left(\frac{\mathcal{U}' - \mathcal{U}}{\mathcal{U}}\right)^2 - \gamma_s \leq 0 \tag{4.7.5}$$

where $\mathcal{U}$ is the strain energy of the system after activation (with no external load applied) and $\mathcal{U}'$ is the strain energy after applying an additional external perturbation load. The limit in relative amount of change in strain energy with and without the final perturbation load is denoted by γ_s. The end-stiffness constraint therefore requires a certain stiffness of the structure in the activated configuration, in order to resist the perturbation pressure applied in the opposite direction of the desired deformation. It should be noted that in case of a thermomechanical problem consisting of homogeneous material under pure thermal expansion (without any mechanical loads applied), the strain energy is zero. This is due to a stress-free state (no mechanical strains) under isotropic

thermal expansion which is the case at the beginning of a combined LS-XFEM-density design optimization process where a uniform material is present in the entire solid domain. See Section 5.3 for numerical examples.

In case of a static and conservative the mechanical model, the adjoint problem only needs to be solved at the end of the loading process [66]. When the end-stiffness constraint is enforced, the design sensitivities for the displacement matching objective need to be evaluated at the load increment t_{Load} while the sensitivities for the end-stiffness constraint are evaluated at t_{Pert}. For more details on computing the design sensitivities for a quasi-static problem, the reader is referred to Section 4.6.1. Further details and applications of the adaptive time stepping approach and the end-stiffness constraint are presented in Appendix C.

Chapter 5

Numerical Studies and Examples

Numerical examples are presented in this chapter to demonstrate the applicability of the previously proposed design optimization and regularization schemes.

5.1   Nonlinear Total Lagrangian Element

A nonlinear total Lagrangian thermomechanical element supporting both FEM and XFEM was developed and implemented for the work presented in this thesis. The corresponding thermomechanical governing equations are presented in Chapter 2 while the XFEM specific considerations are discussed in Section 3.1. To gain confidence in the XFEM implementation and to demonstrate its performance, comparison studies are conducted. These include mesh refinement studies against the commercial FEA package Abaqus [180], body-fitted FEM results, experimental results and a 1D Timoshenko beam model.

5.1.1   Mesh Refinement Studies

A cantilevered beam of size $1.0 \times 2.0 \times 10.0$ is used to conduct mesh refinement studies for different constitutive models. The formulation of each of these hyperelastic material models is presented in Section 2.3.3. The beam is clamped on one end, and a traction load in X_1, X_2, and X_3 direction is applied to the free end. The beam is composed of two materials where phase II does exhibit isotropic thermal expansion while phase I does not. The swelling inclusion which is tilted with respect to the X_3 axis in the center of the beam is either modeled by a body-fitted mesh or

Table 5.1: Properties of the cantilevered beam problem.

Property	Ω_0^I	Ω_0^{II}
Young's Modulus $[N/m^2]$	$E = 1.0 \cdot 10^6$	$E = 5.0 \cdot 10^5$
Poisson's Ratio [-]	$\nu = 0.4$	$\nu = 0.45$
CTE $[1/K]$	$\alpha = 0.0$	$\alpha = 0.027$
Surface Traction $[N/m^2]$	$[T_{X_1}, T_{X_2}, T_{X_3}] = [9.0 \cdot 10^4, 1.5 \cdot 10^4, 9.0 \cdot 10^3]$	-

immersed on a structured background mesh using XFEM. The problem parameters are summarized in Table 5.1. Trilinear hexahedral elements are used to model the beam both using classical FEM and XFEM.

A linear thermal expansion model (see Eqn.(2.3.7)) is used to model the isotropic thermal expansion in phase II. Mesh sizes ranging from $h = 1.0 \times 1.0 \times 1.0$ to $h = 0.0625 \times 0.0625 \times 0.0625$ are used in this study. An adaptive load stepping approach as presented in Section 4.7.2 is used to facilitate convergence of the nonlinear solver. This is especially critical for simulating the equilibrium path of strongly nonlinear structures. A comparison of the displacement predictions obtained by linear elasticity, a Saint Venant-Kirchhoff material, a Neo-Hookean material and an alternative formulation of the Neo-Hookean material in the deformed configuration of the loaded beam is shown in Figure 5.1.
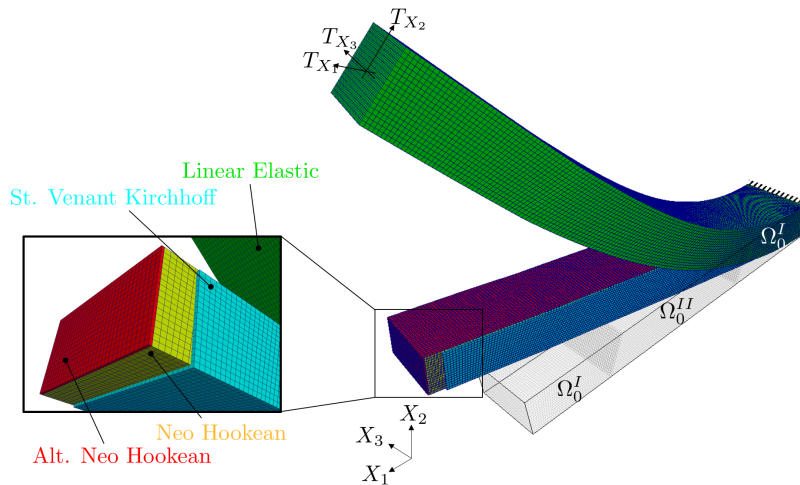
Figure 5.1: Deformed cantilevered beam analyzed by different thermomechanical models.
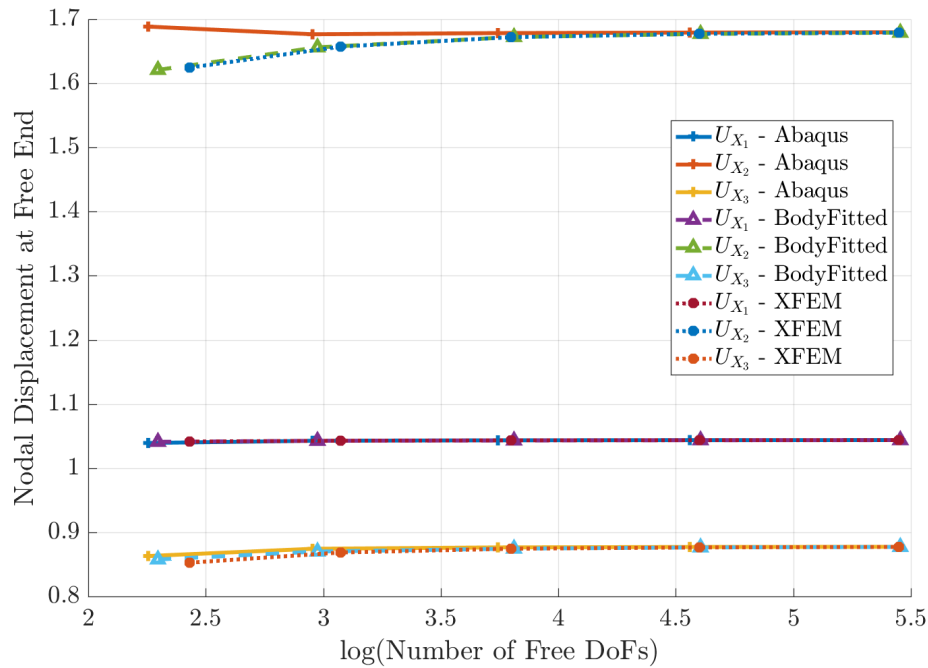
Figure 5.2: Convergence of the tip displacement with mesh refinement, using a Saint Venant-Kirchhoff material model.
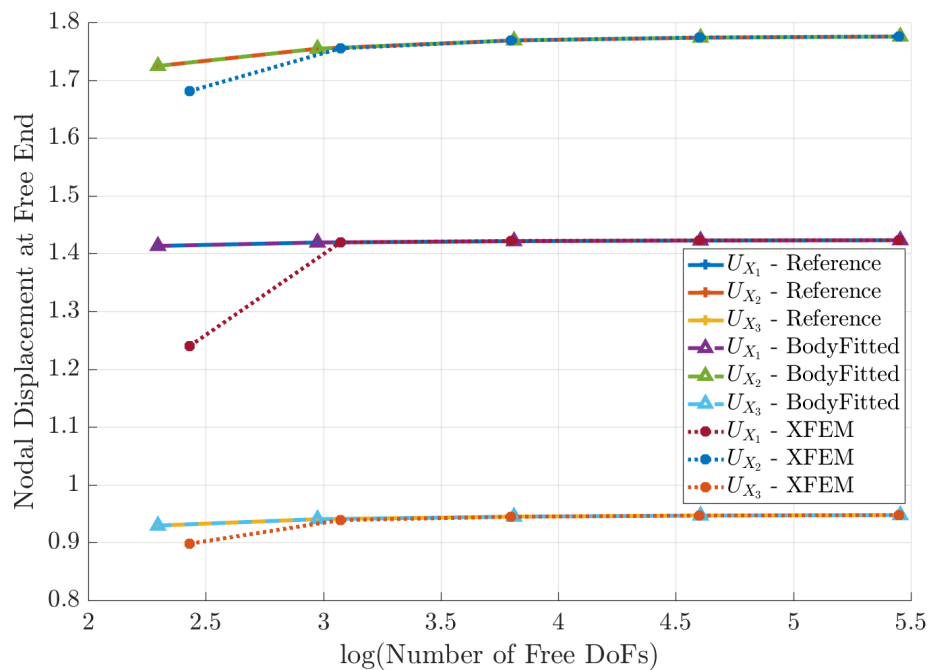
Figure 5.3: Convergence of the tip displacement with mesh refinement, using a Neo-Hookean material model.
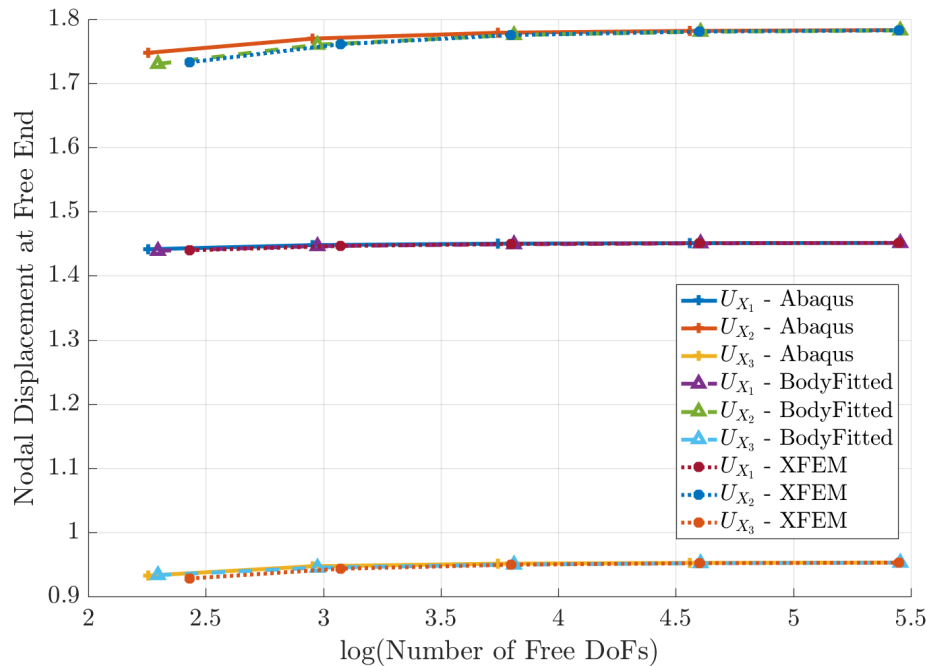
Figure 5.4: Convergence of the tip displacement with mesh refinement, using an alternative formulation of the Neo-Hookean material model.

As expected, significant differences between linear elastic and nonlinear kinematics predictions are observed. The predictions of all hyperelastic material models considering nonlinear kinematics only differ slightly from each other. A quantitative comparison of the displacement prediction of the free end of the beam is studied next for each hyperelastic material model. Comparisons between Abaqus (reference), body-fitted FEM, and XFEM predictions are made.

Using a Saint Venant-Kirchhoff material model (see Section 2.3.3.1), the tip displacement components are shown in Figure 5.2 for different levels of mesh refinement. Moreover, displacement predictions of Abaqus, FEM and XFEM are compared. Good agreement between all three approaches is seen and fast convergence towards the Abaqus (reference) solution is obtained for all three displacement components, U_{X_1}, U_{X_2}, and U_{X_3} measured at the free end.

The same study is repeated for a Neo-Hookean material, as discussed in Section 2.3.3.2. As no Abaqus solution is available for this constitutive model, a body-fitted FEM solution based on an established FEM implementation is used as a reference. The results are presented in Figure 5.3. A
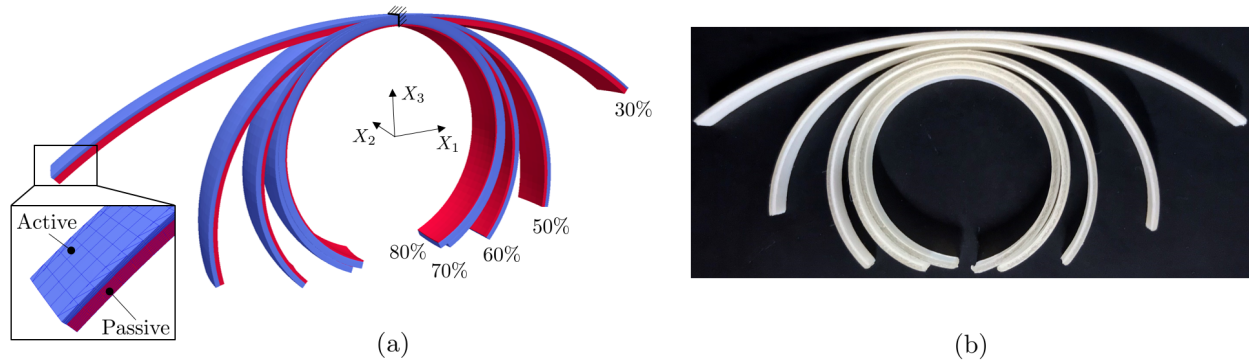
Figure 5.5: Curling strips used for experimental verification using different ratios of expanding (active) material. (a) XFEM results and (b) experimental results.

similar, quick convergence behavior is seen.

Finally, a mesh refinement study for the alternative formulation of the Neo-Hookean material model as used by Abaqus (see Section 2.3.3.3) is performed. The comparison between Abaqus results, FEM and XFEM are presented in Figure 5.4.

For all three investigated constitutive models quick convergence of the thermomechanical XFEM prediction against body-fitted reference FEM solutions is seen. This establishes a first verification of the implemented nonlinear total Lagrangian XFEM element, which is discussed in more detail in the next sections.

5.1.2 Experimental Verification

Self-curling strips are studied next to compare the finite strain hyperelastic thermomechanical model developed in Section 2.3 against experimental results and a 1D Timoshenko beam model presented in [45]. Bi-layer strips, composed of a swelling (active) material at the top and a non-expanding (passive) material at the bottom are modeled via XFEM, where the solid-void interface is along the X_1 direction, see Figure 5.5 (a). The same strips with a varying ratio of active material are also printed and activated via 4D printing [184] which lead to different radii of curvature for different material ratios, see Figure 5.5 (b). Due to the slenderness of the beams ($80.0 \times 5.0 \times 1.0$ mm), quadratic HEX20 elements are used to alleviate element locking, as discussed in Section 3.2.3. For
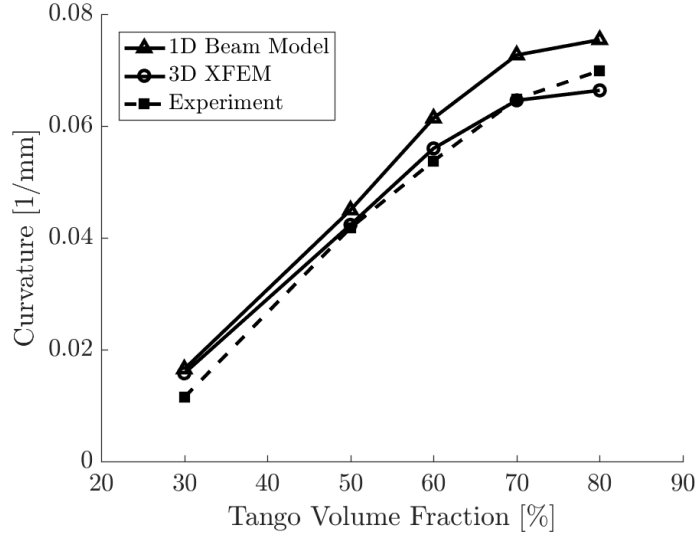
Figure 5.6: Comparison of mean curvatures obtained using the XFEM model, 1D Timoshenko beam model, and experiments.

more details on the problem setup and on the experimental 4D printing approach, see Appendix C. The mean curvatures obtained for five distinct ratios of active material are shown in Figure 5.6. Comparing the XFEM results with experiments and analytical curvature values obtained by a Timoshenko beam model shows good agreement, especially for small ratios of active material. For active material ratios greater 50%, an over-prediction of the curvature occurs by the analytical beam model. This is due to the presence of the Poisson's effect and transverse bending (i.e., cylindrical bending) of the strips, effects which are not accounted for by the simplified 1D beam model. The employed 3D thermomechanical large deformation XFEM model however captures both of these effects and therefore predicts the curvature quite well.

5.1.3   Sensitivity Plateaus

To verify the consistency of the tangent stiffness matrix, insensitivity of the design shape gradients with respect to the finite difference (FD) perturbation size needs to be verified. This is established by changing the FD perturbation size ϵ_{FD} used on a local level in the adjoint method, as discussed in Section 4.6. In addition, global FD is used to verify the obtained design sensitivity.
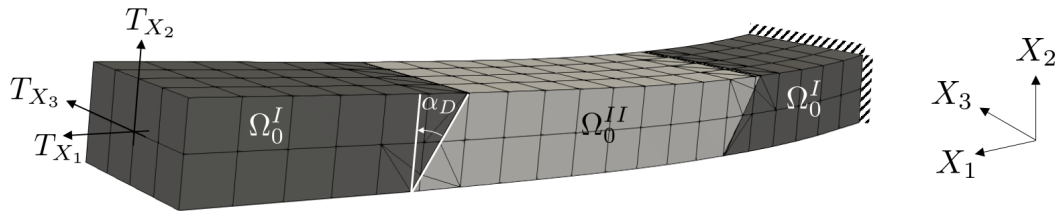
Figure 5.7: Single design variable cantilevered beam setup used for generating sensitivity plateaus.

For this study, a two-material cantilevered beam problem similar to the one introduced in Section 5.1.1 is used. An element edge length of $h = 0.5\ mm$ is used and the inclusion angle α_D is used as a single design variable, as illustrated in Figure 5.7. The objective function in this sweep study is the matching of a target displacement at the free end of the beam, where a traction load is applied. The problem parameters listed in Table 5.1 are again used.

First, it is ensured that a smooth objective function is obtained when varying the inclusion angle $20.0° \leq \alpha_D \leq 40.0°$ as a single design variable in ten steps.
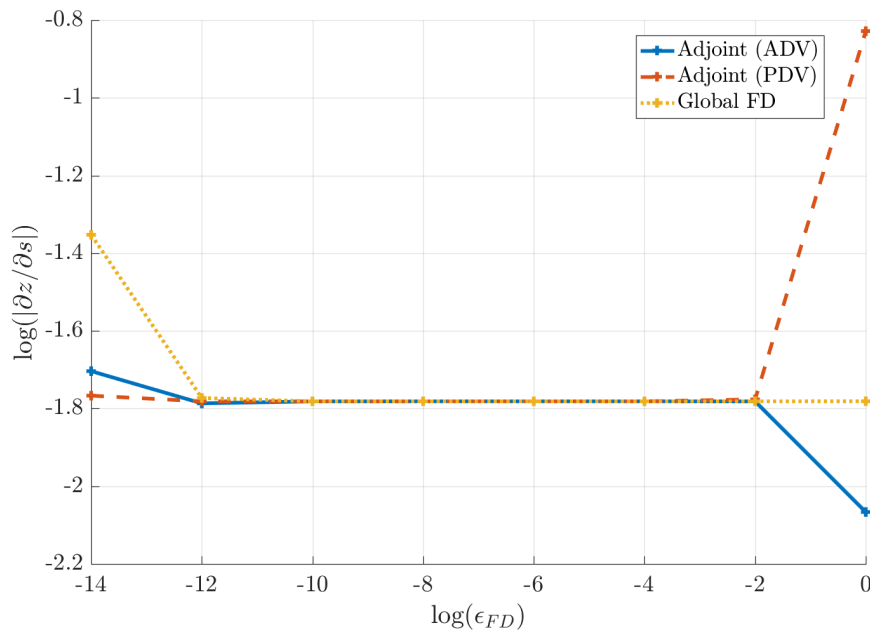
Figure 5.8: Influence of FD perturbation size on objective sensitivity, using a Saint Venant-Kirchhoff material model.
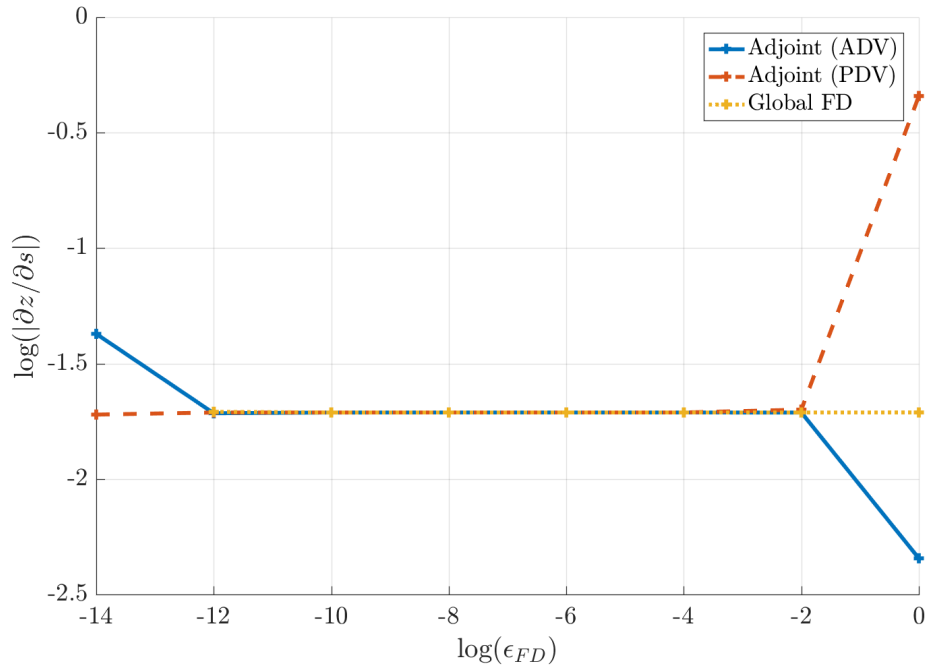
Figure 5.9: Influence of FD perturbation size on objective sensitivity, using a Neo-Hookean material model.
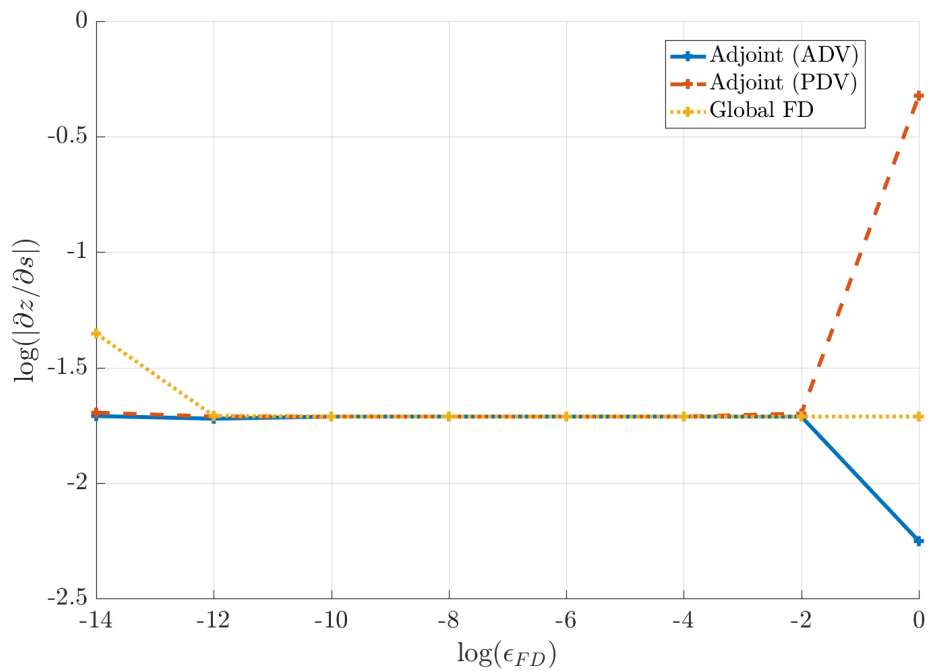
Figure 5.10: Influence of FD perturbation size on objective sensitivity, using an alternative formulation of the Neo-Hookean material model.

Using a LS primitive (see Section 4.1.2.2) in combination with coordinate transformation defines the LS value for each node of the XFEM mesh. Based on a smooth objective behavior, an inclusion angle of $\alpha_D = 30.0°$ is used as the starting point for the sensitivity analysis plateaus.

Insensitivity of the objective gradient with respect to the FD perturbation size needs to be established for a range of ϵ_{FD} values. If the FD perturbation is too large, inaccuracies in the derivative are expected. And if ϵ_{FD} is picked too small, the FD perturbation will be overpowered by numerical noise and inaccuracies are introduced. For a Saint Venant-Kirchhoff material model, the sensitivity plateau is shown in Figure 5.8. It can be seen that for $1.0 \cdot 10^{-10} \leq \epsilon_{FD} \leq 1.0 \cdot 10^{-4}$ the objective sensitivity is not affected by the perturbation size. The same study is repeated for a Neo-Hookean material model and an alternative formulation of the Neo-Hookean material model. The resulting sensitivity plateaus are presented in Figure 5.9 and Figure 5.10, respectively. From these studies, it can also be seen that the objective sensitivity matched the one obtained by global FD within the plateau region.

This concludes the verification of the nonlinear total Lagrangian thermomechanical XFEM element which is used for various design optimization studies in the following sections.

5.2   Design of Self-Folding Origami Structures using LS Primitives

The ancient art of paper folding called "origami" has recently gained large popularity in engineering applications. To maximize the potential offered by origami, systematic design approaches are needed. This has for example been done by [150] where classical crease pattern design rules are employed to design technical origami structures. The performance is predicted by FEA but computationally expensive re-meshing is required to capture the pre-determined folding patterns. Photo-induced self-folding origami structures were designed by [134] and [117] who incorporated simple origami principles in the design process. Alternatively, TO can be used as a systematic origami design tool. In most literature, the optimal folding lines for a desired structure are determined via a ground structure approach, as shown by [60, 62, 57]. While this approach greatly reduces the number of design variables and hence simplifies the design optimization problem, the majority of the design space is largely unexplored. In addition, by modeling origami structures as rigid plates connected by flexible hinges, simplifications, and limitations on the mechanical model are introduced. This approach is called "rigid origami" and is also widely used in literature. Furthermore, TO has also been used by [58] and [56] to design active liquid crystal elastomer origami structures.

However, due to the simplified mechanical modeling assumptions and the simplifications in formulating the design optimization problem based on a ground-structure approach, a strong need for a systematic design and modeling approach for finding optimal folding patterns for active origami structures is identified. In this thesis, a most general LS-XFEM TO approach is adopted to find the crease patterns of pre-stressed light-activated polymer (LAP) composites.

5.2.1   Pre-Stressed Light-Activated Polymer Composites

The use of pre-stressed polymer composites activated by light to create self-folding origami designs was initially introduced by [132] using the name "photo origami". Photo origami describes self-folding structures which transform from a flat 2D shape into a complex 3D shape by non-contact, light inducted activation as demonstrated by [117]. A photo origami composite consists of three
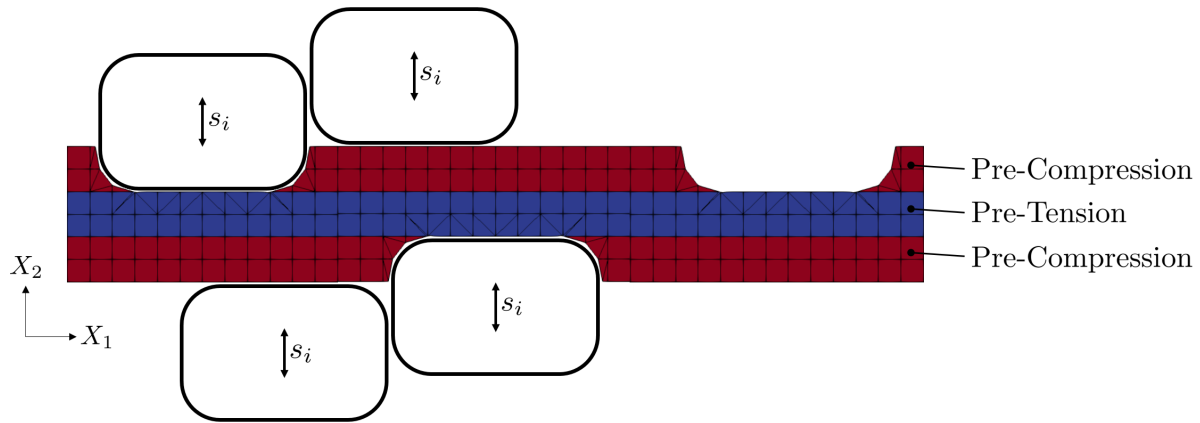
Figure 5.11: Layers of a pre-stressed LAP composite, where void cuboids are used to simulate the localized stress relaxation.

layers, where the outer two layers are made from LAP monomer material with embedded photo initiators and the intermediate layer is made from, for example NOA65, a commercially available elastomer. Initially, the core elastomer material is stretched to about 15.0% tensile strain and held in this stretched configuration during adhesion of the outer two layers. One photo sensitive LAP layer is then bonded to either side of the stretched intermediate layer of the composite. After the composite has fully bonded, the prescribed strain is removed and the composite shrinks due to the contraction of the middle layer. The pre-stressed composite, with the outer two layers in a state of compression and the center elastomer layer in tension has been formed. A schematic illustration discretized on an XFEM mesh is shown in Figure 5.11.

Once exposed to UV radiation, bond exchange reactions take place in the outer most layers which lead to macroscopic relaxation of the compressive stress. If this exposure to UV light and therefore the degradation of the polymer bonds is performed in a selective and unsymmetrical manner (with respect to the three-layer LAP composite layup), the local stress-relaxation causes the laminate to bend or fold. This way of initiating self-folding is contact less and can therefore be easily triggered remotely. Since the eigenstrains are built into the material as it is deposited, no mechanical training load needs to be applied to the structure once it has been fabricated. This enables a wide range of application for pre-stressed self-folding composite structures, especially in aerospace systems. This

is a key advantage of LAP structures since no mechanical loading needs to be removed to perform activation as it is, for example, needed in classical, single layer self-folding origami structures [154].

Even though a sophisticated thermomechanical model is developed by [132], eigenstrains as the internal driving force for self-folding is simulated by simple isotropic temperature induced swelling in this thesis. This simplified modeling approach shows sufficient accuracy while being computationally efficient at the same time. Both of which are critical factors in order to perform design optimization of pre-stressed composites. To model a self-folding behavior, a non-zero positive CTE is assigned only in the top and bottom layer of the LAP composite. Therefore, if crease patterns are introduced in the top layer for example, upwards folding of the composite will be the result of non-counteracted thermal swelling in the bottom layer. Employing a LS-XFEM framework, the localized stress relaxations are modeled via void domains immersed into the structure, as illustrated in Figure 5.11. For a first proof of concept, a small strain linear elastic thermomechanical model is used to simulate the pre-stressed LAPs while solid-void LS-XFEM is used to model the activation process through light-induced, localized stress relaxation.

To design self-folding origami structures from pre-stressed LAP composites, the following optimization problem is solved:

$$\min_{\mathbf{s}} \; z(\mathbf{s}, \mathbf{u}) = w_1 \int_{\Gamma_{Tar}} \mathbf{u} \; dS + w_2 \int_{\Gamma_0^{I,II}} dS$$
$$\text{s.t.} \; g = \gamma_v - \frac{\Omega_0^I}{(\Omega_0^I + \Omega_0^{II})} \leq 0 \tag{5.2.1}$$

where the objective is to minimize/maximize displacements at a target set Γ_{Tar} with a weighted perimeter penalty to prevent the emergence of irregular geometric features [188]. Furthermore, the optimization problem of Eqn.(5.2.1) is subject to a minimum volume constraint on the volume of phase I, limiting the amount of void inclusions permitted in the design domain.

5.2.2   2D Zig-Zag Pattern Example

As discussed in Section 5.2.1, out-of-plane deformation of the initially flat laminate is achieved by locally relaxing the stress in the outer, optically active (receptive to light) layers. The goal of the

optimization process is to find spatial patterns of stress relaxations (e.g., folding patterns) such that the self-deforming laminate assumes a desired target deformation. The necessary stress relaxation can be realized by selective exposure of the top and/or bottom layer to a laser. This approach allows for rather complex and non-intuitive folding patterns which can be determined by solving the optimization problem formulated in Eqn.(5.2.1). The localization of the light exposure by a laser beam, and hence the stress relaxation, is modeled through LS primitives, e.g., cuboids as depicted in Figure 5.11, representing void. The individual cuboids, of which the centroid X_2 coordinate is used as a design variable, are combined via a KS function (Eqn. (4.1.10)) to obtain a nodal LS field for generating the XFEM intersections. The advantage of using LS primitives as design variables is twofold. First, regularization of the design variable field (similar to LS filtering) is introduced and second, explicit geometric control of for example the depth of the void cuts or their width is formulated into the design optimization problem.

The first design example is a 2D pre-stressed composite beam of size $60.0 \times 3.0 \times 1.0\ mm$ which should deform into a zig-zag pattern when the stress is locally relaxed in the top and bottom layer. Due to the symmetry of the design problem, only one half of the beam is modeled using bilinear QUAD4 plane-strain elements with an element edge length of $h = 0.5$. The Young's modulus of the middle layer is $E_M = 1.0 MPa$ and the Young's modulus of the outer layers is $E_O = 10.0 MPa$. The Poisson's ratio is $\nu = 0.3$. A pre-stress of 20.0% is modeled via a CTE of $\alpha_M = -0.1$ in the middle layer and a CTE of $\alpha_O = +0.1$ in the outer layers. The objective of this design problem is to
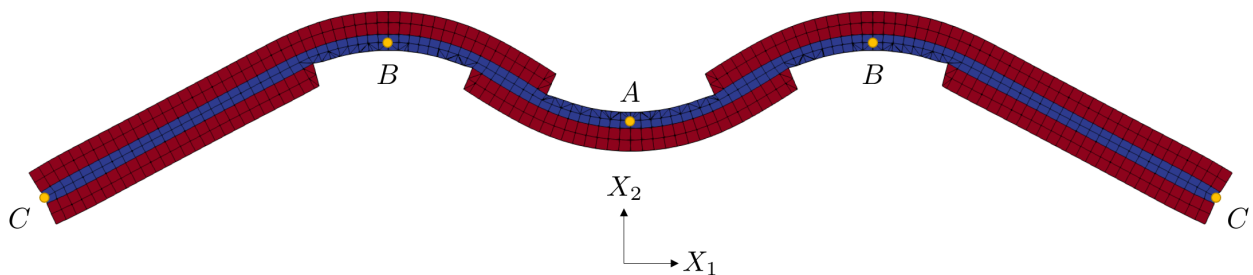
Figure 5.12: Zig-Zag pattern obtained from unsymmetrical stress relaxation of a pre-stressed LAP composite.

Table 5.2: Properties of the 3D LAP examples.

Property	Value
Domain Size	$34.0 \times 34.5 \ mm$
Element Size	$0.5 \times 0.5 \times 0.05 \ mm$
Young's Modulus Middle	$E_M = 6.7 \ MPa$
Young's Modulus Outer	$E_O = 4.1 \ MPa$
Poisson's Ratio	$\nu = 0.3$
CTE Middle	$\alpha_M = 0.0$
CTE Outer	$\alpha_0 = +0.15$

maximize the vertical displacements at points A and C in negative X_2 direction while maximizing the vertical displacement in negative X_2 direction at point B. The volume of stress relaxed material (i.e., void) is constrained to less or equal than 10.0% of the total beam volume.

The final result is shown in Figure 5.12 in its activated, zig-zag configuration. It can be seen that unsymmetrical stress relaxation (with respect to the two active outer layers) was utilized by the optimizer to achieve the desired target deformation. Due to the applied volume constraint on the void phase, locally confined areas of stress relaxation are used, which resemble the cutting lines by a laser source. Alternatively, this multi-criterion optimization problem could be solved by a bound formulation [139] where a single bound parameter is minimized to minimize or maximize multiple sub-criteria.

5.2.3   3D Water Bomb Base Example

A similar design approach is used in 3D to find the crease patterns of the Water Bomb Base, a classical origami example. The problem parameters are listed in Table 5.2 and due to symmetry of the design problem only one quarter of the domain is modeled and optimized. The appropriate mechanical boundary conditions are applied weakly via Nitsche's method (see Eqn.(3.1.3)). The quarter of the design problem is modeled using trilinear HEX8 brick elements and a linear elastic small strain thermomechanical model. The design problem to achieve the Water Bomb Base structure is formulated such that the X_3 displacement in the center of the design domain is maximized while

keeping the out-of-plane displacements of the corner points at a minimum. A volume constraint of 10.0% is enforced on the maximum allowed amount of void domain (i.e., domains with relaxed eigenstrain). The final design in the activated configuration obtained by identifying the appropriate folding lines through LS-XFEM TO is shown in Figure 5.13. It should be noted that both mountain folds (convex) and valley folds (concave) are identified during the optimization process which then lead to the desired 3D structure. A singularity exists in the center of the design domain, where mountain folds and valley folds intersect. To avoid numerical instabilities occurring at this point, a center hole (void) is created and excluded from the design domain. This is a commonly performed means to avoid this geometric singularity, as for example also done by [210].

A smooth evolution of objective and constraint is obtained, where convergence of the optimization problem is achieved after about 350 design iterations. The evolution of normalized objective and volume constraint is shown in Figure 5.14. The slight oscillations towards the end of the design optimization process are attributed to the limits of the linear kinematics model which is used in this design example.

(a)   (b)
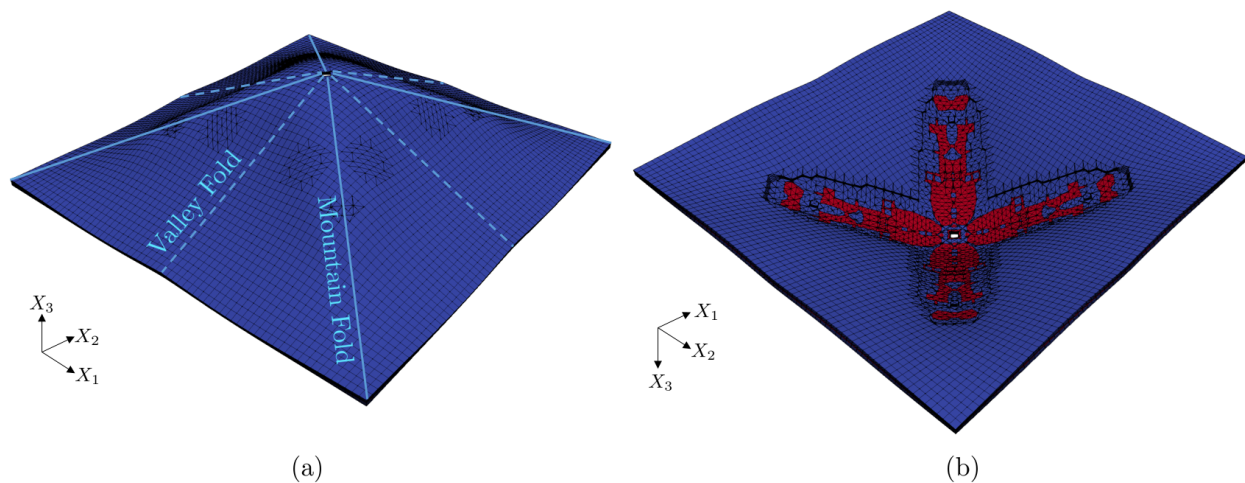
Figure 5.13: Water Bomb Base structure obtained from design optimization of a pre-stressed LAP composite. (a) Top view and (b) bottom view.
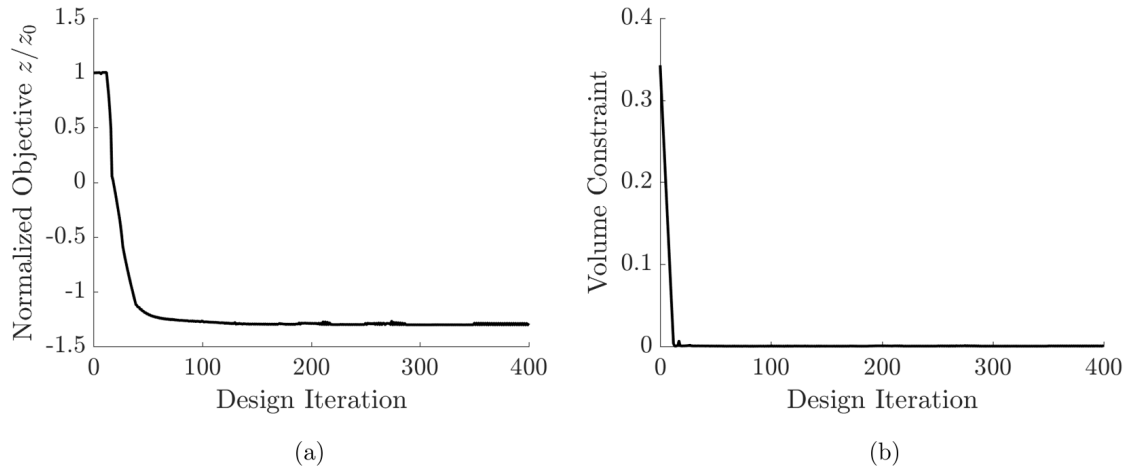
Figure 5.14: Evolution of (a) normalized objective and (b) volume constraint for the Water Bomb Base example.

5.2.4   3D Origami Chomper Example

The final design optimization example used to demonstrate the ability of LS-XFEM TO to identity crease pattern is the origami Chomper [31, 160]. The objective of this example is to maximize the X_3 displacement in the center of the design domain while minimizing the out-of-plane displacements at the ends of the design domain along the X_1 axis. A 10.0% volume constraint on
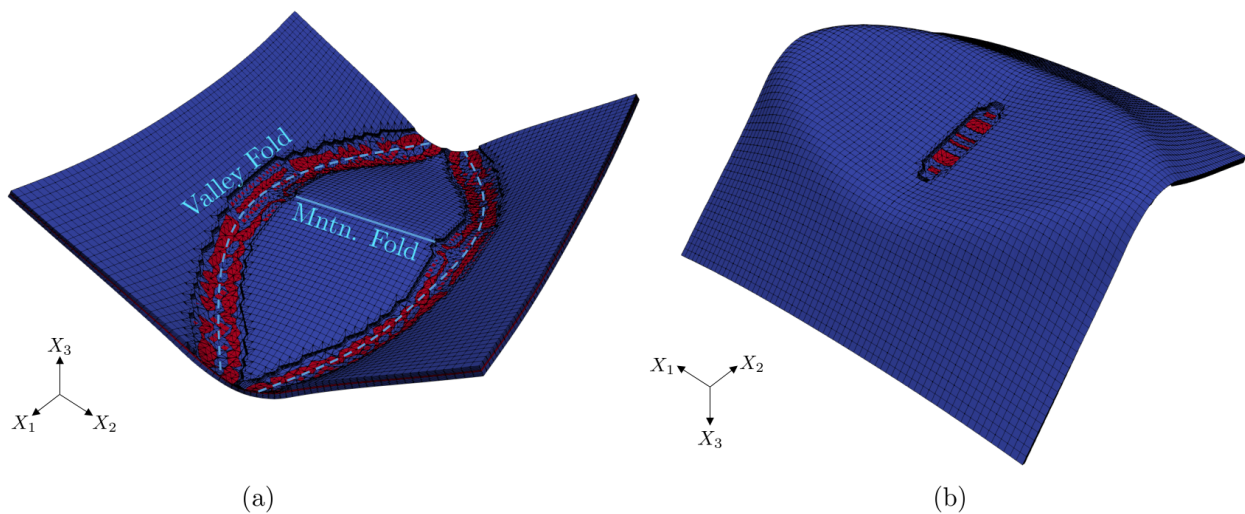
Figure 5.15: Chomper origami structure obtained from design optimization of a pre-stressed LAP composite in (a) top view and (b) bottom view.
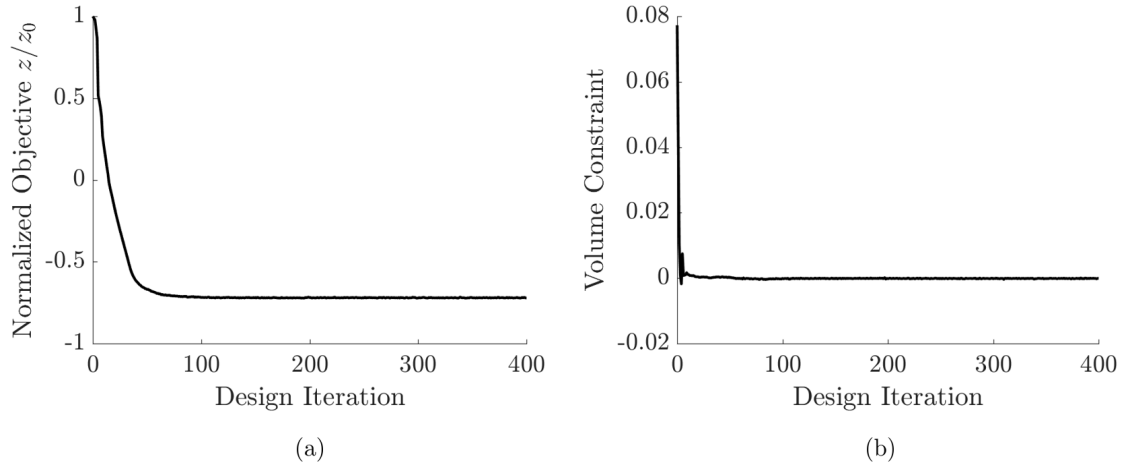
Figure 5.16: Evolution of (a) normalized objective and (b) volume constraint for the Chomper example.

the void phase is applied and symmetry of the design problem is exploited. The problem parameters are listed in Table 5.2. The final design is depicted in Figure 5.15 where clear mountain and valley folds can be identified. It should be pointed out that while the mountain fold is straight and along the X_2 axis, curved valley folds are identified. In the activated stage, these lead to upwards folding of the structure resembling the origami Chomper. As before, a smooth evolution of objective and constraint is observed (see Figure 5.16) where the converged design is obtained after about 350 design iterations.

5.2.5   Discussion

As demonstrated through design optimization examples in 2D and 3D, LS-XFEM TO was successfully used to determine the folding lines of active origami structures made from pre-stressed LAP composites. Even though small strain linear elasticity was used, crease patterns were successfully identified without reducing the design space a-priori, as for example done in a ground-structure approach. It was however also seen that using linear elasticity can only be employed for a first proof of concept of this design approach. Due to the slenderness of the active structures, finite deformations and rotations are experienced which naturally require the use of nonlinear kinematics. Also, locking of low-order elements is experienced due to the high aspect ratios of the XFEM elements, which

requires the use of higher-order XFEM to avoid shear locking effects. Moreover, eigenstrains of up to 15.0% were employed which are far beyond the small strain limit. This is another reason why hyperelastic models should be employed. Finally, structural instabilities commonly experienced by slender structures under compressive stresses are not captured by linear kinematics but are considered in a finite strain thermomechanical model. Through the design optimization examples it was seen that finite width folds are obtained, in contrast to the infinite folds seen in classical paper origami. This is mainly due to finite thickness of the composite sheets used for modeling of the origami structures and can potentially be reduced by utilizing thinner sheets of LAPs. A comprehensive review of state-of-the-art thickness accommodation techniques for technical origami is presented in [108].

The aforementioned limitations of the current, initial design approach are subject to future work as great potential of LS-XFEM TO for identifying non-intuitive crease patterns for active origami structures was seen through this preliminary study.

5.3   Combined Level-Set-XFEM-Density Topology Optimization of 4D Printed Active Structures

Due to the rapid advancement of additive manufacturing technologies in recent years, an increased amount of design freedom is provided which can be utilized to maximize the performance of printed structures. This includes the variety of materials, the accuracy of deposition, and the possibility to combine multiple materials to create active, shape-changing structures. The concept called 4D printing [184] has recently gained great popularity and has, for example, been used by [65, 64] to fabricate active origami structures susceptive to a thermal stimulus. A systematic design approach using LS-XFEM TO was presented by [125] for designing 4D printed shape memory polymer structures assuming a small strain linear elastic response. To alleviate the need for a complex thermomechanical training and activation cycle, which is typically required for shape memory materials, [45] introduced the concept of direct 4D Printing. In this approach, an inelastic printing strain is embedded into parts of a multi-material structure during a polyjet printing process. Once the printed part is heated beyond the glass transition temperature of the glassy polymer (passive material), the printing strain in the rubbery polymer (active material) is released causing a shape change. An overview of recent advancements in 4D printing is given by [104].

A strong need for a systematic design approach is identified, in order to unlock the full potential of 4D printing. Previously, only simplified design approaches for 1D rod structures [199, 44] and simplified geometric structures [45] have been explored. In these works, only intuitive material layouts and geometries have been considered for which the determination of the initial material composition was straightforward. A novel design approach combining LS-XFEM and density-based TO for designing active 4D printed structures was therefore proposed by [69, 68] where small strain linear elasticity is assumed in [69]. A strong need for considering finite deformation nonlinear kinematics has been identified and a more accurate thermomechanical model was used by [68]. Both of those reference are available in Appendices C and B, respectively. The combined LS-XFEM density TO approach used for the subsequent design examples is presented in Section 4.1.3.1.
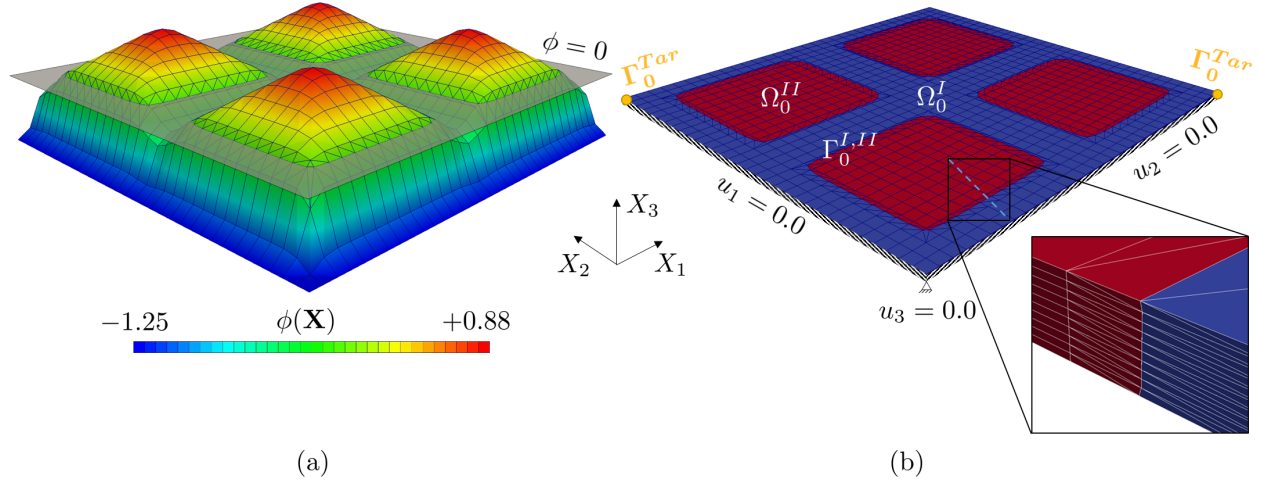
Figure 5.17: Initial quarter design domain for the 4D printed active structures. (a) Initial LSF and (b) XFEM mesh of the quarter domain.

Table 5.3: Properties of the 4D printed active structures.

Property	Value
Young's Modulus Active Material	$E_A = 0.6\ MPa$
Young's Modulus Passive Material	$E_P = 8.0\ MPa$
Poisson's Ratio	$\nu_A = \nu_P = 0.4$
CTE Active Material	$\alpha_A = 0.05$
CTE Passive Material	$\alpha_P = 0.0$

The initial design of all subsequent design problems is shown in Figure 5.17, where only one quarter of the full model is analyzed and optimized. The inclusion radius of the initial void pattern is $\mathbf{r}_i = [14.5, 14.5, 14.5]$. The appropriate mechanical boundary conditions are applied weakly using Nitsche's method. The inelastic printing strain is modeled via an isotropic thermal strain, as suggested by [45]. Quadratic twenty node hexahedral (HEX20) brick elements are used for modeling the thermomechanical response while the density and LS design variables are discretized using trilinear shape functions.

Nodal fictitious density values and nodal LS values are used as design variables for describing the multi-material TO problem. For both sets of design variables a linear filter of radius $r_f = 4.0\ mm$ is used. The goal of each design problem is matching of a target displacement at certain target sets

Table 5.4: Parameters used for each 4D printed design example.

	Propeller	Figure-8	Cylinder Gripper	4-Legged Gripper	Elevated Plane
Quarter Domain Size	$80.0 \times 80.0 \times 1.0\ mm$	$80.0 \times 80.0 \times 1.0\ mm$	$80.0 \times 80.0 \times 1.0\ mm$	$80.0 \times 80.0 \times 1.0\ mm$	$120.0 \times 120.0 \times 1.0\ mm$
Element Edge Length h	$1.0 \times 1.0 \times 0.1\ mm$	$2.5 \times 2.5 \times 0.1\ mm$	$2.5 \times 2.5 \times 0.1\ mm$	$2.5 \times 2.5 \times 0.1\ mm$	$2.5 \times 2.5 \times 0.1\ mm$
Initial Void Pattern	$4 \times 4 \times 1$	$4 \times 4 \times 1$	$4 \times 4 \times 1$	$4 \times 4 \times 1$	$6 \times 6 \times 1$
Volume Constraint γ_v	0.15	0.15	0.20	0.10	0.10
Perimeter Penalty $\gamma_p er$	0.01	0.05	0.05	0.05	0.05
Change in Strain Energy γ_s	-	$5.0 \cdot 10^{-5}$	$5.0 \cdot 10^{-5}$	$1.0 \cdot 10^{-6}$	$5.0 \cdot 10^{-5}$
Perturbation Pressure $\bar{P}$	-	$1.0\ Pa$	$0.1\ Pa$	$1.0\ Pa$	$1.0\ Pa$
GCMMA Step Size	0.05	0.04	0.03	0.03	0.03

Γ_0^{Tar}, in order to achieve a desired target deformation upon activation of the 4D printed structure. The optimization problem is subject to a volume constraint on the maximum amount of solid material and an end-stiffness constraint to ensure structural integrity. More details regarding the end-stiffness constraint are presented in Section 4.7. A linear filtering and a projection scheme is applied to the density design variables to obtain clearly defined active and passive material sub-domains. The projection sharpness parameter is increased from $\gamma_P = 0.01$ to $\gamma_P = 48.0$ using a continuation approach.

To avoid local reduction of the member thickness, independent LS design variables are only applied to the top surface of the plate-like structures. All nodal LS values below the top surface are dependent on the corresponding nodal LS value on the top surface, such that $\phi(X_1, X_2, X_3) = \phi(X_1, X_2)$. To guarantee mechanical connection between the target sets and the base of the structure, strips immediately bordering the mechanical symmetry planes are excluded from the LS-XFEM optimization process, see Figure 5.17. These domains are however still subject to material optimization through variation of the nodal density design variables. Selective structural springs, as discussed in Section 4.2.3, are applied in all design examples. The partial differential equations related to the selective structural springs and the structural mechanics are solved using a staggered solution approach in a one-way coupled manner (see Section 3.4 for more details). The material properties used for active and passive material as well as problem specific parameters are listed in Table 5.3 and Table 5.4, respectively.

The optimization problem to be solved in order to achieve the desired target deformation is formulated as:

$$\min_{\mathbf{s}} \ z(\mathbf{s}, \mathbf{u}) = w_1 \int_{\Gamma_0^{Tar}} (\mathbf{u} - \mathbf{u}_{Tar})^2 dA + w_2 \int_{\Gamma_0^{I,II}} dS$$

$$\text{s.t. } g_1 = \frac{\Omega_0^I}{(\Omega_0^I + \Omega_0^{II})} - \gamma_v \leq 0 \qquad (5.3.1)$$

$$g_2 = \left(\frac{\mathcal{U}' - \mathcal{U}}{\mathcal{U}}\right)^2 - \gamma_s \leq 0$$

where the first term of the objective function aims to achieve a target displacement $\mathbf{u}_0^{Tar}$ at a certain target set Γ_{Tar} and the second term is a perimeter penalty for regularization of the design optimization problem. Furthermore, the optimization problem is subject to a volume constraint g_1 limiting the amount of phase I material as well as an end-stiffness constraint g_2. A detailed discussion on the formulation of the end-stiffness constraint is presented in Section 4.7.3.

Finally, the optimized designs are fabricated and activated via direct 4D printing for qualitative comparison with the XFEM prediction. For more details regarding direct 4D printing and the described design approach, the interested reader is referred to the works of [45, 68, 69].

5.3.1   Small Deformation

First, a linear elastic small strain design example is considered to demonstrate the applicability of the multi-material, combined LS-XFEM density TO approach. In accordance with the quadratic XFEM approach used, higher-order ghost stabilization as discussed in Section 3.2.1 is employed. A ghost penalization parameter of $\gamma_G = 0.001$ is used to provide numerical stabilization.

5.3.1.1   Active Propeller Example

Designing an active propeller from an initially flat plate is the goal of this first design example. To achieve a target twisting angle of $\omega_{Tar} = 45°$ of four propeller arms, the geometry of the structure (solid/void) and the material layout (active/passive) are optimized simultaneously. The design optimization problem is furthermore subject to a volume constraint of $\gamma_v = 0.15$ on the amount of
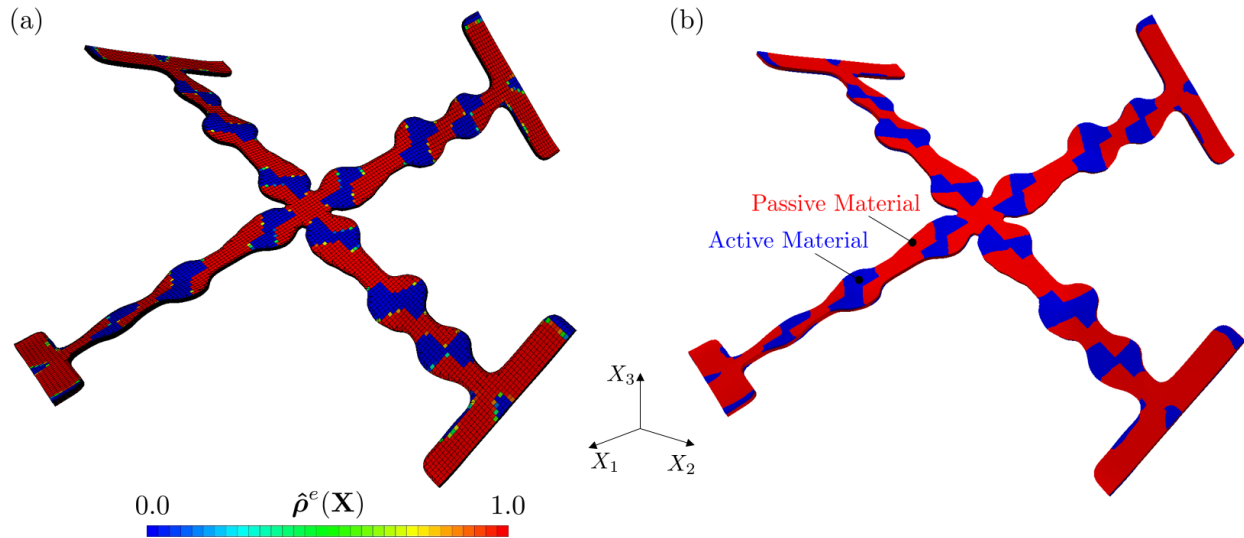
Figure 5.18: Final design in the activated stage for the twisting propeller example. (a) Density field and (b) extracted distinct material phases.

solid material. To allow for the twisting of the propeller arms, simply-supported anti-symmetry conditions are applied along the symmetry boundaries indicated in Figure 5.17.

The final design resembling a self-twisting propeller structure is shown in Figure 5.18 where the quarter domain was reflected to illustrate the full structure. Both (a) the final density field and (b) distinct material phases, which are extracted in a post-processing step, are shown. It can be seen that overall four propeller arms are formed which connect the propeller blades with the center of the structure. These arms are mostly comprised of passive material (red) with distinct strips of active material (blue) aligned at 45°. This special combination of passive and active material leads to the desired twisting of the propeller blades from the base of the structure outwards. To enable the final design to be 4D printed, distinct material phases are extracted along a density threshold of $\hat{\rho}^e = 0.5$, as shown in Figure 5.18 (b).

The evolution of objective and volume constraint are shown in Figure 5.19. Periodic increases in the objective function are seen, which are caused by an increase of the projection parameter through continuation, to mitigate intermediate material densities. It is also seen that the objective function converges to a non-zero value (i.e., $z/z_0 = 0.13$) which means the target twisting angle
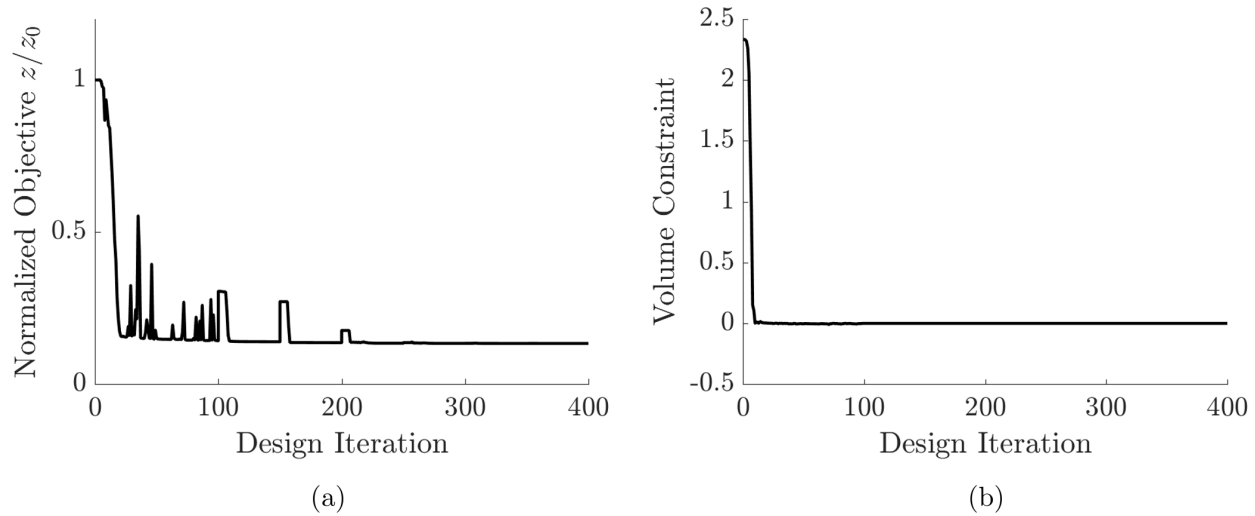
Figure 5.19: Evolution of (a) normalized objective and (b) volume constraint for the twisting propeller example.

of $\omega_{Tar} = 45°$ cannot be fully achieved by the active propeller blades. This is partially due to the simplified linear elastic kinematics and a printing strain of only 5.0% which is insufficient to yield the desired twisting angle.

To understand the error introduced by a linear kinematics model used for this design example, the final design is analyzed using a nonlinear kinematics model for comparison. The deformation results from both analyses are shown in Figure 5.20 in a side-on view. It can clearly be seen
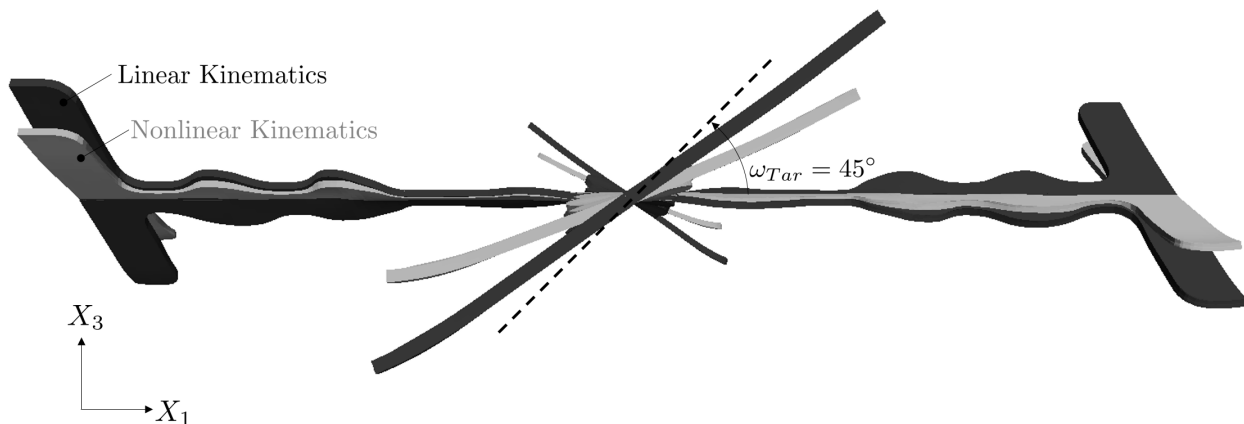
Figure 5.20: Comparison of the deformation prediction for the final propeller design using linear and nonlinear kinematics.

that the linear kinematics assumption significantly over-predicts the twisting motion. Due to the large discrepancy between linear and nonlinear model, it can be seen that the small strain limit is surpassed in this example and using a linear kinematics model introduces a significant modeling error. From this example, it is apparent that a strong need for a fully nonlinear XFEM model exists, which needs to be employed throughout the entire TO process. This is addressed by the following design examples.

5.3.2   Large Deformation

Design optimization of multi-material 4D printed active structures under finite deformation is targeted in this section. As before, a combined LS-XFEM density approach is employed to describe the multi-material TO problem. In addition, an end-stiffness constraint is enforced to ensure sufficient structural rigidity of the final designs. More details on the formulation of the end-stiffness constraint are presented in Section 4.7. For stabilization of the XFEM model, a geometric preconditioning scheme originally proposed by [107] is used.

5.3.2.1   Twisted Figure-Eight Example

The first example studied using a finite deformation kinematics model is the design of a twisted figure-eight structure. The goal of this example is to design a self-deforming structure where two of the target points meet at the top and two target points meet at the bottom, in the center of the design domain, creating a twisted figure-eight like structure. The problem parameters are listed in Table 5.4 and the material parameters used in this example are provided in Table 5.3.

The final design, in the activated deformed configuration is shown in Figure 5.21 for both (a) the XFEM prediction and (b) the printed sample. A clear distinction between areas of active and passive material can be made due to the employed projection scheme using a continuation approach. A slight asymmetry between the top and the bottom legs can be seen.

This is due to a local minimum identified by the optimization algorithm which was then manifested through an increasingly nonlinear design space caused by an increasing projection
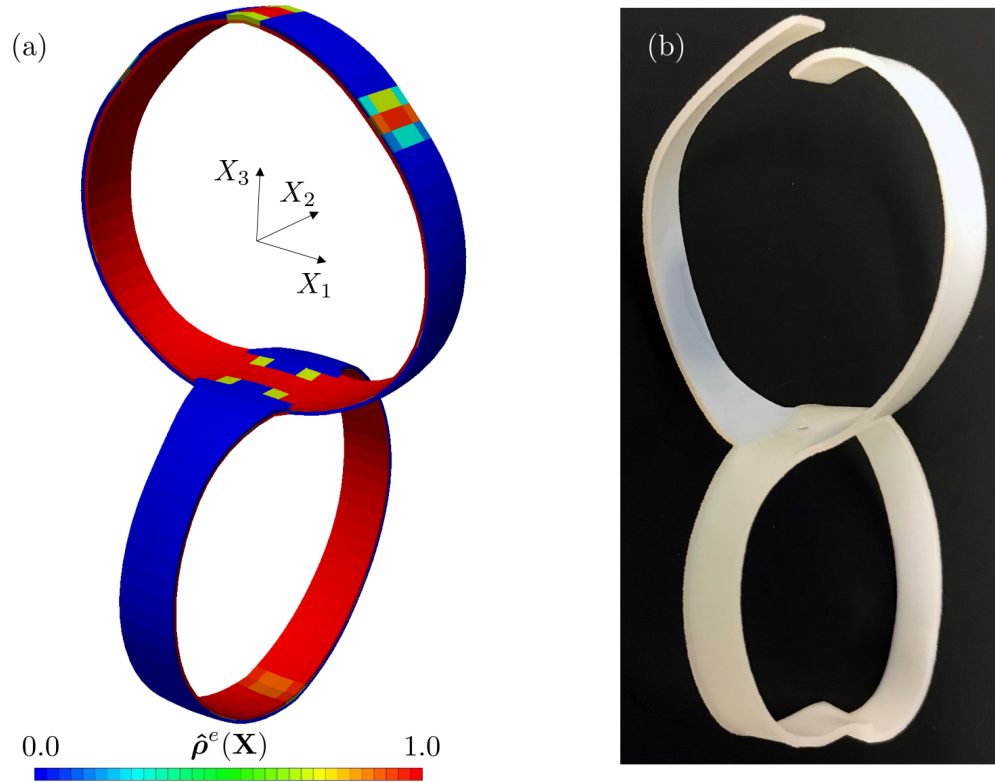
Figure 5.21: Final design of the twisted figure-eight design problem. (a) XFEM prediction and (b) printed and activated specimen.

sharpness parameter. Overall, the anticipated twisted figure-eight target deformation is achieved reasonably well, both by the XFEM model and the activated 4D printed sample. Figure 5.22 shows the initial, undeformed configuration of the final design where (a) distinct material phases were extracted. (b) Shows the printed structure before activation.
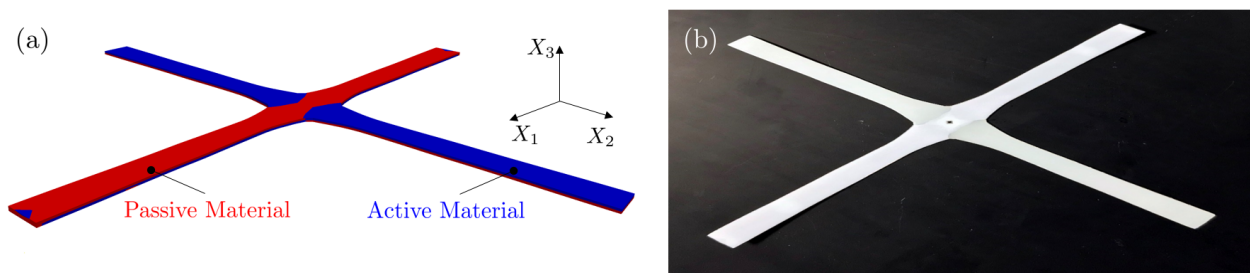
Figure 5.22: Final design of the twisted figure-eight in undeformed state. (a) Extracted material phases and (b) printed inactivated structure.
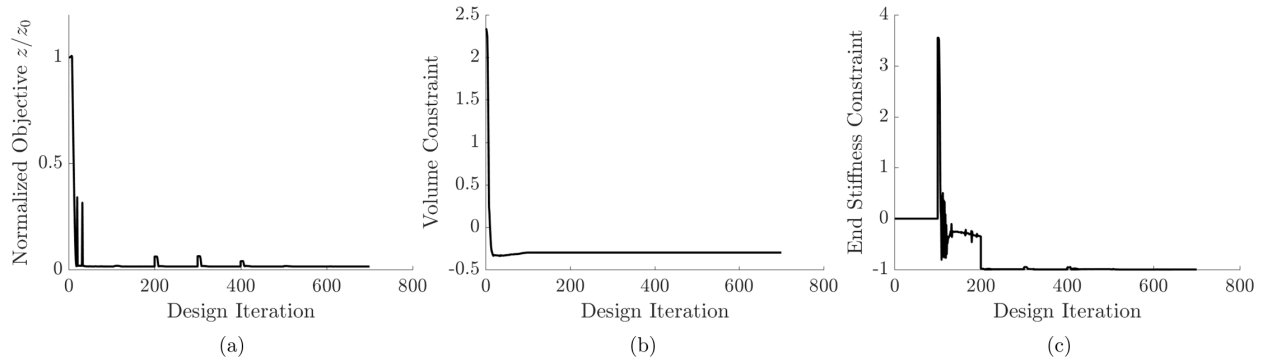
Figure 5.23: Evolution of (a) objective, (b) volume constraint, and (c) end-stiffness constraint for the twisted figure-eight example.

The evolution of objective function, volume constraint and end-stiffness constraint is shown in Figure 5.23. As expected, periodic increases in the objective function are observed, caused by the continuation approach. It should also be pointed out that the volume constraint is only active initially, as the optimizer favors slender arms of the structure to achieve the required curling. This reduces the cylindrical bending effect caused by the isotropic printing strain which, if too dominant, reduces the desired curling effect. Moreover, the end-stiffness constraint is only activated after 100 design iterations, after an initial structural layout was identified.

5.3.2.2   Cylinder Gripper Example

The second example considering finite deformation is the design of a cylinder gripper. The target deformation of the initially flat structure is such that a cylinder of radius $R_{Tar} = 50.0\ mm$ is being enclosed at a depth of $X_{3_{Tar}} = -45.0\ mm$. The activated structure thus resembles gripping of a cylindrical object. The material parameters are listed in Table 5.3 while problem specific parameters are given in Table 5.4.

The final design in the deformed configuration is shown in Figure 5.25. Both the XFEM model and the activated 4D printed structure are shown, which achieve the target deformation very well. Double curvature is used to form four gripping arms with enlarged gripping bars at their tips. To achieve the required minimum stiffness, fillets of passive (stiff) material are placed at the tips of
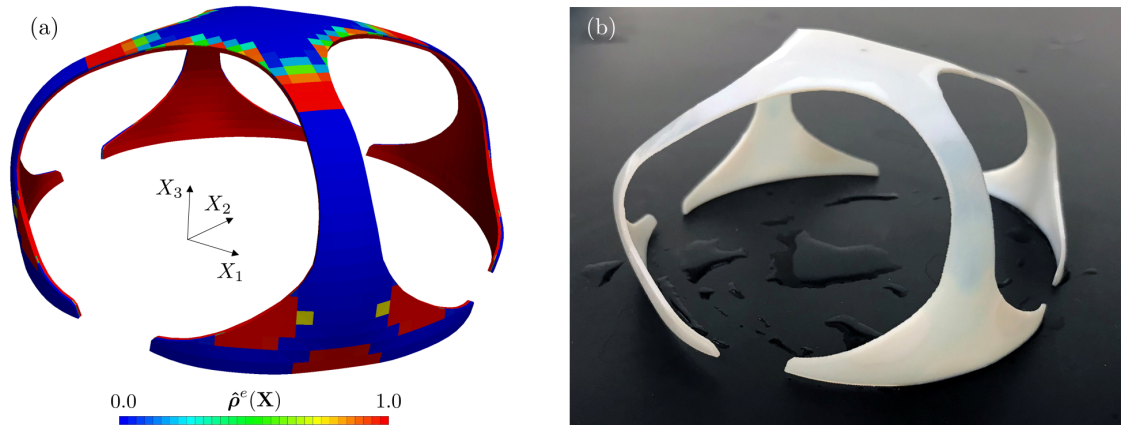
Figure 5.24: Final design of the cylinder gripper design problem. (a) XFEM prediction and (b) printed and activated specimen.

the gripper. The extracted material phases of active and passive material along with the printed specimen are depicted in Figure 5.25.

The evolution of objective and constraints is shown in Figure 5.26. As before, a smooth evolution of the objective is seen, except when an increase of the projection sharpness parameter momentarily causes oscillations. For this example, the volume constraint is active and so is the end-stiffness constraint at convergence.

5.3.2.3 Four-Legged Gripper Example

Next, designing an active four-legged gripper structure is targeted. The initially flat structure is designed to deform such that four gripping legs meet at the bottom center of the design domain.
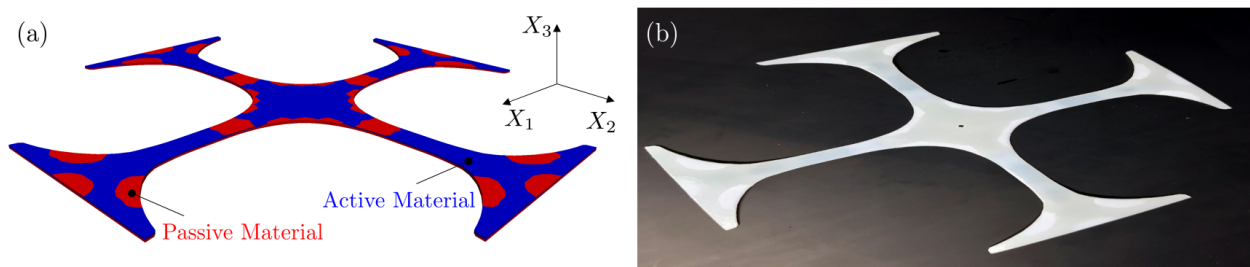
Figure 5.25: Final design of the cylinder gripper in undeformed state. (a) Extracted material phases and (b) printed inactivated structure.
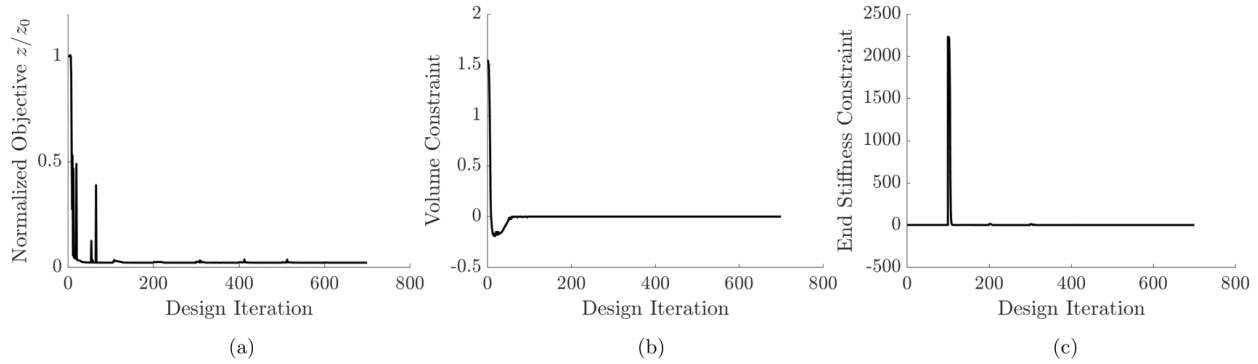
Figure 5.26: Evolution of (a) objective, (b) volume constraint, and (c) end-stiffness constraint for the cylinder gripper example.

Again, the material parameters used for this design example are listed in Table 5.3 while problem specific parameters are presented in Table 5.4. The final design as predicted by the XFEM model as well as the printed and activated specimen of the four-legged gripper is shown in Figure 5.27 (a) and Figure 5.27 (b), respectively.

Interesting design features, e.g., inverted convex-concave sections along the gripping legs, are seen in the deformed structure. These are created in response to a target deformation of increased complexity and help facilitate the required minimum stiffness of the gripper. Due to the lack of a
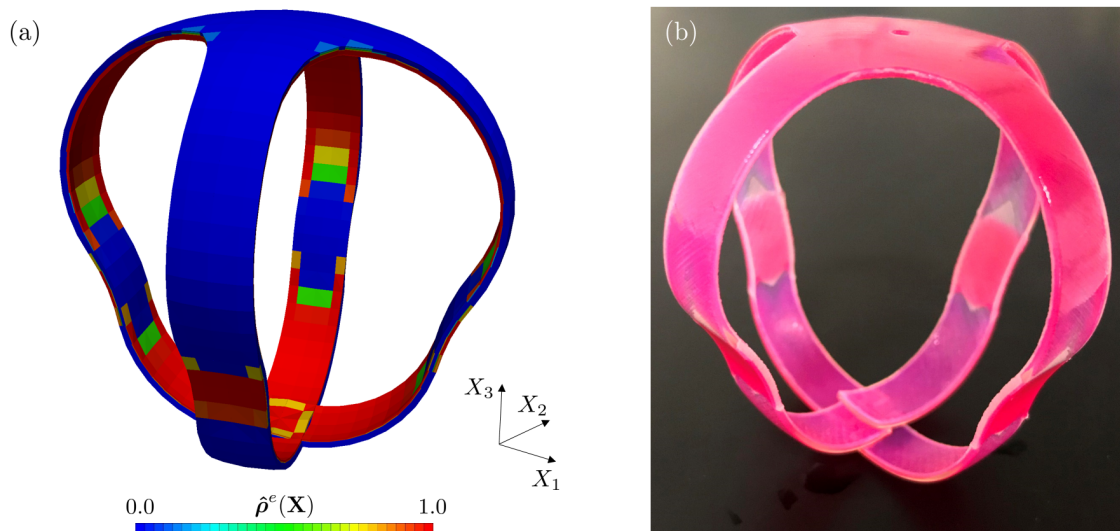
Figure 5.27: Final design of the four-legged gripper design example. (a) XFEM model and (b) printed specimen.
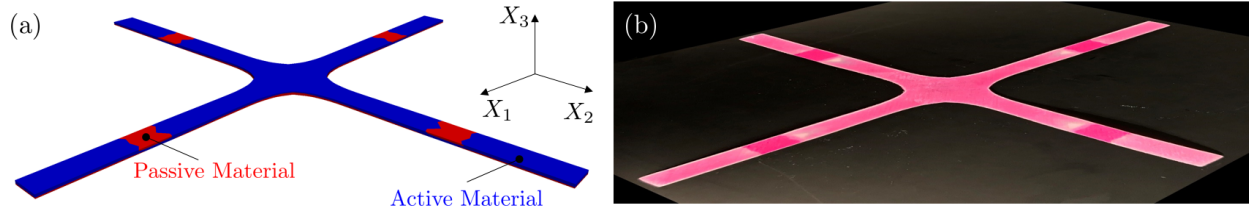
Figure 5.28: Final design of the four-legged gripper in the undeformed configuration. (a) Extracted material phases and (b) printed inactivated structure.

contact formulation in the employed XFEM model, areas of self-penetration are experienced at the tips of the gripper. In the physical specimen, this is alleviated by a slight overlap of the gripping legs at different X_3 depths (see Figure 5.27 (b)).

The evolution of objective and constraints is presented in Figure 5.29. It should be pointed out that for this design example, the end-stiffness constraint is directly affected by an increase in projection sharpness, unlike in the previous example problems. Which means that the optimizer uses as much passive (stiff) material as possible to create the required stiffness of the structure. After every continuation step, a few design iterations are needed before the appropriate re-arrangement of material is performed and the required end-stiffness is again achieved.
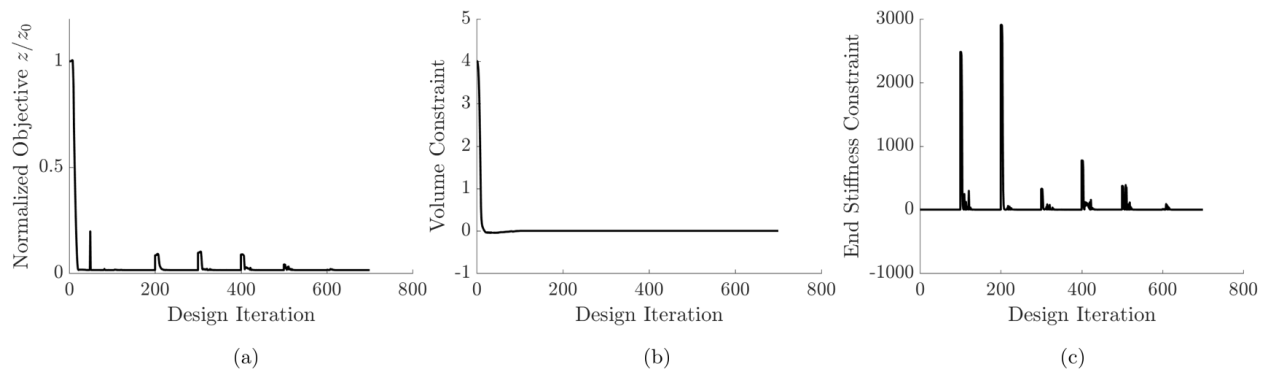
Figure 5.29: Evolution of (a) objective, (b) volume constraint, and (c) end-stiffness constraint for the four-legged gripper design problem.
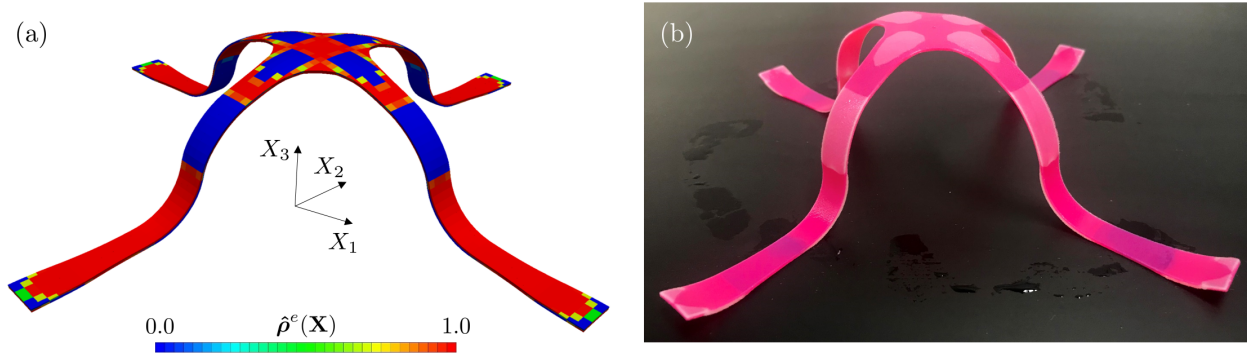
Figure 5.30: Final design of the elevated plane design example. (a) XFEM model and (b) printed specimen.

5.3.2.4 Elevated Plane Example

The final design example discussed in the context of combined LS-XFEM-density-based TO of active 4D printed structures is a self-elevating plane. The objective of this problem is to find the optimal geometry and material layout such that an initially flat plane elevates its center by $+40.0 \; mm$ in the X_3-direction while exhibiting no out-of-plane deformation at the tips. In order to achieve this, the design space is enlarged as stated in Table 5.4. As before, Table 5.3 lists the material parameters used here. The XFEM prediction and the 4D printed and activated structure corresponding to the final design are depicted in Figure 5.30 (a) and (b), respectively.

The corresponding initial, flat structure is shown in Figure 5.31. Inverted sections of active
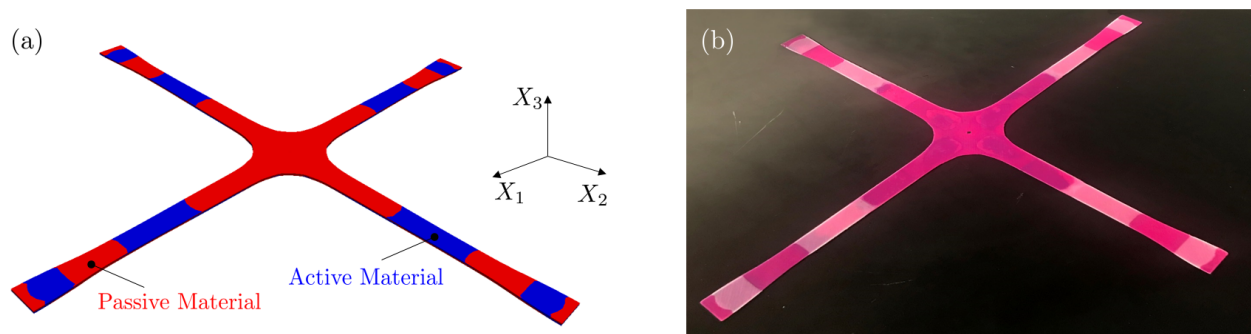
Figure 5.31: Final design of the self-elevating plane in the undeformed configuration. (a) Extracted material phases and (b) printed inactivated structure.
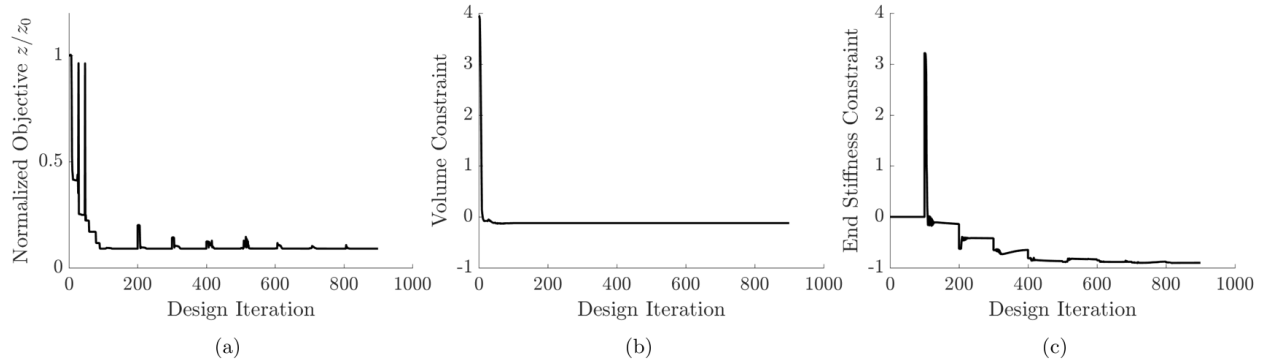
Figure 5.32: Evolution of (a) objective, (b) volume constraint, and (c) end-stiffness constraint for the elevating plane design problem.

and passive material can be seen along all four legs which yield the concave/convex deformation required to achieve the elevation of the center plane after activation of the printed structure. Figure 5.32 shows the evolution of objective function and constraint values. The end-stiffness constraint in this design example tends to decrease with an increasing projection sharpness parameter, as intermediate material domains are removed. At convergence, only the volume constraint limiting the amount of solid phase is active.

5.3.3 Discussion

A multi-material TO approach was developed by combining LS-XFEM and density-based TO approaches. The method was successfully applied to several design optimization problems where the optimal geometry and the material layout were determined to achieve desired target deformations upon activation of 4D printed active structures. An initial design example under the small strain assumption clearly demonstrated the need for considering large deformation nonlinear kinematics. Considering finite deformations in combination with quadratic HEX20 XFEM elements, yielded good qualitative agreement between numerical predictions and experimental results.

However, some limitations of the current design approach were identified. A need for including a contact formulation was seen due to the fact that self-penetrating domains tend to emerge during the optimization process. Furthermore, structural instabilities like buckling and snap-though have

not been considered yet. These are quite prevalent in slender structures with eigenstrains as shown by [209, 48] and should be studied in future work. Finally, to achieve quantitative comparisons between numerical results and experimental specimen, ambient effects like gravity, the viscosity of water and anisotropies introduced through the 4D printing process need to be included in the numerical model for future work.

5.4   Loosely-Coupled Combined Level-Set-XFEM-Density Approach

As discussed in Section 4.1.3.2, introducing a loose coupling between density and LS design variables can be used to create a combined LS-XFEM-density TO approach. Combining those two, traditionally independent, TO approaches, the benefits of both methods can be taken advantage of while mitigating the drawbacks of either approach. Namely, the benefits of the combined method are no need for initial seeding, minimum feature size control, and a crisp definition of the interface geometry. At the same time, downsides of either method (fuzzy interface, need for initial seeding) are eliminated by coupling the density design variable field and the LS design variable field through inequality constraints. More details regarding the loose coupling approach employed here are discussed in Section 4.1.3.2. Linear elasticity is considered for demonstration of the combined LS-XFEM-density TO approach. Solid-void numerical examples in 2D and 3D are presented in the following. The material properties used for all examples are summarized in Table 5.5.

5.4.1   Mass Measure only in Phase I - Hole Nucleation

First, a mass constraint is only considered in phase I, which leads to the hole nucleation property through the lower LS penalty discussed in Section 4.1.3.2. In the following, the initial seeding dependency of a pure LS-XFEM TO approach is demonstrated and it is shown how the hole nucleation ability of the proposed combined LS-XFEM-density approach mitigates this long standing issue.

The strain energy minimization problem with a mass constraint only on the solid phase (i.e., phase I) is therefore formulated as:

$$\min_{\mathbf{s}} \ z(\mathbf{s}, \mathbf{u}) = w_1 \, \mathcal{U} + w_2 \int_{\Gamma_0^{I,II}} dS + w_3 \int_{\Omega_0^D} p_L \, dV + w_4 \int_{\Omega_0^D} p_{Reg} \, dV$$

$$\text{s.t. } g = \frac{\mathcal{M}^I}{(\Omega_0^I + \Omega_0^{II})} - \gamma_m \le 0 \tag{5.4.1}$$

where the objective function consists of four weighted components, such that $w_1 + w_2 + w_3 + w_4 = 1.0$. The first term minimizes the strain energy $\mathcal{U}$, the second term minimizes the perimeter of the XFEM interface, the third term is the lower penalty p_L causing the hole nucleation, and the last objective

Table 5.5: Properties of the combined LS-XFEM-density structures.

Property	Value
Young's Modulus Solid Material	$E_S = 2.0 \ GPa$
Young's Modulus Void Material	$E_V = 1.0 \cdot 10^{-8} \ Pa$
Poisson's Ratio	$\nu_S = \nu_V = 0.4$
Density Solid Material	$\rho_S = 1.0$
Density Void Material	$\rho_V = 0.0$

contribution is the LS regularization discussed in Section 4.3. It should be pointed out that the different objective contributions are enabled sequentially, using a continuation approach. First, a pure strain energy minimization problem is solved, until the lower LS penalty is added. After a XFEM interface exists, the perimeter penalty and the LS regularization term are enabled. Every time an additional objective contribution is added, a re-normalization of all objective contributions is performed, in order to achieve the desired scaling as specified by the weights w_i.

5.4.1.1 2D Short Beam

First, a short cantilevered beam in 2D is studied to demonstrate the hole nucleation capabilities of the combined LS-density approach. The problem setup with loads and boundary conditions is shown in Figure 5.33. It should be noted that domains at which the traction load and the clamped
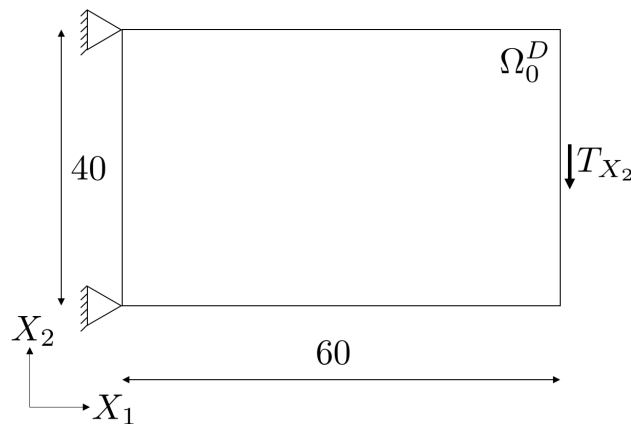
Figure 5.33: Problem setup of the short beam in 2D.
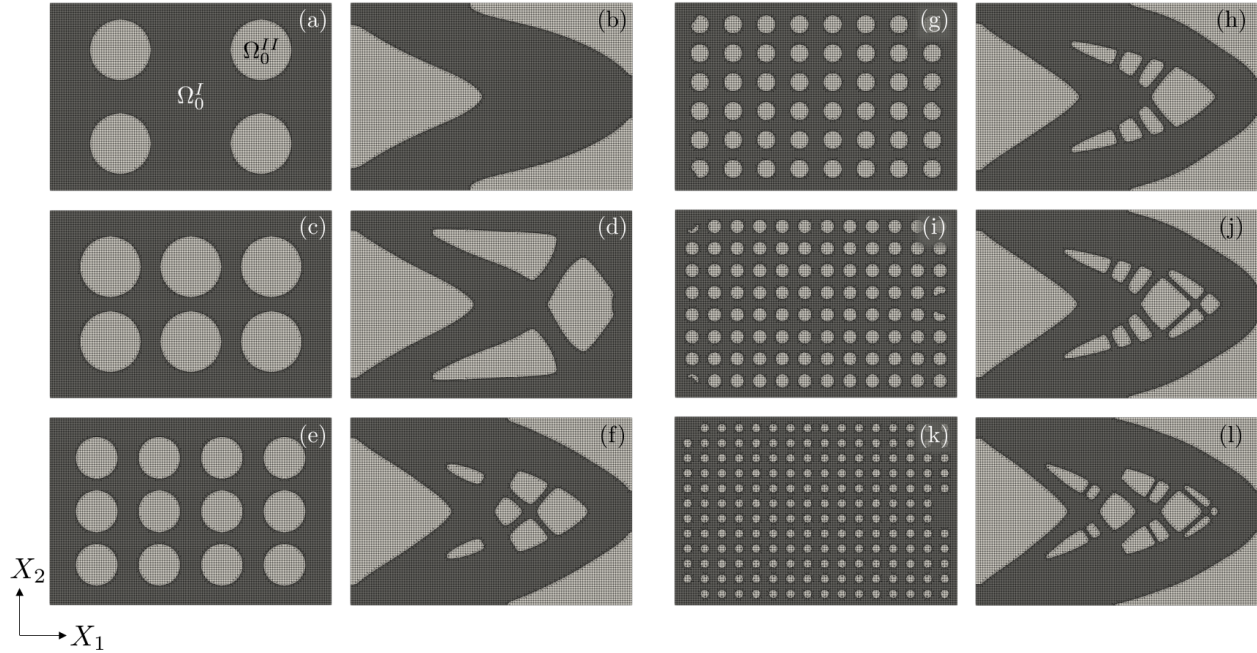
Figure 5.34: Dependency of a LS-XFEM TO final design on the initial hole seeding for the short beam in 2D. (a) Initial design with 4 void inclusions, (b) corresponding final design. (c) Initial design with 6 holes, (d) obtained final design. (e) Initial hole pattern for 12 holes and (f) final design obtained from it. (g) Initial seeding with 48 inclusions and (h) corresponding final design. (i) Initial hole pattern with 96 inclusions, (j) obtained final structure. (k) Initial seeding pattern with 192 holes and (l) obtained final design.

boundary conditions are applied, are excluded from the design domain to ensure a mechanically connected structure. Also, design symmetry about the X_1 axis is assumed in the middle of the design domain. A vertical traction load of $T_{X_2} = -60$ is applied over a length of 2 along the right side of the design domain. A mass constraint of $\gamma_m = 0.6$ is enforced and the objective weights are $w_i = [0.93,\ 0.01,\ 0.05,\ 0.01]$.

The initial design dependency of LS-XFEM TO is illustrated using the 2D short beam example. It is well known, that a large dependency of the final design on the initial guess exists in LS-XFEM TO when no hole nucleation strategies are employed [188, 187]. This dependency is typically mitigated by using a sufficiently large number of initial void inclusions as an initial guess [189]. Figure 5.34 shows different designs obtained from initial seeding patterns of 4, 6, 12, 48, 96, and 192 holes. As can be seen, final designs with increasingly more sophisticated micro structures are

Figure 5.35: Final density distribution of the short beam in 2D obtained by (a) a classical SIMP approach and (b) a combined LS-density approach. The domain decomposition in solid (Ω_0^I) and void (Ω_0^{II}) obtained by the LS-density approach is shown in (c).

obtained when the design optimization process is initialized with an increasing number of holes. Even though the design features get more refined when the number of initial holes is increased, the structural performance (i.e., strain energy) stays largely unaffected by these more complex design features. It is also observed that no convergence is obtained towards one specific final design (and topology), even for a large number of holes.

In contrast, density methods suffer much less from this dependency [188]. The final density field obtained by a SIMP TO approach with an initial density field of $\mathbf{s}^\rho = 0.5$ is shown in Figure 5.35 (a). The final design obtained by the loosely-coupled combined LS-density approach is depicted in Figure 5.35 (b). The lower LS penalty discussed in Section 4.1.3.2 is used in order to create domains of a positive LSF (Ω_0^{II}, void) in areas of low density. Initially, the LS design variables are all negative (Ω_0^I, solid) and the coupling penalty is only enabled after 60 design iterations using a continuation approach. The hole nucleation process takes about 20 design iterations until the LS regularization and the perimeter penalty are activated as additional objective contributions (see Eqn.(5.4.1)). It is important to point out that the hole seeding process (lower LS penalty) is only enabled after a first, converged density field is obtained. This guarantees a fast and clean hole nucleation without leading to oscillating void islands and a very irregular XFEM interface. Moreover, during the hole seeding process, no LS regularization is performed. This ensures that during this stage of the design optimization process, the advancement of the LSF is dominated by
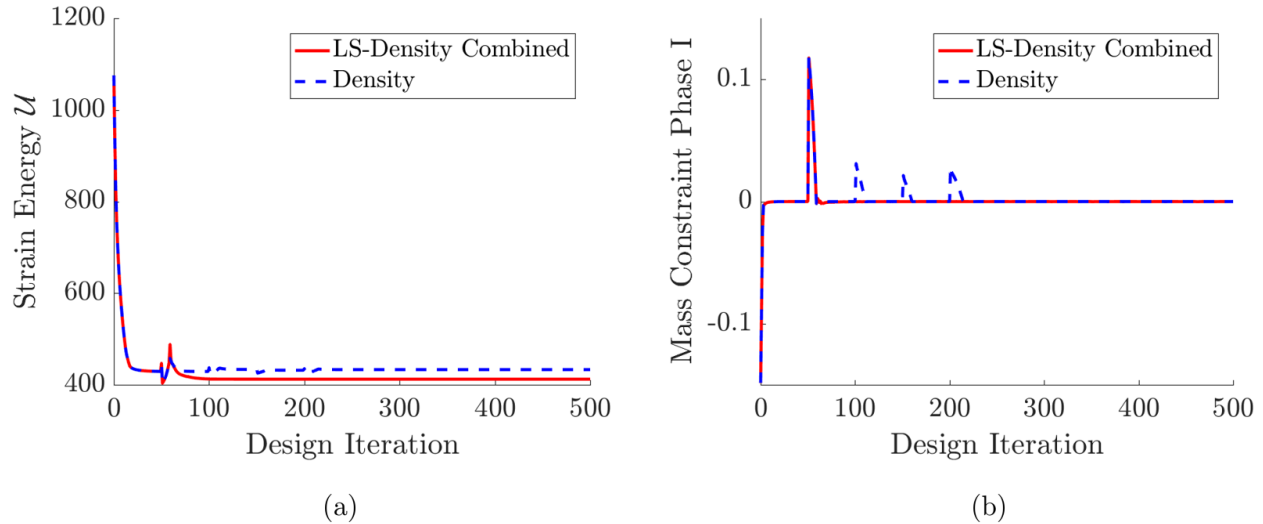
Figure 5.36: Comparison of (a) evolution of strain energy and (b) mass constraint on phase I of pure density TO with combined LS-density TO.

the coupling term (lower LS penalty) and void domains are introduced properly in all areas of low density.

As only the mass in phase I is considered in the mass constraint of Eqn.(5.4.1), an arbitrary amount of high density material can be placed by the optimizer in phase II without violating the prescribed mass ratio γ_m. This can be seen in Figure 5.35 (b) where high density values are obtained even in the void phase (Ω_0^{II}). This shows that as soon as void domains are introduced in the design domain, the SIMP penalization effect is lost and solely the XFEM interface is used to enforce the mass constraint. Undercutting of the density field by the XFEM interface is not prohibited when only the mass of phase I is considered in the mass constraint. This means, the XFEM interface can evolve somewhat independently of the density field as soon as the hole nucleation process is complete. This can be seen by comparing the pure SIMP design shown in Figure 5.35 (a) with the final design obtained by the combined approach shown in Figure 5.35 (c), where one of the internal vertical bars has disappeared leading to a slightly different topology than in the SIMP design.

The evolution of strain energy and mass constraint enforced in phase I is shown in Figure 5.36, for both classical SIMP TO and combined LS-density TO. It can clearly be seen that initially

identical curves are obtained, until the lower LS penalty is enabled at design iteration 60. A few iterations after that, the XFEM interface is introduced in the combined LS-density approach which causes a deviating behavior of the strain energy. As a complete hand-over from a pure SIMP problem to a pure XFEM problem is performed, the strain energy quickly converges to a significantly lower value than in the classical density problem. This difference is attributed to areas of intermediate (weak) material which can never be fully eliminated in a pure density TO approach. A quantitative comparison of the structural performance of the pure density design and the combined LS-density design is not meaningful, as different analysis techniques were employed. The density design is analyzed by classical FEM while the combined LS-density design is analyzed by XFEM, where stabilization techniques (e.g., face-oriented ghost stabilization) and an increased number of integration points in intersected elements may lead to slight differences in the prediction of the physical response. A direct comparison between FEM and XFEM is therefore only possible in the limit of mesh refinement, as performed in Section 5.1.1. To mitigate blurriness in the density field introduced by the linear filter, the projection sharpness parameter and the SIMP exponent are increased in a continuation approach. This leads to periodic increases in strain energy and mass constraint as seen in Figure 5.36 for the pure density-based approach.

5.4.1.2   3D Short Beam

A similar study, as performed in Section 5.4.1.2, is repeated in 3D in this section. For that, the design space is increased to $60.0 \times 40.0 \times 40.0$ while similar load and boundary conditions as shown in Figure 5.33 are used. To increase computational efficiency, only one-half of the design domain in X_3-direction is modeled and optimized. The centrally applied traction load at the right domain boundary is $T_{X_2} = -60.0$ and a mass constraint of $\gamma_m = 0.11$ is enforced.

Unlike in the 2D case, the dependency of the final design obtained by pure LS-XFEM TO on the initial seeding pattern is insignificant. This can be seen in Figure 5.37 for design studies initiated with 24, 48, 192 and 378 void inclusions. Independent of the initial seeding, the expected shear-web design connecting the centrally applied load (on the right) to the four areas of support (on the left) is obtained. The reason for this insensitivity of the 3D short beam to the initial hole seeding stems from the fact that the LSF can evolve much more freely in 3D and has the ability to create holes by "punching" through a solid member in thickness direction. This is not possible in 2D and therefore a much larger dependency of the final design on the initial hole pattern is observed
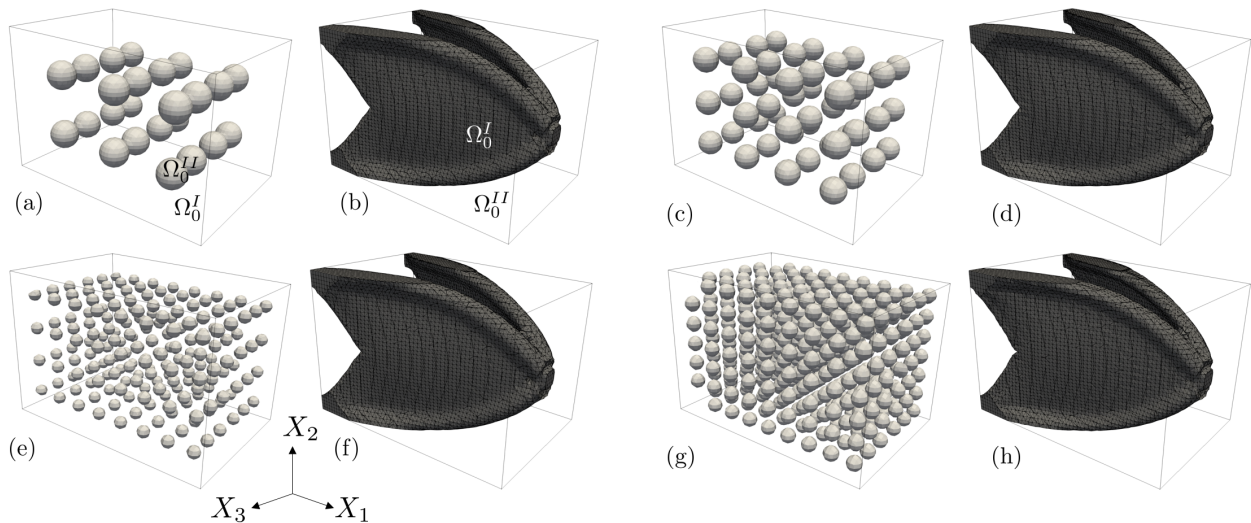
Figure 5.37: Dependency of a LS-XFEM TO final design on the initial hole seeding for the short beam in 3D. (a) Initial design with 24 void inclusions, (b) corresponding final design. (c) Initial design with 48 holes, (d) obtained final design. (e) Initial hole pattern for 192 holes and (f) final design obtained from it. (g) Initial seeding with 378 inclusions and (h) corresponding final design.
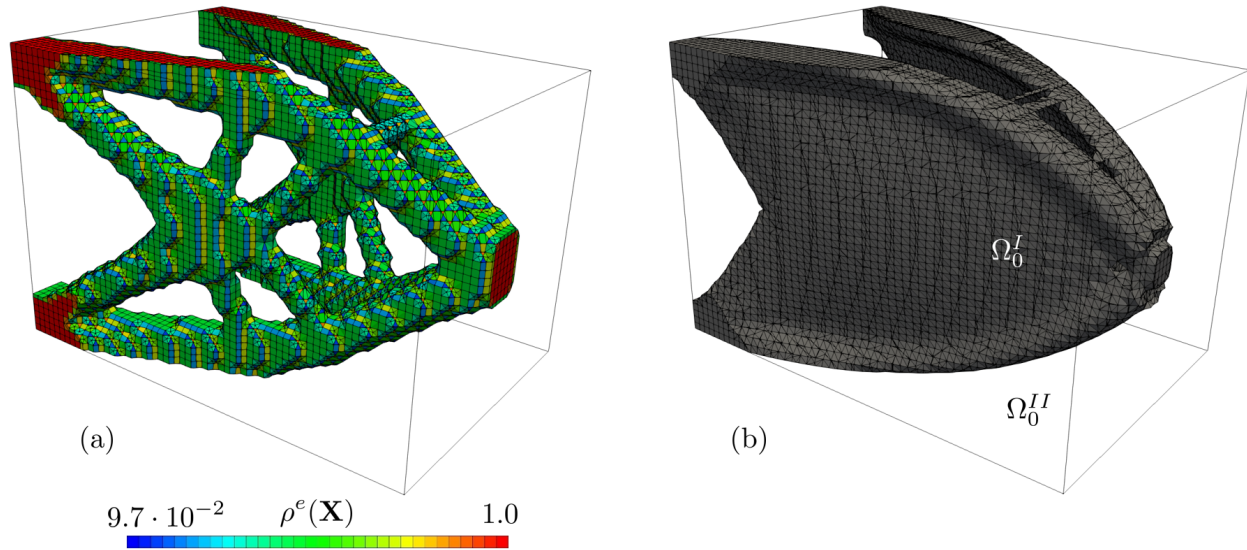
Figure 5.38: Final density distribution of the short beam in 3D obtained by (a) a classical SIMP approach (extracted iso-volume along $\mathbf{s}^\rho = 0.5$) and (b) solid domain (Ω_0^I) obtained by the combined LS-density approach.

in Section 5.4.1.1. No significant difference in physical performance is seen between all final designs shown in Figure 5.37.

A distinctly different final design is obtained when solving this short beam TO problem in 3D with the density method. Figure 5.38 (a) shows the final design obtained by a SIMP approach combined with a continuation scheme to incrementally increase the projection sharpness parameter and the SIMP exponent. As a small filter radius of $r_f = 1.8\ h$ is used, a jagged density boundary closely tracing the underlying background mesh is obtained. In general, 3D SIMP designs are mostly comprised of truss-like features, whereas pure LS-XFEM designs in 3D are dominated by very thin shear-webs (see Figure 5.37). The built-in minimum feature size control through filtering and projection in density methods (see Section 4.1.1) leads to concentrated areas of solid material (truss members), versus the LS-XFEM approach (where no minimum feature size control is achieved through filtering and projection) yields extremely thin walls of continuous material. A similar effect is also observed by the combined LS-density approach, where the density field is only followed initially by the XFEM interface. After the hole nucleation process is complete, an independent
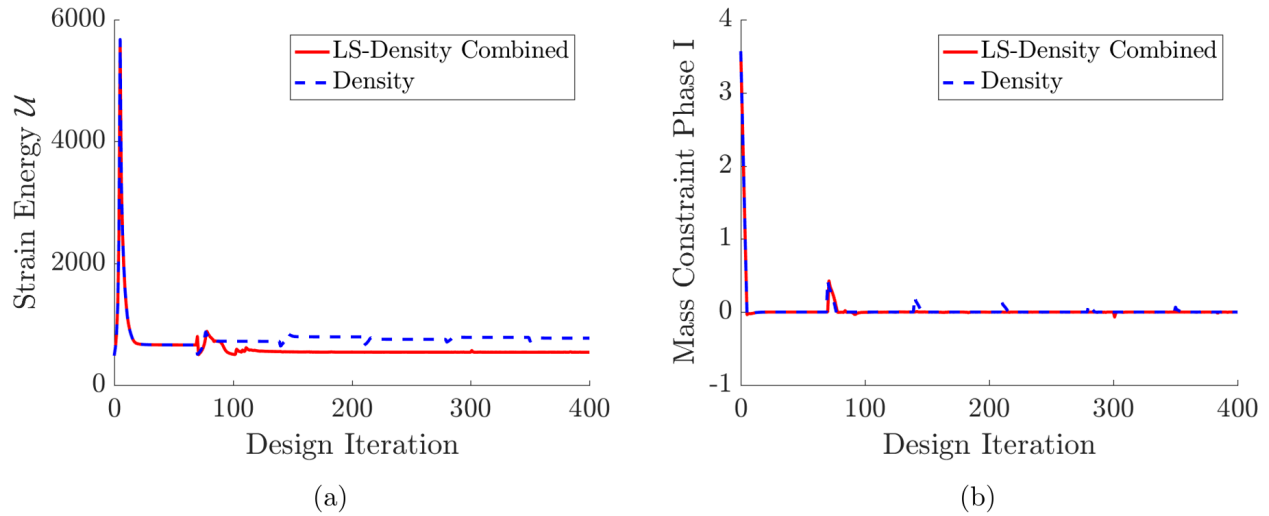
Figure 5.39: Comparison of (a) evolution of strain energy and (b) mass constraint on phase I of pure density TO with combined LS-density TO for the 3D short beam problem.

evolution of the XFEM interface finally leads to the expected shear-web structure (see Figure 5.38 (b)). This happens because the XFEM interface is not tied to the density field and undercutting of the density field is permitted in the formulation of the optimization problem presented in Eqn.(5.4.1).

The evolution of strain energy and the applied mass constraint on phase I are shown in Figure 5.39 for the SIMP design and the combined LS-density design depicted in Figure 5.38. As in the 2D short beam problem, a continuation approach is employed to incrementally increase the projection sharpness as well as the SIMP exponent. This causes periodic increases in strain energy and mass constraint for the classical density design problem. Again, the behaviors of the pure density problem and the combined LS-density problem are identical until the hole nucleation process is initiated at design iteration 70. The combined TO problem then quickly converges to a lower strain energy value as the XFEM interface can evolve independent from the underlying density field.
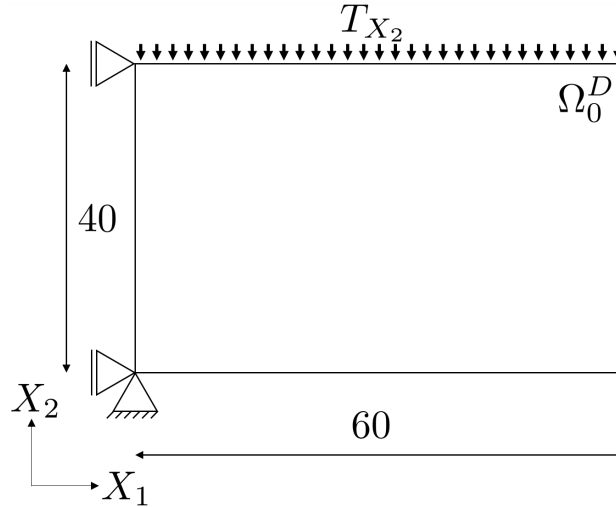
Figure 5.40: Problem setup of the support structure in 2D.

5.4.1.3   2D Support Structure

To gain more insight in the performance of the combined LS-density TO approach, a support structure under a distributed load is studied next. A similar problem was previously studied by [1] using a classical SIMP approach. The roof support structure problem was initially based on the work of [155]. The 2D problem setup with the distributed load at the top and boundary conditions is shown in Figure 5.40. Due to the symmetry of the design problem, only half of the domain is modeled and optimized. Symmetry boundary conditions are applied weakly in the vertical direction. As before, the loading and the support domains are excluded from the design domain. The applied traction load over the entire top edge is $T_{X_2} = -6.0$ and a mass constraint of $\gamma_m = 0.4$ is enforced.

As in the previous examples, the dependency of the final design obtained by pure LS-XFEM TO on the initial hole pattern is investigated. The initial seeding pattern for 8, 12, 24, 96, 192 and 384 holes is shown in Figure 5.41 along with the corresponding final designs (full, reflected design domain). Initially, when increasing the number of void inclusions, an increasingly finer structural layout is obtained. This behavior was previously observed for the short beam example in 2D discussed in Section 5.4.1.1. In contrast to this behavior is however the fact that for the current example, a coarser micro structure is again obtained when increasing the number of initial
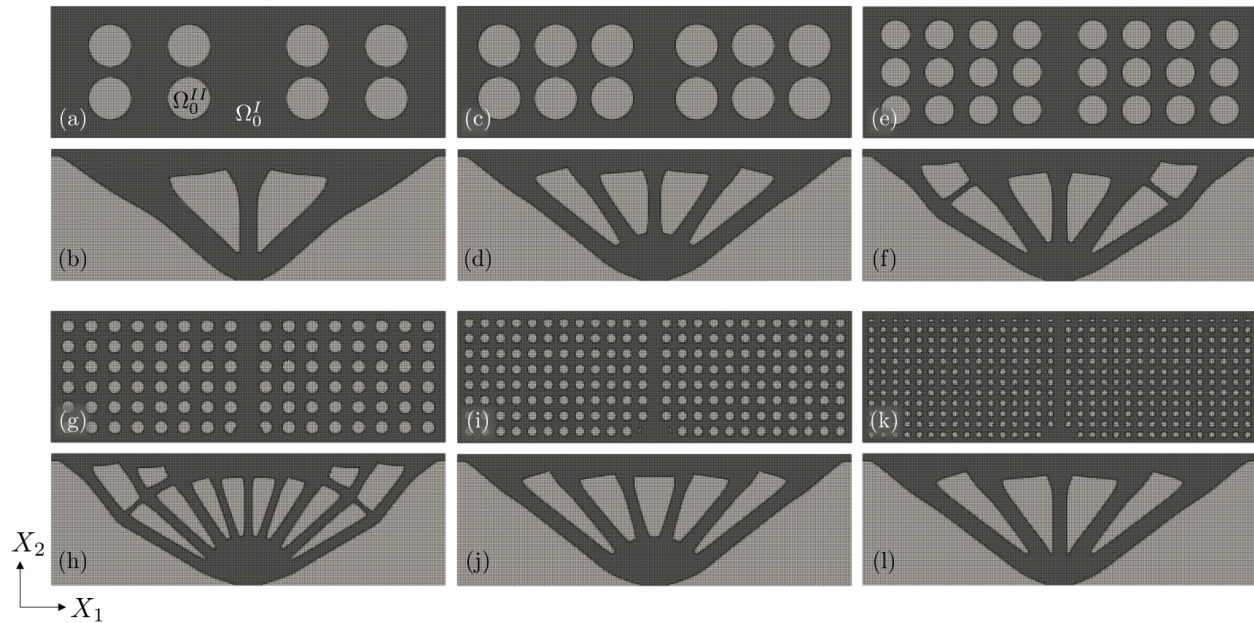
Figure 5.41: Dependency of a LS-XFEM TO final design on the initial hole seeding for the support structure in 2D (reflected design). (a) Initial design with 8 void inclusions, (b) corresponding final design. (c) Initial design with 12 holes, (d) obtained final design. (e) Initial hole pattern for 24 holes and (f) final design obtained from it. (g) Initial seeding with 96 inclusions and (h) corresponding final design. (i) Initial hole pattern with 192 inclusions, (j) obtained final structure. (k) Initial seeding pattern with 384 holes and (l) obtained final design.

holes beyond 96. This is counter-intuitive and can be explained by the fact that when the number of initial holes is too large, lots of small features quickly disconnect which, in turn, coarsens the obtained final structure. Due to this coarsening effect, the structural performance (e.g., strain energy) is worse for designs seeded with an extremely large number of holes compared to designs seeded with an intermediate number of holes. Determining the optimal number of holes is therefore extremely difficult and requires problem specific (iterative) tuning of parameters.

The final density distribution corresponding to a design obtained by a classical SIMP approach is shown in Figure 5.42 (a). A fine micro-structure is obtained which connects the loaded top edge of the structure with the supported domain in the bottom center of the domain. A continuation approach to incrementally increase the projection sharpness and the SIMP exponent is used to minimize the areas of intermediate densities. Figure 5.42 (b) shows the density distribution obtained by the combined LS-density approach at the final design iteration. Similar to the short beam
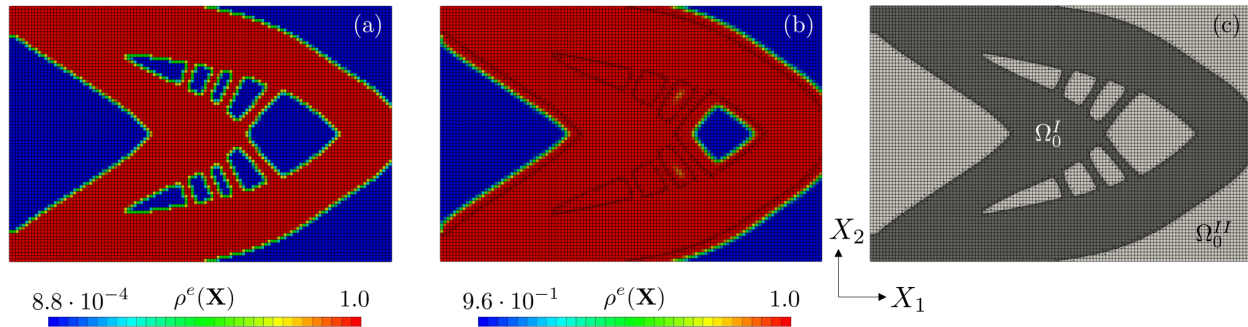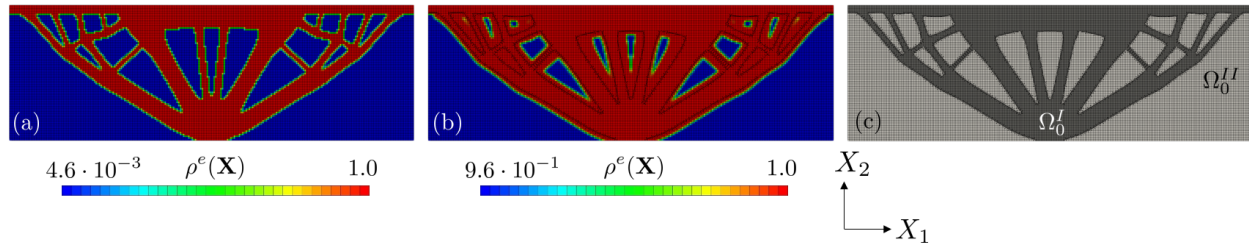
Figure 5.42: Final density distribution of the support structure in 2D obtained by (a) a classical SIMP approach and (b) a combined LS-density approach. The domain decomposition in solid (Ω_0^I) and void (Ω_0^{II}) obtained by the LS-density approach is shown in (c).

example, a uniform density of 1.0 is obtained in the solid (Ω_0^I) while also a significant amount of high density material is placed in the void domain (Ω_0^{II}). This stems from the fact that a mass constraint is only enforced within phase I which allows the XFEM interface to undercut the density field.

By employing the density field for the hole nucleation process, a highly sophisticated micro structure is obtained through the combined LS-density approach (see Figure 5.42 (c)). The hole seeding capability obtained through the lower LS penalty (Eqn.(4.1.11)) places the void inclusions optimally after a first density field was obtained. This does not only circumvent the large computational burden present when using a large number of initial holes, but also eliminates the parameter tuning required to determine the "right" number of initial voids. This is especially critical for structures under distributed loads, where simply increasing the number of initial holes does not necessarily yield finer structures with better physical performance (see Figure 5.41).

The evolution of strain energy and mass constraint on phase I is shown in Figure 5.43. Again, the behavior of the pure density problem and the combined LS-density problem is compared. While initially identical behaviors are seen, the combined LS-density problem quickly converges to a more optimal design once the hole seeding process is complete. The evolution of the density problem is influenced by a periodic increase of the projection parameter and the SIMP exponent using continuation.
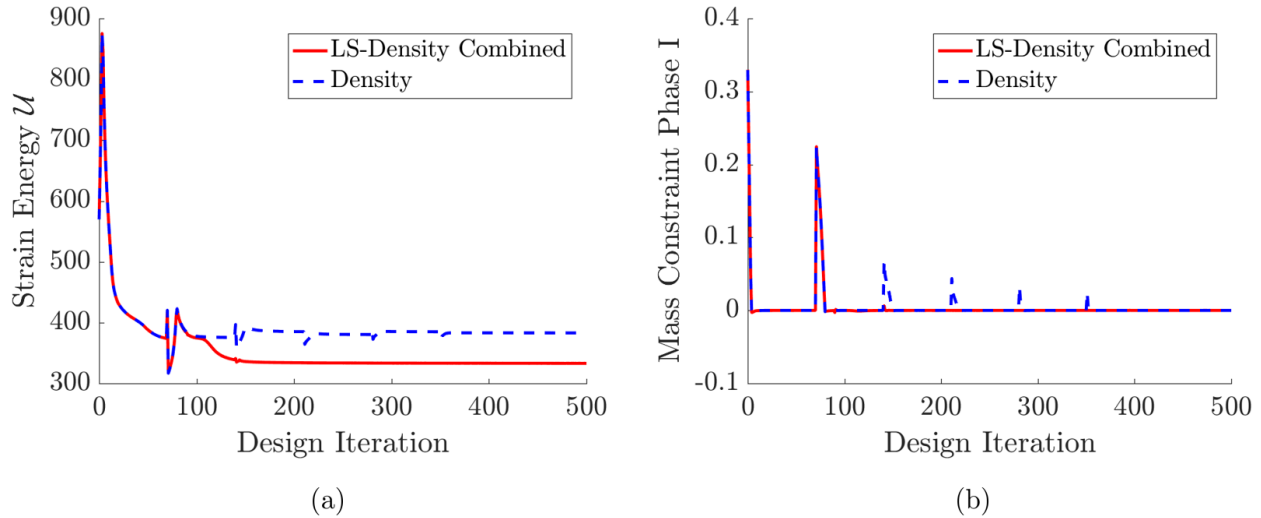
Figure 5.43: Evolution of (a) strain energy and (b) mass constraint on phase I for a classical density approach and the combined LS-density approach for the support structure in 2D.

5.4.1.4   3D Support Structure

The same study as conducted in Section 5.4.1.3 is repeated in 3D. The problem setup shown in Figure 5.40 is extended accordingly and due to the mechanical symmetry of the problem, only one quarter of the full domain is analyzed and optimized in 3D. The applied traction load over the entire top face is set to $T_{X_2} = -2.0$ and the mass constraint is reduced to $\gamma_m = 0.125$.

First, the initial design dependency of the LS-XFEM TO approach is studied for the 3D support structure problem. The initial void patterns of 24, 48, 192 and 756 inclusions along with their corresponding final designs are shown in Figure 5.44. It should be noted that all designs shown in Figure 5.44 are reflected and turned upside down for illustration purposes. For this 3D example, no converging trend towards one design can be identified when increasing the number of initial void inclusions. The obtained final structures vary arbitrarily and therefore a strong dependence of the final design on the initial seeding exists, even in 3D. One common feature of all support structures obtained by pure LS-XFEM TO is the fact that a central shear-web exists. Depending on the initial seeding, more or less pronounced fingers appear from that, connecting the loaded top surface with the base support. In some designs, these fingers are less pronounced (blended into each other),
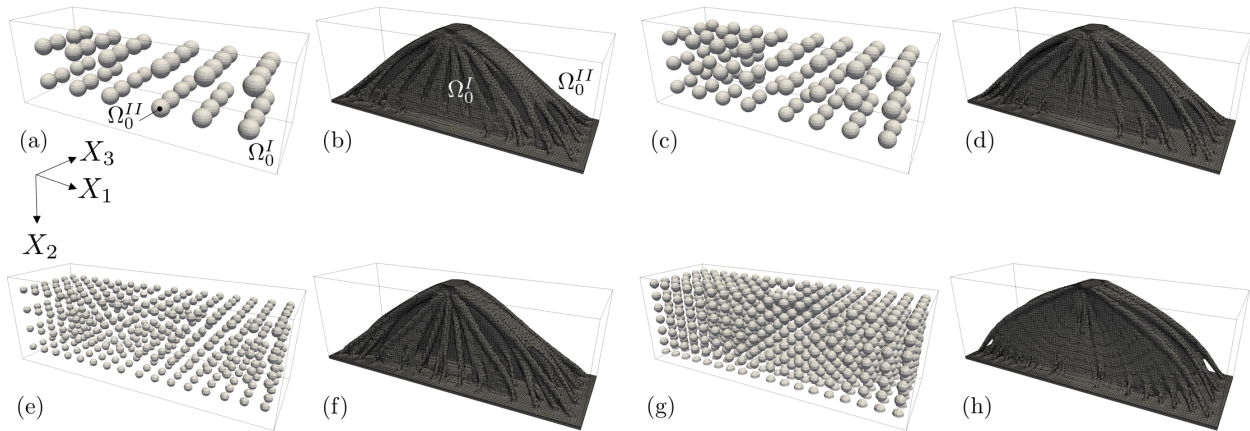
Figure 5.44: Dependency of a LS-XFEM TO final design on the initial hole seeding for the support structure in 3D (reflected design, upside down). (a) Initial design with 24 void inclusions, (b) corresponding final design. (c) Initial design with 48 holes, (d) obtained final design. (e) Initial hole pattern for 192 holes and (f) final design obtained from it. (g) Initial seeding with 756 inclusions and (h) corresponding final design.

such that additional shear-webs are formed. Since no minimum feature size control is imposed on the LS-XFEM design problem, these shear-webs typically tend to have a thickness in the order of the mesh size h. While the XFEM attempts to geometrically resolve those minimum features, the analysis accuracy drastically decreases and the spatial oscillations are observed along the XFEM interface. Moreover, the applied LS regularization suffers in those insufficiently discretized small features. For a more detailed discussion on this, the reader is referred to the discussion in Section 5.5.

The final design obtained by a classical density method is shown in Figure 5.45 (a). Similar to the short beam problem in 3D (Section 5.4.1.2) a drastically different design is obtained compared to the previously discussed LS-XFEM TO results. This is again due to the built-in minimum feature size control exhibited by the density method. Due to that, bar-like features which concentrate the available amount of material are preferred over mass-distributing shear-webs. The close tracing of background elements by the iso-volume extracted along $\mathbf{s}^\rho = 0.5$ is again due to a small filter radius and a high projection sharpness. As before, the projection sharpness parameter and the SIMP exponent are increased incrementally by a continuation approach. The final design obtained
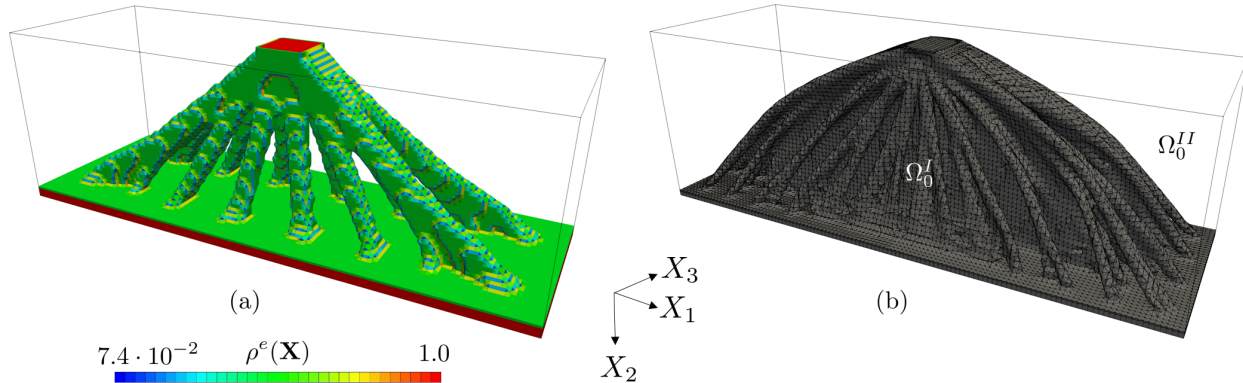
Figure 5.45: Iso-volume of the final density distribution of the support structure in 3D obtained by (a) a classical SIMP approach and (b) the extracted solid phase obtained through a combined LS-density approach. Both designs are reflected and depicted upside down for clarity.

by the combined LS-density approach is shown in Figure 5.45 (b). Great similarities between this design and the pure LS-XFEM designs shown in Figure 5.44 can be seen. Even though the truss-like density field is used for hole nucleation, the XFEM interface quickly departs from the original density field and evolves independently, creating again a shear-web type structure. Without any form of feature size control enabled on the LS-XFEM problem, these thin-walled structures are preferred because of their optimal physical performance.
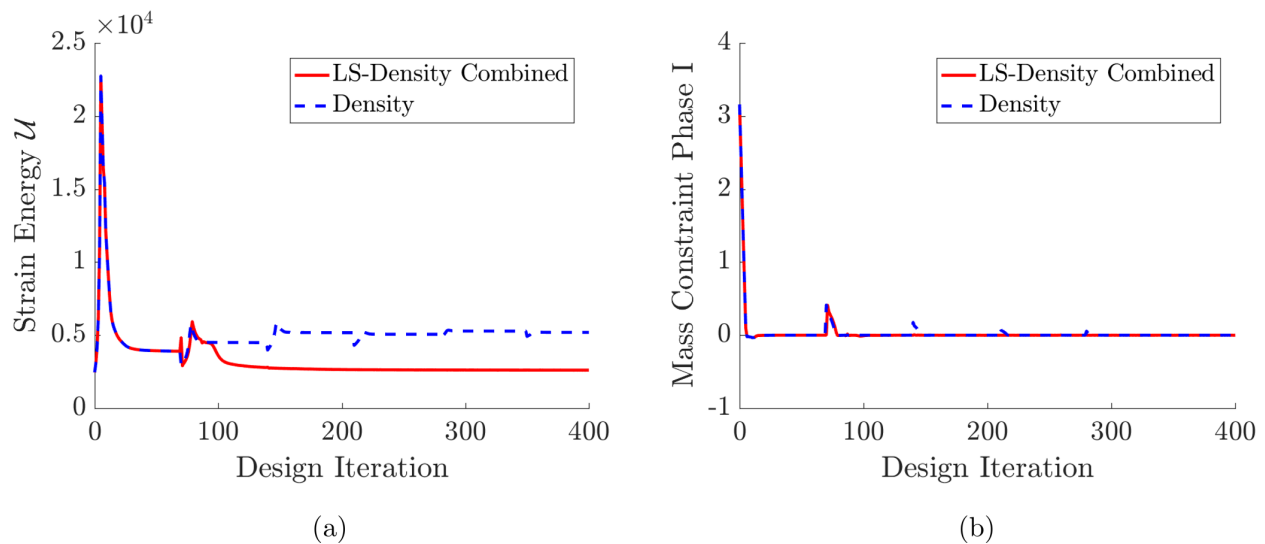
Figure 5.46: Evolution of (a) strain energy and (b) mass constraint on phase I for a classical density approach and the combined LS-density approach for the 3D support structure.

Density Only
$h = 1.0 \times 1.0 \times 1.0$
157,563 free DOFs

Density Only
$h = 0.5 \times 0.5 \times 0.5$
1,205,523 free DOFs

LS-Density Combined
$h = 1.0 \times 1.0 \times 1.0$
262,605 free DOFs

LS-XFEM Only
$h = 1.0 \times 1.0 \times 1.0$
287,800 free DOFs

(a)   (b)   (c)   (d)
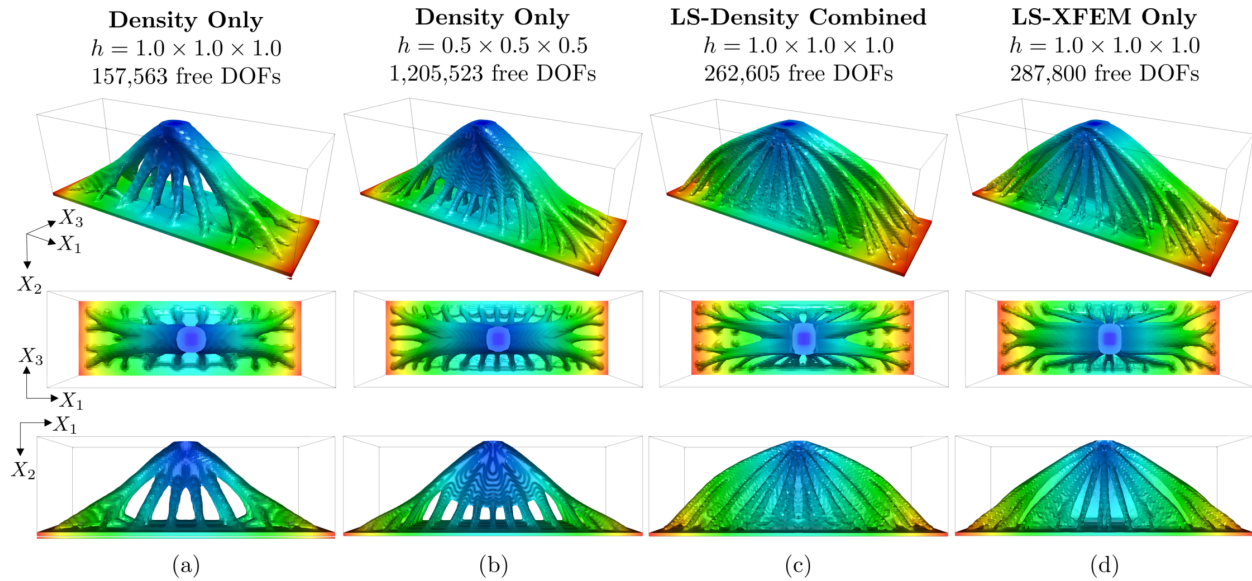
Figure 5.47: Comparison of the support structure final designs obtained by (a) classical density-based TO, (b) density-based TO on a refined mesh, (c) combined LS-density TO and (d) pure LS-XFEM TO.

The evolution of strain energy and mass constraint on phase I is shown in Figure 5.46 for the 3D support structure. As before, an identical behavior of the pure SIMP problem and the combined LS-density problem is seen until the hole nucleation process is initiated. From design iteration 70 onward, the combined LS-density problem quickly convergences to a lower strain energy value than the density problem. The evolution of the density problem is periodically affected by the incremental increase in SIMP exponent and projection sharpness parameter via a continuation approach.

A comparison of final designs obtained for the support structure problem in 3D is shown in Figure 5.47. Figure 5.47 (a) shows different perspectives of the final design obtained by a classical density approach. The reason that this design looks less jagged as the density design shown in Figure 5.45 (a) is due to the fact that for all designs shown in Figure 5.47, no projection and no feature size control is enforced. This leads to a smoother iso-volume extracted from the density field and finer fingers attaching to the loaded surface. Using the same mesh size (i.e., $h = 1.0 \times 1.0 \times 1.0$) and solving the 3D support structure via a pure LS-XFEM approach (initial design with 192 holes), yields the final design shown in Figure 5.47 (d). As discussed before, a centrally located shear-web

with fine structural features connecting to it is obtained. This design is drastically different than the one obtained by a classical density-based TO approach. However, the density methods tends to converge towards the same shear-web type structures as produced by the LS-XFEM approach with mesh refinement. This can be seen in Figure 5.47 (b), where a background mesh of size $h = 0.5 \times 0.5 \times 0.5$ was used. It is apparent that the centrally located shear web has increased compared the same design on a coarser background mesh (see Figure 5.47 (a)). Also, the obtained fingers have been greatly refined in terms of spatial resolution. This trend, that density-based TO yields similar results as obtained by LS-XFEM TO was also found by [189]. The computational cost associated with this increased geometrical resolution is however significant. When comparing computational cost, the LS-XFEM approach is by far more efficient while yielding mechanically more meaningful designs due to its increased spatial resolution on coarser meshes. The combined LS-density approach yields a designs which also benefits of the increased geometrical resolution (see Figure 5.47 (c)), while not suffering from the initial design dependence exhibited by classical LS-XFEM TO.

5.4.2   Mass Measure in Phase I - Hole Nucleation and Prevention of Undercutting

To not only introduce void domains but also prevent the XFEM interface from undercutting the density field, both the lower LS penalty and the upper LS penalty (Eqn.(4.1.11) and Eqn.(4.1.12), respectively) are used. For that, a strain energy minimization problem subject to a mass constraint within phase I and a LS regularization constraint is formulated as:

$$\min_{\mathbf{s}} \; z(\mathbf{s}, \mathbf{u}) = w_1 \, \mathcal{U} + w_2 \int_{\Gamma_0^{I,II}} dS + w_3 \int_{\Omega_0^D} p_L \; dV + w_4 \int_{\Omega_0^D} p_U \; dV + w_5 \, \mathcal{M}^{II}$$
$$\text{s.t. } g_1 = \frac{\mathcal{M}^I}{(\Omega_0^I + \Omega_0^{II})} - \gamma_m \leq 0 \tag{5.4.2}$$
$$g_2 = \int_{\Omega_0^D} p_{Reg} \; dV - \epsilon_{Reg} \leq 0$$

In addition, a penalty on the mass in phase II is added to the objective. The objective weights are $w_i = [0.839, \, 0.01, \, 0.05, \, 0.01, \, 0.1, \, 0.001]$, a mass ratio of $\gamma_m = 0.35$ is enforced, and the LS regularization tolerance is $\epsilon_{Reg} = 0.05$. It should be pointed out that in Eqn.(5.4.2) the LS
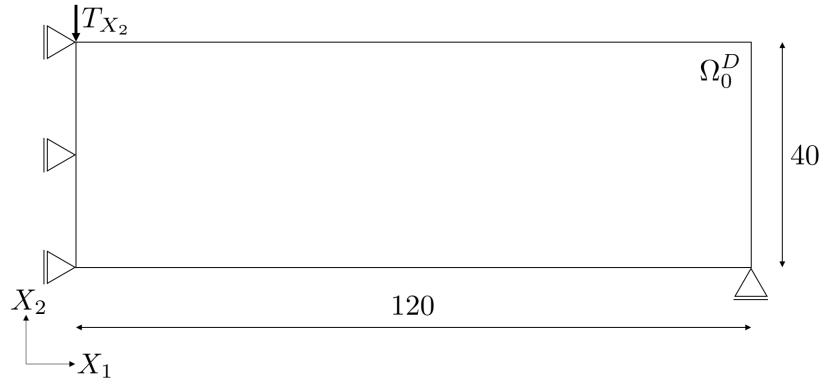
Figure 5.48: Problem setup of the MBB beam in 2D with load and boundary conditions. Due to mechanical symmetry, only one half of the full domain is modeled and optimized.

regularization penalty p_{Reg} is applied as an additional constraint with a tolerance ϵ_{Reg}. This ensures a more strict enforcement of the LS regularization compared to formulating it as an additional penalty term on the objective.

The MBB beam [17, 97], a classical benchmark problem in structural TO, is used to study the formulation of Eqn.(5.4.2) in 2D. The problem setup with load and boundary conditions is shown in Figure 5.48. The final density field is shown in Figure 5.49 (a), while the final LSF is depicted in Figure 5.49 (b). It is observed that the XFEM interface follows the density field much closer, than it did without the upper LS penalty (see Section 5.4.1). Also, any high density values have been
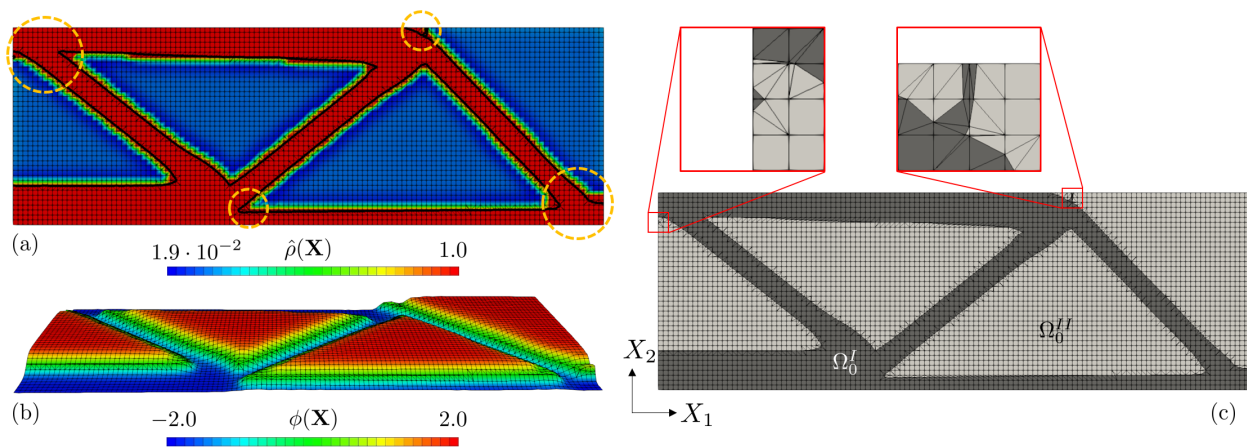
Figure 5.49: Final design of the 2D MBB beam. (a) Nodal density field, (b) nodal LS field warped for illustration purposes, and (c) the domain decomposition into solid (Ω_0^I) and void (Ω_0^{II}) domains.
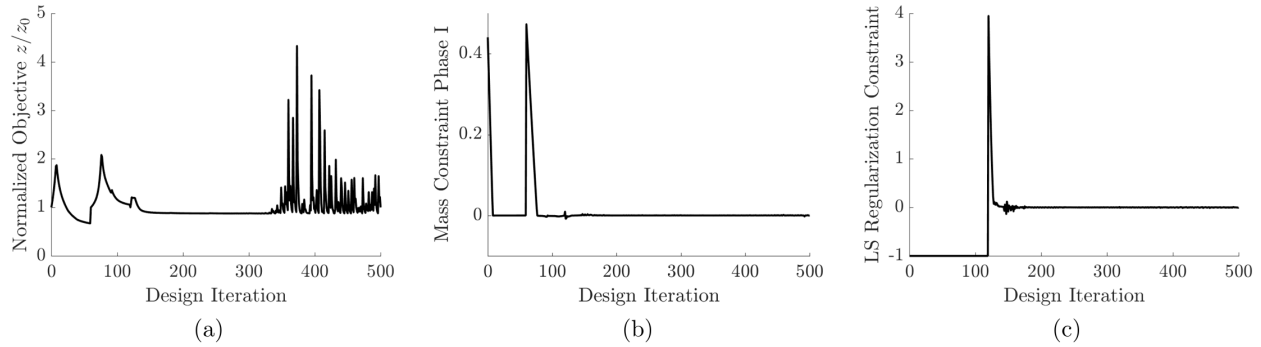
Figure 5.50: Evolution of (a) normalized objective, (b) mass constraint on phase I, and (c) the LS regularization constraint for the 2D MBB beam problem.

removed from the void domain due to the mass phase II penalty added to the objective formulation. However, local undercutting of the density field by the XFEM interface is still observed in some parts of the design domain (see highlighted regions in Figure 5.49 (a)). These are predominately found near sharp, reentrant corners where the XFEM interface favors undercutting and does not follow the density field. The LSF shown in Figure 5.49 (b) is very well regularized, except in areas where the interface undercuts the density field. In those localized regions, the upper LS penalty (which prevents undercutting) is competing with the LS regularization (which enforces a unit gradient of the LSF in the vicinity of the interface). Since neither of them can be achieved fully, a degenerated, flat LSF is obtained in those domains. As discussed in [67], a degenerated LSF leads to spurious oscillations of the interface and may lead random material inclusions in the void domain. This is the case in this 2D MBB beam example and shown in the highlighted regions in Figure 5.49 (c).

This instability caused by the formulation of the optimization problem is also reflected in the evolution of the objective, shown in Figure 5.50 (a). As the design space becomes more nonlinear due to an increased projection sharpness and SIMP exponent, large oscillations appear in the objective. These are caused by the competing formulation of upper LS penalty (to prevent undercutting) and LS regularization (to assure a smooth LSF). Since both of those measures are formulated in the absence of any physical quantity (e.g., strain energy, mass of the structure), the optimizer is unable to properly account for both of them while still satisfying the mass constraint and minimizing

strain energy. This leads eventually to divergence of the optimization problem, because of a locally degenerated LS field causing spurious material inclusions in the void phase. Therefore, using the LS upper penalty to prevent the XFEM interface from undercutting the density field is not further explored in this thesis.

5.4.3   Global Mass Measure - Hole Nucleation and Minimum Feature Size Control

In this section, a globally enforced mass measure (i.e., $\mathcal{M} = \mathcal{M}^I + \mathcal{M}^{II}$) is applied to combine the hole nucleation process with minimum feature size control. Control of minimum features is achieved by preventing the XFEM interface from undercutting the density field. Therefore, minimum feature size on the LS field can be controlled through filtering and projection of the density design variables.

5.4.3.1   Mass Minimization - 2D MBB Beam

First, a global mass minimization formulation subject to a strain energy constraint is explored. It is stated as:

$$\min_{\mathbf{s}} \ z(\mathbf{s}, \mathbf{u}) = w_1 \left(\mathcal{M} \right) + w_2 \int_{\Gamma_0^{I,II}} dS + w_3 \int_{\Omega_0^D} p_L \ dV + w_4 \int_{\Omega_0^D} p_{Reg} \ dV$$

$$\text{s.t. } g = \frac{\mathcal{U}}{\mathcal{U}_{Tar}} - 1.0 \leq 0$$

(5.4.3)

where the target strain energy is denoted by $\mathcal{U}_{Tar}$. In this formulation, an initial, uniform density field of $\mathbf{s}^\rho = 1.0$ is used to initially satisfy the strain energy constraint. The formulation of Eqn.(5.4.3) can be used to achieve designs with small volume/mass fractions without using a continuation approach on the volume or mass constraint. Moreover, the formulation of Eqn.(5.4.3) is advantageous for design studies involving minimum feature size, as no conflict between the minimum feature size measure and the enforced mass constraint is created. The only drawback of the mass minimization formulation presented above is that a proper target strain energy value $\mathcal{U}_{Tar}$ needs to be know a priori. In general, this can be challenging, but can be achieved by first solving a strain energy minimization problem (Eqn.(5.4.1)) to obtain this value. For the subsequent studies, a value of $\mathcal{U}_{Tar} = 20.0$ is used. The weights of the individual objective contributions are $w_i = [0.93, \ 0.01, \ 0.05, \ 0.01]$.

Initially, a classical LS-XFEM approach is used to solve the MBB beam TO problem in 2D, using the formulation of Eqn.(5.4.3). The problem setup shown in Figure 5.48 is used. The initial design and the final design (both reflected to show the full domain) are presented in Figure 5.51 (a) and (b), respectively. The initial design is seeded with 186 void inclusions and a filter radius of $r_f = 1.6 \, h$ is used for the LS design variables. As expected, a network of trusses is obtained as the final design, which transfers the centrally applied load from the top edge to the supported corners at the bottom edge. However, as discussed in Section 4.1.2, minimum feature size cannot be controlled by linear filtering of the LS design variables.

Minimum feature size control through linear filtering and projection is possible in density-based TO, and this feature is also inherited by the combined LS-density approach when a global mass measure is used. The resulting designs show different refinement levels of the obtained micro structure, depending on the employed linear filter radius used on the density design variables. Figure 5.51 (d), (f), (h) and (j) show the final designs obtained by filter radii of $r_f = [1.6 \, h, \; 2.4 \, h, \; 3.2 \, h, \; 6.4 \, h]$ using the combined LS-density approach. The corresponding density fields are shown in Figure 5.51 (c), (e), (g) and (i). It can be seen that the density field is nowhere undercut by the XFEM interface. This is achieved by using a global mass measure, which not only accounts for the mass in phase I (Ω_0^I, solid), but also includes the mass of phase II (Ω_0^{II}, void). This formulation makes it unattractive for the optimizer to place any high-density material in phase II, as it does not contribute towards the stiffness of the structure but only towards the mass measure. On the other hand, it is not advantageous to undercut the density field, as it results in a harm of the stiffness, while still contributing to the mass measure enforced in the entire domain. This penalization effect (similar to the SIMP penalization but now enforced through the XFEM interface which distinguishes between solid and void domain) leads to the fact that the XFEM interface strictly traces the density field without ever undercutting it. Different minimum feature sizes caused by different filter radii on the density field are therefore directly translated to the XFEM interface and therefore the LS field. Increasing the filter radius removes small structural members from the final design and regularizes the overall final geometry (see Figure 5.51). The fact that the minimum achieved features (indicated
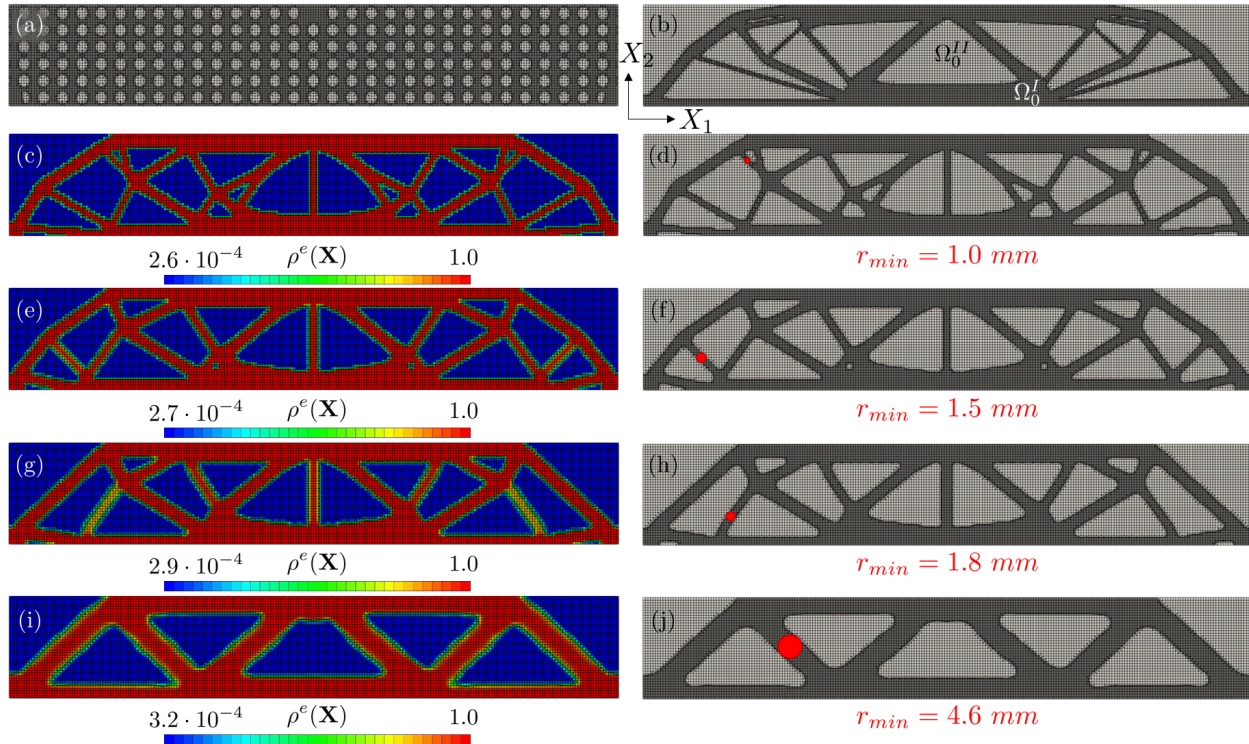
Figure 5.51: Solutions of the 2D MBB beam formulated as a mass minimization problem (reflected for illustration purposes). (a) Shows the initial design of a pure LS-XFEM approach and (b) is the corresponding final design obtained with a filter radius of $r_f = 1.6\ h$. (c) Shows the final density field obtained by the combined LS-density approach with a filter radius of $r_f = 1.6\ h$, (d) is the corresponding solid-void domain decomposition. (e) Shows the final density field obtained by the combined approach with a filter radius of $r_f = 2.4\ h$, (f) is the domain decomposition corresponding to it. (g) Shows the elemental density field obtained with a filter radius of $r_f = 3.2\ h$ and the combined LS-density approach, (h) is the corresponding solid-void layout. (i) Final density field obtained through the combined LS-density approach with a filter radius of $r_f = 6.4\ h$, the corresponding domain layout is shown in (j).

by red circles) are slightly smaller than the applied filter radii, is due to a well-known limitation of density-based TO. Due to the nodal density design variables, it is possible to achieve structural members of reduced thickness when only selected design variables are active (before filtering and a projection) at the final design. In order to achieve exact minimum feature size, controlled by the linear filter radius on the density design variables, a so-called robust optimization approach [166, 76] needs to be employed. In this approach, multiple designs with different filter radii are optimized simultaneously, such that the exact prescribed minimum feature size is achieved globally.
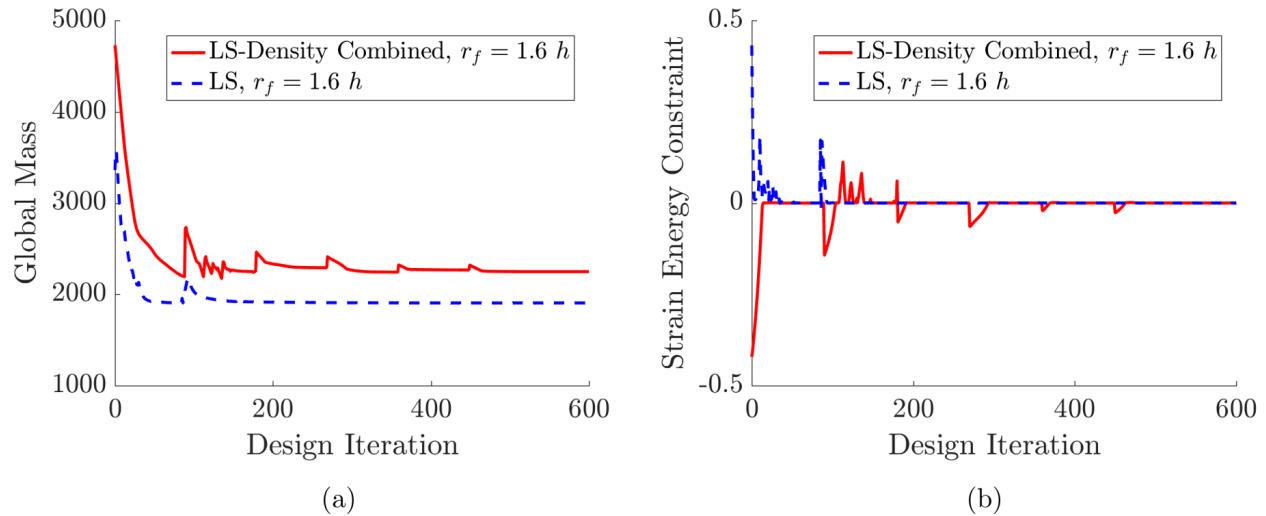
Figure 5.52: Evolution of (a) the global mass measure and (b) the strain energy constraint for the pure LS-XFEM approach and the combined LS-density approach for a filter size of $r_f = 1.6\ h$.

It should also be pointed out that a small fraction of elements with intermediate densities remains in the vicinity of the interface, even at the converged stage. This finite transition region between high-density and low-density material is inherited from the density-based approach and can only partially be mitigated by the XFEM where subphase constant material properties are used.

The evolution of the global mass measure and the strain energy constraint for a classical LS-XFEM approach and the combined LS-density approach are shown in Figure 5.52 (a) and (b), respectively. It can be seen that while the pure LS-XFEM design quickly converges to a lower overall mass, the mass of the combined approach is influenced by the applied continuation approach on the SIMP exponent and the projection sharpness parameter. The reason that the pure LS-XFEM design converges to a much lower mass is the fact that arbitrarily fine features are allowed as no minimum feature size control is imposed. In contrast, the combined LS-density approach inherits the minimum feature size control from classical density methods. The overall mass is therefore higher, to the benefit of a more regularized and feature size controlled final design.

5.4.3.2   Strain Energy Minimization - 3D MBB Beam

The final example used to demonstrate the capabilities of the combined LS-density approach is the MBB beam problem in 3D. Unlike before, a strain energy minimization formulation subject to a global mass constraint is used. The optimization problem is formulated as:

$$
\begin{aligned}
\min_{\mathbf{s}}\ z(\mathbf{s}, \mathbf{u}) &= w_1\, \mathcal{U} + w_2 \int_{\Gamma_0^{I,II}} dS + w_3 \int_{\Omega_0^D} p_L\ dV + w_4 \int_{\Omega_0^D} p_{Reg}\ dV \\
\text{s.t.}\ g &= \frac{\mathcal{M}}{\gamma_m} - 1.0 \leq 0
\end{aligned}
\tag{5.4.4}
$$

where a mass constraint of $\gamma_m = 0.15$ is enforced. An extension of the problem setup shown in Figure 5.48 to 3D is used. Due to the symmetry of the design problem, only one quarter of the full design space is analyzed and optimized.

The final design obtained by classical LS-XFEM TO is shown Figure 5.53 (b) and (c), using the initial void seeding, depicted in Figure 5.53 (a), as a starting point. Similar to the 3D short beam example studied in Section 5.4.1.2, the typical shear-web designs is obtained. While it seems advantageous to use continuous walls connecting the two flanges at the top and bottom of the beam, the wall thickness typically is in the order of the element edge length h. This does not only reach the limit of the geometric resolution of the XFEM, but also leads to reduced analysis accuracy. When using the combined LS-density approach with feature size control, truss-like features are preferred over shear-webs. Figures 5.53 (e) and (f) show the final design obtained by the LS-density approach with a filter radius of $r_f = 2.4\ h$ on the density design variables. The elemental density distribution of the same design is depicted in Figure 5.53 (d). While this design still exhibits a centrally located shear-web, increasing the filter radius to $r_f = 3.6\ h$ fully eliminates this feature. This is shown in Figures 5.53 (h) and (i), where a network of trusses constitutes the final design. Figure 5.53 (g) shows the corresponding density layout.

Identical to the 2D examples, undercutting of the density field by the XFEM interface is successfully prohibited by a global mass measure (see Eqn.(5.4.4)). The XFEM interface essentially extracts an iso-volume along the $\hat{\rho} = 0.5$ iso-volume of the density field. This is a common post-processing step performed (manually) in density TO after a converged design is found. As it is
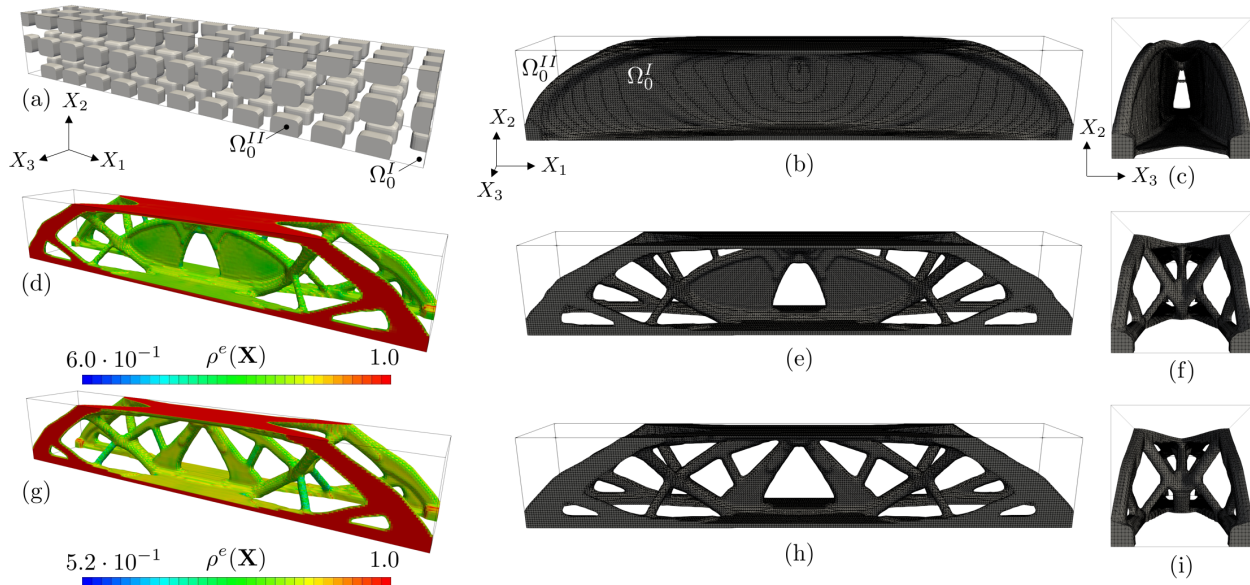
Figure 5.53: Final designs obtained for the MBB beam TO problem in 3D. (a) Initial design and (b) and (c) final design obtained by classical LS-XFEM TO. (d) Elemental density field of the final design obtained by combined LS-density TO for a filter radius of $r_f = 2.4\ h$. (e) and (f) are side-view and front-view of the same final design. (g) Density field on the final design obtained by LS-density TO with a density filter radius of $r_f = 3.6\ h$, (h) and (i) are show the corresponding solid phase of the final design.

done in a post-processing step, the analysis model operates on the jagged, approximated domain boundary. Since in the combined LS-density approach the XFEM interface continuously follows the density field, a highly accurate structural analysis and sensitivity analysis is performed throughout the full design process. Once a converged design is found, the zero LS iso-contour can easily be extracted for manufacturing without the need for additional manual post-processing.

The evolution of strain energy and global mass constraint for the two designs obtained by the combined LS-density approach discussed previously is shown in Figure 5.54. Again, due to the strong coupling of the XFEM interface to the density field, both strain energy and global mass constraint are influenced by the continuation scheme. No significant influence of the employed filter radius on the structural performance of the final designs is observed.
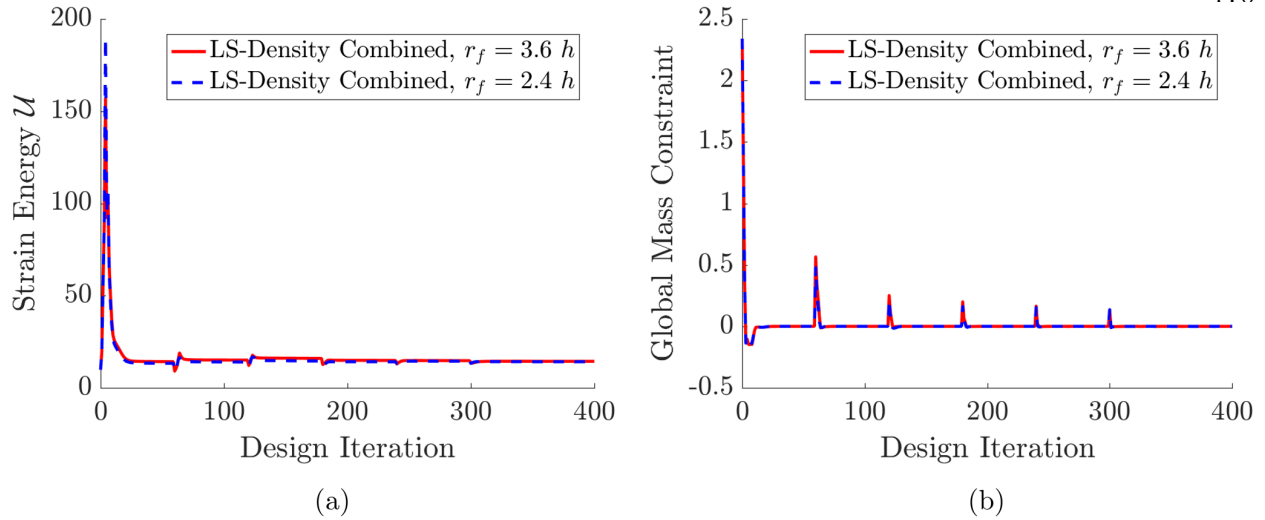
Figure 5.54: Evolution of (a) strain energy and (b) global mass constraint for designs obtained by the combined LS-density approach for different filter radii.

5.4.4 Discussion

Multiple aspects of the proposed combined LS-density TO approach have been demonstrated through the previous numerical examples in 2D and 3D. By combining density-based and LS-XFEM-based TO, the advantages of either method are exploited to eliminate their mutual drawbacks. This leads to a superior TO method. The advantages of the combined approach are that no initial seeding is required, minimum feature size can be achieved through linear filtering and projection of the density field, and a crisp and unambiguous material interface is obtained by the XFEM.

The increased computational cost due to twice the number of design variables is partially offset by the fact that, for example, the void inclusions are placed optimally in the design space through a penalty formulation. This eliminates the drawback of pure LS-XFEM TO where a large number of arbitrarily placed initial holes as a starting point is typically used, which significantly increases the computational cost due to a large number of intersected elements.

It was shown that a physics-based formulation is required in order to prevent undercutting of the density field by the XFEM interface (e.g., global mass constraint). Using the upper LS penalty leads to divergence of the optimization problem as a non-physics-based regularization formulation

competes with the mass constraint on phase I, which is solely enforced by the XFEM interface. When using a global mass measure, a small fraction of elements with intermediate material is obtained in the vicinity of the XFEM interface. This however can be mitigated by mesh refinement or a higher projection parameter on the density field.

Overall, the combined LS-density method showed excellent performance in terms of computational efficiency, robustness and analysis accuracy when compared to either classical density-based TO or pure LS-XFEM TO in both 2D and 3D.

5.5 Explicit Level-Set-XFEM Regularization

The explicit LS regularization approach discussed in Section 4.3 is applied towards numerical examples in 2D and 3D in the following. The optimization problem solved in the subsequent design examples is formulated as:

$$
\min_{\mathbf{s}} \; z(\mathbf{s}, \mathbf{u}) = w_1 \frac{z_1(\mathbf{s}, \mathbf{u})}{z_1(\mathbf{s}^0, \mathbf{u}^0)} + w_2 \frac{\int_{\Gamma_0^{I,II}} dS}{\int_{(\Gamma_0^{I,II})^0} dS} + w_3 \frac{p_{Reg}(\mathbf{s})}{p_{Reg}(\mathbf{s}^0)}
$$
$$
\text{s.t. } g = \frac{\Omega_0^I}{(\Omega_0^I + \Omega_0^{II})} - \gamma_v \leq 0
$$

(5.5.1)

where the objective function depends on a physical performance quantity $z_1(\mathbf{s}, \mathbf{u})$ (e.g., strain energy), a perimeter penalty and the LS regularization penalty p_{Reg} introduced in Section 4.3.2. Each of these contributions is weighted, such that $w_1 + w_2 + w_3 = 1.0$. The optimization problem is furthermore subject to a volume constraint γ_v on the volume of phase I. It should also be noted that all objective contributions in Eqn.(5.5.1) are normalized by their initial value to achieve appropriate scaling of the individual contributions. For design problems discussed in this study, the design variables only consist of LS design variables, such that $\mathbf{s} = \mathbf{s}^\phi$.

The parameters used for all numerical studies in this section are listed in Table 5.6, where the bounds and the target LS value are specified as a function of the element edge length h. It should be pointed out that the design variable bounds are chosen such that the target LSF ϕ_{Bnd} is contained within. The temperature field for the HM is solved in a single time step unless noted otherwise. For

Table 5.6: Problem parameters for all LS regularization examples.

Parameter	Value
Weak BC Penalty	$\gamma_N = 100/h$
Ghost Penalty	$\gamma_G = 0.001$
Perimeter Penalty Weight	$w_2 = 0.01$
Lower Bound of $\mathbf{s}$	$\mathbf{s}_L = -3h$
Upper Bound of $\mathbf{s}$	$\mathbf{s}_U = +3h$
Target of LSF	$\phi_{Bnd} = 2h$
Filter Radius in 2D	$r_f = 1.6h$
Filter Radius in 3D	$r_f = 2.4h$

all structural problems, selective structural springs as discussed in Section 4.2.3 are employed. All systems (i.e., HM, selective structural springs and physics) are solved using a staggered solution approach in a one-way coupled fashion. For more details regarding a block solution approach, see Section 3.4.

5.5.1   Linear Elasticity

As a first set of examples, linear elastic hanging bar design problems are solved in 2D and 3D. These problems are modified versions of the two bar truss example presented in [168] where it is solved with the density method. The problem parameters used for linear elasticity are summarized in Table 5.7.

5.5.1.1   Hanging Bar in 2D

The problem setup and the initial design for the hanging bar problem in 2D, discretized with four-node plane stress XFEM elements is shown in Figure 5.55 (a). The symmetry of the design problem is taken into account, such that only one half of the design domain is modeled and optimized. Symmetry boundary conditions are applied weakly using Nitsche's method. The top of the design domain is clamped while a traction load of $T_{X_2} = -30.0 \ N/mm$ is applied over a width of 12.0 mm at the bottom center. A volume constraint of $\gamma_v = 0.16$ on phase I is applied to the design problem, where minimization of the strain energy is the objective. In addition, a perimeter penalty and the LS regularization penalty as formulated in Eqn.(5.5.1) are minimized.

Table 5.7: Properties for the linear elastic LS regularization design problems.

Parameter	Value
Young's Modulus	$E = 2.0 \cdot 10^3 \ MPa$
Poisson's Ratio	$\nu = 0.0$
LS Regularization Weight	$w_3 = 0.01$
Element Edge Length	$h = 1.0 \ mm$
Selective Spring Ratio	$r_s = 1.0 \cdot 10^{-12}$

Figure 5.55: Problem setup with load and boundary conditions for the 2D hanging bar problem. (a) Initial design and (b) final design.

Figure 5.55 (b) shows the final design, which consists only of a single vertical bar. A comparison of the evolution of objective and constraint with and without LS regularization is shown in Figure 5.56. Initially, significant oscillations are seen in both objective and volume constraint when no LS regularization is applied. These are almost fully removed through the LS regularization. In addition, faster convergence of the optimization problem is seen when the LSF is regularized. Since the regularization contribution vanishes at convergence, the same objective and constraint values are obtained as in the case where no regularization is applied.
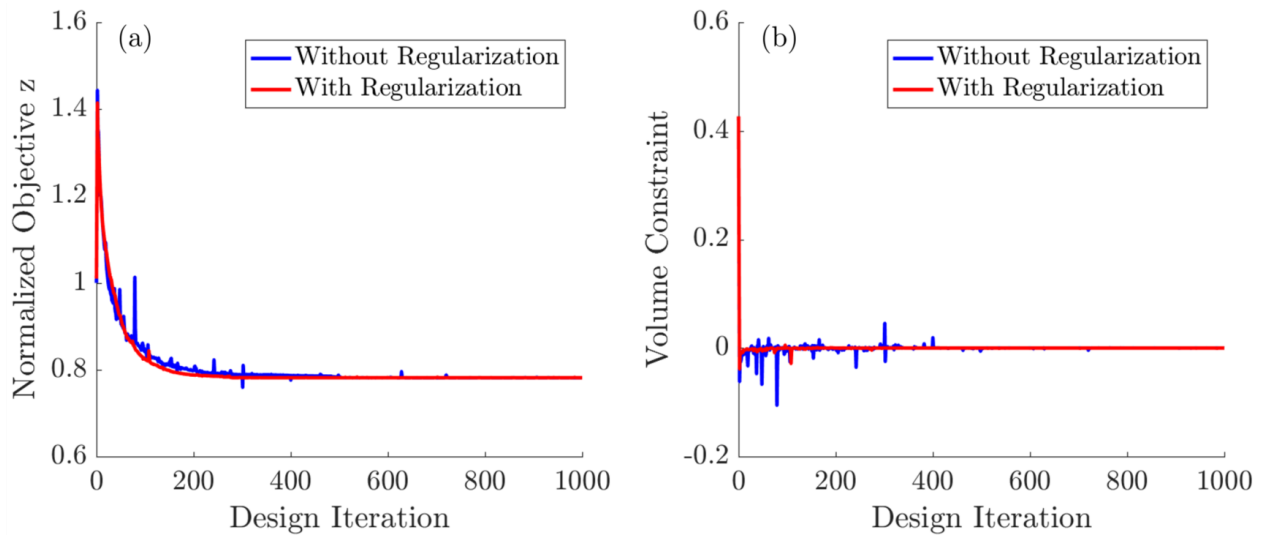
Figure 5.56: Evolution of (a) normalized objective and (b) volume constraint on phase I for the 2D hanging bar problem.
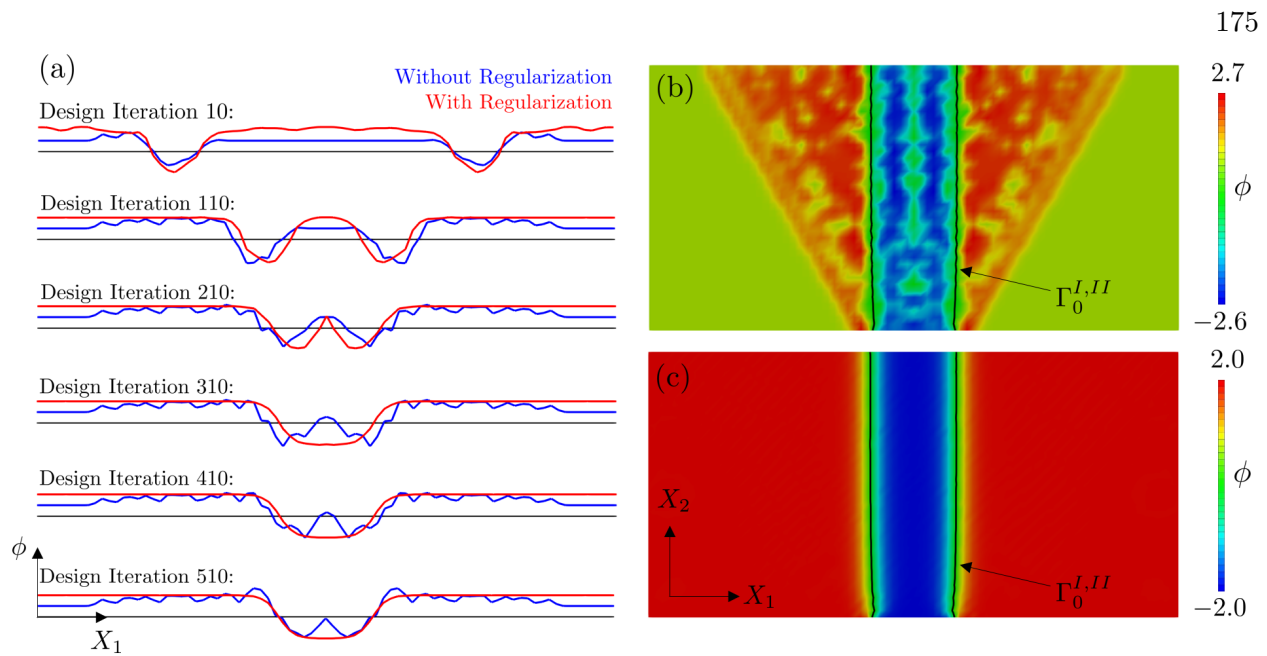
Figure 5.57: (a) Snapshots of the design LSF with and without LS regularization during the optimization process. (b) Final design LSF without LS regularization and (c) with LS regularization.

Snapshots of the design LSF $\phi(\mathbf{X})$ taken during the optimization process are shown in Figure 5.57 (a), where a large effect of the LS regularization on the design LSF is observed. The line at $X_2 = 40.0$ at which these snapshots are taken is highlighted in red in Figure 5.55 (b). It can be seen that LS regularization maintains a unit normal slope of the LSF in the vicinity of the interface while upper and lower LS bounds are assumed away from it. Without any regularization, oscillations in the LSF are seen and a degenerated slope in the vicinity of the interface is observed. A LSF close to zero near the XFEM interface oftentimes leads to isolated material domains in the void caused by numerical noise in the design LSF. These, in turn, lead to ill-conditioning, oscillations in objective and constraint, and potentially to divergence of the optimization problem when no LS regularization is employed. With LS regularization, greater numerical stability of the optimization problem is seen which means larger optimization step sizes can be used without leading to divergence.

Figure 5.57 (b) and (c) show the design LSF at the final design iteration without LS regularization and with LS regularization, respectively. Similar zero LS iso-contours are obtained, but away from the interface, a large effect of the LS regularization is seen. The imprint of the initial
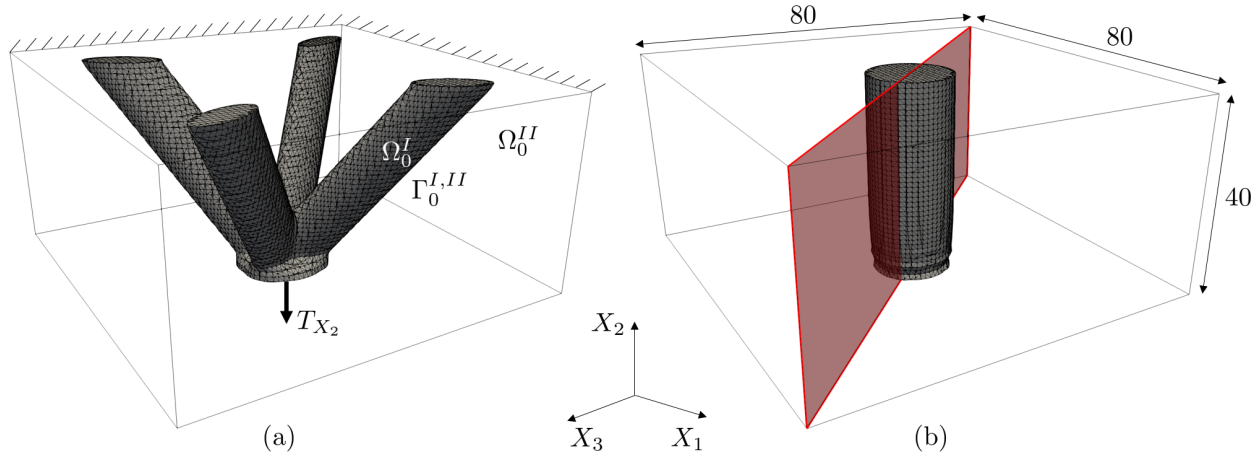
Figure 5.58: Problem setup with load and boundary conditions for the 3D hanging bar problem. (a) Initial design and (b) final design.

design is completely removed in Figure 5.57 (c), while in 5.57 (b) the initial LSF is still observable at convergence. In addition, a smooth unit normal gradient is achieved by the LS regularization in the vicinity of the interface $\Gamma_0^{I,II}$.

5.5.1.2 Hanging Bar in 3D

The design study of Section 5.5.1.1 is extended to 3D next. The initial design along with load and boundary conditions is shown in Figure 5.58 (a). Due to the symmetry of the design problem, only one quarter of the domain is modeled and optimized. The appropriate symmetry boundary conditions are applied weakly. A volume constraint of $\gamma_v = 0.035$ is enforced and the strain energy of the four bar truss is minimized. The final design, comprised of a single cylindrical bar with a nearly constant cross section is shown in Figure 5.58 (b). The evolution of objective and constraint for the 3D hanging bar problem is shown in Figure 5.59 where an effect of LS regularization can be seen. A much smoother design evolution is obtained when the LSF is regularized. Oscillations in objective and constraint, especially early in the design process, are largely mitigated. It is also worth pointing out that with LS regularization a slightly smaller objective value is obtained at convergence. This can potentially be attributed to a local minimum, identified by the optimizer
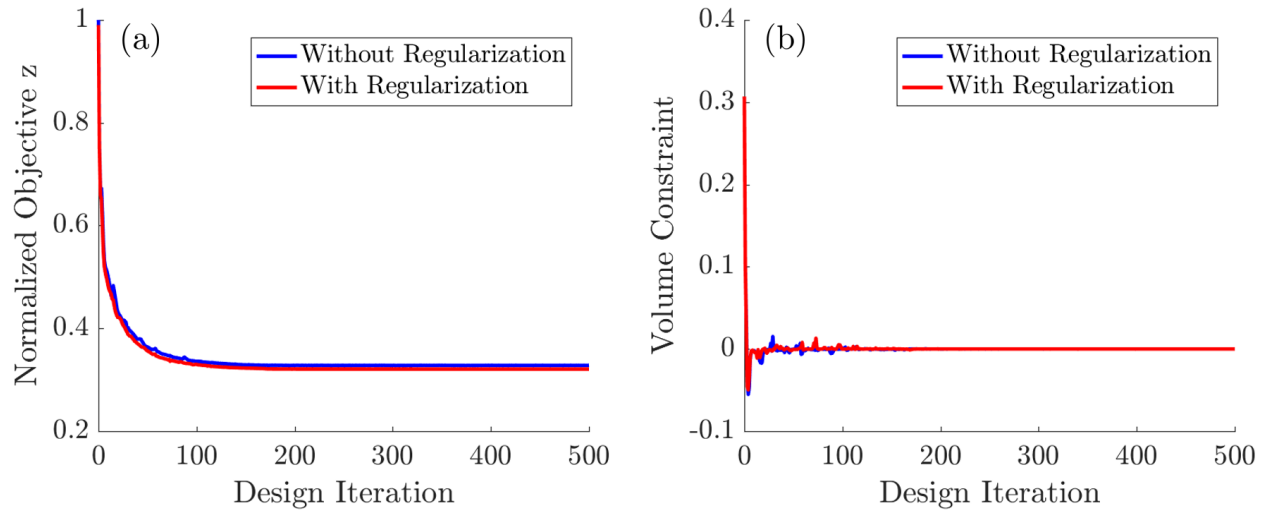
Figure 5.59: Evolution of (a) normalized objective and (b) volume constraint on phase I for the 3D hanging bar problem.

Figure 5.60: Comparison of (a) the final design LSF without LS regularization and (b) with LS regularization for the 3D hanging bar problem.

when no LSF regularization is applied.

Figure 5.60 shows a comparison of the LSFs obtained at convergence, with and without LS

Table 5.8: Properties for the hyperelastic LS regularization design problems.

Parameter	Value
Young's Modulus	$E = 2.0 \cdot 10^3 \ MPa$
Poisson's Ratio	$\nu = 0.4$
LS Regularization Weight	$w_3 = 0.01$
Element Edge Length	$h = 1.0 \ mm$
Selective Spring Ratio	$r_s = 1.0 \cdot 10^{-12}$

regularization. As in the 2D case, a smooth design LSF is obtained which has a unit norm slope in the vicinity of the interface and assumes ϕ_{Bnd} away from it. Without any regularization, the initial design LSF is still imprinted at convergence and spatial oscillations in the LSF are seen. In addition, the slope of the LSF near the interface is not guaranteed to be of unit magnitude. While yielding similar zero LS iso-contours, significant improvements in terms of stability and robustness of the LS-XFEM optimization approach have been observed.

5.5.2 Nonlinear Hyperelasticity

After an initial applicability of the novel LS regularization approach was demonstrated for linear elastic structural problems, finite strain hyperelasticity is considered next. The problem parameters for the beam problems studied in 2D and 3D using a hyperelastic Saint Venant-Kirchhoff material model are listed in Table 5.8.

5.5.2.1 Beam in 2D

First, a beam structure in 2D is optimized, where the initial design with load and boundary conditions is presented in Figure 5.61 (a). A traction load of $T_{X_2} = -10.0 \ N/mm$ is applied to the top center of the structure. Mechanical and design symmetry is used to reduce the model domain to one half. Plane strain 4 node quadrilateral nonlinear XFEM elements are used for modeling in 2D, as suggested by [162]. The objective is again strain energy minimization with a perimeter penalty and a LS regularization penalty. The optimization problem is furthermore subject to a
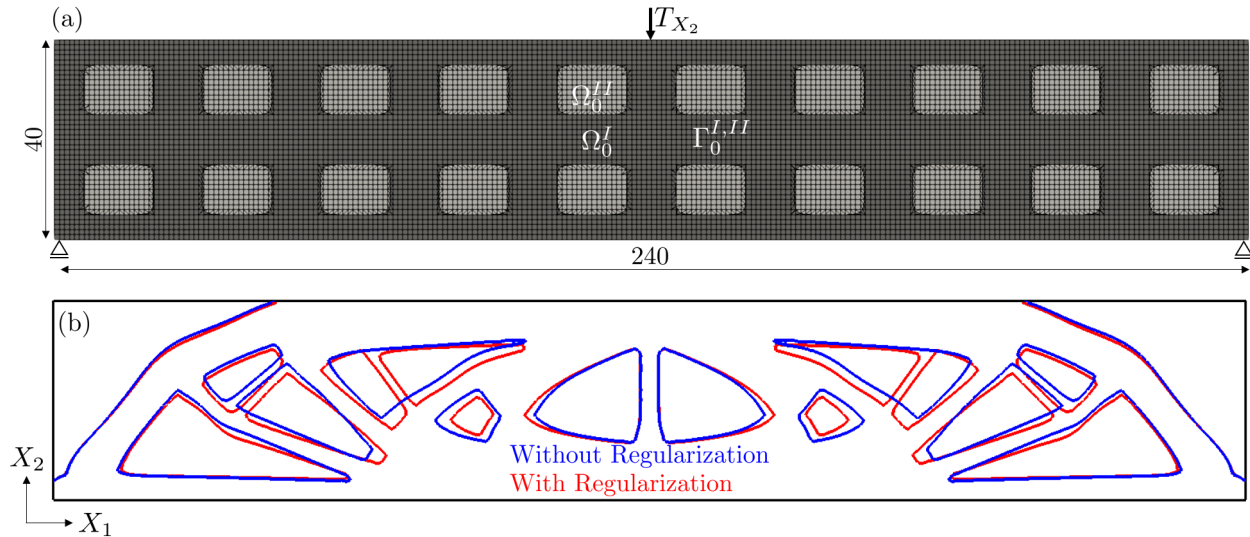
Figure 5.61: 2D beam problem setup with load and boundary conditions. (a) Initial design and (b) zero LS iso-contours of the final designs with and without LS regularization.

volume constraint of $\gamma_v = 0.6$. A comparison of the zero LS iso-contours obtained with and without LS regularization is shown in Figure 5.61 (b). While overall similar designs are obtained, slight differences in the final geometry are observed. These stem from the continuous LS regularization which facilitates convergence of the optimization problem and increases stability of the TO approach. When comparing the performance of the final designs, a slight decrease in strain energy by 0.1% is seen when LS regularization is applied. A similar effect was observed in Section 5.5.1.2 where a local minimum is identified when no LS regularization is used, causing an increased objective value at convergence.

The warped design LSF obtained at convergence with and without LS regularization is shown in Figure 5.62 (a) and (b), respectively. Clear differences can be seen in terms of spatial regularity, smoothness and uniformity of the spatial gradient of the LSF in the vicinity of the XFEM interface. While no specific LS values are obtained without regularization, the target LS value ($\pm\phi_{Bnd}$ with zero LS gradient) is obtained away from the interface through LS regularization. In the vicinity of the interface, a smooth and unit normal gradient is obtained. Figure 5.62 (c) shows the warped SDF corresponding to the final design obtained with LS regularization. As discussed in Section 4.3, the
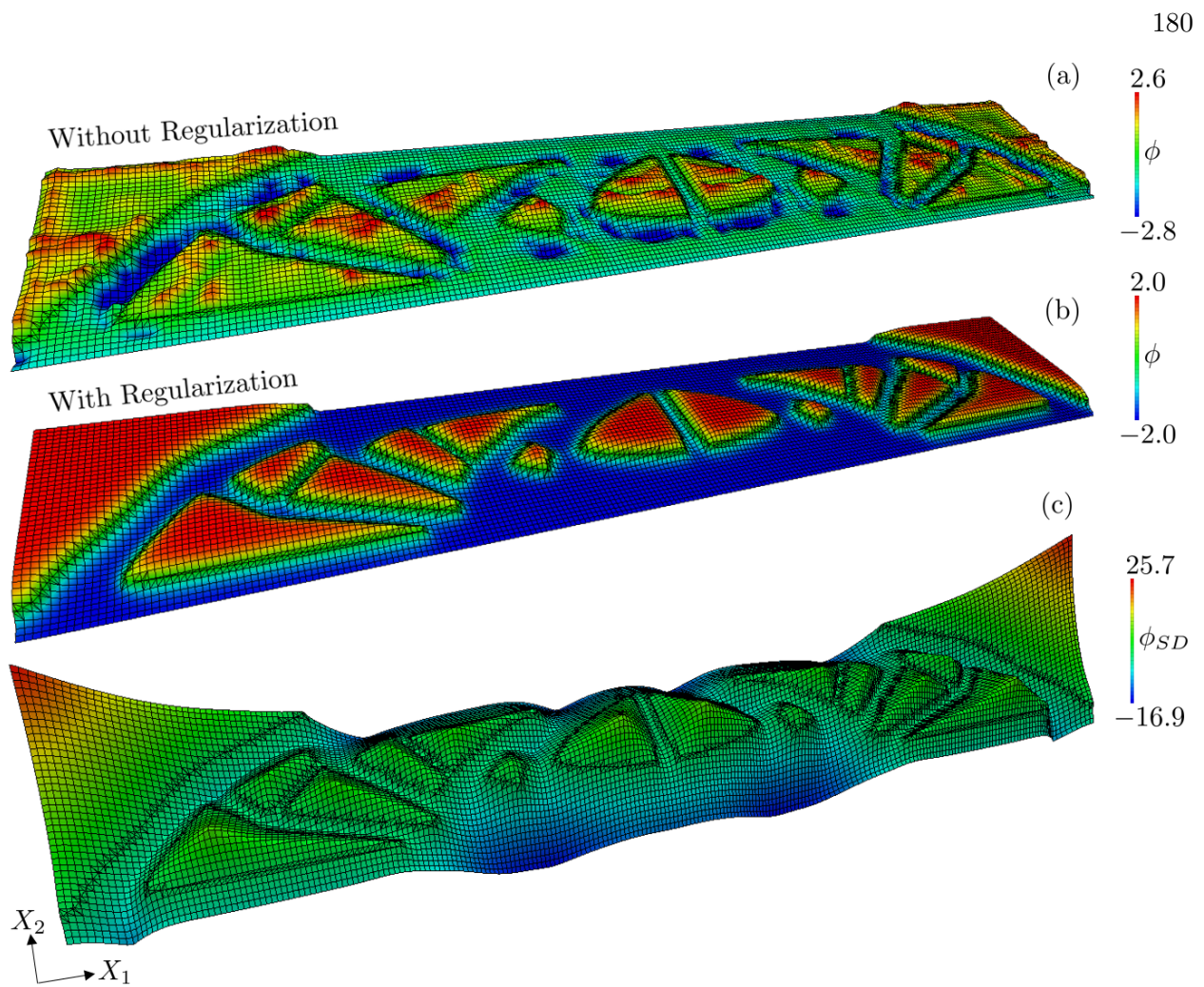
Figure 5.62: Comparison of the warped final design LSF. (a) Without LS regularization and (b) with LS regularization. (c) Shows the corresponding SDF for the final design.

SDF is the starting point for constructing the smoothly truncated LS target field for regularization of the design LSF. Overall, the SDF is well resolved. Except in areas of small geometric features (in the order of the element edge length h), the resolution of the SDF is insufficient and therefore the accuracy of the reconstructed target field (see Enq.(4.3.7)) suffers.

Influence of the LS Regularization Penalty Weight

A common challenge of penalty formulations as the one used in the formulation of the objective in Eqn.(5.5.1) is determining an appropriate weighting of the individual objective contributions.
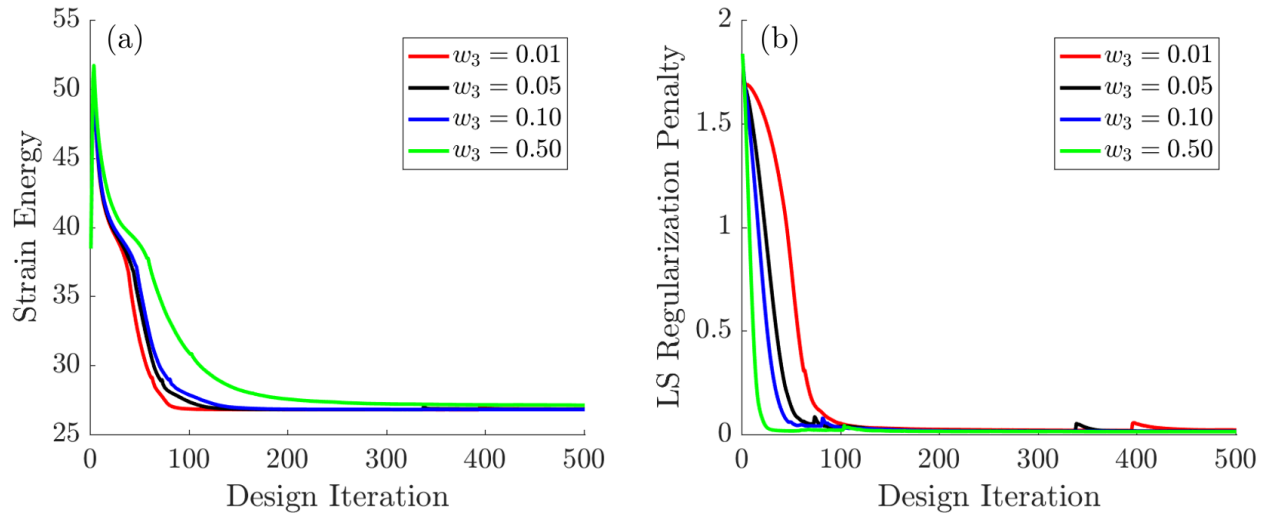
Figure 5.63: Influence of the LS regularization penalty weight on the evolution of (a) the strain energy and (b) the LS regularization penalty.

The influence of the LS regularization penalty weight is therefore studied next. The influence of different penalty weights, i.e., $w_3 = [0.01, 0.05, 0.1, 0.5]$ on the evolution of strain energy and the LS regularization penalty is shown in Figure 5.63 (a) and (b), respectively. With an increasing penalty weight, the minimization of the LS regularization term is favored by the optimizer at the cost of minimizing strain energy. Small increases of the LS regularization penalty are due to disconnecting members of the structure, which occur earlier for higher penalization weights. Based on numerical experiments, a penalization weight of $0.01 \leq w_3 \leq 0.1$ leads to a good balance between regularization and optimization of the structural performance of the beam. When the regularization weight is set too large (e.g., $w_3 = 0.5$), the regularization term dominates the overall objective at the cost of minimization of the strain energy. This essentially leads to a drastically different optimization problem which is not driven by physics anymore and therefore converges to a larger strain energy value. See Figure 5.63 (a).

Influence of Implicit Design Sensitivities on LS Regularization

As discussed in Section 4.3.2, implicit design sensitivities of the LS regularization formulation
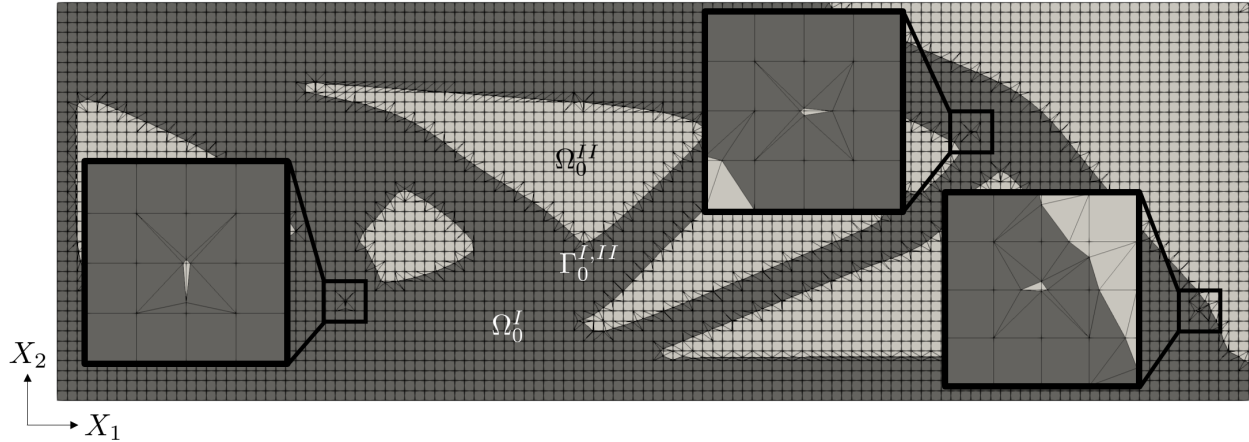
Figure 5.64: Spurious void inclusions in the 2D MBB beam structure for a penalty weight of $w_3 = 0.1$ and consideration of implicit design sensitivities.

(Eqn.(4.3.5)) on the design variables are neglected, as the target LSF $\tilde{\phi}(\mathbf{X})$ is seen as a prescribed target field without any dependencies on the design variables. Therefore, only the explicit dependencies of the LS regularization penalty on the design variables are accounted for in the sensitivity analysis. The advantage of this approach is demonstrated by a counter example in this section, where implicit design sensitivities of the LS regularization penalty are computed via the adjoint method and included in the optimization process.

The final design of the optimized beam in 2D, obtained through considering both explicit and implicit design sensitivities together with a large LS regularization penalty weight of $w_3 = 0.1$, is shown in Figure 5.64. The fairly large penalty weight causes insufficient advancement of the XFEM interface by the physical response as a significant influence of the regularization portion is driving the design evolution. This leads to spurious void inclusions in the vicinity of the interface which cause poor structural performance of the beam. When a much smaller penalty weight, e.g., $w_3 = 0.01$ is used, these effects are not seen and the converged structural design is indistinguishable from the one where no implicit design sensitivities are included. This shows that it is advantageous and computationally more efficient to not include the implicit design sensitivities while using a small LS regularization penalty weight.
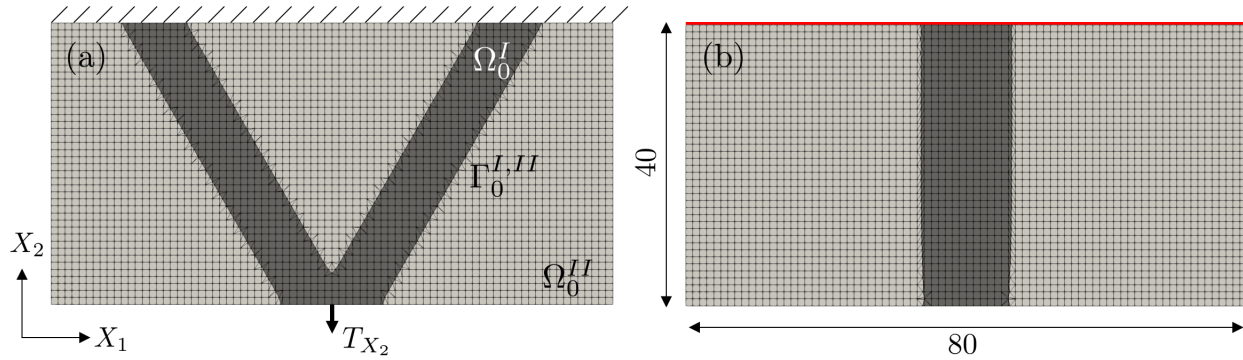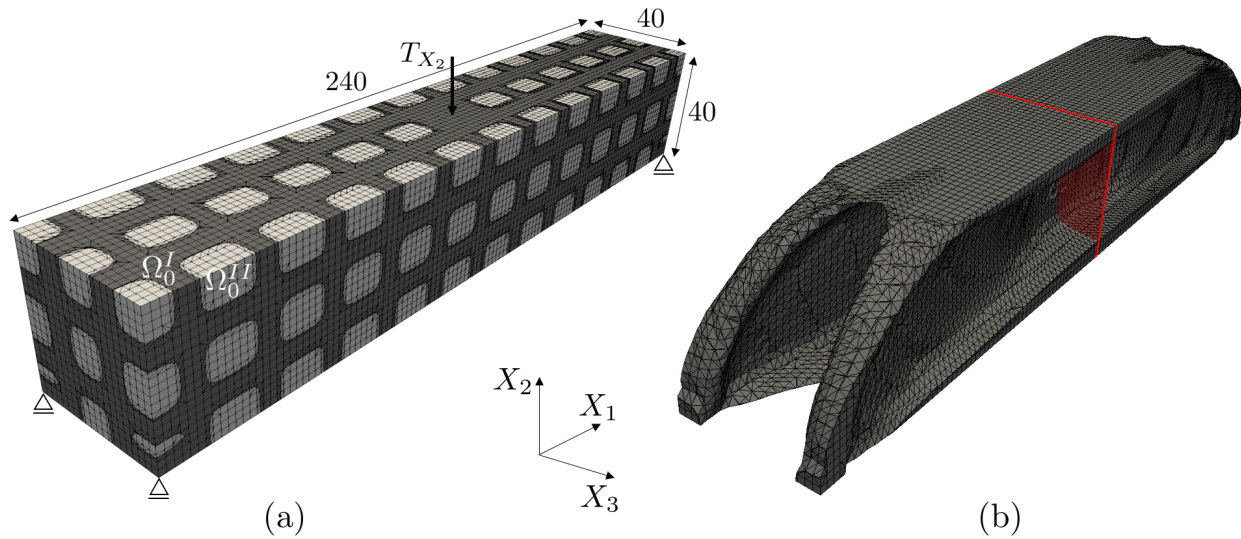
Figure 5.65: Problem setup with load and boundary conditions for the 3D beam problem. (a) Initial design and (b) final design.

5.5.2.2   Beam in 3D

The previously studied 2D beam example is re-addressed in 3D here where significant changes in topology are expected during the design process. The initial design along with load and boundary conditions is shown in Figure 5.65 (a) where an element edge length of $h = 2.0 \ mm$ is used. Due to
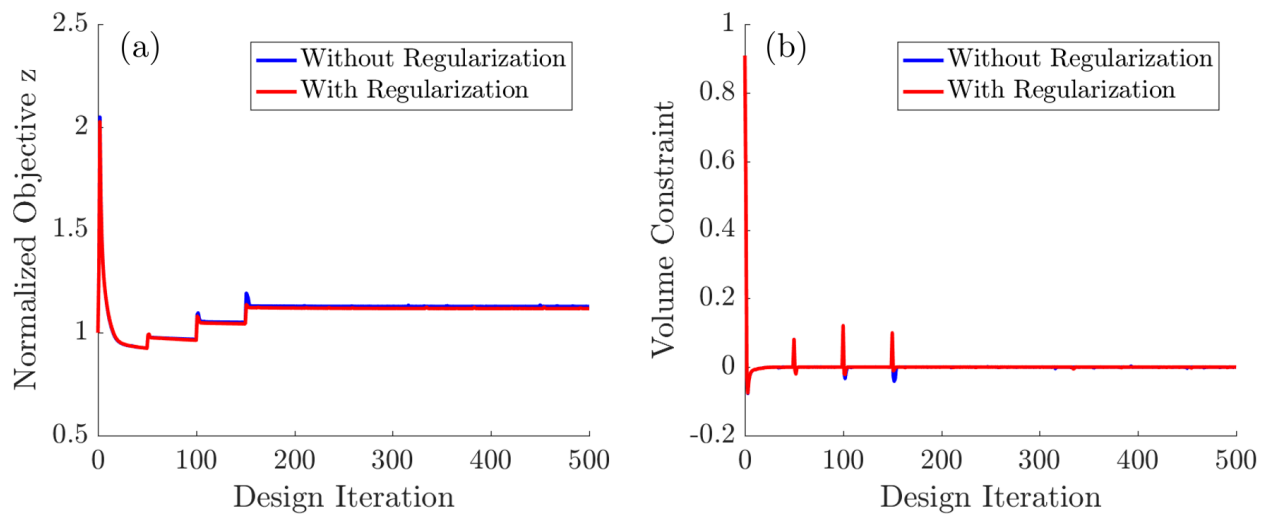
Figure 5.66: Evolution of (a) normalized objective and (b) volume constraint of the 3D beam problem.
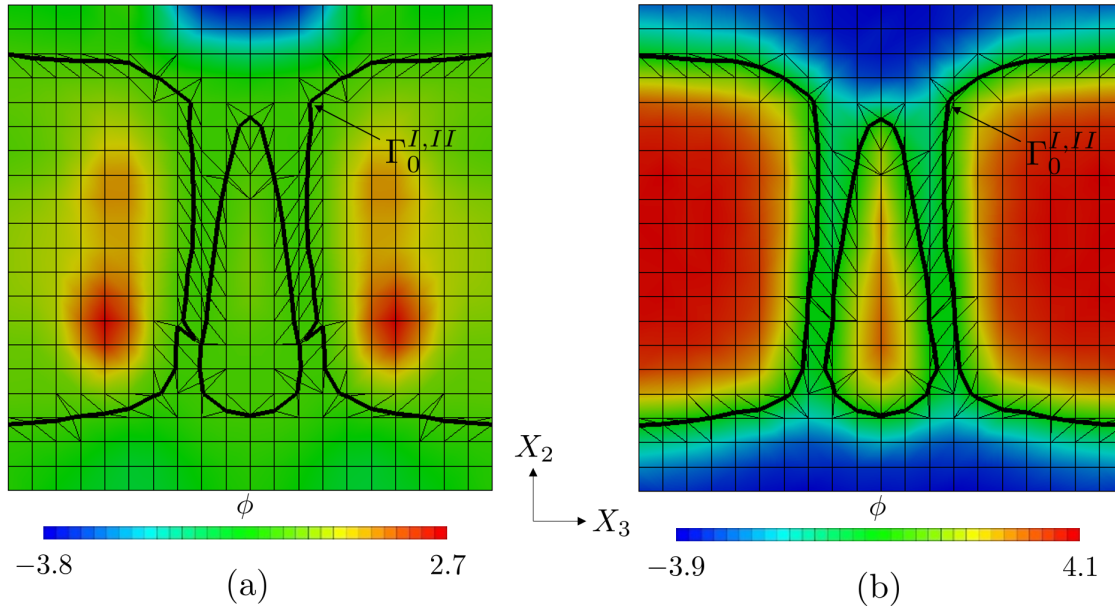
Figure 5.67: Comparison of the design LSF of the final design of the 3D beam, (a) without LS regularization and (b) with LS regularization.

the symmetric design problem, only one quarter of the full domain is modeled and optimized. The appropriate symmetry boundary conditions are again applied weakly. A traction load of $T_{X_2} = -2.0 \ N/mm$ is applied over a circular domain of radius 2.0 mm at the top center of the beam. A volume constraint limiting the amount of phase I (solid) domain to $\gamma_v = 0.3$ is enforced through a continuation approach.

The final design obtained after about 400 design iterations is shown in Figure 5.65 (b). The corresponding evolution of objective and volume constraint is depicted in Figure 5.66 (a) and (b), respectively. The effect of the continuation scheme on the volume constraint results in periodic increases of the objective function. Overall, a smooth and quick convergence of the design problem is seen, especially when LS regularization is employed. A slightly better design (i.e., lower final objective value) is found when using LS regularization during the design process.

A comparison of the final design LSF along the center plane of the 3D beam (see red plane in Figure 5.65 (b)) is shown in Figure 5.67. It can be seen that without any LS regularization, the design LSF is shallow (see Figure 5.67 (a)), while a regularized LSF is obtained through the

Table 5.9: Properties for the fluid LS regularization design problems.

Parameter	Value
Reynolds Number	$Re = 66.0$
Fluid Density	$\rho = 1.0$
LS Regularization Weight	$w_3 = 0.05$
Element Edge Length	$h = 0.25 \; mm$

proposed regularization scheme. See Figure 5.67 (b). As in the 2D beam problem, thin structural members limit the applicability of the regularization scheme due to an insufficiently resolved SDF. This is also the case for the 3D beam, where thin vertical members are formed. From Figure 5.67 (b), it can be seen that in these areas the target LS value ϕ_{Bnd} cannot be achieved, due to insufficient spatial resolution. A strong need for minimum feature size control is therefore seen to provide appropriate spatial discretization and regularization of the LSF. This is an inherent limitation of the XFEM approach as it is unable to properly resolve geometric features on the order of h.

5.5.3 Incompressible Navier-Stokes Flow

A flow problem modeled by the incompressible Navier-Stokes equations at steady state is considered as the final design example to demonstrate the LS regularization scheme. The formulation of the governing equations and the stability terms of the velocity and pressure equations are beyond the scope of this thesis. More details regarding XFEM modeling of incompressible Navier-Stokes flow can be found in [190, 67]. The problem parameters for the fluid design example are listed in Table 5.9.

5.5.3.1 Fluid Nozzle in 3D

A fluid-void nozzle design problem is studied next which is an extension of a similar design problem in 2D presented by [21, 102, 122]. The initial design, with boundary conditions and dimensions is shown in Figure 5.68. A non-design domain of size $0.75 \times 5.0 \times 5.0$ is enforced downstream from the inlet domain. A parabolic inflow with a maximum inlet velocity of 30.0 mm/s
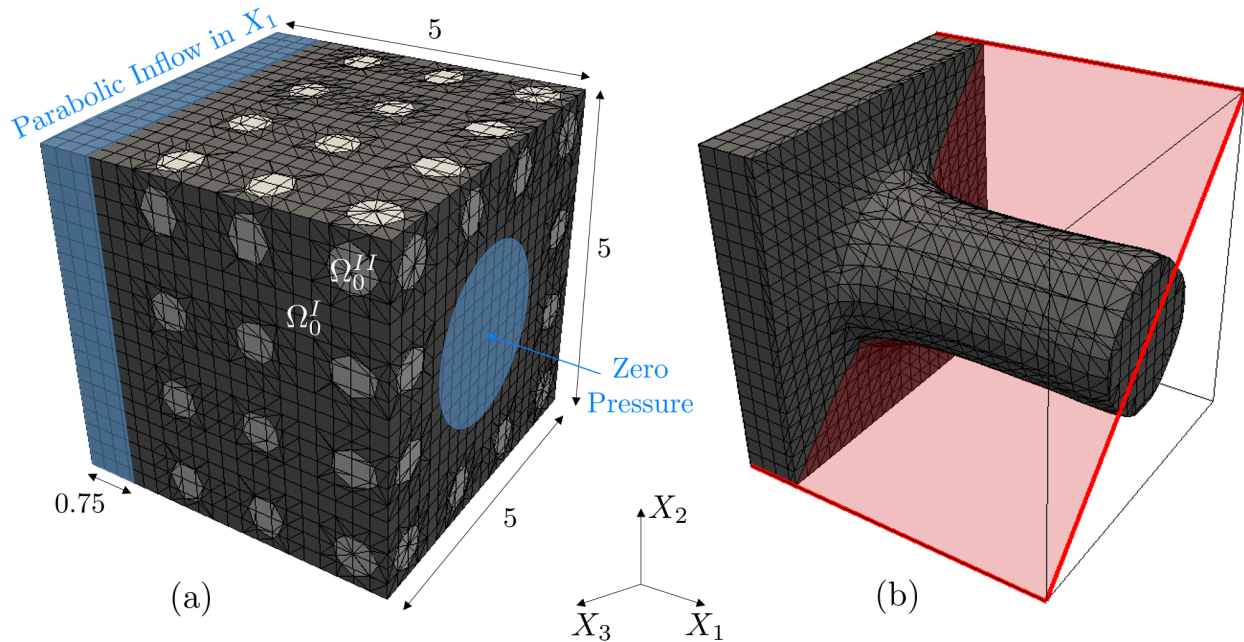
Figure 5.68: Problem setup with boundary conditions for the 3D fluid nozzle problem. (a) Initial design and (b) final design.

in X_1 direction is applied at the inlet. Zero pressure is enforced weakly at the outlet. Both the inlet and the outlet domain are non-design domain. Quarter symmetry of this design problem is used and slip conditions are applied along the symmetry planes. The objective of this design problem is the minimization of the total pressure drop between inlet and outlet, subject to a volume constraint of $\gamma_v = 0.3$ on the fluid phase.

The final design is shown in Figure 5.68 which shows a straight channel upstream from the outlet which blends into the rectangular inlet domain. As the minimum total pressure drop would be obtained from a straight channel, the optimizer tries to achieve such a channel design as good as possible, considering the non-design space at the inlet and outlet domains. This design agrees well with the results presented in literature.

A comparison of the final design LSF along the diagonal plane highlighted in red in Figure 5.68 (b) is shown in Figure 5.69. As in the structural problems, a significantly more regularized LSF is obtained when LS regularization is employed. As before, the target LS value together with a
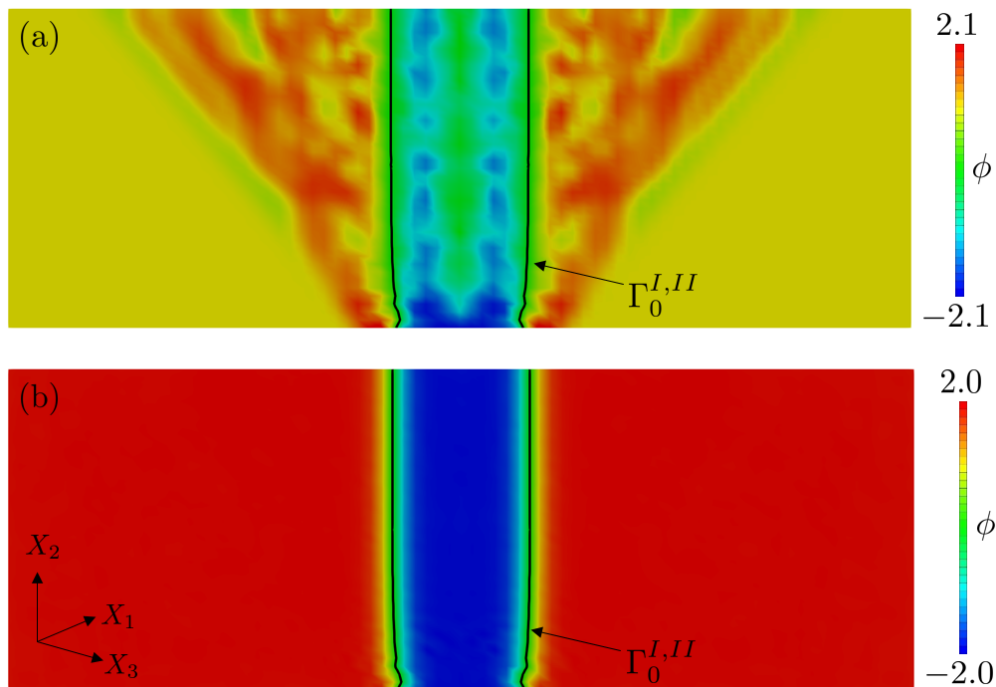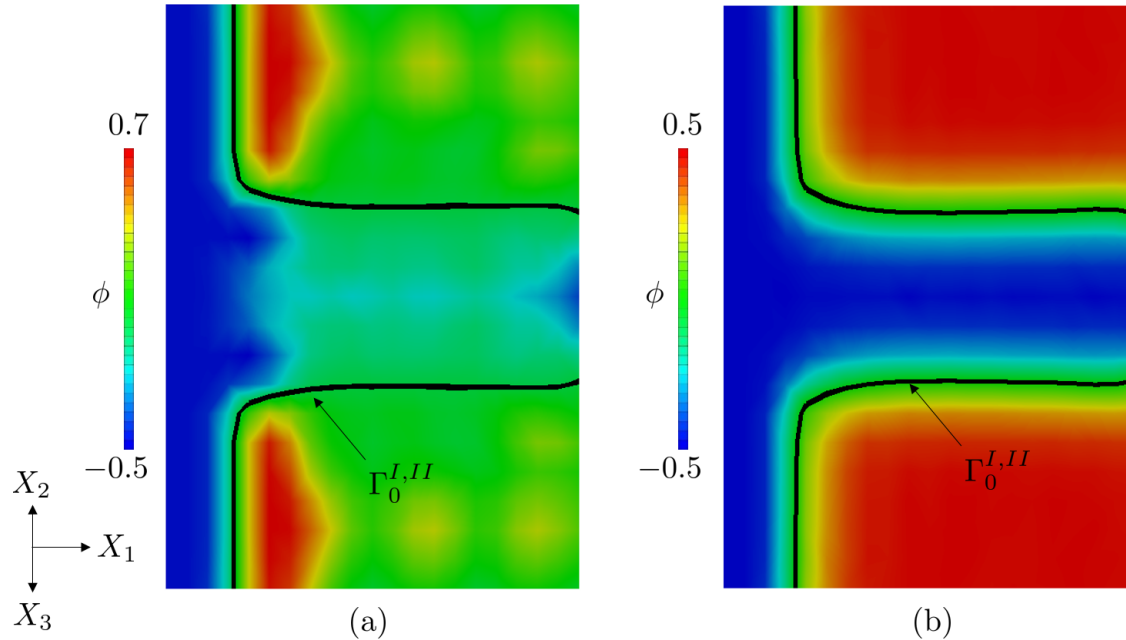
Figure 5.69: Comparison of the final design LSF (a) without LS regularization and (b) with LS regularization for the 3D fluid nozzle example.

zero LS gradient is achieved away from the interface while a unit norm LS gradient is obtained in the vicinity of the XFEM interface. Without regularization, a rather flat LSF is obtained. While no significant difference in final designs is seen, a drastic increase in robustness and stability of the optimization approach was observed when LS regularization is used.

Influence of the number of Time Steps in on LS Regularization

The effect of temporal discretization on the HM used for LS regularization is studied next. As proposed by [40], a single time step for time integrating the transient heat conduction equation (Eqn.(2.1.3)) provides a sufficiently accurate SDF when using the HM. This statement is investigated through variation of the number of time steps used in the Euler backward scheme (Eqn.(2.1.2)) for time integration.

Figure 5.70 shows the evolution of normalized objective function and the LS regularization penalty contribution for different number of time steps. It should be noted that while the number of time
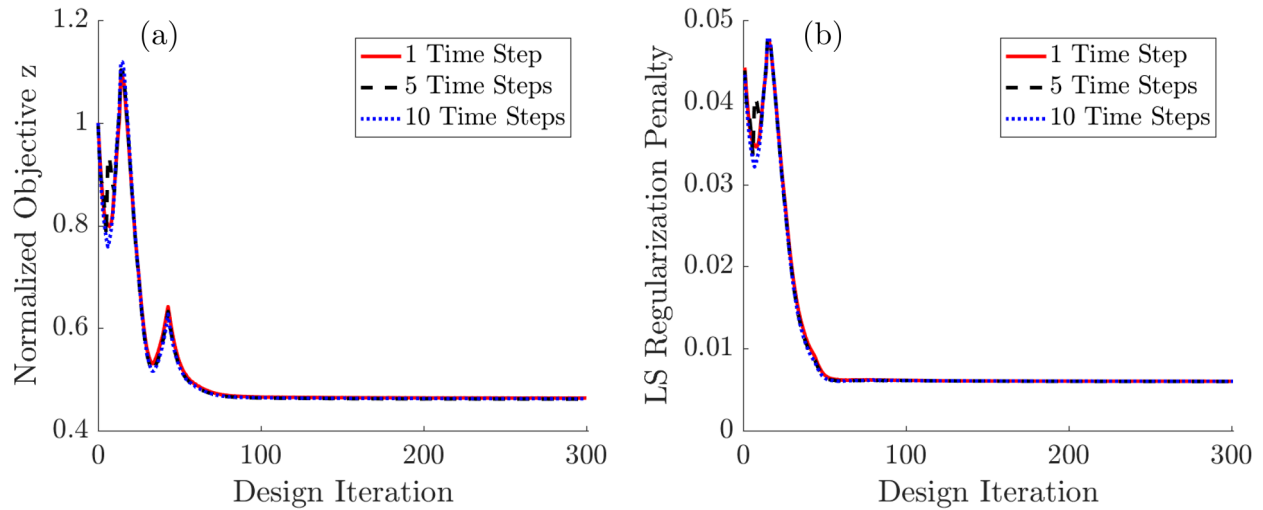
Figure 5.70: Effect of different number of time steps for the HM on (a) normalized objective and (b) LS regularization penalty.

steps was varied, the total simulation time for this example was kept constant at $t_{max} = 1.0\ s$. As can be seen from Figure 5.70, no significant differences are observed when varying the number of time steps used for the HM. This confirms the statement by [40] and significantly reduces the computational effort when using LS regularization based on the HM with only a single time step.

5.5.4   Discussion

In summary, a robust and generally applicable LS regularization scheme based on an extension of the HM was presented. By constructing a smooth and globally unique target LSF, limitations of previously proposed, local regularization schemes are overcome. The performance of the physics-independent regularization scheme was demonstrated using numerical examples in linear elasticity, nonlinear hyperelasticity and fluid flow in 2D and 3D. The influence of the penalty weight, consideration of implicit design sensitivities and the number of time steps used for the HM was investigated. Overall, improved stability and robustness of the LS-XFEM-based design optimization approach was seen when explicit LS regularization was employed. Due to the improved stability, faster convergence was seen and larger optimization step sizes could be used.

However, a strong need for controlling small geometric features was identified. Minimum geometric features in the order of the element edge length h are not only insufficiently resolved and analyzed by the XFEM, but also the accuracy of the HM and therefore the LS regularization scheme suffers. In addition, the added computational cost from solving two additional PDEs needs to be considered when using the proposed LS regularization scheme.

5.6   Minimum Feature Size Control

The approach to control minimum feature size in LS-XFEM TO using the SDF skeleton as discussed in Section 4.4 is studied next. Different numerical examples in 2D and 3D are considered. The basis of the minimum feature size measure defined in Eqn.(4.4.1) is the notion of the skeleton of the SDF and the SDF values at those skeleton locations. A more detailed discussion on the computation of the SDF skeleton using the Laplacian of the SDF is presented in Section 4.4.3. To mitigate boundary effects of the HM on the SDF, immersion of the design domain is performed. Significant boundary effects are exhibited by the HM when the XFEM interface (location of the temperature source) exits the design domain. When the design domain is immersed, this is prevented by construction. Alternatively, averaging a Dirichlet and Neumann temperature solution field as the source for the SDF (see Eqn.(4.4.4)) could be used to mitigate boundary effects on the HM. In addition, as pointed out by [116, 203], boundary effects on the skeleton can lead to unintended design features where feature size is artificially enforced. [116, 203] therefore perform a trimming of the SDF skeleton before using it to enforce feature size. This extra step is not required in the presented approach where the corners of the immersed design domain are sufficiently rounded in order to avoid undesired skeletons. Numerical studies have demonstrated general applicability of this approach.

5.6.1   Effect of Discretization on Skeleton

First, the effect of spatial discretization on the obtained SDF skeleton is studied. It is crucial to understand the relationship of XFEM discretization on the computation of the SDF and the SDF skeleton as both fields are key for the minimum feature size measure presented in this thesis. An immersed bar as shown in Figure 5.71 (a) is used in combination with a sweep over its rotation angle α_{Rot} to study this effect. Initially, the bar is immersed vertically in the quadratic domain. The corresponding SDF and the Laplacian of the SDF are depicted in Figure 5.71 (b) and (c), respectively. It can be seen that initially, when the valley of the SDF $\phi_{SD}(\mathbf{X})$ is aligned with the
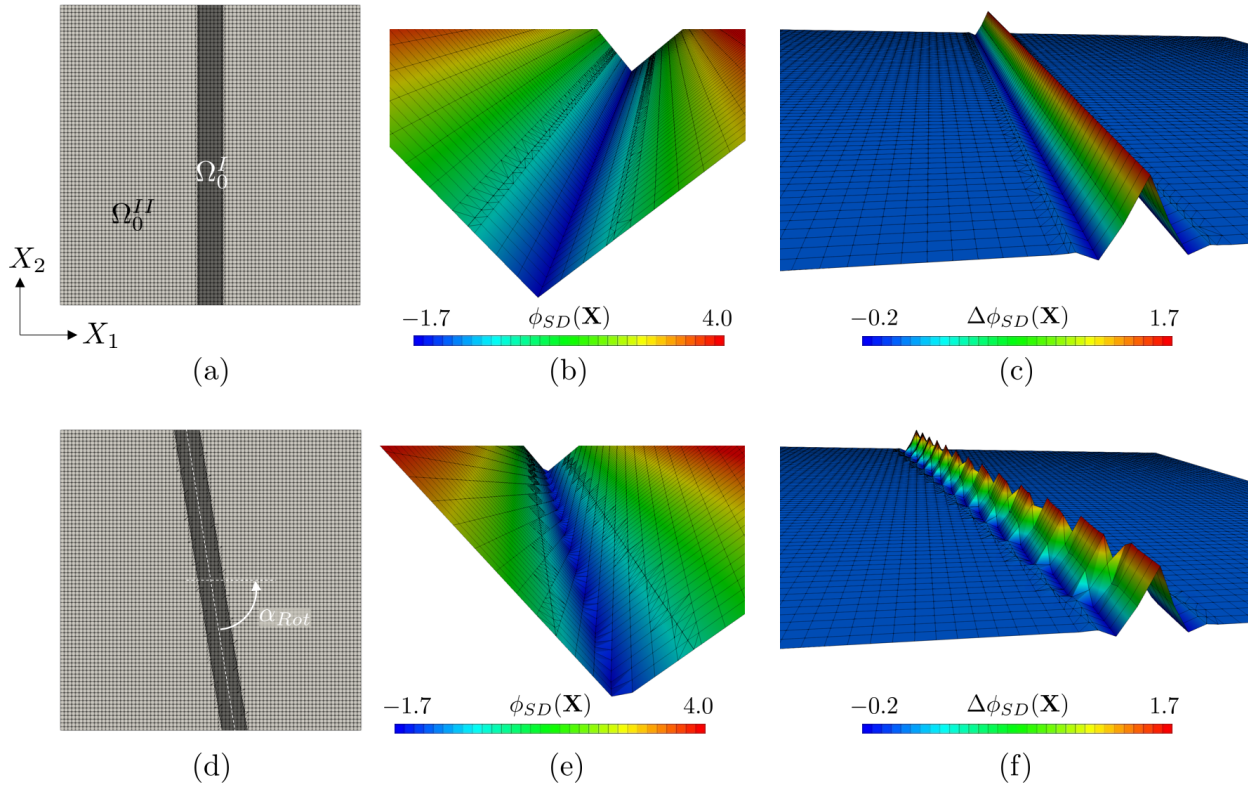
Figure 5.71: Rotating immersed bar example. The initial, vertical configuration (a) leads to (b) a uniform SDF and (c) a uniform skeleton. For a rotated configuration (d), (e) the SDF and (f) the skeleton become non-uniform.

background mesh, a clear and uniform skeleton (i.e., ridge of $\Delta\phi_{SD}(\mathbf{X})$) is obtained. The fact that the ridge has a finite width of $4h$ is caused by the operator splitting technique used to compute the SDF normal field $\eta(\mathbf{X})$ and the SDF Laplacian field $\lambda(\mathbf{X})$, as discussed in Section 4.4.2.2 and Section 4.4.2.3, respectively. In addition, Helmholtz smoothing is applied to mitigate spatial oscillations on both of those fields across the XFEM interface which also contributes to a spreading of the skeleton.

For a non-zero rotation angle (e.g., $\alpha_{Rot} = 10.0°$), the obtained valley of the SDF and therefore the skeleton (i.e., Laplacian of the SDF) is not anymore aligned with the background mesh. This is illustrated in Figure 5.71 (d), (e), and (f), respectively. It can clearly be seen that the minimum of the SDF cannot be properly represented by the regular (linear) background grid. This, in turn, leads to spatial oscillations, i.e., non-uniformity of the skeleton. Depending on the rotation angle of the bar this effect may be more or less pronounced.
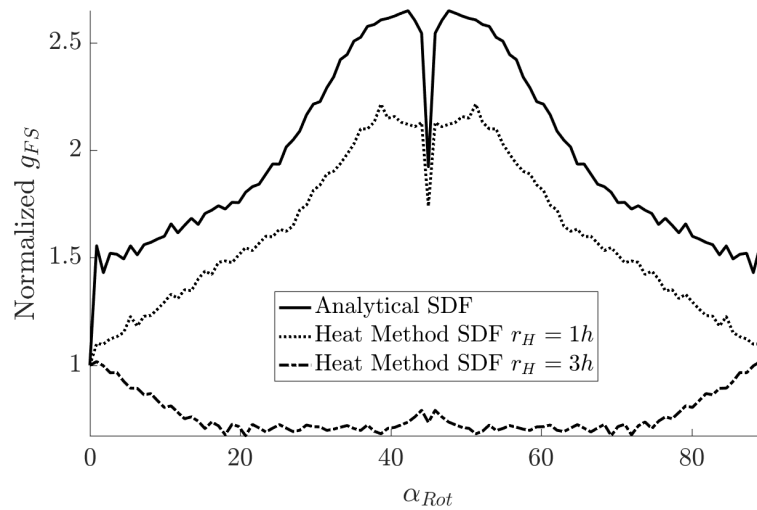
Figure 5.72: Dependency of the feature size measure on the rotation angle of the immersed bar using different SDF computations.

This change in resolution of the extremum of the Laplacian however causes significant oscillations of the feature size measure in this example where the immersed bar is rotated, such that $0° \leq \alpha_{Rot} \leq 90°$. The variation of the feature size measure (Eqn.(4.4.1)) over the rotation angle is shown in Figure 5.72 for a SDF obtained by the HM with a Helmholtz smoothing radius of $r_H = 1h$ and $r_H = 3h$ and a prescribed analytical (i.e., exact) SDF. A similar non-uniform magnitude of the feature size measure depending on the rotation of the bar is seen, for both HM SDF with $r_H = 1h$ and the analytical SDF. A more uniform feature size measure with respect to the investigated rotation angles is obtained when using $r_H = 3h$. Ideally, a constant measure would be expected, as in fact the width of the bar remains unchanged and only the orientation of the bar with respect to the total design domain is changed. The cause for these oscillations is two-fold and does not stem from using the HM to obtain the SDF (since a similar oscillating feature size measure is seen when using a perfect, analytical SDF).

The first cause for the high dependency of the feature size measure on the spatial discretization stems from the non-uniformity of the SDF Laplacian, as shown in Figure 5.71 (c) and (f) when a Helmholtz smoothing radius of $r_H = 1h$ is used. This, in turn, comes from the inability of the

uniform (linear) background mesh to accurately capture the discontinuities in the SFD when these are not aligned with the regular background elements. As discussed above, this causes a non-uniform magnitude of the SDF skeleton and thus oscillations in the feature size measure. Secondly, the SDF value itself is used to compute the feature size measure at the location of the skeleton, see Eqn.(4.4.1). Since also the SDF value is not captured accurately on a non-aligned background mesh, see Figure 5.71 (e), additional variations in the feature size measure are introduced.

When a larger smoothing radius (e.g., $r_H = 3h$) is used, spatial variations in both the SDF and the Laplacian are reduced and a more uniform feature size measure is obtained, regardless of the rotation angle. This however comes with the drawback of a spatially more spread skeleton, which then leads to wider features as the sharp definition of the skeleton is sacrificed. In order to obtain both a pronounced skeleton and a smooth, discretization independent behavior, extremely fine background meshes are required. Alternatively, adaptive mesh refinement could be used to accurately capture discontinuities in the SDF gradient which define the LS skeleton. Numerical studies have shown, that the finer the background mesh, the better the Dirac-delta-like skeleton is resolved. In combination with a large Helmholtz filtering, the required smoothness of the feature size measure is obtained. Alternatively, XFEM triangulation of the background mesh not only along the zero LS iso-contour but also along the ridge of the Laplacian (i.e., skeleton) could potentially be performed to obtain discretization independence of the proposed feature size measure.

5.6.2   Minimization of Volume Phase I - A purely geometric Example

As a first design optimization example, a volume minimization example under a minimum feature size constraint in 2D is considered. This purely geometrical example has previously been studied by [191, 4, 78]. Mathematically, the constrained optimization problem is formulated as:

$$\min_{\mathbf{s}} \ z(\mathbf{s}, \mathbf{u}) = w_1 \frac{\Omega_0^I}{(\Omega_0^I)^0} + w_2 \frac{\int_{\Gamma_0^{I,II}} dS}{\int_{(\Gamma_0^{I,II})^0} dS} + w_3 \frac{p_{Reg}(\mathbf{s})}{p_{Reg}(\mathbf{s}^0)}$$

$$\text{s.t. } g = \frac{p_{FS}}{(\Omega_0^I + \Omega_0^{II})} - \epsilon_{FS} \leq 0$$

(5.6.1)

Table 5.10: Properties for the geometric minimum feature size design problems.

Parameter	Value
Objective Weights	$w_i = [0.89, 0.01, 0.1]$
Minimum Feature Size Epsilon	$\epsilon_{FS} = 1.0 \cdot 10^{-4}$
Minimum Feature Size Radius	$r_m = 1h$
Helmholtz Smoothing Radius	$r_H = 1h$
Element Edge Length	$h = 0.5\ mm$
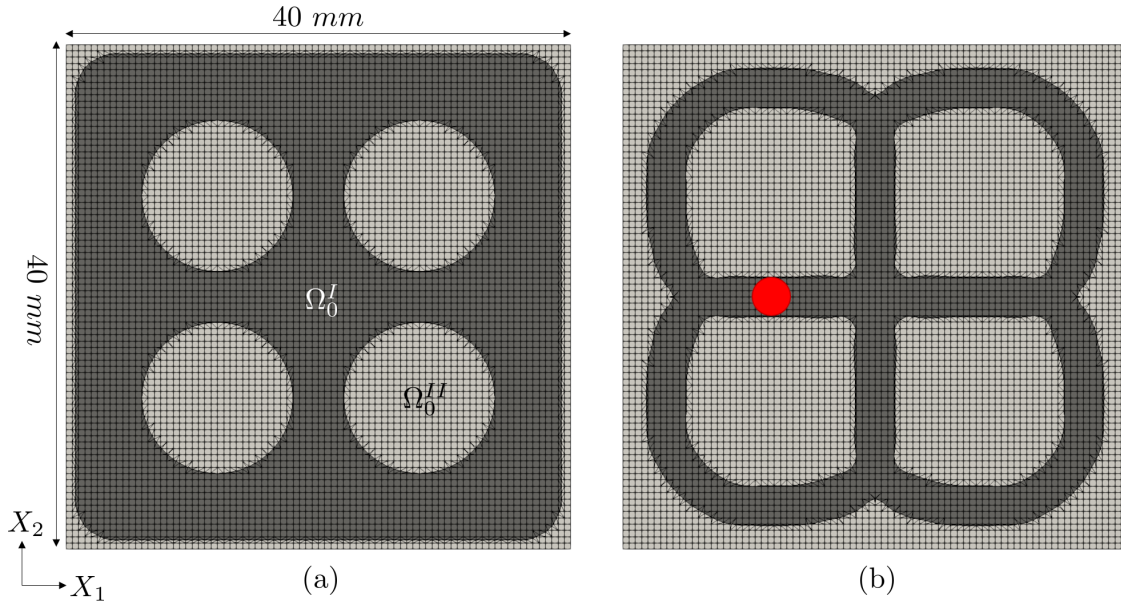
Figure 5.73: Problem setup for the 4 inclusion geometrical example. (a) Initial design and (b) final design.

where the objective components are weighted and normalized. The first component minimizes the volume of phase I (Ω_0^I), the second component is a perimeter penalty, and the last component is the LS regularization term discussed in Section 4.3.2. The minimum feature size constraint is normalized by the total design domain volume to avoid any length scale dependence and it is enforced using a tolerance ϵ_{FS}. The parameters used for this geometrical design example are summarized in Table 5.10.

The initial design with four phase II inclusions is shown in Figure 5.73 (a). It should be pointed out that the design domain is immersed and rounded corners are used to eliminate any undesired
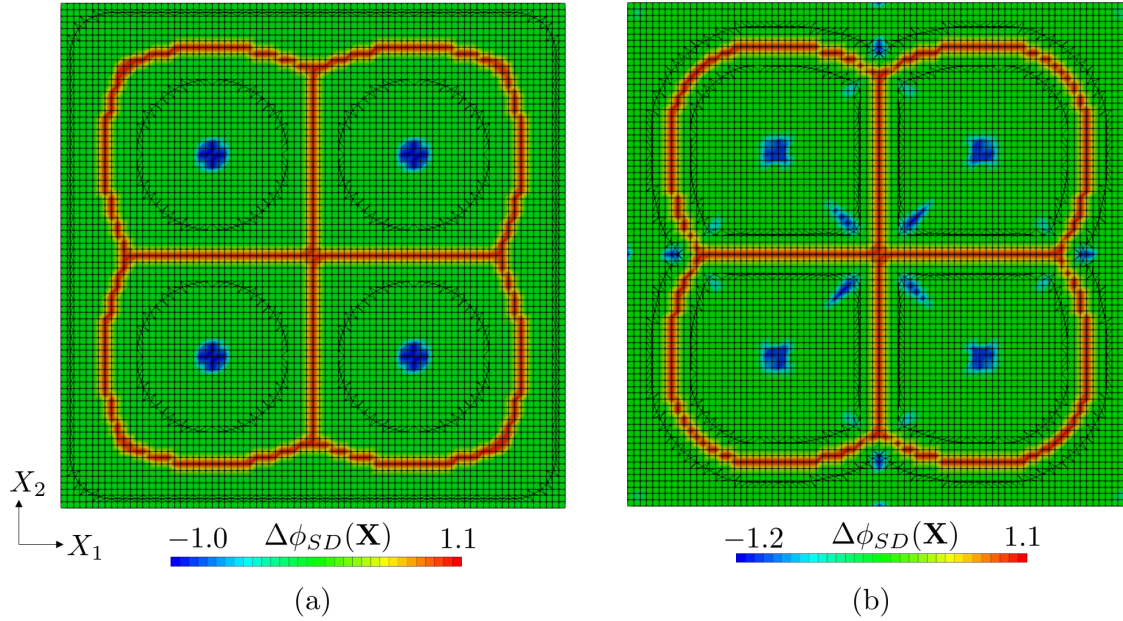
Figure 5.74: Smoothly projected Laplacian of the SDF for (a) the initial design and (b) the final design.

boundary skeleton effects. Three-fold symmetry is enforced on the design variable field. The final design is shown in Figure 5.73 (b). It can be seen that a phase I domain with almost constant width is obtained, resembling the shape of a rounded window. The obtained result matches results found in literature for this problem, however it is only a local minimum. An equally valid solution with even less phase I volume would be a circle of minimum feature size in the center of the design domain, or no phase I volume at all. Since the minimum feature measure is (strictly) enforced as a constraint, topological changes are prohibited and the initial topology of four inclusions is retained at the final design. The width of the obtained features is of radius $r_{min} = 3h$, which is indicated by a red disc in Figure 5.73 (b). The increase in minimum feature size from $r_m = 1h$ to $r_{min} = 3h$ is caused by the spreading of the skeleton as discussed in Section 5.6.1. This widening of the enforced minimum feature size is described by Eqn.(4.4.17).

The skeleton (i.e., Laplacian of the SDF) for the initial design and the final design are depicted in Figure 5.74. Smooth Laplacian projection is used for this design example, which greatly improves the uniformity of the skeleton and thus the robustness of the skeleton-based feature size approach.
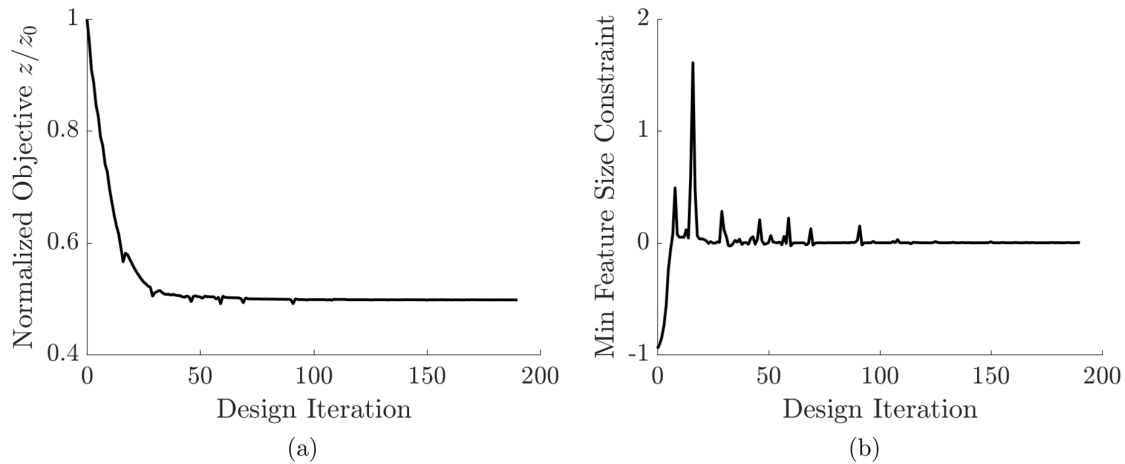
Figure 5.75: Evolution of (a) objective and (b) minimum feature size constraint for the four inclusion geometrical example.

Since the overall topology stays unchanged during the design optimization process, the skeleton only changes slightly, between the initial and the final design. The effect of smooth Laplacian projection can clearly be seen where the Laplacian in the majority of the design space is projected to zero, except at the skeleton it is either plus or minus one.

Figure 5.75 shows the evolution of the normalized objective function and the minimum feature size constraint. A converging behavior of the optimization problem with only minor oscillations is seen. These stem from the discretization dependence of the skeleton and the SDF as discussed in Section 5.6.1. Oscillations appear as long as the XFEM interface evolves during the optimization process. Once a converged design is obtained, the feature size constraint is satisfied and therefore constant in magnitude.

5.6.2.1   Enforcement of Minimum Feature Size Control along Domain Boundaries

To (partially) offset the computational cost stemming from additional fields and from the need for rather fine meshes for the skeleton-based minimum feature size control, selectively enforcing feature size control along domain (e.g., symmetry) boundaries is investigated. This is a unique capability of the proposed approach and only possible because a Helmholtz-type PDE is solved to obtain the Laplacian of the SDF. Therefore, boundary conditions can be enforced weakly on the
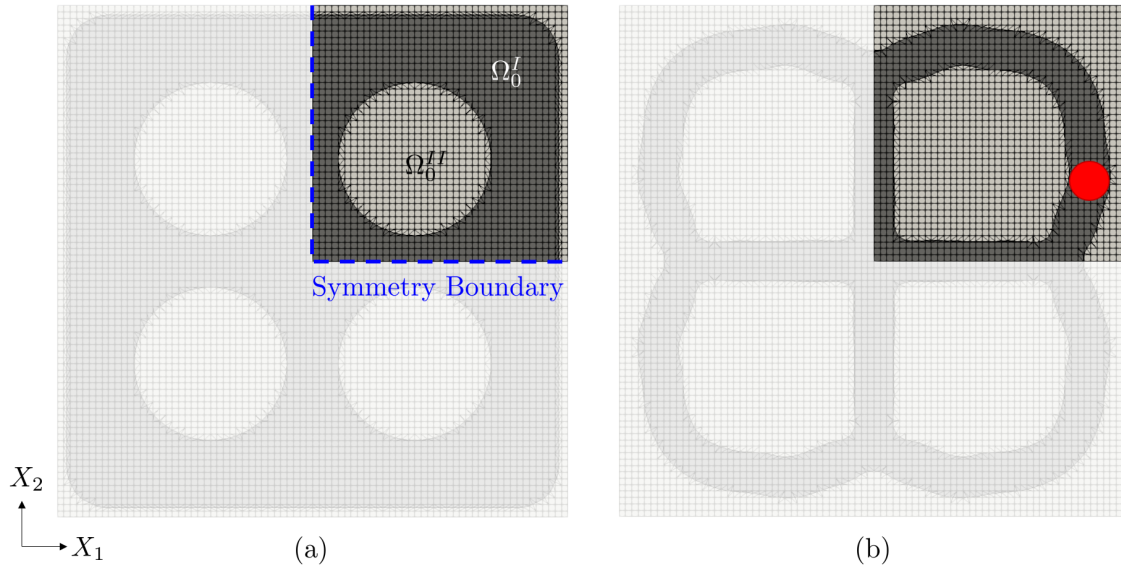
Figure 5.76: Problem setup for the 4 inclusion geometrical example using quarter symmetry. (a) Initial design and (b) final design.

Laplacian field $\lambda(\mathbf{X})$ to selectively enforce feature size along the respective boundary.

To demonstrate the effectiveness of the selectively applied feature size control along symmetry boundaries, the geometric four inclusion problem discussed in Section 5.6.2 is re-addressed. The initial design using only one quarter of the full design domain with symmetry boundaries is shown in Figure 5.76 (a). Along the symmetry boundaries, a prescribed Laplacian value of $\lambda = 1.0$ is enforced weakly using Nitsche's method. Through that, a skeleton is created along the symmetry boundaries which leads to enforcement of feature size control. The final design is shown in Figure 5.76 (b) which is very similar to the one obtained on the full domain (see Figure 5.73 (b)).

The corresponding Laplacian fields are shown in Figure 5.77 (a) and (b), respectively. Compared to the Laplacian fields for the full domain shown in Figure 5.74, slight differences can be seen. The weakly enforced skeleton along the symmetry boundaries in Figure 5.77 (a) slightly extends past the outer skeleton in vertical and horizontal direction, respectively. See domains highlighted by the red circles in Figure 5.77 (a). This is due to the fact that the selectively enforced Laplacian is formulated such that it only enforces feature size normal to the respective boundary, but not tangential to it. In other words, the weakly enforced Laplacian value can be reduced in tangential,
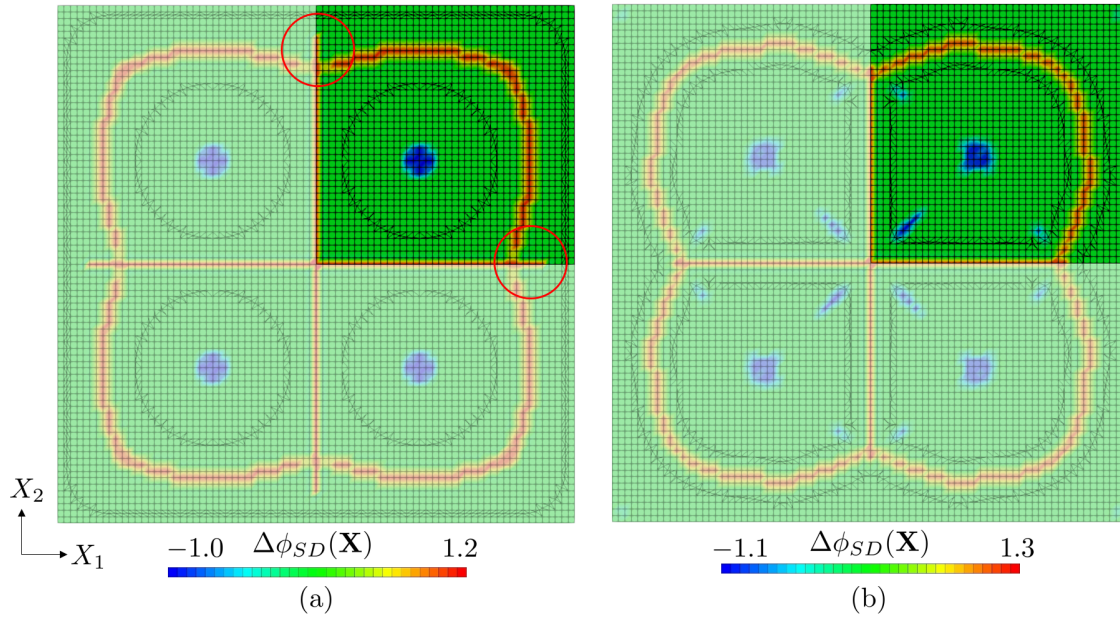
Figure 5.77: Laplacian of the SDF for (a) the initial design and (b) the final design using quarter symmetry. The extension of the weakly enforced Laplacian along the symmetry boundaries is circled in red.

but not in normal direction by an approaching XFEM interface and the corresponding SDF. During the design optimization process, the Laplacian enforced along the symmetry boundaries is shortened towards the center of the design domain such that it does not extend past the outer skeleton in the final design (Figure 5.77 (b)). The evolution of normalized objective and minimum feature size
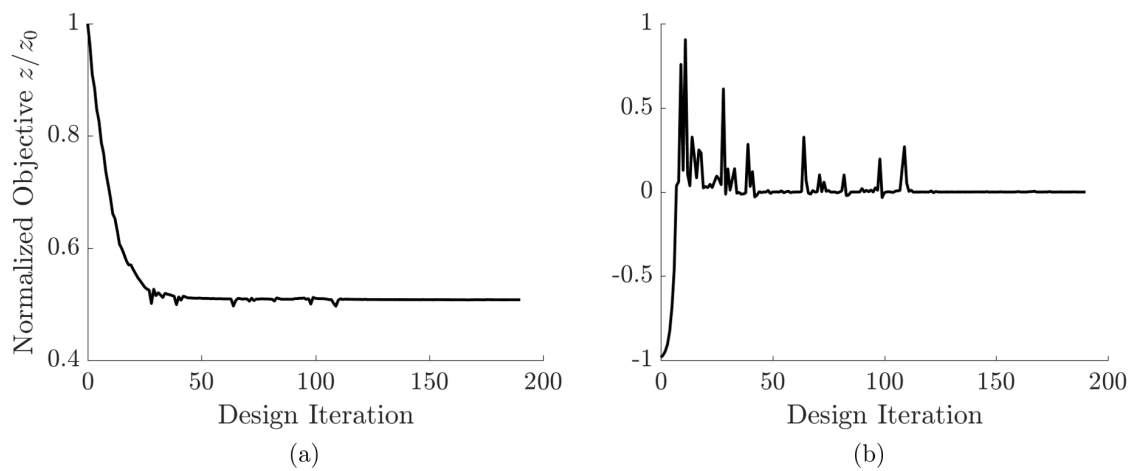
Figure 5.78: Evolution of (a) objective and (b) minimum feature size constraint for the four inclusion quarter symmetric geometrical example.

Table 5.11: Properties for the 2D short beam design problems.

Parameter	Value
Objective Weights	$w_i = [0.98, 0.01, 0.01]$
Minimum Feature Size Epsilon	$\epsilon_{FS} = 1.0 \cdot 10^{-4}$
Minimum Feature Size Radius	$r_m = 1h$
Helmholtz Smoothing Radius	$r_H = 1h$
Element Edge Length	$h = 0.5 \ mm$
Volume Constraint	$\gamma_v = 0.5$
Young's Modulus Phase I	$E = 2.0 \ GPa$
Poisson's Ratio Phase I	$\nu = 0.4$

constraint is shown in Figure 5.78. A similar behavior as observed for the same design problem solved on the full domain (see Figure 5.75) is seen.

5.6.3 Short Beam in 2D

Next, a solid-void linear elastic cantilevered short beam problem is studied in 2D. The main problem parameters are summarized in Table 5.11. The strain energy minimization problem subject to a volume constraint on phase I and a minimum feature size constraint is formulated as:

$$\min_{\mathbf{s}} \ z(\mathbf{s}, \mathbf{u}) = w_1 \frac{\mathcal{U}}{\mathcal{U}^0} + w_2 \frac{\int_{\Gamma_0^{I,II}} dS}{\int_{(\Gamma_0^{I,II})^0} dS} + w_3 \frac{p_{Reg}(\mathbf{s})}{p_{Reg}(\mathbf{s}^0)}$$

$$\text{s.t. } g_1 = \frac{\Omega_0^I}{(\Omega_0^I + \Omega_0^{II})} - \gamma_v \leq 0 \tag{5.6.2}$$

$$g_2 = \frac{p_{FS}}{(\Omega_0^I + \Omega_0^{II})} - \epsilon_{FS} \leq 0$$

The initial design with load and boundary conditions is shown in Figure 5.79 (a) where a traction load of $T_{X_2} = -3.0 \cdot 10^1 N/mm$ is applied at the free end. As before, the design domain is immersed and loading and boundary condition domains are prescribed to strictly be solid, thus excluded from the design domain. In addition, design symmetry along the X_1 axis is enforced. This is valid as under linear elasticity a compressional load case is equal and opposite of a tensional load case. The initial design is seeded with six circular void inclusions. The corresponding Laplacian field identifying the skeleton of the SDF is shown in Figure 5.79 (b). To improve stability of the feature
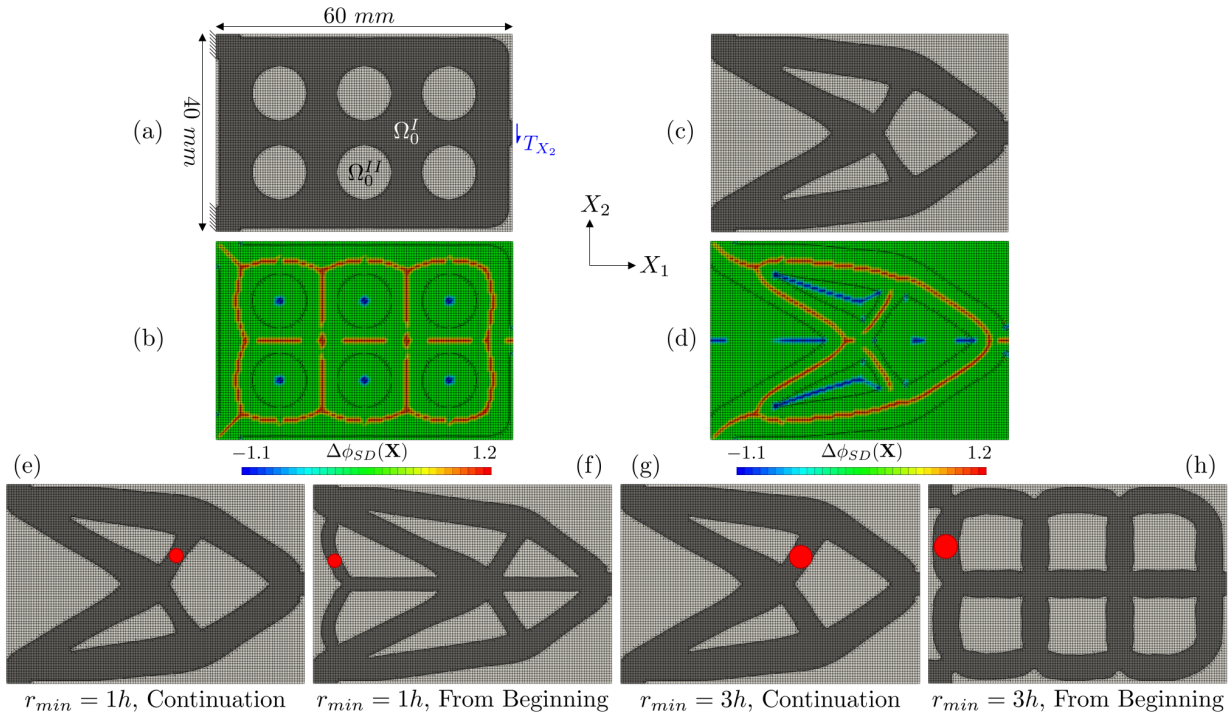
Figure 5.79: Different designs for the short beam problem in 2D. (a) Initial design, (b) corresponding Laplacian field, (c) final design without feature size control and (d) corresponding Laplacian field. (e) - (f) are designs with feature size control enforced.

size measure, smooth Laplacian projection is used. Therefore, gaps in the skeleton can be identified. The final design, without any feature size constraint is shown in Figure 5.79 (c), along with its Laplacian field shown in Figure 5.79 (d). It should be pointed out that the skeleton is clearly identified both in phase I (in red) and in phase II (in blue).

Using the skeleton-based feature size control, different design studies are conducted. First, a minimum feature size radius of $r_m = 1h$ is enforced in a continuation approach after 150 design iterations. The result is shown in Figure 5.79 (e). Only slight differences between the design without feature size control (Figure 5.79 (c)) and the one where a feature size constraint of $r_m = 1h$ was enforced after 150 design iterations (Figure 5.79 (e)) can be seen. If the feature size constraint of $r_m = 1h$ is enforced from the beginning of the design process, the design shown in Figure 5.79 (f) is obtained for this short beam design problem. As discussed before, topological changes are prevented by the feature size constraint and therefore a total of six void inclusions is retained at the final

Table 5.12: Relative change in strain energy of different 2D short beam designs using feature size control compared to a design without feature size control.

Problem	$r_m = 1h$ Continuation	$r_m = 1h$ From Beginning	$r_m = 3h$ Continuation	$r_m = 3h$ From Beginning
Relative Change in Strain Energy	-0.3 %	+12.7 %	+0.1 %	+191.7 %

design. It should be noted that even though a minimum feature size radius of $r_m = 1h$ is specified, the minimum obtained feature size radius is $r_{min} = 3h$. This is again due to the spreading of the skeleton by virtue of operator splitting for computing the SDF normal field and the SDF Laplacian field. For more details regarding this, see Section 4.4.3.3. The same studies are repeated with a minimum feature size of $r_m = 3h$, both using a continuation approach and enforcing the feature size constraint from the beginning. The results are shown in Figure 5.79 (g) and (h), respectively. While enforcing a minimum feature size of $r_m = 3h$ does not lead to a significantly different final design when employed in a continuation approach, enforcing it from the beginning significantly influences the final design.

The influence of enforcing a minimum feature size constraint on the strain energy of the final design is compared in Table 5.12. The relative change in strain energy of all designs with minimum feature size is computed with respect to the nominal design without feature size control, shown in Figure 5.79 (c). As expected, enforcing a minimum feature size constraint which leads to significant design changes drastically reduces the mechanical performance of the design. This can be mitigated if the feature size constraint is enforced after an initial geometry has been determined and enforcing a minimum feature size is only used to slightly modify the design, in a shape optimization sense. It is however not trivial to determine when to enable this additional constraint, as through this, the design space becomes inherently more non-convex and local minima are more likely to be identified.

5.6.4   Short Beam in 3D

The short beam design problem studied in Section 5.6.3 is repeated in 3D in this section. Design symmetries are enforced along the X_2 plane and the X_3 plane and mechanical symmetry along the X_3 plane is used to only analyze one half of the domain. The main problem parameters of Table 5.11 are used, whereas the element edge length is $h = 1.0 \ mm$. Smooth Laplacian truncation, as discussed in Section 4.4.3.1, is used for all 3D examples using feature size control.

5.6.4.1   Minimization of Strain Energy under Volume Phase I Constraint

The formulation of the optimization problem of Eqn.(5.6.2) is used where a volume constraint of $\gamma_v = 0.12$ is gradually enforced using a continuation approach. The initial design setup along with load and boundary conditions is shown in Figure 5.80 (a). A traction load of $T_{X_2} = -3.0 \cdot 10^1 N/mm$ is applied at the free end of the cantilevered beam. The final design, obtained without feature size control is shown in Figure 5.80 (b).

When in addition to the volume constraint a minimum feature size constraint is enforced (using a continuation approach), the final design shown in Figure 5.80 (d) is obtained. It can be seen that while the nominal design (Figure 5.80 (b)) is comprised of two vertical shear-webs resembling a shell-like structure, the design with a feature size constraint is made from a set of trusses arranged in a cross shape. When using LS-XFEM-based TO, it is well known that thin-walled structures are favored in 3D, while density-based TO typically forms truss-like structures [189]. It has been speculated by [189] that when enforcing minimum feature size control in combination with a LS-XFEM TO approach, similar truss-structures as obtained with density-based methods are obtained in 3D. This has however not been shown until this thesis. The clear difference between the final design without and with minimum feature size control can also be seen in the sliced view in Figure 5.80 (c) and (e) which are colored by the SDF Laplacian. It can also be seen that in Figure 5.80 (e) minimum feature size is enforced where the Laplacian (i.e., skeleton) is clearly developed in the center of the truss. When comparing the structural performance of both final designs (with and
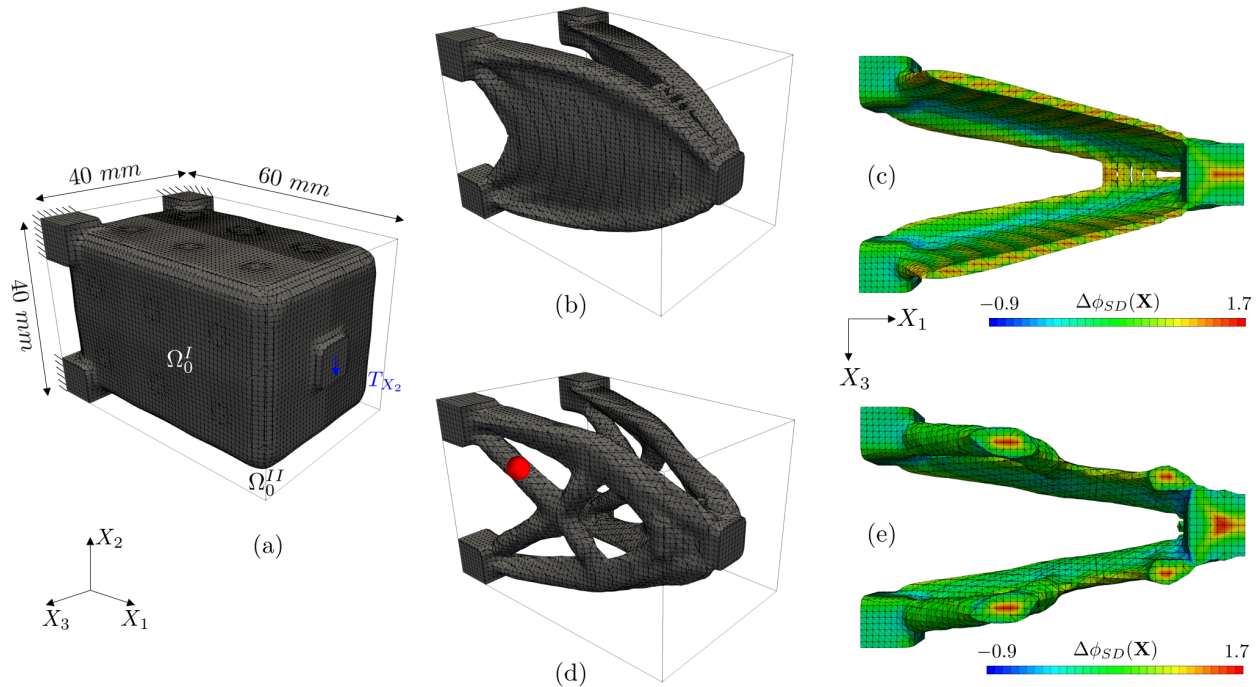
Figure 5.80: Short Beam problem in 3D, (a) initial design with boundary conditions, (b) final design under a volume constraint only, and (c) corresponding Laplacian field on the sliced final design. (d) Final design obtained with a volume constraint and a minimum feature size constraint, and (e) corresponding Laplacian field on the sliced final design.

without feature size control), a 9.0% increase in strain energy is observed when minimum feature size is enforced using a continuation approach.

The evolution of the normalized objective, the volume constraint and the minimum feature size
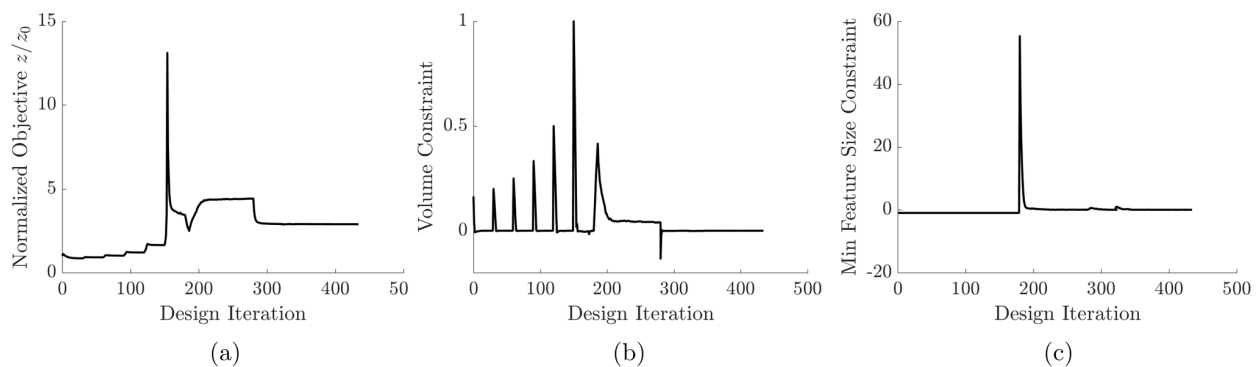
Figure 5.81: Evolution of (a) normalized objective, (b) volume constraint, and (c) minimum feature size constraint for the 3D short beam problem.

constraint is shown in Figure 5.81 where periodic increases of the volume constraint are due to the applied continuation scheme. Initially, a volume constraint of $\gamma_v = 0.6$ is enforced which is then reduced by 0.1 every 30 design iterations until a volume constraint of $\gamma_v = 0.1$ is reached at design iteration 150. At design iteration 180, the minimum feature size constraint is enabled. As it is however not possible to achieve both the minimum feature size constraint along with a volume constraint of $\gamma_v = 0.1$ (see violated volume constraint between design iteration 200 and 280), the volume constraint is relaxed to $\gamma_v = 0.12$ at design iteration 280. By doing so, both, the volume constraint and the minimum feature size constraint, can be satisfied. Overall, a smooth convergence of the design optimization problem is observed.

5.6.4.2   Minimization of Volume Phase I under Strain Energy Constraint

The drawback of formulating the short beam optimization problem as minimizing the strain energy subject to a volume constraint and a minimum feature size constraint is the need to use a continuation approach in order to gradually reduce the volume constraint, as discussed in Section 5.6.4.1. An alternative to this formulation is a volume phase I minimization problem subject to a strain energy constraint, which is studied in this section. In addition, the minimum feature size control is formulated as an objective penalty as opposed to a second constraint. The optimization problem is formulated as:

$$\min_{\mathbf{s}} \ z(\mathbf{s}, \mathbf{u}) = w_1 \Omega_0^I + w_2 \frac{\int_{\Gamma_0^{I,II}} dS}{\int_{(\Gamma_0^{I,II})^0} dS} + w_3 \frac{p_{Reg}(\mathbf{s})}{p_{Reg}(\mathbf{s}^0)} + w_4 \frac{p_{FS}}{(\Omega_0^I + \Omega_0^{II})} \tag{5.6.3}$$

$$\text{s.t. } g = \mathcal{U} - \bar{\mathcal{U}} \leq 0$$

where the strain energy threshold is set to $\bar{\mathcal{U}} = 2.3 \cdot 10^3 \ N/mm$. This reference value was chosen based on the results obtained in Section 5.6.4.1. The same initial design with load and boundary conditions as depicted in Figure 5.80 (a) is used for this study.

The final designs obtained without any minimum feature size penalty, with a feature size penalty applied through a continuation approach, and with minimum feature size penalty applied from the beginning of the optimization process are shown in Figure 5.82 (a), (c), and (e), respectively.
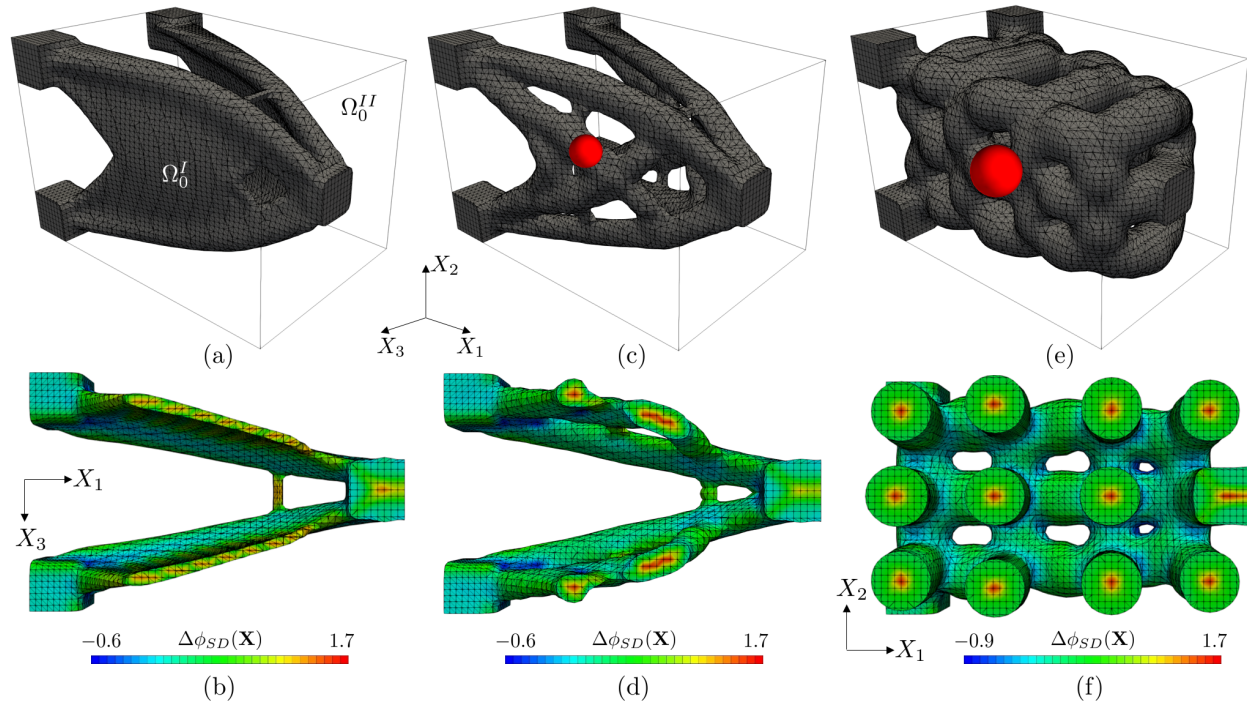
Figure 5.82: Short beam problem in 3D, where the volume of phase I is minimized under a strain energy constraint. (a) Final design obtained without minimum feature size penalty and (b) corresponding Laplacian field. (c) Final design obtained with a minimum feature size penalty using a continuation approach with (d) the Laplacian field for it. (e) Final design obtained with a minimum feature size penalty from the beginning and (f) it's Laplacian field on the sliced design.

The corresponding Laplacian field on the sliced designs are depicted in Figure 5.82 (b), (d), and (f), respectively. As can be seen, the alternative formulation of Eqn.(5.6.3) leads to a similar final design when no feature size is enforced. Comparing the final design shown in Figure 5.82 (a) with the corresponding one in Figure 5.80 (b) yields a decrease in volume of phase I of about 6.0% for the final design obtained by solving Eqn.(5.6.3). This can also be seen by the fact that the design in Figure 5.82 (a) has holes near the front of the beam while the design of Figure 5.80 (b) has continuous vertical shear-webs.

The design in Figure 5.82 (c), which was obtained by enforcing a minimum feature size penalty of 10.0% after 150 design iterations does exhibit a less pronounced truss structure compared to Figure 5.80 (d). This is due to the less restrictive formulation of the feature size control as a penalty (versus a constraint) in combination with minimizing the volume of phase I. The corresponding
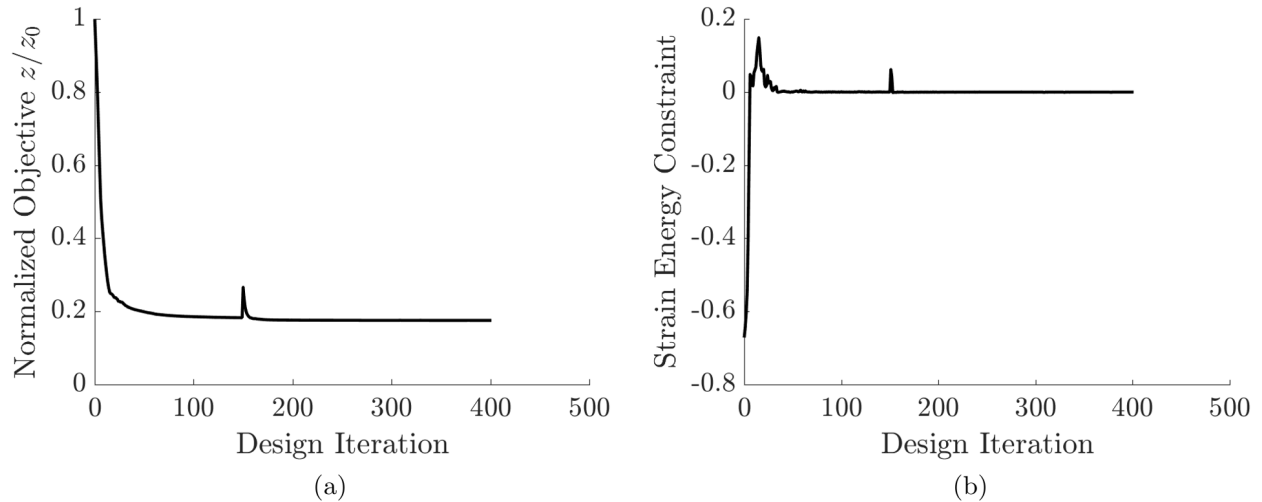
Figure 5.83: Evolution of (a) normalized objective and (b) strain energy constraint for the 3D short beam problem using a continuation approach for the feature size penalty.

evolution of normalized objective and strain energy constraint is shown in Figure 5.83. An increase in objective and constraint at design iteration 150 caused by the enforcement of the minimum feature size penalty can be seen. Compared to the design without any feature size penalty, the volume of phase I of this final design has only increased by about 7.0%.

The third final design shown in Figure 5.82 (e) is obtained by solving the optimization problem formulated in Eqn.(5.6.3) whereas a minimum feature size penalty of 5.0% is enabled from the beginning. This allows only for minimal changes in topology and leads to a final structure comprised of a network made of curved rods. Due to the strain energy constraint and the minimum feature size penalty, the overall volume of phase I cannot be minimized as much as in the previous two examples. Compared to the design without any feature size penalty (Figure 5.82 (a)), the volume of phase I has significantly increased by about 245.0%. It should also be pointed out that the minimum feature size obtained in Figure 5.82 (e) (indicated by a red sphere) is much larger than the one obtained in Figure 5.82 (c). This is attributed to a more pronounced Laplacian (i.e., skeleton) and more available volume which is preserved when the feature size penalty is enforced from the beginning on. As the feature size control is enforced as a penalty, it is looser than when employed through an additional constraint. This however results in the fact that local violations can occur. The
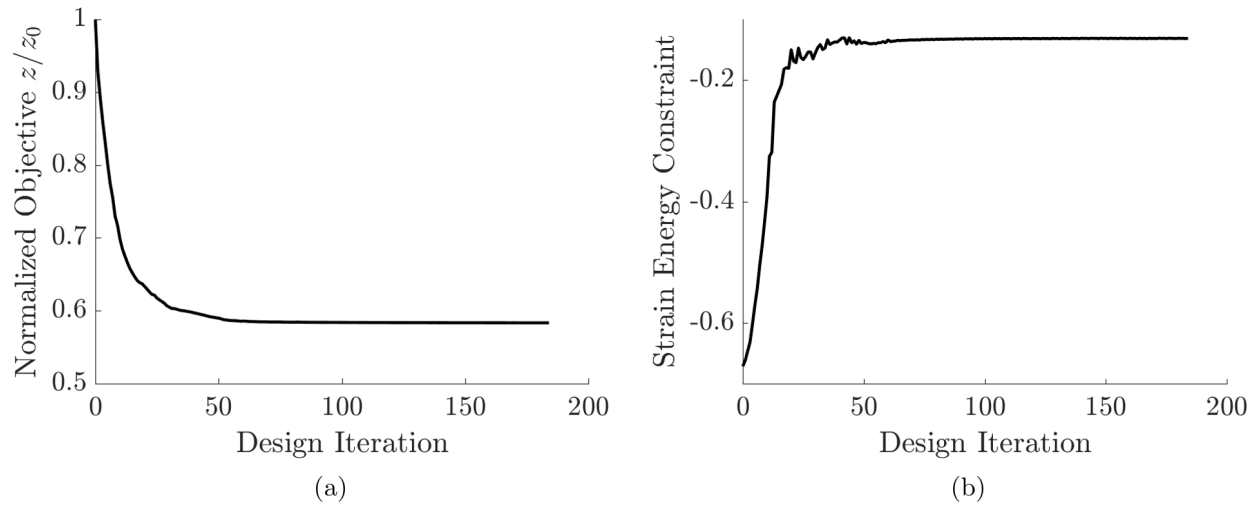
Figure 5.84: Evolution of (a) normalized objective and (b) strain energy constraint for the 3D short beam problem enforcing a feature size penalty from the beginning.

enforcement of different objective components thus highly depends on their weighting parameters w_i which are non-trivial to per-determine. The evolution of normalized objective and strain energy constraint is shown in Figure 5.84. While a smooth convergence behavior is seen, it should be pointed out that the converged objective value is significantly higher than the one obtained in Figure 5.83 (a) where the feature size penalty is enforced only after 150 design iterations.

5.6.5   Discussion

A minimum feature size measure for explicit LS-XFEM TO based on the SDF skeleton has been developed and demonstrated through numerical examples in 2D and 3D. While the skeleton approach comes with its own set of advantages and disadvantages (see Section 4.4.1), a wide applicability of the feature size control method was shown. The skeleton is identified by the Laplacian of the SDF which is computed using operator splitting and the SDF computed by the HM as a starting point. For a more detailed discussion, see Section 4.4.2. The applicability of the feature size control scheme was demonstrated via a purely geometrical example and linear elastic short beam examples in 2D and 3D. It was also shown that minimum feature size control can be achieved along domain boundaries if desired. This is especially useful when exploiting design symmetries in

order to reduce the computational cost. In addition, a long standing claim of obtaining truss-like structures in 3D LS-XFEM TO was proven, when minimum feature size is enabled. Typically, shear-web-type structures are obtained for 3D structural TO problems when a LS-XFEM is used, unlike density methods, which naturally favor truss-like designs. Through numerical examples, it was shown that the discretization dependency of the SDF Laplacian discussed in Section 5.6.1 is of minor importance for physics-driven problems. While slight oscillations in the evolution of the purely geometrical optimization problem (see Section 5.6.2) were observed, smooth behaviors were seen for all linear elastic examples in 2D and 3D. Smoothness in the SDF skeleton was introduced by smooth Laplacian truncation and smooth Laplacian projection, as discussed in Section 4.4.3.1 and 4.4.3.2, respectively.

As with most feature size approaches, a few open issues remain. The first one is the question of when to enable it and how to enforce it. It was shown that when using it from the beginning, local minima are identified and topological changes are prohibited. This oftentimes leads to clumsy and structurally low performing structures, especially when the feature size measure is enforced through a constraint. This can be avoided by only enabling the minimum feature size measure after a first design is found and topology changes have been performed. Then, the minimum feature size measure acts in a shape-optimization sense where only slight modifications of the design are made. It was seen that in those cases, the structural performance remains relatively unaffected. Alternatively, minimum feature size can also be enforced using a penalty method. Using this approach, topological changes are permitted to a certain degree, as the feature size measure enforcement is less strict. However, local violations of the feature size measure are also possible and the success of enforcing minimum feature size via an objective penalty largely depends on the weighting of the individual objective contributions. Since the current approach is based on computation of the SDF Laplacian via operator splitting, spreading of the SDF skeleton cannot be avoided. This means, exact feature size, as specified as a parameter in Eqn.(4.4.1) can never be achieved. In practice, a spreading of the skeleton to a minimum width of $4h$ was observed which was in parts caused by the applied Helmholtz smoothing required to achieve sufficient smoothness of higher-order spatial derivatives.

Finally, the proposed scheme requires rather fine background meshes in order to properly capture the SDF skeleton. This becomes however computationally costly, especially in 3D. In addition, discretization dependence of the SDF Laplacian on the orientation within the background mesh was seen. This may lead to undesired oscillations in the evolution of objective and constraints and needs to be addressed in future studies.
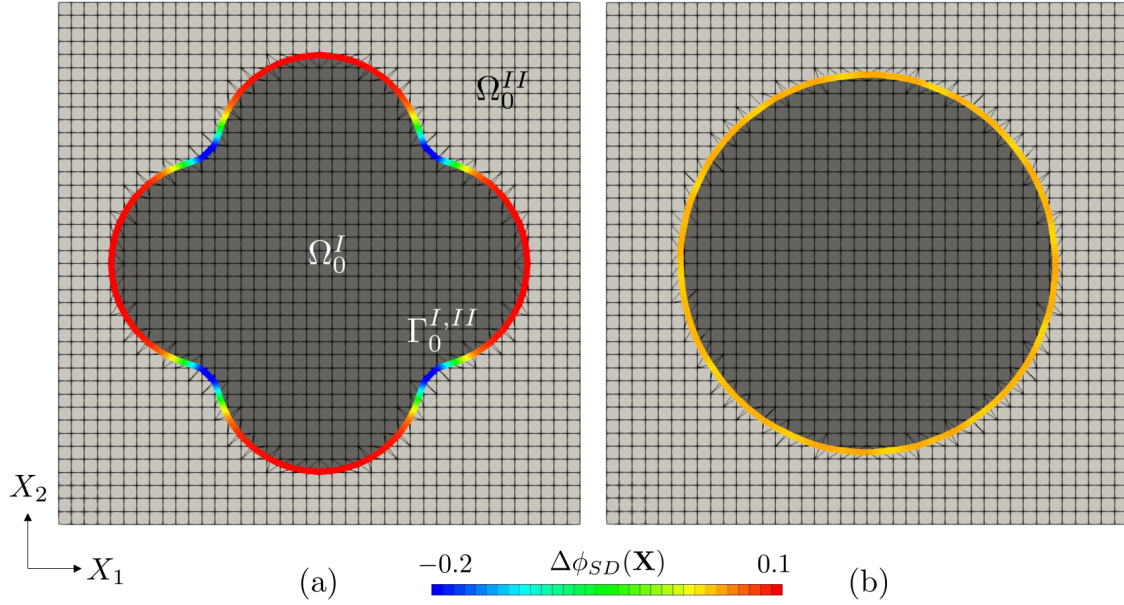
Figure 5.85: Mean curvature squared minimization problem. (a) Initial design and (b) final design.

5.7   Mean Curvature Measure

The mean curvature measure discussed in Section 4.5 is applied for regularization of a geometrical design optimization problem in this section. In order to compute the mean curvature at the XFEM interface, the smooth Laplacian projection scheme discussed in Section 4.4.3 cannot be used, since all Laplacian (i.e., mean curvature) information is projected to zero at the interface. Instead, the smooth truncation approach of the Laplacian field (see Section 4.4.3.1) is used. The purely geometric design optimization problem considered here is formulated as:

$$\min_{\mathbf{s}} \ z(\mathbf{s}, \mathbf{u}) = w_1 p_\kappa + w_2 \frac{p_{Reg}(\mathbf{s})}{p_{Reg}(\mathbf{s}^0)}$$

$$\text{s.t.} \ g = \Omega_0^I - (\Omega_0^I)^0 \leq 0$$

(5.7.1)

where p_κ is the squared mean curvature measure and $(\Omega_0^I)^0$ is the phase I domain volume at the initial design. The initial design of this geometrical design optimization problem is shown in Figure 5.85 (a). The initial design is chosen such that a non-uniform curvature is obtained along the XFEM interface. It should be pointed out that both positive and negative curvatures are represented well by the Laplacian field evaluated at the XFEM interface. As minimization of the mean curvature
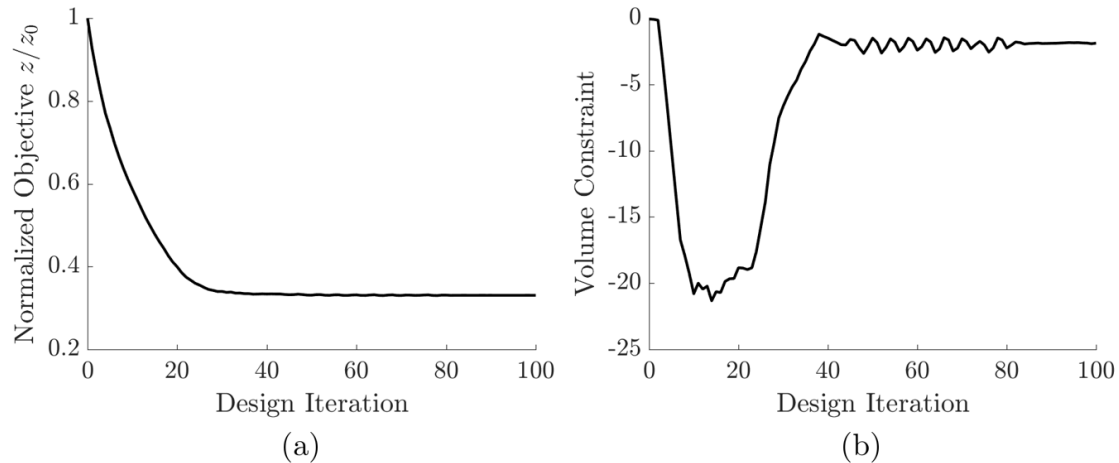
Figure 5.86: Evolution of (a) normalized objective and (b) volume constraint for the 2D mean curvature squared minimization problem.

squared is the main objective of Eqn.(5.7.1), a uniform interface geometry is obtained as shown in Figure 5.85 (b). The corresponding evolution of normalized objective and a volume constraint on phase I is shown in Figure 5.86.

While a smooth objective evolution is seen, it should be pointed out that the volume constraint is not active. This is due to the fact that the solution of the posed optimization problem is not unique. While the solution of Eqn.(5.7.1) only yields a regularized, i.e., uniform or circular interface geometry, neither the radius of this circle nor its center position are uniquely determined.

As presented by the numerical example considered in this section, minimizing the mean curvature squared based on the Laplacian of the SDF largely yields a regularized interface geometry. However, a closer look at the interface curvature of Figure 5.85 (b) needs to be taken. Slight oscillations of the mean curvature at the circular interface can be seen, even though the optimization problem has converged. These oscillations in the Laplacian field most likely stem from the fact that only straight XFEM interfaces are considered in this thesis. This means, the evaluation of the mean curvature by numerical integration of Eqn.(4.5.2) is in reality always slightly inward from the true, curved interface, as the triangulated XFEM interface is a straight line. From a numerical perspective, this leads to a small discrepancy between the true interface geometry and the desired

one, which is a perfect circle for the current problem.

Even though future work is needed to further study the oscillatory behavior of the regularized geometry obtained by minimization of the mean curvature squared, its applicability within LS-XFEM TO was successfully demonstrated. Since the mean curvature can directly be obtained from the Laplacian field, which is also used for minimum feature size control (see Section 4.4.3), it is computationally efficient to use mean curvature-based interface regularization in combination with skeleton-based minimum feature size control.

Chapter 6

Conclusions and Future Work

A design and analysis framework based on combined LS-XFEM-density TO was developed and presented in this thesis. Motivated by the goal to systematically design and predict the performance of active, self-folding structures, several aspects regarding computational design optimization have been studied and extended in this work. The main ideas are summarized in the following and areas of future work are identified.

In order to design active structures using TO, a most general analysis framework needed to be established. The work presented in this thesis is based on a multi-physics XFEM TO framework previously used for fluid-structure interaction problems [89], contact problems [109], optimization of flow problems [191, 190], and small strain structural mechanics [189].

A need for finite deformation kinematics is inherently present when simulating active structures that exhibit large deformations. Typically, self-deforming structures undergo large deformations and rotations either during the training process in the case of shape memory structures, during the activation or deployment process, or both. To accurately capture these phenomena, a finite strain computational XFEM framework was developed and tested in this thesis. The finite deformation model includes thermoelasticity at large strains which is essential for modeling inelastic printing strains as suggested by [45]. In order to obtain correct design sensitivities via the adjoint method, consistent tangent stiffness matrices needed to be derived. Moreover, XFEM interface conditions and weak boundary condition formulations using Nitsche's method [136] were developed for the large strain thermomechanical model. The finite strain thermomechanical model was validated

against a commercial FE package for three different nonlinear constitutive models. In addition, an experimental validation of the XFEM model for slender beam structures was performed.

To accurately capture the deformation of slender structures, locking phenomena of low order FEs need to be alleviated. This can either be achieved by reduced integration, shell element formulations or by higher-order spatial discretization. Similar locking phenomena are also experienced by low-order XFEM interpolation. A need for higher-order XFEM discretization in order to accurately predict the deformation of slender structures was identified in this thesis. With that, higher-order stabilization techniques need to be employed. A strong need for higher-order ghost stabilization in combination with higher-order XFEM was demonstrated in order to obtain well-conditioned linear systems. Through mesh refinement studies, it was demonstrated that higher-order convergence rates of the XFEM are only achieved if the geometric interface representation is increased in accordance with the underlying spatial discretization order of the background mesh. This means, for higher-order XFEM, capturing of curved interface geometries is necessary to obtain higher-order convergence rates with mesh refinement. Future studies should therefore address the currently lacking ability of the employed XFEM framework to capture curved interfaces in order to accurately resolve arbitrary interface geometries with improved accuracy.

As an alternative to higher-order XFEM discretization, an EAS method was studied for XFEM. The work initially proposed by [46] was followed and successfully applied to simple immersed geometries in 2D. An extension to more complex, arbitrarily intersected geometries however showed the limitations of the originally proposed approach. A need for a generally applicable EAS formulation for XFEM where the intersections are not aligned with the background mesh was identified and should be developed in future work.

During a solid-void TO process, isolated material domains may be present when features merge or disconnect. To stabilize these disconnected domains and to prevent rigid body motion, [190] proposed a selective springs approach based on an auxiliary indicator field for fluid flow problems. This approach was extended to structural mechanics in this thesis and successfully applied to stabilize small strain and large strain structural TO problems. Alternatively, globally

applied weak springs can be used which do not require the solution of an additional indicator field. It was however observed, that especially under consideration of finite deformations, global springs significantly influence the displacement prediction. It is therefore crucial to use selective springs for structural solid-void TO of active structures under consideration of finite deformations.

To further stabilize the XFEM framework, a nonlinear Jacobi preconditioner was proposed. Similar to a classical diagonal preconditioner, the Jacobi preconditioner is used on the nonlinear system to facilitate convergence of the nonlinear problem. Moreover, a consistent LS shifting scheme was developed in this thesis which should be studied in more depth in future work.

The developed LS-XFEM TO framework was used in this thesis for the design of self-folding origami structures. LS primitives were used to model the crease pattern which were determined through TO. While an initial applicability of TO as a systematic design tool for self-folding origami structures was shown, further studies are needed. Large strain kinematics should be included and higher-order XFEM discretization needs to be used to properly predict the physical performance of the origami structures. Moreover, the final designs should be printed and activated in order to validate the feasibility of the computationally determined origami designs.

Development and testing of combined LS-density TO approaches is a core part of this thesis. An uncoupled LS-density approach was used for solving multi-material TO problems. Optimizing the geometric layout of active structures and simultaneously the material distribution within the structure was successfully demonstrated. Active structures of various complexities were designed via the developed large strain LS-XFEM-density TO framework. The final designs where then printed and activated via direct 4D printing. While overall a good match between numerical predictions and experimental results was obtained, a strong need for including a contact formulation into the TO framework was identified. This is especially crucial when considering more complex self-folding structures where the unfolding sequence of multiple parts plays a critical role. As this was not the case in the presented work, a significant amount of self-penetration was seen for some structures. In addition, structural instabilities (e.g., buckling and snap-through) should be considered in future design studies of active structures. As studied by [148, 209, 48], accounting for structural instabilities

is crucial when analyzing slender structures subject to large amounts of compressive stress. These instabilities should be captured during the optimization process and either avoided or leveraged as a desired design feature.

In addition to the uncoupled LS-density approach, a loosely coupled combined approach was used to eliminate the mutual drawbacks of both pure density-based and pure LS-based TO. It was shown that by introducing a loose coupling between density and LS design variables through inequality constraints, hole nucleation is facilitated. This has been a long standing issue in explicit LS-XFEM TO where a large dependency of the final design on the initial hole seeding is typically observed. The newly proposed combined approach fully eliminates this issue. In addition, combining density-based and LS-based TO can be used for minimum feature size control, while retaining a crisp material interface modeled by the XFEM. While this superior TO approach was successfully applied to small strain structural TO problems in 2D and 3D, an extension to large strain kinematics and other physics should be considered in a next step.

A regularization scheme for explicit LS-XFEM TO was developed and studied in this thesis. It was demonstrated that a regularized and uniquely defined LSF is critical to ensure stability of the optimization problem. The novel regularization approach is based on the SDF obtained by the HM. General applicability of the regularization approach was shown for a wide range of physics through numerical examples in 2D and 3D. Moreover, a significant improvement in stability and convergence behavior of TO problems was seen when the explicit LS regularization scheme was used. However, more efficient distributed linear solver technologies should be explored in future work to offset the added computational cost by solving additional fields and degrees of freedom in order to reconstruct the SDF at every design iteration.

The SDF obtained though the HM can furthermore be used for minimum feature size control in LS-based TO. This is achieved through the skeleton approach by computing the Laplacian of the SDF. The work of [78] was followed and extended in this thesis to formulate a minimum feature size measure along the skeleton of the SDF. Moreover, the Laplacian of the SDF was used to obtain a penalty formulation on the mean curvature of the XFEM interface. It was shown that design

regularization can be obtained by that. A strong need for local (adaptive) mesh refinement was identified in order to more accurately resolve the SDF gradient and its discontinuities. This is crucial in order to unambiguously identify the SDF skeleton on which the minimum feature size measure is based. Moreover, a more robust skeleton identification method should be developed which is independent of the background discretization and the alignment of the XFEM intersections.

Chapter 7

Contributions

The original contributions made in the field of combined LS-XFEM-density TO of structural problems through the work presented in this thesis are summarized in the following:

(1) **Study of higher-order XFEM for TO of slender structures.** Higher-order XFEM discretization was studied in this thesis to accurately model the structural response for TO of slender structures. It is critical for both small strain and large strain kinematics, to use higher-order spatial discretization as one means to alleviate shear locking of low-order XFEM elements. More details on this are discussed in Section 3.2.3 and in Appendix B. In addition, mesh refinement studies of higher-order XFEM elements were conducted in Section 3.2.2.2. It was shown that higher-order convergence rates are only obtained when the order at which the interface geometry is captured corresponds to the discretization order of the background mesh. To achieve higher-order convergence rates with the XFEM, it is crucial to allow for a curved interface representation.

(2) **Extension of higher-order face-oriented ghost stabilization to problems with non-homogeneous materials.** The face-oriented ghost stabilization scheme originally proposed by [30, 156] was extended to a more generally applicable formulation in this thesis. Since the original, displacement gradient-based, penalty formulation is limited to homogeneous materials within a domain, an extension for combined LS-density-based TO was required. A novel stress-based and a virtual work-based ghost penalty formulation were

developed in Section 3.2.1. A verification of and application towards higher-order XFEM problems is presented in Section 3.2.2.1 and in Appendix B.

(3) **Extension of selective structural springs to linear elastic and nonlinear hyperelastic TO problems.** The selective spring concept originally proposed by [190] was extended and applied to structural problems in linear elasticity and nonlinear elasticity in this thesis. The formulation of the auxiliary indicator field and the selectively applied structural stabilization were discussed in Section 4.2.3. It was shown that selectively applying structural springs to only floating material domains is crucial when considering nonlinear kinematics for slender structures. This stabilization scheme was successfully applied for TO of active structures as presented in the publications listed in Appendices B and C.

(4) **Application of LS-XFEM TO for finding optimal crease patterns for self-folding origami structures.** LS-based TO using void primitives for modeling origami crease patterns was demonstrated in this thesis. As discussed in Section 4.1.2.2 and in Section 5.2, a unique LS-XFEM TO approach was proposed to solve design problems of self-folding origami structures made out of pre-stressed LAP sheets. The design approach was successfully applied towards traditional origami structures where the required folding lines were identified by the optimization scheme.

(5) **Combination of LS and density-based TO methods for optimization of multimaterial problems.** A novel multi-material TO approach was proposed through the combination of density-based and LS-based TO schemes. Two sets of independent design variables are introduced to simultaneously optimize the geometric layout and the material distribution of active structures. This approach was applied towards several design problems of self-deforming active structures as presented in Section 5.3 and in the publications included in Appendices B and C. It was shown that non-intuitive design layouts are obtained through the additional design freedom provided by the combined LS-density TO approach.

(6) **Experimental validation of optimized active structures through 4D printing.**
The optimized active structures presented in Section 5.3 and in Appendix C were fabricated
and activated via direct 4D printing. This provided additional confidence in the performance
of the developed LS-XFEM TO approach and demonstrated the applicability of the design
methodology towards real-world design optimization problems. Furthermore, 4D printed
physical samples were used for validation of the developed finite strain thermoelastic XFEM
model. For more details, see Section 5.1.2.

(7) **Development of a combined LS-density-based TO approach for hole nucleation
and minimum feature size control.** A coupled LS-density TO approach was proposed
yielding a superior TO scheme which builds on the advantages of pure density-based TO
and pure LS-XFEM-based TO (see Section 4.1.3.2). The novel method has the ability to
nucleate holes during the TO process, removing the need for initial seeding. This has been
a long-standing issue in explicit LS-XFEM TO as pointed out by [191]. Moreover, a physics-
based coupling approach can also be used to include minimum feature size control through
the density design variable field onto the LS field. Multiple design examples illustrating the
unique capabilities of this combined LS-density approach are presented in Section 5.4.

(8) **Development of a regularization scheme for explicit LS XFEM TO using the
HM.** A LS regularization scheme for explicit LS-XFEM TO was developed and tested in this
thesis. The regularization scheme is based on a penalty formulation between the design LSF
and a globally constructed target LSF (see Section 4.3). The target LSF is obtained from
the SDF which is computed using the HM [39, 40] at every design iteration. It was shown
that a significant amount of stability and increased convergence of optimization problems is
obtained when a smooth and regularized LS field is retained throughout the optimization
process. Numerical examples demonstrating the capabilities of the regularization scheme in
2D and 3D are discussed in Section 5.5 and in the publication presented in Appendix D.

(9) **Development of a feature size and curvature measure for explicit LS-XFEM TO based on the skeleton approach.** Using the SDF obtained by the HM, a minimum feature size measure is developed in this thesis. The approach originally proposed by [78] is applied to explicit LS-XFEM TO, where the Laplacian of the SDF is used for identification of the SDF skeleton. Operator splitting and L^2 projections are used in this thesis to compute higher-order spatial derivatives of the SDF. In addition, Helmholtz smoothing as originally proposed by [110] is used to introduce regularity into the SDF normal and Laplacian fields. The formulation of the feature size measure and the computation of the SDF Laplacian are presented in Section 4.4. Through numerical examples shown in Section 5.6, the applicability of the minimum feature size measure for explicit LS-XFEM TO was demonstrated. It was also shown for the first time that truss-like designs are obtained by LS-XFEM TO for 3D structures when a constraint on the minimum feature size is imposed. Without this constraint, shear-web designs are obtained. This claim was originally posed by [189] and was verified for the first time in this thesis. Moreover, an approach to selectively apply minimum feature size control along domain (symmetry) boundaries was developed. Finally, the computed Laplacian field of the SDF was used to control the mean curvature of the XFEM interface during TO. The formulation of the mean curvature measure and a numerical example demonstrating the applicability are presented in Sections 4.5 and 5.7, respectively.

Bibliography

[1] Niels Aage, Erik Andreassen, and Boyan Stefanov Lazarov. Topology optimization using PETSc: An easy-to-use, fully parallel, open source topology optimization framework. Structural and Multidisciplinary Optimization, 51(3):565–572, mar 2015.

[2] Oleg Alexandrov and Fadil Santosa. A topology-preserving level set method for shape optimization. Journal of Computational Physics, 204(1):121–130, mar 2005.

[3] G. Allaire, F. Jouve, and G. Michailidis. Casting constraints in structural optimization via a level-set method. In 10th World Congress on Structural and Multidisciplinary Optimization, number 1, pages 1–10, may 2013.

[4] G. Allaire, F. Jouve, and G. Michailidis. Thickness control in structural optimization via a level set method. Structural and Multidisciplinary Optimization, 53(6):1349–1382, jun 2016.

[5] Grégoire Allaire, François Jouve, and Anca Maria Toader. Une méthode de lignes de niveaux pour l'optimisation de forme. Comptes Rendus Mathematique, 334(12):1125–1130, jan 2002.

[6] Grégoire Allaire, François Jouve, and Anca Maria Toader. Structural optimization using sensitivity analysis and a level-set method. Journal of Computational Physics, 194(1):363–393, feb 2004.

[7] Grégorie Allaire, Frédéric de Gournay, François Jouve, and Anca-Maria Toader. Structural optimization using topological and shape sensitivity via a level set method. Control and cybernetics, 34(1):59–80, 2005.

[8] Samuel Amstutz. Connections between topological sensitivity analysis and material interpolation schemes in topology optimization. Structural and Multidisciplinary Optimization, 43(6):755–765, jun 2011.

[9] U. Andelfinger and E. Ramm. EAS-elements for two-dimensional, three-dimensional, plate and shell structures and their equivalence to HR-elements. International Journal for Numerical Methods in Engineering, 36(8):1311–1337, apr 1993.

[10] Ulrich Andelfinger. Untersuchungen zur Zuv. hybrid-gemischter FE fur Flachentragwerke. PhD thesis, Universität Stuttgart, 1991.

[11] J. S. Arora and Q. Wang. Review of formulations for structural and mechanical system optimization. Structural and Multidisciplinary Optimization, 30(4):251–272, oct 2005.

[12] Y. Bazilevs and T. J.R. Hughes. Weak imposition of Dirichlet boundary conditions in fluid mechanics. Computers and Fluids, 36(1):12–26, jan 2007.

[13] T. Belytschko and T. Black. Elastic crack growth in finite elements with minimal remeshing. International Journal for Numerical Methods in Engineering, 45(5):601–620, jun 1999.

[14] Ted Belytschko, Robert Gracie, and Giulio Ventura. A review of extended/generalized finite element methods for material modeling. Modelling and Simulation in Materials Science and Engineering, 17(4):043001, jun 2009.

[15] Ted Belytschko, Wing Kam Liu, and Brian Moran. Nonlinear Finite Elements For Continua And Structures, volume 104. Wiley, 2000.

[16] M. P. Bendsøe. Optimal shape design as a material distribution problem. Structural Optimization, 1(4):193–202, dec 1989.

[17] Martin P. Bendsøe and Ole Sigmund. Topology Optimization. Springer Berlin Heidelberg, Berlin, 2004.

[18] Martin Philip Bendsøe and Noboru Kikuchi. Generating optimal topologies in structural design using a homogenization method. Computer Methods in Applied Mechanics and Engineering, 71(2):197–224, nov 1988.

[19] P. Betsch, F. Gruttmann, and E. Stein. A 4-node finite shell element for the implementation of general hyperelastic 3D-elasticity at finite strains. Computer Methods in Applied Mechanics and Engineering, 130(1-2):57–79, mar 1996.

[20] Manfred Bischoff, E. Ramm, and J. Irslinger. Models and Finite Elements for Thin-Walled Structures. In Encyclopedia of Computational Mechanics Second Edition, volume 2, pages 1–86. John Wiley & Sons, Ltd, Chichester, UK, dec 2017.

[21] Thomas Borrvall and Joakim Petersson. Topology optimization of fluids in Stokes flow. International Journal for Numerical Methods in Fluids, 41(1):77–107, jan 2003.

[22] Blaise Bourdin. Filters in topology optimization. International Journal for Numerical Methods in Engineering, 50(9):2143–2158, mar 2001.

[23] Allan F. Bower. Applied Mechanics of Solids. CRC Press, oct 2010.

[24] Tyler E. Bruns and Daniel A. Tortorelli. Topology optimization of non-linear elastic structures and compliant mechanisms. Computer Methods Applied Mechanical Engineering, 190(26):3443–3459, mar 1999.

[25] Martin Burger, Benjamin Hackl, and Wolfgang Ring. Incorporating topological derivatives into level set methods. Journal of Computational Physics, 194(1):344–362, feb 2004.

[26] Erik Burman, Susanne Claus, Peter Hansbo, Mats G. Larson, and André Massing. CutFEM: Discretizing geometry and partial differential equations. International Journal for Numerical Methods in Engineering, 104(7):472–501, nov 2015.

[27] Erik Burman, Daniel Elfverson, Peter Hansbo, Mats G. Larson, and Karl Larsson. Cut Topology Optimization for Linear Elasticity with Coupling to Parametric Nondesign Domain Regions. arxiv.org, sep 2018.

[28] Erik Burman and Peter Hansbo. Fictitious domain finite element methods using cut elements: I. A stabilized Lagrange multiplier method. Computer Methods in Applied Mechanics and Engineering, 199(41-44):2680–2686, oct 2010.

[29] Erik Burman and Peter Hansbo. Fictitious domain finite element methods using cut elements: II. A stabilized Nitsche method. Applied Numerical Mathematics, 62(4):328–341, apr 2012.

[30] Erik Burman and Peter Hansbo. Fictitious domain methods using cut elements: III. A stabilized Nitsche method for Stokes' problem. ESAIM: Mathematical Modelling and Numerical Analysis, 48(3):859–874, may 2014.

[31] Philip R. Buskohl, Kazuko Fuchi, Greg W. Reich, James J. Joo, and Richard A. Vaia. Design tools for adaptive origami devices. In Thomas George, Achyut K. Dutta, and M. Saif Islam, editors, Micro- and Nanotechnology Sensors, Systems, and Applications VII, volume 9467, page 946719. International Society for Optics and Photonics, jun 2015.

[32] Rui P.R. Cardoso, Jeong Whan Yoon, M. Mahardika, S. Choudhry, R. J.Alves de Sousa, and R. A.Fontes Valente. Enhanced assumed strain (EAS) and assumed natural strain (ANS) methods for one-point quadrature solid-shell elements. International Journal for Numerical Methods in Engineering, 75(2):156–187, jul 2008.

[33] Shikui Chen, Michael Yu Wang, and Ai Qun Liu. Shape feature control in structural topology optimization. CAD Computer Aided Design, 40(9):951–962, sep 2008.

[34] Kwok Wah Cheng and Thomas Peter Fries. Higher-order XFEM for curved strong and weak discontinuities. International Journal for Numerical Methods in Engineering, 82(5):564–590, apr 2010.

[35] Christof Hausser. Effiziente Dreieckselemente für Flächentragwerke. PhD thesis, Universität Stuttgart, 1996.

[36] Peter Coffin and Kurt Maute. Level set topology optimization of cooling and heating devices using a simplified convection model. Structural and Multidisciplinary Optimization, 53(5):985–1003, may 2016.

[37] Peter B Coffin. LS-XFEM TO with Applications to Convective Heat Transfer. PhD thesis, University of Colorado Boulder, jan 2015.

[38] Robert D Cook, Davis S Malkus, Michael E Plesha, and Robert J Witt. Concepts and applications of finite element analysis. Wiley, 2002.

[39] Keenan Crane, Clarisse Weischedel, and Max Wardetzky. Geodesics in Heat. ACM Transactions on Graphics, 32(5):1–11, sep 2012.

[40] Keenan Crane, Clarisse Weischedel, and Max Wardetzky. The Heat Method for Distance Computation. Communications of the ACM, 60(11):90–99, oct 2017.

[41] M. J. De Ruiter and F. Van Keulen. Topology optimization: approaching the material distribution problem using topological function description. In Computational techniques for materials, composites and composite structures, pages 111–119. Civil-Comp, 2001.

[42] E.A. de Souza Neto, D. Perić, M. Dutko, and D.R.J. Owen. Design of simple low order finite elements for large strain analysis of nearly incompressible solids. International Journal of Solids and Structures, 33(20-22):3277–3296, aug 1996.

[43] Joshua D. Deaton and Ramana V. Grandhi. A survey of structural and multidisciplinary continuum topology optimization: Post 2000. Structural and Multidisciplinary Optimization, 49(1):1–38, jan 2014.

[44] Zhen Ding, Oliver Weeger, H. Jerry Qi, and Martin L. Dunn. 4D rods: 3D structures via programmable 1D composite rods. Materials & Design, 137:256–265, jan 2018.

[45] Zhen Ding, Chao Yuan, Xirui Peng, Tiejun Wang, H. Jerry Qi, and Martin L. Dunn. Direct 4D printing via active composite materials. Science Advances, 3(4):e1602890, apr 2017.

[46] J. E. Dolbow and A. Devan. Enrichment of enhanced assumed strain approximations for representing strong discontinuities: Addressing volumetric incompressibility and the discontinuous patch test. International Journal for Numerical Methods in Engineering, 59(1):47–67, jan 2004.

[47] Kristell Dréau, Nicolas Chevaugeon, and Nicolas Moës. Studied X-FEM enrichment to handle material interfaces with higher order finite element. Computer Methods in Applied Mechanics and Engineering, 199(29-32):1922–1936, jun 2010.

[48] Martin L. Dunn, Yanhang Zhang, and Victor M. Bright. Deformation and structural stability of layered plate microstructures subjected to thermal loading. Journal of Microelectromechanical Systems, 11(4):372–384, aug 2002.

[49] Alexander Düster. High Order Finite Elements for 3D, Thin Walled Nonlinear Continua. PhD thesis, Technische Universität München, 2002.

[50] Ata A. Eftekharian and Horea T. Ilie. Distance functions and skeletal representations of rigid and non-rigid planar shapes. Computer-Aided Design, 41(12):865–876, dec 2009.

[51] Hans A Eschenauer and Niels Olhoff. Topology optimization of continuum structures: A review. Applied Mechanics Reviews, 54(4):331, 2001.

[52] Carlos Felippa. Advanced Finite Element Methods. CAS, 1(April):1–62, 2018.

[53] Moritz A Frenzel. Adv. Structural FEM of Arterial Walls for Patient-Specific Geometries. PhD thesis, Technische Universität München, 2009.

[54] Thomas Peter Fries and Ted Belytschko. The extended/generalized finite element method: An overview of the method and its applications. International Journal for Numerical Methods in Engineering, 84(3):253–304, aug 2010.

[55] Junjian Fu, Hao Li, Mi Xiao, Liang Gao, and Sheng Chu. Topology optimization of shell-infill structures using a distance regularized parametric level-set method. Structural and Multidisciplinary Optimization, pages 1–14, aug 2018.

[56] Kazuko Fuchi, Philip R. Buskohl, Giorgio Bazzan, Michael F. Durstock, Gregory W. Reich, Richard A. Vaia, and James J. Joo. Design Optimization Challenges of Origami-Based Mechanisms With Sequenced Folding. Journal of Mechanisms and Robotics, 8(5):051011, may 2016.

[57] Kazuko Fuchi, Philip R. Buskohl, James J. Joo, Gregory W. Reich, and Richard A. Vaia. Topology Optimization for Design of Origami-Based Active Mechanisms. In Proceedings of the ASME 2014 International Design Engineering Technical Conferences & Computers and Information in Engineering Conference (IDETC/CIE 2014), pages DETC2014–35153. ASME, aug 2014.

[58] Kazuko Fuchi, Philip R. Buskohl, Taylor Ware, Richard A. Vaia, Timothy J. White, Gregory W. Reich, and James J. Joo. Inverse Design of LCN Films for Origami Applications Using Topology Optimization. ASME 2014 Conference on Smart Materials, Adaptive Structures and Intelligent Systems, pages V001T01A011–V001T01A011, sep 2014.

[59] Kazuko Fuchi and Alejandro R. Diaz. Origami Design by Topology Optimization. Journal of Mechanical Design, 135(11):111003, sep 2013.

[60] Kazuko Fuchi and Alejandro R. Diaz. Origami Design by Topology Optimization. Journal of Mechanical Design, 135(11):111003, sep 2013.

[61] Kazuko Fuchi, Taylor H. Ware, Philip R. Buskohl, Gregory W. Reich, Richard A. Vaia, Timothy J. White, and James J. Joo. Topology optimization for the design of folding liquid crystal elastomer actuators. Soft Matter, 11(37):7288–7295, 2015.

[62] Kazuko Fuchi, Taylor H. Ware, Philip R. Buskohl, Gregory W. Reich, Richard A. Vaia, Timothy J. White, and James J. Joo. Topology optimization for the design of folding liquid crystal elastomer actuators. Soft Matter, 11(37):7288–7295, sep 2015.

[63] Arun L. Gain and Glaucio H. Paulino. A critical comparative assessment of differential equation-driven methods for structural topology optimization. Structural and Multidisciplinary Optimization, 48(4):685–710, oct 2013.

[64] Qi Ge, Conner K Dunn, H Jerry Qi, and Martin L Dunn. Active origami by 4D printing. Smart Materials and Structures, 23(9):094007, sep 2014.

[65] Qi Ge, H. Jerry Qi, and Martin L. Dunn. Active materials by four-dimension printing. Applied Physics Letters, 103(13):131901, sep 2013.

[66] Hae Chang Gea and Jianhui Luo. Topology optimization of structures with geometrical nonlinearities. Computers and Structures, 79(20-21):1977–1985, aug 2001.

[67] Markus J. Geiss, Jorge L. Barrera, Narasimha Bodetti, and Kurt Maute. A Regularization Scheme for Explicit Level-Set XFEM Topology Optimization. Frontiers of Mechanical Engineering, 2019.

[68] Markus J. Geiss, Narasimha Boddeti, Oliver Weeger, Kurt Maute, and Martin L. Dunn. Combined Level-Set-XFEM-Density Topology Optimization of 4D Printed Structures undergoing Large Deformation. Journal of Mechanical Design, nov 2018.

[69] Markus J. Geiss and Kurt Maute. Topology Optimization of Active Structures using a Higher-Order Level-Set-XFEM-Density Approach. In 2018 Multidisciplinary Analysis and Optimization Conference, Reston, Virginia, jun 2018. American Institute of Aeronautics and Astronautics.

[70] Axel Gerstenberger and Wolfgang A. Wall. An eXtended Finite Element Method/Lagrange multiplier based approach for fluid-structure interaction. Computer Methods in Applied Mechanics and Engineering, 197(19-20):1699–1714, mar 2008.

[71] Frederic Gibou, Ronald Fedkiw, and Stanley Osher. A review of level-set methods and some recent applications. Journal of Computational Physics, 353:82–109, jan 2017.

[72] Stephanie Golmon, Kurt Maute, and Martin L. Dunn. Multiscale design optimization of lithium ion batteries using adjoint sensitivity analysis. International Journal for Numerical Methods in Engineering, 92(5):475–494, nov 2012.

[73] José Gomes and Olivier Faugeras. Reconciling distance functions and level sets. Journal of Visual Communication and Image Representation, 11(2):209–223, jun 2000.

[74] J. K. Guest, J. H. Prévost, and T. Belytschko. Achieving minimum length scale in topology optimization using nodal design variables and projection functions. International Journal for Numerical Methods in Engineering, 61(2):238–254, 2004.

[75] James K. Guest. Imposing maximum length scale in topology optimization. Structural and Multidisciplinary Optimization, 37(5):463–473, feb 2009.

[76] James K. Guest. Topology optimization with multiple phase projection. Computer Methods in Applied Mechanics and Engineering, 199(1-4):123–135, dec 2009.

[77] Xu Guo, Weisheng Zhang, and Wenliang Zhong. Doing Topology Optimization Explicitly and GeometricallyA New Moving Morphable Components Based Framework. Journal of Applied Mechanics, 81(8):081009, may 2014.

[78] Xu Guo, Weisheng Zhang, and Wenliang Zhong. Explicit feature control in structural topology optimization via level set method. Computer Methods in Applied Mechanics and Engineering, 272:354–378, apr 2014.

[79] Bertil Gustafsson. The Convergence Rate for Difference Approximations to Mixed Initial Boundary Value Problems. Mathematics of Computation, 29(130):396, apr 1975.

[80] R. B. Haber, C. S. Jog, and M. P. Bendsøe. A new approach to variable-topology shape design using a constraint on perimeter. Structural Optimization, 11(1):1–12, feb 1996.

[81] R.B. Haber and M.P. Bendsøe. Problem formulation, solution procedures and geometric modeling: Key issues in variable-topology optimization. In 7th AIAA/USAF/NASA/ISSMO Symposium on Multidisciplinary Analysis and Optimization, Reston, Virigina, sep 1998. American Institute of Aeronautics and Astronautics.

[82] Anita Hansbo and Peter Hansbo. A finite element method for the simulation of strong and weak discontinuities in solid mechanics. Computer Methods in Applied Mechanics and Engineering, 193(33-35):3523–3540, aug 2004.

[83] Daniel Hartmann, Matthias Meinke, and Wolfgang Schröder. The constrained reinitialization equation for level set methods. Journal of Computational Physics, 229(5):1514–1535, mar 2010.

[84] Z. Hashin and S. Shtrikman. A variational approach to the theory of the elastic behaviour of multiphase materials. Journal of the Mechanics and Physics of Solids, 11(2):127–140, mar 1963.

[85] W.S. Hemp. Michell's structural continua optimum structures. Clarendon Press, 1973.

[86] G Holzapfel. Nonlinear solid mechanics: A continuum approach for engineering, volume First Edit. Kluwer Academic Publishers, 2000.

[87] Thomas J. R. Hughes, Robert L. Taylor, and Worsak Kanoknukulchai. A simple and efficient finite element for plate bending. International Journal for Numerical Methods in Engineering, 11(10):1529–1543, jan 1977.

[88] Miche Jansen. Explicit level set and density methods for topology optimization with equivalent minimum length scale constraints. Structural and Multidisciplinary Optimization, pages 1–14, dec 2018.

[89] Nicholas Jenkins and Kurt Maute. Level set topology optimization of stationary fluid-structure interaction problems. Structural and Multidisciplinary Optimization, 52(1):179–195, jul 2015.

[90] Long Jiang and Shikui Chen. Parametric structural shape & topology optimization with a variational distance-regularized level set method. Computer Methods in Applied Mechanics and Engineering, 321:316–336, jul 2017.

[91] Wen Jiang, Chandrasekhar Annavarapu, John E. Dolbow, and Isaac Harari. A robust Nitsche's formulation for interface problems with spline-based finite elements. International Journal for Numerical Methods in Engineering, 104(7):676–696, jun 2015.

[92] Milan Jirásek. Comparative study on finite elements with embedded discontinuities. Computer Methods in Applied Mechanics and Engineering, 188(1):307–330, jul 2000.

[93] Zhan Kang and Yiqiang Wang. Integrated topology optimization with embedded movable holes based on combined description by material density and level sets. Computer Methods in Applied Mechanics and Engineering, 255:1–13, mar 2013.

[94] Atsushi Kawamoto, Tadayoshi Matsumori, Shintaro Yamasaki, Tsuyoshi Nomura, Tsuguo Kondoh, and Shinji Nishiwaki. Heaviside projection based topology optimization by a PDE-filtered scalar function. Structural and Multidisciplinary Optimization, 44(1):19–24, jul 2011.

[95] Roman Kemmler. Große Verschiebungen und Stabilität in der Topologie- und Formoptimierung. PhD Thesis, Universität Stuttgart, page 187, 2004.

[96] R. Kimmel and A. M. Bruckstein. Shape offsets via level sets. Computer-Aided Design, 25(3):154–162, 1993.

[97] Anders Klarbring and Niclas Strömberg. Topology optimization of hyperelastic bodies including non-zero prescribed displacements. Structural and Multidisciplinary Optimization, 47(1):37–48, jan 2013.

[98] Frank Koschnick. Geom. Locking-Eff. bei FE und ein allg. Konzept zu ihrer Vermeidung. PhD thesis, Technische Universität München, 2004.

[99] Frank Koschnick, Manfred Bischoff, Natalia Camprubí, and Kai Uwe Bletzinger. The discrete strain gap method and membrane locking. Computer Methods in Applied Mechanics and Engineering, 194(21-24 SPEC. ISS.):2444–2463, jun 2005.

[100] Gerhard Kreisselmeier and Reinhold Steinhauser. Application of vector performance optimization to a robust control loop design for a fighter aircraft. International Journal of Control, 37(2):251–284, feb 1983.

[101] Sebastian Kreissl and Kurt Maute. Levelset based fluid topology optimization using the extended finite element method. Structural and Multidisciplinary Optimization, 46(3):311–326, sep 2012.

[102] Sebastian Kreissl, Georg Pingen, and Kurt Maute. An explicit level set approach for generalized shape optimization of fluids with the lattice Boltzmann method. International Journal for Numerical Methods in Fluids, 65(5):496–519, feb 2011.

[103] Sebastian Kreissl, Georg Pingen, and Kurt Maute. Topology optimization for unsteady flow. International Journal for Numerical Methods in Engineering, 87(13):1229–1253, 2011.

[104] Xiao Kuang, Devin J. Roach, Jiangtao Wu, Craig M. Hamel, Zhen Ding, Tiejun Wang, Martin L. Dunn, and Hang Jerry Qi. Advances in 4D Printing: Materials and Applications. Advanced Functional Materials, page 1805290, nov 2018.

[105] Tsz-Ho Kwok, Charlie C. L. Wang, Dongping Deng, Yunbo Zhang, and Yong Chen. Four-Dimensional Printing for Freeform Surfaces: Design Optimization of Origami and Kirigami Structures. Journal of Mechanical Design, 137(11):111413, oct 2015.

[106] Patrick Laborde, Julien Pommier, Yves Renard, and Michel Salaün. High-order extended finite element method for cracked domains. International Journal for Numerical Methods in Engineering, 64(3):354–381, sep 2005.

[107] Christapher Lang, David Makhija, Alireza Doostan, and Kurt Maute. A simple and efficient preconditioning scheme for heaviside enriched XFEM. Computational Mechanics, 54(5):1357–1374, nov 2014.

[108] Robert J. Lang, Kyler Tolman, Erica Crampton, Spencer P. Magleby, and Larry L. Howell. Accommodating Thickness in Origami-Inspired Engineered Systems. Applied Mechanics Reviews, 70(1):010805, feb 2018.

[109] Matthew Lawry and Kurt Maute. Level set shape and topology optimization of finite strain bilateral contact problems. International Journal for Numerical Methods in Engineering, 113(8):1340–1369, 2018.

[110] B. Lazarov and Ole Sigmund. Sensitivity filters in topology optimisation as a solution to Helmholtz type differential equation. In 8th World Congress on Structural and Multidisciplinary Optimization, pages 1–10, 2009.

[111] B. S. Lazarov and O. Sigmund. Filters in topology optimization based on Helmholtz-type differential equations. International Journal for Numerical Methods in Engineering, 86(6):765–781, may 2011.

[112] Boyan S. Lazarov, Fengwen Wang, and Ole Sigmund. Length scale and manufacturability in density-based topology optimization. Archive of Applied Mechanics, 86(1-2):189–218, jan 2016.

[113] A. Legay, H. W. Wang, and T. Belytschko. Strong and weak arbitrary discontinuities in spectral finite elements. International Journal for Numerical Methods in Engineering, 64(8):991–1008, oct 2005.

[114] Chunming Li, Chenyang Xu, Changfeng Gui, and Martin D. Fox. Level set evolution without re-initialization: A new variational formulation. In Proceedings - 2005 IEEE Computer Society Conference on Computer Vision and Pattern Recognition, CVPR 2005, volume I, pages 430–436. IEEE, 2005.

[115] Chunming Li, Chenyang Xu, Changfeng Gui, and Martin D. Fox. Distance regularized level set evolution and its application to image segmentation. IEEE Transactions on Image Processing, 19(12):3243–3254, dec 2010.

[116] Jikai Liu, Lei Li, and Yongsheng Ma. Uniform thickness control without pre-specifying the length scale target under the level set topology optimization framework. Advances in Engineering Software, 115:204–216, jan 2018.

[117] Ying Liu, Julie K. Boyles, Jan Genzer, and Michael D. Dickey. Self-folding of polymer sheets using local light absorption. Soft Matter, 8(6):1764–1769, jan 2012.

[118] Junzhao Luo, Zhen Luo, Shikui Chen, Liyong Tong, and Michael Yu Wang. A new level set method for systematic design of hinge-free compliant mechanisms. Computer Methods in Applied Mechanics and Engineering, 198(2):318–331, dec 2008.

[119] Zhen Luo, Micheal Yu Wang, Shengyin Wang, and Peng Wei. A level set-based parameterization method for structural shape and topology optimization. International Journal for Numerical Methods in Engineering, 76(1):1–26, oct 2008.

[120] Richard H. Macneal. A theorem regarding the locking of tapered fournoded membrane elements. International Journal for Numerical Methods in Engineering, 24(9):1793–1799, sep 1987.

[121] David Makhija and Kurt Maute. Numerical instabilities in level set topology optimization with the extended finite element method. Structural and Multidisciplinary Optimization, 49(2):185–197, feb 2014.

[122] David Makhija and Kurt Maute. Level set topology optimization of scalar transport problems. Structural and Multidisciplinary Optimization, 51(2):267–285, feb 2015.

[123] Tadayoshi Matsumori, Atsushi Kawamoto, Tsuguo Kondoh, Tsuyoshi Nomura, and Hidetaka Saomoto. Boundary shape design by using PDE filtered design variables. Structural and Multidisciplinary Optimization, 56(3):619–629, sep 2017.

[124] Kurt Maute. Topology Optimization. In Encyclopedia of Computational Mechanics Second Edition, pages 1–34. John Wiley & Sons, Ltd, Chichester, UK, dec 2017.

[125] Kurt Maute, Anton Tkachuk, Jiangtao Wu, H. Jerry Qi, Zhen Ding, and Martin L. Dunn. Level Set Topology Optimization of Printed Active Composites. Journal of Mechanical Design, 137(11):111402, 2015.

[126] Ursula M. Mayer, Axel Gerstenberger, and Wolfgang A. Wall. Interface handling for three-dimensional higher-order XFEM-computations in fluid-structure interaction. International Journal for Numerical Methods in Engineering, 79(7):846–869, aug 2009.

[127] Georgios Michailidis. Manufacturing Constraints and Multi-Phase Shape and TO via a LSM. PhD thesis, Ecole Polytechnique, jan 2014.

[128] A.G.M. Michell. The limits of economy of material in frame-structures. Philosophical Magazine Series 6, 8(47):589–597, nov 1904.

[129] H. P. Mlejnek. Some aspects of the genesis of structures. Structural Optimization, 5(1-2):64–69, mar 1992.

[130] Nicolas Moës, John Dolbow, and Ted Belytschko. A finite element method for crack growth without remeshing. International Journal for Numerical Methods in Engineering, 46(1):131–150, sep 1999.

[131] U. Montanari. A Method for Obtaining Skeletons Using a Quasi-Euclidean Distance. Journal of the ACM, 15(4):600–624, oct 1968.

[132] Xiaoming Mu, Nancy Sowan, Julia A. Tumbic, Christopher N. Bowman, Patrick T. Mather, and H. Jerry Qi. Photo-induced bending in a light-activated polymer laminated composite. Soft Matter, 11(13):2673–2682, mar 2015.

[133] T. Mura and P. C. Cheng. The Elastic Field Outside an Ellipsoidal Inclusion. Journal of Applied Mechanics, 44(4):591, 1977.

[134] Jun Hee Na, Arthur A. Evans, Jinhye Bae, Maria C. Chiappelli, Christian D. Santangelo, Robert J. Lang, Thomas C. Hull, and Ryan C. Hayward. Programming reversibly self-folding origami with micropatterned photo-crosslinkable polymer trilayers. Advanced Materials, 27(1):79–85, jan 2015.

[135] H. Neuber. Ein neuer Ansatz zur Lösung räumlicher Probleme der Elastizitätstheorie. Der Hohlkegel unter Einzellast als Beispiel. ZAMM - Zeitschrift für Angewandte Mathematik und Mechanik, 14(4):203–212, jan 1934.

[136] J A Nitsche. Über ein Variationsprinzip zur Lösung von Dirichlet-Problemen bei Verwendung von Teilräumen, die keinen Randbedingungen unteworfen sind,. Abh. Math. Sem. Univ. Hamburg, 36:9–15, 1971.

[137] Lise Noël and Pierre Duysinx. Shape optimization of microstructural designs subject to local stress constraints within an XFEM-level set framework. Structural and Multidisciplinary Optimization, 55(6):2323–2338, jun 2017.

[138] Julian A. Norato, Martin P. Bendsøe, Robert B. Haber, and Daniel A. Tortorelli. A topological derivative method for topology optimization. Structural and Multidisciplinary Optimization, 33(4-5):375–386, apr 2007.

[139] N. Olhoff. Multicriterion structural optimization via bound formulation and mathematical programming. Structural Optimization, 1(1):11–17, mar 1989.

[140] N Olhoff and J E Taylor. On Structural Optimization. Journal of Applied Mechanics, 50(4b):1139–1151, dec 1983.

[141] Niels Olhoff, Martin P. Bendsøe, and John Rasmussen. On CAD-integrated structural topology and design optimization. Computer Methods in Applied Mechanics and Engineering, 89(1-3):259–279, aug 1991.

[142] Carl Olsson and Yuri Boykov. Curvature-based regularization for surface approximation. In Proceedings of the IEEE Computer Society Conference on Computer Vision and Pattern Recognition, pages 1576–1583. IEEE, jun 2012.

[143] Stanley Osher and Ronald Fedkiw. Level Set Methods and Dynamic Implicit Surfaces, volume 153. Springer-Verlag New York, 2003.

[144] Stanley Osher and Nikos Paragios. Geometric LSM in Imaging, Vision, and Graphics. Springer-Verlag, New York, 2003.

[145] Stanley Osher and James A. Sethian. Fronts propagating with curvature-dependent speed: Algorithms based on Hamilton-Jacobi formulations. Journal of Computational Physics, 79(1):12–49, nov 1988.

[146] Stanley J. Osher and Fadil Santosa. Level Set Methods for Optimization Problems Involving Geometry and Constraints I. Frequencies of a Two-Density Inhomogeneous Drum. Journal of Computational Physics, 171(1):272–288, jul 2001.

[147] M. Otomori, T. Yamada, K. Izui, and S. Nishiwaki. Level set-based topology optimisation of a compliant mechanism design using mathematical programming. Mechanical Sciences, 2(1):91–98, may 2011.

[148] Joseph M. Pajot, Kurt Maute, Yanhang Zhang, and Martin L. Dunn. Design of patterned multilayer films with eigenstrains by topology optimization. International Journal of Solids and Structures, 43(6):1832–1853, 2006.

[149] P F Papkovich. An Expression for a General Integral of the Equations of the Theory of Elasticity in Terms of Harmonic Functions. Izv. Akad. Nauk SSSR, Phys.-Math. Ser, 1(1425):90, 1932.

[150] Edwin A. Peraza Hernandez, Darren J. Hartl, Richard J. Malak, Ergun Akleman, Ozgur Gonen, and Han-Wei Kung. Design Tools for Patterned Self-Folding Reconfigurable Structures Based on Programmable Active Laminates. Journal of Mechanisms and Robotics, 8(3):031015, mar 2016.

[151] Joakim Petersson and Ole Sigmund. Slope constrained topology optimization. International Journal for Numerical Methods in Engineering, 41(8):1417–1434, apr 1998.

[152] J. Poblet-Puig and A. RodrÍguez-Ferran. The block Gauss Seidel-method in sound transmission problems. Journal of Computational Acoustics, 18(1):13–30, mar 2010.

[153] G. I. N. Rozvany. Front Matter. Soil Organic Matter (Second English Edition), 0(Pergamon, Oxford):3 –, 1966.

[154] Jennie Ryu, Matteo D'Amato, Xiaodong Cui, Kevin N. Long, H. Jerry Qi, and Martin L. Dunn. Photo-origamiBending and folding polymers with light. Applied Physics Letters, 100(16):161908, apr 2012.

[155] Mutsuro Sasaki. Morphogenesis of flux structure. AA Publications, London, 2007.

[156] B. Schott, U. Rasthofer, V. Gravemeier, and W. A. Wall. A face-oriented stabilized Nitsche-type extended variational multiscale method for incompressible two-phase flow. International Journal for Numerical Methods in Engineering, 104(7):721–748, nov 2015.

[157] B. Schott and W. A. Wall. A new face-oriented stabilized XFEM approach for 2D and 3D incompressible Navier-Stokes equations. Computer Methods in Applied Mechanics and Engineering, 276:233–265, 2014.

[158] J. A. Sethian. Fast Marching Methods. SIAM Review, 41(2):199–235, jan 1999.

[159] J. A. Sethian and Andreas Wiegmann. Structural Boundary Design via Level Set and Immersed Interface Methods. Journal of Computational Physics, 163(2):489–528, sep 2000.

[160] Jeremy Shafer. Origami Ooh La La! Action Orgami for Performance and Play. Shafer, Jeremy, 2010.

[161] Ashesh Sharma. Advances in Design and Optimization using Immersed Boundary Methods. PhD thesis, University of Colorado at Boulder, jan 2017.

[162] Ashesh Sharma and Kurt Maute. Stress-based topology optimization using spatial gradient stabilized XFEM. Structural and Multidisciplinary Optimization, 57(1):17–38, jan 2018.

[163] Ashesh Sharma, Hernan Villanueva, and Kurt Maute. On shape sensitivities with heaviside-enriched XFEM. Structural and Multidisciplinary Optimization, 55(2):385–408, feb 2017.

[164] O. Sigmund. Design of multiphysics actuators using topology optimization - Part II: Two-material structures. Computer Methods in Applied Mechanics and Engineering, 190(49-50):6605–6627, oct 2001.

[165] Ole Sigmund. Morphology-based black and white filters for topology optimization. Structural and Multidisciplinary Optimization, 33(4-5):401–424, feb 2007.

[166] Ole Sigmund. Manufacturing tolerant topology optimization. Acta Mechanica Sinica/Lixue Xuebao, 25(2):227–239, apr 2009.

[167] Ole Sigmund. On the usefulness of non-gradient approaches in topology optimization. Structural and Multidisciplinary Optimization, 43(5):589–596, may 2011.

[168] Ole Sigmund and Kurt Maute. Topology optimization approaches: A comparative review. Structural and Multidisciplinary Optimization, 48(6):1031–1055, dec 2013.

[169] J. C. Simo and F. Armero. Geometrically non-linear enhanced strain mixed methods and the method of incompatible modes. International Journal for Numerical Methods in Engineering, 33(7):1413–1449, may 1992.

[170] J. C. Simo, F. Armero, and R. L. Taylor. Improved versions of assumed enhanced strain tri-linear elements for 3D finite deformation problems. Computer Methods in Applied Mechanics and Engineering, 110(3-4):359–386, dec 1993.

[171] J. C. Simo and M. S. Rifai. A class of mixed assumed strain methods and the method of incompatible modes. International Journal for Numerical Methods in Engineering, 29(8):1595–1638, jun 1990.

[172] F. L. Stazi, E. Budyn, J. Chessa, and T. Belytschko. An extended finite element method with higher-order elements for curved cracks. Computational Mechanics, 31(1-2 SPEC.):38–48, may 2003.

[173] Simon Sticko and Gunilla Kreiss. Higher Order Cut Finite Elements for the Wave Equation. Computing Research Repository, aug 2016.

[174] M. Stolpe and K. Svanberg. An alternative interpolation scheme for minimum compliance topology optimization. Structural and Multidisciplinary Optimization, 22(2):116–124, sep 2001.

[175] M. Stolpe and K. Svanberg. On the trajectories of penalization methods for topology optimization. Structural and Multidisciplinary Optimization, 21(2):128–139, apr 2001.

[176] Mark Sussman. A level set approach for computing solutions to incompressible two-phase flow. Journal of Computational Physics, 114(1):146–159, sep 1994.

[177] Krister Svanberg. The method of moving asymptotesa new method for structural optimization. International Journal for Numerical Methods in Engineering, 24(2):359–373, feb 1987.

[178] Krister Svanberg. A Class of Globally Convergent Optimization Methods Based on Conservative Convex Separable Approximations. SIAM Journal on Optimization, 12(2):555–573, jan 2002.

[179] Magnus Svärd and Jan Nordström. Response to Convergence of Summation-by-Parts Finite Difference Methods for the Wave Equation. Journal of Scientific Computing, 74(2):1188–1192, apr 2018.

[180] Dassault Systèmes. ABAQUS User's & Theory ManualsRelease 6.14-1, Providence, RI, USA. page 1306, 2013.

[181] J. E. Tarancón, A. Vercher, E. Giner, and F. J. Fuenmayor. Enhanced blending elements for XFEM applied to linear elastic fracture mechanics. International Journal for Numerical Methods in Engineering, 77(1):126–148, jan 2009.

[182] Robert L. Taylor, Peter J. Beresford, and Edward L. Wilson. A nonconforming element for stress analysis. International Journal for Numerical Methods in Engineering, 10(6):1211–1219, jan 1976.

[183] Kenjiro Terada, Mitsuteru Asai, and Michihiro Yamagishi. Finite cover method for linear and non-linear analyses of heterogeneous solids. International Journal for Numerical Methods in Engineering, 58(9):1321–1346, nov 2003.

[184] Skylar Tibbits. 4D Printing: Multi-Material Shape Change. Architectural Design, 84(1):116–121, jan 2014.

[185] A. B. Tran, J. Yvonnet, Q. C. He, C. Toulemonde, and J. Sanahuja. A multiple level set approach to prevent numerical artefacts in complex microstructures with nearby inclusions within XFEM. International Journal for Numerical Methods in Engineering, 85(11):1436–1459, mar 2011.

[186] C. Truesdell and W. Noll. The Non-Linear Field Theories of Mechanics. Springer Berlin Heidelberg, Berlin, Heidelberg, 2004.

[187] N. P. Van Dijk, M. Langelaar, and F. Van Keulen. Explicit level-set-based topology optimization using an exact Heaviside function and consistent sensitivity analysis. International Journal for Numerical Methods in Engineering, 91(1):67–97, jul 2012.

[188] N. P. Van Dijk, K. Maute, M. Langelaar, and F. Van Keulen. Level-set methods for structural topology optimization: A review. Structural and Multidisciplinary Optimization, 48(3):437–472, sep 2013.

[189] Carlos H. Villanueva and Kurt Maute. Density and level set-XFEM schemes for topology optimization of 3-D structures. Computational Mechanics, 54(1):133–150, jul 2014.

[190] Carlos H. Villanueva and Kurt Maute. CutFEM topology optimization of 3D laminar incompressible flow problems. Computer Methods in Applied Mechanics and Engineering, 320(Supplement C):444–473, 2017.

[191] Carlos Hernan Villanueva. Top Opt using the Level Set and XFEM: Theory and Appl. PhD thesis, University of Colorado Boulder, jan 2016.

[192] L. Vujosevic and V.a. Lubarda. Finite-strain thermoelasticity based on multiplicative decomposition of deformation gradient. Theoretical and Applied Mechanics, 28(28-29):379–399, 2002.

[193] Wolfgang Wall. Fluid-Struktur-Interaktion mit stabilisierten Finiten Elementen. PhD thesis, Universität Stuttgart, 1999.

[194] L. J. Walpole. The determination of the elastic field of an ellipsoidal inclusion in an anisotronic medium. Mathematical Proceedings of the Cambridge Philosophical Society, 81(2):283–289, 1977.

[195] Michael Yu Wang and Xiaoming Wang. "Color" level sets: A multi-phase method for structural topology optimization with multiple materials. Computer Methods in Applied Mechanics and Engineering, 193(6-8):469–496, feb 2004.

[196] Michael Yu Wang, Xiaoming Wang, and Dongming Guo. A level set method for structural topology optimization. Computer Methods in Applied Mechanics and Engineering, 192(1-2):227–246, jan 2003.

[197] Shengyin Wang and Michael Yu Wang. Radial basis functions and level set method for structural topology optimization. International Journal for Numerical Methods in Engineering, 65(12):2060–2090, mar 2006.

[198] Yiqiang Wang, Lei Zhang, and Michael Yu Wang. Length scale control for structural optimization by level sets. Computer Methods in Applied Mechanics and Engineering, 305:891–909, jun 2016.

[199] Oliver Weeger, Yue Sheng Benjamin Kang, Sai-Kit Yeung, and Martin L. Dunn. Optimal Design and Manufacture of Active Rod Structures with Spatially Variable Materials. 3D Printing and Additive Manufacturing, 3(4):204–215, 2016.

[200] Peng Wei, Michael Yu Wang, and Xianghua Xing. A study on X-FEM in continuum structural optimization using a level set model. CAD Computer Aided Design, 42(8):708–719, aug 2010.

[201] E.L. Wilson, R.L. Taylor, W.P. Doherty, and J. Ghaboussi. Incompatible Displacement Models. In Numerical and Computer Methods in Structural Mechanics, pages 43–57. Academic Press, jan 1973.

[202] Tony Wong and Shingyu Leung. A Fast Sweeping Method for Eikonal Equations on Implicit Surfaces. Journal of Scientific Computing, 67(3):837–859, may 2016.

[203] Qi Xia and Tielin Shi. Constraints of distance from boundary to skeleton: For the control of length scale in level set based structural topology optimization. Computer Methods in Applied Mechanics and Engineering, 295:525–542, oct 2015.

[204] Shengli Xu, Yuanwu Cai, and Gengdong Cheng. Volume preserving nonlinear density filter based on heaviside functions. Structural and Multidisciplinary Optimization, 41(4):495–505, apr 2010.

[205] Riye Xue, Rui Li, Zongliang Du, Weisheng Zhang, Yichao Zhu, Zhi Sun, and Xu Guo. Kirigami pattern design of mechanically driven formation of complex 3D structures through topology optimization. Extreme Mechanics Letters, 15:139–144, 2017.

[206] Takayuki Yamada, Kazuhiro Izui, Shinji Nishiwaki, and Akihiro Takezawa. A topology optimization method based on the level set method incorporating a fictitious interface energy. Computer Methods in Applied Mechanics and Engineering, 199(45-48):2876–2891, nov 2010.

[207] Weisheng Zhang, Dong Li, Jian Zhang, and Xu Guo. Minimum length scale control in structural topology optimization based on the Moving Morphable Components (MMC) approach. Computer Methods in Applied Mechanics and Engineering, 311:327–355, nov 2016.

[208] Weisheng Zhang, Wenliang Zhong, and Xu Guo. An explicit length scale control approach in SIMP-based topology optimization. Computer Methods in Applied Mechanics and Engineering, 282:71–86, dec 2014.

[209] Yanhang Zhang and Martin L. Dunn. Geometric and material nonlinearity during the deformation of micron-scale thin-film bilayers subject to thermal loading. Journal of the Mechanics and Physics of Solids, 52(9):2101–2126, sep 2004.

[210] Zeang Zhao, Jiangtao Wu, Xiaoming Mu, Haosen Chen, H. Jerry Qi, and Daining Fang. Origami by frontal photopolymerization. Science Advances, 3(4):e1602326, apr 2017.

[211] M. Zhou and G. I N Rozvany. The COC algorithm, Part II: Topological, geometrical and generalized shape optimization. Computer Methods in Applied Mechanics and Engineering, 89(1-3):309–336, aug 1991.

[212] Benliang Zhu and Xianmin Zhang. A new level set method for topology optimization of distributed compliant mechanisms. International Journal for Numerical Methods in Engineering, 91(8):843–871, aug 2012.

[213] Benliang Zhu, Xianmin Zhang, and Sergej Fatikow. Structural topology and shape optimization using a level set method with distance-suppression scheme. Computer Methods in Applied Mechanics and Engineering, 283:1214–1239, jan 2015.

Appendix A

XFEM 1D Bar Example

To illustrate the enforcement of interface conditions using Nische's method, a single element, linear elastic 1D bar example is discussed. The problem setup along with loads and boundary conditions is shown in Figure A.1 (a). The modeling problem consists of two distinct material phases (i.e. Ω_0^I and Ω_0^{II}) with a material interface at X_Γ. A generalized Heaviside enrichment strategy (Eqn.(3.1.1)) is used. Two enrichments levels ($l = [1, 2]$) are required in this example to represent two distinct material phase ($m = [\text{I, II}]$), leading to two DOFs per node. Figure A.1 (b) shows the associated 1D shape functions where solid lines indicate active areas and dashed lines denote areas in which the corresponding shape function is (physically) inactive. These are identical to a classical 1D FEM bar problem and stated here for completeness as:

$$N_i = \begin{bmatrix} N_A \\ N_B \end{bmatrix} = \begin{bmatrix} 1 - \frac{x}{L} \\ \frac{x}{L} \end{bmatrix} \tag{A.0.1}$$

where i denotes the node index (i.e. $i = [A, B]$). The global, enriched nodal displacement solution vector for two enrichment levels is:

$$\hat{\mathbf{u}} = \begin{bmatrix} \hat{u}_A^1 \\ \hat{u}_B^1 \\ \hat{u}_A^2 \\ \hat{u}_B^2 \end{bmatrix} \tag{A.0.2}$$

It should be noted that only displacement components $\hat{u}_A^1$ and $\hat{u}_B^2$ have a physical meaning whereas the remaining two (enriched) DOFs ($\hat{u}_A^2$, $\hat{u}_B^1$) solely serve the purpose of representing an intra-element
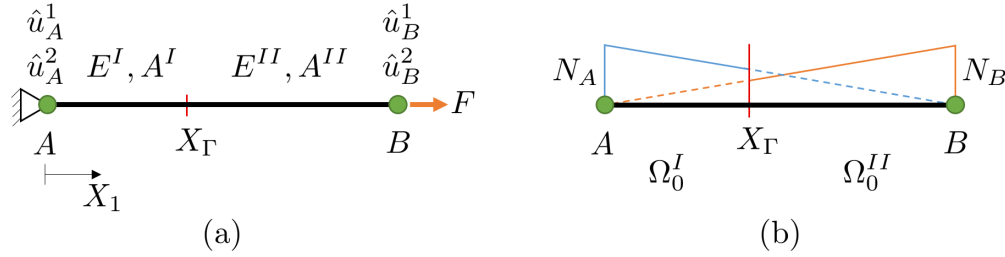
Figure A.1: 1D bar example decomposed into two material sub-domains using XFEM. (a) Problem setup and (b) shape functions.

discontinuity using Heaviside-enriched XFEM.

Bulk and Interface Contributions

In order to enforce continuity of displacements and traction at the interface via Nitsche's method, the total elemental residual consists of three terms. Two bulk contributions (i.e. one from each material phase) and an interface contribution. It can be stated as:

$$\mathbf{R} = \mathbf{R}_B^I + \mathbf{R}_B^{II} + \mathbf{R}_{IF}\big|_{X_\Gamma} \tag{A.0.3}$$

where the bulk residual contributions are denoted by $\mathbf{R}_B^m$ for phase m, respectively. The bulk contributions are computed using the weak form of the linear elastic governing equation (Eqn.(2.2.11)) as:

$$\mathbf{R}_B^m = \int_{X_l}^{X_u} \boldsymbol{\epsilon}^m(\delta\mathbf{u}) E^m \boldsymbol{\epsilon}^m(\mathbf{u})\ dX \tag{A.0.4}$$

where E^m denotes the Young's modulus of phase m and the integration limits are determined by X_l^m and X_u^m for the respective material phase. The 1D strain tensor for enrichment level l is computed as $\boldsymbol{\epsilon}(\mathbf{u}^l) = \frac{N_B \hat{u}_B^l - N_A \hat{u}_A^l}{L}$ and the variation of strain is $\boldsymbol{\epsilon}(\delta\mathbf{u}^l) = \frac{N_B - N_A}{L}$. Evaluating Eqn.(A.0.4)

yields the bulk residual contributions for phase I and phase II as:

$$\mathbf{R}_B^I = \frac{E^I A^I}{L^2} X_\Gamma \begin{bmatrix} \hat{u}_A^1 - \hat{u}_B^1 \\ -\hat{u}_A^1 + \hat{u}_B^1 \\ 0 \\ 0 \end{bmatrix} \quad , \qquad \mathbf{R}_B^{II} = \frac{E^{II} A^{II}}{L^2} (L - X_\Gamma) \begin{bmatrix} 0 \\ 0 \\ \hat{u}_A^2 - \hat{u}_B^2 \\ -\hat{u}_A^2 + \hat{u}_B^2 \end{bmatrix} \qquad (A.0.5)$$

where L denotes the total length of the bar element and A^m is the cross sectional area of the bar within each material phase.

Nitsche's interface residual (Eqn.(3.1.3)) simplifies in the 1D case to:

$$\mathbf{R}_{IF} = -[\![\delta \mathbf{u}]\!]\{E\boldsymbol{\epsilon}(\mathbf{u})\}\mathbf{N}\big|_{X_\Gamma} + \{E\boldsymbol{\epsilon}(\delta \mathbf{u})\}\mathbf{N}[\![\mathbf{u}]\!]\big|_{X_\Gamma} + \gamma_N [\![\delta \mathbf{u}]\!][\![\mathbf{u}]\!]\big|_{X_\Gamma} \qquad (A.0.6)$$

where it should be noted that Eqn.(A.0.6) is evaluated at the interface (point) X_Γ only and therefore the normal vector $\mathbf{N}$ on the interface degrades to a unit scalar. Expanding Eqn.(A.0.6) leads to:

$$\begin{aligned} \mathbf{R}_{IF} = &-(\delta u_i^1 - \delta u_i^2)\left(\frac{E^I A^I}{2}\frac{\hat{u}_B^1 - \hat{u}_A^1}{L} + \frac{E^{II} A^{II}}{2}\frac{\hat{u}_B^2 - \hat{u}_A^2}{L}\right) \\ &-\left(\frac{E^I A^I}{2}\frac{\delta\hat{u}_B^1 - \delta\hat{u}_A^1}{L} + \frac{E^{II} A^{II}}{2}\frac{\delta\hat{u}_B^2 - \delta\hat{u}_A^2}{L}\right)[\![u]\!] \\ &+\gamma(\delta u_i^1 - \delta u_i^2)[\![u]\!] \end{aligned} \qquad (A.0.7)$$

where $i = [A, B]$, $u_i^m = N_i \hat{u}_i^m$ and $\delta u_i^m = N_i$. The displacement jump at the interface is computed as:

$$[\![u]\!] = \sum_i N_i \hat{u}_i^1 - \sum_i N_i \hat{u}_i^2 = (N_A \hat{u}_A^1 + N_B \hat{u}_B^1) - (N_A \hat{u}_A^2 + N_B \hat{u}_B^2) \qquad (A.0.8)$$

It should be noted that in Eqn.(A.0.7) an equal traction weighting of $w^I = w^{II} = 0.5$ is used for simplicity. Separating out the interface residual equation for each nodal DOF, Eqn. (A.0.7)

becomes:

$$
\mathbf{R}_{IF} = -\frac{E^I A^I}{2L}
\begin{bmatrix}
N_A(\ \ \hat{u}_B^1 - \hat{u}_A^1) \\
N_B(\ \ \hat{u}_B^1 - \hat{u}_A^1) \\
N_A(-\hat{u}_B^1 + \hat{u}_A^1) \\
N_B(-\hat{u}_B^1 + \hat{u}_A^1)
\end{bmatrix}
- \frac{E^{II} A^{II}}{2L}
\begin{bmatrix}
N_A(\ \ \hat{u}_B^2 - \hat{u}_A^2) \\
N_B(\ \ \hat{u}_B^2 - \hat{u}_A^2) \\
N_A(-\hat{u}_B^2 + \hat{u}_A^2) \\
N_B(-\hat{u}_B^2 + \hat{u}_A^2)
\end{bmatrix}
$$

$$
-\frac{1}{2L}
\begin{bmatrix}
E^I A^I\ (-[\![u]\!]) \\
E^I A^I\ (\ \ [\![u]\!]) \\
E^{II} A^{II}(-[\![u]\!]) \\
E^{II} A^{II}(\ \ [\![u]\!])
\end{bmatrix}
$$

$$
+\gamma_N
\begin{bmatrix}
N_A(\ \ [\![u]\!]) \\
N_B(\ \ [\![u]\!]) \\
N_A(-[\![u]\!]) \\
N_B(-[\![u]\!])
\end{bmatrix}
\tag{A.0.9}
$$

Finally, the total elemental tangent stiffness matrix is computed by linearization of Eqn.(A.0.3) as:

$$
\mathbf{K} = \frac{\partial \mathbf{R}_B^I}{\partial \hat{\mathbf{u}}} + \frac{\partial \mathbf{R}_B^{II}}{\partial \hat{\mathbf{u}}} + \frac{\partial \mathbf{R}_{IF}}{\partial \hat{\mathbf{u}}}
\tag{A.0.10}
$$

As in a classical FE case, the nodal (physical and enriched) displacement DOFs are obtained by solving the master stiffness equation:

$$
\mathbf{K}\hat{\mathbf{u}} - \hat{\mathbf{F}} = \mathbf{R}
\tag{A.0.11}
$$

where $\hat{\mathbf{F}}$ is some external force vector. It should be noted that if the same material is used in phase I and phase II, an identical solution is obtained for each enrichment level. The solution is then also identical to a classical FE problem, as no discontinuity and therefore no intra-element interface exists.

Influence of interface position X_Γ on the Residual R

An investigation of the influence of the interface position X_Γ on the total elemental residual (Eqn.(A.0.3)) is studied next. The total sensitivity is computed from three terms as:

$$\frac{\partial \mathbf{R}}{\partial X_\Gamma} = \frac{\partial \mathbf{R}_B^I}{\partial X_\Gamma} + \frac{\partial \mathbf{R}_B^{II}}{\partial X_\Gamma} + \frac{\partial \mathbf{R}_{IF}}{\partial X_\Gamma} \tag{A.0.12}$$

The sensitivities of the phase I and phase II bulk residuals of Eqn.(A.0.12) are computed as:

$$\frac{\partial \mathbf{R}_B^I}{\partial X_\Gamma} = \frac{E^I A^I}{L^2} \begin{bmatrix} \hat{u}_A^1 - \hat{u}_B^1 \\ -\hat{u}_A^1 + \hat{u}_B^1 \\ 0 \\ 0 \end{bmatrix}, \qquad \frac{\partial \mathbf{R}_B^{II}}{\partial X_\Gamma} = -\frac{E^{II} A^{II}}{L^2} \begin{bmatrix} 0 \\ 0 \\ \hat{u}_A^2 - \hat{u}_B^2 \\ -\hat{u}_A^2 + \hat{u}_B^2 \end{bmatrix} \tag{A.0.13}$$

The sensitivity of the interface residual (Eqn.(A.0.9)) with respect to the interface position X_Γ is computed as:

$$\frac{\partial \mathbf{R}_{IF}}{\partial X_\Gamma} = -\frac{E^I A^I}{2L^2} \begin{bmatrix} -(\ \hat{u}_B^1 - \hat{u}_A^1) \\ (\ \hat{u}_B^1 - \hat{u}_A^1) \\ -(-\hat{u}_B^1 + \hat{u}_A^1) \\ (-\hat{u}_B^1 + \hat{u}_A^1) \end{bmatrix} - \frac{E^{II} A^{II}}{2L^2} \begin{bmatrix} -(\ \hat{u}_B^2 - \hat{u}_A^2) \\ (\ \hat{u}_B^2 - \hat{u}_A^2) \\ -(-\hat{u}_B^2 + \hat{u}_A^{II}) \\ (-\hat{u}_B^2 + \hat{u}_A^2) \end{bmatrix}$$

$$-\frac{1}{2L} \begin{bmatrix} E^I A^I \ (-\frac{\partial \llbracket u \rrbracket}{\partial x_\Gamma}) \\ E^I A^I \ (\ \frac{\partial \llbracket u \rrbracket}{\partial x_\Gamma}) \\ E^{II} A^{II} (-\frac{\partial \llbracket u \rrbracket}{\partial x_\Gamma}) \\ E^{II} A^{II} (\ \frac{\partial \llbracket u \rrbracket}{\partial x_\Gamma}) \end{bmatrix} \tag{A.0.14}$$

$$+\gamma_N \begin{bmatrix} N_A(\ \frac{\partial \Delta u}{\partial x_\Gamma} - \frac{1}{L} \llbracket u \rrbracket) \\ N_B(\ \frac{\partial \Delta u}{\partial x_\Gamma} + \frac{1}{L} \llbracket u \rrbracket) \\ N_A(-\frac{\partial \Delta u}{\partial x_\Gamma} + \frac{1}{L} \llbracket u \rrbracket) \\ N_B(-\frac{\partial \Delta u}{\partial x_\Gamma} - \frac{1}{L} \llbracket u \rrbracket) \end{bmatrix}$$

where the sensitivity of the interface jump with respect to the interface position X_Γ is obtained

from:

$$\frac{\partial [\![u]\!]}{\partial X_\Gamma} = \sum_i \frac{\partial N_i}{\partial x_\Gamma} \hat{u}_i^1 - \sum_i \frac{\partial N_i}{\partial x_\Gamma} \hat{u}_i^2 = \frac{1}{L}(-\hat{u}_A^1 + \hat{u}_B^1) - (-\hat{u}_A^2 + \hat{u}_B^2) \qquad (A.0.15)$$

It should be noted that if the same material is used in phase I and phase II, just as before, there is no influence of the intersection on the element sensitivity as the element can be treated as a regular, non-intersected element. This is accounted for in Nitsche's formulation such that the sensitivities of the bulk contributions and the interface sensitivity cancel each other out. For different materials in phase I and phase II, a non-zero $\frac{\partial \mathbf{R}}{\partial X_\Gamma}$ is obtained since the (different) stresses in each domain do not fully cancel out.

Lorem ipsum dolor sit amet, consectetuer adipiscing elit. Ut purus elit, vestibulum ut, placerat ac, adipiscing vitae, felis. Curabitur dictum gravida mauris. Nam arcu libero, nonummy eget, consectetuer id, vulputate a, magna. Donec vehicula augue eu neque. Pellentesque habitant morbi tristique senectus et netus et malesuada fames ac turpis egestas. Mauris ut leo. Cras viverra metus rhoncus sem. Nulla et lectus vestibulum urna fringilla ultrices. Phasellus eu tellus sit amet tortor gravida placerat. Integer sapien est, iaculis in, pretium quis, viverra ac, nunc. Praesent eget sem vel leo ultrices bibendum. Aenean faucibus. Morbi dolor nulla, malesuada eu, pulvinar at, mollis ac, nulla. Curabitur auctor semper nulla. Donec varius orci eget risus. Duis nibh mi, congue eu, accumsan eleifend, sagittis quis, diam. Duis eget orci sit amet orci dignissim rutrum.

Nam dui ligula, fringilla a, euismod sodales, sollicitudin vel, wisi. Morbi auctor lorem non justo. Nam lacus libero, pretium at, lobortis vitae, ultricies et, tellus. Donec aliquet, tortor sed accumsan bibendum, erat ligula aliquet magna, vitae ornare odio metus a mi. Morbi ac orci et nisl hendrerit mollis. Suspendisse ut massa. Cras nec ante. Pellentesque a nulla. Cum sociis natoque penatibus et magnis dis parturient montes, nascetur ridiculus mus. Aliquam tincidunt urna. Nulla ullamcorper vestibulum turpis. Pellentesque cursus luctus mauris.

Nulla malesuada porttitor diam. Donec felis erat, congue non, volutpat at, tincidunt tristique, libero. Vivamus viverra fermentum felis. Donec nonummy pellentesque ante. Phasellus adipiscing semper elit. Proin fermentum massa ac quam. Sed diam turpis, molestie vitae, placerat a, molestie nec, leo. Maecenas lacinia. Nam ipsum ligula, eleifend at, accumsan nec, suscipit a, ipsum. Morbi blandit ligula feugiat magna. Nunc eleifend consequat lorem. Sed lacinia nulla vitae enim. Pellentesque tincidunt purus vel magna. Integer non enim. Praesent euismod nunc eu purus. Donec bibendum quam in tellus. Nullam cursus pulvinar lectus. Donec et mi. Nam vulputate metus eu enim. Vestibulum pellentesque felis eu massa.

Quisque ullamcorper placerat ipsum. Cras nibh. Morbi vel justo vitae lacus tincidunt ultrices. Lorem ipsum dolor sit amet, consectetuer adipiscing elit. In hac habitasse platea dictumst. Integer tempus convallis augue. Etiam facilisis. Nunc elementum fermentum wisi. Aenean placerat. Ut imperdiet, enim sed gravida sollicitudin, felis odio placerat quam, ac pulvinar elit purus eget enim.

Nunc vitae tortor. Proin tempus nibh sit amet nisl. Vivamus quis tortor vitae risus porta vehicula.

Appendix B

Publication 1: Topology Optimization of Active Structures using a Higher-Order Level-Set-XFEM-Density Approach

Topology Optimization of Active Structures using a Higher-Order Level-Set-XFEM-Density Approach

Markus J. Geiss[*], Kurt Maute[†], *University of Colorado Boulder, Boulder, CO 80309*

To fully use the potential of emerging manufacturing technologies like additive manufacturing (AM), a need for novel design tools is inherently created. In this work, topology optimization (TO) is used to automate the design process of active, 3D structures. A linear elastic thermomechanical model together with higher-order finite elements (FE) is utilized to capture the physical behavior of a self-deforming structure where self-actuation is caused by internal swelling strains. A gradient-based level-set (LS) TO approach is adopted to describe the evolving interface geometry between a solid and void domain. Simultaneously, a density-based TO approach is used within the solid domain to define the distribution of different materials. The extended finite element method (XFEM) is employed to predict the structural response using a well-resolved geometry representation and spatial discretization. In addition, the need for higher-order XFEM elements is identified in order to accurately predict the deformations of slender structures. Face-oriented ghost stabilization is studied for stabilization of the higher-order XFEM. Finally, a stabilization scheme to suppress rigid body motion of isolated solid sub-domains appearing during the optimization process is investigated. An example of an optimized shape-changing structure is presented and the performance of the final design is analyzed. Potential aerospace applications of this design methodology are discussed.

I.   Introduction

With emerging manufacturing technologies like additive manufacturing (AM) providing unprecedented design freedom, design tools are needed that take advantage of the increased flexibility of these novel manufacturing techniques. Multi-disciplinary design optimization has the potential to unlock the full capabilities of AM, in particular 3D printing. Topology optimization (TO), being the most general form of design optimization, is used in this work to automatically generate the design of shape-changing 3D structures. A level-set (LS) extended finite element method (XFEM)-based TO approach is combined with a density-based TO approach to create a multi-material optimization framework, which leverages the advantages of each method. The focus of this work is on slender active structures where locking of low-order finite elements (FE) prevents the accurate prediction of the structural response. Therefore, a higher-order element interpolation is used to improve the deformation prediction using the XFEM. Another challenge being addressed in this work is the need for numerical stabilization of the higher-order XFEM in the vicinity of the material-void interface. Therefore, a face-oriented ghost penalization scheme is employed and verified against an analytical example. Selective structural springs are utilized to provide numerical stability while having no effect on the deformation prediction of the remaining, connected solid domain.

II.   Extended Finite Element Modeling of Slender Structures

The XFEM, initially used by [1] for capturing crack growth phenomena, is an accurate approach to describe evolving interfaces on a fixed background mesh. It is therefore popular in combination with a LS geometry description to capture changing designs throughout a TO process [2]. In this work, a generalized Heaviside enrichment strategy is used to enhance the classical FE interpolation with additional shape functions which allow for independent interpolation into disconnected sub-domains. Triangulation of material sub-domains for volume and surface integration is performed and interface conditions need to be enforced in order to achieve a continuous solution across the discontinuous material interface.

---

*Graduate Research Assistant, Ann and H.J. Smead Department of Aerospace Engineering Sciences, AIAA Student Member, Markus.Geiss@Colorado.edu

†Professor, Ann and H.J. Smead Department of Aerospace Engineering Sciences, Kurt.Maute@Colorado.edu
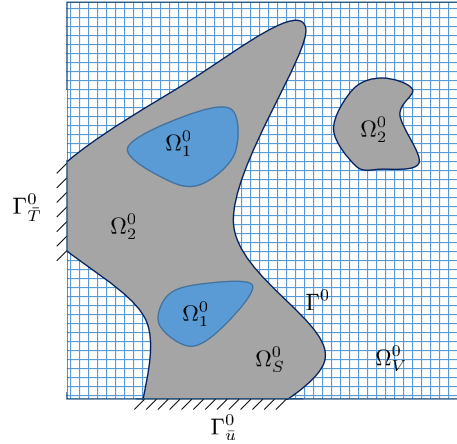
Figure 1. Domain decomposition into solid (Ω_S^0) and void (Ω_V^0) sub-domains along the material-void interface Γ^0 using LS-XFEM. Within the solid domain, a further distinction is made between two different materials (Ω_1^0 and Ω_2^0). The hatched lines on the left and bottom edge of the design domain represent Neumann and Dirichlet boundary conditions, respectively.

A. Linear Elastic Thermomechanical Model

Static equilibrium is considered, enforcing balance of linear momentum within the solid domain Ω_S^0 (see Figure 1). The weak form of the linear elastic governing equation is stated as:

$$R_{lin} = \int_{\Omega_S^0} \left(\delta\epsilon_{ij}\sigma_{ij} - \delta u_i \rho B_i \right) dV - \int_{\Gamma_{\bar{T}}^0} \delta u_i \cdot \bar{T}_i \, dA = 0 \tag{1}$$

where ϵ_{ij} is the total strain tensor, σ_{ij} is the symmetric Cauchy stress tensor, and u_i are the nodal displacements. The density is denoted by ρ, B_i is the body-force vector, and $\bar{T}_i$ is the prescribed traction vector on the surface $\Gamma_{\bar{T}}^0$. The isotropic eigenstrain causing a shape-change in active structures is modeled by a residual, isotropic thermal swelling strain. The total strain ϵ_{ij} is computed as:

$$\epsilon_{ij} = (\epsilon_u)_{ij} - (\epsilon_s)_{ij} \tag{2}$$

where $(\epsilon_u)_{ij}$ denotes the symmetric infinitesimal strain tensor defined as:

$$(\epsilon_u)_{ij} = \frac{1}{2}\left(\frac{\partial u_i}{\partial X_j} + \frac{\partial u_j}{\partial X_i} \right) \tag{3}$$

and $(\epsilon_s)_{ij}$ is the isotropic thermal swelling strain defined as:

$$(\epsilon_s)_{ij} = \alpha_m \Delta T \delta_{ij} \tag{4}$$

where α_m is the coefficient of thermal expansion (CTE) of Material 1 or Material 2 (i.e. $m = 1, 2$), $\Delta T = 1$ is a pseudo temperature increment and, δ_{ij} is the Kronecker delta. The Cauchy stress is finally computed using Eqn. (2) as:

$$\sigma_{ij} = D_{ijkl}\epsilon_{kl} \tag{5}$$

where the fourth-order constitutive tensor D_{ijkl} is defined as:

$$D_{ijkl} = \frac{E_m}{2(1+\nu_m)}(\delta_{il}\delta_{jk} + \delta_{ik}\delta_{jl}) + \frac{E_m\nu_m}{(1+\nu_m)(1-2\nu_m)}\delta_{ij}\delta_{kl} \tag{6}$$

The elastic modulus of material m is denoted by E_m and ν_m is the Poisson's ratio of an isotropic, linear elastic material.

B.   Nonlinear Hyperelastic Thermomechanical Model

For verification purposes of the optimized design, a nonlinear kinematics model is used which is briefly introduced here for completeness. The weak form of the governing equation is formulated as:

$$R_{NonLin} = \int_{\Omega_S^0} \left(\delta F_{ij} P_{ij} - \delta u_i \rho B_i \right) dV - \int_{\Gamma_{\bar{T}}^0} \delta u_i \cdot \bar{T}_i \, dA = 0 \tag{7}$$

where $F_{ij} = \partial x_i / \partial X_j$ is the total deformation gradient tensor with $x_i = u_i + X_i$ defining the relation between spatial coordinates in the undeformed (X_i) and deformed (x_i) configurations Ω_S^0 and Ω_S, respectively. The first Piola-Kirchhoff stress tensor is denoted by P_{ij}. A multiplicative decomposition of the total deformation gradient into a mechanical and thermal deformation gradient is used, where a linear thermal expansion model is assumed for calculation of the thermal deformation gradient. Moreover, a Saint-Venant Kirchhoff hyperelastic material model is used. For more details on the nonlinear kinematics model, the interested reader is referred to [3].

C.   XFEM for Slender Structures

Just like in classical FE, element locking needs to be considered when modeling slender structures with the XFEM. Element locking is an artifact of low-order FEs occurring when the interpolation order is too low to properly capture the displacement field. This introduces artificial element strains which lead to over-stiffening of the FE approximation and hence to a large under-prediction of the displacements. In particular shear locking, caused by high aspect ratio elements, is a major problem when modeling slender structures. The artificial element locking can, for example, be mitigated by using shell formulations, reduced-order integration or by increasing the interpolation order of the elements.

In order to illustrate the effect of shear locking, a simple bi-layer beam example is modeled using linear and quadratic XFEM elements for different levels of mesh refinement as well as linear and nonlinear kinematics models. The obtained tip displacements are then compared against the results from a 1D Timoshenko beam model outlined in [4]. A bi-layer, slender 3D beam is considered where the XFEM is used to decompose a slender beam into two different materials layers (see Figure 2). The material in the top layer has an elastic modulus of $E_1 = 0.6 \, MPa$, a Poisson's ratio of $\nu_1 = 0$, and a uniaxial swelling strain of $\alpha_1 = 0.045$ in X_1-direction. The material in the bottom layer is stiffer with an elastic modulus of $E_2 = 6 \, MPa$, the same Poisson's ratio but no swelling strain (i.e. $\alpha_2 = 0$). The beam of dimensions 80 mm x 2.5 mm x 1 mm is clamped on the left end. Boundary conditions are applied weakly using Nitsche's method [5]. Isotropic swelling of the active material at the top of each beam leads to downward curling of the structure, as depicted in Figure 2.
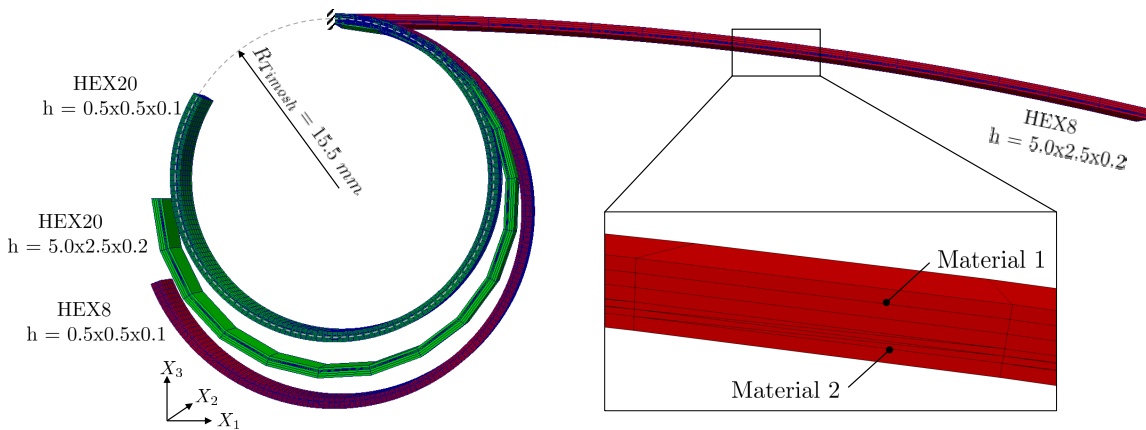
Figure 2.   Nonlinear deformation prediction of a cantilevered bi-layer beam using different order XFEM elements and different element sizes. The insert shows the XFEM mesh of the two-layer beam. Deformation predictions using the linear kinematics model are not shown.

The linear and the nonlinear kinematics models introduced previously are used for the XFEM analysis where a strong influence of the spatial discretization on the accuracy of the XFEM prediction is observed. However, even for the finest mesh with a mesh size of $h = 0.5 \text{x} 0.5 \text{x} 0.1$ and 10 elements through the thickness, a large discrepancy between the 1D analytical model (indicated by the dashed circle in Figure 2) and the nonlinear XFEM solution is observed when

trilinear HEX8 elements are used (shown in red). Using higher-order serendipity HEX20 elements with 20 nodes and a total of 60 degrees of freedom (DOF) in 3D in combination with a nonlinear analysis (shown in green), a much better agreement and convergence towards the analytical Timoshenko beam theory-based radius of curvature $R_{Timosh} = 15.5\ mm$ is obtained. It can also be seen that even the coarsest spatial discretization shown in Figure 2 performs much better using HEX20 elements compared to the finest HEX8 mesh considered here. A quantitative comparison of the tip displacement L^2 norm between HEX8 and HEX20 elements using linear and nonlinear kinematics is shown in Table 1. It should be noted that the comparison shown in Table 1 is only made within each kinematics model, as a cross-comparison of displacements between linear and nonlinear kinematics for large deformations and rotations is physically meaningless.

Table 1. Comparison of the tip displacement L^2 norm against a 1D Timoshenko model using linear and nonlinear kinematics.

	Linear		Nonlinear	
Mesh Size	HEX8	HEX20	HEX8	HEX20
h = 5.0x2.5x0.2	93.6 %	3.7 %	90.1 %	4.3 %
h = 0.5x0.5x0.1	14.7 %	2.6 %	6.3 %	1.2 %

It can clearly be seen that when using coarse meshes for modeling slender structures, low-order FEs exhibit large amounts of locking. For both, linear and nonlinear kinematics, the difference in tip displacements between a coarse XFEM prediction and the respective analytical reference solution is over 90%. With mesh refinement, these discrepancies reduce, however the computational cost increases. When using a higher-order spatial discretization, locking effects are largely mitigated for both, linear and nonlinear kinematics. Therefore, a closer match between the XFEM predictions and the respective Timoshenko model predictions is obtained. These results demonstrate the need for higher-order spatial discretization to accurately predict the displacement behavior of slender structures modeled by solid brick XFEM elements.

III.   Higher-Order Face-Oriented Ghost Stabilization

To stabilize the higher-order XFEM approach described in Section II, face-oriented ghost stabilization as proposed by [6] is adopted for linear elastic structural problems. Instabilities of the XFEM approach arise when the material-void interface Γ^0 moves too close to a FE node in the background mesh, which may lead to a vanishing zone of influence of a DOF. Numerically, this leads to ill-conditioning of the linear system and to inaccuracies in the linear solve. To cure this issue, face-oriented ghost stabilization is applied in the vicinity of the solid-void interface by augmenting the linear elastic governing equation with a penalty term. The most simple ghost formulation as originally proposed by [6] penalizes the jump in the displacement gradient and is stated as:

$$R_G = h\gamma_G E \sum_{F\in\Xi} \int_F \left[\!\left[\frac{\partial v_i}{\partial X_j}n_j\right]\!\right]\left[\!\left[\frac{\partial u_i}{\partial X_j}n_j\right]\!\right] dS + h^3\gamma_G E \sum_{F\in\Xi} \int_F \left[\!\left[\frac{\partial}{\partial X_k}\left(\frac{\partial v_i}{\partial X_j}n_j\right)\right]\!\right]\left[\!\left[\frac{\partial}{\partial X_k}\left(\frac{\partial u_i}{\partial X_j}n_j\right)\right]\!\right] dS$$

(8)

where h is the element edge length, γ_G is a constant ghost penalization parameter, and E is the elastic modulus of the solid material. The subset Ξ contains all element facets F in the immediate vicinity of the solid-void interface, for which at least one of the two adjacent elements is intersected [7]. The admissible test functions are denoted by $v_i = \delta u_i$. The jump operator is defined as:

$$[\![\bullet]\!] = \bullet|_{\Omega_{e_1}^0} - \bullet|_{\Omega_{e_2}^0}$$

(9)

and is evaluated along the face between two adjacent elements, $\Omega_{e_1}^0$ and $\Omega_{e_2}^0$. The outward facing normal between element $\Omega_{e_1}^0$ and $\Omega_{e_2}^0$ is denoted by n_j. The first term in Eqn.(8) penalizes the jump in the first-order spatial gradients of the displacements while the second term penalizes the jump in the second-order spatial gradients of the displacements. Because the integration domain of Eqn.(8) is always an entire face, regardless of the intersection configuration, face-oriented ghost stabilization overcomes numerical issues associated with small intersections and the associated vanishing zone of influence of certain DOFs.

For general applications, where a uniform, homogeneous material is present within the solid domain, the displacement gradient-based ghost formulation presented in Eqn.(8) is sufficient. However, if the solid domain consists of a non-uniform material, as it is the case in combined LS-XFEM-Density TO, a more general ghost penalization formulation is required. The originally proposed formulation directly penalizes jumps in the spatial displacement

gradients, which need to vanish between elements of the same phase. However, if spatially varying material properties are present within the solid phase, displacement gradient jumps exist by construction. Using the displacement gradient-based ghost formulation presented in Eqn.(8) would therefore falsely penalize jumps which are not caused by numerical instabilities but by spatially varying material properties. To address this issue and to correctly apply face-oriented ghost stabilization only to jumps caused by the XFEM discretization, a stress-based ghost stabilization is proposed. It is formulated as:

$$R_G = \frac{h}{\tilde{E}} \gamma_G \sum_{F \in \Xi} \int_F [\![\sigma_{ij}(v)\, n_j]\!]\, [\![\sigma_{ij}(u)\, n_j]\!]\, dS + \frac{h^3}{\tilde{E}} \gamma_G \sum_{F \in \Xi} \int_F \left[\!\!\left[\frac{\partial \sigma_{ij}(v)}{\partial X_k}\, n_j \right]\!\!\right] \left[\!\!\left[\frac{\partial \sigma_{ij}(u)}{\partial X_k}\, n_j \right]\!\!\right]\, dS \qquad (10)$$

where $\tilde{E}$ a scaling factor based on the geometric mean of the elastic moduli of the two adjacent elements. The advantage of this stress-based formulation is that the scaling of the individual contributions by the Young's modulus is performed elementally, which eliminates jumps in the displacement gradients solely caused by varying material properties. Even though the ghost penalization formulation stated in Eqn.(10) is most general, computing the linearization of the variation of the gradient of the stress $\partial/\partial u_l(\partial \sigma_{ij}(v)/\partial X_k)$ needed for stabilizing second-order spatial gradients leads to a significant increase in computational efforts. Therefore, a hybrid formulation based on the principle of virtual work is proposed. The ghost penalization residual contribution is formulated as:

$$R_G = h\, \gamma_G \sum_{F \in \Xi} \int_F \left[\!\!\left[\frac{\partial v_i}{\partial X_j} n_j \right]\!\!\right] [\![\sigma_{ij}(u)\, n_j]\!]\, dS \; + \; h^3 \gamma_G \sum_{F \in \Xi} \int_F \left[\!\!\left[\frac{\partial}{\partial X_k} \left(\frac{\partial v_i}{\partial X_j} n_j \right) \right]\!\!\right] \left[\!\!\left[\frac{\partial \sigma_{ij}(u)}{\partial X_k}\, n_j \right]\!\!\right]\, dS \quad (11)$$

This formulation is computationally efficient while still being accurate for non-uniform material distributions within the solid domain.

A. Verification against an Analytical Spherical Inclusion Problem

To verify the performance of the face-oriented ghost stabilization formulation for higher-order XFEM elements, as proposed in Section III, a mesh refinement study is performed. The convergence behavior of the L^2 error norm, the H^1 error semi-norm, and the effect on the condition number is studied for the virtual work-based formulation presented in Eqn.(11). A cubic domain with a spherical inclusion as depicted in Figure 3a is considered. Both, the inclusion material (Phase I) and the matrix material (Phase II) have an elastic modulus of $E = 10\,MPa$ and a Poisson's ratio of $\nu = 0.3$. The inclusion material has a CTE of $\alpha = 0.1$, while the matrix material has no eigenstrain. Isotropic linear elasticity is assumed for each material phase and the interface conditions along the Phase I/Phase II material interface are enforced weakly using Nitsche's method [8]. The interface condition ensures continuity of the displacements and the traction across the interface in material-material problems. Details of the formulation are omitted here for brevity, but the interested reader is referred to [9] for further information.

a) Setup of spherical inclusion problem.

b) Deformation due to expansion of spherical inclusion (cut-away view)
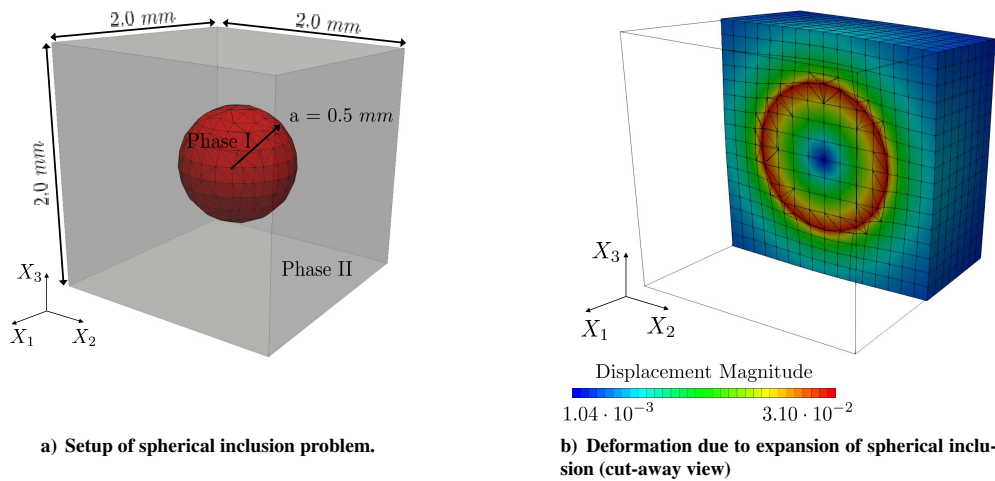
Figure 3. Verification problem of a spherical inclusion in cubical host matrix.

An analytical solutions for the strain and stress fields within a spherical inclusion embedded in an infinite isotropic linear elastic solid were first proposed by [10]. Due to the existence of a uniform eigenstrain ϵ_s^I within the spherical inclusion (Phase I), a uniform strain field is obtained as:

$$\epsilon_{ij}^I = S_{ijkl}^* (\epsilon_s^I)_{kl} \tag{12}$$

where S_{ijkl}^* is the constant, fourth-order Eshelby tensor. For a spherical inclusion, it is defined as:

$$S_{ijkl}^* = \frac{5\nu - 1}{15(1-\nu)} \delta_{ij}\delta_{kl} + \frac{4-5\nu}{15(1-\nu)} (\delta_{ik}\delta_{jl} + \delta_{il}\delta_{jk}) \tag{13}$$

The displacement field inside the spherical inclusion $u_i^I(\mathbf{X})$ is obtained by integration of Eqn.(12) whereas the spatial gradient of the displacement field $\partial u_i^I(\mathbf{X})/\partial X_j$ equals the strain defined in Eqn.(12).

Based on the work of [11], an analytical expression for the displacement field outside the spherical inclusion (Phase II) can be obtained as well. For that, a transformation stress $\bar{\sigma}_{ij}^I$ is computed from the eigenstrain as [12]:

$$\bar{\sigma}_{ij}^I = \frac{E}{1+\nu} \left((\epsilon_s^I)_{ij} + \frac{\nu}{1-2\nu} (\epsilon_s^I)_{kk}\delta_{ij} \right) \tag{14}$$

The transformation stress is then used in combination with the Papkovich-Neuber potentials [13, 14] to compute the displacements. The Papkovich-Neuber potentials reduce for a spherical inclusion case to:

$$\Psi_i = \frac{a^3 \bar{\sigma}_{ij} X_j}{3R^3} \quad \text{and} \quad \phi = \frac{a^3 \bar{\sigma}_{ij}}{15R^3} \left((5R^2 - a^2)\delta_{ij} + 3a^2 \frac{X_i X_j}{R^2} \right) \tag{15}$$

where the radial distance from the origin is compute as $R = \sqrt{X_k X_k}$ and a is the inclusion radius. The displacements outside the spherical inclusion are calculated by using:

$$u_i^{II}(\mathbf{X}) = \frac{2(1+\nu)}{E} \left(\Psi_i + \frac{1}{4(1-\nu)\frac{\partial}{\partial X_i}}(\phi - \Psi_k X_k) \right) \tag{16}$$

Substituting Eqn.(15) into Eqn.(16) yields the final expression for the displacements in Phase II, stated as:

$$u_i^{II}(\mathbf{X}) = \frac{(1+\nu)a^3}{2(1-\nu)E} \left(\frac{2\bar{\sigma}_{ik}X_k + \bar{\sigma}_{kk}X_i}{15R^5}(3a^2 - 5R^2) + \frac{\bar{\sigma}_{jk}X_i X_j X_k}{R^7}(R^2 - a^2) + \frac{4(1-\nu)\bar{\sigma}_{ik}X_k}{3R^3} \right) \tag{17}$$

The calculation of the spatial derivatives of the outside displacements $\partial u_i^{II}(\mathbf{X})/\partial X_j$ is straightforward and omitted here for brevity.

a) Comparison of L^2 error norms.   b) Comparison of H^1 error semi-norms.   c) Comparison of condition numbers.
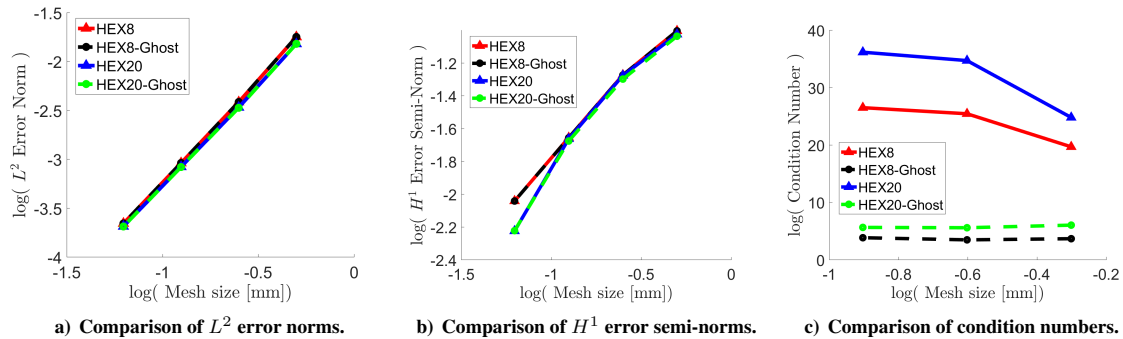
Figure 4. Convergence of linear and quadratic hexahedral elements over mesh size, with and without ghost stabilization.

In order for the aforementioned analytical solutions to be a valid reference, an infinite host matrix needs to be modeled using XFEM. To achieve this, "infinity" boundary conditions are applied to all six faces of the cubical matrix domain shown in Figure 3a. These are location dependent Dirichlet boundary conditions applied along the domain

a) Initial design and problem setup.

b) Selective springs during the design process.
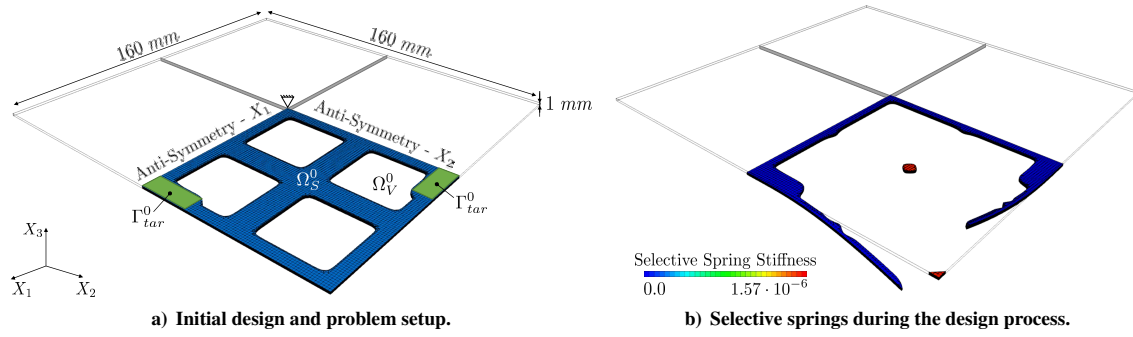
Figure 5. Problem setup for self-twisting propeller.

boundaries which prescribe the analytical displacement values computed using Eqn.(17). This approach allows for a finite simulation domain while simulating a swelling spherical inclusion within an infinite host matrix. Using the previously discussed problem setup and the derived analytical solutions within and outside the spherical inclusion as a reference, a mesh-refinement study is conducted. The aim of the study is to determine the effect of higher-order ghost stabilization on the displacement solution, the spatial gradient of the displacement solution, and the condition number of the linear system when using quadratic XFEM elements. The results are presented in Figure 4.

From Figure 4a it can be seen that using quadratic HEX20 elements versus linear HEX8 elements leads to a slightly smaller L^2 error in the displacement solution. The convergence behavior with respect to mesh refinement is however not affected by employing face-oriented ghost penalization. A similar effect is observed with respect to the H^1 error semi-norm in the displacement gradients, depicted in Figure 4b. Therefore, using higher-order spatial discretization leads to an improved convergence rate with mesh refinement. Regarding the condition number, a significant improvement is observed when using higher-order ghost penalization in combination with HEX20 XFEM elements (see Figure 4c). Compared to HEX8 elements, an increase in condition number is naturally expected due to the increased number of DOFs. This effect is however almost entirely mitigated by employing second-order face-oriented ghost stabilization, as shown in Figure 4c.

IV.   Definition of the Multi-Material Design Optimization Problem

To take advantage of the benefits of both a LS-XFEM-based approach and a density-based TO approach, a combined strategy is used in this work. This approach follows the work of [3] and is applied to linear elastic structural problems in this paper. For completeness, a brief overview of the definition of the multi-material topology optimization problem is stated here. A discretized nodal LS function $\phi(\mathbf{X})$ is used in order to represent the solid and void domains. The distinction is defined as:

$$\begin{aligned}
\phi(\mathbf{X}) &< 0, \ \forall \, \mathbf{X} \in \Omega_S^0 \\
\phi(\mathbf{X}) &> 0, \ \forall \, \mathbf{X} \in \Omega_V^0 \\
\phi(\mathbf{X}) &= 0, \ \forall \, \mathbf{X} \in \Gamma^0
\end{aligned} \tag{18}$$

where Ω_S^0 and Ω_V^0 denote the solid and void domain respectively and Γ^0 denotes the interface between them (see Figure 1). Just as in classical LS-XFEM, the nodal LS values are introduced as design variables. In addition, continuous nodal design variables $0 \leq \rho(\mathbf{X}) \leq 1$ are introduced within the solid domain Ω_S defining the material distribution by the Solid Isotropic Material with Penalization (SIMP) [15] law as:

$$E(\rho) = E_{\min} + (E_{\max} - E_{\min})\rho^\beta \tag{19}$$

where the elastic modulus is interpolated between a minimum and maximum property value using a SIMP exponent of $\beta = 3$. The minimum and maximum material properties represent Material one (Ω_1^0) and Material two (Ω_2^0), respectively. A schematic illustration of this distinction is shown in Figure 1. A similar interpolation with a SIMP exponent of $\beta = 1$ is used for interpolating the nodal densities ρ. A slightly modified SIMP interpolation scheme is used for interpolating the CTE of the two materials. It is defined as:

$$\alpha(\rho) = \alpha_{\min} + (\alpha_{\max} - \alpha_{\min})(1 - \rho)^\beta \tag{20}$$

where the SIMP exponent is $\beta = 3$.

The combined LS-XFEM and SIMP optimization problem can be formulated as:

$$\min_{\mathbf{s}} \ z(\mathbf{s}, \mathbf{u})$$
$$\text{s.t. } g_j(\mathbf{s}, \mathbf{u}) \leq 0 \qquad j = 1...N_g$$
$$\mathbf{s} \in \Pi = \{\mathbb{R}^{N_s} | \mathbf{s}_L \leq \mathbf{s} \leq \mathbf{s}_U\} \tag{21}$$
$$\mathbf{u} \in \mathbb{R}^{N_u}$$

where the design variables $\mathbf{s}$ include both the nodal LS values $\phi(\mathbf{X})$ and the nodal densities $\rho(\mathbf{X})$. Target shape matching is the main objective of this work. The objective function is defined as:

$$z(\mathbf{s}, \mathbf{u}) = \int_{\Gamma_{tar}^0} (\hat{\mathbf{u}} - \mathbf{u}_{tar})^2 dA + \gamma_{per} \int_{\Gamma^0} dA \tag{22}$$

where $\hat{\mathbf{u}}$ are the nodal displacements and $\mathbf{u}_{tar}$ is the target displacement defined over the target surface Γ_{tar}^0 (see Figure 5a). The perimeter penalty factor is denoted by γ_{per}. The first term of Eqn.(22) corresponds to a measure of how well the target shape is matched and the second term is a perimeter penalty. The perimeter penalty is applied to regularize the optimized design and to avoid small, irregular geometric features. A volume constraint is applied to the LS-XFEM problem in order to only allow for a maximum amount of solid phase within the entire design domain. A constraint on the maximum amount of solid phase is needed in order for the structure to achieve its desired target shape. This is not possible with the initial, plate-like design shown in Figure 5a. Mathematically, this inequality constraint is formulated as:

$$g_1(\mathbf{s}, \mathbf{u}) = \frac{\Omega_S^0}{(\Omega_S^0 + \Omega_V^0)} - \gamma_v \leq 0 \tag{23}$$

where γ_v is the maximum allowed amount of solid phase. In this work, a nested analysis and design approach, also known as NAND [16] is used. In this approach the equilibrium equations are solved separately from the optimization problem. Therefore, different solution algorithms are utilized for solving the "forward" problem and the optimization problem.

It should also be noted, that in addition to the interpolation schemes defined in Eqn.(18), Eqn.(19), and Eqn.(20) linear filtering techniques are used to regularize the design variable fields and to accelerate convergence. This also provides the ability for controlling the minimum feature size within the solid domain. The nodal density design variables are averaged for each FE to compute elementally constant material properties. A smoothed Heaviside projection [17] is used to obtain a well-defined material interface between Ω_1^0 and Ω_2^0 removing intermediate densities introduced through the linear filter.

V. Selective Structural Springs

As reported by [18], during a material-void TO process, isolated material islands can occur which will then lead to ill-conditioning of the linear system due to rigid body motion (RBM). Conceptually this is illustrated in Figure 1

Table 2. Parameters of the twisting propeller problem

	Value
Mesh Size	80 x 80 x 10 (Quarter Domain)
Element Size	$h = 1 \text{ x } 1 \text{ x } 0.1 \ mm$
Elastic Modulus Material 1	$E_1 = 8.0 \ MPa$
CTE Material 1	$\alpha_1 = 0.0$
Poisson's Ratio	$\nu_1 = \nu_2 = 0.4$
Elastic Modulus Material 2	$E_2 = 0.6 \ MPa$
CTE Material 2	$\alpha_2 = 0.054$
Ghost Penalization Parameter	$\gamma_G = 0.001$
Smoothing Filter Radius	$4 \ mm$
Number of Design Variables	286,900 (Quarter Domain)
Number of initial free DOFs	626,500 (Quarter Domain)

a) Evolution of normalized objective.

b) Evolution of volume constraint.
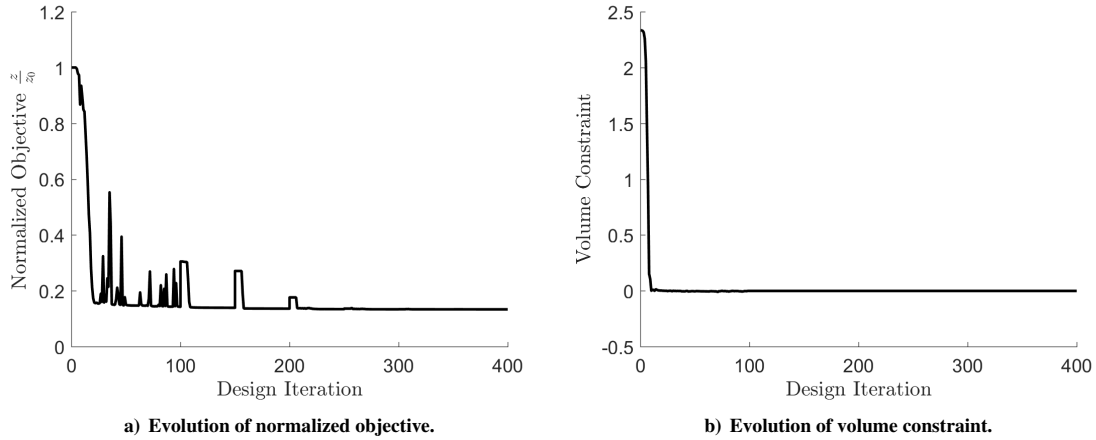
Figure 6. Evolution of objective and constraint.

where a sub-domain of Ω_2^0 is disconnected from the bulk of the solid domain Ω_S^0 and unconstrained. It was therefore suggested to add a small perturbation to the diagonal of the global stiffness matrix in order to prevent ill-conditioning of the linear system. Physically, this perturbation represents the attachment of weak linear springs to every DOF in the entire system. This was proven to be a simple and effective means to prevent RBM when using trilinear HEX8 elements. For quadratic elements which do not suffer from shear locking effects, a significant influence of the globally applied springs was seen on the deformation prediction.

One way to mitigate this problem is to apply the weak structural springs only to selective sub-domains which are isolated and need to be constrained in order to suppress RBM. To identify disconnected sub-domains, the solution of an auxiliary indicator field is used. Prior to solving the structural problem, a linear diffusion problem with bulk convection is solved. This determines whether a sub-domain is disconnected from mechanical boundary conditions or not. Dirichlet boundary conditions of $\tilde{\theta} = 0$ are applied to the same boundaries where the structural problem is constrained (indicated by hatched lines in Figure 1). In addition, a volumetric flux is applied to those boundaries. The residual equation for the auxiliary indicator field can be formulated as:

$$R_{Diff} = \int_{\Omega_S^0} \frac{\partial \delta\tilde{\theta}}{\partial X_i} \left(k \frac{\tilde{\theta}}{\partial X_i} \right) + \delta\tilde{\theta}(\kappa(\tilde{\theta} - \tilde{\theta}_{ref})) dV \tag{24}$$

where k is the thermal conductivity set to 20, $\tilde{\theta}$ is the scalar indicator value, κ is the bulk heat transfer coefficient set to 0.01, and $\tilde{\theta}_{ref}$ is the reference indicator value set to 1. The solution of Eqn.(24) will lead to indicator values of close to 0 in sub-domains connected to mechanical boundary conditions and indicator values close to 1 in disconnected sub-domains. Note that a non-physical "bulk" convection term in Eqn.(24) prevents ill-conditioning of the linear diffusion system due to disconnected sub-domains. To project the indicator values, to either exactly 0 or exactly 1, a smoothed Heaviside projection is used and defined as:

$$\bar{\theta} = \frac{1}{2} + \frac{1}{2} \tanh(k_w(\tilde{\theta} - k_t\tilde{\theta}_{ref})) \tag{25}$$

where $\bar{\theta}$ is the projected indicator value, k_w is the projection sharpness parameter, and k_t is the projection threshold. After the auxiliary indicator field solution has been obtained, the residual of the linear structural problem (1) is augmented by the following selective spring stiffness term:

$$R_{Spr_j} = \int_{\Omega_S^0} u_i \delta_{ij} \, r E_m \, \bar{\theta} \, dV \tag{26}$$

where the relative spring stiffness ratio is $r = 1.0 \cdot 10^{-6}$, and E_m is the elastic modulus of either solid material. An illustration of selectively applied structural springs for stabilization of isolated material domains is shown in Figure 5b. It can clearly be seen that a non-zero spring stiffness value is only applied to solid sub-domains disconnected from any mechanical boundary condition, which naturally arise during a solid-void LS-XFEM TO process.

a) **XFEM model of the final design of the active propeller.**

b) **Extracted material phases of the active propeller.**
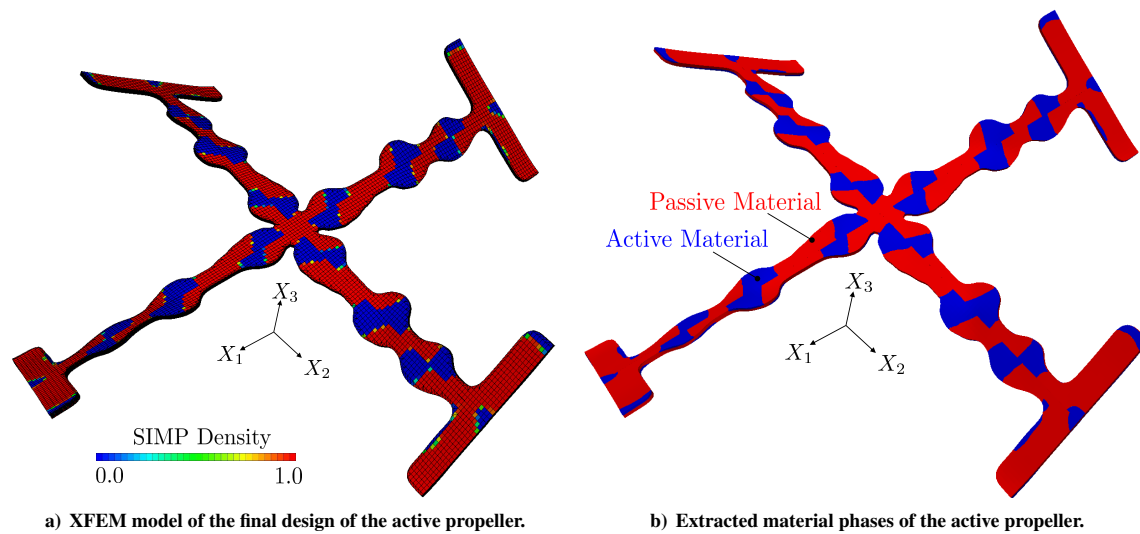
Figure 7. **Final design of the active propeller. Reflected to obtain the full design (void phase is not shown).**

VI.   Numerical Example

A numerical example is presented to demonstrate the applicability the proposed combined LS-XFEM and density-based TO framework for designing 3D self-deforming structures. For simplification of the numerical design process, the linear kinematics model introduced in Section A combined with higher-order XFEM elements is used. In order to meet a certain target shape, the topology of the solid domain as well as the material distribution within are altered during the optimization process. The linear "forward" problems are solved using the Multifrontal Massively Parallel Solver (MUMPS) [19, 20]. The optimization problem is solved using the Globally Convergent Method of Moving Asymptotes (GCMMA) [21] for which the objective and constraint gradients are obtained through the adjoint method. For more details regarding the computation of shape sensitivities using the XFEM, the interested reader is referred to [22].

A shape-changing propeller structure is designed by optimizing the arrangement of an active material (with a non-zero eigenstrain) and a passive material (with zero eigenstrain) within a solid domain. Simultaneously, the geometry of the solid domain itself is also subject to the optimization. The symmetry of the mechanical problem is taken advantage of and only one quarter of the domain is modeled and analyzed (see Figure 5a). Anti-symmetry boundary conditions are applied by clamping a single row of nodes along the internal edges to only allow for rotations about the respective axes. In addition, the center of the design domain is constrained in X_3-direction. The objective of this problem is to match a $\omega = 45°$ twisted target shape of the target domains Γ_{tar}^0. A perimeter penalty of $\gamma_{per} = 0.01$ and a volume constraint of $\gamma_v = 0.15$ are enforced.

The design variables defining the LS field exist only on the top surface of the domain which leads to constant nodal LS values through the thickness of the plate in X_3-direction (e.g. $\phi(X_1, X_2, X_3) = \phi(X_1, X_2)$). This ensures straight cuts through the thickness and prevents the optimizer from reducing the plate thickness in X_3-direction. Moreover, to prevent disconnection of the tips where the target displacement is measured from the base at the center of the propeller, the domain immediately bordering the anti-symmetry boundaries is prescribed to be solid phase throughout the optimization process. The parameters used for this design problem are listed in Table 2. An initial uniform density distribution of $\rho = 0.5$ is used to initialize the SIMP design variables. To initialize the LS design variables, an initial seeding with four square holes within one quarter of the entire domain is used as shown in Figure 5a.

The TO is performed using HEX20 XFEM elements with higher-order ghost stabilization and a linear elastic constitutive model. In addition, selective structural springs are employed. The evolution of objective and constraint is depicted in Figure 6. A quick drop in the objective function is seen, while initially the volume constraint is violated. Initial oscillations in the objective disappear after about 100 design iterations as an optimum material arrangement and solid-domain topology is identified. At this point, a continuation approach is enabled which increases the projection parameter every 50 design iterations, from initially 3 to 96 after 400 design iterations. This is reflected in slight

increases in the objective every 50 iterations, as shown in Figure 6a. The objective converges to a non-zero value of about 0.13, which means the desired target rotation angle of $\omega_{tar} = 45°$ cannot be full achieved (see Figure 8). This is due to the simplified linear elastic model used in the analysis in combination with an eigenstrain of 4.5% which is insufficient to fully reach the target angle.

The final, converged design in the deformed configuration is shown in Figure 7a where the solution of the quarter domain was reflected to complete the entire propeller for illustration purposes. The final design exhibits interesting features in order to assume the desired twisting of its tips. The overall shape corresponds to a cross structure with perpendicular tips forming the propeller "blades". The four arms are comprised of mostly passive material (red) with distinct strips of active material (blue) braided from the center outward. The alignment of these bands of active material is about 45° and they are placed at three "bulges" where the width of the propeller arms increases locally. These three areas at which twisting occurs are connected by two sections of purely passive material leading to incremental twisting of the propeller in the outward direction. Overall, the target shape of a twisting propeller comprised of four arms is achieved reasonably well. Figure 7b shows the extracted distinct material phases highlighting the interwoven active and passive material regions. The extracted geometries of each of the material phases could for example be used for AM of this active structure comprised of active and passive material.
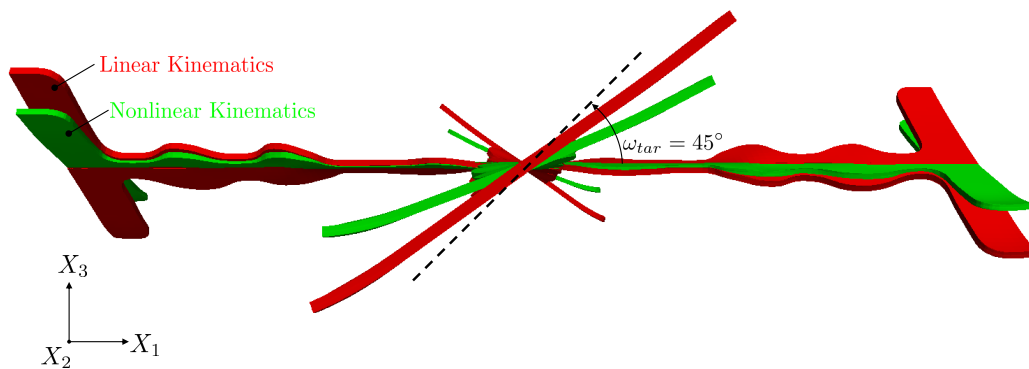
Figure 8. Comparison of the final design analyzed with a linear kinematics model and a nonlinear kinematics model with the desired target rotation angle $\omega_{tar} = 45°$ indicated by a dashed line.

To understand the error introduced in the design optimization process by employing a simplified linear elastic mechanical model, the final design is analyzed with the nonlinear kinematic model of Eqn.(7). Figure 8 shows the deformed twisted propeller in side view analyzed by both a linear kinematics model (red) and a nonlinear kinematics model (green). It can be seen that the linear elastic model significantly over-predicts the twist angle compared to a more realistic prediction by the nonlinear model using the same optimized material layout. Since the linear elastic model served as the basis during the design optimization process, the performance of the identified optimal design is worse than predicted by the linear model. This shows the need for using a nonlinear analysis during the entire optimization process, as performed by [3] in order to provide the proper guidance towards a more accurate optimal design.

VII. Conclusions and Outlook

This work employed a combined LS-XFEM and density-based multi-material TO framework for the design of shape-changing slender structures. The solid-void distinction is described by using LS-XFEM while the distribution of two different materials within the solid domain is modeled by a SIMP interpolation. A need for higher-order XFEM elements to accurately predict the deformation of slender structures was identified. To provide numerical stabilization of the XFEM, higher-order face-oriented ghost stabilization was employed. The originally proposed displacement gradient-based stabilization formulation was extended to a more general case and a verification against a 3D linear elastic, analytical solution was performed. Moreover, a scheme to selectively apply linear springs to isolated solid sub-domains was discussed. This approach prevents RBM and ill-conditioning of the global linear system as isolated solid sub-domains appear during the TO process. The identification of disconnected solid areas is achieved through the solution of a linear diffusion problem. Finally, a design optimization example was presented which demonstrates the applicability and the performance of the proposed framework. An active twisting propeller was designed and the respective target shape matched reasonably well. Moreover, a comparison of the performance of the optimized

design between a linear elastic and a nonlinear analysis was performed. Overall, robustness and applicability of the proposed framework using higher-order XFEM elements with higher-order ghost stabilization to design slender, self-deforming structures was demonstrated in this work. The need for incorporation of nonlinear kinematics during the entire optimization process was identified. Various applications, especially within the aerospace sector, can be considered for using the proposed design optimization framework. These include deployable space mechanisms such as solar sails, antennas or reflectors where a shape-change is triggered remotely. Alternatively, shape changing gripper structures or holding mechanisms can be designed and fabricated through AM using the interplay between active and passive materials.

Acknowledgments

References

[1] N. Moes, J. D. and T. Belytschko., 46, ., "A finite element method for crack growth without remeshing." *International Journal for Numerical Methods in Engineering*, 1999.

[2] N.P. Dijk, K. Maute, M. L. and Keulen, F., "Level-set methods for structural topology optimization: A review," *Structural and Multidisciplinary Optimization*, 2013.

[3] M. Geiss, N. Bodetti, O. W. K. M. M. D., "Combined Level-Set-XFEM-Density Topology Optimization of 4D Printed Structures undergoing Large Deformation," *ASME, J. Mech. Des*, 2018, (submitted).

[4] Ding, Z., Yuan, C., Peng, X., Wang, T., Qi, H. J., and Dunn, M. L., "Direct 4D printing via active composite materials," *Science Advances*, Vol. 3, No. 4, 2017.

[5] Nitsche, J., "Über ein Variationsprinzip zur Lösung von Dirichlet-Problemen bei Verwendung von Teilräumen, die keinen Randbedingungen unterworfen sind," *Abh. Math. Sem. Univ. Hamburg*, 1971.

[6] Burman, E. and Hansbo, P., "Fictitious domain methods using cut elements: III. A stabilized Nitsche method for Stokes problem," *ESAIM: Mathematical Modelling and Numerical Analysis*, Vol. 48, No. 3, 2014, pp. 859874.

[7] Villanueva, C. H. and Maute, K., "CutFEM topology optimization of 3D laminar incompressible flow problems," *Computer Methods in Applied Mechanics and Engineering*, Vol. 320, No. Supplement C, 2017, pp. 444 – 473.

[8] Stenberg, R., "On some techniques for approximating boundary conditions in the finite element method," *Journal of Computational and Applied Mathematics*, Vol. 63, No. 1, 1995, pp. 139 – 148, Proceedings of the International Symposium on Mathematical Modelling and Computational Methods Modelling 94.

[9] Sharma, A. and Maute, K., "Stress-based topology optimization using spatial gradient stabilized XFEM," *Structural and Multidisciplinary Optimization*, Vol. 57, No. 1, Jan 2018, pp. 17–38.

[10] Eshelby, J., "The determination of the elastic field of an ellipsoidal inclusion, and related problems," *Proceedings of the Royal Society of London A: Mathematical, Physical and Engineering Sciences*, Vol. 241, No. 1226, 1957, pp. 376–396.

[11] Eshelby, J., "The elastic field outside an ellipsoidal inclusion," *Proceedings of the Royal Society of London A: Mathematical, Physical and Engineering Sciences*, Vol. 252, No. 1271, 1959, pp. 561–569.

[12] Bower, A. F., *Applied Mechanics of Solids*, CRC Press, 2010.

[13] Papkovich, P., "The representation of the general integral of the fundamental equations of elasticity theory in terms of harmonic functions (in Russian," *Izv. Akad. Nauk SSSR, Phys.-Math. Ser*, Vol. 10, No. 1425, 1932, pp. 90.

[14] Neuber, H., "Ein neuer Ansatz zur Lösung räumlicher Probleme der Elastizitätstheorie. Der Hohlkegel unter Einzellast als Beispiel," *ZAMM - Journal of Applied Mathematics and Mechanics / Zeitschrift für Angewandte Mathematik und Mechanik*, Vol. 14, No. 4, pp. 203–212.

[15] Bendsøe, M. P., "Optimal shape design as a material distribution problem," *Structural optimization*, Vol. 1, No. 4, 1989, pp. 193–202.

[16] Arora, J. and Wang, Q., "Review of formulations for structural and mechanical system optimization," *Structural and Multidisciplinary Optimization*, Vol. 30, No. 4, 2005, pp. 251–272.

[17] Wang, F., Lazarov, B. S., and Sigmund, O., "On projection methods, convergence and robust formulations in topology optimization," *Structural and Multidisciplinary Optimization*, Vol. 43, No. 6, Jun 2011, pp. 767–784.

[18] Villanueva, C. H. and Maute, K., "Density and level set-XFEM schemes for topology optimization of 3-D structures," *Computational Mechanics*, Vol. 54, No. 1, Jul 2014, pp. 133–150.

[19] Amestoy, P. R., Guermouche, A., LExcellent, J.-Y., and Pralet, S., "Hybrid scheduling for the parallel solution of linear systems," *Parallel Computing*, Vol. 32, No. 2, 2006, pp. 136 – 156, Parallel Matrix Algorithms and Applications (PMAA04).

[20] Amestoy, P. R., Guermouche, A., L'Excellent, J.-Y., and Pralet, S., "Hybrid Scheduling for the Parallel Solution of Linear Systems," *Parallel Comput.*, Vol. 32, No. 2, Feb. 2006, pp. 136–156.

[21] Svanberg, K., "A Class of Globally Convergent Optimization Methods Based on Conservative Convex Separable Approximations," *SIAM Journal on Optimization*, Vol. 12, No. 2, 2002, pp. 555–573.

[22] Sharma, A., Villanueva, H., and Maute, K., "On shape sensitivities with heaviside-enriched XFEM," *Structural and Multidisciplinary Optimization*, Vol. 55, No. 2, Feb 2017, pp. 385–408.

Appendix C

Publication 2: Combined Level-Set-XFEM-Density Topology Optimization of 4D Printed Structures undergoing Large Deformation

Markus J. Geiss
Ann and H. J. Smead Department of
Aerospace Engineering Sciences,
University of Colorado at Boulder,
Boulder, CO 80309-0429
e-mail: Markus.Geiss@Colorado.edu

Narasimha Boddeti
SUTD Digital Manufacturing and Design Centre,
Singapore University of Technology and Design,
8 Somapah Road,
Singapore 487372
e-mail: Gowri_Boddeti@SUTD.edu.sg

Oliver Weeger
SUTD Digital Manufacturing and Design Centre,
Singapore University of Technology and Design,
8 Somapah Road,
Singapore 487372
e-mail: Oliver_Weeger@SUTD.edu.sg

Kurt Maute
Ann and H. J. Smead Department of
Aerospace Engineering Sciences,
University of Colorado at Boulder,
Boulder, CO 80309-0429
e-mail: Kurt.Maute@Colorado.edu

Martin L. Dunn
College of Engineering and Applied Sciences,
University of Colorado Denver,
1200 Larimer Street,
Denver, CO 80217-3364
e-mail: Martin.Dunn@UCDenver.edu

Combined Level-Set-XFEM-Density Topology Optimization of Four-Dimensional Printed Structures Undergoing Large Deformation

Advancement of additive manufacturing is driving a need for design tools that exploit the increasing fabrication freedom. Multimaterial, three-dimensional (3D) printing allows for the fabrication of components from multiple materials with different thermal, mechanical, and "active" behavior that can be spatially arranged in 3D with a resolution on the order of tens of microns. This can be exploited to incorporate shape changing features into additively manufactured structures. 3D printing with a downstream shape change in response to an external stimulus such as temperature, humidity, or light is referred to as four-dimensional (4D) printing. In this paper, a design methodology to determine the material layout of 4D printed materials with internal, programmable strains is introduced to create active structures that undergo large deformation and assume a desired target displacement upon heat activation. A level set (LS) approach together with the extended finite element method (XFEM) is combined with density-based topology optimization to describe the evolving multimaterial design problem in the optimization process. A finite deformation hyperelastic thermomechanical model is used together with an higher-order XFEM scheme to accurately predict the behavior of nonlinear slender structures during the design evolution. Examples are presented to demonstrate the unique capabilities of the proposed framework. Numerical predictions of optimized shape-changing structures are compared to 4D printed physical specimen and good agreement is achieved. Overall, a systematic design approach for creating 4D printed active structures with geometrically nonlinear behavior is presented which yields nonintuitive material layouts and geometries to achieve target deformations of various complexities.
[DOI: 10.1115/1.4041945]

1 Introduction

Advanced additive manufacturing technologies like three-dimensional (3D) printing have improved vastly in recent years in terms of accuracy, material variety, and reliability. Recently, the concept of four-dimensional (4D) printing was introduced by Tibbits [1], where external stimuli are used to trigger shape changes after a structure is 3D printed. The shape change over time is therefore seen as the fourth dimension. In Ref. [2], this concept was used to design transforming shape memory polymer structures utilizing the thermomechanical response of a glassy polymer within an elastomer matrix. A similar material response was studied in Ref. [3] to create active origami structures. Exploiting the shape memory behavior of a 3D printed glassy polymer, Maute et al. [4] used level set (LS) topology optimization to create printed active composites, which assume a target shape after a thermomechanical training and activation cycle. As stated by Ding et al. [5], the drawback of these traditional approaches of 4D printing is the fact that a complex thermomechanical training and activation cycle is required through which a shape change can be triggered. To alleviate this issue, [5] introduced a novel approach called "direct 4D printing" where no external training cycle is required before the shape change occurs upon printing. The so called "printing strain" used in this method for creating a shape change is an inelastic eigenstrain that is programmed into the 3D printed structure during the printing process. This strain is compressive, and its magnitude can be designed by controlling the time and intensity of the UV-curing of photo polymers in the polyjet process. In the current work, two polymers with different magnitudes of eigenstrain and different glass transition temperatures are used to achieve a desired shape change upon release of the built-in eigenstrain. A component fabricated in this manner therefore consists of multiple well-bonded polymers with a high-fidelity geometry, and with each polymer containing a spatially variable eigenstrain. Upon printing, the component is heated to release the built-in eigenstrain of the rubbery polymer (active material) by lowering the stiffness of the glassy polymer (passive material). This is achieved through heating of the printed structure beyond the glass transition temperature of the passive material causing a permanent shape change. Alternatively, a frontal polymerization process has been proposed by Zhao et al. [6] and Zhao et al. [7]. This process uses the change in intensity of photo polymerization to create spatially varying material parameters leading to 4D printed self-folding origami structures. Shape changes are triggered by a solvent entering a loose polymer matrix which then causes isotropic swelling. In this work, the direct 4D printing method is employed as a convenient way to incorporate spatially varying eigenstrains during fabrication of self-actuating plate-like structures. For a more detailed study of the process of direct 4D printing, the interested reader is referred to Ref. [5].

In order to exploit spatially varying inelastic strains to obtain complex target displacements upon activation, an inverse design problem is formulated and solved. Given a desired target deformation, the optimal geometry and material layout of active 4D

www.manaraa.com

printed components are determined in a systematic manner. In previous works [8] and [9], this has only been done for one-dimensional (1D) rod structures or for simple target shapes [5] where it was possible to predetermine the optimal material layout intuitively. A similar approach based on classical origami designs is demonstrated in Ref. [10] for self-folding composite structures. In this paper, a new multimaterial topology optimization formulation is used to determine the material arrangement of shape-changing 4D printed structures undergoing large deformation. The proposed computational design framework accurately captures the physical response of the structure by employing a hyperelastic thermomechanical model combined with an higher-order extended finite element method (XFEM) formulation. The shape of the structure is defined by a LS method. A hybrid approach combining LS-XFEM and density-based topology optimization is introduced to solve the multimaterial design problem. These topology optimization schemes have each demonstrated individually a wide range of applicability. An overview of LS and density topology optimization methods is given in Refs. [11–13], respectively. Some applications of topology optimization can also be found in the field of design optimization of self-folding structures, for example: Fuchi et al. [14] used a density-based method to optimize the layout of monolithic liquid crystal elastomers in order to create folding liquid crystal elastomer actuators. However, a simplified linear elastic model operating in the small strain regime greatly limits the accuracy of this approach. A different simplified approach was taken by Kwok et al. [15] where shape optimization is employed to determine the optimal layout of cuts to design active 3D origami and kirigami structures using 4D printing. And just recently, Xue et al. [16] applied the concept of moving morphable components [17] in combination with a genetic algorithm for topology optimization of post-buckled 3D kirigami structures. Even though each of these approaches greatly reduces the number of design variables and hence the complexity of the optimization problem, only a subspace of all possible designs is explored. To take advantage of the entire design space while considering a fully nonlinear structural response, a combined LS-XFEM and density topology optimization framework for designing 4D printed active structures is proposed in this paper.

The design, fabrication, and activation process of 4D printed structures as proposed in this work are conceptually shown in Fig. 1, where target displacement matching is the objective. This can be achieved by either specifying the desired target shape, i.e., position of points of the structure in the deformed (activated) configuration, or by specifying the required displacement of certain points of the structure to achieve the desired deformation. In this work, the displacement of target points on the domain boundary is specified to achieve target deformations, see Fig. 1(a). Starting from an initially flat plate (b), a level set function (LSF) is used to define an initial arrangement of solid and void domains. Within the solid domain, a fictitious density field is used to interpolate the different properties of an active and a passive material. Both the LSF and the density distributions are discretized on the XFEM background mesh. The resulting parameter optimization problem is then solved by a nonlinear programming method. After a final design (i.e., geometry and material distribution) has been found (c), subdomains of active and passive material are extracted in a postprocessing step (d). Once the flat structure has been printed (e), the shape change is activated through relaxation of the compressive printing strain in the active material in a hot water bath. This is achieved by heating up the structure above the glass transition temperature of the passive, stiff material at which its stiffness is significantly reduced. At this state, the eigenstrains of the active material can relax leading to the desired change in shape. After a subsequent cool-down, the passive material stiffens and a permanently deformed structure is obtained (f).

The theoretical background of the physical model, the spatial discretization of state and optimization variables, and the optimization problem along with examples are presented in the remainder of this paper, which is organized as follows: Section 2 introduces the continuum model of the nonlinear thermomechanical phenomena. Section 3 provides details on the optimization approach and the XFEM model. Section 4 describes the validation of the thermomechanical model, and design optimization examples are presented in Sec. 5 along with experimental results. A summary of the work is presented in Sec. 6.

2 Hyperelastic Thermomechanical Model

The total design domain Ω_D^0 is comprised of solid and void subdomains (i.e., Ω_S^0 and Ω_V^0), such that $\Omega_D^0 = \Omega_S^0 \cup \Omega_V^0$. Within the solid domain Ω_S^0 (see Fig. 2(a)), balance of linear momentum in the undeformed configuration is described by the static equilibrium. The weak form of the governing equation using a total Lagrangian formulation is stated as

$$\mathbf{R} = \int_{\Omega_S^0} (\delta\mathbf{F} : \mathbf{P} - \delta\mathbf{u}\rho_0\mathbf{B})dV - \int_{\Gamma_{\overline{T}^0}} \delta\mathbf{u}\overline{\mathbf{T}}dA = 0 \qquad (1)$$
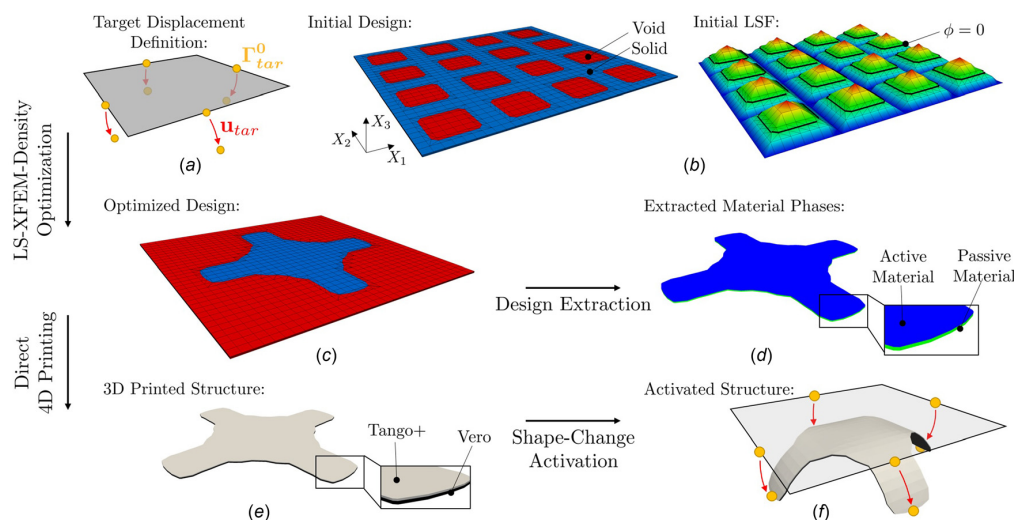

Fig. 1 Conceptual steps of the design process from (a) the definition of a target displacement to (f) an activated structure using direct 4D printing
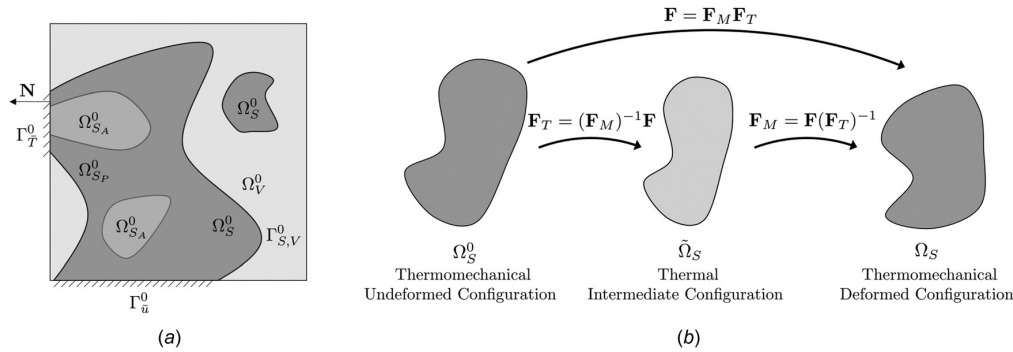
Fig. 2 (*a*) Design domain decomposition into solid (Ω_S^0) and void (Ω_V^0) subdomains using LS-XFEM along the interface $\Gamma_{S,V}^0$. Within the solid domain, a further distinction is made between an active material ($\Omega_{S_A}^0$) and a passive material ($\Omega_{S_P}^0$). (*b*) Multiplicative decomposition of the total deformation gradient into thermal and mechanical deformation gradient.

where $\mathbf{F} = \partial\mathbf{x}/\partial\mathbf{X}$ is the total deformation gradient tensor with $\mathbf{x} = \mathbf{u} + \mathbf{X}$ defining the relation between spatial coordinates in the undeformed ($\mathbf{X}$) and deformed ($\mathbf{x}$) configurations Ω_S^0 and Ω_S, respectively. The displacements are denoted by $\mathbf{u}$ and $\delta\mathbf{u}$ are the admissible test functions. The first Piola-Kirchhoff stress tensor is denoted by $\mathbf{P}$, and $\mathbf{B}$ is the prescribed body force vector in the undeformed configuration. The density is denoted by ρ_0 and $\overline{\mathbf{u}}$ is the prescribed displacement field on $\Gamma_{\overline{u}}^0$, see Fig. 2(*a*). The prescribed traction vector on $\Gamma_{\overline{T}}^0$ is $\overline{\mathbf{T}}$ and the total design domain boundary Γ^0 is comprised of $\Gamma^0 = \Gamma_{\overline{T}}^0 \cup \Gamma_{\overline{u}}^0$. A hyperelastic Saint Venant-Kirchhoff constitutive model for isotropic compressible solids is used in the current work. The hyperelastic Saint Venant-Kirchhoff material model is suitable for large deformations at small strains, which is the case for the slender structures targeted in this work. The proposed design optimization framework can easily be extended to operate on nonlinear constitutive models for both compressible and incompressible materials. This is especially relevant for simulating rubbery, nearly-incompressible polymers and therefore should be studied in future work. The Saint Venant-Kirchhoff material model is defined as

$$\tilde{\mathbf{S}} = 2\mu\mathbf{E}_M + \lambda\text{tr}(\mathbf{E}_M)\mathbf{I} \tag{2}$$

where $\tilde{\mathbf{S}}$ is the second Piola-Kirchhoff stress tensor in the intermediate configuration (see Fig. 2(*b*)) and $\mathbf{E}_M$ is the Green-Lagrange strain tensor defined as the deformation of the intermediate configuration to the thermomechanical deformed configuration. The second-order identity tensor is denoted by $\mathbf{I}$. The Lamé constants are denoted by μ and λ which are related to the Young's modulus E and Poisson's ratio ν as follows:

$$\mu = \frac{E}{2(1+\nu)} \quad\text{and}\quad \lambda = \frac{E\nu}{(1+\nu)(1-2\nu)} \tag{3}$$

In the context of topology optimization using the density method, the Young's modulus is manipulated as a function of the design variables whereas the Poisson's ratio is kept constant. A more detailed discussion of the optimization problem is presented in Sec. 3.1.

To model the inelastic printing strain built into the elastomer, a residual thermal strain model is used as suggested by Ding et al. [5]. In a finite deformation case, special consideration with respect to the decomposition of the total deformation gradient is required. As indicated in Fig. 2(*b*), a multiplicative decomposition of the total deformation gradient $\mathbf{F}$ into an inelastic thermal deformation gradient $\mathbf{F}_T$ and an elastic mechanical deformation gradient $\mathbf{F}_M$ is used. The multiplicative decomposition of the total deformation gradient can be stated as

$$\mathbf{F} = \mathbf{F}_M\mathbf{F}_T \tag{4}$$

For the thermal deformation gradient tensor, a linear thermal expansion model is assumed

$$\mathbf{F}_T = (1 + \alpha_k[\overline{T} - T_0])\mathbf{I} \tag{5}$$

where α_k is the linear coefficient of thermal expansion (CTE) of either solid material (k = active or passive) representing the amount of inelastic expansion. The externally applied temperature is $\overline{T}$, which is a linear function of pseudo time of the deformation process, and T_0 is the reference temperature. Using the previously defined relationships, the Green-Lagrange strain tensor is defined as

$$\mathbf{E}_M = \frac{1}{2}(\mathbf{C}_M - \mathbf{I}) \tag{6}$$

where the right Cauchy–Green deformation tensor is $\mathbf{C}_M = (\mathbf{F}_M)^{\text{T}}\mathbf{F}_M$.

For integration of the governing equation stated in Eq. (1) in the undeformed configuration, the second Piola-Kirchhoff stress tensor $\tilde{\mathbf{S}}$ is pulled back from the intermediate configuration $\tilde{\Omega}_S$ to the undeformed configuration Ω_S^0 using the Piola-transform. This transformation is defined as

$$\mathbf{S} = (\mathbf{F}_T)^{-1}\tilde{\mathbf{S}}(\mathbf{F}_T)^{-\text{T}}J_T \tag{7}$$

where J_T is the Jacobian of the thermal deformation gradient tensor $J_T = \det(\mathbf{F}_T)$. The first Piola-Kirchhoff stress tensor in the undeformed configuration is finally computed as

$$\mathbf{P} = \mathbf{F}\,\mathbf{S} \tag{8}$$

2.1 Follower Pressure Load. In order to enforce an end-stiffness constraint on the final, deformed structure, a follower pressure load is introduced and added to the weak form of the governing Eq. (1). To this end, a deformation-dependent (i.e., follower) Neumann boundary condition is employed, which is formulated in the deformed configuration and mapped back to the undeformed configuration. Using Nanson's formula [18], the relationship between surface areas in the undeformed and deformed configuration is defined. The follower pressure can simply be evaluated in the undeformed configuration as follows:

$$\mathbf{R}_{\Gamma_P} = -\int_{\Gamma_{\overline{T}}^0} \delta\mathbf{u}(\mathbf{F})^{-\text{T}}\mathbf{N}\,\mathbf{J}\,\overline{P}dA \tag{9}$$

where dA is an infinitesimal surface area in the undeformed configuration, $J = \det(\mathbf{F})$ is the determinant of the total deformation gradient, and $\mathbf{N}$ is the surface normal in the undeformed configuration. The surface pressure scalar reformulated in the undeformed configuration is denoted by $\overline{P}$. For simplicity, it is assumed that $\overline{P}$ is not state dependent. A more detailed discussion of the end-stiffness constraint is presented in Sec. 3.4.

2.2 Adaptive Load-Stepping Approach. To efficiently predict the nonlinear deformation of 4D printed self-deforming structures, an adaptive load-stepping scheme is used for the XFEM analysis. Schematically, the evolution of the temperature load $T(t)$, applied follower load $P(t)$, and displacement response $\mathbf{u}(t)$ as a function of pseudo time t are depicted in Fig. 3. An adaptive time-stepping scheme is used such that the initially set time-step size Δt_0 is reduced by a factor f in case a Newton–Raphson solve does not converge to an equilibrium solution for a set maximum number of nonlinear iterations. This is, for example, encountered when domains of intermediate (weak) material dominate the structural response during the topology optimization process. In such an event, the time-step is adaptively reduced until a specified number of (converged) nonlinear solutions are obtained at the reduced time-step. After that, the original time-steps size is gradually restored. The total number of time-steps is adjusted accordingly to reach the final loading time t_{Load}. The temperature load T is increased linearly between t_0 and t_{Load} to achieve a maximum value $\overline{T}$ while the follower surface pressure load P is zero during this time. Conceptually, this is shown in Figs. 3(a) and 3(b), respectively. The maximum value of $\overline{T}$ corresponds to the inelastic printing strain. Between t_{Load} and t_{Pert}, the external temperature load is kept constant at $\overline{T}$ while a constant nonzero follower perturbation load $\overline{P}$ is applied. The magnitude of the non-zero follower perturbation load is chosen sufficiently small in order to achieve fast convergence of the nonlinear solver, ideally in a single iteration. This is valid for enforcing an end-stiffness constraint measuring the change in total strain energy based on a linear concept.

3 Multimaterial Topology Optimization

A multimaterial topology optimization approach is adopted to determine the geometry and the spatial material arrangement of 4D printed active structures. This approach builds on a LS-XFEM optimization framework previously used to study problems in structural mechanics [4,19,20] and fluid mechanics [21,22]. This section provides an overview of the multimaterial topology optimization approach, while more details regarding immersed boundary techniques used for design optimization are provided in Ref. [23].

3.1 Combined Level Set-Density Geometry and Material Description. The three-material problem depicted in Fig. 2(a) is described by a combined LS-density approach. A nodally discretized LSF is used to distinguish between a solid and a void domain where negative LS values ($\phi_i < 0$) represent the solid domain Ω_S^0 and positive LS values ($\phi_i > 0$) represent the void domain $\Omega_V^{0^*}$. The zero LS iso-contour ($\phi_i = 0$) represents the phase boundary $\Gamma_{S,V}^0$ between the solid and the void domain. Nodal LS values ϕ_i are explicitly defined in terms of nodal design variables s_j^ϕ using a

linear filtering scheme as proposed by Kreissl and Maute [24]. This linear filtering technique enhances convergence of the optimization problem by increasing the zone of influence of each design variable and is formulated as

$$\phi_i = \frac{\sum_{j=1}^{N_n} w_{ij} s_j^\phi}{\sum_{j=1}^{N_n} w_{ij}}, \quad w_{ij} = \max\left(0, r_s - |\mathbf{X}_i - \mathbf{X}_j|\right) \quad (10)$$

where N_n is the number of finite element (FE) nodes within the smoothing radius, r_s, and $|\mathbf{X}_i - \mathbf{X}_j|$ is the Euclidean distance between node i and j measured in the undeformed configuration (indicated by a superscript ^{0}). Index i denotes the current node for which the LS value is computed and index j denotes each node within the smoothing radius contributing to the LS value ϕ_i.

Combining the level set method with the XFEM yields a crisp solid–void interface, which is naturally suited for additive manufacturing reducing the need for postprocessing. However, as mentioned in Refs. [12] and [24], a strong influence of the final solution on the initial guess is observed in LS-XFEM topology optimization. Moreover, since LS-XFEM topology optimization is solely driven by localized sensitivities along the interface, the appearance of new holes within the solid domain is not possible [4]. One way to mitigate this issue and the dependency of the final design on the initial guess is to use topological derivatives, as suggested by Norato et al. [25]. In the current work, a sufficiently large number of initial void inclusions are used to mitigate this dependency.

In addition, a density-based topology optimization approach is used within the solid domain Ω_S^0 in order to distinguish between an active material ($\Omega_{S_A}^0$) and a passive material ($\Omega_{S_P}^0$). This combined approach allows for the description of the multimaterial topology optimization problem at hand. Nodally discretized, fictitious density design variables $0 \leq s_i^{\bar{\rho}} \leq 1$ are used to track the material distribution within the solid phase. A standard solid isotropic material with penalization (SIMP) approach [26] is adopted. Considering an element-wise constant density interpolation, the material property within an element is defined as

$$p^e(\hat{\rho}_i^e) = p_{\min}^e + (p_{\max}^e - p_{\min}^e)(\hat{\rho}_i^e)^\beta \quad (11)$$

where p^e represents any elemental material property like the Young's modulus, density, or CTE. Physical properties corresponding to the active material and passive material are denoted by $p_{\min}^e$ and $p_{\max}^e$, respectively, and β is the so-called SIMP exponent used to achieve different interpolation behavior. Different SIMP exponents are used for interpolation of different material properties. Elementally averaged fictitious density values $\tilde{\rho}_j^e$ are obtained from nodal fictitious density design variables $s_i^{\bar{\rho}}$ as

$$\tilde{\rho}_j^e = \frac{\sum_{i=1}^{N_n^e} s_i^{\bar{\rho}}}{N_n^e} \quad (12)$$
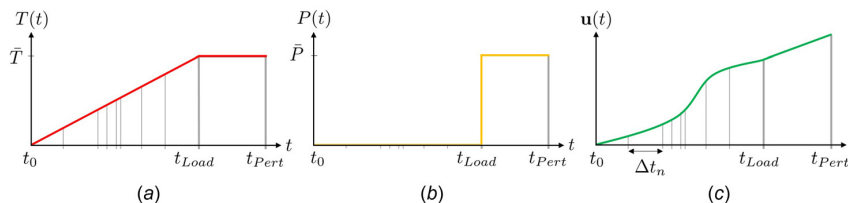

Fig. 3 Adaptive load-stepping technique used to solve the nonlinear problem: (a) temperature load profile, (b) follower load profile, and (c) displacement response over pseudo time

where N_n^e is the number of nodes per element j. A linear elemental filter similar to the one stated in Eq. (10) is then used to compute a smoothed fictitious elemental density $\overline{\rho}_i^e$ from the elementally averaged fictitious densities $\tilde{\rho}_j^e$. In addition, a smoothed Heaviside projection scheme proposed by Lazarov et al. [27] is used subsequently to mitigate the blurriness introduced by the linear filtering scheme. The projection function used to compute the fictitious projected elemental density $\hat{\rho}_i^e$ is stated as

$$\hat{\rho}_i^e = \frac{\tanh(\gamma(\overline{\rho}_i^e - \eta)) + \tanh(\gamma\eta)}{\tanh(\gamma(1 - \eta)) + \tanh(\gamma\eta)} \tag{13}$$

where γ is the projection sharpness parameter and η is the projection threshold parameter. The projection (13) is applied through a continuation approach where the projection sharpness parameter is gradually increased in the optimization process. More details regarding this approach are found in the discussion of the results in Sec. 5.

3.2 Extended Finite Element Method Model.
The XFEM is used in this work to discretize the weak form of the governing Eq. (1) on nonconforming subdomains. This immersed boundary method is utilized to distinguish between the solid (Ω_S^0) and the void (Ω_V^0) subdomains along the interface ($\Gamma_{S,V}^0$) defined by the zero LS iso-contour as depicted in Fig. 2(a). The advantage of this discretization method is that a high spatial resolution of the interface described by the level set method is retained throughout the optimization process while operating on a fixed background mesh, thus avoiding the need for remeshing. The XFEM approach, however, requires enriching the classical FE approximation spaces with additional shape functions [28] in order to avoid spurious coupling and load transfer between physically disconnected domains. Note that, in general, enrichment functions are also needed to capture weak and strong discontinuities across material phases. However, this requirement does not apply here, as the XFEM is applied to distinguish only between the solid (Ω_S^0) and the void (Ω_V^0) phase. Thus, the displacement field only exists within the solid subdomain and any element within the void phase can be omitted. A generalized Heaviside enrichment approach [29] is used where the displacements in the solid phase are approximated by standard FE shape functions. The nodal displacements $\mathbf{u}_i(\mathbf{X})$ of node i within the solid domain Ω_S^0 are approximated as [22]

$$\mathbf{u}_i(\mathbf{X}) = \sum_{m=1}^{M} \left(H(-\phi(\mathbf{X})) \sum_{k=1}^{N_n^e} N_k(\mathbf{X}) \delta_{mq}^k \mathbf{u}_{im}^k \right) \tag{14}$$

where H is the Heaviside function as a function of the LS value $\phi(\mathbf{X})$ defined as

$$H(\phi) = \begin{cases} 1 & \text{if } \phi(\mathbf{X}) > 0 \\ 0 & \text{if } \phi(\mathbf{X}) < 0 \end{cases} \tag{15}$$

The maximum number of enrichment levels is denoted by M, $N_k(\mathbf{X})$ is the elemental shape function and δ_{mq}^k is the Kronecker delta which selects the active enrichment level q for node k. δ_{mq}^k ensures that displacements at node k are only interpolated by a single set of degrees-of-freedom (DOFs) defined at node position $\mathbf{X}$ such that the partition of unity principle is satisfied [20]. The Heaviside function H is used to only activate shape functions within the solid phase as displacement solutions in the void domain would be physically meaningless. For more details about the generalized Heaviside enrichment strategy employed in this work, the interested reader is referred to Refs. [23], [30], and [31].

For stabilization of the XFEM discretization, a geometric preconditioning scheme as proposed by Lang et al. [32] is used. This geometric preconditioner ensures that DOFs with vanishing zones

of influence, which arise when the LS intersection is too close to a FE node, are rescaled or eliminated in order to provide numerical stability.

Dirichlet boundary conditions applied to the solid subdomain Ω_S^0 are enforced weakly using Nitsche's method [33]. The weak form of the governing Eq. (1) is augmented with the weak boundary condition residual contribution $\mathbf{R}_\Gamma^D$ stated as

$$\mathbf{R}_\Gamma^D = -\int_{\Gamma_{\overline{u}}^0} [[\delta\mathbf{u}]] \ \mathbf{P}(\mathbf{u}) \ \mathbf{N} dA$$
$$- \int_{\Gamma_{\overline{u}}^0} \mathbf{P}(\delta\mathbf{u}) \ \mathbf{N} \ [[\mathbf{u}]] dA$$
$$+ \gamma_D \int_{\Gamma_{\overline{u}}^0} [[\delta\mathbf{u}]] \ [[\mathbf{u}]] dA \tag{16}$$

where the jump operator $[[\bullet]]$ is defined as

$$[[\mathbf{u}]] = \mathbf{u} - \overline{\mathbf{u}}, \quad [[\delta\mathbf{u}]] = \delta\mathbf{u} - \delta\overline{\mathbf{u}} \tag{17}$$

The penalty factor to enforce the prescribed Dirichlet boundary condition $\overline{\mathbf{u}}$ is denoted by γ_D. The first term in Eq. (16) corresponds to the standard consistency term, the second term to the adjoint consistency, and the last term is the Nitsche penalty term which explicitly controls the accuracy at which the Dirichlet boundary condition is enforced.

3.3 Selective Structural Springs.
To avoid ill-conditioning of the linear system due to rigid body modes of disconnected solid subdomains surrounded by the void phase (see Fig. 2(a)), selective structural springs are introduced. This approach was initially proposed by Villanueva and Maute [21] for fluid problems and is extended to nonlinear structural mechanics in this work. To identify disconnected solid domains "floating" within the void domain, an auxiliary indicator field modeled as a linear diffusion problem is introduced within the solid domain. The weak form of the governing equation for the auxiliary scalar indicator field $\tilde{\theta}$ is formulated as

$$\mathbf{R}_{\text{Aux}} = \int_{\Omega_S^0} \delta\nabla\tilde{\theta}(\kappa\nabla\tilde{\theta}) + \delta\tilde{\theta}h(\tilde{\theta} - \tilde{\theta}_{\text{ref}})dV \tag{18}$$

where $\delta\tilde{\theta}$ are the admissible test functions and κ denotes the thermal conductivity. The bulk heat transfer coefficient is denoted by h and $\tilde{\theta}_{\text{ref}}$ is the reference indicator value. The diffusion problem (18) along with the appropriate boundary conditions will lead to indicator values of close to 0.0 in domains that are connected to where the Dirichlet boundary condition of $\tilde{\theta} = 0.0$ is applied and indicator values close to 1.0 in disconnected subdomains. It should be noted that a nonphysical "bulk" convection term in Eq. (18) prevents ill-conditioning of the linear diffusion system even if disconnected subdomains exist. After the auxiliary indicator field solution has been obtained, a smoothed Heaviside projection function is used to enforce a 0–1 indicator field. The weak form of the governing equation of the nonlinear structural problem (1) is augmented by the following selective spring stiffness term

$$\mathbf{R}_{\text{Spr}} = \int_{\Omega_S^0} \delta\mathbf{u} \, \mathbf{I} \, \mathbf{u} \, r \, E_k \overline{\theta} \, dV \tag{19}$$

where r is the relative spring stiffness ratio, $\overline{\theta}$ is the projected indicator field value, and E_k is the Young's modulus of either solid material ($k = $ active or passive). For more details regarding selective structural springs, the reader is referred to Ref. [34].

In summary, the governing equation in weak form is composed of the following terms which have been introduced above, see Eqs. (1), (9), (16), (18), and (19):

$$\tilde{\mathbf{R}} = \mathbf{R} + \mathbf{R}_{\Gamma_P} + \mathbf{R}_{\Gamma}^D + \mathbf{R}_{\text{Aux}} + \mathbf{R}_{\text{Spr}} = \mathbf{0} \qquad (20)$$

3.4 Formulation of Optimization Problem. The combined LS-XFEM and density approach introduced in Sec. 3.1 describes the geometry and the material distribution in parameterized form. These parameters define the optimization variables $\mathbf{s}$. The optimization problem considered here can be written as follows:

$$\min_{\mathbf{s}} \ z(\mathbf{s}, \mathbf{u}) = z_{\text{tar}}(\mathbf{s}, \mathbf{u}) + z_{\text{reg}}(\mathbf{s})$$
$$\text{s.t.} \ \ g_j(\mathbf{s}, \mathbf{u}) \leq 0 \quad j = 1 \ldots N_g$$
$$\mathbf{s} \in \Pi = \{\mathbb{R}^{N_s} | \mathbf{s}_L \leq \mathbf{s} \leq \mathbf{s}_U\} \qquad (21)$$
$$\mathbf{u} \in \mathbb{R}^{N_u}$$

where the nodal displacements $\mathbf{u}$ satisfy the discretized governing equation $\tilde{\mathbf{R}} = \mathbf{0}$ and implicitly depend on the design variables $\mathbf{s}$. The number of design variables is denoted by N_s and the number of state variables is N_u. The design variables include both the nodal LS values s_i^ϕ and the fictitious nodal SIMP densities $s_i^{\bar{\rho}}$, such that $s_i = [s_i^\phi, s_i^{\bar{\rho}}]$. The lower and upper bounds of the optimization variables are denoted by $\mathbf{s}_L$ and $\mathbf{s}_U$, respectively. The number of inequality constraints g_j is denoted by N_g. In this work, a nested analysis and design approach [35] is used where the displacements $\mathbf{u}$ are considered dependent variables of $\mathbf{s}$ and satisfy the governing equations for a given design. The advantage of this approach is that different solution algorithms can be utilized for solving the "forward" analysis problem and the optimization problem.

Displacement matching of active structures is the main objective of this work. The first part of the objective function is therefore formulated as a minimization of the squared difference between the nodal displacements $\mathbf{u}$ and the target displacements $\mathbf{u}_{\text{tar}}$ at a specified target set $\Gamma_{\text{tar}}^0 \subset \Gamma^0$.

$$z_{\text{tar}}(\mathbf{s}, \mathbf{u}) = \int_{\Gamma_{\text{tar}}^0} (\mathbf{u} - \mathbf{u}_{\text{tar}})^2 dA \qquad (22)$$

It should be noted that even though a target displacement is specified a priori, no constraints with respect to the required geometry and material layout are imposed. The resulting, in general, nonintuitive geometry and material layout required to achieve a deformation that best matches the target displacements $\mathbf{u}_{\text{tar}}$ is solely a result of solving the optimization problem of Eq. (21). Selecting the target set Γ_{tar}^0, which in this work is defined as a subset of the design domain boundary Γ^0, is in general nontrivial and dependent on the desired target deformation. Mechanical constraints like self-penetration or nonuniqueness of geometric mappings of planar structures onto the desired target deformation need to be considered in order to define a well-posed optimization problem. More details on the target displacements and the corresponding target sets considered in this work are provided in Sec. 5.

In addition to target displacement matching, a regularization term is added to the objective function in order to avoid the emergence of irregular geometric artifacts [11]. Here, regularization is introduced through a perimeter penalty that is formulated as

$$z_{\text{reg}}(\mathbf{s}, \mathbf{u}) = \gamma_{\text{per}} \int_{\Gamma_{S,V}^0} dA \qquad (23)$$

where γ_{per} is the perimeter penalty factor chosen such that smoothing of the interface geometry is obtained while not allowing Eq. (23) to dominate the overall objective.

Besides the objective contributions defined in Eqs. (22) and (23) two inequality constraints are imposed. The first one is a volume constraint bounding the maximum amount of solid phase allowed within the entire design domain

$$g_1(\mathbf{s}, \mathbf{u}) = \frac{\Omega_S^0}{(\Omega_S^0 + \Omega_V^0)} - \gamma_v \leq 0 \qquad (24)$$

where γ_v controls the maximum allowed solid volume Ω_S^0 relative to the entire design domain volume $\Omega_D^0 = \Omega_S^0 \cup \Omega_V^0$. To control the stiffness of the structure in the activated state, an end-stiffness constraint is enforced. Following the work of Kemmler [36], it is formulated as:

$$g_2(\mathbf{s}, \mathbf{u}) = \left(\frac{\mathcal{S}' - \mathcal{S}}{\mathcal{S}}\right)^2 - \gamma_s \leq 0 \qquad (25)$$

where $\mathcal{S}$ is the strain energy of the system after activation (with no external load applied) and $\mathcal{S}'$ is the strain energy after applying an additional external perturbation load. The limit in relative amount of change in strain energy with and without the final perturbation load is denoted by γ_s. The end-stiffness constraint therefore requires a certain stiffness of the structure in the activated configuration in order to resist the perturbation pressure applied in the opposite direction of the desired deformation.

3.5 Design Sensitivity Analysis Using the Adjoint Method. Due to a large number of design variables, the design sensitivities of objective and constraints are computed using the adjoint method. Since the mechanical model is static and conservative, the adjoint problem only needs to be solved at the end of the loading process [37]. When the end-stiffness constraint is enforced, the design sensitivities for the displacement matching objective need to be evaluated at the load increment t_{Load} while the sensitivities for the end-stiffness constraint are evaluated at t_{Pert}.

Following the work of Refs. [24] and [38], the derivative of the objective z with respect to the vector of design variables $\mathbf{s}$ for a quasi-static case is:

$$\frac{dz}{d\mathbf{s}} = \frac{\partial z}{\partial \mathbf{s}} + \left(\frac{\partial z}{\partial \mathbf{u}}\right)^{\text{T}} \frac{d\mathbf{u}}{d\mathbf{s}} \qquad (26)$$

where the first term represents explicit dependencies while the second term represents the implicit sensitivities. Considering the two sets of nodal design variables, $\mathbf{s}^\phi$ and $\mathbf{s}^{\bar{\rho}}$, and the filtering and projection relationships defined in Sec. 3.1, the total derivative of Eq. (26) can be further expanded into

$$\frac{d\mathbf{u}}{d\mathbf{s}} = \begin{cases} \dfrac{\partial \mathbf{u}}{\partial \phi} \dfrac{d\phi}{d\mathbf{s}^\phi} \\[2mm] \dfrac{\partial \mathbf{u}}{\partial \hat{\rho}^e} \dfrac{\partial \hat{\rho}^e}{\partial \overline{\rho}^e} \dfrac{\partial \overline{\rho}^e}{\partial \tilde{\rho}^e} \dfrac{d\tilde{\rho}^e}{d\mathbf{s}^{\bar{\rho}}} \end{cases} \qquad (27)$$

Satisfying the governing Eq. (20) for every design, i.e., $\tilde{\mathbf{R}} = \mathbf{0}$, the derivative $d\mathbf{u}/d\mathbf{s}$ can be computed from

$$\frac{d\tilde{\mathbf{R}}}{d\mathbf{s}} = \frac{\partial \tilde{\mathbf{R}}}{\partial \mathbf{s}} + \frac{\partial \tilde{\mathbf{R}}}{\partial \mathbf{u}} \frac{d\mathbf{u}}{d\mathbf{s}} = \mathbf{0} \qquad (28)$$

Solving Eq. (28) for $d\mathbf{u}/d\mathbf{s}$ and combining it with Eq. (26) yields

$$\frac{dz}{d\mathbf{s}} = \frac{\partial z}{\partial \mathbf{s}} - \left(\frac{\partial z}{\partial \mathbf{u}}\right)^{\text{T}} \left(\frac{\partial \tilde{\mathbf{R}}}{\partial \mathbf{u}}\right)^{-1} \frac{\partial \tilde{\mathbf{R}}}{\partial \mathbf{s}} \qquad (29)$$

where the following adjoint problem can be identified:

$$\left(\frac{\partial \tilde{\mathbf{R}}}{\partial \mathbf{u}}\right)^{\text{T}} \boldsymbol{\lambda} = \frac{\partial z}{\partial \mathbf{u}} \qquad (30)$$

The adjoint solution is denoted by $\boldsymbol{\lambda}$, which is used to finally compute the expression for the design sensitivities as

$$\frac{dz}{d\mathbf{s}} = \frac{\partial z}{\partial \mathbf{s}} - \boldsymbol{\lambda}^{\mathrm{T}}\frac{\partial \tilde{\mathbf{R}}}{\partial \mathbf{s}} \qquad (31)$$

It should be noted that in the current work, the explicit contribution $\partial z/\partial \mathbf{s}$ and the post-multiplication term $\partial \tilde{\mathbf{R}}/\partial \mathbf{s}$ are obtained via finite differences on an elemental level. In a similar fashion as discussed above, the design sensitivities of the constraints with respect to the design variables can be obtained. For more details regarding the computation of design sensitivities with the XFEM, the interested reader is referred to Ref. [39].

4 Validation of the Hyperelastic Thermomechanical Model

The finite deformation thermomechanical model introduced in Sec. 2 is validated against experimental results and an analytical beam model to establish confidence in the XFEM model for design optimization. The test specimen for model validation are rectangular, bilayer strips with different volume ratios of active versus passive material, leading to different curvature values. The bilayer composite is made out of Tango+ as the active elastomer in the top layer ($\Omega^0_{S_A}$) and Vero as the passive glassy polymer in the bottom layer ($\Omega^0_{S_P}$) printed on a Stratasys Keshet J750 multimaterial 3D printer, with a printing layer thickness of 27 μm. The XFEM predictions of the bilayer strips are shown in Fig. 4(a) while the printed and activated specimen are shown in Fig. 4(b).

The model parameters and the material parameters of the XFEM model are given in Tables 1 and 2, respectively. Only one quarter of the domain is simulated and mechanical symmetry boundary conditions are applied along the X_1-X_3 and X_2-X_3 plane using the weak boundary condition formulation stated in Eq. (16). The XFEM is used to describe the solid-void boundary of the bilayer strips along the X_1 axis as highlighted in the insert in Fig. 4(a). Note that the void domain is not shown in Fig. 4(a) for clarity. This approach replicates a nonconforming mesh for analyzing the solid domain just as it is present during the subsequent design optimization process. The varying volume fraction of active material (Tango+ in the top layer) and passive material (Vero in the bottom) is modeled by uniformly changing the material ratios, respectively. The computational mesh consists of 1630 HEX20 XFEM elements of which 400 are intersected resulting in a total of 26,227 DOFs. HEX20 elements are 20 node hexahedral serendipity elements with a total of 60 DOFs.

The bending behavior of the bilayer strips due to different thermal expansion of the layers is studied for five distinct volume fractions of active material. The curvature is measured at the midplane of the strips in the X_2-X_3 symmetry plane. A comparison of the curvature values obtained by the 3D XFEM model, a 1D Timoshenko beam model as outlined in Ref. [5] and physical experiments for different Tango+ volume fractions is presented in Fig. 5. It should be noted that due to a small sample size of 8 samples per volume fraction, error bars are not meaningful and therefore omitted when plotting the mean curvature in Fig. 5. Good agreement is achieved between the 3D XFEM model and the

Table 1   Extended finite element method model of bilayer validation strips

Dimensions	$80.0 \times 5.0 \times 1.0$ mm
Mesh size	$80 \times 5 \times 10$
Weak BC penalty	$\gamma_D = 250.0$
Prescribed thermal load	$T = 1.0$ K
Reference temperature	$T_0 = 0.0$ K

Table 2   Material parameters of Tango+ and Vero

Young's modulus Tango+	$E_T = 0.6$ MPa
Young's modulus Vero	$E_V = 8.0$ MPa
Printing strain Tango+	$\alpha_T = 0.05(1/\mathrm{K})$
Printing strain Vero	$\alpha_V = 0.0(1/\mathrm{K})$
Poisson's ratio of Tango+, Vero	$\nu_T = \nu_V = 0.4$
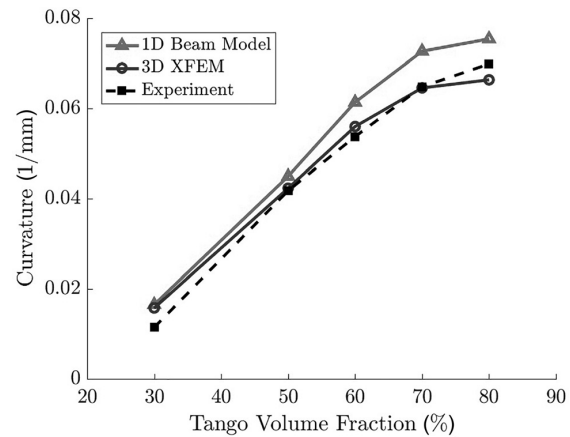
Fig. 5   Comparison of mean curvatures obtained by simulations and experiments for different Tango+ volume ratios

physical experiments, whereas the 1D model tends to overestimate the curvature, especially for large volume fractions of Tango+. This is due to assumptions made by the Timoshenko beam model which do not account for Poisson effect as well as transverse thermal expansion. Both of those phenomena are, however, present in the physical experiments where a double curvature (i.e., cylindrical bending) is observed for Tango+ volume fractions greater than 50%. These phenomena are accurately captured in the 3D XFEM model where the curvature along the X_1 direction is in fact reduced due to an increasing effect of curvature along the X_2 direction.

5 Design Optimization Examples

The proposed design methodology for finding the optimal design of 4D printed active structures is applied to four design
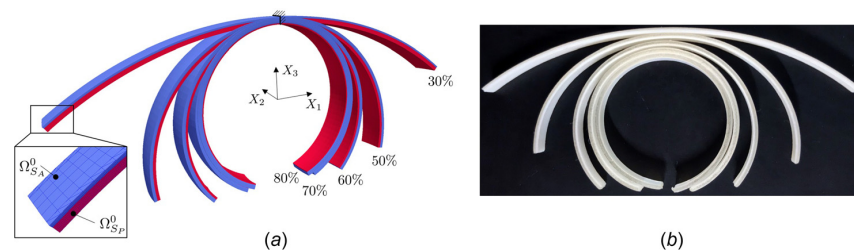
Fig. 4   Bilayer strips with different active material ratios (in %) used for XFEM model validation. The solid–void interface of the strips along the X_1 axis is cut by the XFEM and tetrahedralized for volume integration: (a) simulation results and (b) experimental results.

Table 3   Optimization problem parameters

Perimeter penalty	$\gamma_{per} = 5.0 \times 10^{-2}$
Lower bound for LS design variables	$s_L^\phi = -1.25$
Upper bound for LS design variables	$s_U^\phi = +1.25$
Lower bound for density design variables	$s_{L\tilde{\rho}} = 0.0$
Upper bound for density design variables	$s_{U\tilde{\rho}} = 1.0$
GCMMA initial asymptote adaption parameter	0.5
GCMMA asymptote adaption parameter	0.7

problems. The LSF and the nodal densities for all design examples are discretized using trilinear shape functions. The material properties are approximated element-wise constant and are obtained using an elemental average of all nodal fictitious density values (12) together with the SIMP power law (11). In this work, $\beta = 3.0$ is used for interpolating the Young's modulus and CTE while $\beta = 1.0$ is used for interpolating the physical density. The values of the SIMP exponent β have been chosen such that a good convergence toward either active or passive material is achieved.

The projection (13) is applied through a continuation approach which represents a trade-off between convergence behavior and computational efficiency of the optimization process. Initially, the projection threshold parameter is set to $\eta = 0.5$ and the sharpness parameter is $\gamma = 0.01$. After a converged initial design is obtained, (e.g., after 100 design iterations), the sharpness parameter is increased to $\gamma = 3.0$ and the end-stiffness constraint is enforced. The projection sharpness parameter is then doubled every 100 design iterations. This procedure is repeated four times until $\gamma = 48.0$ and a sufficient approximation to a bimaterial design within the solid domain is obtained. After the overall geometry has converged to an optimum (e.g., after 100 design iterations), the LS design variables stay unchanged while the material distribution within the solid domain is further optimized, to yield a bimaterial design with a certain end-stiffness. For both sets of design variables (nodal LS values s_i^ϕ and nodal fictitious densities s_i^ρ), a smoothing radius of $r_s = 4.0$ mm is used.

The optimization problem (21) is solved using the convergent method of moving asymptotes (GCMMA) [40] without inner iterations. The parameters of the optimization problem are listed in Table 3. The optimization problem is considered converged once a relative residual norm drop of the Karush–Kuhn–Tucker (KKT) conditions [41] greater 1.0×10^{10} is achieved and all constraints are satisfied.

For all examples, the initial design is a flat square plate composed of uniform, intermediate material of density $s^{\tilde{\rho}} = 0.5$ in Ω_S^0 with an initial seeding of square holes representing Ω_V^0, see Fig. 6(b). The size of the cuboid inclusions is $\mathbf{r}_i = [14.5, 14.5, 14.5]$ mm for all examples. Different target displacements are prescribed to certain subsets of the domain boundary Γ^0 in order to achieve target deformations of varying complexities. A design with the desired mechanical response is found through optimizing the solid-void geometry as well as the active–passive material distribution within the solid domain by solving the optimization problem outlined in Sec. 3.4. The material properties used for all design examples are listed in Table 2 and parameters specific for each design example are listed in Table 4.

For all subsequent design problems, quarter symmetry of the mechanical problem about the X_1-X_3 and the X_2-X_3 plane is exploited by analyzing only one quarter of the design domain and enforcing appropriate mechanical boundary conditions weakly via Nitsche's method (16). In addition, for the design problems of Secs. 5.2–5.4, design symmetry about the $X_1 - X_2$ diagonal is introduced by assigning a set of independent nodal LS values and nodal fictitious density values to only one eighth of the total design domain. The initial design used for all design optimization examples along with the symmetry boundary conditions is depicted in Fig. 6(b).

The LSF of the initial design is shown in Fig. 6(a) and computed as a signed-distance function from an array of cuboids defined as

$$\phi(\mathbf{X}) = 1 - \min_i \left(\left(\frac{X_1 - \tilde{X}_{1_i}}{r_{1i}} \right)^n + \left(\frac{X_2 - \tilde{X}_{2_i}}{r_{2_i}} \right)^n + \left(\frac{X_3 - \tilde{X}_{3_i}}{r_{3_i}} \right)^n \right)^{\frac{1}{n}}$$

(32)
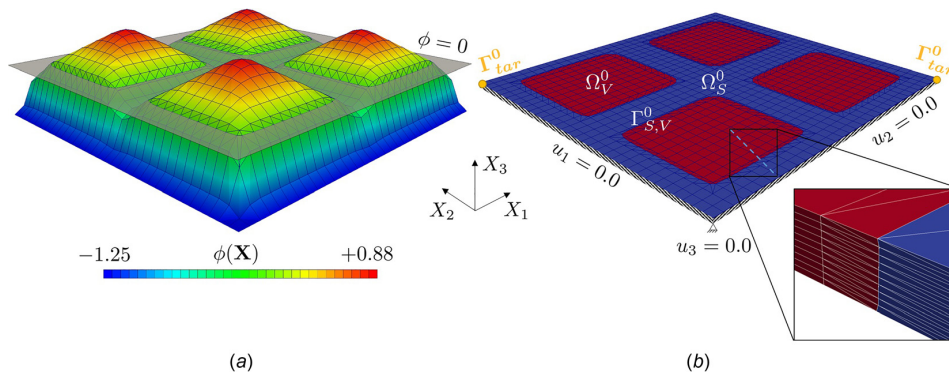
Fig. 6   Initial design of a quarter of the self-deforming structure with (a) the initial LSF and (b) the mechanical boundary conditions

Table 4   Parameters used for each design example

	Twisted figure-eight	Cylinder gripper	Four-legged gripper	Elevated plane
Initial void pattern	$4 \times 4 \times 1$	$4 \times 4 \times 1$	$4 \times 4 \times 1$	$6 \times 6 \times 1$
Volume constraint, γ_v	0.15	0.20	0.10	0.10
Change in strain energy, γ_s	5.0×10^{-5}	5.0×10^{-5}	1.0×10^{-6}	5.0×10^{-5}
Perturbation pressure, $\bar{P}$	1.0 Pa	0.1 Pa	1.0 Pa	1.0 Pa
GCMMA step size	0.04	0.03	0.03	0.03

where i is the number of individual cuboids, $\mathbf{r}_i$ is the radius of the ith cuboid, and $\bar{\mathbf{X}}_i$ is the position of the center of the ith cuboid in X_1, X_2, and X_3 direction, respectively. The roundness parameter is set to $n = 100.0$. The parameters of this arbitrary initial design have been determined through numerical studies to minimize the dependence of the final design on the initial geometry.

The plane creating the zero LS iso-contour is shown in gray (Fig. 6(a)) and the corresponding solid-void material layout is depicted in Fig. 6(b). It should be noted that LS design variables are only defined on the top surface of the initially flat plate, such that $\phi(X_1, X_2, X_3) = \phi(X_1, X_2)$. The LS values of all nodes which are not on the upper surface are dependent on the corresponding design variable hosted by the respective node on the top surface. This guarantees to always have a vertical cut in X_3 direction represented by the XFEM (see insert in Fig. 6(b)) and it prevents the optimizer from locally reducing the plate thickness during the optimization process.

The target displacements are monitored at target sets Γ_{tar}^0 defined at the tips of the structure (along the symmetry boundaries). To guarantee that these tips are mechanically connected to the base of the structure, the LS field along the symmetry boundaries is fixed to be negative (see Fig. 6(a)). This means, strips along the symmetry boundaries are excluded from the LS-XFEM design domain and remain solid throughout the optimization process. However, regarding the density optimization, this domain is still considered design domain in which the material distribution can be altered.

The nonlinear thermomechanical model is discretized by quadratic HEX20 XFEM elements. While the in-plane discretization varies for each example, 10 HEX20 brick elements are used for discretization in thickness direction in order to accurately capture the bending behavior of the slender structures and to avoid shear locking exhibited by lower-order brick elements. An iterative Newton–Raphson scheme is used to solve the nonlinear problem that is considered as converged when a relative nonlinear residual norm drop greater 1.0×10^6 is achieved. Convergence is facilitated by the adaptive load-stepping approach discussed in Sec. 2.2 where the time-step reduction factor is set to $f = 0.25$ and the maximum number of nonlinear iterations is set to 40. Again, the importance of the adaptive load-stepping scheme with respect to the convergence of the nonlinear problem during the optimization process should be emphasized. Especially for designs with large amounts of weak material, i.e., material with intermediate densities, adaptively reducing the load step is crucial in order to facilitate convergence of the Newton–Raphson scheme. The linearized subsystems are solved using the Multifrontal Massively Parallel Solver (MUMPS) [42,43].

To improve the computational efficiency of the optimization approach, the converged nonlinear solution of the state variables of the previous design is used as an initial guess for analyzing the current design. This approach is well suited for problems with static conservative mechanical models and incremental design changes where the displacement solution of the current design only differs slightly from the displacement behavior of the previous design [44]. If the design change and the resulting change in the displacement response is too large, i.e., no equilibrium configuration is obtained using the converged solution of the previous design as an initial guess, the design is analyzed by simulating the entire load path.

In order to stabilize disconnected solid subdomains throughout the optimization process, selective structural springs as introduced in Sec. 3.3 are used. The thermal conductivity in this auxiliary diffusion problem is set to $\kappa = 10.0$, the bulk heat transfer coefficient is $h = 0.01$ and the reference indicator value is $\tilde{\theta}_{\text{ref}} = 1.0$. A uniform initial indicator value of $\tilde{\theta}_0 = 1.0$ is applied to the entire domain and a relative spring stiffness ratio of $r = 1.0 \times 10^{-6}$ is used. Adiabatic boundary conditions on the auxiliary indicator field are assumed on boundaries where no displacements are prescribed. To further improve the numerical stability of the proposed approach, a staggered solution algorithm is employed. First,

the linear diffusion problem of the auxiliary indicator field (18) is solved and subsequently the nonlinear thermomechanical problem (1) is solved in a one-way coupled manner.

The final design for each example problem is fabricated and activated using the direct 4D printing method introduced by Ding et al. [5]. As described in Sec. 4, for fabrication of the optimized shape-changing structures, a Stratasys Keshet J750 multimaterial 3D printer is used to deposit the Tango+ and Vero material accurately onto a build tray. The zero LS iso-contour is used to extract the solid-void boundary of the final design, while an iso-volume created along a fictitious density threshold of $\hat{\rho}^e = 0.5$ is extracted to create distinct active and passive material domains. These post-processing steps are performed in ParaView [45], as it provides a convenient interface between the ExodusII mesh format and many computer-aided design file types. In the current work, a stereo-lithography mesh file is extracted from the converged optimization result (provided in ExodusII format by the employed LS-XFEM optimization framework) for each material subdomain. The stereo-lithography file format is commonly supported by 3D printing software and therefore used to import the computer-aided design data into the Stratasys printing software. In the Stratasys preprocessing environment, Tango+ is assigned to the active material domain represented by $0 \le \hat{\rho}^e < 0.5$, while Vero is assigned to the passive material domain corresponding to $0.5 \le \hat{\rho}^e \le 1$. The active structures are printed in a flat configuration and only deform upon release of the inelastic printing strain in the Tango+ material. This is triggered by submerging the initially flat, bimaterial structures into a water bath of $65.0\,^\circ$C which causes the stiffer Vero material to soften due to its glass transition temperature at around $53.0\,^\circ$C. This allows the built-in compressive printing strain in Tango+ to be released resulting in a shape change. The deformation is made permanent after the structure has cooled off to room temperature. A more detailed discussion of the direct 4D printing process as well as the activation steps can be found in Ref. [5].

It should be noted that all experimental results are shown for qualitative comparison only as a quantitative comparison is beyond the scope of this paper. The experimental verifications show the feasibility of the numerically determined designs and demonstrate the applicability of the proposed design framework to solving real-world design problems in a systematic manner.

5.1 Twisted Figure-Eight Example. The first example demonstrates the proposed computational design framework with the design of an initially flat plate that deforms into a twisted figure-eight like structure. The target displacement is tracked at the following target set $\Gamma_{\text{tar}}^0 = [\mathbf{X}_1, \mathbf{X}_2]$; at $\mathbf{X}_1 = [80.0, 0.0, 0.0]$ mm the target displacement is set to $\mathbf{u}_{\text{tar}} = [-80.0, 0.0, +50.0]$ mm and at $\mathbf{X}_2 = [0.0, 80.0, 0.0]$ mm the target displacement is set to $\mathbf{u}_{\text{tar}} = [0.0, -80.0, -50.0]$ mm (see Fig. 6(b)). This target displacement corresponds to a structure where two of the target points meet at the top center, and the other two target points meet at the bottom in the center of the full domain. The dimensions of the (quarter) design space and the mesh size used for this example are listed in Table 5. Representative for the first three design optimization problems, a total number of 47,200 design variables result from the problem setup shown in Fig. 6. The number of DOFs of the XFEM model reduces from initially about 126,000–30,500 at the lowest due to an expanding void phase which is excluded from the XFEM analysis.

The final design, obtained after 624 design iterations is shown in Fig. 7(a) in the activated, deformed stage. A clear solid-void interface defined by the zero iso-contour of the LS field can be seen along with an almost binary material layout within the solid phase. A small fraction of elements with intermediate fictitious densities remains which is attributed to the finite transition regions between active and passive material. Using a yet higher projection, smaller filter radius or finer background mesh would help to further reduce those intermediate density domains, however, their

Table 5 Extended finite element method model parameters for design optimization problems

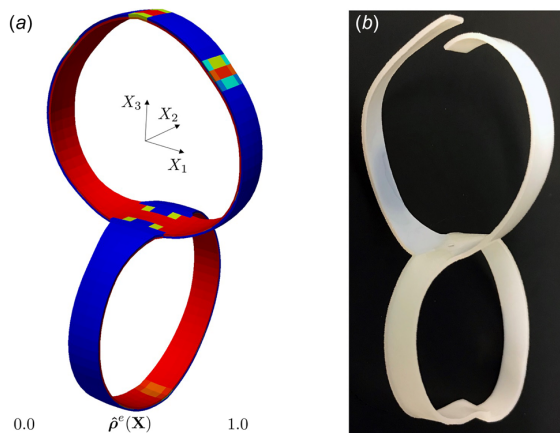| Dimensions (quarter domain)	$80.0 \times 80.0 \times 1.0\,\mathrm{mm}$
Mesh size (quarter domain)	$32 \times 32 \times 10$
Weak BC penalty	$\gamma_D = 250.0$
Prescribed thermal load	$\bar{T} = 1.0\,\mathrm{K}$
Reference temperature	$T_0 = 0.0\,\mathrm{K}$

Fig. 7 Final design of the twisted figure-eight example in deformed configuration: (a) XFEM prediction and (b) activated 4D printed sample

effect on the performance of the final design is negligible. Figure 7(b) shows the corresponding printed and activated structure with good qualitative agreement compared to the XFEM prediction. Both the numerical XFEM model as well as the physical sample assume the twisted figure-eight target deformation well. A slight overlap of the tips of the four legs is seen in the numerical prediction. This is due to the lack of a self-contact formulation which is beyond the scope of this work. Intuitively, a perfectly symmetric design is expected in order to meet the twisted figure-eight target deformation. A slight asymmetry can, however, be observed in Fig. 7, for both the XFEM simulation and the physical experiment. This is attributed to a local minimum identified by the GCMMA during the design optimization process. The increasing projection parameter then locks the design into this local minimum as the design space becomes increasingly more nonconvex with a higher projection parameter γ.

The evolution of the normalized objective z/z_0, where z_0 is the objective value of the initial design, the volume constraint (24) and the end-stiffness constraint (25) are shown in Fig. 8 for this first design optimization example. A similar behavior is also observed for all other numerical examples. After initial oscillations in the objective, which are due to the violation of the volume constraint, a smooth and converging behavior is seen. The slight increase of the objective every 100 iterations is due to an increasing projection parameter γ which makes the design space increasingly more nonlinear. Therefore, the optimization algorithm needs a few design iterations to minimize the objective again until convergence is obtained. It is observed that even though initially the volume constraint is active, it becomes inactive within the first 20 design iterations. The motivation for the solid strips to become thinner is to reduce the effect of double curvature due to the isotropic inelastic printing strain which impedes on the primary bending behavior. Therefore, the volume constraint stays inactive for the remainder of the optimization process. As mentioned before, the end-stiffness constraint is not enabled during the first 100 design iterations. Once enabled, it is initially violated but quickly becomes inactive after about 50 design iterations. Using the smoothed Heaviside projection in combination with the end-stiffness constraint greatly benefits the final stiffness of the structure as intermediate material is mitigated with an increasing projection parameter γ.

Figure 9(a) shows the final design in the undeformed configuration after two distinct material phases have been extracted in a postprocessing step. In the current and in future examples, Tango+ is printed transparent while Vero is printed in either white or magenta, see Fig. 9(b). Overall, this example shows a first application of the proposed method and it demonstrates that desired target deformations can be achieved upon activation of an initially flat, plate-like structure.

5.2 Cylinder Gripper Example. A similar design study as performed in Sec. 5.1 is repeated for finding the optimal design of an initially flat structure which deforms into a gripper enclosing a cylinder as its target. The target displacement of the gripper is monitored at the target set Γ_{tar}^0 which is comprised of $\mathbf{X}_1 = [0 \leq X_1 \leq 30.0, 75.0 \leq X_2 \leq 80.0, -0.5]\,\mathrm{mm}$ and $\mathbf{X}_2 = [75.0 \leq X_1 \leq 80.0, 0 \leq X_2 \leq 30.0, -0.5]\,\mathrm{mm}$ spanning the tips of the gripper. The desired deformation of the tips of the structure is described by a surface of a cylinder aligned with the X_3 axis, with radius $R_{\mathrm{tar}} = 50.0\,\mathrm{mm}$ and a depth of $X_{3_{\mathrm{tar}}} = -45.0\,\mathrm{mm}$. The XFEM model parameters listed in Table 5 are used. Parameters specific to this example are found in Table 4.

A smooth evolution of objective and constraints is observed as discussed before. The convergence history plots are omitted here for brevity. Figure 10 shows the final design (a) in the deformed configuration next to (b) the experimental result for the cylinder gripper. Qualitatively, the structure fabricated and activated through direct 4D printing assumes the anticipated target deformation well. From the predicted XFEM simulation it can clearly be seen that the optimizer took advantage of the possibility to use double curvature in order to achieve the cylindrical target
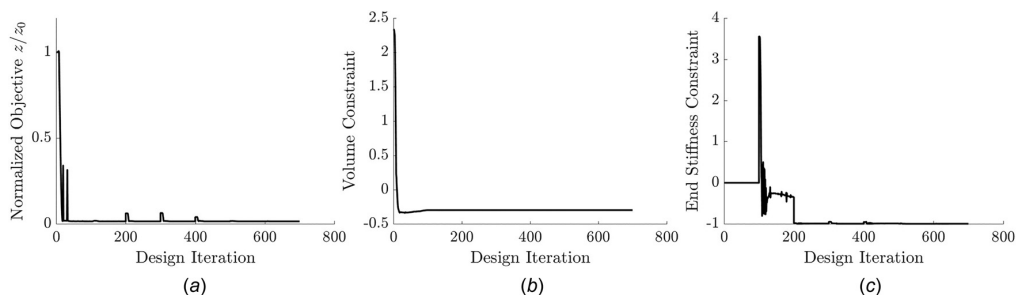

Fig. 8 Evolution of (a) normalized objective, (b) volume constraint, and (c) end-stiffness constraint for the twisted figure-eight example
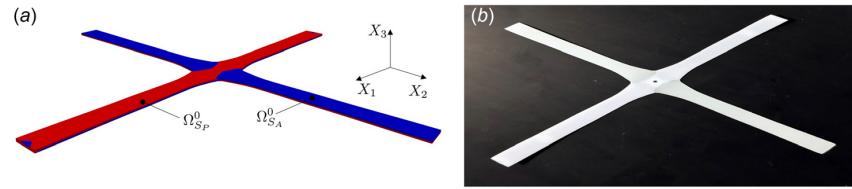
Fig. 9 Final twisted figure-eight design in undeformed configuration: (*a*) extracted material phases and (*b*) printed structure
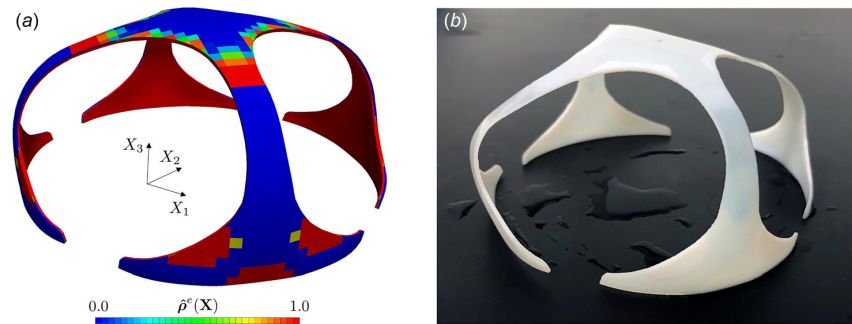

Fig. 10 Final design of the cylinder gripper in deformed configuration: (*a*) XFEM prediction and (*b*) activated experiment
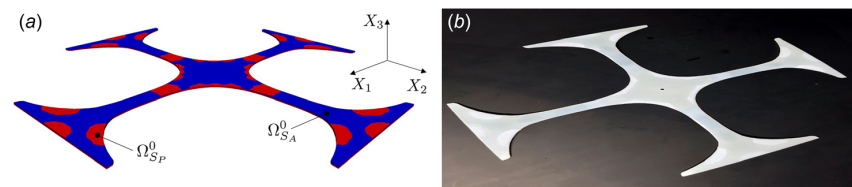

Fig. 11 Final cylinder gripper design in undeformed configuration: (*a*) extracted material phases and (*b*) printed specimen

deformation. Moreover, a nonuniform curvature in the outward pointing legs is used to best match the target deformation at the tips of the gripper. The optimal curvature is controlled by the amount of stiff, passive Vero material along the top of the gripper. Pure Vero is also placed as filets at the tips of the gripper to control the bending behavior and to also contribute toward a higher stiffness of the overall structure.

In Fig. 11 the corresponding initial, flat configuration of the optimal design is shown. As before, distinct material phases were extracted from the final fictitious density field in a postprocessing step; see Fig. 11(*a*). Figure 11(*b*) shows the printed physical specimen for the self-deforming cylinder gripper. This example successfully demonstrates that the proposed design method is not limited to finding the optimal geometry of simple target deformations, but also handles more sophisticated ones. Nonuniform double curvature is used in the optimized gripper design to obtain the desired deformation upon activation.

5.3 Four-Legged Gripper Example. The design of an active four-legged gripper is the aim of the third design optimization example. The target displacement is formulated such that gripping of an object is simulated. In order to achieve this, a target displacement of $\mathbf{u}_{tar} = [-80.0, 0.0, -50.0]$ mm is defined at $\mathbf{X}_1 = [0.0, 80.0, 0.0]$ mm and a similar target displacement of $\mathbf{u}_{tar} = [0.0, -80.0, -50.0]$ mm is prescribed at $\mathbf{X}_2 = [80.0, 0.0, 0.0]$ mm. This target displacement describes a structure where all four target

points coincide in the center of the design domain below its initial, flat configuration. As in previous examples, the XFEM model parameters listed in Table 5 are used and the parameters specific to this four-legged gripper example are found in Table 4.

The optimal design layout in the deformed configuration is depicted in Fig. 12 showing (*a*) the XFEM prediction and (*b*) the physical sample of the four-legged gripper. Due to the increased complexity of the target deformation, this design problem exhibits design phenomena previously not observed in Secs. 5.1 and 5.2.
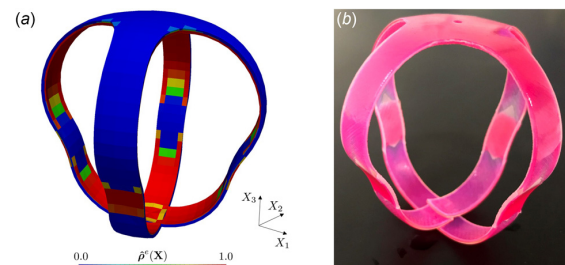

Fig. 12 Final design of the four-legged gripper example in deformed configuration: (*a*) XFEM prediction and (*b*) activated experiment
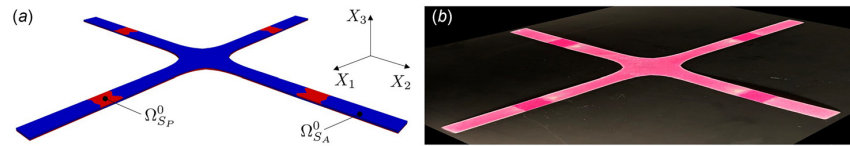
Fig. 13 Final four-legged gripper design in undeformed configuration: (*a*) extracted material phases and (*b*) printed sample
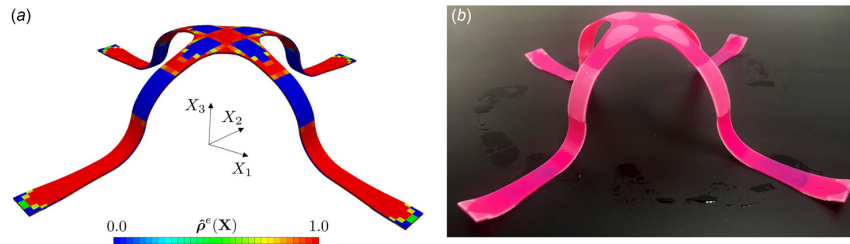

Fig. 14 Final design of the self-elevating plane in the deformed configuration: (*a*) XFEM prediction and (*b*) direct 4D printed specimen
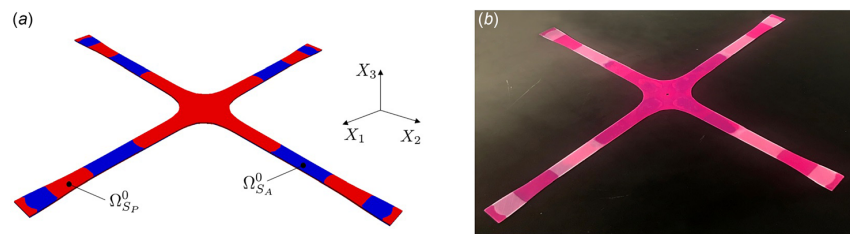

Fig. 15 Final elevated plane design in undeformed configuration: (*a*) extracted material phases and (*b*) printed sample

The final design of the gripper consists of four legs, which deform to match the target deformation in a nonintuitive manner. Since an end-stiffness constraint is enforced, convex–concave curvature sections are created to increase the stiffness of the four legs. These interesting features demonstrate how geometry features triggered by a mechanical stiffness constraint yield a meaningful, complex active gripper structure. Due to the finite width of the legs, self-penetration of all four gripper legs is observed at the bottom center of the structure. This is caused by inability of the XFEM model to account for contact. In the physical experiment, self-penetration is avoided by overlapping of the four gripper legs at different X_3 depths. However, in order to more accurately account for a behavior like this, contact should be included in future work. Overall, good qualitative agreement between the XFEM prediction and the direct 4D printed four-legged gripper is observed.

Figure 13 shows the corresponding initial, undeformed design for the four-legged gripper. The distinct domains of convex–concave curvature can be identified in both the XFEM model (Fig. 13(*a*)) as well as the printed specimen (Fig. 13(*b*)) where the bilayer beam composition is locally inverted at about the half-way point of each gripper leg.

5.4 Elevated Plane Example. The last example used to demonstrate the capabilities of the proposed multimaterial topology optimization framework is the design of a self-elevating plane. For this design example, the domain size is increased to $120.0 \times 120.0 \times 1.0$ mm for the quarter domain. This increase in in-plane domain size improves the ability to capture double

curvature with the given eigenstrain provided by the active material. A mesh size of $48 \times 48 \times 10$ elements is used to discretize one quarter of the design domain, leading to initially 276,000 free DOFs. To achieve self-elevation of the domain in the center of the design space by 40.0 mm in the X_3 direction, a target displacement of $\mathbf{u}_{\mathrm{tar}} = [0.0, 0.0, +40.0]$ mm is defined at the center of the domain spanned by $\mathbf{X}_1 = [0.0 \le X_1 \le 15.0, 0.0 \le X_2 \le 15.0, 0.0]$ mm. In addition, the out-of-plane displacement is fixed at the tips along the symmetry planes defined by $\mathbf{X}_1 = [105.0 \le X_1 \le 120.0, 0.0 \le X_2 \le 5.0, 0.0]$ mm and $\mathbf{X}_2 = [0.0 \le X_1 \le 5.0, 105.0 \le X_2 \le 120.0, 0.0]$ mm. The remaining XFEM model parameters for this example are listed in Table 5 and all other problem specific parameters are listed in Table 4.

The final design of the self-elevating plane in the deformed configuration is shown in Fig. 14. Both (a) the XFEM prediction and (b) the direct 4D printed physical specimen are depicted. The target deformation is achieved well in both simulation and physical experiments. A cross-shaped structure attached to the platform at the center is created. Each member of the cross exhibits a nonuniform active–passive material layout to yield distinct domains of concave–convex bending upon activation. This change in curvature is necessary to elevate the center of the structure in X_3 direction while introducing no out-of-plane displacement and rotation at the tips.

Figure 15 shows the undeformed structures of the elevated plane corresponding to (a) the XFEM simulation and (b) the printed sample before activation. A thresholding scheme is employed to eliminate any remaining intermediate densities and

to clearly identify active and passive material domains required for direct 4D printing.

6 Conclusions

A topology optimization approach for designing direct 4D printed, shape-changing structures undergoing large deformations was proposed. A combined LS-XFEM and density-based topology optimization approach was introduced in order to describe the multimaterial optimization problem. The LS-XFEM was employed to describe the solid-void domains in a crisp manner, while the SIMP method was used within the solid domain to distinguish between active and passive material subdomains. The hyperelastic thermomechanical model was discretized by quadratic displacement elements using an XFEM formulation. The inelastic printing strain introduced through the direct 4D printing process was modeled as a residual isotropic eigenstrain. Accurate prediction of the behavior of self-deforming structures by the proposed large strain thermomechanical XFEM model was verified by comparing numerical results against physical experiments and an analytical beam model.

The capabilities of the proposed design optimization methodology were demonstrated through four example problems. The objective was to match a given target displacement subject to a volume constraint and an end-stiffness constraint in order to assure structural integrity of the final design. Optimal designs matching target displacements of a twisted figure-eight design, a cylinder gripper, a four-legged gripper, and a self-elevating plane were successfully obtained using the proposed framework. Geometries and material arrangements of increasing complexity were created that take advantage of mechanical phenomena such as double curvature, locally concave–convex curvatures, and domains of uniform passive material in order to meet the end-stiffness constraint.

To further improve the capabilities of the proposed framework, a few shortcomings should be addressed in future work. These include the simplifications made with regards to structural instabilities, such as buckling and snap-through, which are a common phenomenon in slender structures. These structural instabilities have been avoided by using sufficiently thick structures in the current work, but need to be considered in general, when large compressive stresses are present in the structure initiated by the active material. Previous works in the field of modeling of slender structures incorporating eigenstrains include [44] and [46] where especially [46] and [47] consider fully nonlinear behavior including instabilities. Future work should study the influence of structural instabilities on the optimal design of 4D printed structures and develop a systematic optimization approach to either leverage them as a desired design feature or to avoid them in order to increase design robustness.

Moreover, the third example experienced a significant amount of self-penetration in the activated stage due to the lack of a self-contact formulation within the employed XFEM framework. Incorporating an XFEM contact formulation with multimaterial topology optimization as studied by Lawry and Maute [20] into the proposed design framework is another topic, which needs to be addressed in future work.

This paper has presented an initial demonstration of a systematic design approach for 4D printed structures undergoing large deformations. In addition, design problems with more complex target displacements should be studied in future work.

Physical specimen for all design examples were fabricated using direct 4D printing. Upon activation, qualitatively good agreement between the XFEM prediction and the physical response was seen. Discrepancies between the numerical results and the experiments are mainly attributed to minor anisotropy of the material properties with respect to the print direction, ambient effects like gravity, and viscosity of the water bath on the soft structures during the activation process. None of those physical effects have been accounted for in this work. However, in order to achieve better agreement between XFEM simulations and 4D printed specimen, all of those effects should be accounted for in future studies.

References

[1] Tibbits, S., 2014, "4D Printing: Multi-Material Shape Change," Archit. Des., **84**(1), pp. 116–121.
[2] Ge, Q., Qi, H. J., and Dunn, M. L., 2013, "Active Materials by Four-Dimension Printing," Appl. Phys. Lett., **103**(13), p. 131901.
[3] Ge, Q., Dunn, C. K., Qi, H. J., and Dunn, M. L., 2014, "Active Origami by 4D Printing," Smart Mater. Struct., **23**, p. 094007.
[4] Maute, K., Tkachuk, A., Wu, J., Jerry Qi, H., Ding, Z., and Dunn, M. L., 2015, "Level Set Topology Optimization of Printed Active Composites," ASME J. Mech. Des., **137**(11), p. 111402.
[5] Ding, Z., Yuan, C., Peng, X., Wang, T., Qi, H. J., and Dunn, M. L., 2017, "Direct 4D Printing Via Active Composite Materials," Sci. Adv., **3**(4), p. e1602890.
[6] Zhao, Z., Wu, J., Mu, X., Chen, H., Qi, H. J., and Fang, D., 2017, "Desolvation Induced Origami of Photocurable Polymers by Digit Light Processing," Macromol. Rapid Commun., **38**(13), p. 1600625.
[7] Zhao, Z., Wu, J., Mu, X., Chen, H., Qi, H. J., and Fang, D., 2017, "Origami by Frontal Photopolymerization," Sci. Adv., **3**(4), p. e1602326.
[8] Weeger, O., Kang, Y. S. B., Yeung, S.-K., and Dunn, M. L., 2016, "Optimal Design and Manufacture of Active Rod Structures With Spatially Variable Materials," 3D Print. Addit. Manuf., **3**(4), pp. 204–215.
[9] Ding, Z., Weeger, O., Qi, H. J., and Dunn, M. L., 2018, "4D Rods: 3D Structures Via Programmable 1D Composite Rods," Mater. Des., **137**, pp. 256–265.
[10] Tolley, M. T., Felton, S. M., Miyashita, S., Aukes, D., Rus, D., and Wood, R. J., 2014, "Self-Folding Origami: Shape Memory Composites Activated by Uniform Heating," Smart Mater. Struct., **23**(9), p. 94006.
[11] Van Dijk, N. P., Maute, K., Langelaar, M., and Van Keulen, F., 2013, "Level-Set Methods for Structural Topology Optimization: A Review," Struct. Multidiscip. Optim., **48**(3), pp. 437–472.
[12] Sigmund, O., and Maute, K., 2013, "Topology Optimization Approaches: A Comparative Review," Struct. Multidiscip. Optim., **48**(6), pp. 1031–1055.
[13] Deaton, J. D., and Grandhi, R. V., 2014, "A Survey of Structural and Multidisciplinary Continuum Topology Optimization: Post 2000," Struct. Multidiscip. Optim., **49**(1), pp. 1–38.
[14] Fuchi, K., Ware, T. H., Buskohl, P. R., Reich, G. W., Vaia, R. A., White, T. J., and Joo, J. J., 2015, "Topology Optimization for the Design of Folding Liquid Crystal Elastomer Actuators," Soft Matter, **11**(37), pp. 7288–7295.
[15] Kwok, T.-H., Wang, C. C. L., Deng, D., Zhang, Y., and Chen, Y., 2015, "Four-Dimensional Printing for Freeform Surfaces: Design Optimization of Origami and Kirigami Structures," ASME J. Mech. Des., **137**(11), p. 111413.
[16] Xue, R., Li, R., Du, Z., Zhang, W., Zhu, Y., Sun, Z., and Guo, X., 2017, "Kirigami Pattern Design of Mechanically Driven Formation of Complex 3D Structures Through Topology Optimization," Extreme Mech. Lett., **15**, pp. 139–144.
[17] Guo, X., Zhang, W., and Zhong, W., 2014, "Doing Topology Optimization Explicitly and Geometrically a New Moving Morphable Components Based Framework," ASME J. Appl. Mech., **81**(8), p. 081009.
[18] Holzapfel, G. A., 2000, *Nonlinear Solid Mechanics: A Continuum Approach for Engineering Science*, 1st ed., Wiley, Hoboken, NJ.
[19] Villanueva, C. H., and Maute, K., 2014, "Density and Level Set-XFEM Schemes for Topology Optimization of 3-D Structures," Comput. Mech., **54**(1), pp. 133–150.
[20] Lawry, M., and Maute, K., 2018, "Level Set Shape and Topology Optimization of Finite Strain Bilateral Contact Problems," Int. J. Numer. Methods Eng., **113**(8), pp. 1340–1369.
[21] Villanueva, C. H., and Maute, K., 2017, "CutFEM Topology Optimization of 3D Laminar Incompressible Flow Problems," Comput. Methods Appl. Mech. Eng., **320**(Suppl. C), pp. 444–473.

[22] Jenkins, N., and Maute, K., 2015, "Level Set Topology Optimization of Stationary Fluid-Structure Interaction Problems," Struct. Multidiscip. Optim., **52**(1), pp. 179–195.

[23] Makhija, D., and Maute, K., 2014, "Numerical Instabilities in Level Set Topology Optimization With the Extended Finite Element Method," Struct. Multidiscip. Optim., **49**(2), pp. 185–197.

[24] Kreissl, S., and Maute, K., 2012, "Levelset Based Fluid Topology Optimization Using the Extended Finite Element Method," Struct. Multidiscip. Optim., **46**(3), pp. 311–326.

[25] Norato, J. A., Bendsøe, M. P., Haber, R. B., and Tortorelli, D. A., 2007, "A Topological Derivative Method for Topology Optimization," Struct. Multidiscip. Optim., **33**(4–5), pp. 375–386.

[26] Bendsøe, M. P., 1989, "Optimal Shape Design as a Material Distribution Problem," Struct. Optim., **1**(4), pp. 193–202.

[27] Lazarov, B. S., Wang, F., and Sigmund, O., 2016, "Length Scale and Manufacturability in Density-Based Topology Optimization," Arch. Appl. Mech., **86**(1–2), pp. 189–218.

[28] Fries, T. P., and Belytschko, T., 2010, "The Extended/Generalized Finite Element Method: An Overview of the Method and Its Applications," Int. J. Numer. Methods Eng., **84**(3), pp. 253–304.

[29] Hansbo, A., and Hansbo, P., 2004, "A Finite Element Method for the Simulation of Strong and Weak Discontinuities in Solid Mechanics," Comput. Methods Appl. Mech. Eng., **193**(33–35), pp. 3523–3540.

[30] Terada, K., Asai, M., and Yamagishi, M., 2003, "Finite Cover Method for Linear and Non-Linear Analyses of Heterogeneous Solids," Int. J. Numer. Methods Eng., **58**(9), pp. 1321–1346.

[31] Tran, A. B., Yvonnet, J., He, Q. C., Toulemonde, C., and Sanahuja, J., 2011, "A Multiple Level Set Approach to Prevent Numerical Artefacts in Complex Microstructures With Nearby Inclusions Within XFEM," Int. J. Numer. Methods Eng., **85**(11), pp. 1436–1459.

[32] Lang, C., Makhija, D., Doostan, A., and Maute, K., 2014, "A Simple and Efficient Preconditioning Scheme for Heaviside Enriched XFEM," Comput. Mech., **54**(5), pp. 1357–1374.

[33] Nitsche, J. A., 1971, "Über Ein Variationsprinzip Zur Lösung Dirichlet-Problem Bei Verwendung Von Teilräumen, Die Keinen Randbedingungen Unteworfen Sind," Abh. Math. Sem. Univ. Hamburg, **36**(1), pp. 9–15.

[34] Geiss, M. J., and Maute, K., 2018, "Topology Optimization of Active Structures Using a Higher-Order Level-Set-XFEM-Density Approach," AIAA Paper No. AIAA-2018-4053.

[35] Arora, J. S., and Wang, Q., 2005, "Review of Formulations for Structural and Mechanical System Optimization," Struct. Multidiscip. Optim., **30**(4), pp. 251–272.

[36] Kemmler, R., 2004, "Große Verschiebungen Und Stabilität in Der Topologie- Und Formoptimierung," Ph.D. thesis, Universität Stuttgart, Stuttgart, Germany, p. 187.

[37] Gea, H. C., and Luo, J., 2001, "Topology Optimization of Structures With Geometrical Nonlinearities," Comput. Struct., **79**(20–21), pp. 1977–1985.

[38] Kreissl, S., Pingen, G., and Maute, K., 2011, "An Explicit Level Set Approach for Generalized Shape Optimization of Fluids With the Lattice Boltzmann Method," Int. J. Numer. Methods Fluids, **65**(5), pp. 496–519.

[39] Sharma, A., Villanueva, H., and Maute, K., 2017, "On Shape Sensitivities With Heaviside-Enriched XFEM," Struct. Multidiscip. Optim., **55**(2), pp. 385–408.

[40] Svanberg, K., 1987, "The Method of Moving Asymptotes—A New Method for Structural Optimization," Int. J. Numer. Methods Eng., **24**(2), pp. 359–373.

[41] Kuhn, H. W., and Tucker, A. W., 1951, "Nonlinear Programming," *Proceedings of the 2nd Berkeley Symposium on Mathematical Statistics and Probability*, University of California Press, Berkeley, CA, pp. 481–492.

[42] Amestoy, P. R., Duff, I. S., L'Excellent, J.-Y., and Koster, J., 2001, "A Fully Asynchronous Multifrontal Solver Using Distributed Dynamic Scheduling," SIAM J. Matrix Anal. Appl., **23**(1), pp. 15–41.

[43] Amestoy, P. R., Guermouche, A., L'Excellent, J. Y., and Pralet, S., 2006, "Hybrid Scheduling for the Parallel Solution of Linear Systems," Parallel Comput., **32**(2), pp. 136–156.

[44] Pajot, J. M., Maute, K., Zhang, Y., and Dunn, M. L., 2006, "Design of Patterned Multilayer Films With Eigenstrains by Topology Optimization," Int. J. Solids Struct., **43**(6), pp. 1832–1853.

[45] Ahrens, J., Geveci, B., and Law, C., 2005, "ParaView: An End-User Tool for Large-Data Visualization," Los Alamos National Laboratory, Los Alamos, NM, Technical Report No. LA-UR-03-1560.

[46] Zhang, Y., and Dunn, M. L., 2004, "Geometric and Material Nonlinearity During the Deformation of Micron-Scale Thin-Film Bilayers Subject to Thermal Loading," J. Mech. Phys. Solids, **52**(9), pp. 2101–2126.

[47] Dunn, M. L., Zhang, Y., and Bright, V. M., 2002, "Deformation and Structural Stability of Layered Plate Microstructures Subjected to Thermal Loading," J. Microelectromech. Syst., **11**(4), pp. 372–384.

Appendix D

Publication 3: A Regularization Scheme for Explicit Level-Set XFEM Topology Optimization

RESEARCH ARTICLE

Markus J. GEISS, Jorge L. BARRERA, Narasimha BODDETI, Kurt MAUTE

A regularization scheme for explicit level-set XFEM topology optimization

Abstract Regularization of the level-set (LS) field is a critical part of LS-based topology optimization (TO) approaches. Traditionally this is achieved by advancing the LS field through the solution of a Hamilton-Jacobi equation combined with a reinitialization scheme. This approach, however, may limit the maximum step size and introduces discontinuities in the design process. Alternatively, energy functionals and intermediate LS value penalizations have been proposed. This paper introduces a novel LS regularization approach based on a signed distance field (SDF) which is applicable to explicit LS-based TO. The SDF is obtained using the heat method (HM) and is reconstructed for every design in the optimization process. The governing equations of the HM, as well as the ones describing the physical response of the system of interest, are discretized by the extended finite element method (XFEM). Numerical examples for problems modeled by linear elasticity, nonlinear hyperelasticity and the incompressible Navier-Stokes equations in two and three dimensions are presented to show the applicability of the proposed scheme to a broad range of design optimization problems.

Keywords level-set regularization, explicit level-sets, XFEM, CutFEM, topology optimization, heat method, signed distance field, nonlinear structural mechanics, fluid mechanics

Markus J. GEISS, Jorge L. BARRERA, Kurt MAUTE (✉)
Ann and H.J. Smead Department of Aerospace Engineering Sciences, University of Colorado at Boulder, Boulder, CO 80309-0429, USA
E-mail: Kurt.Maute@Colorado.edu

Narasimha BODDETI
Singapore University of Technology and Design, SUTD Digital Manufacturing and Design Centre, Singapore 487372, Singapore

1 Introduction

Topology optimization (TO), with its large design freedom, has emerged as a powerful design tool for a variety of applications including structural mechanics, fluid flow and heat transfer [1–3]. The two most commonly used TO approaches are density-based methods and level-set (LS)-based implicit boundary methods. Since the introduction of the level-set method (LSM) [4], the method has gained great popularity in the areas of image processing, computer graphics, computational geometry and computational physics [5–7]. LSMs describe geometry changes by evolving an implicit boundary, conventionally defined as the zero-level iso-contour of a level-set function (LSF), $\phi(\boldsymbol{X})$. When applied to TO, LSMs enable a clear and unambiguous definition of the material interface [2,8]. van Dijk et al. [8] classified LSMs into two broad categories based on the LSF update procedure: i) *Implicit methods* where some form of the Hamilton-Jacobi (HJ) equation is used to evolve the LSF based on a velocity field defined by shape sensitivities that are in turn governed by the physics [9–12], and ii) *explicit methods* where a parametrized LSF is updated using mathematical programming techniques [8,13–17].

By construction, shape sensitivities only exist in the vicinity of the domain boundary, i.e., zero iso-contour of the LSF, and depend on the spatial LSF gradient. Furthermore, locally too flat or too steep LSF gradients affect the stability and the rate of convergence of LSMs, while a uniform and uniquely defined LSF improves those features. To this end, several regularization schemes for LSMs have been proposed [8]. Perimeter regularization is used to obtain a well-posed optimization problem [18] whereas Tikhonov regularization is used to control the smoothness of the LSF gradient [19,20]. These methods, however, do not guarantee a unique LSF and may lead to a flat LSF [8]. For both, explicit LS descriptions and implicit LSMs using the HJ equation, there exists a strong need for better regularization schemes to improve convergence of

the optimization process and avoid convergence to local minima [8].

An LSF with a uniform gradient along the interface, e.g., $|\nabla\phi(X)| = 1$, is desired for both explicit and implicit approaches [5,8]. A uniform, unit norm gradient is a unique property of the signed distance function (SDF), and hence the SDF is commonly used to reinitialize the LSF. However, as it evolves, the LSF quickly loses its SDF characteristics [21]. To alleviate this issue, several SDF regularization techniques have been proposed [22–29]. For the implicit LSMs, typically an auxiliary HJ equation [25] is solved, or a fast marching method [26] is used to reinitialize the LSF intermittently during the optimization process. For a more detailed discussion of HJ methods, the interested reader is referred to Refs. [5,30]. Even though LSF reinitialization is widely used, it slightly moves the zero LS iso-contour during the reinitialization process [5,31] and therefore affects the convergence of the design optimization process. Moreover, if the HJ equations are solved by an explicit time integration scheme, the design step size is limited by the Courant-Friedrichs-Lewy stability criterion.

To overcome the LSF reinitialization issues discussed above, an energy functional that penalizes the deviation from a unit norm LSF gradient is most commonly added to the objective function [13,22–24,32]. However, these measures do not allow for sufficient control of the LSF gradient away from the interface and may lead to oscillations [27,28]. Double-well energy functionals were introduced in Refs. [27–29] to enforce a unit norm gradient near the interface and a zero LSF gradient away from the interface, thus leading to an LSF that has an SDF characteristic near the interface and is constant away from it. The fundamental limitation of these local LS regularization approaches is that they operate directly on the local design LS value, or its gradient, and lack information about the minimum distance of a point to the interface. Thus, they cannot distinguish between points that have the same LS value but differ in their distance to the interface. This inability may cause undesirable material inclusions away from the original interface as illustrated in Fig. 1. Enforcing a unit norm gradient of the LSF at points with LS values close to zero but away from the interface at iteration n (Fig. 1(a)) may create new intersections at iteration $n + 1$ (Fig. 1(b)), without these intersections being necessarily beneficial for improving the performance of the design.

Using the local design LS value, either a zero gradient is achieved away from the interface or a unit norm gradient is enforced in the vicinity of it (see Fig. 1(a) for a simplified one-dimensional LSF and the corresponding interface). Due to the local enforcement of the different targets, the local measure lacks the ability to distinguish between areas where the LSF is within the LS bound ϕ_{Bnd} (i.e., $-\phi_{\text{Bnd}} \leqslant \phi \leqslant \phi_{\text{Bnd}}$) at which an interface exists and areas at which no interface is present. The local regularization
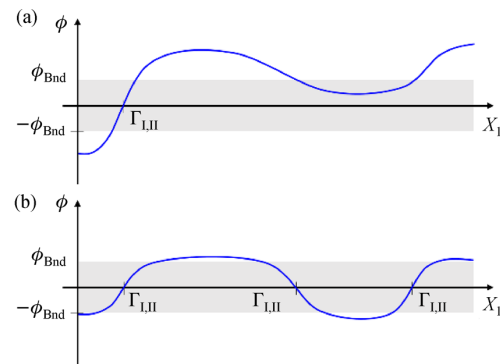

Fig. 1 Effect of a local LS regularization scheme on a simplified one-dimensional design problem for two distinct design iterations: (a) n and (b) $n + 1$

scheme enforces $|\nabla\phi| = 1$ anywhere, where $-\phi_{\text{Bnd}} \leqslant \phi \leqslant \phi_{\text{Bnd}}$ and thus has the tendency to create spurious material inclusions (Fig. 1(b)). Limiting the enforcement of the unit norm gradient to only intersected elements does not reliably alleviate this issue. Based on the authors' experience, adding energy functionals to the objective while formulating a well-posed optimization problem is challenging and requires problem dependent fine-tuning of parameters defining the regularization.

To overcome the shortcomings of the previously discussed regularization schemes, this paper introduces a novel LS regularization approach for explicit LS-based TO. This approach penalizes the difference between the design LSF $\phi(X)$ and a target LSF. The target LSF is constructed at every design iteration from the SDF, which is obtained using an extension of the heat method (HM) [33,34]. The SDF is computed at every design iteration for the current interface geometry and treated as a prescribed target field for the design LSF. The governing equations of the physics models and the HM are discretized in space by the extended finite element method (XFEM). The advantage of this novel approach is that a smooth and unique target field is used as reference for a locally enforced LS regularization. Using a differentiable penalty formulation to match the design LSF with the computed target LSF alleviates the need for reinitialization and therefore does not introduce discontinuities in the optimization process. The implementation of the HM is straightforward and can easily be coupled with explicit LSMs. The effectiveness of the proposed scheme is demonstrated via LS-based TO numerical examples in two (2D) and three (3D) spatial dimensions. Linear elasticity, nonlinear hyperelasticity and fluid flow examples are studied to demonstrate the general applicability of the novel LS regularization scheme.

The remainder of the paper is organized as follows: Section 2 gives a brief summary of the explicit LS-based TO framework; Section 3 introduces the HM; Section 4

278

Markus J. GEISS et al. A regularization scheme for explicit level-set XFEM topology optimization   3

discusses the XFEM discretization; Section 5 provides details of the explicit LS regularization scheme; numerical examples are presented in Section 6; and Section 7 concludes and summarizes the paper.

2 Explicit level-set topology optimization

The LSM implicitly describes the geometry of a body and its evolution using a scalar LSF $\phi(\boldsymbol{X})$. The material layout within a design domain Ω_D composed of two distinct phases is given by

$$\begin{cases} \phi(\boldsymbol{X}) < 0, \ \forall \boldsymbol{X} \in \Omega_\mathrm{I} \\ \phi(\boldsymbol{X}) > 0, \ \forall \boldsymbol{X} \in \Omega_\mathrm{II}, \\ \phi(\boldsymbol{X}) = 0, \ \forall \boldsymbol{X} \in \Gamma_\mathrm{I,II} \end{cases} \tag{1}$$

where Ω_I and Ω_II are the material domains of Phases I and II, respectively, such that $\Omega_\mathrm{D} = \Omega_\mathrm{I} \cup \Omega_\mathrm{II}$. The interface between them is denoted by $\Gamma_\mathrm{I,II}$ which corresponds to the zero LS iso-contour $\phi(\boldsymbol{X}) = 0$. In explicit LS-based TO, the nodal values of the discretized LS field $\phi_i(\boldsymbol{X})$ are defined as an explicit function of the design variables. Here, the design variable field is discretized using linear finite element (FE) shape functions, and each node j is assigned one design variable s_j. The LSF function is defined by filtering the discretized design variable field as follows:

$$\phi_i = \frac{\sum_{j=1}^{N_\mathrm{n}} w_{ij} s_j}{\sum_{j=1}^{N_\mathrm{n}} w_{ij}}, \ w_{ij} = \max(0, \ r_\mathrm{f} - |\boldsymbol{X}_i - \boldsymbol{X}_j|), \tag{2}$$

where N_n is the number of nodes within a filter radius r_f and $|\boldsymbol{X}_i - \boldsymbol{X}_j|$ is the Euclidean distance between Nodes i and j. This linear filtering scheme Eq. (2) initially proposed by Ref. [35] for LSMs increases the area of influence of every design variable and therefore enhances convergence of the optimization problem. The LSF is then used to discretize distinct physical sub-domains using the XFEM (see Section 4). The optimization problems considered in this work are formulated as

$$\begin{cases} \min_{\boldsymbol{s}} z(\boldsymbol{s},\boldsymbol{u}) = w_1 \dfrac{z_1(\boldsymbol{s},\boldsymbol{u})}{z_1(\boldsymbol{s}^0,\boldsymbol{u}^0)} + w_2 \dfrac{\int_{\Gamma_\mathrm{I,II}} \mathrm{d}A}{\int_{\Gamma_\mathrm{I,II}^0} \mathrm{d}A} + w_3 \dfrac{p(\boldsymbol{s})}{p(\boldsymbol{s}^0)} \\[2ex] \text{s.t. } g_1(\boldsymbol{s}) = \dfrac{\Omega_\mathrm{I}}{\Omega_\mathrm{I} + \Omega_\mathrm{II}} - \gamma_V \leqslant 0 \\[2ex] \boldsymbol{s} \in \Pi = \{\mathbb{R}^{N_s} | \boldsymbol{s}_\mathrm{L} \leqslant \boldsymbol{s} \leqslant \boldsymbol{s}_\mathrm{U}\} \\[1ex] \boldsymbol{u} \in \mathbb{R}^{N_u} \end{cases}, \tag{3}$$

where $\boldsymbol{s}$ denotes the vector of design variables and $\boldsymbol{u}$ is the vector of state variables. The objective function consists of a weighted contribution z_1 that characterizes the physical performance (e.g., strain energy, total fluid pressure drop) and two weighted penalty contributions, such that $w_1 + w_2 + w_3 = 1$. All objective function contributions are normalized by their values of the initial design, denoted by the superscript 0. The first penalty contribution minimizes the perimeter to avoid the emergence of irregular geometric features, and the second penalty is the newly introduced LS regularization that is discussed in detail in Section 5. When no LS regularization is used, $w_3 = 0$. All optimization problems considered in this work are subject to a volume constraint γ_V on Ω_I which prevents trivial solutions. The lower and upper bounds of the design variables are denoted by $\boldsymbol{s}_\mathrm{L}$ and $\boldsymbol{s}_\mathrm{U}$, respectively. The number of design variables is denoted by N_s and the number of state variables is N_u. The state variables $\boldsymbol{u}$ are governed by a set of discretized partial differential equations. These equations are satisfied for each design in the optimization process.

3 The heat method

The basis of the proposed regularization scheme for explicit LSMs is the construction of the SDF at every design iteration. Most commonly used approaches to obtain the SDF are fast marching methods [36] and fast sweeping approaches [37]. These methods however require non-trivial implementations within an FE-based software platform and present issues with parallelization [33]. In the current work, the SDF is obtained using an extension of the HM. First, a transient heat conduction equation is solved on the entire design domain, with a heat source at the material interface (Fig. 2(a)). The strong form of the governing equation of the temperature field $\theta(\boldsymbol{X})$ is

$$\dot{\theta} = \Delta\theta, \tag{4}$$

where Δ is the Laplace operator, and the temperature time derivative is denoted by $\dot{\theta}$. The initial and Dirichlet boundary conditions at the XFEM interface are $\theta^0(\boldsymbol{X}) = 0$ and $\theta(\Gamma_\mathrm{I,II}) = 1$, respectively. Adiabatic boundary conditions are applied to the temperature field at the domain boundary.

The distance field $\phi_\mathrm{D}(\boldsymbol{X})$ is obtained by solving a Poisson's equation with a volumetric flux that depends on the normalized gradient of the temperature field $\theta(\boldsymbol{X})$. The governing equation of the distance field $\phi_\mathrm{D}(\boldsymbol{X})$ is

$$\Delta\phi_\mathrm{D} = \nabla \cdot \left(-\frac{\nabla\theta}{|\nabla\theta|}\right), \tag{5}$$

with the Dirichlet boundary condition $\phi_\mathrm{D}(\Gamma_\mathrm{I,II}) = 0$ at the material interface and homogeneous Neumann boundary
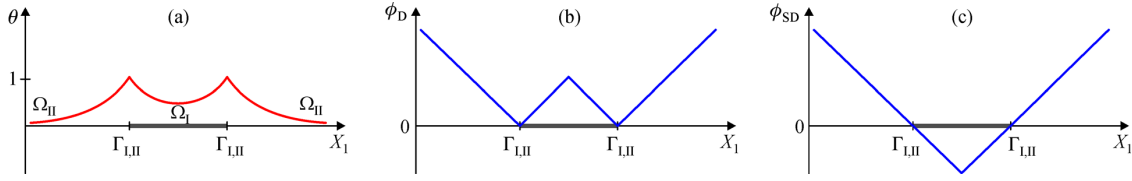
Fig. 2 Construction of the SDF using the HM. (a) A heat distribution is obtained from heat sources at the material interface; (b) the normalized temperature gradient is utilized to compute a distance field; from that, (c) the SDF is obtained

conditions at the domain boundary. The solution of Eq. (5) is illustrated in Fig. 2(b). The SDF $\phi_{SD}(X)$ is then computed by multiplying the distance field with the sign of the original design LSF $\phi(X)$ (Fig. 2(c)). Mathematically, this is stated as

$$\phi_{SD} = \text{sign}(\phi)\phi_D. \tag{6}$$

Note that due to enforcing $\phi_D = 0$ at the interface, constructing the SDF from the distance field via Eq. (6) does not introduce spurious fluctuations.

From a design optimization point of view, it is important to distinguish between the design LSF $\phi(X)$ which is an explicit function of the design variables s (Eq. (2)) and the reconstructed SDF $\phi_{SD}(X)$. The design LSF $\phi(X)$ determines the decomposition of the design domain into distinct phases and the material interface, which is the starting point of the HM and the SDF computation.

The weak form of the residual equation of the temperature field $\theta(X)$ is

$$R_\theta = \int_\Omega \delta\theta\dot{\theta}dV + \int_\Omega \delta\nabla\theta\nabla\theta dV = 0, \tag{7}$$

where the admissible test functions are denoted by $\delta\theta$. The time derivative at the current time step $m+1$ is approximated using an implicit Euler backward scheme as

$$\dot{\theta}^{m+1} \approx \frac{\theta^{m+1} - \theta^m}{\Delta t}, \tag{8}$$

where θ^m is the temperature field at the previous time step m and Δt is the time step size. To obtain an accurate distance field, Crane et al. [33] recommended a time step size in the order of $\Delta t = h^2$ where h is the element edge length. To increase computational efficiency of the HM, only a single time step is used for solving the temperature field $\theta(X)$ of Eq. (7). The time step size Δt is set sufficiently large to obtain a non-zero temperature gradient in the entire design domain and a meaningful SDF. This greatly reduces the computational overhead compared to a fully transient problem while only slightly effecting the accuracy of the obtained SDF away from the interface. For selecting a sufficiently large, single time step size, the following guideline can be used:

$$\Delta t \geqslant \left(\frac{L}{\ln\theta_L}\right)^2, \tag{9}$$

where L is defined as $L = L_{max}\sqrt{d}$ and θ_L represents a small temperature value at the far end of the design domain, e.g., $\theta_L = 1\times10^{-4}$. The maximum side length of the design domain bounding box is denoted by L_{max} and d is the spatial dimensionality, e.g., $d = 2$ in 2D. When employing the HM within a TO process, computational efficiency is more important than a high accuracy of the SDF. As discussed in Section 6.3.1, numerical studies have shown that solving Eq. (7) only for a single time step does not impede the functionality of the LS regularization but significantly simplifies the application of the HM for TO.

It is not necessary to compute the distance field $\phi_D(X)$ and the signed distance field $\phi_{SD}(X)$ in two sequential steps. The residual equation for the signed distance field $\phi_{SD}(X)$ is obtained by integration by parts of Eq. (5) and stated as

$$R_{\phi_{SD}} = \int_\Omega \delta\nabla\phi_{SD}(\nabla\phi_{SD} - G)dV = 0, \tag{10}$$

where the coupling term G is computed as the normalized temperature gradient times the negative of the sign of the design LS field:

$$G = -\text{sign}(\phi)\frac{\nabla\theta}{|\nabla\theta|}. \tag{11}$$

It should be noted that Eq. (10) does not contain any boundary contribution, as $\nabla\phi_{SD} = G$ is assumed over the outer domain boundary.

4 The extended finite element method

The XFEM [38] is used for discretization of the physics and the HM governing equations on a non-conforming background mesh. Being an immersed boundary method, it alleviates the need for re-meshing, which can be challenging and computationally costly during an optimization process.

Enrichment of the classical FE approximation spaces with additional shape functions is used for interpolation into disconnected sub-domains [39]. Multiple levels of enrichment are used to avoid spurious coupling or load transfer between disconnected material sub-domains. In this work, a generalized Heaviside enrichment strategy [40] is employed where the degrees of freedom within each

280

Markus J. GEISS et al. A regularization scheme for explicit level-set XFEM topology optimization   5

unique sub-domain are approximated by standard FE shape functions. The HM state variables $u = \{\theta, \phi_{\mathrm{SD}}\}$ at Node i are therefore approximated as

$$u_i(\boldsymbol{X}) = \sum_{m=1}^{M} \left(H(-\phi(\boldsymbol{X})) \sum_{k=1}^{N_{\mathrm{n}}^e} N_k(\boldsymbol{X}) \delta_{mq}^k u_{im}^{k,\mathrm{I}} \right.$$
$$\left. + H(\phi(\boldsymbol{X})) \sum_{k=1}^{N_{\mathrm{n}}^e} N_k(\boldsymbol{X}) \delta_{mq}^k u_{im}^{k,\mathrm{II}} \right), \qquad (12)$$

where the Heaviside function H is a function of the LS value and is defined as

$$H(\phi(\boldsymbol{X})) = \begin{cases} 1 & \text{if } \phi(\boldsymbol{X}) > 0 \\ 0 & \text{if } \phi(\boldsymbol{X}) < 0 \end{cases}. \qquad (13)$$

The maximum number of enrichment levels is denoted by M, N_{n}^e is the number of nodes per element and $N_k(\boldsymbol{X})$ is the elemental shape function. The Kronecker delta δ_{mq}^k selects the active enrichment Level q for Node k such that the partition of unity principle is satisfied. More details regarding Heaviside enriched XFEM can be found in Refs. [41,42].

Face-oriented ghost penalization, as proposed by Refs. [43,44], is used to stabilize the XFEM discretization. Numerical instabilities arise in the XFEM when the material interface $\Gamma_{\mathrm{I,II}}$ moves too close to a FE node, leading to a vanishing zone of influence of certain degrees of freedom. Face-oriented ghost stabilization cures this ill-conditioning independent of the intersection configuration. For stabilization of the solution fields, face-oriented ghost penalization is applied in the vicinity of the interface. It is formulated as

$$R_G = h\gamma_G \sum_{F \in F_{\mathrm{cut}}} \int_F [\![\delta \nabla u \boldsymbol{N}_{\mathrm{e}}]\!][\![\nabla u \boldsymbol{N}_{\mathrm{e}}]\!] \, \mathrm{d}A = 0, \qquad (14)$$

where γ_G is the ghost penalization parameter and F_{cut} contains all element faces in the immediate vicinity of the material interface for which at least one of the two adjacent elements is intersected [45]. The jump operator is defined as $[\![\bullet]\!] = \bullet|_{\Omega_{\mathrm{e}_1}} - \bullet|_{\Omega_{\mathrm{e}_2}}$. The ghost penalty is evaluated along all faces between two adjacent elements, Ω_{e_1} and Ω_{e_2}. The outward facing normal vector between Ω_{e_1} and Ω_{e_2} is denoted by $\boldsymbol{N}_{\mathrm{e}}$. This form of stabilized XFEM is also referred to as CutFEM in Ref. [46].

Boundary conditions and interface conditions are applied weakly in this work using the unsymmetrical version of Nitsche's method [47]. Weakly enforced boundary and interface conditions are essential in LS-based XFEM TO where the material phase of a domain boundary at which Dirichlet boundary conditions are applied may change. The weakly enforced conditions are applied using

$$R_N^p = -\int_\Gamma [\![\delta u^p]\!] \nabla u^p \boldsymbol{N} \, \mathrm{d}A + \int_\Gamma \nabla \delta u^p \boldsymbol{N} [\![u^p]\!] \, \mathrm{d}A$$
$$+ \gamma_{\mathrm{N}} \int_\Gamma [\![\delta u^p]\!][\![u^p]\!] \, \mathrm{d}A$$
$$= 0, \qquad (15)$$

where the phase index is denoted by $p = \{\mathrm{I,II}\}$ and $\boldsymbol{N}$ denotes the normal vector on the domain or interface boundary. The first term in Eq. (15) is the standard consistency, the second term is the adjoint consistency, and the last term is a penalty term on the jump of the state variables. The Nitsche penalty parameter is denoted by γ_{N}.

The same XFEM approach, stabilization and application of Dirichlet boundary conditions via Nitsche's method as outlined in this section is also used for discretization of all physics governing equations discussed in Section 6.

5 Explicit level-set regularization

The SDF obtained by the HM is used for regularization of the design LSF during the optimization process. Instead of reinitializing the design LSF $\phi(\boldsymbol{X})$ with the SDF $\phi_{\mathrm{SD}}(\boldsymbol{X})$, the following penalty formulation is proposed to achieve a continuous LS regularization:

$$p = \frac{\int_{\Omega_{\mathrm{D}}} (\phi - \tilde{\phi})^2 \, \mathrm{d}V}{\int_{\Omega_{\mathrm{D}}} \phi_{\mathrm{Bnd}}^2 \, \mathrm{d}V} + \frac{\int_{\Omega_{\mathrm{D}}} |\nabla \phi - \nabla \tilde{\phi}|^2 \, \mathrm{d}V}{\int_\Omega \mathrm{d}V}, \qquad (16)$$

where ϕ_{Bnd} denotes an upper (lower) bound for the target LSF. The penalty measures the difference between the design LSF $\phi(\boldsymbol{X})$ and a target LSF $\tilde{\phi}(\boldsymbol{X})$, as well as the difference in the spatial gradients. The target LSF $\tilde{\phi}(\boldsymbol{X})$ is constructed from the SDF $\phi_{\mathrm{SD}}(\boldsymbol{X})$. As the design LSF $\phi(\boldsymbol{X})$ converges to the target LSF $\tilde{\phi}(\boldsymbol{X})$, both contributions in Eq. (16) vanish. Penalizing the difference in the spatial gradients of the design and target LSFs, in addition to the difference in their values, increases the accuracy and avoids spatial oscillations. Both contributions are integrated over the entire design domain $\Omega_{\mathrm{D}} = \Omega_{\mathrm{I}} \cup \Omega_{\mathrm{II}}$. In the authors' experience, equal weighting of the two contributions in Eq. (16) provides a good balance between matching the target LS value and avoiding oscillations. To avoid length scale dependence, the penalty terms are normalized.

In this work, upper and lower bounds are imposed on the design LSF. To obtain a bounded design LSF away from the material interface, the following piecewise linear LSF is proposed as a target:

$$\hat{\phi}(\boldsymbol{X}) = \begin{cases} \phi_{\mathrm{Bnd}} & \text{if } \phi_{\mathrm{SD}}(\boldsymbol{X}) \geqslant \phi_{\mathrm{Bnd}} \\ -\phi_{\mathrm{Bnd}} & \text{if } \phi_{\mathrm{SD}}(\boldsymbol{X}) \leqslant -\phi_{\mathrm{Bnd}} \\ \phi_{\mathrm{SD}}(\boldsymbol{X}) & \text{else} \end{cases}. \qquad (17)$$

The truncated target LSF $\hat{\phi}(X)$ matches the SDF in the vicinity of the interface. Away from the interface, the lower bound $-\phi_{\mathrm{Bnd}}$ is matched in Ω_{I} and the upper bound ϕ_{Bnd} is matched in Ω_{II}. To avoid the non-differentiability of the piecewise linear target LSF $\hat{\phi}(X)$, a smooth target LSF $\tilde{\phi}(X)$ is used to approximate Eq. (17). This is achieved by the following sigmoid function:

$$\tilde{\phi} = \left(\frac{2}{1 + \mathrm{e}^{\frac{-2\phi_{\mathrm{SD}}}{\phi_{\mathrm{Bnd}}}}} - 1 \right) \phi_{\mathrm{Bnd}}. \tag{18}$$

A comparison between the piecewise linear target LSF and the smooth target LSF is illustrated in Fig. 3 for a one-dimensional interface configuration.

The target LSF $\tilde{\phi}(X)$ depends implicitly on the geometry of the interface, defined by the zero iso-contour of the design LSF $\phi(X)$ that depends explicitly on the optimization variables. The implicit dependence of $\tilde{\phi}(X)$ is described by the governing equations of the HM. In general, these implicit and explicit dependencies need to be considered for computing consistent design sensitivities of the LS regularization penalty Eq. (16). However, if the weight w_3 for the LS regularization term in the formulation of the objective function Eq. (3) is large and the implicit dependency of the target LSF $\tilde{\phi}(X)$ on the optimization variables is accounted for, the evolution of the design may be dominated by the LS regularization and the optimization process may converge to a design with poor physical performance. To overcome this issue, the LS regularization weight should be chosen small, e.g., $w_3 < 0.1$; a motivation for this recommendation will be presented in Section 6.2.1.1.

In addition, the authors found it advantageous to consider the target LSF $\tilde{\phi}(X)$ as a prescribed field which is reconstructed at every design iteration of the optimization process. Using this interpretation of $\tilde{\phi}(X)$, the penalty term Eq. (16) depends only explicitly on the optimization variables and the implicit sensitivities are ignored. As it will be shown in Section 6.2.1.2, this approach reduces the influence of the LS regularization term on the evolution of the design LSF in the vicinity of the zero iso-contour, i.e.,

the interface geometry. In addition, ignoring the implicit sensitivity contributions enhances the convergence of the optimization process to a design with optimized physical performance. Furthermore, the computational cost is noticeably reduced by omitting the computation of the adjoint solution of the HM. The LS regularization mainly controls the slope of the LSF along the interface and ensures that the LSF converges to either upper or lower bounds, $\pm\phi_{\mathrm{Bnd}}$, away from the interface. The reader may note that the LS regularization penalty Eq. (16) provides non-zero sensitivities in the entire design domain. This is usually not the case in LS-based TO using the XFEM, where shape sensitivities only exist in the vicinity of the interface [8].

Instead of introducing the LS regularization by the penalty term Eq. (16) into the formulation of the optimization problem, one could also add a constraint in the form of $p \leqslant \varepsilon$ with $\varepsilon \ll 1$. As the authors obtained satisfactory results with the penalty formulation for a wide range of penalty weights (see Section 6), the constraint formulation has not been considered in this work.

6   Numerical examples

Numerical examples considering different physical phenomena in 2D and 3D are presented in this section to study the characteristics of the proposed regularization approach. The examples include structural design problems modeled by linear and nonlinear elasticity and a flow problem described by the incompressible Navier-Stokes equations at steady-state.

Common to all examples is that the governing equations, including the ones of the HM, are discretized by the XFEM. An iterative Newton-Raphson scheme is used to solve the nonlinear problems that are considered as converged when a relative nonlinear residual norm drop greater than 10^6 is achieved. A single load increment is used in all numerical examples. The linearized sub-systems are solved using the Multifrontal Massively Parallel Solver (MUMPS) [48]. Bilinear four node quadrilateral elements are used in 2D, and trilinear eight node hexahedral
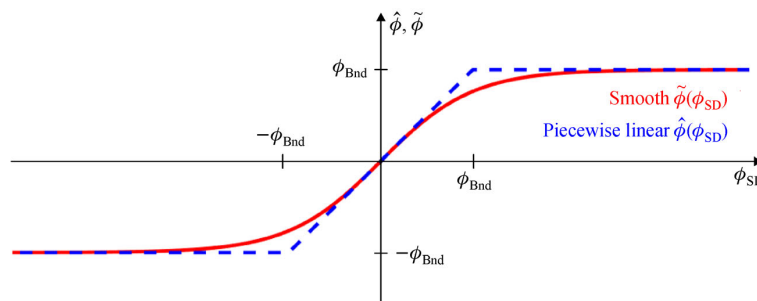

Fig. 3   Piecewise and smooth approximation of the design LSF

282

Markus J. GEISS et al. A regularization scheme for explicit level-set XFEM topology optimization   7

elements are used in 3D. The same discretization is used for the design LSF. The parameter optimization problem Eq. (3) is solved using a gradient-based nonlinear programming scheme, namely the Globally Convergent Method of Moving Asymptotes (GCMMA) [49], with no inner iterations.

The optimization problem is considered converged if the constraint is satisfied and the relative change in objective between two consecutive design iterations is less than 1×10^{-5}. The design sensitivities are obtained using the adjoint method. For more details on design sensitivities using XFEM, the interested reader is referred to Ref. [50]. Selective structural springs [51] are applied for all structural problems to suppress rigid body motion of isolated material domains that may emerge in solid-void LS-based TO. The initial seeding of the design domain with holes is performed using primitives in the form of squares in 2D and cubes in 3D.

The parameters used for the following numerical examples are listed in Table 1. Self-consistent units are used for all numerical examples and therefore not stated explicitly. The bounds for the design and target LSF are set as a function of the element edge length h. Note that the bound ϕ_{Bnd} for the target LSF $\tilde{\phi}(\boldsymbol{X})$ is within the range of values of the discretized design LSF $\phi(\boldsymbol{X})$. As discussed in Section 3, the temperature field in the HM is advanced in time by a single time step, unless otherwise stated. A staggered solution approach is used to separately solve the two partial differential equations of the HM in a one-way coupled fashion. This improves computational efficiency as each sub-problem is linear and of smaller size.

Table 1 Parameters used for all numerical examples with h denoting the element size

Parameter	Value
Weak boundary condition penalty Eq. (15)	$\gamma_{\mathrm{N}} = 100/h$
Ghost penalty Eq. (13)	$\gamma_G = 0.001$
Perimeter penalty weight Eq. (3)	$w_2 = 0.01$
Lower bound of s	$s_{\mathrm{L}} = -3h$
Upper bound of s	$s_{\mathrm{U}} = +3h$
Target bound of LSF	$\phi_{\mathrm{Bnd}} = 2h$
Filter radius used in 2D	$r_{\mathrm{f}} = 1.6h$
Filter radius used in 3D	$r_{\mathrm{f}} = 2.4h$

6.1 Examples for linear elasticity

The physical response in the first set of examples is described by linear elasticity. The weak form of the governing equation is

$$\boldsymbol{R} = \int_{\Omega_{\mathrm{I}}} \delta\boldsymbol{\varepsilon}\boldsymbol{\sigma}\mathrm{d}V - \int_{\Gamma_T} \delta\boldsymbol{u}\overline{\boldsymbol{T}}\mathrm{d}A = \boldsymbol{0}, \tag{19}$$

with $\boldsymbol{u} = \overline{\boldsymbol{u}}$ on Γ_u, where the displacement vector is denoted by $\boldsymbol{u}$. The surface traction applied on Γ_T is $\overline{\boldsymbol{T}}$. The infinitesimal strain tensor is defined by $\boldsymbol{\varepsilon} = \frac{1}{2}(\nabla\boldsymbol{u}^{\mathrm{T}} + \nabla\boldsymbol{u})$, and the Cauchy stress is $\boldsymbol{\sigma} = \boldsymbol{D}\boldsymbol{\varepsilon}$. The fourth-order material tensor is denoted by $\boldsymbol{D}$, and for isotropic, linear elastic homogeneous materials considered in this work it is defined in terms of the Lamé constants λ and μ as follows:

$$D_{ijkl} = \lambda\delta_{ij}\delta_{kl} + \mu(\delta_{ik}\delta_{jl} + \delta_{il}\delta_{jk}), \tag{20}$$

where δ_{ij} is the Kronecker delta. The Lamé constants can be expressed in terms of the Young's modulus E and the Poisson's ratio ν as

$$\lambda = \frac{E\nu}{(1+\nu)(1-2\nu)}, \ \mu = \frac{E}{2(1+\nu)}. \tag{21}$$

The problem parameters used for linear elastic problems are listed in Table 2. For more details about the linear elastic XFEM formulation used in this section, the reader is referred to Ref. [52].

Table 2 Parameters used for the linear elastic design problems

Parameter	Value
Young's modulus	$E = 2 \times 10^3$
Poisson's ratio	$\nu = 0$
LS regularization weight	$w_3 = 0.01$
Element edge length	$h = 1$

6.1.1 Hanging bar in 2D

As a first design example, a 2D linear elastic plane stress "hanging bar" design optimization problem is solved. This example problem is a modified version of the two-bar truss solid-void problem that was studied in Ref. [2] with the density method. The initial design of size 80×40 with boundary conditions is shown in Fig. 4(a). Only one half of the design is analyzed and optimized, with weakly enforced symmetry boundary conditions along the vertical center line. The top edge of the domain is clamped while a traction load of $T_{X_2} = -30$ is applied in X_2 direction at the center of the bottom edge over a length of 12. The region at the center of the bottom edge, at which the load is applied, is excluded from the design domain. The optimization problem Eq. (3) is to minimize the strain energy with a perimeter penalty and an LS regularization penalty subject to a volume constraint of $\gamma_V = 0.16$. A relative GCMMA optimization step size of 0.1 and a time step size of $\Delta t = 4$ is used in the HM.

The final design is shown in Fig. 4(b) and consists of only a single vertical bar, to transfer the applied traction load at the bottom to the support at the top of the domain.
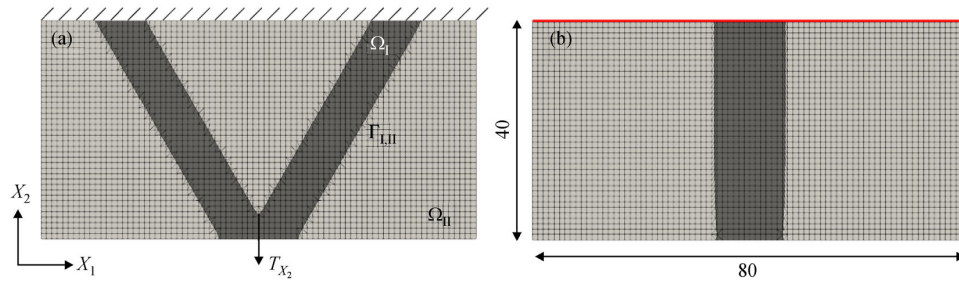
Fig. 4   (a) Initial design of the 2D hanging bar problem; (b) final design with boundary conditions and dimensions

Figure 5 shows a comparison of the evolution of objective and constraint with and without LS regularization. Early on in the design process, oscillations are observed without LS regularization, while with LS regularization a smooth design evolution is obtained. Moreover, the design problem converges significantly faster when LS regularization is applied: About 300 design iterations versus about 500 design iterations. Since the LS regularization contribution vanishes at the optimum, the regularized design problem converges to the same objective and constraint values as without regularization.

Figure 6(a) shows snapshots of the design LSF at discrete steps during the optimization process, comparing the evolution of the design LSFs with and without LS regularization. The LSFs are plotted over X_1 at the top of the design domain, i.e., $X_2 = 40$. When no LS regularization is used, irregularities of the design LSF are observed as the design is changed and a quick degradation of the slope of the LSF at the interface is seen. With regularization, a non-oscillatory LSF is obtained in the entire design domain. Even though the design problem without regularization also eventually converges, the LSF is noisy and at some locations close to zero. Due to numerical noise, LS values close to zero often create unintended isolated material islands in the vicinity of the interface. These may cause ill-conditioning of the analysis

and potential divergence of the design problem. Thus, when using the proposed LS regularization, a much larger optimization step size can be used, owing to the enhanced stability of the optimization problem.

Figure 6 on the right shows the design LSFs at design iteration 200 without regularization applied (Fig. 6(b)) and with LS regularization (Fig. 6(c)). Even though the same zero iso-contour is obtained, the non-regularized LSF is noisy, and the initial design can still be observed even at convergence. In contrast, LS regularization achieves a design LSF with LS values at the target boundary values ϕ_{Bnd} and a unit norm gradient in the vicinity of the interface. Due to the exclusion of the bottom center from the design domain, slight irregularities in the final iso-contour and in the regularized LSF are seen in this region.

6.1.2   Hanging bar in 3D

A 3D configuration of the 2D problem discussed in Section 6.1.1 is considered here. The initial design with loads and boundary conditions is shown in Fig. 7(a). Due to the symmetry of the design problem, only one quarter of the domain is modeled and optimized. Again, the area at the bottom of the domain at which the traction load is applied (circular area of radius 8.5) is excluded from the design
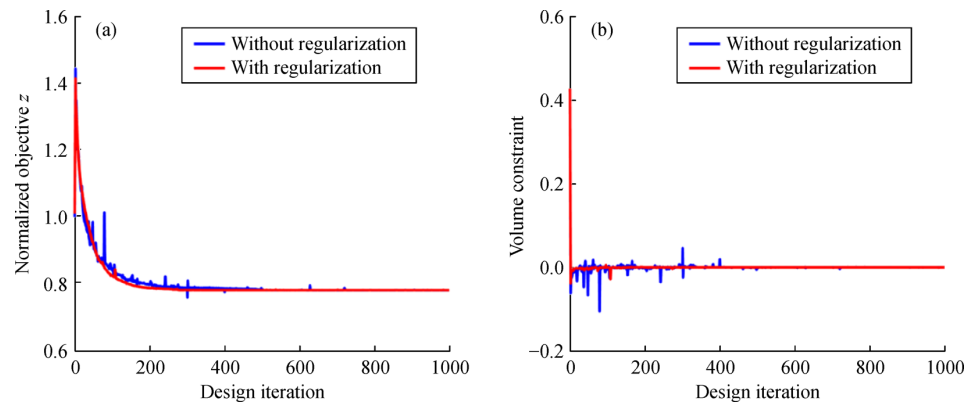

Fig. 5   Evolution of (a) objective and (b) constraint with and without regularization for the 2D hanging bar

284

Markus J. GEISS et al. A regularization scheme for explicit level-set XFEM topology optimization   9
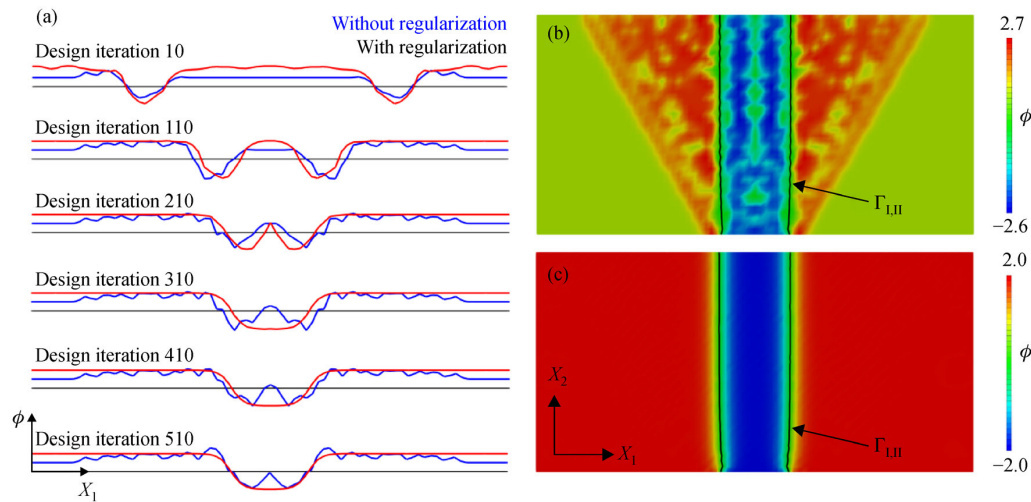
Fig. 6   (a) Comparison of the design LSFs with and without regularization at different snapshots during the optimization process (see Fig. 4), final design LSF (b) without regularization and (c) with regularization

domain. The dimensions of the design domain are $80 \times 40 \times 80$. A volume constraint of $\gamma_V = 0.035$ is enforced, and a relative GCMMA step size of 0.2 is used. A time step size of $\Delta t = 6$ is used in the HM.

As in the 2D problem, the optimization process converges to a single vertical bar (Fig. 7(b)). Figure 8 shows the design LSFs of the final design obtained without and with LS regularization. The 2D plane shown here is taken along the diagonal of the design domain as indicated in red in Fig. 7(b).

It can clearly be seen that when LS regularization is used the LS values are at the target bounds away from the interface, while a smoothed LSF with a unit norm gradient is obtained near the solid-void interface. Without regularization, the LSF of the initial design is clearly preserved at convergence, and large spatial oscillations exist throughout the entire design domain. As before, slight oscillations in

the design LSF are observed in the vicinity of the loaded edge since this domain is excluded from the design domain. Overall, increased stability and higher convergence rates are observed for this initial set of design problems when the LS regularization is applied.

6.2   Examples for nonlinear hyperelasticity

To demonstrate the applicability of the proposed LS regularization scheme to design problems with increased complexity, examples are considered next where the structural response is described by a finite strain hyperelastic model. The weak form of the governing equation is stated as

$$\boldsymbol{R} = \int_{\Omega_{\mathrm{I}}} \delta \boldsymbol{F}\boldsymbol{P}\mathrm{d}V - \int_{\Gamma_T} \delta \boldsymbol{u}\overline{\boldsymbol{T}}\mathrm{d}A = 0, \tag{22}$$
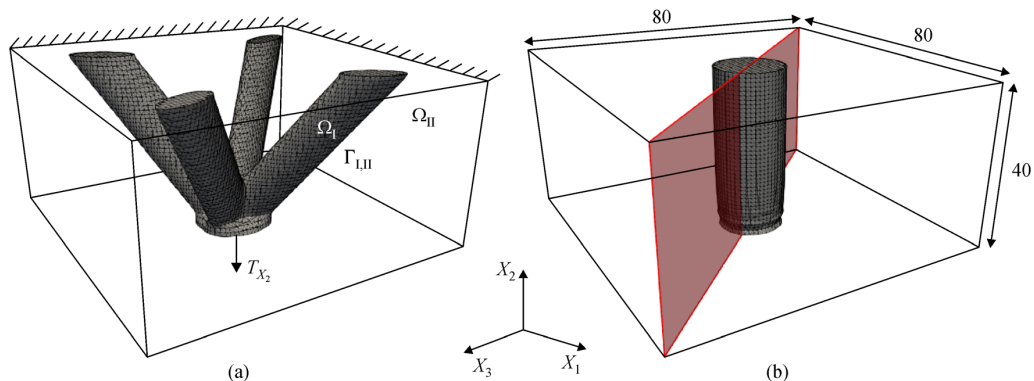

Fig. 7   (a) Initial design of the 3D hanging bar problem and (b) final design with boundary conditions and dimensions. The diagonal area highlighted in red represents the plane in which the design LSFs with and without regularization are being compared in Fig. 8
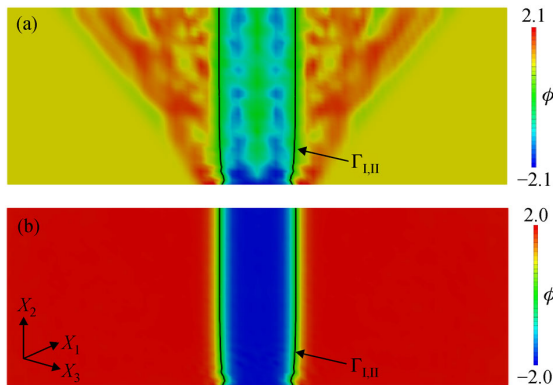
Fig. 8 Comparison of the final design LSFs (a) without LS regularization and (b) with regularization

where $\boldsymbol{F} = \partial\boldsymbol{x}/\partial\boldsymbol{X}$ is the deformation gradient tensor, and $\boldsymbol{x} = \boldsymbol{u} + \boldsymbol{X}$ describes the relationship between reference $\boldsymbol{X}$ and current $\boldsymbol{x}$ coordinates. The first Piola-Kirchhoff stress is denoted by $\boldsymbol{P}$. A hyperelastic Saint Venant-Kirchhoff constitutive model for homogeneous, isotropic compressible materials is used, which is formulated as

$$S = 2\mu E + \lambda\mathrm{tr}(E)I, \tag{23}$$

where $\boldsymbol{S}$ is the second Piola-Kirchhoff stress tensor and $\boldsymbol{E}$ is the Green-Lagrange strain tensor. The second order identity tensor is denoted by $\boldsymbol{I}$. The Lamé constants defined in Eq. (21) are used.

The Green-Lagrange strain tensor is defined as:

$$E = \frac{1}{2}(C - I), \tag{24}$$

where the right Cauchy-Green deformation tensor $\boldsymbol{C}$ is computed as $\boldsymbol{C} = \boldsymbol{F}^{\mathrm{T}}\boldsymbol{F}$. Finally, the first Piola-Kirchhoff

stress is obtained from

$$P = FS. \tag{25}$$

For more details on the formulation and verification of the nonlinear XFEM formulation used in this work, the interested reader is referred to Ref. [53]. The parameters listed in Table 3 are used for all hyperelastic design optimization problems, unless stated otherwise.

Table 3 Parameters used for the hyperelastic design problems

Parameter	Value
Young's modulus	$E = 2 \times 10^3$
Poisson's ratio	$\nu = 0.4$
LS regularization weight	$w_3 = 0.01$
Element edge length	$h = 1$

6.2.1 Beam in 2D

First, we consider the design of a beam-type structure in 2D. The initial design with loads and boundary conditions is shown in Fig. 9(a). The design domain is of size 240×40. A traction load of $T_{X_2} = -10$ is applied at the top center of the domain over a length of 3 while the structure is simply supported on either ends on the bottom of the domain. Due to the symmetry of the design problem, only half of the domain is modeled and optimized. Symmetry boundary conditions are applied weakly. The structural response is described by the hyperelastic model outlined above and discretized by the XFEM. Following the work of Ref. [54], a plane strain model is used in 2D. The objective of the optimization problem is to minimize the strain energy with a 1% penalty weight on the perimeter and a 1% penalty weight on the LS regularization. The optimization problem is subject to a volume constraint of
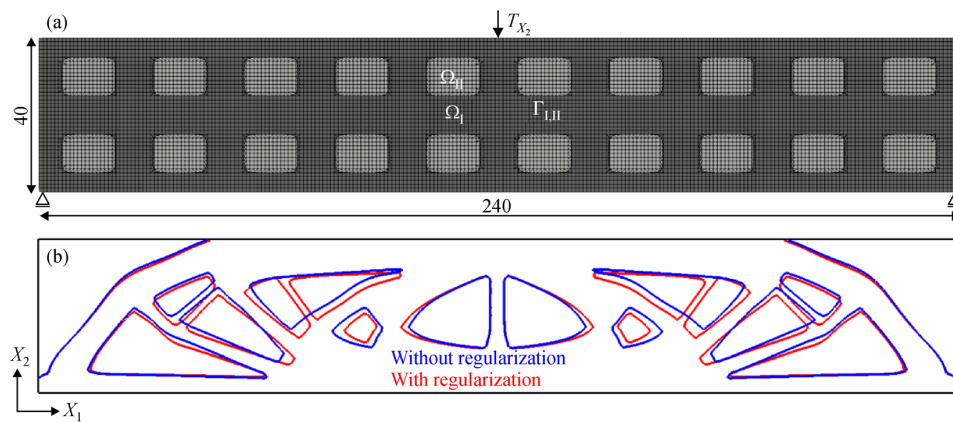

Fig. 9 (a) Initial design of the 2D beam problem with boundary conditions and dimensions; (b) comparison of the zero LS iso-contours of the final designs without and with LS regularization

286

Markus J. GEISS et al. A regularization scheme for explicit level-set XFEM topology optimization 11

$\gamma_V = 0.6$, and an optimization step size of 0.025 is used. A single time step of size $\Delta t = 35$ is used in the HM.

Figure 9(b) shows a comparison of the zero LS iso-contour of the final beam designs obtained without and with LS regularization. The typical truss-like structure is obtained for both methods with only slight differences in the final geometries. These differences can be attributed to different evolutions of the LSFs during the optimization process. The proposed LS regularization scheme leads to an increased convergence behavior due to a uniform LS gradient in the vicinity of the interface. This is also reflected in a slightly (0.1%) lower strain energy of the regularized design versus the non-regularized design.

The design LSFs, $\phi(\boldsymbol{X})$, at the final optimization iteration are shown in Figs. 10(a) and 10(b) without LS regularization and with regularization, respectively. Both LSFs are warped for illustration purposes. An oscillatory LSF is obtained without regularization, while with LS regularization the optimization process converges to a smoothly truncated design LSF. The regularized LSF shows a unit norm gradient in the vicinity of the material interface while having a zero gradient away from the interface. Figure 10(c) shows the SDF obtained by the HM for the final design of the 2D beam. It can be seen that overall the SDF is well resolved. Only in areas with small geometric features, with a size of h, the XFEM discretization insufficiently resolves the SDF. Consequently, the LS regularization suffers in these areas from a degraded target LSF due to the limited resolution of spatial discretization.

6.2.1.1 Influence of the LS regularization penalty weight

The influence of different weights w_3 for the LS regularization penalty is studied in Fig. 11. Figure 11(a) shows the evolution of strain energy and Fig. 11(b) shows the LS regularization penalty for regularization weights of $w_3 = \{0.01, 0.05, 0.1, 0.5\}$. With an increased LS regularization penalty weight, the minimization of the LS regularization term is favored early in the design process, while the minimization of strain energy is given less importance. The reader may note small jumps in the evolution of strain energy and the LS regularization penalty, for example, at iteration 350 and iteration 400. The jumps are caused by thin structural members disconnecting. The design iteration at which this happens depends on the weight of the LS regularization term.

For a weighting parameter in the range of $1\% \leqslant w_3 \leqslant 10\%$, both the strain energy and the regularization penalty assume similar values after about 200 design iterations. If the LS regularization weight is too large (e.g., 50%), the optimization problem changes noticeably and the physical performance of the optimized design is affected. The LS regularization term then dominates the overall objective and the physics contribution is of lesser importance (Fig. 11 (a)). In the authors' experience with the current problem and other design problems, an LS regularization weight up to 10% provides a good balance between sufficient regularization while not impairing the performance of the optimized design.
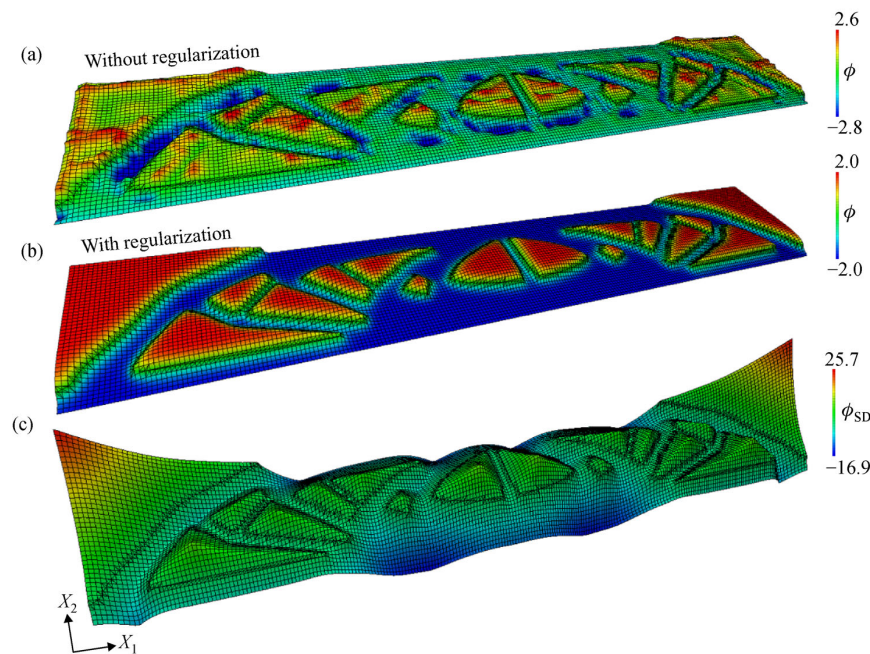

Fig. 10 Comparison of the warped final design LSFs (a) without LS regularization, (b) with regularization, and (c) SDF of the 2D beam
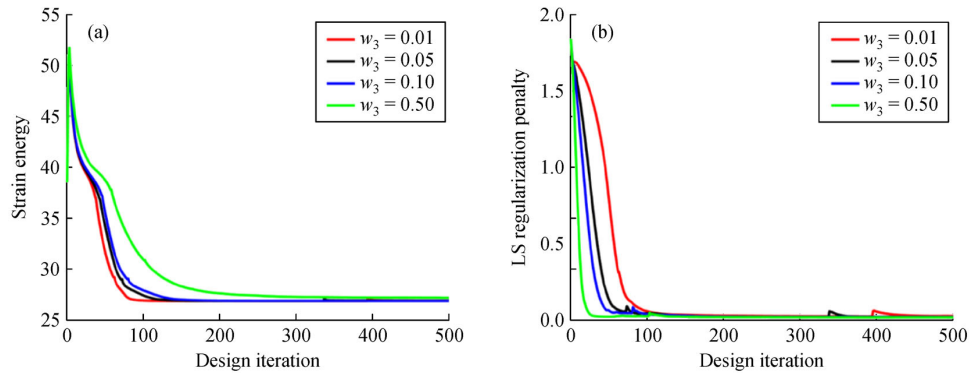
Fig. 11 Evolution of (a) strain energy and (b) regularization penalty for different penalization weights

6.2.1.2 Influence of implicit design sensitivities on LS regularization

As discussed in Section 5, the proposed regularization scheme considers the target LSF $\tilde{\phi}(X)$ as a prescribed field and ignores the implicit contributions of the penalty term Eq. (16) to the design sensitivities. Only the explicit dependency of the design LSF on the optimization variables is accounted for in the sensitivity analysis. To illustrate the benefits of this approach, the influence of including the implicit design sensitivities is investigated. The implicit contributions are computed by the adjoint approach.

Figure 12 shows the optimized beam design obtained with an LS regularization weight of $w_3 = 0.1$ and including implicit sensitivities of the target LSF. Due to a fairly large weight of the regularization on the objective, the implicit design sensitivities influence significantly the evolution of the zero LS iso-contour. The design evolution is predominantly influenced by the regularization scheme and insufficiently driven by the physics performance. This leads to spurious void inclusions, premature convergence, and poor physical performance of the optimized structure (Fig. 12). For a sufficiently low regularization penalty (e.g., $w_3 = 0.01$) these issues are not observed, and the

design convergence is indistinguishable from the one where the implicit design sensitivities are omitted. Thus, to prevent an undesired influence of the regularization on the design evolution and to gain computational efficiency, it is recommended to ignore design sensitivities of the target LSF on the design variables and to use a low penalty weight for the regularization term.

6.2.2 Beam in 3D

The hyperelastic beam example is studied next in 3D to demonstrate the applicability of the proposed LS regularization scheme to 3D problems where the geometry undergoes significant changes during the optimization process. Figure 13(a) shows the initial design with boundary conditions for a design domain of size $240 \times 40 \times 40$. An element edge length of $h = 2$ is used for this example, along with a time step size of $\Delta t = 51$ in the HM. Analogous to the 2D configurations, a traction load of $T_{X_2} = -2$ is applied within a circular region of radius 2 at the center of the top face of the domain. The structure is simply supported at all four corners at the bottom face of the design domain. The loading and the support domains are excluded from the design domain, respectively.
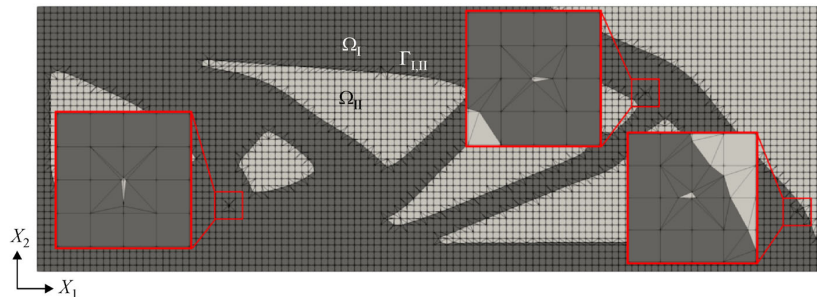

Fig. 12 Spurious void inclusions within the structure as a result of including implicit design sensitivities of the target LSF with a regularization penalty weight of 10%
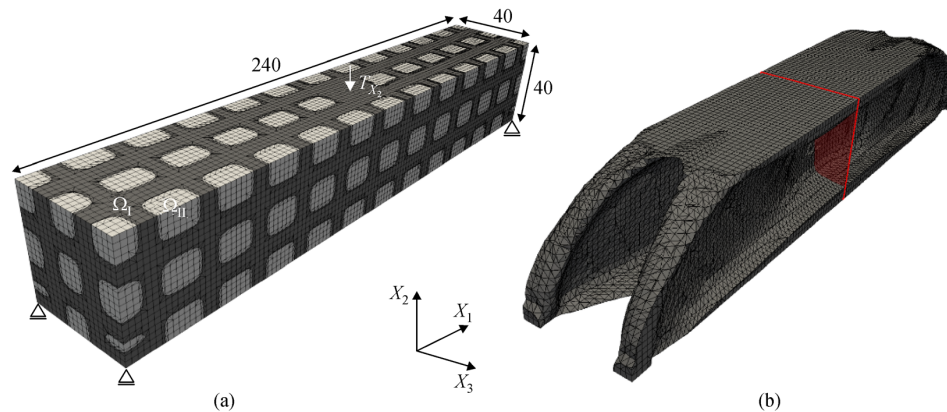
Fig. 13 (a) Initial design of the 3D beam problem with boundary conditions and dimensions; (b) final design. The central area highlighted in red represents the plane in which the design LSFs are being compared in Fig. 14

Two-fold symmetry is exploited for the mechanical and the design problem. A relative optimization step size of 0.0125 is used and a volume constraint of $\gamma_V = 0.3$ is enforced through a continuation approach.

Figure 13(b) depicts the final design obtained after 400 optimization iterations, using the proposed LS regularization. As before, a smooth evolution of objective and constraint is achieved when employing the LS regularization scheme.

Figure 14 shows the design LSFs at convergence obtained without the LS regularization and with LS regularization, extracted in the center of the design domain (indicated by the red plane in Fig. 13(b)). As before, a clear difference can be observed with respect to the smoothness of the LSF and the uniformity of the spatial gradient along the zero LS iso-contour. While the non-regularized LSF is shallow, the regularized LSF quickly approaches the LS bounds away from the interface.

Figure 14 shows thin vertical members in the optimal design, which represent shear webs in between the top and bottom flanges of the beam. Because their thickness is in the order of the mesh size h, the XFEM discretization provides insufficient resolution of both the stress and strain fields, as well as the SDF. Due to the inability of the discretization to capture the SDF in areas of small features, the target LSF is not well developed and, therefore, the LS regularization suffers. The result of this can be seen in Fig. 14(b) where the lower LS bound of $-\phi_{\mathrm{Bnd}} = -2$ is not reached by the design LSF within the thin vertical members of the structure. While this effect has already been observed in the 2D beam example (Section 6.2.1) this issue is more pronounced here. This is not an inherent drawback of the proposed LS regularization scheme, but rather stems for the underlying XFEM discretization and its limitations to resolve features with a size in the order of h. Minimum feature size control (e.g., Ref. [55]) or local mesh refinement would be required to properly regularize the design LSF.
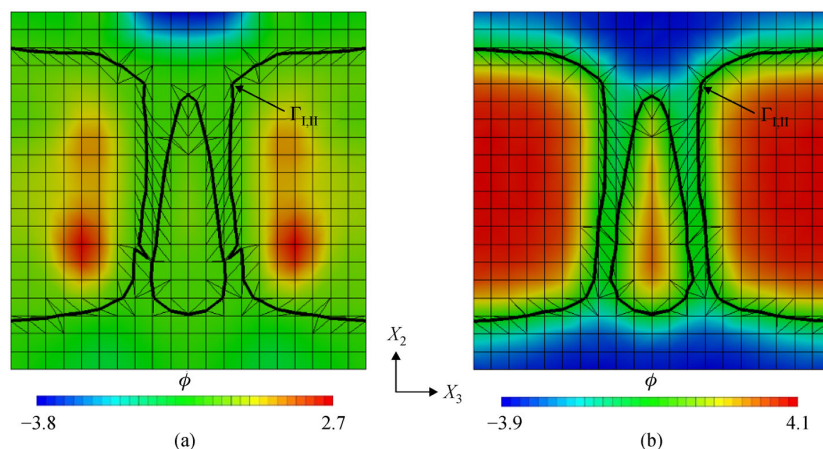

Fig. 14 Comparison of the design LSFs at the mid-plane of the beam (a) without and (b) with LS regularization

6.3 Example for incompressible Navier-Stokes flow

The goal of the final example is to demonstrate the applicability of the proposed LS regularization scheme to a flow problem, modeled by the incompressible Navier-Stokes equations at steady state. Furthermore, the influence of the accuracy with which the HM is time integrated is studied.

The non-stabilized weak form of the volumetric contribution ($\boldsymbol{R}$) of the governing equation is stated as

$$\boldsymbol{R} = \int_{\Omega_I} [\delta\boldsymbol{v}\rho(\boldsymbol{v}\nabla\boldsymbol{v}) + \boldsymbol{\varepsilon}(\delta\boldsymbol{v})\boldsymbol{\sigma}(\boldsymbol{v},p)]\mathrm{d}V$$
$$+ \int_{\Omega_I} \delta p\nabla\boldsymbol{v}\mathrm{d}V = 0, \qquad (26)$$

where $\boldsymbol{v}$ is the velocity vector, p is the pressure, and ρ is the density. The admissible test functions for velocity and pressure are denoted by $\delta\boldsymbol{v}$ and δp, respectively. The infinitesimal strain rate tensor $\varepsilon(\boldsymbol{v})$ is defined as

$$\boldsymbol{\varepsilon}(\boldsymbol{v}) = \frac{1}{2}(\nabla\boldsymbol{v}^{\mathrm{T}} + \nabla\boldsymbol{v}). \qquad (27)$$

The Cauchy stress tensor for Newtonian fluids is denoted by $\boldsymbol{\sigma}(\boldsymbol{v},p)$ and is defined as

$$\boldsymbol{\sigma}(\boldsymbol{v},p) = -p\boldsymbol{I} + 2\mu_D\boldsymbol{\varepsilon}(\boldsymbol{v}), \qquad (28)$$

where μ_D is the dynamic viscosity. The governing Eq. (26) is augmented by sub-grid stabilization to suppress spurious velocity and pressure oscillations, as well as by ghost penalization. For more details on the XFEM discretization and the corresponding stabilization techniques, the reader is referred to Ref. [45]. The fluid domain boundary is decomposed into the fluid-void interface $\Gamma_{\mathrm{I,II}}$, and Dirichlet and Neumann external boundaries, Γ_u and Γ_T, respectively. No-slip conditions are applied weakly at the fluid-void

interface; the other boundary conditions are problem dependent and are specified below.

An extension of the fluid nozzle problem studied by Refs. [56–58], to 3D is studied here. The design domain with boundary conditions and the initial design are shown in Fig. 15(a). The computational domain is a $5\times5\times5$ cube with a $0.75\times5\times5$ non-design domain downstream from the inlet face. A parabolic velocity profile with a maximum inlet velocity of 30 in X_1 direction is applied to the inlet face, and zero pressure is enforced weakly at the circular outlet of radius 1.25. Both, the inlet domain and the circular outlet face are excluded from the design domain. Only one quarter of the design domain is modeled. Slip conditions are imposed on the $X_1 - X_2$ and $X_1 - X_3$ symmetry planes.

Assuming a constant density of $\rho=1$ and a dynamic viscosity of $\mu_D=1$, the flow conditions correspond to a Reynolds number of Re = 66 with the reference velocity being the average inlet velocity and the reference length being the edge length of the design domain, i.e., $L_{\mathrm{Ref}}=5$. A ghost stabilization parameter of 0.005 is used for stabilization of the pressure and a ghost penalization parameter of 0.05 is used for stabilization of velocities; for details see Ref. [45].

The objective of this nozzle design problem is the minimization of the total pressure drop between inlet and outlet along with a 1% perimeter penalty and a 5% LS regularization penalty. The optimization problem is subject to a $\gamma_V=0.3$ volume constraint on the fluid phase. A relative GCMMA step size of 0.01 and a single time step of $\Delta t=0.1$ is used for the HM. The main problem parameters are listed in Table 4.

The final design obtained after 90 design iterations is shown in Fig. 15(b). These results agree with the ones presented in the literature. As before, a smooth evolution of objective and constraint is obtained when LS
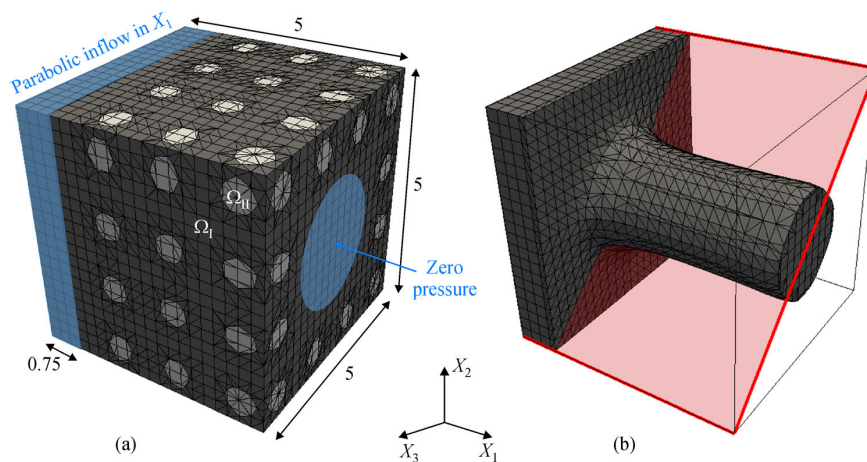

Fig. 15 (a) Initial design of the 3D fluid nozzle with boundary conditions and dimensions; (b) final nozzle design. The diagonal highlighted in red represents the plane in which the design LSFs are being compared

290

Markus J. GEISS et al. A regularization scheme for explicit level-set XFEM topology optimization   15

regularization is used. The design LSFs at convergence without and with the LS regularization are compared in Fig. 16. Again, a rather oscillatory LSF with flat gradients near the interface is obtained when no LS regularization is employed. With LS regularization, the design LSF assumes the target bounds away from the interface while having a unit norm gradient in the vicinity of the fluid-void interface. The final designs obtained without and with the HM do not differ significantly. However, improved numerical stability and robustness during the optimization process was observed due to the regularization of the LSF.

To provide insight into the dependence of the optimization results on the accuracy with which the temperature field in the HM is time integrated (Eq. (7)), the number of time steps in the Euler backward scheme Eq. (8) is varied. The total time is kept constant at $t_{max} = 1$. Comparisons of objective and LS regularization penalty evolution for different number of time steps of the HM Eq. (7) are shown in Fig. 17. No significant differences are observed when solving the HM with multiple time steps and reduced time step sizes. This confirms the observations by Ref. [33], and shows that a single time step is sufficient for LS regularization using the HM.

7   Conclusions

A regularization scheme for explicit LS XFEM design

optimization in 2D and 3D was presented. The regularization scheme augments the objective function by a penalty term that measures the difference between the design LSF and a target LSF, both in regard to the field value and its spatial derivatives. The target LSF has a unit norm gradient in the vicinity of the interface and assumes either an upper or lower bound away from the interface, depending on the material phase. The target LSF is constructed from the SDF that is computed by an XFEM discretization of the HM at every design iteration for the current interface geometry. Numerical experiments on 2D and 3D problems in solid and fluid mechanics showed that the proposed regularization scheme is largely insensitive to the penalty weight for the regularization term. As long as the weights are less than 10%, the LS regularization does not influence noticeably the final design. A small influence on the design evolution has been observed for larger penalty weights. Furthermore, it was observed that it is beneficial to ignore the dependence of the target LSF on the interface geometry for computing the design sensitivities.

Omitting the sensitivities of the target LSF on the design variables leads to an improved convergence to a design with improved physical performance and reduces the computational cost. The numerical results further suggest that the temperature field of the HM can be computed by a single time step without significantly affecting the accuracy of the SDF. The time step size is a function of the domain length. Good results were obtained with a time step size determined by Eq. (9).

Comparing the results obtained with and without the proposed regularization scheme suggests that the proposed scheme significantly improves the convergence of the optimization process and mitigates issues in the XFEM analysis due to the emergence of small inclusions of one phase within a domain occupied by another phase. The scheme mitigates irregular interface evolution and promotes a uniform LS gradient at the zero LS iso-contour. It
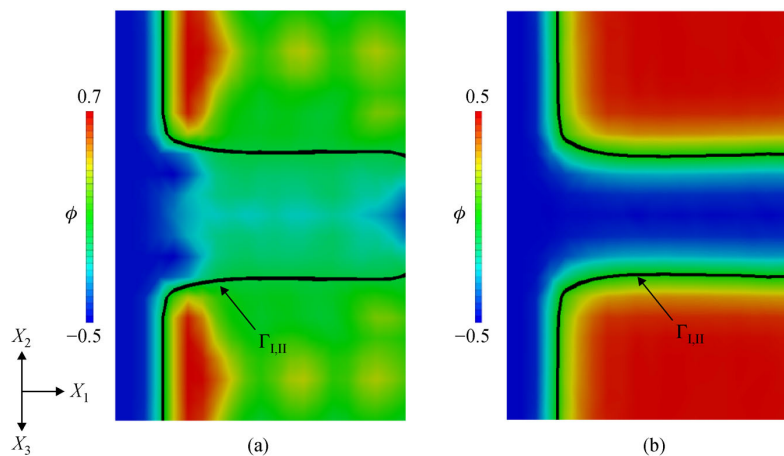

Fig. 16 Comparison of the design LSFs across the diagonal of the fluid nozzle final design (a) without and (b) with LS regularization
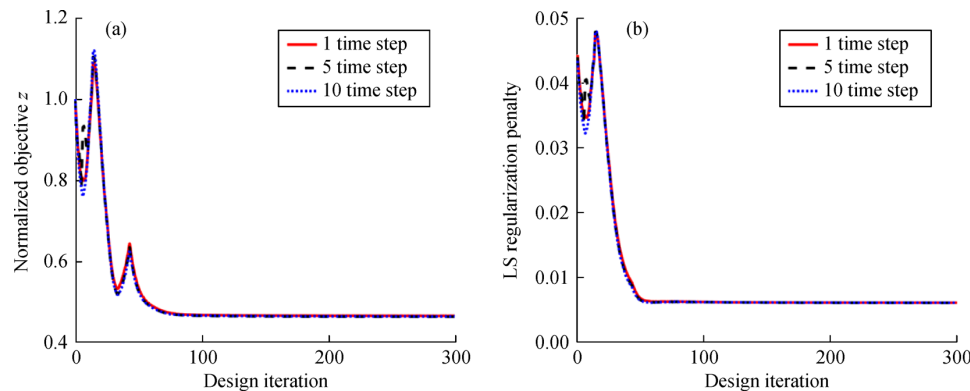
Fig. 17 Evolution of (a) normalized objective and (b) LS regularization penalty for different number of time steps

eliminates the need for reinitialization. Furthermore, the proposed method mitigates robustness issues observed with regularization schemes that solely operate on the value or the spatial gradients of the design LSF. The capabilities of the proposed method were demonstrated through numerical examples in 2D and 3D, including problems in linear and nonlinear elasticity and fluid mechanics.

The numerical studies presented in this paper have revealed a few shortcomings of the proposed method that need to be addressed in future work. These include overcoming the limited resolution of a fixed XFEM background mesh with linear interpolation. When features of dimensions in the order of the element edge length of the background mesh emerge in the optimization process, the resolution of a linear interpolation is insufficient to accurately compute the target LSF. Therefore, the performance of the regularization is reduced. This could be addressed by adding feature size control to the design problem, locally refining the background mesh or by using higher order spatial discretizations. In addition, an increase in computational cost was observed due to the need for solving two additional partial differential equations in the HM. Depending on the complexity of the physics model, this additional cost may become significant when compared to runs without the LS regularization scheme. However, the additional cost is partially offset by an increased convergence rate and by the ability to use larger optimization step sizes. Future work needs to address ways to improve the computational efficiency of the scheme. For example, the temperature and SDF fields in the HM could be solved only approximately, using a few iterations of an iterative linear solver. Finally, due to the regularization of the LSF, the nucleation of new holes is impaired. In order to mitigate the dependency of the final design on the initial seeding, systematic approaches for the creation of new holes during the optimization process need to be explored in combination with the proposed LS regularization. This includes but is not limited to using additional LSFs [59] or topological derivatives.

References

1. Bendsøe M P, Sigmund O. Topology Optimization. Berlin: Springer, 2004

2. Sigmund O, Maute K. Topology optimization approaches: A comparative review. Structural and Multidisciplinary Optimization, 2013, 48(6): 1031–1055

3. Deaton J D, Grandhi R V. A survey of structural and multidisciplinary continuum topology optimization: Post 2000. Structural and Multidisciplinary Optimization, 2014, 49(1): 1–38

4. Osher S, Sethian J A. Fronts propagating with curvature-dependent speed: Algorithms based on Hamilton-Jacobi formulations. Journal of Computational Physics, 1988, 79(1): 12–49

5. Osher S, Fedkiw R. Level Set Methods and Dynamic Implicit Surfaces. Vol. 153. New York: Springer, 2003

292

Markus J. GEISS et al. A regularization scheme for explicit level-set XFEM topology optimization   17

6. Osher S, Paragios N. Geometric Level Set Methods in Imaging, Vision, and Graphics. New York: Springer, 2003

7. Gibou F, Fedkiw R, Osher S. A review of level-set methods and some recent applications. Journal of Computational Physics, 2018, 353: 82–109

8. van Dijk N P, Maute K, Langelaar M, et al. Level-set methods for structural topology optimization: A review. Structural and Multidisciplinary Optimization, 2013, 48(3): 437–472

9. Osher S J, Santosa F. Level set methods for optimization problems involving geometry and constraints I. Frequencies of a two-density inhomogeneous drum. Journal of Computational Physics, 2001, 171(1): 272–288

10. Allaire G, Jouve F, Toader A M. A level-set method for shape optimization. Comptes Rendus Mathématique, 2002, 334(12): 1125–1130 (in French)

11. Wang M Y, Wang X, Guo D. A level set method for structural topology optimization. Computer Methods in Applied Mechanics and Engineering, 2003, 192(1–2): 227–246

12. Allaire G, Jouve F, Toader A M. Structural optimization using sensitivity analysis and a level-set method. Journal of Computational Physics, 2004, 194(1): 363–393

13. Wang S, Wang M Y. Radial basis functions and level set method for structural topology optimization. International Journal for Numerical Methods in Engineering, 2006, 65(12): 2060–2090

14. Luo Z, Wang M Y, Wang S, et al. A level set-based parameterization method for structural shape and topology optimization. International Journal for Numerical Methods in Engineering, 2008, 76(1): 1–26

15. Kreissl S, Pingen G, Maute K. An explicit level set approach for generalized shape optimization of fluids with the lattice Boltzmann method. International Journal for Numerical Methods in Fluids, 2011, 65(5): 496–519

16. van Dijk N P, Langelaar M, van Keulen F. Explicit level-set-based topology optimization using an exact Heaviside function and consistent sensitivity analysis. International Journal for Numerical Methods in Engineering, 2012, 91(1): 67–97

17. de Ruiter M J, van Keulen F. Topology optimization using a topology description function. Structural and Multidisciplinary Optimization, 2004, 26(6): 406–416

18. Haber R B, Jog C S, Bendsøe M P. A new approach to variable-topology shape design using a constraint on perimeter. Structural Optimization, 1996, 11(1): 1–12

19. Yamada T, Izui K, Nishiwaki S, et al. A topology optimization method based on the level set method incorporating a fictitious interface energy. Computer Methods in Applied Mechanics and Engineering, 2010, 199(45–48): 2876–2891

20. Otomori M, Yamada T, Izui K, et al. Level set-based topology optimisation of a compliant mechanism design using mathematical programming. Mechanical Science, 2011, 2(1): 91–98

21. Gomes J, Faugeras O. Reconciling distance functions and level sets. Journal of Visual Communication and Image Representation, 2000, 11(2): 209–223

22. Zhu B, Zhang X. A new level set method for topology optimization of distributed compliant mechanisms. International Journal for Numerical Methods in Engineering, 2012, 91(8): 843–871

23. Li C, Xu C, Gui C, et al. Level set evolution without re-initialization: A new variational formulation. In: Proceedings of 2005 IEEE

24. Coffin P, Maute K. Level set topology optimization of cooling and heating devices using a simplified convection model. Structural and Multidisciplinary Optimization, 2016, 53(5): 985–1003

25. Sussman M, Smereka P, Osher S. A level set approach for computing solutions to incompressible two-phase flow. Journal of Computational Physics, 1994, 114(1): 146–159

26. Osher S. Book review: Level set methods and fast marching methods: Evolving interfaces in computational geometry, fluid mechanics, computer vision, and materials science. Mathematics of Computation, 2001, 70(233): 449–451

27. Li C, Xu C, Gui C, et al. Distance regularized level set evolution and its application to image segmentation. IEEE Transactions on Image Processing, 2010, 19(12): 3243–3254

28. Zhu B, Zhang X, Fatikow S. Structural topology and shape optimization using a level set method with distance-suppression scheme. Computer Methods in Applied Mechanics and Engineering, 2015, 283: 1214–1239

29. Jiang L, Chen S. Parametric structural shape & topology optimization with a variational distance-regularized level set method. Computer Methods in Applied Mechanics and Engineering, 2017, 321: 316–336

30. Burger M, Osher S J. A survey in mathematics for industry a survey on level set methods for inverse problems and optimal design. European Journal of Applied Mathematics, 2005, 16(2): 263–301

31. Hartmann D, Meinke M, Schröder W. The constrained reinitialization equation for level set methods. Journal of Computational Physics, 2010, 229(5): 1514–1535

32. Fu J, Li H, Xiao M, et al. Topology optimization of shell-infill structures using a distance regularized parametric level-set method. Structural and Multidisciplinary Optimization, 2018, 1–14 (in press)

33. Crane K, Weischedel C, Wardetzky M. Geodesics in heat. ACM Transactions on Graphics, 2013, 32(5): 1–11

34. Crane B K, Weischedel C, Wardetzky M. The heat method for distance computation. Communications of the ACM, 2017, 60(11): 90–99

35. Kreissl S, Maute K. Levelset based fluid topology optimization using the extended finite element method. Structural and Multidisciplinary Optimization, 2012, 46(3): 311–326

36. Sethian J A. Fast marching methods. SIAM Review, 1999, 41(2): 199–235

37. Wong T, Leung S. A fast sweeping method for eikonal equations on implicit surfaces. Journal of Scientific Computing, 2016, 67(3): 837–859

38. Daux C, Moës N, Dolbow J, et al. Arbitrary branched and intersecting cracks with the extended finite element method. International Journal for Numerical Methods in Engineering, 2000, 48(12): 1741–1760

39. Fries T P, Belytschko T. The extended/generalized finite element method: An overview of the method and its applications. International Journal for Numerical Methods in Engineering, 2010, 84(3): 253–304

40. Hansbo A, Hansbo P. A finite element method for the simulation of strong and weak discontinuities in solid mechanics. Computer Methods in Applied Mechanics and Engineering, 2004, 193(33–35):

3523–3540

41. Makhija D, Maute K. Numerical instabilities in level set topology optimization with the extended finite element method. Structural and Multidisciplinary Optimization, 2014, 49(2): 185–197

42. Tran A B, Yvonnet J, He Q C, et al. A multiple level set approach to prevent numerical artefacts in complex microstructures with nearby inclusions within XFEM. International Journal for Numerical Methods in Engineering, 2011, 85(11): 1436–1459

43. Burman E, Hansbo P. Fictitious domain methods using cut elements: III. A stabilized Nitsche method for Stokes' problem. Mathematical Modelling and Numerical Analysis, 2014, 48(3): 859–874

44. Schott B, Rasthofer U, Gravemeier V, et al. A face-oriented stabilized Nitsche-type extended variational multiscale method for incompressible two-phase flow. International Journal for Numerical Methods in Engineering, 2015, 104(7): 721–748

45. Villanueva C H, Maute K. CutFEM topology optimization of 3D laminar incompressible flow problems. Computer Methods in Applied Mechanics and Engineering, 2017, 320(Suppl C): 444–473

46. Burman E, Claus S, Hansbo P, et al. CutFEM: Discretizing geometry and partial differential equations. International Journal for Numerical Methods in Engineering, 2015, 104(7): 472–501

47. Nitsche J A. On a variational principle for the solution of Dirichlet problems under the use of subspaces which are subject to no boundary conditions. Abhandlungen aus dem Mathematischen Seminar der Universität Hamburg, 1971, 36(1): 9–15 (in German)

48. Amestoy P R, Guermouche A, L'Excellent J Y, et al. Hybrid scheduling for the parallel solution of linear systems. Parallel Computing, 2006, 32(2): 136–156

49. Svanberg K. The method of moving asymptote—A new method for structural optimization. International Journal for Numerical Methods in Engineering, 1987, 24(2): 359–373

50. Sharma A, Villanueva H, Maute K. On shape sensitivities with Heaviside-enriched XFEM. Structural and Multidisciplinary Optimization, 2017, 55(2): 385–408

51. Geiss M J, Maute K. Topology optimization of active structures using a higher-order level-set-XFEM-density approach. In: Proceedings of 2018 Multidisciplinary Analysis and Optimization Conference, AIAA AVIATION Forum, (AIAA 2018-4053). Atlanta, 2018

52. Villanueva C H, Maute K. Density and level set-XFEM schemes for topology optimization of 3-D structures. Computational Mechanics, 2014, 54(1): 133–150

53. Geiss M J, Bodeti N, Weeger O, et al. Combined level-set-XFEM-density topology optimization of 4D printed structures undergoing large deformation. Journal of Mechanical Design, 2018 (in press)

54. Sharma A, Maute K. Stress-based topology optimization using spatial gradient stabilized XFEM. Structural and Multidisciplinary Optimization, 2018, 57(1): 17–38

55. Guo X, Zhang W, Zhong W. Explicit feature control in structural topology optimization via level set method. Computer Methods in Applied Mechanics and Engineering, 2014, 272: 354–378

56. Kreissl S, Pingen G, Maute K. Topology optimization for unsteady flow. International Journal for Numerical Methods in Engineering, 2011, 87(13): 1229–1253

57. Makhija D, Maute K. Level set topology optimization of scalar transport problems. Structural and Multidisciplinary Optimization, 2015, 51(2): 267–285

58. Borrvall T, Petersson J. Topology optimization of fluids in Stokes flow. International Journal for Numerical Methods in Fluids, 2003, 41(1): 77–107

59. Dunning P D, Alicia Kim H. A new hole insertion method for level set based structural topology optimization. International Journal for Numerical Methods in Engineering, 2013, 93(1): 118–134